The relationship between the radio and gamma-ray emission of blazars

Thesis by

Walter Kennerth Max-Moerbeck Astudillo

In Partial Fulfillment of the Requirements

for the Degree of

Doctor of Philosophy

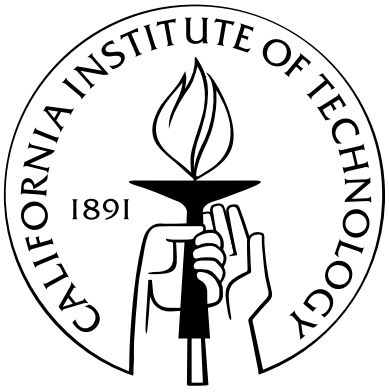

California Institute of Technology

Pasadena, California

2013

(Defended January 31, 2013)

Acknowledgements

I would like to start by thanking professor Anthony Readhead for all his support, first as the option representative and then as my thesis adviser. The opportunity he gave me to work on this project resulted to be a very interesting experience that exposed me to a broad range of ideas from astrophysics, radio astronomy, optimization and statistics. Even with his busy schedule he was always open to discuss my ideas on how to solve the problem of the day, but more importantly he always had excellent questions and suggestions that got me thinking on how to improve my initial solutions and their presentation.

Another important mentor was Tim Pearson who always provided invaluable advice and hard questions, always going straight to the weakest points of an analysis. Special thanks go to my fellow student Joseph Richards with whom we ran the monitoring program and pondered about the properties of blazars. It was with him that we managed to tame the 40 meter telescope with all its quirks, while also having fun in the process.

A number of other people played a role in the success of the radio monitoring program. The work of Talvikki Hovatta was key during the last couple of years, and I thank her for running the program during the last year of my thesis, for providing the gamma-ray light curves I use in this investigation, and also for many interesting conversations about the behavior of blazars. Vasiliki Pavlidou, our resident theorist, provided a lot of astrophysical and data analysis insight along with words of encouragement and always a big smile. Matthew Stevenson was critical during the early stages of the monitoring program, and although this was not the subject of his thesis he was always available to help us when Joey and I were not able to work on the telescope. Another very important person for the monitoring program and the Owens Valley Radio Observatory is Russell Keeney. Russ has a number of outstanding technical skills and a work ethic that I really admire. I thank him for keeping the telescope running and for the fun conversations we had at the prime focus of the 40 meter during many calibration runs. Martin Shepherd did an excellent job developing the new telescope control system and was always happy to answer my questions. Oliver King and Rodrigo Reeves were extremely generous and always willing to help me learn a little bit more about microwave electronics and radio receivers in general. I thank Kieran Cleary and Rohit Gawande for their help on my brief forays to the radio lab. Sincere thanks go to Althea Keith, Sandy Lester, Gita Patel, Gina Armas,

Judith Mack, Patrick Shopbell, Anu Mahabal, Tess Legaspi, Daniel Yoder, Laura Flower Kim, Jim Endrizzi, Rosa Carrasco, Mary Daniel, Rick Hobbs, Cecil Patrick and all the staff at Caltech and Owens Valley. They were always helping me by giving prompt solution to my requests and allowing me to concentrate on my research. A special mention to my friends Elvira Serpa, Marta Robles, Efrain Hernández and Engracia Álvarez. They were always concerned about my well being and I already miss them.

I thank the staff of the Fulbright Commission in Chile and the Institute of International Education, in particular Karina Sapunar, for all their support. Ann Kerr-Adams from the UCLA International Institute did an excellent job at helping the Fulbrighters of Southern California made the most out of the experience of living in the US and I am sincerely grateful for that.

The *Fermi*-LAT collaboration, and specially the AGN science group, have been a constant source of scientific collaborations as testified by the numerous papers that have benefited from the simultaneous radio and gamma-ray monitoring. I am particularly thankful to Jeff Scargle, James Chiang, Roger Blandford, Roger Romani, Steve Healey and Michael Shaw, for many interesting conversations about active galactic nuclei, gamma-ray astronomy and science in general. Another important source of motivation was David Meier who let us read a preliminary version of his book on black hole astrophysics. It was a great pleasure to read the close to 1000 pages of almost anything you could think about black holes. All the participants of the reading group are thankful for the opportunity to be part this project. The book made a nice addition to my collection, and it is getting a lot of use. I am also thankful for the support of the National Radio Astronomy Observatory in Socorro, New Mexico where I spent the final two months of the writing of this thesis.

My classmates at Caltech deserve a special acknowledgement for being so awesome. I learnt a lot from them about looking at things from other perspectives and to appreciate the value of different backgrounds in the science enterprise. I had the nice surprise of finding out that they were not only very intelligent and passionate people, but also extremely nice and reliable persons. Yacine Ali-Haïmoud and Varun Bhalerao were a lot of fun as classmates and made our brief stay on the second basement of the Robinson building a lot more enjoyable. Thanks to Mansi Kasliwal for advice and for inviting me to her wedding with Setu; Laura and I really had a wonderful time in India. Ann Marie Cody (and Tommy) will be missed too, as will be my office mates (Milan Bogosavljević, Dan Stark, Shriharsh Tendulkar, Drew Newman and Ben Montet) whose hard work and the occasional joke, always provided a very important source of inspiration. Special thanks go to the Stevensons, Matthew, Jennifer, and their kids, Bronson and Edmund. The last years in Villa where a lot of fun, specially seeing the kids grow and do silly things. Karín Menéndez-Delmestre and Thiago Gonçalves were a source of inspiration and invaluable tips about enjoying our time at Caltech. I am glad they have moved to Rio de Janeiro because I will get to see them often once I go back to Chile.

An important part of this experience was getting to meet the small Chilean community at

Caltech and surrounding areas (Daniel, Margarita, Francisco, Emerson, Javier, Roberto, Jorge, Jolana, Rodrigo, Javiera, Gustavo, Mariana, Solange, Adolfo, Fabian, Carolina, Guillermo and Isidora). They played a significant role in keeping me sane, specially during the first and last parts of this adventure. I am glad to see a new batch of Chileans (Carlos, Ruby, Cristian and Camila) take our torch and hope to see them back in Chile helping improve our long and thin stripe of land, or finding their own path in foreign lands without forgetting their roots.

Even though this work was done at Caltech, I would have never come here without the help of a lot of people who supported me from way before this project started. Special thanks go to all the teachers I had at school and college. I learned a lot from my hardworking and perseverant classmates at the *Instituto Nacional*. My time at the School of Engineering and Sciences at *Universidad de Chile* (or as we called *la escuela*) was another wonderful experience to which I really owe being a scientist. It was there that I had my first and definitive encounter with astronomy with the classes of Diego Mardones and Héctor Álvarez, with the amateur astronomy club Auriga, and the summer school at Las Campanas Observatory. Thanks to all the astronomy professors there and in particular to Jorge May and Leonardo Bronfman, the advisers of my undergraduate thesis. I wish Jorge was here to thank him for his support, and I hope we are able to continue with his vision for the development of astronomy in Chile.

The strongest supporter of my early career was my mother, Marta Astudillo. Thanks for her encouragment and for having taught me not to be satisfied with what the circumstances offered me. A great deal of my perseverance comes from my grandmother Lidia Guerra who never gave up. She is not with us anymore, but her memory still gives me strength in times when things are getting hard. I also have a large and supportive family and I thank all of them for having helped me in one way or another.

And finally comes the time to thank my loved Laura for having shared this long journey with me. I cannot even imagine how all this adventure would have been without her love and support. I am glad we have come this far as a couple and also as scientists, we have been very fortunate to have each other, and I am hopeful the future will be full of even more amazing adventures.

This work has been funded in part by a fellowship from the Fulbright Program and the chilean government through the *Comisión Nacional de Investigación Científica y Tecnológica* (CONYCIT) that partially funded the first four years of my graduate studies at Caltech. Part of the funds for the radio monitoring program came from NASA grants NNX08AW31G and NNX11A043G and NSF grants AST-0808050 and AST-1109911.

Abstract

Blazars are active galaxies with a jet closely oriented to our line of sight. They are powerful, variable emitters from radio to gamma-ray wavelengths. Although the general picture of synchrotron emission at low energies and inverse Compton at high energies is well established, important aspects of blazars are not well understood. In particular, the location of the gamma-ray emission region is not clearly established, with some theories favoring a location close to the central engine, while others place it at parsec scales in the radio jet.

We developed a program to locate the gamma-ray emission site in blazars, through the study of correlated variations between their gamma-ray and radio-wave emission. Correlated variations are expected when there is a relation between emission processes at both bands, while delays tell us about the relative location of their energy generation zones. Monitoring at 15 GHz using the Owens Valley Radio Observatory 40 meter telescope started in mid-2007. The program monitors 1593 blazars twice per week, including all blazars detected by the Fermi Gamma-ray Space Telescope (*Fermi*) north of -20° declination. This program complements the continuous monitoring of gamma-rays by *Fermi*.

Three year long gamma-ray light curves for bright *Fermi* blazars are cross-correlated with four years of radio monitoring. The significance of cross-correlation peaks is investigated using simulations that account for the uneven sampling and noise properties of the light curves, which are modeled as red-noise processes with a simple power-law power spectral density. We found that out of 86 sources with high quality data, only three show significant correlations (AO 0235+164, B2 2308+34 and PKS 1502+106). Additionally, we find a significant correlation for Mrk 421 when including the strong gamma-ray/radio flare of late 2012. In all four cases radio variations lag gamma-ray variations, suggesting that the gamma-ray emission originates upstream of the radio emission. For PKS 1502+106 we locate the gamma-ray emission site parsecs away from the central engine, thus disfavoring the model of Blandford & Levinson (1995), while other cases are inconclusive. These findings show that continuous monitoring over long time periods is required to understand the cross-correlation between gamma-ray and radio-wave variability in most blazars.

Contents

List of Figures

List of Tables

Chapter 1

Introduction

Active galaxies are characterized by very bright nuclei, whose luminosity cannot be explained by conventional nuclear fusion that powers stars. These bright nuclei, known as active galactic nuclei (AGN), show great variety and are characterized by some combination of very small angular size, high luminosity, broadband continuum emission, emission lines, variability, polarization and radio emission. An extremely comprehensive discussion of these objects may be found in the review by Begelman et al. (1984). The presence of certain features and absence of others gives rise to the several different observational classes of objects that form the AGN class.

The current understanding of AGNs is that their emission is produced by accretion of matter onto a central black hole. Material surrounding the black hole forms an accretion disk that gets heated through viscous dissipation of gravitational energy, thus generating its energy output. The class known as radio-loud AGN is defined by having a ratio between the radio flux density (at 5 GHz, $F_{\rm r}$) and the optical flux density (in the B-band, F_o) of $F_{\rm r}/F_{\rm o} \geqslant 10$ (Kellermann et al., 1989). These radio-loud objects have jets of plasma that are ejected perpendicular to the accretion disk. The energy for these jets could be extracted from a rotating black and the accretion disk (Blandford & Znajek, 1977; Blandford & Payne, 1982). The matter in these jets moves at relativistic speeds giving rise to much of the extreme phenomenology of the radio-loud objects.

The commonly accepted model of an AGN is summarized in the so-called unified model. In this model, all the different classes are the result of looking at the source from a different point of view and by the presence of radio jets in radio-loud objects. The role of orientation and relativistic beaming as the origin for the different classes of radio sources was already recognized in the late 1970s, as briefly reviewed in Readhead (1980). Readhead et al.

(1978) argued that projection effects could explain the large bends in the jets of compact radio sources. This was followed by Scheuer & Readhead (1979), who proposed beaming as an explanation of the relationship between superluminal and radio-quiet objects and their relative source counts. Their idea was later modified to relate flat-spectrum and steep-spectrum sources in Orr & Browne (1982), who also introduced the "unified scheme" terminology. These early developments are reviewed in Begelman et al. (1984), while later extensions of the unified model that include all classes of AGNs are reviewed in Antonucci (1993) and Urry & Padovani (1995). Figure 1.1 presents a schematic view of the unified model in which all the basic components of an AGN can be seen. In the following we provide a brief description for each component, accompanied with a reference scale of their size. At the center there is a supermassive black hole surrounded by an accretion disk ($R_{BH} \sim 3 \times 10^{13}$ cm for $M_{BH} \sim 10^8$ $M_\odot$, and $10^{14} - 10^{15}$ cm for the disk), which converts gravitational energy into radiation in the UV/soft-X-rays range and launches the jets in the radio-loud objects. Just above the accretion disk, a hot electron corona produces hard X-ray radiation (a few times the size of the black hole). Surrounding it there are high velocity clouds that form the broad-line region ($\sim 10^{15} - 10^{16}$ cm), which is responsible for broad emission lines directly observed in objects seen close to the line of sight, or in reflected and polarized light in the ones observed almost edge on (Antonucci & Miller, 1985). Further out, a torus or warped disk of gas and dust blocks and absorbs radiation produced by the inner components (at distances $\geq 10^{17}$ cm from the center). This obscuring material generates objects with optical spectra of different classes depending on the ability of the observer to directly see the internal regions of the AGN. In Type 1 objects we can directly observe the broad line region while in Type 2 objects we only get a direct view of the narrow line region. At even larger distances ($10^{18} - 10^{20}$ cm) from the black hole/accretion disk system, there are slowly moving clouds that produce narrow emission lines. Jets of plasma that move relativistically in small scales of a few parsecs are present in radio-loud objects. These jets can extend out to megaparsec scales in the most powerful radio galaxies.

Research in AGN not only provides a better understanding of this class of objects. Their study allows us to probe extreme physics near black holes, the mechanisms for the formation of jets and the production of high energy emission, thus making them excellent tools for fundamental physics. In addition, AGNs play an important role in the formation of supermassive black holes and their relation to galaxy formation and evolution (Fabian,

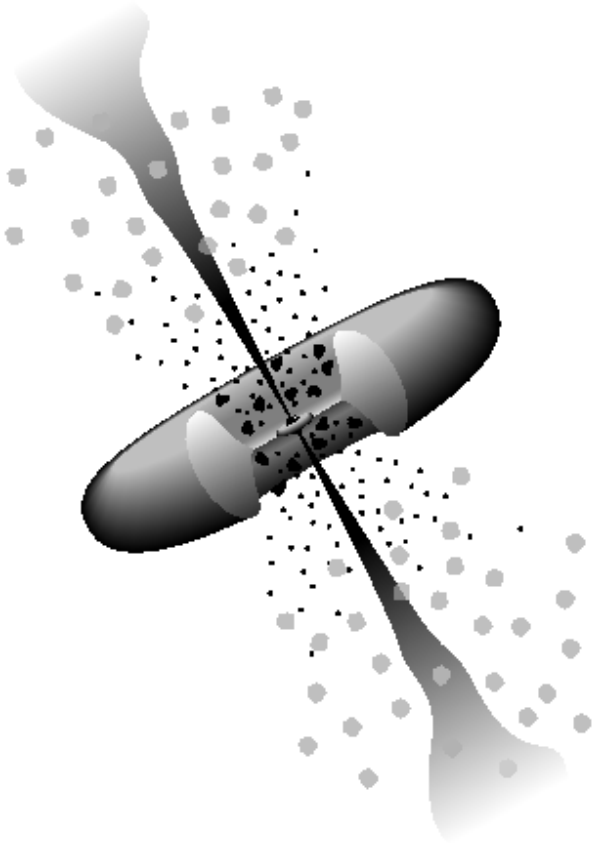

Figure 1.1: Schematic model of an AGN (Urry & Padovani, 1995). The main components are a supermassive black hole and accretion disk in the center, a hot electron corona, broad line region, torus or warped disk of dust and gas, the narrow line region and jets in the radio-loud objects. Credit: Urry, C. M., & Padovani, P. 1995, PASP, 107, 803, reproduced by permission of the University of Chicago Press.

2012). Their high luminosity makes them suitable background sources for the study of the intervening intergalactic medium at very long distances, through the study of absorption lines (Rauch, 1998) first pioneered by Sargent et al. (1980), and the investigation of the star formation and accretion history through the effects of their emitted radiation, the so-called extragalactic background light, in the gamma-ray spectra of distant AGN (Ackermann et al., 2012). They have also been used for measurements of cosmological parameters when lensed by foreground clusters (e.g., Biggs et al., 1999).

This thesis is concerned with the study of a particular type of active galaxies known as blazars, and the details of their high energy emission mechanisms through the study of their radio and gamma-ray variability properties. In this chapter we present an overview of the main characteristics of these objects and current models of their inner workings. This

is followed by a brief review of previous studies on the variability properties of their radio emission, and its relation to the high energy properties and of current efforts to shed light onto the details of their emission mechanisms. The chapter ends with an outline of this thesis.

1.1 Observational characteristics of blazars

Blazars are powerful emitters of radiation from the radio band to the highest gamma-ray energies. Their spectral energy distributions (SED) are characterized by the presence of two broad peaks: a low energy peak with a maximum in the IR/optical/UV/X-rays and a high energy peak with a maximum at gamma-ray energies, as found with the Energetic Gamma-Ray Experiment Telescope (EGRET) by von Montigny et al. (1995) and confirmed with the Fermi Gamma-ray Space Telescope by Abdo et al. (2010). Figure 1.2 illustrates the typical blazar SED as obtained by a recent multi-wavelength campaign on 3C 279 (Hayashida et al., 2012). Blazars are characterized by a flat spectrum in the radio band.

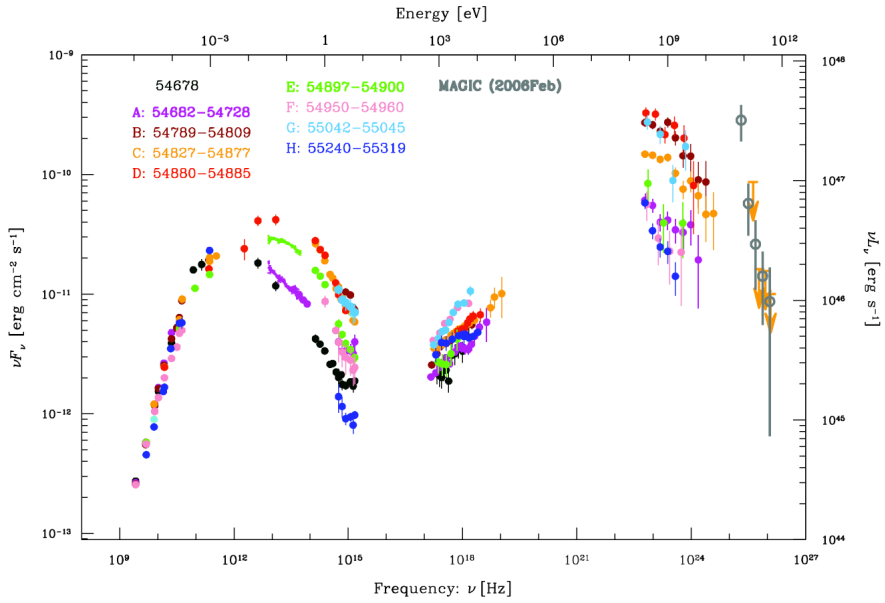

Figure 1.2: Spectral energy distribution for 3C 279 for multiple epochs from Hayashida et al. (2012). The different epochs are color coded and labeled with letters from A to H as indicated in the figure. The time period for each epoch is given as an MJD range next to the labels. In addition to the broadband SED, variability is also apparent. Credit: Hayashida, M., et al. 2012, ApJ, 754, 114, reproduced by permission of the AAS.

In addition to the extreme energy range at which blazars can be observed, they are

also polarized in radio and optical emission. Furthermore, blazars have a rich time domain behavior showing variability in all the observed bands (for a review see Ulrich et al., 1997). An example of blazar variability is shown in Figure 1.3, from a recent multi-wavelength campaign in 3C 279 (Hayashida et al., 2012).

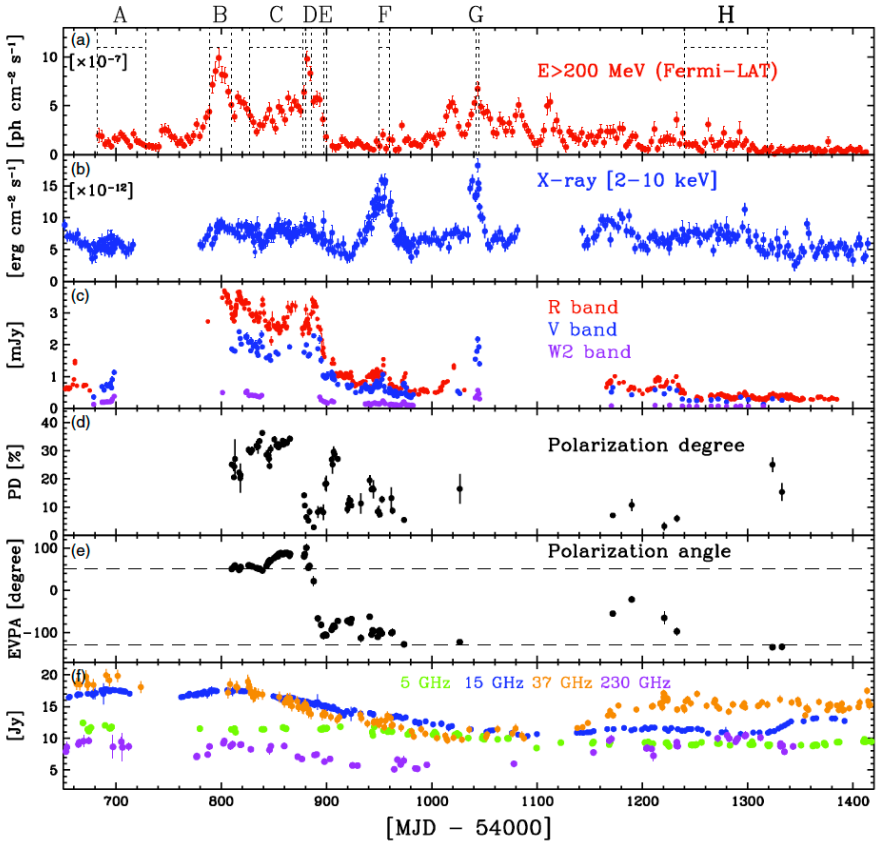

Figure 1.3: Multi-wavelength variability of 3C 279 from Hayashida et al. (2012). The light curves cover a period of two years from 2008 August to 2010 August. (a) Gamma-rays. (b) X-rays. (c) R, V and W2 bands. (d) Polarization degree in the optical band. (e) Polarization angle in the optical band with horizontal dashed lines indicating angles of 50° and −130°. (f) Radio flux density at 5, 15, 37 and 230 GHz. Credit: Hayashida, M., et al. 2012, ApJ, 754, 114, reproduced by permission of the AAS.

These observational characteristics make the study of blazars an intrinsically multi-wavelength endeavor that also requires time domain information, as the large variability needs to be incorporated in the models.

Based on their optical spectroscopic properties blazars can be divided into two classes: flat-spectrum radio quasars (FSRQ) and BL Lacs (named after the prototypical source BL Lacertae, originally identified as a highly variable star). FSRQs have strong broad emission

lines while BL Lacs have weak emission lines with equivalent widths of < 5 Å (e.g. Healey et al., 2008, and references therein).

By number, blazars are only a small fraction of the radio-loud AGNs, which in turn are only about 10% of the radio-quiet AGNs. Nonetheless they are the dominant population in energy bands where non-thermal emission processes are important, as for example in the radio and millimeter-wave bands where blazars become a prominent point source contamination of cosmic microwave background experiments like Planck (Planck Collaboration et al., 2011). They are also dominant in gamma-rays, as was discovered with EGRET (Hartman et al., 1999) and more recently confirmed with the Fermi Gamma-ray Space Telescope (Abdo et al., 2010; Nolan et al., 2012).

Another fundamental characteristic is their small angular size, which makes it extremely difficult to obtain spatially resolved observations, except by very long baseline interferometry (VLBI) in the radio band, where submilli-arcsecond angular resolution allows us to study their detailed structure. VLBI observations have shown the presence of single sided jets in which bright components are ejected at superluminal apparent speeds (Cohen et al., 1977; Zensus, 1997), and gave us the first observational evidence for unified theories of AGN (Readhead et al., 1978; Readhead, 1980). These observations have provided us with a basic picture of a blazar as an AGN with a jet of material moving at relativistic speeds and oriented close to our line of sight (e.g., Begelman et al., 1984; Blandford & Rees, 1978; Blandford & Königl, 1979).

1.2 Theoretical models for blazars

The general picture of a blazar as an AGN with a relativistic jet pointing close to the line of sight has been widely accepted since the late 1970s, but the understanding of its details is still incomplete. A basic requirement for any model of blazar emission is to reproduce the observed SED which is basically understood as a result of synchrotron emission for the low energy peak and inverse Compton for the high energy peak. However, alternatives models for the origin of the high energy peak based on particle cascades initiated by high energy proton-photon interactions have been proposed and are referred as hadronic models (e.g., Mannheim & Biermann, 1992). The basic idea of the low energy peak originating from synchrotron emission is in good standing, as it is the best candidate to reproduce

the observed high polarization degree (e.g., Angel & Stockman, 1980). The details of the high energy emission peak are less clear, even for the inverse Compton model in which a definitive answer on the source of the seed photon field is not available. This photon field could be the same synchrotron photons (Jones et al., 1974), or it could be an external photon field originating near the black hole (Blandford & Levinson, 1995), in the accretion disk (Dermer & Schlickeiser, 1993), the broad line region (Sikora et al., 1994) or the dust torus (Błażejowski et al., 2000). A recent review of blazar SED modeling is given by Boettcher (2012).

One of the largest uncertainties for blazar emission modeling concerns the location of the gamma-ray emission site, which is the main topic of this thesis. There are two main alternative locations for the gamma-ray emission: one is close to the central engine, as proposed in the pair cascade model of Blandford & Levinson (1995), and the other is in shocks located in the parsec scale jets observed with VLBI as proposed in Jorstad et al. (2001).

In the model that locates the gamma-ray emission close to the central engine, the gamma-rays are produced by interactions between scattered soft X-ray photons from near the black hole and electron/positrons or other gamma-ray photons already in the jet. An interaction with another high energy photon can result in the production of an electron positron pair, while interactions with electrons or positrons can produce gamma-rays via inverse Compton scattering. Due to the presence of the scattered soft X-rays and other high energy photons in the jet, a pair-production opacity is present. This opacity is energy dependent and gives rise to unity opacity surfaces for the gamma-ray photons that are called gamma-spheres. Photons can only escape the source once they reach the surface of the gamma-sphere. The radius of this surfaces increases with energy, so the lower energy photons originate closer to the central engine. An schematic representation is shown in Figure 1.4.

In the model that locates gamma-ray emission site in the parsec scale jet, the radio and gamma-ray emission are produced in the same region, with the gamma-rays originating from inverse Compton scattering of the same synchrotron photons or some external radiation field present at this distance from the central engine. A schematic representation is shown in Figure 1.5.

The fast time scales of variability observed at high energies are easier to explain for an

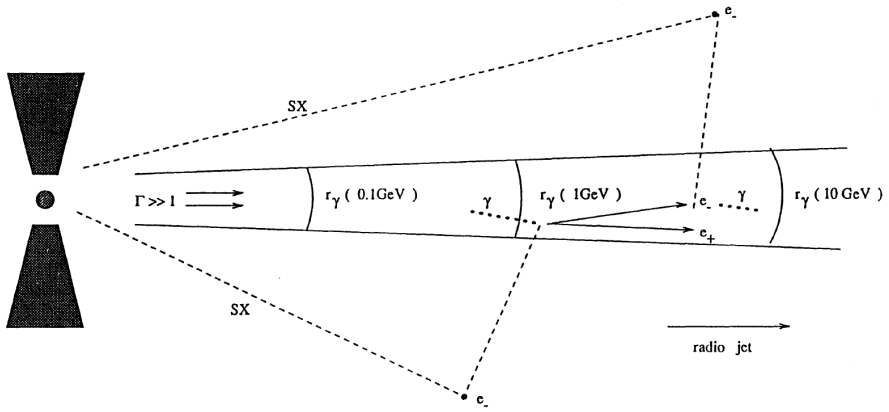

Figure 1.4: Schematic representation of the Blandford & Levinson (1995) model. In this model, soft X-ray photons denoted SX emitted near the black hole may be Thomson-scattered into the jet. There they can both combine with gamma-rays to form electrons and positrons and be inverse Compton scattered by electrons and positrons to form gamma-rays. In this way a pair cascade can develop. Also shown are the gamma-spheres from which gamma-rays of a given energy can escape from the jet. Credit: Blandford, R. D., & Levinson, A. 1995, ApJ, 441, 79, reproduced by permission of the AAS.

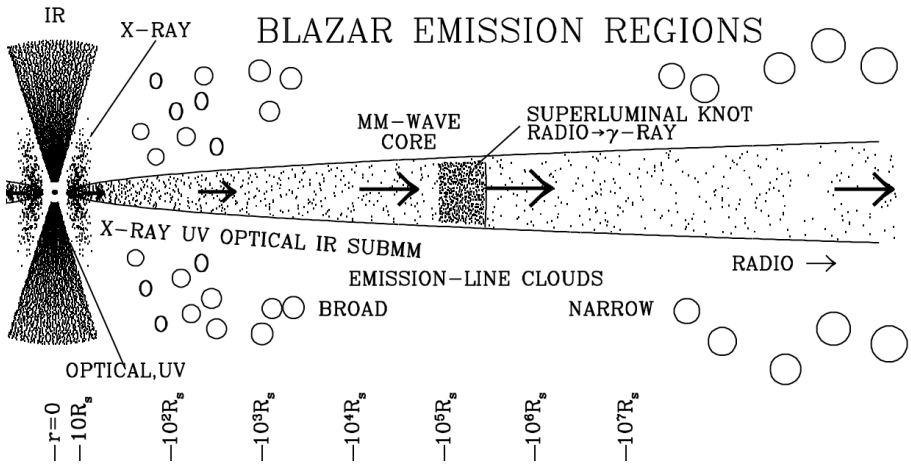

Figure 1.5: Schematic representation of the model proposed in Jorstad et al. (2001) and taken from Marscher (2006). In this model, the radio and gamma-rays are produced in the mm-wave core, located parsecs away from the black hole. The gamma-ray emission is produced by inverse Compton scattering of the synchrotron photons or some external photon field present at this distance from the central engine. Credit: Marscher, A. P. 2006, Blazar Variability Workshop II: Entering the GLAST Era, 350, 155, reproduced by permission of the ASP.

emission site close to black hole, where the jet has a smaller cross-section (e.g., Tavecchio et al., 2010). However, SED modeling does not provide a unique answer and contradictory

claims are found in the literature. Some authors argue for external Compton emission from the broad line region (Ghisellini et al., 2010), while other authors locate it at parsec scales, where the external Compton from the dust torus dominates (Sikora et al., 2009). This complicated theoretical picture could certainly be helped by observational constraints on the location of the high energy emission, these are the major concerns of this thesis and are discussed in Section 1.3 and 1.4.

The problem of the location of the gamma-ray emission in blazars is not the only one that is missing to complete our understanding of AGN. Other areas in which progress is needed are on the mechanisms for the acceleration of relativistic particles in the jets, the composition of the jets and the mechanisms for launching the jets (e.g., Blandford, 2008). All these areas can benefit from observational constraints as well as from theoretical investigations, especially simulations as has been done for the study of the processes by which the black hole/accretion disk system is able to launch the observed relativistic jets. The most promising ideas were proposed by Blandford & Znajek (1977), in which the jet is launched by a rotating black hole threaded with a magnetic field, and by Blandford & Payne (1982), where jets are launched by the accretion disk which is also threaded with a magnetic field. These ideas can currently be tested by detailed general relativistic magnetohydrodynamics simulations, like those of Tchekhovskoy et al. (2010), who studied the dependence of the output power on the spin of the black hole. These authors find differences of factors up to 1000 in the power output of the black hole when the accretion disk is thick, providing a possible explanation for the radio-loud/quiet dichotomy in AGN (Kellermann et al., 1989). A complete review of the progress in this active area of research is outside the scope of this introduction, but an excellent starting point is Meier (2012), in which a thorough account of the basic physics along with recent theoretical and observational results are presented.

1.3 Previous studies of the radio variability and its relation to gamma-ray emission

In spite of their small angular sizes, blazar jets can be resolved using VLBI in the radio band, where submilli-arcsecond resolution is possible. However, this level of resolution is out of reach for current gamma-ray instruments which can only achieve resolutions of a few tenths of a degree at the highest energies. This implies that other approaches are

necessary when trying to locate the site of the gamma-ray emission in these objects, because direct imaging in gamma-rays is not possible. One possible approach is to study the time correlation between the radio and gamma-ray band flux density measurement, which in the case of a common spatial origin for the two bands would produce simultaneous variations. This requires the monitoring of sources at different energy bands and was attempted for the first time with CGRO/EGRET in the 1990s.

The first studies of correlated variability between the radio and gamma-ray band were carried out by Valtaoja & Teräsranta (1995) and Valtaoja & Teräsranta (1996). They used 70 sources observed at 22 and 37 GHz with the 13.7 meter Metsähovi radio telescope and 202 EGRET pointings. Instead of a proper cross-correlation analysis, which was not possible because of the sparse gamma-ray sampling, the epochs of EGRET detections were compared to the state of the source in the radio band. They found an excess of gamma-ray detections during periods in which the radio activity was increasing or at a maximum, and interpreted this as a sign of a common spatial location of the radio and gamma-ray emission regions. However, this result cannot be considered robust due to limitations in the dat sets available at the time, which have very sparse gamma-ray coverage as illustrated in Figure 1.6. Similar conclusions were obtained by Aller et al. (1996), who used radio data from the University of Michigan Radio Observatory (UMRAO) 26 meter telescope at 14.5, 8.0 and 4.5 GHz, but in this case the authors were more cautious and correctly stated that better sampling would be required to confirm the association between the radio and gamma-ray activity.

Monitoring using the Very Long Baseline Array (VLBA) at 22 and 43 GHz was used to determine the epoch of ejection of superluminal components and the times of high gamma-ray fluxes were measured with EGRET by Jorstad et al. (2001). An illustration of the data they analyzed is shown in Figure 1.7, where again the sparsity of the gamma-ray light curves used in these early studies is evident. These authors observed a sample of 42 sources and found that 10 out of 23 gamma-ray flares coincided with the extrapolated time of zero separation between radio knots and cores. This result and the variability of the total and polarized radio flux density is interpreted as evidence for a common spatial origin of the radio and gamma-ray emission in the parsec-scale radio jet.

The results discussed above, obtained during the EGRET era, might provide some evidence of a connection between the radio and gamma-ray emission in blazars, and point

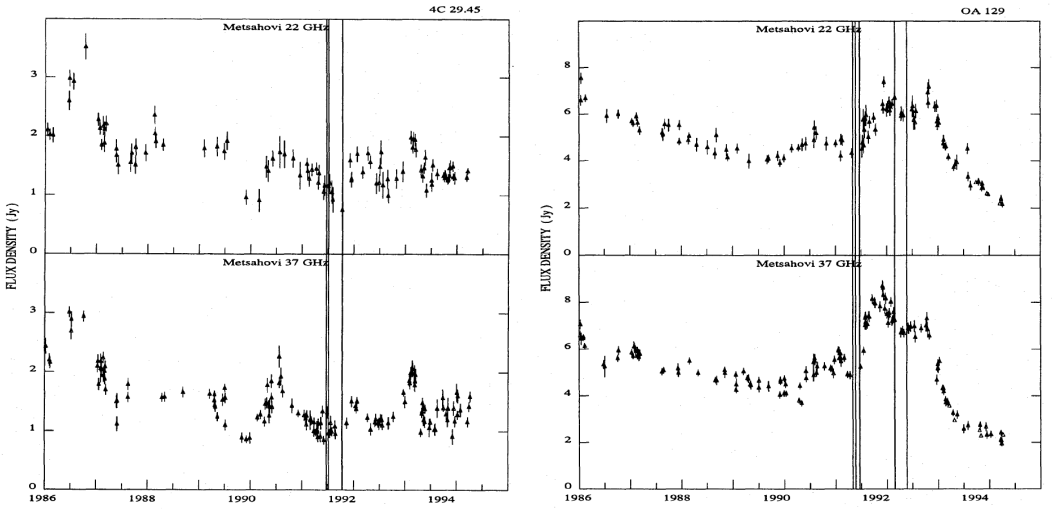

Figure 1.6: Example radio and gamma-ray observations from EGRET and Metsähovi (Valtaoja & Teräsranta, 1995). Left, 4C 29.45 with three EGRET observations (vertical lines) and no detections. Right, OA 129 with 5 EGRET observations (vertical lines) and 2 detections (first and fourth lines). Credit: Valtaoja, E., & Teräsranta, H. 1995, A&A, 297, L13, reproduced with permission © ESO.

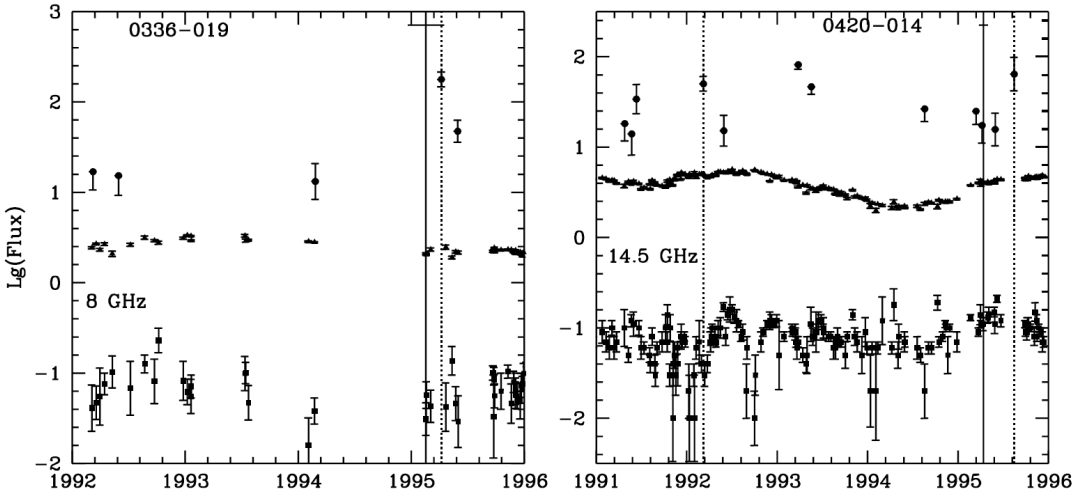

Figure 1.7: Example radio and gamma-ray observations from EGRET, VLBA and UMRAO monitoring (Jorstad et al., 2001). Gamma-ray flux (circles), total radio flux density (triangles), and polarized radio flux density (squares) on a logarithmic scale. Solid lines indicate extrapolated times of zero separation between radio knots and cores, and dotted lines correspond to observed maxima of the gamma-ray emission. Credit: Jorstad, S. G., et al. 2001, ApJ, 556, 738, reproduced by permission of the AAS.

to a common spatial origin of these two bands, but these claims are far from being a robust statistical proof of a connection: they are based on small samples of sources that have been

selected with subjective criteria, and furthermore use light curves with sparse coverage in the gamma-ray band.

1.4 Radio monitoring in the era of *Fermi*

These early EGRET results opened the door to new questions and a need for a better understanding of the gamma-ray sky, that had to wait until the next gamma-ray observatory. The *Fermi Gamma-Ray Space Telescope* (*Fermi*) was launched in June 2008, and began science operations in August 2008 when it started scanning the sky continuously, obtaining a complete image of the gamma-ray sky every two orbits, or approximately 3 hours. The continuous survey observing mode and the increased sensitivity completely changed the way in which gamma-ray observations could be used, by allowing the study of the time domain in a very natural way. This feature of *Fermi* is extremely well suited to the problem of understanding the time domain relation between the radio and gamma-ray band for blazars.

To make the best use of these new capabilities the Caltech group started a monitoring program of blazars using the Owens Valley Radio Observatory 40 meter telescope (OVRO 40 m) in mid 2007. The main goals of the program are to characterize the radio variability of a large number of sources in the radio band, and to study the relation between the variability in the radio and the gamma-ray bands to constrain the location of the high energy emission in blazars.

The OVRO 40 m program started in mid 2007 with the monitoring of all the sources north of -20° declination from the Candidate Gamma-ray Blazars Survey (CGRaBS, Healey et al., 2008), which were selected as candidate gamma-ray emitters based on their radio characteristics. Sources detected by *Fermi* that are associated with blazars detected at lower energies and are visible from Owens Valley have been added. All the sources are observed at 15 GHz, within a three day cycle that is repeated twice a week.

In addition to the OVRO 40 m monitoring program, a few other programs using single-dish radio telescopes were started or continued to complement *Fermi*. Their basic characteristics are shown in Table 1.1.

In terms of cadence, number of sources and sample selection the OVRO 40 m program stands out. In spite of their smaller samples and slower cadences, other programs also provide important information. For example the F-GAMMA program (Angelakis et al.,

Table 1.1: Current single-dish radio monitoring programs of blazars (adapted from Aller et al., 2010)

Program	frequency [GHz]	sampling	size/advantage
OVRO 40 m[a]	15	2 / week	>1000 sources
			low flux density limit
Effelsberg 100-m[b]	2.64 – 43	monthly	≈60 sources
			spectra
IRAM 30-m[b]	86 – 270	monthly	≈60 sources
			high frequency
UMRAO 26-m[c]	4.8, 8.0, 14.5	1–2 / week	35 sources
			multifrequency, linear polarization
Metsähovi[d]	37	monthly	≈100 sources
			high frequency
RATAN-600[e]	1 – 22	2–4 / year	600 sources
			spectra

[a] OVRO 40 m, Richards et al. (2011)
[b] F-GAMMA, Angelakis et al. (2012)
[c] UMRAO 26-m, Aller et al. (2009)
[d] Metsähovi, Nieppola et al. (2011)
[e] RATAN-600, Kovalev et al. (2002)

2012), which uses the Effelsberg 100-m and IRAM 30-m telescopes, provides multifrequency information with a number of high frequency bands that are particularly useful to study the inner regions of the jet, which are not accessible at lower frequencies due to synchrotron opacity. Decade long light curves are important to study the long term variability of the sources and are provided by the UMRAO (Aller et al., 2009) and Metsähovi (Nieppola et al., 2011) program. The UMRAO program also provides linear polarization, which allows for a study of the evolution of the magnetic fields in the radio emitting regions. Unfortunately the UMRAO program was discontinued in mid-2012, but a program to implement polarization measurements on the OVRO 40 m telescope is under way, with commissioning of a new Ku-band (12 – 18 GHz) receiver planned for mid-2013.

These monitoring programs are also accompanied by programs using very long baseline interferometry to monitor smaller samples of sources at high resolution, thus enabling studies of the relation between the gamma-ray properties and the properties of the blazar jets on parsec scales. Among these programs are the Monitoring of Jets in Active Galactic Nuclei with VLBA Experiments (MOJAVE, Lister et al., 2011) and the Boston University Blazar Program (Jorstad et al., 2009), both looking at sources in the northern hemisphere. In the southern hemisphere Tracking Active Galactic Nuclei with Austral Milliarcsecond Interferometry (TANAMI, Ojha et al., 2010) is looking at a different set of sources from all

the other programs, either single dish or VLBI.

All these projects are already producing interesting results. For example, the early suggestions of a common mechanism regulating the total luminosity at high and low energies are confirmed by the correlation between the mean radio flux density and mean gamma-ray flux (e.g., Kovalev et al., 2009; Mahony et al., 2010; Nieppola et al., 2011). By using a large sample of objects with quasi-simultaneous data from the *Fermi* and the OVRO 40 m program Ackermann et al. (2011a) and Pavlidou et al. (2012) have shown that this correlation is real and not an effect of distance modulation. The OVRO 40 m program has also shed light on the search for the radio characteristics that determine the gamma-ray emission properties of blazars. Richards et al. (2011) found a large difference between the radio variability properties of gamma-ray detected versus non-detected blazars, namely, that the fractional variability (as characterized by the modulation index) for the gamma-ray detected sources is twice the value for those not detected by *Fermi*. Other studies have found time-lagged correlation between these two energy bands, but without a large number of objects with well-sampled light curves it is difficult to assess the significance of the correlations for the complete blazar population (e.g., Marscher et al., 2008; Abdo et al., 2010a; Agudo et al., 2011a,b). In a statistical study of a sample of 183 bright *Fermi*-detected sources with monthly binned light curves and radio data from MOJAVE, Pushkarev et al. (2010) found that, on average, the radio flares occur later than the gamma-ray flares. In a study of 60 sources with monthly binned mm-wave and gamma-ray light curves, León-Tavares et al. (2011) found a mean delay between the beginning of the mm-wave flare to the peak of the gamma-ray emission of 70 day.

Our radio monitoring program of blazars stands apart from other programs by its complete source sample and fast cadence. The sources in the sample are monitored independently of their gamma-ray state, providing an unbiased view of their radio activity and complete coverage of the *Fermi* detected blazars north of -20° of declination. These advantages, combined with the *Fermi* coverage at gamma-rays and the use of robust statistical techniques, give us an excellent chance to characterize the radio variability properties of the largest sample of sources ever monitored at 15 GHz, and its relation to the gamma-ray emission through the study of correlated variability, thus constraining the location of the gamma-ray emission site in blazars.

1.5 Structure of this thesis

The main observational effort required to monitor about 1600 sources twice a week is described in Chapter 2, in which a detailed description of the source sample and the technical details of the radio observational program are presented. This chapter also presents a description of the basic characteristics of *Fermi* and the steps required to convert the raw data into the gamma-ray light curves that we use in our studies. The chapter closes with a description of the sample of sources used in the cross-correlation study.

A prerequisite to estimating the significance of the cross-correlations between the radio and gamma-ray bands is a characterization of the variability properties of the light curves. The method used in this task is described in detail in Chapter 3, in which we develop a new technique, inspired by methods used to model X-ray light curves of AGNs to suit the characteristics of our data sets. The results of the application of this technique to the modeling of the complete sample of radio sources observed by the OVRO 40 m program is presented in Chapter 4. This chapter also presents a comparative study of the variability properties for a subset of sources observed by the UMRAO program from the mid 1970s to early 1990s.

Constraints on the location of the gamma-ray emission site are obtained through the study of correlated variability between these bands. This requires a rigorous evaluation of the significance of cross-correlations, which cannot be performed using standard cross-correlation tests that do not take into account the variability properties of the sources, or the uneven sampling of the light curves. A detailed discussion of our implementation of these methods is presented in Chapter 5.

Chapters 3 and 5 provide the basic foundation for the study of correlated variability we present in Chapter 6 where these techniques are applied to a sample of 86 sources with 4 year light curves in the radio band and 3 year light curves in the gamma-ray band.

The physical interpretation of the observational results is discussed in Chapter 7 and Chapter 8 contains a summary of this thesis.

Chapter 2

The OVRO 40 meter telescope blazar monitoring program

2.1 Introduction

In order to carry out the program of constraining the location of the gamma-ray emission site with respect to the radio emission site by studying correlated variability, we require continuous monitoring in both energy bands. The monitoring of the gamma-ray band is secured by the continuous operation of the *Fermi Gamma-ray Space Telescope* (*Fermi*) which in normal scanning mode scans the whole sky every three hours. In order to take full advantage of this capability, a matching program in the radio band is highly desirable. For that purpose we are carrying out a comprehensive monitoring program using the Owens Valley Radio Observatory 40 meter telescope (OVRO 40 m) located near Bishop, CA. The monitoring program started in mid-2007, before the launch of *Fermi*, starting with a sample of candidate gamma-ray blazars and adding the blazars detected by *Fermi* which have high confidence associations with radio sources.

In this chapter we give a description of the OVRO 40 meter blazar monitoring program, the source sample, the instrument and the observational techniques used for the radio monitoring. A brief discussion of the most important aspects of the program is given with an emphasis on the areas in which my involvement has been most critical and most significant, these include the scheduling of the observations and development or improvement of calibration procedures and their implementation and execution. This is followed by a description of the gamma-ray side of the project and includes an outline of the main capabilities of *Fermi* and its principal instrument the Large Area Telescope (LAT). A brief description is

given of the main ideas required to convert the raw photon detections to photon flux light curves, which are the main data product used in our investigations. The chapter ends with a description of the sample of sources which are used in the study of correlated variability.

2.2 Sample description

Radio monitoring observations started in mid-2007 before I joined the program. At that time the sample consisted of 1158 sources which comprise a subset of the *Candidate Gamma-ray Blazar Sample* (CGRaBS, Healey et al., 2008). The CGRaBS sources were selected by their similarity to the blazars detected in the third catalog of the *Energetic Gamma Ray Experiment Telescope* (EGRET, Hartman et al., 1999) on the *Compton Gamma-ray Observatory* (CGRO). The selection of candidate gamma-ray blazars starts with a parent sample of high latitude ($|b| > 10^{\circ}$), bright (> 65 mJy at 4.8 GHz) and flat spectrum ($\alpha > -0.5$ for $S \propto \nu^{\alpha}$) radio sources observed at 8.4 GHz which form the *Combined Radio All-Sky Targeted Eight GHz Survey* (CRATES, Healey et al., 2007). The selection criterion is based on a "figure of merit" that ranks the sources on CRATES according to their likelihood of being like the blazars detected with EGRET, and uses their radio flux density, radio spectral index and x-ray flux. The CGRaBS catalog consists of 1625 sources with the largest likelihood of association. The original monitored sample consisted of all the CGRaBS sources north of -20° declination.

That original sample has been augmented at the time of each *Fermi* source catalog release by adding all the blazars detected in gamma-rays by *Fermi*-LAT. The current sample contains all the original CGRaBS sources plus the blazars in the first LAT AGN catalog (1LAC, Abdo et al., 2010) and the second LAT AGN catalog (2LAC, Ackermann et al., 2011) included in the clean samples (see Section 2.8.2 for further discussion on these catalogs). The current sample contains 1593 blazars plus calibration sources and sources observed for other programs. These are all monitored twice a week. The extent of the coverage can be best appreciated by looking at their distribution in the sky as shown in Figure 2.1.

A list of the monitored blazars is included in Appendix A along with properties of interest for this study. Besides the sources mentioned above, we obtain daily observations of a group of calibration sources which are used to determine the flux density scale of the radio observations. These sources are 3C 286, DR 21, 3C 161 and 3C 274, and are known

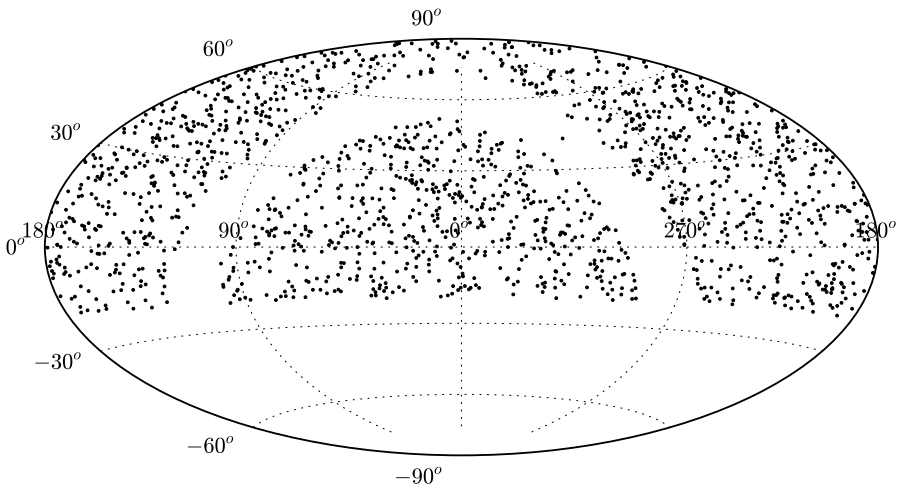

Figure 2.1: Monitored sources in equatorial coordinates

to be stable and have well determined flux densities (Baars et al., 1977).

2.3 The radio monitoring program

2.3.1 Instrument description

The OVRO 40 m telescope (Figure 2.2) is a $f/0.4$ parabolic reflector 130-foot (or 39.624 meters) in diameter on an altitude-azimuth mount. The telescope is located in Owens Valley near Big Pine, California at 37°13′53.″7 N latitude, 118°16′53.″83 W longitude, and 1236 m elevation (Pearson, 1999) and was dedicated in 1968. It surface accuracy is approximately 1.1 mm rms. Two off-axis corrugated horn feeds are located in the prime focus. Each horn has a main beam Full Width at Half Maximum (FWHM) of 157″ and they are separated in azimuth by 12.′95. We deliberately underilluminate the antenna to obtain an aperture efficiency of about 25%. This reduces the effects of pointing errors which are the main limitation when observing bright sources, and in addition minimizes exposure to thermal noise from ground spillover. An increase in aperture efficiency provides little benefit as we already achieve acceptable thermal noise levels for the sources in our sample, but would significantly degrade pointing errors. The reduction of flux density errors due to mispointing also plays a determinant role in the scheduling and calibration of the observations as described in Section 2.4.

The altitude-azimuth mount and drive system can point the telescope from −90° to

+335° in azimuth and in elevation from 11.5° to 10° past zenith, but in practice this is restricted to 90° by the control system. Normal observations are performed in the range between $za = 20°$ and $za = 60°$. The upper limit in zenith angle is set to avoid large atmospheric contributions, while the lower limit is due to limitations on the tracking performance of the telescope at high elevations. The telescope can be driven up to a maximum speed of about 15° per minute, but it can only track sources up to half that speed.

Figure 2.2: The OVRO 40 m telescope

Observations are performed using a Dicke-switched dual-beam system which provides suppression of atmospheric noise allowing longer integrations. The receiver system is a homodyne total power receiver with cooled LNAs and it has a receiver temperature of 30 K with bandwidth of 3 GHz centered at 15 GHz and equivalent noise bandwidth of 2.5 GHz. The receiver is sensitive to right circular polarization on the sky, which allows us to observe linearly polarized sources with any orientation. The Dicke switch alternates with a frequency of 500 Hz between the beams and the receiver provides for each millisecond a total power in each beam. The total system temperature considering contributions from the receiver, atmosphere, CMB and ground is about 55 K. A schematic of the receiver is shown in Figure 2.3.

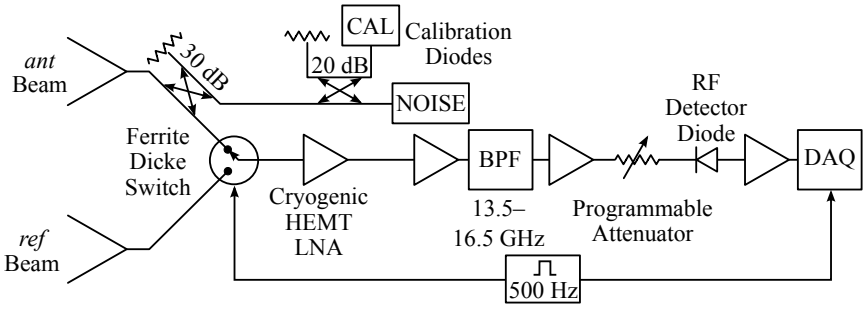

Figure 2.3: The Ku-band receiver. Credit: Richards, J. L., et al. 2011, ApJS, 194, 29, reproduced by permission of the AAS.

Flux density measurements are performed by double switching. In this technique a flux density measurement is divided into four steps which we call A, B, C and D as illustrated in Figure 2.4.

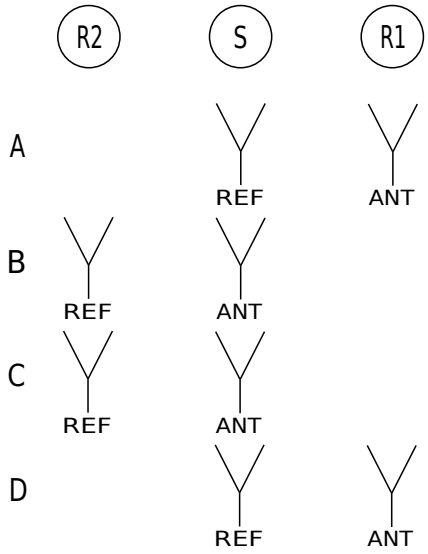

Figure 2.4: Illustration of the double switching procedure. The circles at the top of the figure represent the field containing the source (S), and the two reference fields used to subtract atmospheric contributions (R1 and R2). A flux density measurement consists of four segments called A, B, C and D. For each one the positions of the antenna and reference fields are indicated with respect to the sky fields.

In the A step the source is on the reference beam and the antenna beam looks at reference field R1. In the second and third steps B and C, the antenna beam looks at the source while the reference beam looks at reference field R2. In the last step D, the antenna

beam looks at reference field R1 and the reference beam at the source. The resulting flux density measurement and its error are given by

$$S = \frac{\kappa}{4}(\xi_{\rm B} + \xi_{\rm C} - \xi_{\rm A} - \xi_{\rm D}) \quad (2.1)$$

$$\sigma = \frac{\kappa}{4}\sqrt{\sigma_{\rm A}^2 + \sigma_{\rm B}^2 + \sigma_{\rm C}^2 + \sigma_{\rm D}^2} \quad (2.2)$$

In the equations, κ is the calibration factor that takes digital units to janskys, $\xi_i = P_{{\rm ant},i} - P_{{\rm ref},i}$ is the power difference for step i, and σ_i is the standard deviation in the millisecond samples of power difference for step i.

A similar procedure is used to measure the calibration diodes with the difference that the telescope looks at a blank patch of sky and does not slew between segments A and B, and C and D. The diode is enabled during the C and D integrations.

During the time span of this project two control systems were used. Before 11 August 2010 we were working with a control system running on a Digital Equipment Corporation VAX microcomputer, we call this the *VAX control system*. This original control system had a very simple command line interface and required some familiarity with the VMS operating system. The code was hard to modify, so its development was frozen and during its last year of operations it started failing frequently. The only option to resume observations after some failure was to restart the control program which had to be done with user intervention. This required frequent monitoring of the system by an observer and resulted in unnecessary difficulties in the operation of the telescope. Since 11 August 2010, we have been using a new control system developed by Martin C. Shepherd. The new control system, which we call *MCS control system*[1], works on a real-time variant of Linux operating system and has added increased flexibility and reliability to the operations, reducing the interventions by the observer. As part of that development we have also improved the way pointing corrections are measured and the capabilities of our data flagging procedures. The new system also makes it easier to monitor the status of the receiver and has been key to fast identification and solution of occasional problems.

Further information on the hardware and calibration procedures can be found in Richards

[1]Complete documentation on the *MCS control system* can be found online at `http://www.astro.caltech.edu/~mcs/ovro/40m/help/`.

(2012) and references therein. An entertaining account of the history of the Owens Valley Radio Observatory, including the 40 meter telescope can be found in Cohen (1994, 2007).

2.4 Scheduling of the observations

The only feasible way to continuously monitor the large number of sources at the cadence we require for our program is to make all observations automatic. This requires a scheduling algorithm that can program the observations and calibrations, minimizing the slewing times, and that can run unsupervised. Early in the program I discovered that using the original algorithm, some of the sources showed very large flux density variations from day to day, some of those even seemed to have two light curves tracking each other, with one of them at systematically lower flux density levels than the other. The problem was narrowed down to time and sky position variations of the pointing corrections as described in Section 2.5.1. This section presents a discussion of the requirements and the solution we adopted to solve the scheduling problem.

2.4.1 The problem

Due to the large aperture of the telescope and the moderately high brightness of our sources, short integrations provide adequate noise levels in most sources. For the normal monitoring we can obtain a thermal noise level of 4 mJy in just 32 seconds of integration, which becomes 63 seconds when we add the overhead associated with moving the telescope between the 4 segments of the measurement. A first lower limit in the time required to observe all the sources in the program comes from adding the time to make a flux density measurement, this time is about $1700 \times 63/3600 \approx 30$ hours. To this we have to add the time needed to move the telescope from source to source which can amount to a significant fraction. A quick estimate can be obtained by assuming all the sources are uniformly distributed in the observable region north of -20° in declination. This comprises an area of 2.7π sr, and a mean distance between sources of 4.5°. The telescope slews at 15 degrees per minute and requires around 12 seconds to settle on each source; taking this into account we can get a lower limit assuming that we can observe all the sources just by jumping into the next one which is at the average distance, in this case we obtain a total slewing time of $1700 \times (12 + 4.5/(15/60))/3600 \approx 14$ hours. To these we have to add the time required to

calibrate the flux densities and measure pointing model corrections. Relative flux density calibration requires a calibration diode measurement about once an hour, which adds an approximate overhead of one minute every hour of observations, including slewing. Pointing model corrections are the main restriction as we found that these corrections vary with time and are only valid in regions of less than about 25° in diameter (see Section 2.5.1 for more on this). If we divide the sky into about 100 regions, each one requiring a pointing calibration, which takes about 7 minutes, this amounts to about $7 \times 100/60 \approx 12$ hours. Adding all these numbers we estimate a lower limit on the total observing time of about 60 hours.

An observing sequence in which we visit each source traveling an average distance of 4.5° is far from what really happens as it ignores the details of the source distribution and its interaction with other observing constraints such as the limits on zenith angle of the observations. The variation of the pointing model corrections constrains the possible source arrangements by forcing us to divide the sky into pointing regions of about 25° in diameter, so the observing problem can be separated into two parts, a first level optimization in which the sources are sorted within an observing region and a second level optimization in which these regions are sorted. The scheduling problem consists in observing all the sources once in each cycle, minimizing the slewing times and respecting the restrictions imposed by the pointing and calibration requirements, and observability of the sources.

This problem is related to a classical optimization problem, the Traveling Salesman Problem (frequently referred as the TSP) in which a traveler salesman has to visit a number of cities minimizing the distance traveled. Each city has to be visited only once and the trip ends in the starting city. This problem does not have a known exact solution and requires numerical techniques to search the solution space and find an appropriate solution which in most cases is only close to the optimum. A direct search of the solution space is only feasible for small number of cities making the problem hard even for current computational capabilities. This is due to the fact that the number of possible solutions is $N!$, where N is number of cities, a number that becomes very large even for problems of moderate size (e.g., 100 cities). Various methods have been applied to solve the TSP, among them are the nearest neighbor heuristic, simulated annealing, or problem specific heuristics. The problem has found application in many areas of science and engineering including logistics, genome sequencing, electronic circuit manufacturing and many others. In astronomy it has already been used to help in the scheduling of observations of up to a few hundred sources.

Large instances of its most simple form have been solved and software that is able to handle them is freely available. A complete and recent review of solution techniques and references for its various application is given in Applegate et al. (2006)[2]. Even though the particular example we face is a more complicated version which cannot be handled by these standard tools, we can get some insight from the existing approaches currently used to tackle this problem.

2.4.2 A solution

In the particular version of the problem we have to solve there are some additional complications. The first one is that the sources are moving in horizontal coordinates, which are the relevant coordinates for the scheduling problem, and the second one is that the sources can only be visited during a time window in which they are sufficiently high in the sky to reduce the effects of the atmosphere and far from the zenith where the telescope has problems tracking the sources. All these factors make the solution more challenging than the traditional TSP problem. After some experimentation with some of the basic tools used for the TSP, a scheme that solves the practical problem of fitting the sources to the desired 3 day cycle was found and is described below.

The requirement of having pointing model corrections for regions of less than 25° in diameter, requires us to divide the sky into smaller regions. We chose the HealPix grid to accomplish this as it is widely used in astronomy and has the property of generating regions of equal area and thus a similar number of sources (Górski et al., 2005). The main restriction of having a distance between the source and pointing calibrator of less than 25°, can be accomplished by using a grid with 192 pixels over the full sky, each one with 14°.7 of diameter.[3] This requirement reduces the complexity of the optimization problem by naturally dividing the problem into two levels, one in which sources are sorted in a region and a second one in which the regions are sorted to make a complete observing cycle.

The first step in the optimization is to assign each source to a region. For each region we need to select a source for pointing calibrations. This source is used to obtain the local pointing model corrections that are later applied to the other sources in the region. A

[2]A collection of interesting resources related to the TSP can be found in a website maintained by W. J. Cook at `http://www.tsp.gatech.edu/`

[3]This diameter is actually an equivalent angular size given by $\theta_{\rm pix} = \Omega_{\rm pix}^{1/2}$, where $\Omega_{\rm pix}$ is the solid angle subtended by each pixel.

pointing calibrator needs to be bright, unresolved and located in a region free of confusion. Almost all the sources in our monitoring program satisfy the unresolved requirement and are far from the Galactic plane in regions which are usually not affected by confusion; the few which are not suitable are excluded from this procedure. The pointing calibrator is chosen from the sources that are brighter than a certain threshold. Regions with one of the flux density calibrators use this for pointing. For other regions we select among the sources brighter than 400 mJy and choose the one with the minimum average distance to other sources. In regions with no sources brighter than 400 mJy we simply choose the brightest source. For a couple of special cases near the Galactic plane where contamination of the reference fields is severe, sources have been incorporated in nearby regions always ensuring a distance of less than 20° to the pointing calibrator.

For each region we have to solve the problem of visiting the sources starting with the pointing calibrator in an order that minimizes the slewing time. Regions with fewer than 10 sources can be optimized by direct search of the best solution. For regions with at least 10 sources this approach is too costly and we resort to simulated annealing which can find a good solution in a reasonable time[4]. The extent of this problem can be appreciated by looking at Figure 2.5 which shows that only a small fraction of the regions can be optimized by direct search.

Even though we cannot hope to solve the problem exactly with a direct search, we can use simulated annealing which is an approximation algorithm used to find solutions in optimization problems that do not have exact solutions or when finding such would take an unreasonable amount of time. The basic idea is to simulate the processes of annealing in a metal, in which the material is heated and slowly cooled in order to remove strain and imperfections as a result of minimizing the free energy in the material. In a practical optimization problem, instead of reducing the free energy we are interested in reducing some cost function and we choose a quantity analogous to the temperature that is a measure of the variability of the cost function. This method is easy to implement and although it does not ensure an optimum solution it has proven to be good at finding good solutions with a reasonable amount of computation (Laarhoven & Aarts, 1987; Reinelt, 1994). In practice

[4]The time it takes for a direct search is proportional to the number of possible solutions. Using our implementation on a desktop computer it takes 108 seconds to test the 9! possibilities for 9 sources. By simply scaling this we can predict that it would take 300 days for 14 sources and 80% of the age of the universe for 22 sources. It was not fun to realize this in my second year of graduate school.

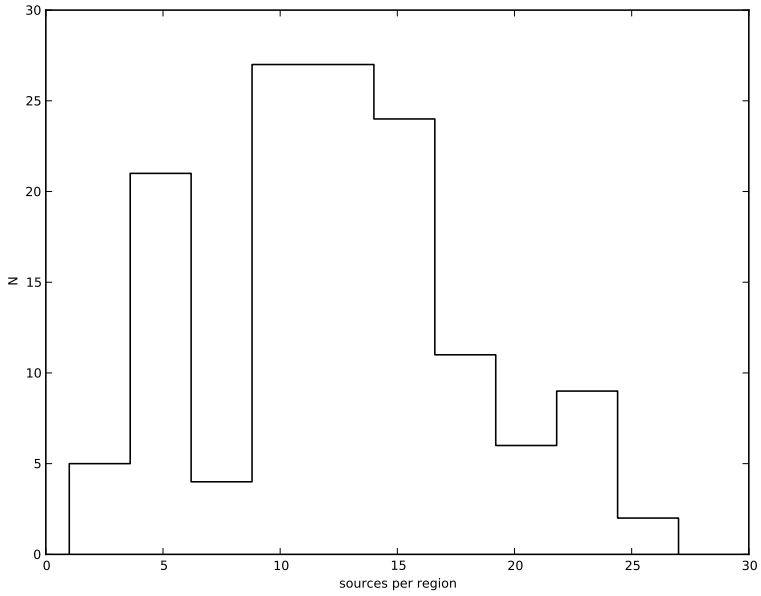

Figure 2.5: Number of sources per region in the sky. Only regions with fewer than 10 sources can be optimized by direct search; for most of them we use simulated annealing.

we find appropriate solutions in very short times with only a few thousand iterations. The simulated annealing algorithm is summarized below (adapted from Reinelt, 1994). Here a tour is a path that goes from source to source and we denote it by T. The time length is the cost function for the minimization and we called it $C(T)$,

- Compute an initial tour of the sources T and choose an initial temperature $\theta > 0$ and a repetition factor r.
    - As long as the stopping criterion is not satisfied perform the following steps
        - Do the following r times.
            - Perform a random modification of the current tour T_{mod} and compute the time length difference $\Delta = C(T_{\mathrm{mod}}) - C(T)$.
            - Draw a uniformly distributed random number x, $0 \leq x \leq 1$.
            - If $\Delta < 0$ or $x < \exp(-\Delta/\theta)$ then set $T = T_{\mathrm{mod}}$.
        - Update θ and r
- Output the current tour as solution

This is only a general description of the algorithm that leaves a number of points out. The first one is how to choose a starting temperature θ. There are various recipes for this: one is to explore a number of random paths and use a quantity proportional to the standard deviation on those random tours. In our case we simulate $N = 100$ random tours and start with $\theta = \theta_i = 3\sigma$, where σ is the variance in those N random tours. Another point is the repetition factor r. After some trial we decided to use $r = 100$, as we did not find significant improvements for larger values. The last point is a rule to update θ and r, which is the so-called cooling schedule. We use the simplest cooling schedule in which r is fixed and θ is reduced by a constant factor, in this case 0.9. The procedure ends when $\theta < 0.01\theta_i$. We initialize the optimization by choosing a random tour which is modified at each step by swapping the order of two sources[5].

The solution will depend slightly on the elevation for the observations, but the dependence can be ignored and a fixed value obtained at 45° of elevation can be used for the following stage which is described below. The sample path on the sky for one of the regions is illustrated in Figure 2.6 for a region with 21 sources.

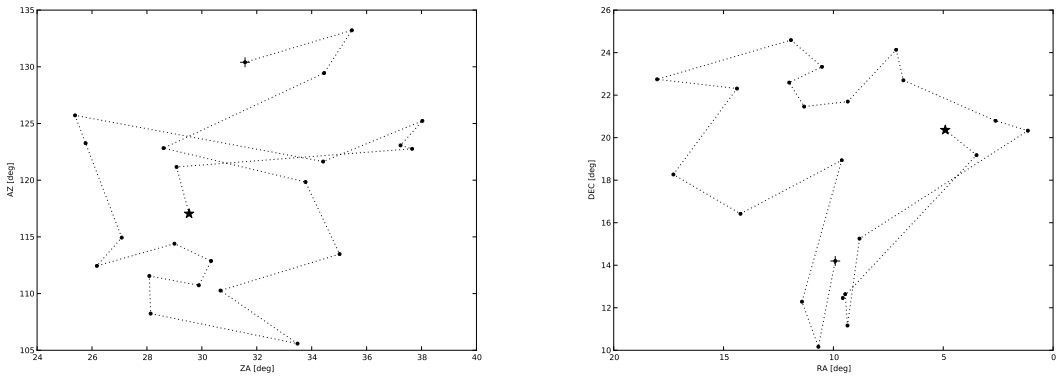

Figure 2.6: Sample path of the telescope for one of the regions in horizontal coordinates (left panel) and equatorial coordinates (right panel). The first source is marked with a star and the last one with a cross. There are a total of 21 sources in this region.

The second stage consists of sorting the regions. This has the extra complication that the regions are only observable for a limited time and that calibrators have to be observed every day. Several approaches were tested, including sorting by declination and right ascension, or by nearest neighbor, but none of them was able to accommodate all the sources in the

[5]In the context of the TSP this is the *city-swap heuristic*

required 3 day cycle. After some experimentation it was found that a heuristic approach that starts by giving higher priority to observations of southern sources and then moves slightly to the north is able to fit all the sources in the 3 day cycle. This heuristic approach is motivated by the fact that southern sources have a very limited observing window while circumpolar sources are observable at any time. The heuristic approach effectively uses circumpolar sources to fill gaps in the schedule where no other regions are observable. An example path through all the 136 regions with sources is shown in Figure 2.7.

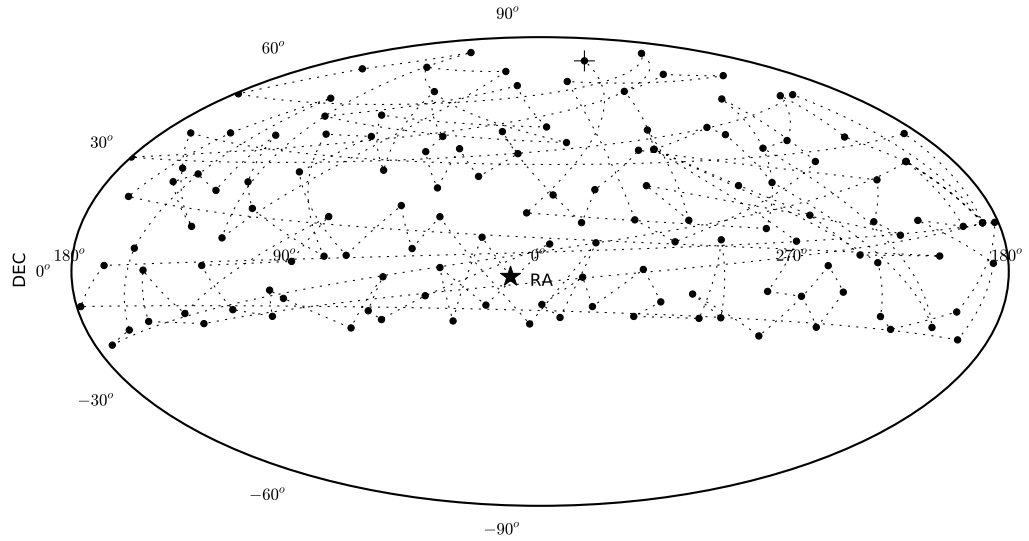

Figure 2.7: Sample telescope path in equatorial coordinates for a full observing cycle of three days. The first region is marked with a star and the last one with a cross.

This system has been in use since March 2009 and allowed us to solve large systematic errors associated with the inadequacy of the pointing model corrections more than about 25° away from the pointing source, a problem that affected a fraction of our early light curves (before March 2009). All those problematic data points have been eliminated and we increased the reliability of our measurements and increased the effective cadence on each source. Although this original heuristic approach has been revised since then we still use the software infrastructure developed in 2009, which has proven to be flexible enough to accommodate new developments.

2.5 Calibration

To obtain precise flux density measurements for the sources we need to perform a number of calibrations aimed at characterizing the behavior of the telescope under different operating conditions. Most of these have been described in Richards et al. (2011) and Richards (2012) so here we only include some points that were not included in that discussion and of which I was the principal responsible. Appendix B includes a summary of the results of these calibration runs until mid 2012.

2.5.1 Pointing

Around December 2008 it became clear that a systematic problem regarding the pointing model corrections was affecting many of our light curves. After some tests we showed that pointing corrections were only valid for a period of about one hour and in a sky region of about 25° in diameter. Figure 2.8 shows the difference between pointing corrections measured at different sky positions and separated by less than one hour as a function of angular distance. The scatter in the measurements is much larger for angular distances of more than 20°; this degrades the repeatability of the observations by reducing the flux density as a result of pointing errors. The same is true, but not shown, if measurements separated by more than an hour are included.

Pointing errors translate directly into a systematic flux density error. An approximate idea of how this affects the data can be obtained by looking at Figure 2.9, which shows the range of the correction factor assuming a Gaussian main beam with a FWHM of 157″. The figure shows that pointing model corrections taken at large separations in the sky differ and can produce dramatic drops in the measured flux density. For example for angular distances larger than 20° a large fraction of the time we got flux density drops larger than 5% which is at the limit of what is acceptable for our monitoring program.

This experiment shows that the pointing corrections are local and time varying. This error is not correctable in the data reduction stage so the only way to reduce it is by limiting the distance between measurements of the pointing model corrections and flux density measurements as explained in Section 2.4.

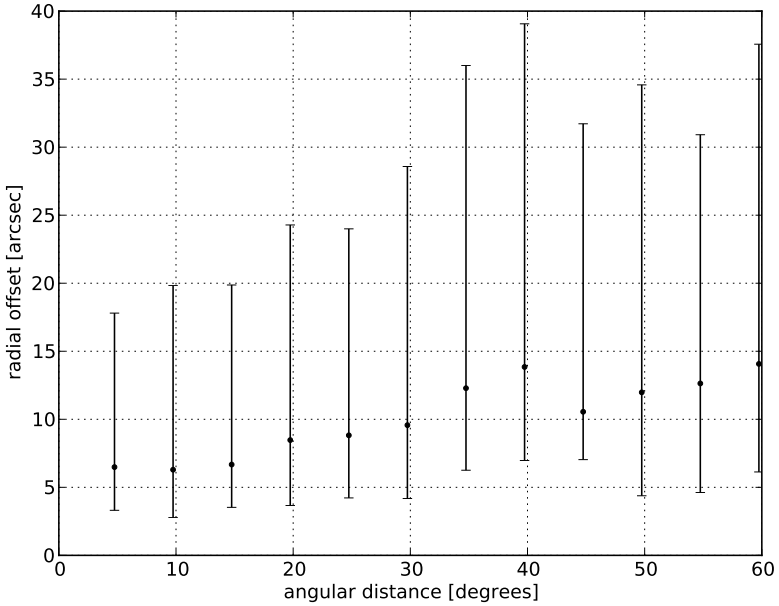

Figure 2.8: Difference between pointing model corrections as a function of angular distance. All the measurements have been taken within an hour of each other. A larger scatter is found for larger angular distances between corrections; this directly affects the repeatability of the flux density observations.

2.5.2 Focus curve model

The 40 meter telescope antenna has been optimized at a zenith angle of about 40°. As the telescope is moved to different zenith angles gravitational forces deform the telescope changing the position of the focus and the antenna gain (see Section 2.5.3). The optimal focus position can be determined experimentally by measuring strong point sources at different focus positions and finding the one that maximizes the antenna gain. In theory, the focus position should only depend on the zenith angle so the original procedure used to characterize the focus curve was to measure a source from rise to set, and fitting a second order polynomial to find the optimum focus position. By using this procedure on multiple sources at different times of the day, we discovered in May 2008 that there was a clear difference between focus curve measurements taken at day and night. Understanding the effect using the current methodology was not possible so a new approach was devised in which we selected a large number of calibration sources that covered different portions of the sky in horizontal coordinates. With this approach we were able to study the dependence

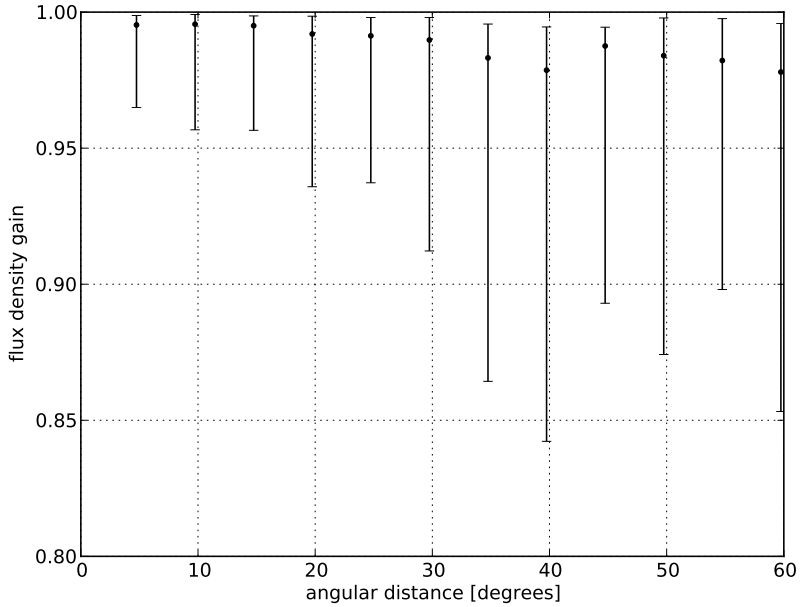

Figure 2.9: The conversion between pointing errors and flux density error can be approximated by the normalized beam pattern which in this case is assumed Gaussian with a FWHM of 157″. For angular distances larger than 20° the flux density drop is larger than 5% for a large fraction of the cases.

of the focus model on a number of other variables. Using this new approach and a more complete model we were able to explain most of the variability and to reduce the residuals by adding new terms for the angle between the Sun and astronomical source (elongation) and the zenith angle of the Sun (we added a linear and quadratic term in each case). The results of an example fit are shown in Figure 2.10 for the model using only the zenith angle and in Figure 2.11 for the complete model. In both figures the upper panel shows the measured position of the optimum focus as a function of the zenith angle, while the lower panel shows the distribution of residuals for a number of variables of interest. Correlations in the residuals for the model using only the zenith angle are evident (Figure 2.10), but these are not present in the model including the terms for the Sun zenith angle and elongation (Figure 2.11). The mathematical expressions for the models with their coefficients for different epochs can be found in Appendix B.

The model implemented in the *MCS control system* is still the simple one and the complete model is incorporated as a correction which is applied during the data reduction.

This was a necessity at the time we first developed the new model, because we were unable to incorporate the correction online using the original *VAX control system*.

The model for the correction is obtained using data from individual focus curve measurements in which we test a number of different focus positions and fit a quadratic model that uses the focus position of maximum gain as the optimum value. We can normalize all the measurements by the model fit and offset the focus positions relative to the optimum focus. In this way all the focus tests can be fitted simultaneously and the dependence of gain as a function of focus error with respect to the optimum can be obtained as shown in Figure 2.12. The focus model and the focus correction model are regularly fitted and it was found that the focus correction model is not epoch dependent while the focus model itself is. The mathematical expression of the focus model correction and its coefficients are included in Appendix B.

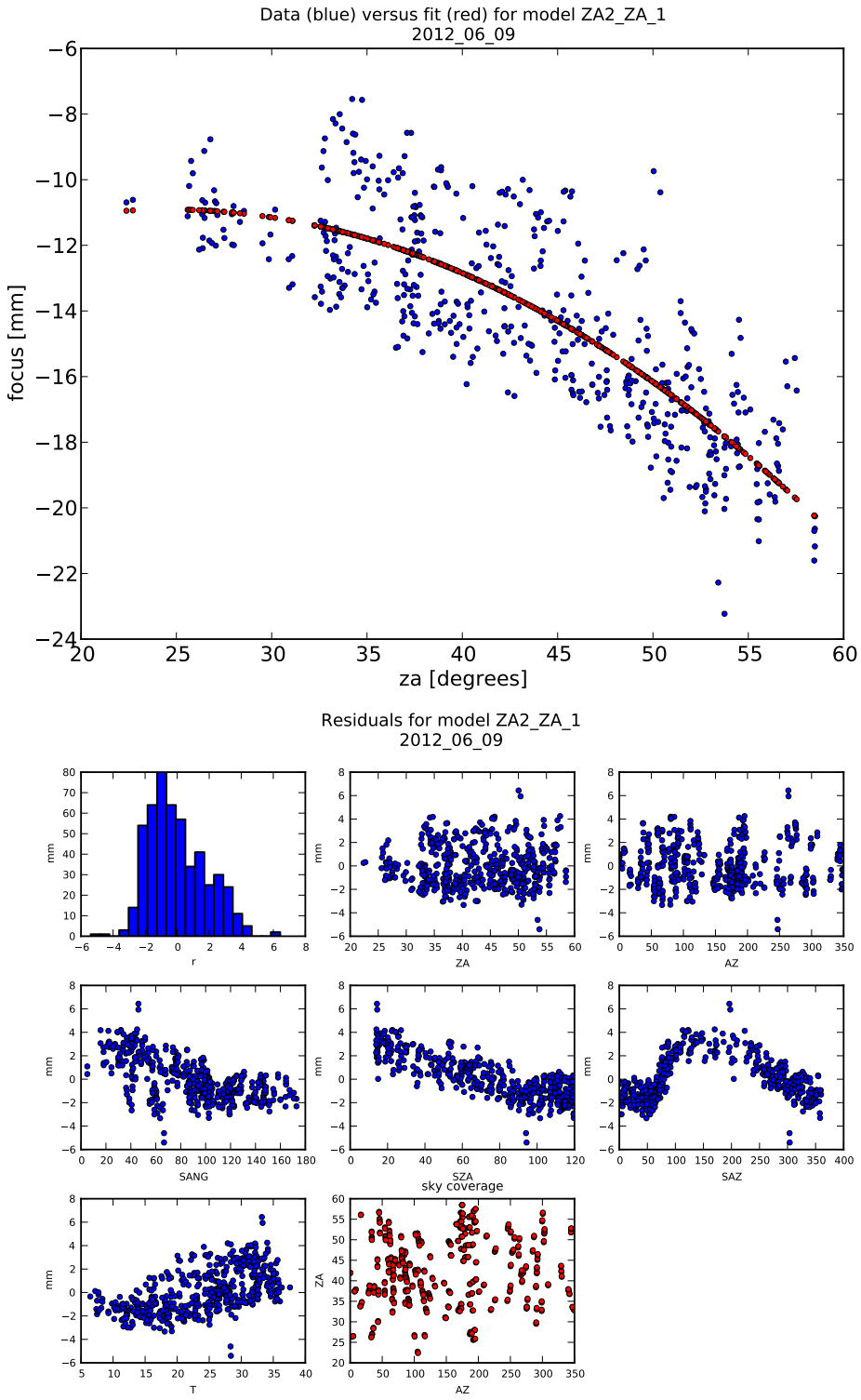

Figure 2.10: Example of a focus curve model fit with the simple model. The upper panel is the measured optimum focus position as a function of zenith angle in blue and the value predicted by the model fitting in red. The lower panel show a histogram of the residuals (upper left) and their distribution as a function of various variables of interest. Correlations are evident with the solar elongation (SANG), the Sun zenith angle (SZA), the Sun azimuth (SAZ) and the ambient temperature (T).

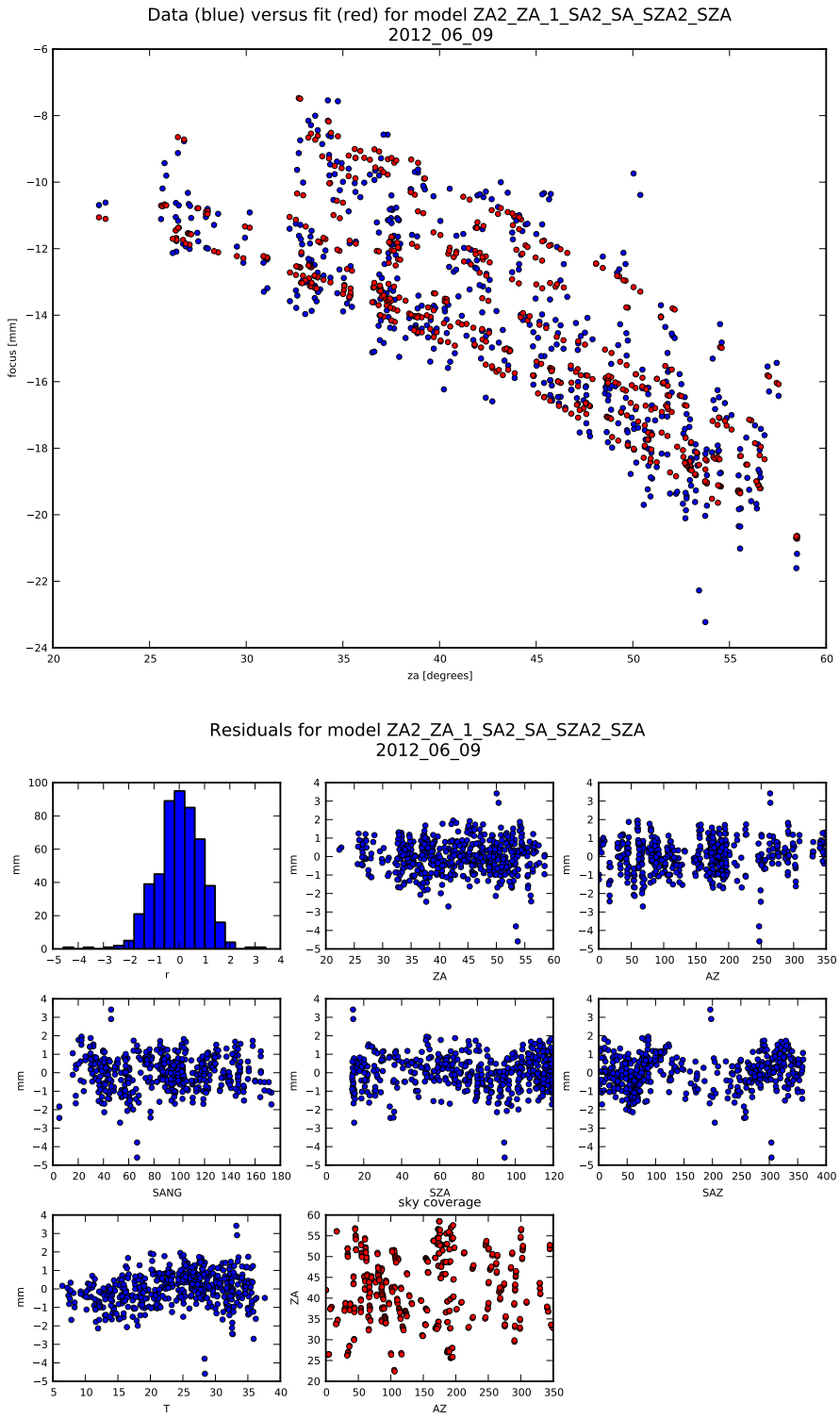

Figure 2.11: Example of a focus curve model fit with the complete model. The upper panel is the measured optimum focus position as a function of zenith angle in blue and the value predicted by the model fitting in red. The lower panel show a histogram of the residuals (upper left) and their distribution as a function of various variables of interest. Correlations are smaller than in Figure 2.10.

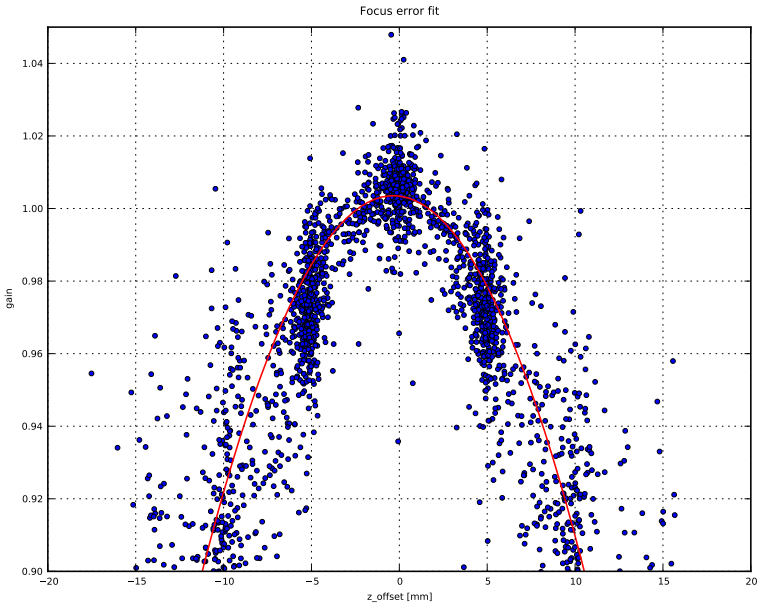

Figure 2.12: Example of a focus curve error model data and fit. The horizontal axis is the offset from the tried focus position with respect to the fitted best position for all the trials of the focus curve measurements. The vertical axis is the normalized gain of the telescope, in which the normalization is with respect to a quadratic model to the focus curve data. The red line is the best quadratic fit which is used to describe the effect of out-of-focus observations.

2.5.3 Gain curve

As described in Section 2.5.2, changes in antenna zenith angle deform the telescope, modifying the antenna gain. This change is characterized by measuring a calibration source at different elevations in the range in which observations are to be performed. A gain curve measurement is obtained by tracking the source from rise to set while doing frequent noise diode calibration, pointing model correction measurements, optimum focus corrections and flux density measurements. In this way we can obtain the effective telescope gain at different elevations. An example data and gain curve from November 2011 is shown in Figure 2.13.

Periodic gain curve measurements have shown that no big changes in the model occur except after major maintenance when the receiver has been taken down from the prime focus. Given this as general practice we characterize the gain curve at least twice a year

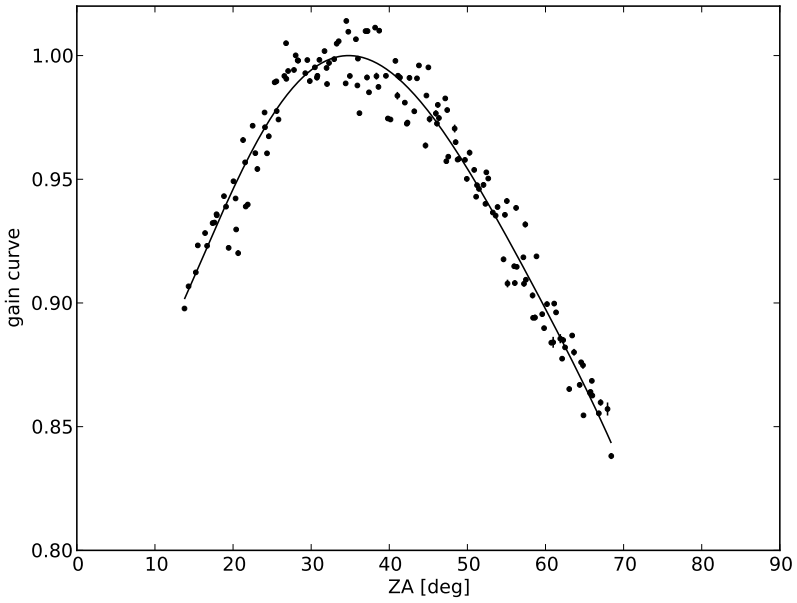

Figure 2.13: Example of a gain curve data and fit with the units normalized to the peak of the fit. These data were taken on November 1, 2011.

and every time the receiver is moved out of the prime focus. The coefficients of the gain curve for different epochs are included in Appendix B.

2.5.4 Effect of the varying atmospheric opacity at 15 GHz

Flux density measurements have to be corrected for the effects of the atmosphere which can be modeled by using the equation of radiative transfer in terms of temperatures for the Rayleigh-Jeans limit,

$$T_{\rm A}(za) = T_{\rm rx} + T_{\rm ground} + T_{\rm sky} e^{-\tau \sec(za)} + T_{\rm atm}(1 - e^{-\tau \sec(za)}) \tag{2.3}$$

Where $T_{\rm A}$ is the antenna temperature, $T_{\rm rx}$ is the receiver temperature which can be determined with a hot/cold test and is about 30 K, $T_{\rm sky} = 2.75$ is approximated by the CMB temperature, $T_{\rm atm}$ is the effective atmospheric temperature and τ is the atmospheric opacity at zenith. In the limit of low atmospheric opacity τ, we can expand the exponential

terms to get,

$$T_{\rm A}(\sec(za)) = T_{\rm rx} + T_{\rm ground} + T_{\rm sky} + (T_{\rm atm} - T_{\rm sky})\tau \sec(za) \tag{2.4}$$

This equation is linear in $\sec(za)$ so the parameters can be estimated by a linear fit. For the temperature of the atmosphere we use a value of $T_{\rm atm} = 270$ K. This is justified by Serabyn et al. (1998) who, using a detailed analysis, find that $T_{\rm atm} \approx T_{\rm air\,at\,ground} - 11.2$ K in the low atmospheric opacity limit. Assuming an average temperature 283.15 K for OVRO we can reasonably assume $T_{\rm atm} \approx 270$ K.

Skydip measurements are performed during every calibration run and they indicate a low atmospheric opacity of about $\tau \approx 0.02$ under typical observing conditions. The atmospheric opacity has two effects in the observations, one is an increased noise due to the emission of the atmosphere and the other is an attenuation of the flux density of the source. The attenuation is equal to $e^{-\tau \sec(za)}$ and has a value of 0.972 at zenith angle of 45°. This small 3% reduction in flux density is calibrated by the gain curve which along with the effects of the deformation of the telescope also accounts for the varying atmospheric opacity with elevation. This is a good assumption as long as the atmospheric opacity does not change from day to day, in which case there will be some residual correction due to the different atmospheric conditions at which the gain curve was measured. Regular skydips obtained during each calibration run show small changes in the atmospheric opacity and are not very useful for estimating variations on shorter time scales. Unfortunately skydips are costly in telescope time and would add a significant overhead to the monitoring observations so we wanted to verify that they were not necessary using only historic data from our monitoring program. With this goal we studied the effects of the varying atmospheric opacity at 15 GHz by producing synthetic skydips that take advantage of our monitoring observations to obtain average atmospheric properties. These were obtained by using the total power signal from one the channels for the beam that was looking at the reference field while the telescope performed noise diode measurements. In this study we used data from 12 June 2007 through 27 September 2009, and only days in which we have at least 20 data points are used. Figure 2.14 shows the variation of the atmospheric opacity at zenith for this period. Its mean value is 0.023 and its scatter is about 40%. More important than the value of the atmospheric opacity are the effects of variations on the calibrated flux

densities. In the absence of atmospheric opacity variations we can remove all the effect by just applying the gain curve, but this is not true if the atmospheric opacity varies. The effects of a varying atmospheric opacity are explored by computing the correction from a median value of the atmospheric opacity versus the daily values for a flux density measured at 45° zenith angle. Figure 2.15 shows that the effect of atmospheric opacity variations in calibrated flux densities at 45° is only a 1% effect. Similar computations at 20° show an even smaller effect while at 70° its value is very close to 3%.

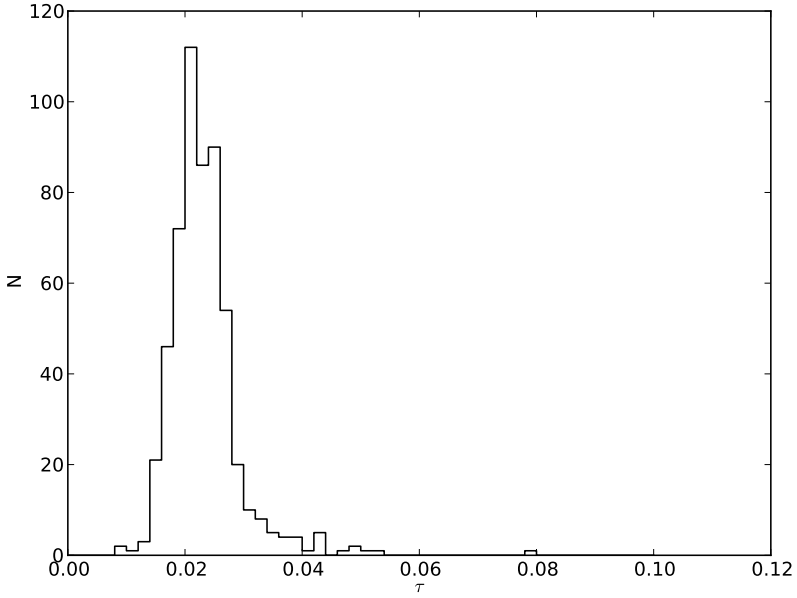

Figure 2.14: Daily averaged atmospheric opacity variations from 12 June 2007 through 27 September 2009. The distribution can be described by $\tau = 0.023 \pm 0.0097$.

2.6 Data reduction

The data reduction is performed using custom software developed by Joseph Richards as part of his Ph.D. thesis (Richards, 2012). The main steps involved in the data reduction are presented in Richards et al. (2011) and Richards (2012); here we only describe the main ideas and steps behind the production of radio light curves. This task was performed by Joseph Richards from the beginning of the program until September 2011 when Talvikki Hovatta took over responsibility for this task.

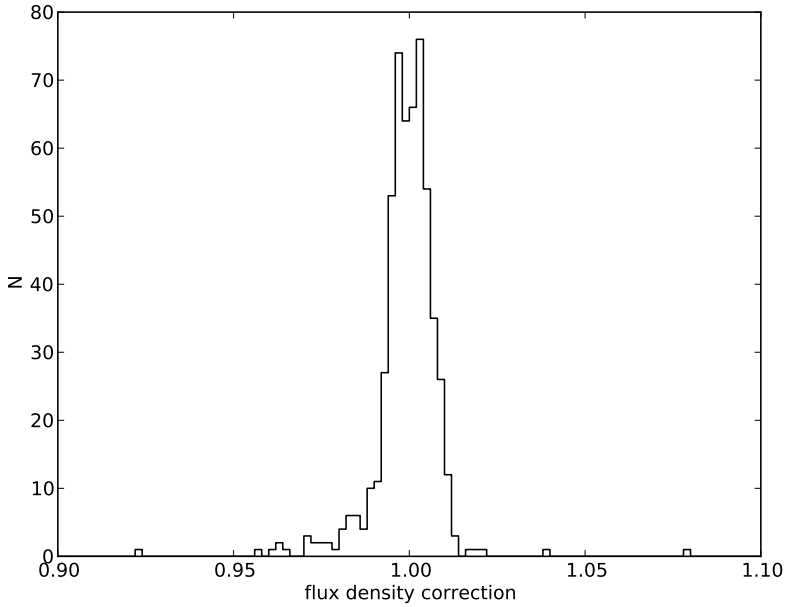

Figure 2.15: Variations in the calibrated flux density at 45° zenith angle due to atmospheric opacity variations shown in Figure 2.14. The magnitude of the corrections is described by $f = 0.999 \pm 0.013$, which is a 1% effect.

The data reduction pipeline is divided into three levels, a *low-level* that converts the data set saved by the control system into flux densities, calibrator noise fluxes and pointing procedures. This level is different for the two control systems (*VAX control system* and *MCS control system*). The results are saved to a reduction database for further processing. The next two levels are *high-level* processing of the data and take care of gain curve and focus corrections, error model, data editing and filtering and flux density calibration.

In what follows we describe the general steps that take us from the uncalibrated flux densities in digital units to the calibrated flux densities we use to study the behavior of astronomical sources.

2.6.1 Data editing and flagging

Some fraction of our data get corrupted by various systematic effects. These data are removed with a combination of manual and automatic procedures briefly described below.

Wind High winds degrade pointing and tracking, systematically reducing the measured flux densities. Periods with average wind speed above 6.7 m s^{-1} (15 mph) are dis-

carded.

Sun and Moon Observations with solar or lunar elongations less than 10° are discarded to avoid additional flux contamination through the sidelobes of the antenna pattern.

Pointing failure Observations with failed pointing offset measurements, or with offsets measured more than 4800 s from the flux density measurements are discarded.

Calibration failure Only observations for which there are at least 2 successful calibration diode measurements within a 2 hour period and in which the difference between the smaller and larger calibration diode is less than 10% are retained, all the rest are discarded.

Saturation or total power anomalies Observations that indicate saturation or other total power anomalies are rejected. Heavy cloud cover or precipitation often causes large fluctuations in total power. Such periods are identified by inspection of the total power time series and manually discarded.

Measured uncertainty We reject flux density measurements with anomalously large measured uncertainties. Since the flux density error has components that are dependent on the source flux (e.g., tracking and pointing errors) a simple cut will be biased against larger flux densities. To avoid this bias we use a flux density-dependent threshold (Richards et al., 2011).

Switched difference The switched difference, defined as $\mu = \frac{\kappa}{4}(\xi_{\rm C} + \xi_{\rm D} - \xi_{\rm A} - \xi_{\rm B})$ (see Section 2.3.1 for definitions of these quantities), should be zero in the absence of gain and atmospheric variations. Deviations of this quantity from zero can be used to determine problematic measurements. A flux density-dependent threshold that avoids a bias against large flux densities is used (Richards et al., 2011).

2.6.2 Relative calibration

Slow gain variations of the receiver are corrected by using a noise diode with power level similar to astronomical sources (see Figure 2.3 for a receiver schematics). The noise diode is measured immediately after pointing corrections with a typical interval between measurements of less than one hour. The calibration factor is the average of all the measurements obtained in a 2 hour window centered on a given flux density measurement.

Variations of the telescope gain due to deformation of the ideal parabolic shape for different elevations are characterized by the gain curve (Section 2.5.3) and the correction is also applied in this stage. Likewise, corrections to the focus position are done online based on the focus model (Section 2.5.2). The online model only includes the variation related to different zenith angle. Further corrections to include the solar zenith angle and elongation as described in Section 2.5.2 are applied at this stage.

2.6.3 Absolute calibration

We divide our observation period into epochs characterized by a consistent ratio between the calibration diode and feed horn inputs to the receiver. This ratio might change if, for example, the signal path is disconnected and reconnected for maintenance, resulting in a slight change in loss along one path. Within a single epoch, the ratio of the calibration diode signal to a stable astronomical source should therefore be constant. For each epoch, a calibration factor is determined from regular observations of the primary calibrator, 3C 286. We adopt the spectral model and coefficients from Baars et al. (1977). At our 15 GHz center frequency, this yields 3.44 Jy, with a quoted absolute uncertainty of about 5%.

2.6.4 Uncertainties in individual flux density measurements

The system noise which includes contributions from the receiver and atmosphere introduces a thermal error component into our flux density measurements. Besides this there are a number of other possible sources of errors that are not accounted for by σ in Equation 2.1. Among possible sources of additional uncertainty are the weather and atmosphere, pointing and focus errors. An error model is used to consider those additional components

$$\sigma^2_{\mathrm{total}} = \sigma^2 + (\epsilon \cdot S)^2 + (\eta \cdot \psi)^2 \tag{2.5}$$

This is an extension of the model used by Angelakis et al. (2009). The first term is the scatter measured during the flux density measurement. The second one is proportional to the flux density of the source and includes contributions which are multiplicative like pointing and tracking errors and variations of the atmospheric opacity. The third term is proportional to the switch difference $\psi = \frac{\kappa}{4}(\xi_{\mathrm{B}} + \xi_{\mathrm{D}} - \xi_{\mathrm{A}} - \xi_{\mathrm{C}})$ which accounts for systematic effects that cause the A-B segment of the flux density measurement to differ from the C-D

segment, such as a pointing offset between the A and D segments, or some rapidly varying weather conditions.

The error model requires a determination of two parameters, ϵ and η. The value of ϵ is the contribution from pointing errors and could be different for pointing calibrators and the rest of the sources. The values of the parameters are determined using the set of stable flux density calibrators to represent the pointing sources and a set of 100 sources with slow variability to represent the rest of the program sources. Ideally we would use non-varying sources but all the sources in our monitoring program present some slow trends that are removed by low order polynomials assumed to account for slow intrinsic source variability (see Richards et al., 2011, for details).

Long-term Trends in 3C 286, 3C 274, and DR 21 A coherent long term trend at 1% to 2% level is observed in these sources. We combine the flux densities from these three sources by normalizing with the median and fit a cubic spline to model the common trend. This trend is then removed from the sources leaving a 1% systematic residual variation. The corresponding correction is applied to all the other sources in our program.

2.7 Scaling of the non-thermal error[6]

The reported error for each flux density measurement has two qualitatively different components as described in Section 2.6.4. The first component is directly obtained during the flux density measurement and it represents random errors such as thermal noise and rapid atmospheric fluctuations, while the second is introduced to take into account flux-density-dependent effects. This error model requires the determination of two constant factors, ϵ and η, which are assumed to be source independent. However, after applying these corrections with the values of ϵ and η that we had derived for our sample, we found that there were many cases in which the data points lay much closer to a low-order polynomial fit to the data than expected from the size of the errors bars – i.e., the value of χ^2 per degree of freedom was significantly less than unity. This is a clear indication that in certain cases the simple assumption of source-independent ϵ and η resulted in overestimated errors.

To correct these constant scale factors on a source-by-source basis, we have used cubic

[6]A version of this section has been published in the *Astrophysical Journal Supplement Series* (Richards et al., 2011). It is reproduced here with permission from AAS.

spline fits and required the χ^2 per degree of freedom to be one for the residuals. Due to the large number of sources and the requirement of a uniform and consistent method for all the sources, an automatic method was developed for this procedure. For each source we can in principle use a range of number of polynomial sections to construct a spline fit. We construct a spline fit for each possible number of polynomial sections[7]. An outlier rejection filter which uses a cubic spline fit with a small number of knots is used to fit the light curve. Points with absolute residuals above the 95% percentile are not used for the following stage of the fitting procedure. Not all the fits are acceptable, as some cases will have correlated residuals or a large departure from normality. Acceptable fits are selected by using two statistical tests: Lilliefors test for normality (Lilliefors, 1967) and the runs test for randomness (e.g., Wall et al., 2003).[8] Only the fits for which both null hypotheses, normally distributed residuals for the Lilliefors test and non correlated residuals for the runs test, cannot be rejected at the 10^{-3} level are considered acceptable. For each acceptable fit, a scale factor that makes the χ^2 per degree of freedom equal to one is calculated. Among the scale factors for all the acceptable fits, the median scale factor is selected as the final correction. The value of the scale factor is not very sensitive to the exact number of polynomial sections. A typical example of the behavior of the scale factor is shown in Figure 2.16.

Note that we have only rescaled the non-thermal part of the errors (the ϵ and η terms in Equation 2.5), and only for those sources for which the resulting correction factor was smaller than one (i.e., the rescaling would result in smaller errors). The latter choice was made for two reasons. First, a correction factor larger than one simply indicates that the spline fit cannot provide an adequate description of the data. This may result from a light curve more variable than can be fitted by a spline with a given number of knots, so such a correction could mask real variability. Only the reverse is cause for concern – when the spline fit is too good a fit, given the quoted errors. Second, this choice ensures a smooth transition between scaled and non-scaled errors, as the transition point (correction factor equal to one) is equivalent to no error scaling.

[7]We use the MATLAB Spline Toolbox function spap2, which automatically selects the positions of the knots for the spline.

[8]We have used the implementations of both tests that are part of the MATLAB Statistics Toolbox.

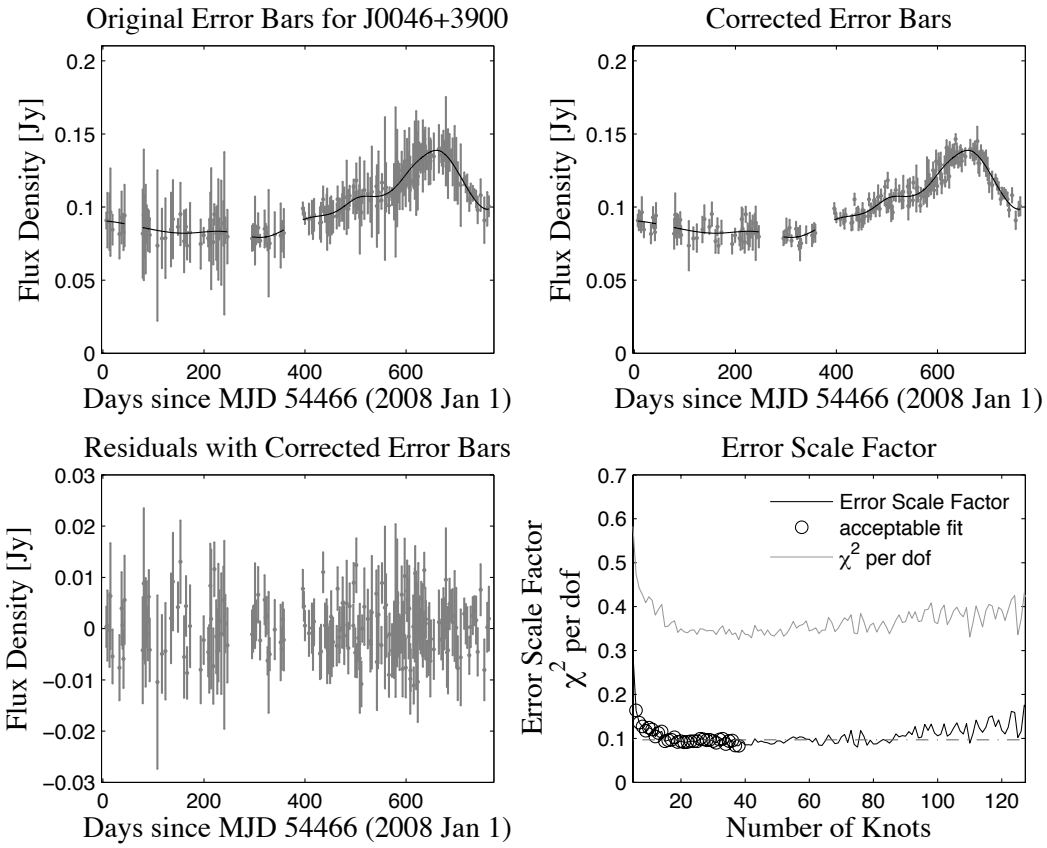

Figure 2.16: Example of the error bar scale factor correction for J0046+3900. The two upper panels show the light curve with the original (left) and corrected (right) error bars (gray points) and a typical spline fit (black line). The bottom left panel shows the residuals from the spline fit using the corrected error bars. In the bottom right panel, the χ^2 per degrees of freedom (solid gray line) and correction factor (solid black line) are shown, with black circles marking the correction factors for fits that pass the acceptance tests, and a dashed line showing the adopted correction factor for the source. Credit: Richards, J. L., et al. 2011, ApJS, 194, 29, reproduced by permission of the AAS.

2.7.1 Additional flagging of the light curves

All the data flagging described above is done with the raw data at the time of data reduction. None of it considers any model of the individual light curves to determine if a data point can be problematic. A visual inspection of the data shows that some of the radio light curves have extreme outliers that were not filtered out by the reduction pipeline. Most of these are extremely low points that appear in isolation, while others correspond to extremely high flux densities or have error bars of large magnitude compared to typical measurements. Bad weather conditions, wind gusts and interference can produce this type of behavior, which

is not expected for the phenomenon under study. A series of additional filters have been applied to the data to reduce negative effects associated with these outliers. We are well aware that this type of filtering precludes the discovery of completely unexpected behavior, which could be due to real physical effects. For this reason we do plan to look at these instances individually in order to determine whether we have edited out data that might be of real interest. For example, it is possible that an extreme scattering event might reduce the flux density of a source for a short time – this would be extremely interesting. Likewise a transient source either associated with the blazar or simply in the same field could cause a sudden increase in flux density. We are now in a position to follow up such cases and we will be doing so in future.

The first filter eliminates measurements with the highest 2% error bars. Then a flux density outlier filter consistent of a moving filter which removes the lowest and highest flux densities in independent windows of 400 days. In some cases when this automatic procedure erroneously removes points in the peak of a flare, the data points have been restored manually for the sources in the cross-correlation sample. For the other sources, the results of the application of this filter have been checked and the most problematic cases have been handled by hand, either by restoring or deleting a few data points. An additional problem is caused by large gaps in the light curves. Although these can be handled without serious problems by the cross-correlation analysis (Chapter 5), they present a more serious problem for the analysis described in Chapter 3 and are thus removed from the light curves by keeping the largest "continuous" segment, where "continuous" means no gaps larger than 90 days.

2.7.2 Example radio light curves

A collection of example radio light curves is shown to illustrate the quality of the data and the variety of observed behaviors. The first two (Figures 2.17 and 2.18) are examples of the flux density calibrators 3C 286 and DR 21 which are also among the brightest sources. Figures 2.19 and 2.20 show two bright blazars with large variability in the radio band. Figures 2.21 and 2.22 show two sources with more typical flux densities of about a few hundred mJy. Even at this much lower flux density level it is possible to discern clearly the source variability and the observational noise. An example of one of the dimmest sources is included in Figure 2.23 where the noise level is comparable with the source flux. Figure

2.24 shows a source with high flux but low variability.

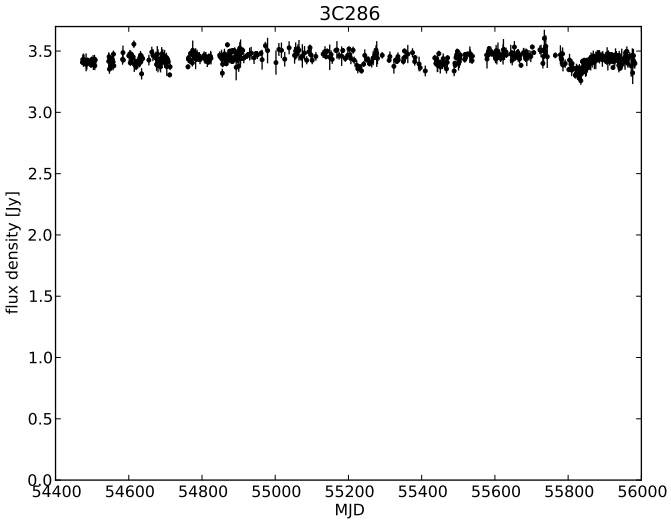

Figure 2.17: The primary flux density calibrator for the radio monitoring program 3C 286. Variations in the source measured flux density are expected from small atmospheric opacity variations and pointing errors. The flux density scale is set by assuming an average value for the 3C 286 flux density of 3.44 Jy (Baars et al., 1977) instead of assuming a strictly constant flux density (Richards et al., 2011).

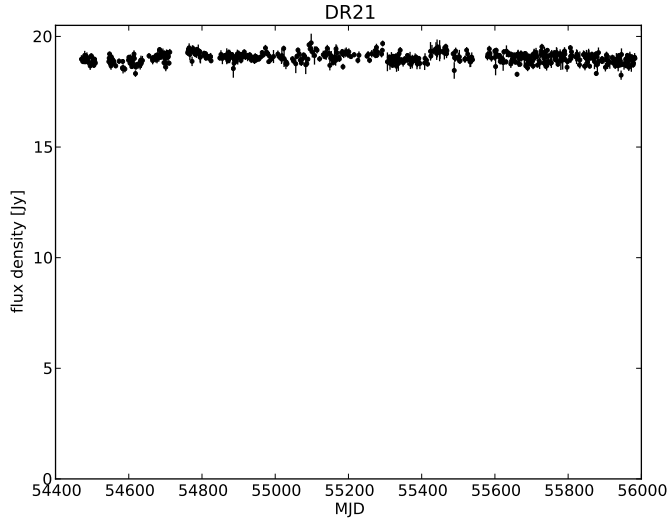

Figure 2.18: A secondary flux density calibrator for the radio monitoring program DR 21. This source is a large molecular cloud and star-forming region for which we do not expect variations at 15 GHz. A few low flux densities are observed possibly due to pointing errors or atmospheric opacity variations.

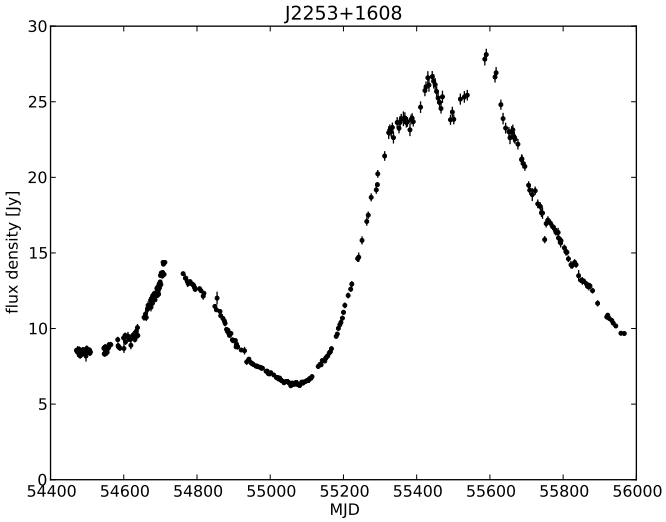

Figure 2.19: Radio light curve for a bright blazar 3C 454.3. The relatively low noise level of the flux density measurements compared to the average flux density of this object provides an excellent view of the source variability.

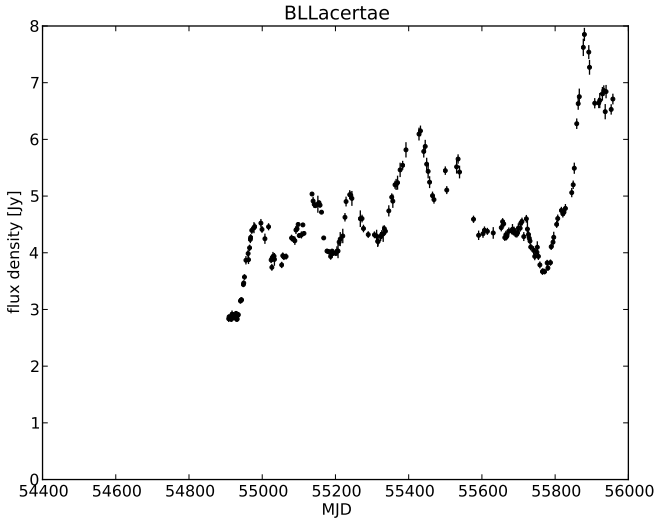

Figure 2.20: Radio light curve for a bright blazar BL Lac. The relatively low noise level of the flux density measurements compared to the average flux density of this object provides an excellent view of the source variability.

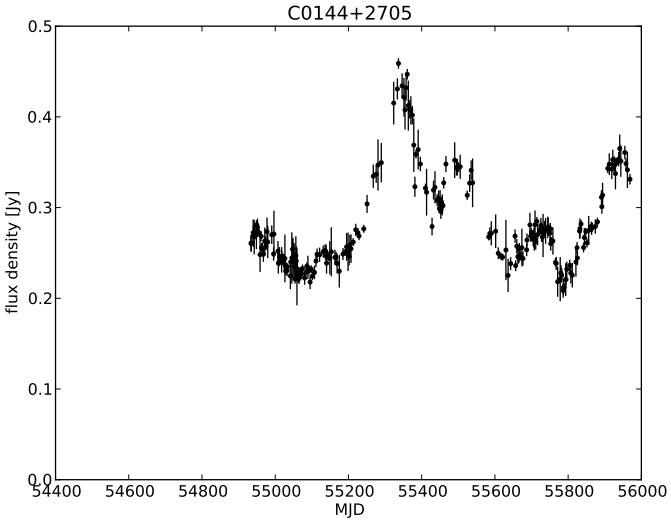

Figure 2.21: Radio light curve for a source with a typical flux density of about 300 mJy, close to the median of the sample. Even at this lower flux density level, source variability is clearly observable.

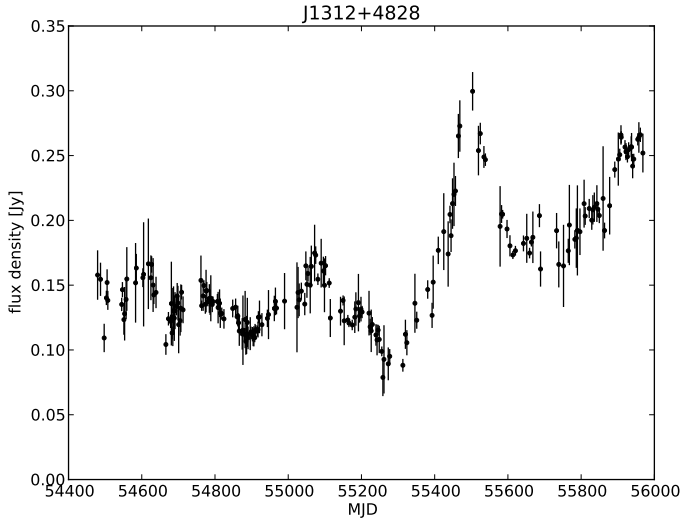

Figure 2.22: Radio light curve for a source with a typical flux density of about 200 mJy, slightly below the median of the sample. Even at this lower flux density level, source variability is clearly observable.

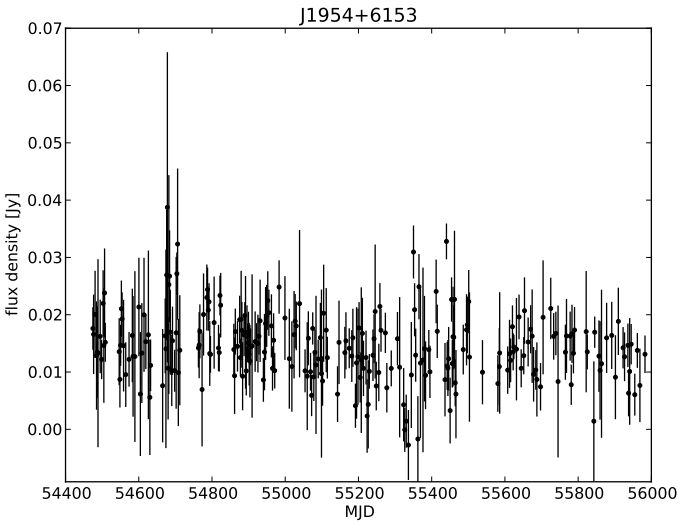

Figure 2.23: Radio light curve for a source with a flux density of about 15 mJy, which is among the dimmest sources in the sample.

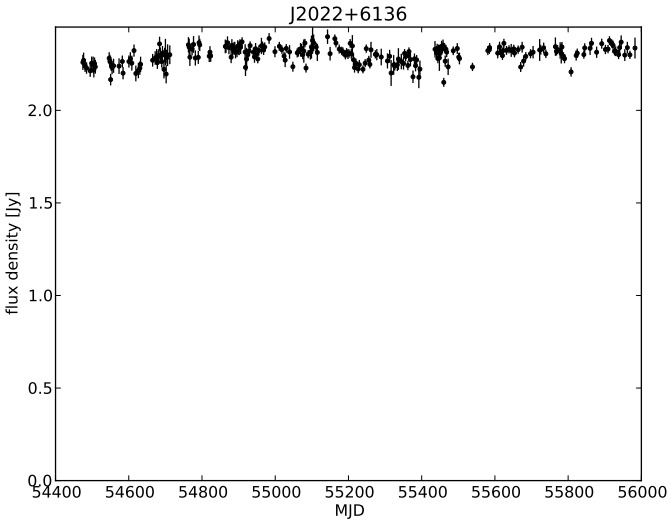

Figure 2.24: Radio light curve for a source with high flux density and low variability. A fraction of our sources show low levels of variability like this one.

2.8 Observations with *Fermi*-LAT

Besides our main effort running the monitoring program we also need to produce gamma-ray light curves for the monitored sources. This is in principle possible for any source as most of the time *Fermi* operates in scanning mode, covering the whole sky in about 3 hours, thus providing a quasi-continuous monitoring of the whole gamma-ray sky. A given source can be observed by integrating its photons for any desired period, with the brightest sources being observable in daily or shorter time bins when in periods of high activity, while dimmer sources require longer integrations. Weekly integrations are well matched to the cadence of the radio monitoring program and allow us to get a reasonable number of sources which are detected on this time scale. This relatively fast gamma-ray cadence limits our studies to only the brightest 86 blazars (see Section 2.9 for a description of the sample), for which higher quality light curves can be obtained. In the future we plan to extend our studies to dimmer gamma-ray sources which will require longer integrations.

In this section we describe the basic characteristics of the Large Area Telescope (LAT) and the *Fermi Gamma-ray Space Telescope* (*Fermi*), followed by a brief description of the basic data products delivered by the *Fermi*-LAT collaboration that are the basis for this and other studies of blazars at gamma-ray energies. All the *Fermi* data are made public along with the software tools necessary to convert the raw photon data into the most common data products. It is by using these tools that we produce the gamma-ray light curves used in this study. A brief description of the main ideas used in the production of gamma-ray light curves from the raw photon data is provided, along with some technical details on the analysis parameters used to produce the gamma-ray light curves. These gamma-ray light curves were produced by Talvikki Hovatta who had previous experience working with the data reduction software. I provided some input on the required cadence, number of sources and characteristics of the analysis. In order to do that I had to familiarize myself with the data reduction procedures and performed a couple of test light curve analyses that are not used in this work. We end this section by presenting a few examples of the gamma-ray light curves.

2.8.1 The Fermi Gamma-ray Space Telescope

The *Fermi Gamma-ray Space Telescope* was launched by NASA on 11 June 2008 as the *Gamma-ray Large Area Space Telescope* (GLAST) to an orbit of about 565 km with an inclination of 25.°5 and an orbital period of about 96 minutes. It carries two science instruments, the Large Area Telescope (LAT) and the Gamma-ray Burst Monitor (GBM). The LAT is a pair-conversion telescope designed to measure the directions, energies (from 20 MeV to 300 GeV) and arrival times of gamma-ray photons over a large field of view, while rejecting a large background of cosmic rays. A brief description of its main components and working principle is given in Section 2.8.1.1, based on Atwood et al. (2009) where additional details can be found. The GBM detects and measures the prompt emission from Gamma-Ray Bursts in a broad energy band (from 8 keV to 40MeV) over the full sky not occulted by the Earth and notifies the LAT and ground observers. A catalog of the sources it detected during the first two years of operation and details on the instrument can be found in Paciesas et al. (2012) and references therein.

In order to take full advantage of the LAT large field of view, *Fermi* operates primarily in scanning survey mode in which the telescope is pointed north and south of zenith in alternate orbits. As a result, after two orbits, about 3 hours, an almost uniform sky exposure is obtained. The rocking angle about zenith was 35° until July 2009, then it was 39° and it was finally set to 50° in September 2009 in order to lower the temperature of the spacecraft batteries and extend their lifetime (Nolan et al., 2012).

2.8.1.1 Large Area Telescope

The LAT detects gamma-ray photons by the pair-conversion mechanism in which a high-energy photon produces an electron-positron pair by interacting with a nucleus of high atomic number. The pair production and tracking of the resulting electron and positron occurs in the *converter-tracker* which is composed of 16 planes of tungsten converter material. These converter planes are interleaved with position-sensitive silicon-strip detectors (a total of 18 (x, y) planes) that record the tracks of the charged particles and allow for a reconstruction of the incoming gamma-ray direction. After passing through the tracker the electron and positron hit the *calorimeter* made of an eight-layer array of CsI crystals which is responsible for measuring the energy deposited by the particles and the spatial

development of the electromagnetic shower which is used for background discrimination. The *converter-tracker* and *calorimeter* consist of a 4 × 4 array of 16 modules. A segmented *anti-coincidence detector* surrounding the tracker permits the rejection of an intense background of charged particles. Detection of gamma-rays is coordinated by an electronic data acquisition system that triggers when a gamma-ray is detected by the instrument and rejects background events, thus reducing the amount of data to be downloaded for further processing on the ground. Figure 2.25 shows a schematic representation of the LAT and the disposition of its main components while Table 2.1 contains a summary of its main parameters.

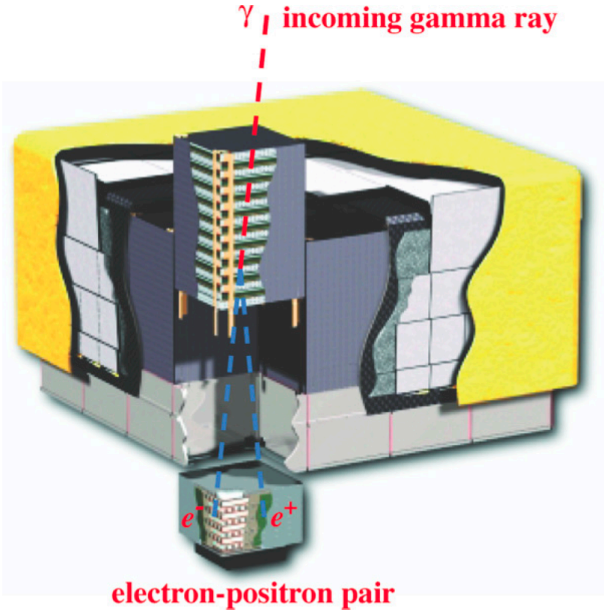

Figure 2.25: Schematic diagram of the LAT. Its dimensions are 1.8 m × 1.8 m × 0.72 m. It consist of a 4 × 4 array of 16 modules for the converter-tracker and calorimeter. An anti-coincidence detector covers the converter-tracker array. Credit: Atwood, W. B., et al. 2009, ApJ, 697, 1071, reproduced by permission of the AAS.

2.8.2 *Fermi* source catalogs

Source catalogs using the survey data have been produced by the *Fermi*-LAT collaboration. These catalogs include all the gamma-ray sources detected and also identifications with lower energy counterparts when possible. Three main catalogs of sources have been released to date, the LAT Bright Source List (0GFL, Abdo et al., 2009), the first *Fermi*-LAT catalog

Table 2.1: Summary of LAT instrument parameters

Parameter	Value or Range[a]
Energy range	20 MeV – 300 GeV
Effective area at normal incidence	6,500 cm^2 at 1 GeV
Energy resolution (equivalent Gaussian 1σ):	
100 MeV – 1 GeV (on-axis)	8% – 17%
1 GeV – 10 GeV (on-axis)	8%
10 GeV – 300 GeV (on-axis)	8% – 15%
Single photon angular resolution (space angle)	
on-axis, 68% containment radius:	
>10 GeV	$\leq 0.^\circ 3$
1 GeV	$0.^\circ 9$
100 MeV	6°
Field of View (FoV)	>2 sr
Timing accuracy[b]	< 10 μs
Event readout time (dead time)[b]	26.5 μs

[a] Values as reported in Fermi-LAT Collaboration (2012), except when indicated
`http://www.slac.stanford.edu/exp/glast/groups/canda/archive/pass7v6/lat_Performance.htm`

[b] These values are from Atwood et al. (2009).

(1FGL, Abdo et al., 2010) and the second *Fermi*-LAT catalog (2FGL, Nolan et al., 2012). These source catalogs are complemented by detailed studies of the blazars and other AGNs as reported in the LAT bright AGN sample (LBAS, Abdo et al., 2009), the first LAT AGN catalog (1LAC, Abdo et al., 2010) and the second LAT AGN catalog (2LAC, Ackermann et al., 2011). The Bright Source List and LAT bright AGN sample were based on the first three months of *Fermi* data, while the first and second year catalogs used 11 and 24 months of data respectively. Besides the additional amount of data, each subsequent iteration of the catalogs has benefited by improved understanding of the instrument and the methods used to analyze the data as is detailed in the references given above. For these reasons we use the source list reported in the second LAT AGN catalog when discussing gamma-ray detections and identifications with radio counterparts. A summary of the main findings of the second LAT AGN catalog which is commonly referred as 2LAC is given here for reference.

A total of 886 gamma-ray sources at high Galactic latitude ($|b| > 10°$) are included in the 2LAC Clean Sample which contains sources detected with high statistical significance and that are not affected by analysis issues like multiple associations, or drastic changes when different versions of the diffuse emission are used. These are divided among the different classes shown in Table 2.2 and Figure 2.26 shows their distribution in the sky along with a map of the integrated high energy emission as seen with the first two years of *Fermi* operations. In contrast 1LAC only contained 599 in the clean sample; the larger number of sources in 2LAC is not only explained by the availability of more data but also by refinements in the analysis, association methods and counterpart catalogs as described in Ackermann et al. (2011).

Besides this high Galactic latitude sample, 2LAC contains a sample of low Galactic latitude AGNs with 104 sources. Due to the difficulties of AGN studies at low latitudes, mainly contamination in the reference beams for our radio observations, these sources are not included in the 2LAC clean sample nor in our study of correlated variability.

The 95% error radius on the source localization is $0.^{\circ}01$ for one of the brightest[9] blazars 3C 454.3 and is about $0.^{\circ}2$ for sources just above the detection threshold. The limiting photon flux depends on Γ, the photon index[10], but it is about 10^{-9} ph cm^{-2} s^{-1} for the hardest sources with $\Gamma = 1.5$ and about 10^{-8} ph cm^{-2} s^{-1} for $\Gamma = 2.5$.

[9]Blazars are extremely variable so this statement is only valid within a given time frame

[10]Using a single power-law model for the photon flux density this is defined as $dN/dE = N_0(E/E_0)^{-\Gamma}$.

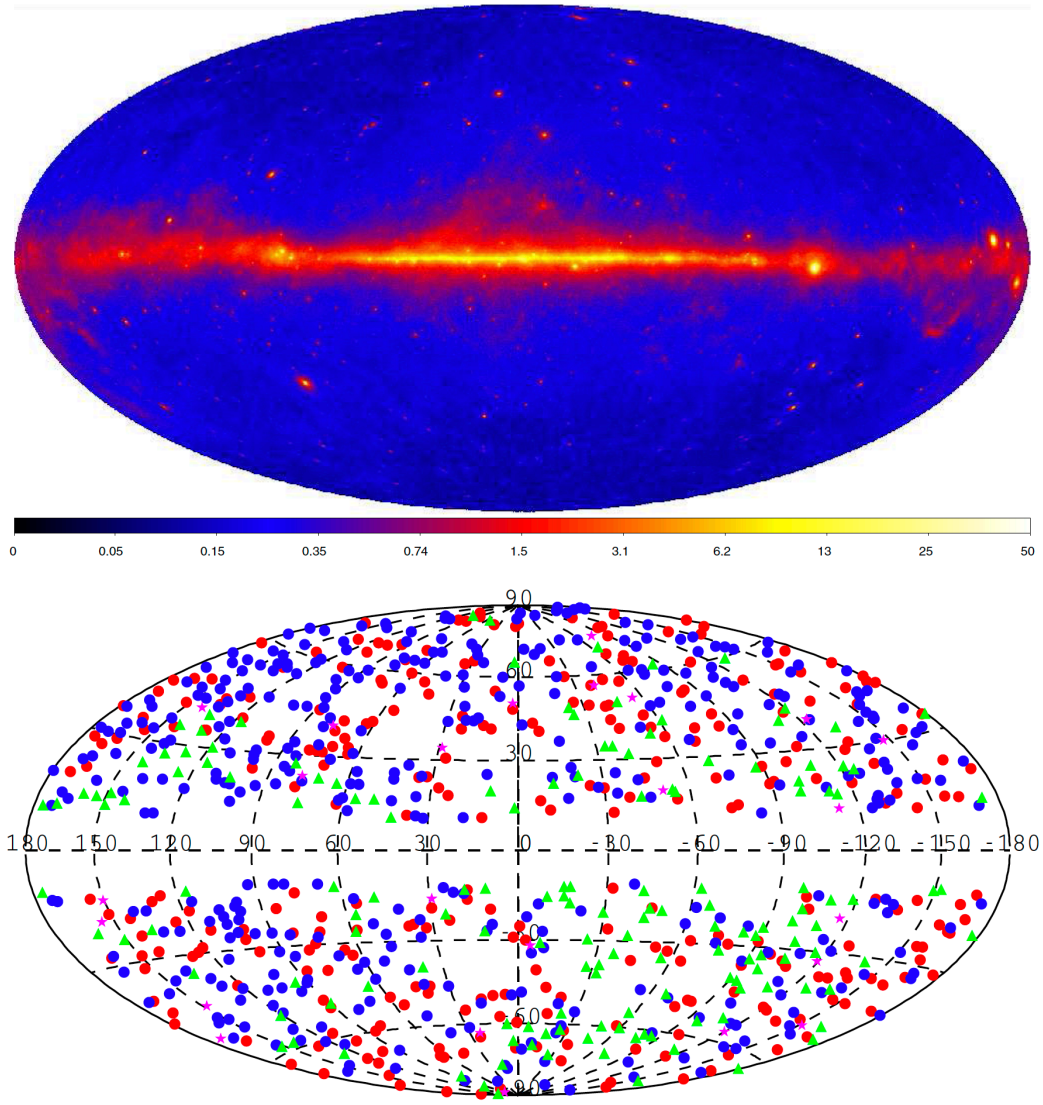

Figure 2.26: 2LAC sky map in Galactic coordinates for 24 months of observations (upper panel) and sources in the clean sample also in Galactic coordinates (lower panel). The upper panel shows the gamma-ray energy flux in units of 10^{-7} erg cm^{-2} s^{-1} sr^{-1}. The lower panel uses different colors to represent source classes. Red: FSRQs, blue: BL Lac objects, magenta: non-blazar AGNs, and green: AGNs of unknown type. The sky map is from Nolan et al. (2012) and source map from Ackermann et al. (2011). Credit: Nolan, P. L., et al. 2012, ApJS, 199, 31 and Ackermann, M., et al. 2011, ApJ, 743, 171, reproduced by permission from the AAS.

Table 2.2: 2LAC clean sample source class distribution from Ackermann et al. (2011)

Class	Number of sources
FSRQ	310
BL Lac	395
Blazar of unknown type	157
All blazars	862
Other AGNs	24
All AGNs	886

2.8.3 Producing gamma-ray light curves

Detailed information on the data products and software tools is provided by the *Fermi Science Support Center* (FSSC)[11]. Based on this online documentation, and other references when indicated, we provide an outline of the process with explanations for the most important concepts.

2.8.3.1 Obtaining data

The raw photon data can be obtained from the FSSC through a web interface,[12] and are usually available within hours of observations to facilitate time sensitive science. Besides the raw photon data, a few other high level products are provided. For example daily and weekly time-binned light curves for a list of monitored sources have been provided since the beginning of the mission. More recently aperture photometry light curves have been provided for the sources in the second year LAT catalog. All these products are intended to point out to interesting activity and trigger follow up studies. The raw data products consist of two data file types which are required for the science analysis. An *events file* type which contains the events detected by LAT and a *spacecraft file* type which contains position and orientation information in 30 second intervals for the telescope. There are two types of *event file*, *photon data* and *extended data*. For most purposes, including ours, only *photon data* are needed.

[11] http://fermi.gsfc.nasa.gov/ssc/

[12] `http://fermi.gsfc.nasa.gov/cgi-bin/ssc/LAT/LATDataQuery.cgi`

2.8.3.2 Source detection, flux determination and spectral modeling

The primary task required to build a light curve is to detect a source, determine its flux density and model its spectrum. The main idea behind the data reduction process is the use of a maximum likelihood technique that is described below.

The observations are modeled using the likelihood function and Poisson statistics required by the small number of photons. If we consider a data set binned in space and frequency the likelihood function has the form

$$\mathcal{L} = \prod_k \frac{m_k^{n_k} e^{-m_k}}{n_k!}, \tag{2.6}$$

where m_k is the expected number of counts in the k-th bin and n_k is the observed value. Each bin contains all the photons in an interval around the energy, sky position and time. This is the case for the binned likelihood which is only an approximation. If we reduce the bin size up to a point in which all bins have one or no photon ($n_k = 0$ or 1) we get into the regime of unbinned likelihood which is the most accurate. Since unbinned likelihood is more accurate it is always the first choice, but in practice as the number of counts gets larger the computational time becomes large and binned likelihood is sometimes the only option.

We are usually interested in detecting a source and quantifying the significance of the detection when compared to a model with no source and only background gamma-ray photons. For that purpose a *Test Statistic* (TS) is defined and often referred to when discussing *Fermi*-LAT results. The TS is

$$\mathrm{TS} = -2 \log \left(\frac{\mathcal{L}_{\mathrm{max},0}}{\mathcal{L}_{\mathrm{max},1}} \right) \tag{2.7}$$

where $\mathcal{L}_{\mathrm{max},0}$ is the maximum likelihood of a model with only background and no sources, while $\mathcal{L}_{\mathrm{max},1}$ is the maximum likelihood of a model with background and the source. This TS is larger when the likelihood of the model with the source is larger and is thus a measure of the significance of the source detection. For a large number of counts Wilks' theorem (Wilks, 1938) states that under the null hypothesis of no source, TS is distributed as χ^2_ν where the number of degrees of freedom, ν, is the number of parameters specifying the additional source. The probability distribution for TS is not exactly a χ^2_ν as Wilks' theorem

does not directly apply to the case of detecting a source on a background as explained in Protassov et al. (2002), but Monte Carlo studies can be used to characterize it in particular cases. In the case of testing a model source with known position on a background, it has been shown by Mattox et al. (1996) that TS is distributed as a $\chi^2_1/2$. The χ^2 distribution and the number of degrees of freedom are a consequence of Wilks' theorem, while the factor of 1/2 comes from the fact that only positive flux fluctuations are considered. Based on a generalization of this finding a useful rule of thumb is that the distribution of TS is $\chi^2_\nu/2$ where ν is the number of additional parameters specifying the source (e.g., flux, flux and spectral slope, etc).

For a given region a general form of a source and background model is given by

$$S(E,\hat{p},t) = \sum_i S_i(E,t)\delta(\hat{p}-\hat{p}_i) + S_{\rm G}(E,\hat{p}) + S_{\rm EG}(E,\hat{p}) + \sum_l S_l(E,\hat{p},t) \qquad (2.8)$$

where S is the number of photons per solid angle, area and time as a function of energy E, position in the sky $\hat{p}$ and time t. S_i is a point source at $\hat{p}_i$, $S_{\rm G}$ and $S_{\rm EG}$ are the Galactic and extra Galactic diffuse emission, and S_l are additional sources (e.g., the extended sources used for the construction of the second *Fermi*-LAT source catalog[13]).

In the analysis of blazars we are usually interested in obtaining a light curve for a source at a known position. The problem of finding the point sources and their positions is solved by comparing the likelihoods of model sources at different positions, but for our purposes we start from the results of the second *Fermi*-LAT source catalog and use the positions reported there. Besides positions, mean flux densities and spectral models for point sources, models for the Galactic, extra Galactic diffuse emission and other extended sources are provided by the *Fermi*-LAT collaboration and are used as the starting point for other analyses.

One last degree of freedom concerning point sources is the spectral model. For blazars a good fit can be obtained using a single power-law function ($dN/dE = N_0(E/E_0)^{-\Gamma}$) or a Log-Parabola function ($dN/dE = N_0(E/E_0)^{-\alpha-\beta\log(E/E0)}$) (Ackermann et al., 2011).

In order to use the model of the sky and the likelihood function with the *Fermi*-LAT observable, which is a list of photons with energy, direction and time of arrival whose properties have been modified by the detection process, a model of the instrument is needed.

[13] `http://fermi.gsfc.nasa.gov/ssc/data/access/lat/2yr_catalog/`

This model is encoded in the instrument response functions (IRFs) which are parameterized representations of the instrument performance. This accounts for the imperfect energy and position reconstruction and the efficiency of detections of gamma-rays reaching the instrument, and it is symbolized by $R(E', \hat{p}', t; E, \hat{p})$, where X represents the original value and X' the observed quantity. The observation is given by

$$M(E', \hat{p}', t) = \int_{\mathrm{SR}} dE d\hat{p} R(E', \hat{p}', t; E, \hat{p}) S(E, \hat{p}, t) \tag{2.9}$$

where $M(E', \hat{p}', t)$ is the number of photons per solid angle, area and time at energy E', from direction $\hat{p}'$ at time t. The integration is over the source region (SR), which contains all the sources that contribute flux to the region we are modeling.

A knowledge of the IRFs is essential to interpret and reconstruct the flux distribution of the source. In practice the IRF is separated into three components which account for different instrumental effects. These are the effective area, the point spread function and energy dispersion. At the start of the *Fermi* mission these were derived using Monte Carlo simulations of the instrument behavior. The currently used ones have been updated using flight data (Fermi-LAT Collaboration, 2012).

If we take the log of the likelihood and drop terms that are independent of the model parameters, we are left with the following log-likelihood to be maximized

$$\log(\mathcal{L}) = \sum n_k \log(m_k) - \sum m_k \tag{2.10}$$

The maximization can be computationally intensive but fortunately the data reduction software provided by the FSSC has all the tools required to obtain source flux densities and spectral models.

In cases when the significance of the flux density measurement is low, an upper limit can be obtained and reported instead. This is done using the profile likelihood method (Nolan et al., 2012; Rolke et al., 2005). Following the conventions of the *Fermi*-LAT collaboration 2σ upper limits are reported.

2.8.3.3 Technical details of the light curves

Hovatta has produced light curves with 7 day time bins from 4 August 2008 to 12 August 2011 for the 86 sources bright enough to be detected in a large number of weekly time bins.

We use an unbinned likelihood, with the positions and spectral models used for 2LAC. The data have been reduced using Fermi-LAT `ScienceTools-v9r23p1` using P7_V6 Source event selection and IRFs, diffuse models `gal_2yearp7v6_v0.fits` and `iso_p7v6source.txt`, and the standard data cuts and filters recommended by the FSSC. Photon integral flux densities for the band from 100 MeV to 200 GeV are reported when TS ≥ 4 and a 2σ upper limit when TS < 4. Some sources are near the ecliptic and have periods with significant contamination due to the Sun's gamma-ray emission which can affect the measured flux when it is closer than $2\overset{\circ}{.}5$ from the source. Although the Moon is similarly bright in gamma-rays the conjunctions are brief and do not affect the data (see Nolan et al., 2012, for a discussion). The affected time bins are eliminated for three sources in which this happens (J0238+1636, J1256−0547 and J2229−0832). Two examples of gamma-ray light curves are presented in Figure 2.27.

2.9 Source sample and basic properties of the light curves

For this study of correlated variability between the radio and gamma-ray band we use the radio data taken during a period of 4 years and two months of the blazar monitoring program from 1 January 2008 through the 26 February 2012. The gamma-ray band data covers a period of about 3 years from the start of the *Fermi*-LAT science mission in 4 August 2008 to 8 August 2011, with a time binning of 7 days. The overlap between the light curves is variable and depends on the date the particular source was added to the radio monitoring program. Only the brightest gamma-ray blazars are included.

Out of 1593 blazars in our radio monitoring program, 645 have been detected at gamma-rays and associated with high confidence with known sources as reported in the 2LAC catalog. Of those, 86 have gamma-ray light curves are bright enough to be detected in at least 75% of the monthly time bins as reported in Nolan et al. (2012) and we have used these for the cross-correlation study. Most of the monitored blazars not detected in gamma-rays come from the CGRaBS sample (Healey et al., 2008). A number of blazars have tentative associations with gamma-ray sources but do not make all the cuts to be included in the 2LAC clean sample. These are still being monitored but are not considered high confidence associations. Note that 39 of our monitored blazars were in the 1LAC clean sample but are not in the 2LAC clean sample, so that for this study they are considered to be non-gamma

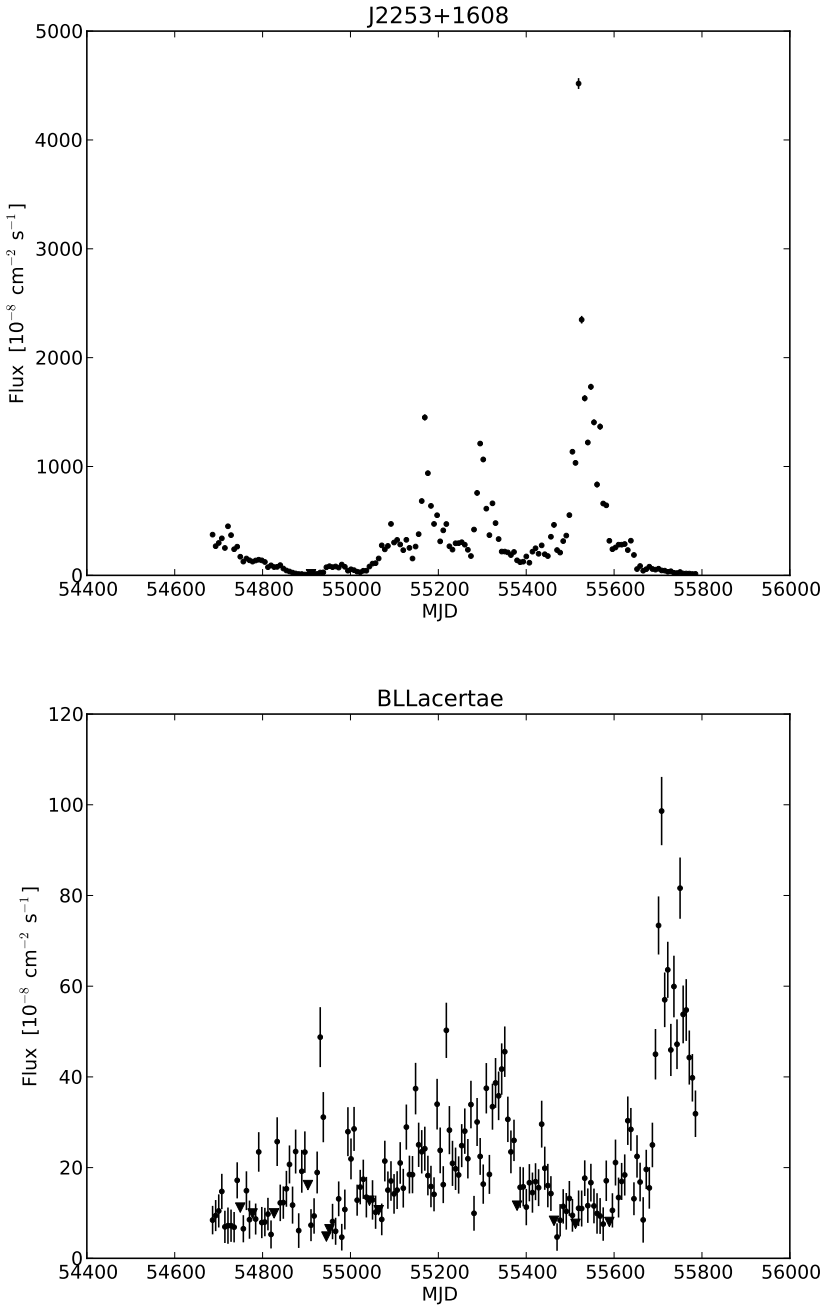

Figure 2.27: Gamma-ray light curves for 3C 454.3 and BL Lac. Black dots with error bars are time bins for which TS ≥ 4 and black downward pointing triangles 2σ upper limits for time bins with TS < 4.

ray detected blazars.

Figure 2.28 shows the distribution of time lengths for the radio light curves, the mean

sampling interval and number of data points. The sources are separated into two groups, those used for cross-correlation and all the rest. An equivalent summary for the gamma-ray light curves is not necessary as they form a more uniform set. They are sampled at a regular interval and each have 158 data points. The main difference is the percentage of the time that we obtain a proper flux density measurement, which ranges from 36% to 100%, and the mean sampling interval can be as large as 20 days (Figure 2.29).

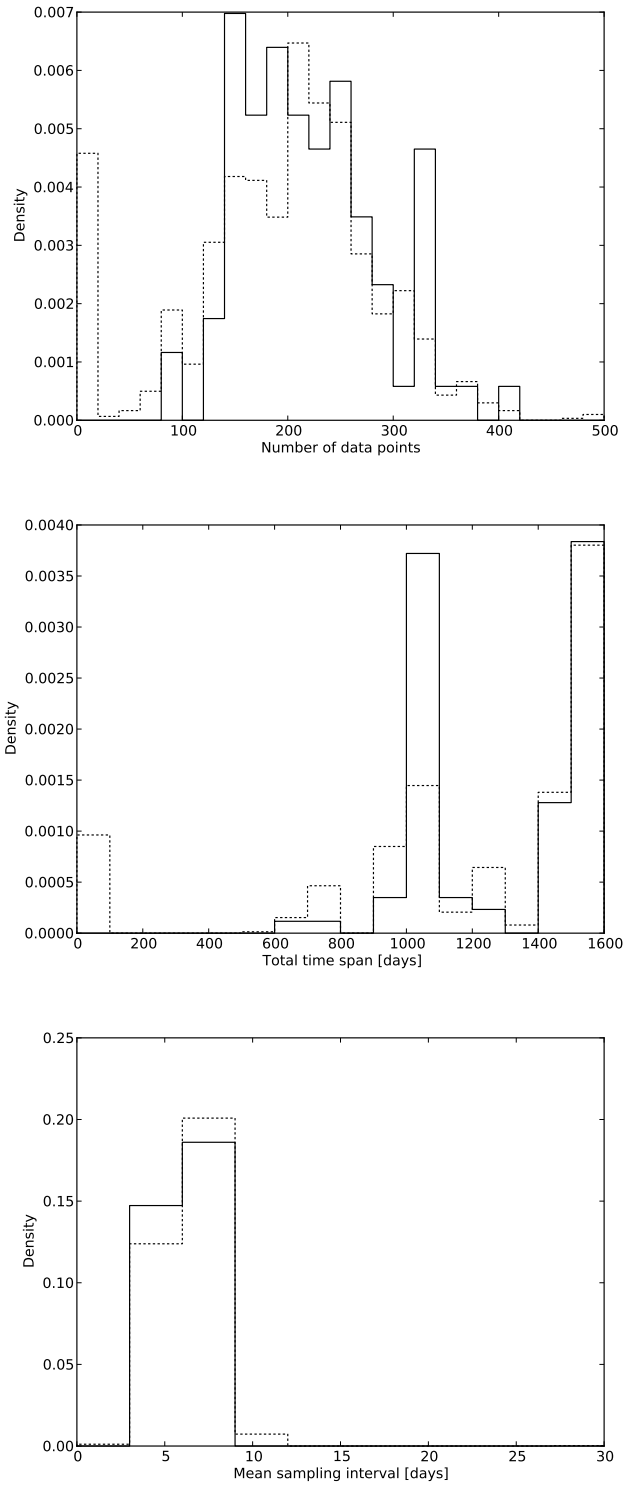

Figure 2.28: Summary of the radio light curve properties for the cross-correlation sample of 86 sources (solid line) and the rest of the blazars in the monitoring program with 1507 sources (dotted line). Upper panel is the normalized distribution for the number of data points in each light curve. Middle panel for the total time span of the light curves in days. Lower panel for the mean sampling interval in days.

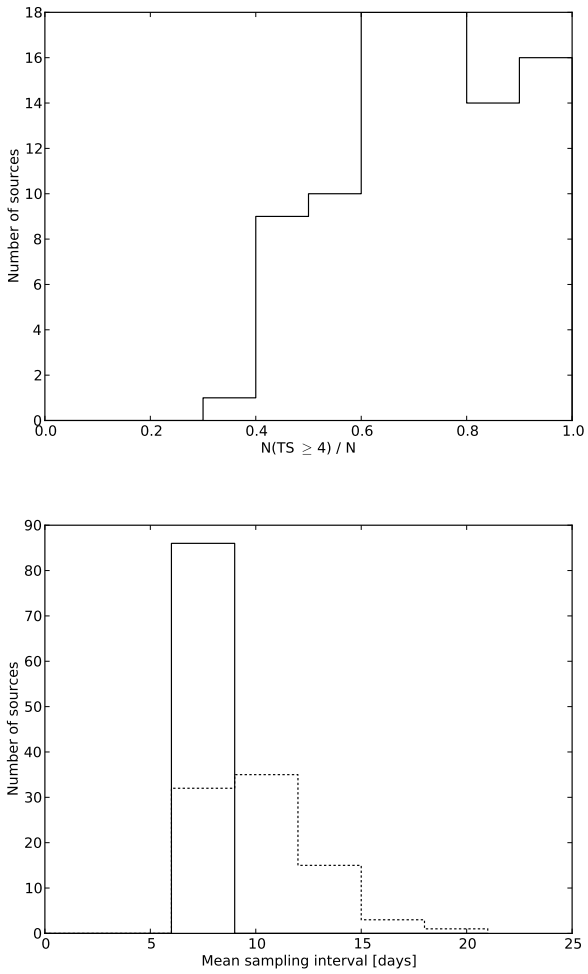

Figure 2.29: Summary of the gamma-ray light curve properties for the cross-correlation sample of 86 sources. Upper panel is the distribution of fraction of time bins with high TS detections. Lower panel is for the mean sampling interval in days.

Chapter 3

Power spectral density estimation for unevenly sampled time series of short duration

3.1 Introduction

An important goal of this program is to characterize the radio variability of the sources and find if it correlates to some other characteristic of the sources like gamma-ray flux density or optical class. More importantly this characterization is also key to the estimation of the significance of correlations as demonstrated in Chapter 5. In this chapter we present the method used to model the light curves in terms of their power spectral density (PSD). Traditional Fourier transform methods were developed for the case of evenly sampled time series ideally of long duration, a situation seldom found in typical astronomical monitoring data sets. For the purposes of this study, the light curves are modeled as noise processes with a single power-law power spectral density. To date, only a few studies have been published of PSDs of radio and gamma-ray light curves and these are for a limited number of sources (Abdo et al., 2010; Chatterjee et al., 2008; Hufnagel & Bregman, 1992; Hughes et al., 1992). The data we have collected allow us to determine the PSD power-law indexes of the largest sample of light curves ever studied. This chapter describes the methods used in this investigation, while its application to our data set is presented in Chapters 4 and 6.

The structure of this chapter is as follows. We start with a brief summary of the theory and standard methods used for the estimation of the PSD and then move to the uneven sampling and short time series case. This discussion is based on the method presented in Uttley et al. (2002) which is modified to suit our data set and the range of PSDs we fit.

The modifications we introduce are discussed in detail along with additional justification of the need for binning and interpolation of the light curves in more detail than in the original paper. We also present an example of the application of the method to a simulated light curve and a number of tests using the OVRO sampling on simulated light curves that demonstrates the accuracy of the fitting procedure under different conditions. A study of the effect of increasing the number of simulations in the fitting procedure is performed in order to guide our choice of parameters for the data analysis. We close the chapter by summarizing the method, with special emphasis on the improvements we add to the original formulation.

3.2 The basics of power spectral density estimation

Before getting into the details of power spectral density estimation for our particular application, it is helpful to review the basics of the standard case of evenly sampled time series. We define a time series as a time ordered sequence of triplets (t_i, f_i, e_i), where t_i is the observation time, f_i is the measured value of the quantity of interest (e.g., flux density, photon flux, etc.), and e_i is an estimate of the observational error associated with the measurement. We assume that the time series is sorted in time and $i = 1, ..., N$. [1]

An estimation of the power spectral density can be obtained through the periodogram which is conventionally defined as the squared modulus of the discrete Fourier transform:

$$P(\nu_k) = \left[\sum_{i=1}^{N} f_i \cos(2\pi\nu_k t_i)\right]^2 + \left[\sum_{i=1}^{N} f_i \sin(2\pi\nu_k t_i)\right]^2 \tag{3.1}$$

where the periodogram is evaluated at the discrete set of frequencies $\nu_k = k/T$ for $k = 1, ..., N/2$ for N even, or $k = 1, ..., (N-1)/2$ for N odd, $\nu_{\rm Nyq} = \frac{N}{2T}$ is the Nyquist frequency and $T = N(t_N - t_1)/(N-1)$.[2]

Estimating the PSD in this way requires sampling a continuous time series at discrete times for a finite amount of time. The sampling operation is equivalent to multiplication of the time series by an infinite train of Dirac delta functions, while sampling for a finite time amounts to a multiplication by a rectangular observing window. These two multiplications

[1] In what follows we use ν for the time frequency and f_i for time series data, e.g., flux density, photon flux, etc.

[2] This choice of T is consistent with the definition of the discrete Fourier transform (Brigham, 1988) and allows us to make use of the Fast Fourier Transform algorithm to increase the speed of the computations.

appear as convolutions in frequency space, with the consequence that we observe the original spectrum convolved with the Fourier transform of the infinite train of Dirac delta functions and the Fourier transform of the rectangular window. As a final step we only look at a discrete set of frequencies which is equivalent to multiplication by an infinite train of Dirac delta function in frequency space.[3]

Ignoring the effect of sampling with an infinite train of Dirac delta functions in time and frequency domain, we find that the periodogram is given by

$$P(\nu) = |W(\nu) * F(\nu)|^2, \tag{3.2}$$

where $F(\nu)$ is the Fourier transform of the time series (t_i, f_i) and $W(\nu)$ is the Fourier transform of the sampling window function, which is by default a rectangular window, and $*$ denotes convolution.

As a result, we do not have access to the original spectrum but a modified version that repeats periodically, whose shape is modified by convolution with the frequency window function and that is sampled at a set of discrete frequencies. All these factors have to be taken into account when analyzing data and interpreting the results. The periodic repetition of the spectrum gives rise to aliasing, in which high frequency components are mistaken as low frequency components. Convolution with the window function can be a serious problem when the sidelobes of the frequency window function lie on regions of the spectrum where the power is much higher than at the frequency of interest – this is the origin of the red-noise leakage problem. Finally, having the spectrum sampled at a number of discrete frequencies can be problematic if we are searching for narrow spectral components which can be smeared or missed.

For the case of evenly sampled time series, power spectral density estimation amounts to using the discrete Fourier transform (DFT) along with periodogram or frequency averaging to decrease the noise which is distributed as a χ^2_2 for a single frequency component. Each of these averaging processes can reduce the variance at the price of reduced spectral resolution. For example, in the case of frequency or periodogram averaging of M components the resulting distribution is χ^2_{2M}, which reduces the variance by a factor of $1/M$ with respect to the non-averaging case.

[3] A graphical representation of these operations can help the reader understand their effect. See Figure 6.1 in Brigham (1988) or elsewhere.

The application of these methods is straightforward in the case of long time series where a good estimate of the PSD can be obtained at the expense of reduced frequency resolution. Nonetheless problems of aliasing and red-noise leakage can still complicate the analysis of broadband signals like the simple power-law PSDs we fit to our data ($P(\nu) \propto 1/\nu^{\beta}$), for the reasons outlined below. For relatively flat spectra (β from 0 to 2) aliasing can be a problem as high frequency power above the Nyquist frequency contaminates low frequencies. This problem is less serious for steep spectra ($\beta \geq 2$) that have relatively small amounts of power at high frequencies, but in this case red-noise leakage can flatten the high frequency part of the spectrum as power from low frequencies contaminates the low amplitude high frequency parts of the spectrum through sidelobes on the sampling window functions. To reduce the effects of these problems a combination of filters and sampling window functions can be used (e.g. Brigham, 1988; Press et al., 1992; Shumway and Stoffer, 2011).

3.3 Power spectral density estimation for unevenly sampled data and short time series

When working with time series data, problems often arise because the time series is unevenly sampled and relatively short. The uneven sampling requires the use of a different estimate of the periodogram: the best known alternatives are the Deeming periodogram (Deeming, 1975) and the Lomb-Scargle periodogram (Scargle, 1982). The Lomb-Scargle periodogram is well suited to the detection of periodic signals in white noise, because it has well understood statistical properties. For the analysis of broadband signals the Deeming periodogram is often used for reasons that are mainly historical as it does not present any real advantages. These two methods allows us to directly obtain an estimate of the periodogram for unevenly sampled time series, but do not provide ways to correct for the distortions produced by the sampling window functions, which in the case of unevenly sampled time series can significantly modify the shape of the periodogram as explained below.

We use the method to estimate the PSD of unevenly sampled and short time series presented by Uttley et al. (2002). A description of our implementation along with a discussion of the necessity of some of the approximations included is presented in this chapter. Uttley et al. (2002) used a number of approximations that were motivated by particularities in their data that do not apply to ours. For example they divided their light curves into three

categories: *long-term*, *intensive* and *long-look*[4], but the cadence of our data is fairly uniform so that this subdivision is unnecessary. This division of the light curves can effectively reduce the red-noise leakage in their implementation but it is not appropriate for the more regular cadence of our data set. In our case we use window functions to reduce the effects of red-noise leakage. This is not part of the original implementation but it is absolutely necessary to deal with steep PSDs and to be able to set an upper bound to the values of β when fitting PSDs of the form $\propto 1/\nu^{\beta}$. Another difference is that we simulate the effects of aliasing by simulating light curves with high frequency components with a sampling period of 1 day, instead of adding a constant noise term to the power spectral density of the simulated light curves as in the original formulation. The high frequency cut at 1 day^{-1} is justified by the small amount of power seen at higher frequencies specially in the radio band. At gamma-rays this is not necessarily true as fast variability has been observed, but given that gamma-ray photon fluxes correspond to mean values of long integrations of at least a week for most blazars the effects of fast variability are less important as they are averaged out.

3.3.1 Description of the method

The method as originally implemented is described in detail in Uttley et al. (2002). We describe the main steps here and describe the differences between their implementation and ours.

- Obtain the periodogram for the light curve and bin it in frequency to reduce scatter. The periodogram is given by a frequency binned version of the following expression

$$P(\nu_k) = \frac{2T}{N^2}\left(\left[\sum_{i=1}^{N} f_i \cos(2\pi\nu_k t_i)\right]^2 + \left[\sum_{i=1}^{N} f_i \sin(2\pi\nu_k t_i)\right]^2\right) \tag{3.3}$$

  where the frequencies are $\nu_k = k/T$ for $k = 1, ..., N/2$ for N even, or $k = 1, ..., (N-1)/2$ for N uneven. The minimum frequency is $\nu_{\min} = \frac{1}{T}$, the maximum frequency is the Nyquist frequency $\nu_{\rm Nyq} = \frac{N}{2}\frac{1}{T}$, and $T = N(t_N - t_1)/(N-1)$. The multiplicative factor is a normalization that has the property that the integral from ν_i to ν_f is equal to the variance contributed to the light curve by this frequency range. The time series

[4]These are the names they give to light curves that sample different time scales for different lengths of time.

(t_i, f_i) is evenly sampled and is obtained from the original one by interpolation onto a regular grid. Also the interpolated time series is first multiplied by an appropriate sampling window in order to reduce red-noise leakage. A justification of these steps is given in Sections 3.3.2 and 3.3.3.

- Choose a PSD model to test against the data. In this case we are fitting simple power-laws of the form $P(\nu) \propto 1/\nu^{\beta}$ but this can be generalized to any functional dependence. For the given model simulate M time series, where M is a large number that allows us to represent a variety of possible realizations of this PSD model.

- For each simulated light curve apply the same sampling, add observational noise and interpolate into the same even grid. Calculate the periodogram for each one. From these M periodograms determine the mean periodogram and its associated error as the scatter at each frequency bin.

- Using the mean periodogram and errors obtained in the last part construct a χ^2 like test defined by

$$\chi^2_{\rm obs} = \sum_{\nu=\nu_{\rm min}}^{\nu_{\rm max}} \frac{[\overline{P_{\rm sim}}(\nu) - P_{\rm obs}(\nu)]^2}{\Delta\overline{P_{\rm sim}}(\nu)^2} \tag{3.4}$$

  This $\chi^2_{\rm obs}$ is then compared to the distribution of χ^2 which is obtained by replacing each of the simulations by the observations in Equation 3.4. The fraction of the distribution for which $\chi^2 > \chi^2_{\rm obs}$ is the significance level at which the tested PSD model can be rejected or the p-value which we simply call p. Thus a high value of this percentage represents a good fit and a low one a poor fit.

The process described above can be repeated for a number of models with different parameters. The final step consists in selecting the best as the one with highest value of p. As with any statistical procedure a measurement of the uncertainty in the parameters of the model needs to be given. In this point we also depart from the original formulation and provide uncertainties based on Monte Carlo simulations of the model fitting process as described in Section 3.3.6.

The most significant differences with the original implementation are the use of sampling window functions to reduce red-noise leakage and the Monte Carlo estimation of fitting

uncertainties. Another important difference, although less important conceptually, is the use of the Fast Fourier Transform to perform the computations, which surprisingly is not part of the original formulation but which it is a rather obvious step for evenly sampled time series, which we have to work with in order to use sampling window functions. Further discussions of the most important elements of the method are given below.

3.3.2 The necessity for rebinning and interpolation of the light curves

In the original formulation this step is justified by just saying that it reduces the distortion of the periodogram but in practice it turns out to be key to obtain any result at all when estimating steep PSDs. We tried to use the original unevenly sampled data in combination with a number of window functions to reduce the effects of red-noise leakage but it turns out that window functions for unevenly sampled data do not behave in the same way as window functions for the evenly sampled case. An example is presented in Figure 3.1, where we show the frequency response of a uneven sampling pattern with a rectangular and Hanning windows for the periodogram of power-law PSDs with different values of β from 0 to 5. The rectangular and Hanning windows used in these examples are given by the expressions in Equation 3.5 and 3.6 respectively.

$$w(t) = \begin{cases} 1, & 0 \leq t \leq T \\ 0, & \text{otherwise} \end{cases} \tag{3.5}$$

$$w(t) = \begin{cases} \cos(\pi \frac{(t-T/2)}{T})^2, & 0 \leq t \leq T \\ 0, & \text{otherwise} \end{cases} \tag{3.6}$$

An equivalent test for the case of even sampling is shown in Figure 3.2.

From Figure 3.1 it can be seen that even though we can calculate the periodogram directly for an unevenly sampled time series the results we obtain are very noisy and do not vary much among different values of β. The main problem is that all the PSDs with $\beta \geq 1$ look very similar, showing almost the same slope when fitted with a linear function after a log-log transformation. This is problematic as the fitting procedure relies on the differences between different PSD power-law indices to choose the best model. Doing the same exercise for a time series with the same time length and number of data points but

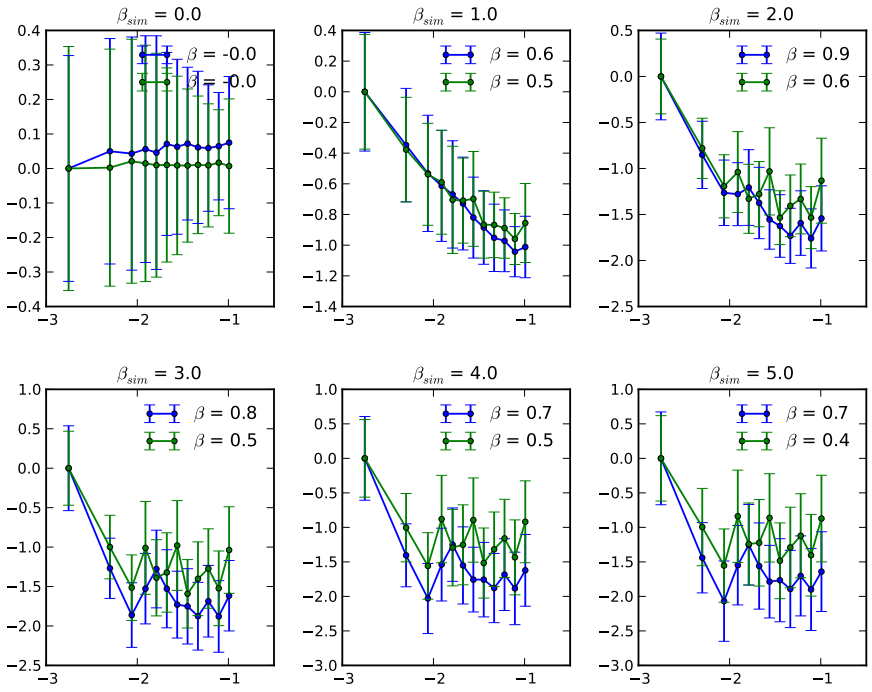

Figure 3.1: Effect of the use of window functions for uneven sampling cases using the rectangular (blue) and Hanning window (green). Each figure shows the result of simulating 1000 light curves with a given simple power-law PSD $\propto 1/\nu^{\beta}$, with β given in each figure title. The data points are the mean PSD and the error the spread in the simulation, while the units of power (vertical axis) and frequency (horizontal axis) are arbitrary. Also included are direct fits of the slopes of the mean PSDs for the simulated data for each window. Notice how the linear fits can hardly discriminate between different slopes and how all the estimated PSDs look very similar.

with even sampling we obtain the results shown in Figure 3.2. In this case the results are much less noisy and the estimated PSDs look different from each other even for very steep PSDs. This allows for better discrimination and is required to find an upper limit to the source power-law exponent of the PSD.

This problem is evident when trying to apply the fitting method using the unevenly sampled data and shows up as an inability to find an upper limit to the power-law exponent β due to the lack of difference between the estimated PSDs for the simulated data. This problem can be solved by the use of interpolation and an appropriate window function, a subject that is discussed in Section 3.3.3.

Another thing we can learn from Figures 3.1 and 3.2 is the limited use we can make

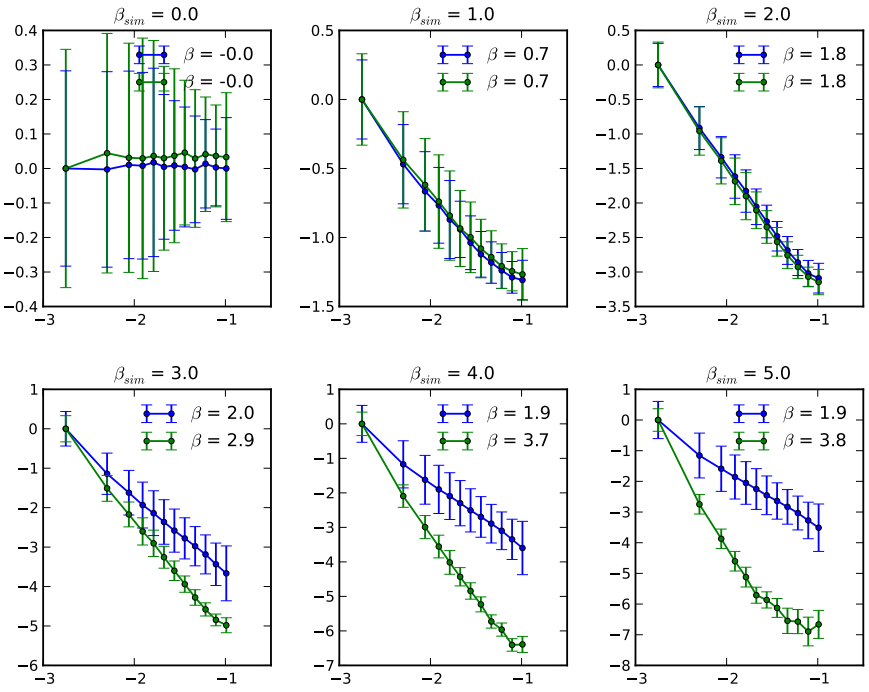

Figure 3.2: Effect of the use of window functions for even sampling cases using the rectangular (blue) and Hanning window (green). Each figure shows the result of simulating 1000 light curves with a given simple power-law PSD $\propto 1/\nu^{\beta}$, with β given in each figure title. The data points are the mean PSD and the error the spread in the simulation, while the units of power (vertical axis) and frequency (horizontal axis) are arbitrary. Also included are direct fits of the slopes of the mean PSDs for the simulated data for each window. In this case the shape of the PSDs is less noisy and the estimated PSDs for steep cases look different from each other.

of direct PSD fitting even for the case of long time series. In this case it is the red-noise leakage which makes it impossible to recover the right power-law index for steep PSDs.

The subject of windowing of unevenly sampled data is briefly discussed in Scargle (1982). In particular their figure 3 shows a few example window functions for the cases of even and uneven sampling using the classic periodogram. From those we can see the very different sidelobe structure that is obtained for the uneven sampling case which is at the root of the problem described here.

To clarify this point we also include the window functions for our test data along with the results of applying the Hanning window. An examination of Figure 3.3 helps understand the results described below. In conventional Fourier analysis window functions change

the frequency response of the sampling, changing the sidelobe structure and thus helping mitigate the effects of red-noise leakage and aliasing. This behavior can be seen when using evenly sampled data sets. The green curve is for a rectangular window and the cyan curve is for a Hanning window. The sidelobe structure is regular and decays as frequency increases. The case for uneven sampling is very different as can be seen in the blue curve for the rectangular window and red curve for the Hanning window. The shapes of the window functions for the case of uneven sampling explains the strong red-noise leakage seen in the simulations and the increased noise. In the case of even sampling we recover the results of conventional Fourier analysis with all the good properties of window functions.

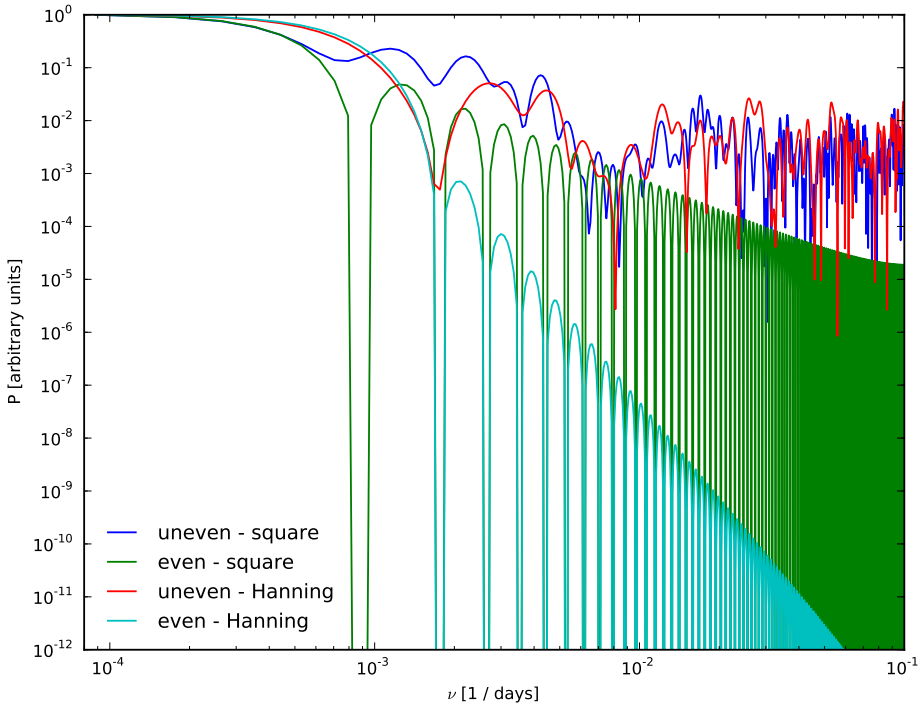

Figure 3.3: Effect of data windowing in the cases of even and uneven sampling. In the uneven sampling case we see that both the rectangular (blue curve) and Hanning (red curve) windows have a response with a relatively high sidelobe level that do not decay as the frequency increases. For the even sampling case with the same time length and number of data points we see that the rectangular (green curve) and Hanning window (cyan curve) behave as expected in the usual case, with a regular sidelobe structure whose amplitude decreases as the frequency increases.

3.3.3 Spectral window function

One fundamental difference between the implementation of the method of Uttley et al. (2002) and ours is that we use window functions to reduce the effects of red-noise leakage. It was found that this is absolutely necessary to deal with steep power spectral densities like those used in this study. In our first attempts to fit the PSDs we found that with a rectangular window we were not able to set an upper limit to the value of β and were only able to set a lower limit. The upper limit on β is absolutely necessary to constrain the significance of cross-correlations as described in Chapter 5. In this section we describe the origin of that problem and the solution we implemented.

For broadband time series a big problem is the leakage of power through far sidelobes of the spectral window response. This problem is evident when dealing with high dynamic range PSDs such as steep power-laws. For these simple power-laws, it is seen as a flattening of the high frequency part of the periodogram due to power leaking from the high power low frequency part. In practical terms it means that after some critical value of the power-law index all the periodograms have a flat slope which does not depend strongly on the PSD. Most of this high frequency power is actually coming from low frequencies through sidelobes of the window function. One way to deal with this problem is by using window functions with low level sidelobes; some details about their application to our data set are presented below.

3.3.3.1 Spectral window functions for our data sets

There is a great variety of window functions, which differ mainly in the width of their main lobe, the maximum level and the fall-off rate of the sidelobes. The ideal window function will depend on the application and some experimentation might be necessary. Properties of various window functions can be found elsewhere (e.g. Harris, 1978)

We tried a number of them and compared their performance in recovering steep PSDs. We found that among the ones we tested the most suitable one was the Hanning window which is able to recover a steep spectrum in a range that allows us to fit our light curves. Among the special characteristics of this window are its low sidelobe level, more than 32 dB below main lobe, and the fast fall-off at -18 dB/decade. As a downside the Hanning window has a broader main lobe at 3 dB ($1.44 \cdot 1/T$) when compared to the rectangular

window $(0.89 \cdot 1/T)$, where T is the length of the time series.

The low level and fast sidelobe fall-off are the key to reducing the effects of red-noise leakage to a level that makes discriminating between different steep PSDs possible. This effect is illustrated in Figure 3.4, which shows the periodogram for a series of steep PSDs. From the figure is also clear why other window functions fail to distinguish between steep PSDs, and thus are not suitable to use with this method.

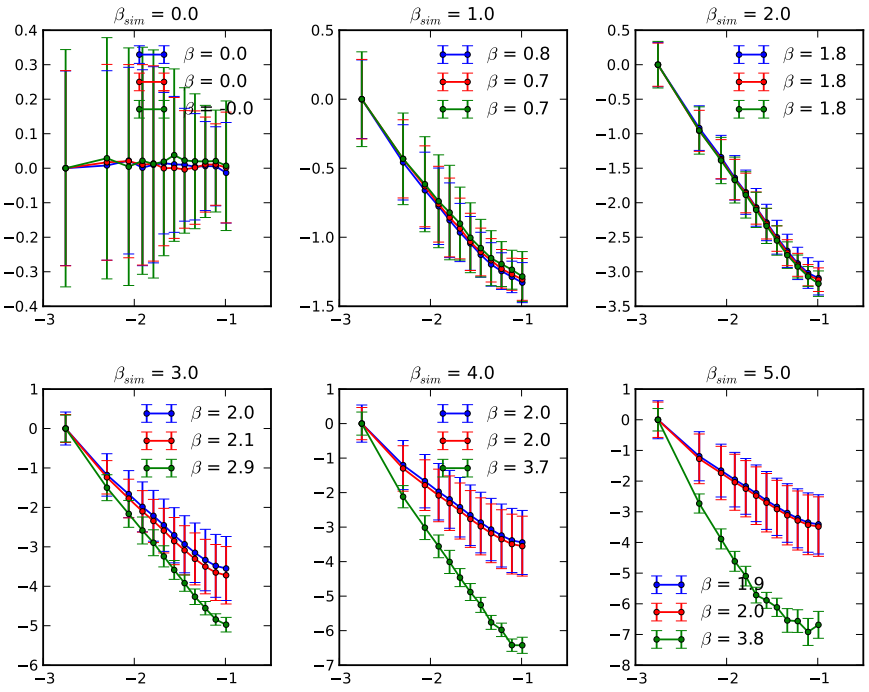

Figure 3.4: Comparison of windowed periodogram for steep PSDs. Each figure shows the result of simulating 1000 light curves with a given simple power-law PSD $\propto 1/\nu^{\beta}$, with β given in each figure title. The data points are the mean PSD and the error the spread in the simulation, while the units of power (vertical axis) and frequency (horizontal axis) are arbitrary. Also included are direct fits of the slopes of the mean PSDs for the simulated data in each case using a rectangular (blue), triangular (red) and Hanning (green) windows.

The results of Figure 3.4 can be understood by comparing the properties of the window functions shown in Table 3.1 (Harris, 1978). The reduction of the red-noise leakage when using the Hanning window is due to the lower sidelobe level and the faster fall-off.

Although there exist other window functions with lower sidelobe levels and faster fall-off it is not necessary to use them in this case, but they are worth considering if fitting

Table 3.1: Properties of selected window functions

Window	Sidelobe Level (dB)	Sidelobe Fall-Off (dB/oct)	3-dB BW (bins)
Rectangular	−13	−6	0.89
Triangle or Barlett	−27	−12	1.28
$\cos^2(x)$ or Hanning	−32	−18	1.44

of steeper PSDs is required. Windowing is good for fitting a featureless PSD, but it can be a source of problems if the goal is to find narrow spectral components. The reason is that by making the sidelobes smaller we make the main beam wider which smears localized features. This has to be considered when searching for periodic components, a case which is outside of the scope of the current analysis.

3.3.4 Filtering

The windowing technique is able to solve the problem with red-noise leakage but another method that can be used to deal with steep spectra is filtering in the time domain and correction to the frequency domain result. We also tested this alternative and compare it to windowing. The idea of filtering is to eliminate the low-frequency components that produce the red-noise leakage before computing the periodogram. Since this changes the spectrum of the time series, it has to be compensated in the final periodogram by the application of a frequency filter.

One of these techniques is called pre-whitening and post-blackening by first differencing. In this case the original time series (t_i, f_i) which has even sampling is transformed to $(t_i, g_i \equiv f_i - f_{i-1})$. In the frequency domain this is equivalent to filtering with $|H(\nu)|^2 = 2[1 - \cos(2\pi\nu)]$. Higher order filtering is possible, for example by the application of first order differencing multiple times (Shumway and Stoffer, 2011).

Figure 3.5 shows the result of applying this procedure to simulated data with even sampling and a range of values of the power-law of the PSD. It can be seen that this method has problems recovering flat PSDs with $\beta \leq 2$ and very steep PSDs with $\beta \geq 4$. We also tested it with the OVRO data set and found that in a large number of cases it was not able to provide good upper limits for β and was outperformed by windowing with the Hanning window. We therefore use Hanning windowing for the data analysis.

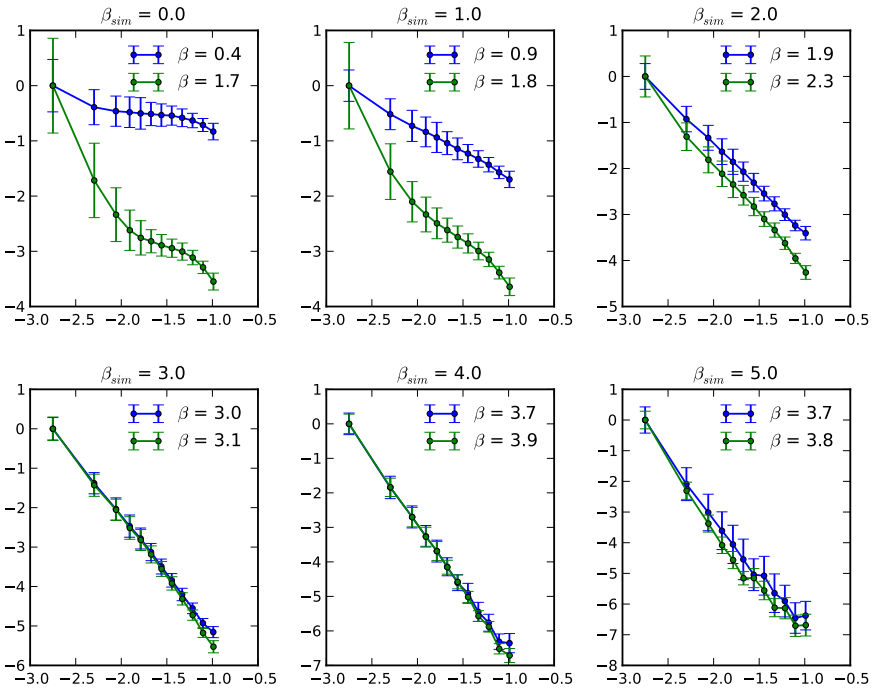

Figure 3.5: Effect of the use of pre-whitening and post-darkening in evenly sampled time series. Each figure shows the result of simulating 1000 light curves with a given simple power-law PSD $\propto 1/\nu^{\beta}$, with β given in each figure title. The data points are the mean PSD and the error the spread in the simulation, while the units of power (vertical axis) and frequency (horizontal axis) are arbitrary. Also included are direct fits of the slopes of the mean PSDs for the simulated data in each case using first difference (blue curve) and second difference (green curves).

3.3.5 Adding noise to the simulated light curves

A final issue is the addition of noise to the simulated light curves, a step which is absolutely necessary in order to consider the effect of observational uncertainties on our ability to measure the PSD. This is not a serious problem for the radio light curves, which in most cases have very high signal-to-noise ratio, but it is important for most gamma-ray light curves which have moderate signal-to-noise ratios.

In order to add the observational noise to the light curves we first need to normalize the simulated data to match the observations. One way to obtain an approximate normalization

is by using the Parseval's theorem, which with the normalization we use implies that

$$\sigma^2 = \sum_{\nu_{\min}}^{\nu_{\max}} P(\nu)\Delta\nu \tag{3.7}$$

We can estimate the variance for the observations and the simulations and use a constant factor to make them equal, thus getting an approximate normalization of the PSD. One problem is that the data already contain the observational noise added to the signal, so for each data point we have $d_i = s_i + n_i$, where d is the data, s the signal and n the noise. We can estimate the variance to obtain $\sigma_{\rm d}^2 = \sigma_{\rm s}^2 + \sigma_{\rm n}^2$, under the assumption that the noise and signal are uncorrelated.

The variance of the noise can be obtained from the error bars by $\sigma_{\rm n}^2 \approx \bar{e_i^2}$, where e_i is the error bar associated with the i-th measurement. The final normalization equation is

$$\sigma_{\rm sim}^2 = A^2(\sigma_{\rm d}^2 - \bar{e_i^2}) \tag{3.8}$$

We can multiply the originally arbitrarily normalized simulated data by A^{-1} to get a normalization equivalent to the one in the observations. In practice we use A to transfer the observational error bars to the simulations, to which we add Gaussian observational noise to the time domain signal such that $e_{\rm sim,i} = A\, e_i$. In the original formulation the noise is applied to the periodogram, but we choose to apply it directly to the time series to be able to account for the different sizes of the observational uncertainties. The assumption of Gaussian error bars is only approximate for the gamma-ray data which have a Poisson distribution. Since in this analysis we are only considering highly significant gamma-ray detections we usually have at least 5 photons in each integration, and in most cases a lot more. In this regime the difference between Poisson and Gaussian distributed errors is negligible.

3.3.6 Estimation of the uncertainty in the model parameters

In the original formulation the authors defined regions of confidence for the fitted model parameters as the region for which $p(\hat{\theta}) > p_{\rm conf}$, where $p(\hat{\theta})$ is the p-value for a given set of parameters $\hat{\theta}$. For example a 68.3% confidence interval has $p_{\rm conf} = 0.317$, while a 95.5% confidence interval has $p_{\rm conf} = 0.045$. Although this rule seems sensible, we found in our

tests using simulated data sets that the confidence intervals thus obtained are not consistent with the scatter in the best fit when the procedure is repeated a large number of times for simulated light curves with known and fixed PSDs. Other problem with the proposed rule is that it is not possible to get 68.3% confidence intervals for fits in which $p < 0.317$. The problem is that even fitting simulated data, we will get a significant fraction of cases with such a small p-value. These are not necessarily bad fits for which we would have no ability to get 68.3% confidence intervals. This contrast with the usual approach to measure uncertainties from χ^2 fits that defines a 68.3% (or any other level) confidence interval by the region of parameter space for which $\chi^2(\theta) - \chi^2_{\rm min} \leq \Delta\chi^2$ where $\Delta\chi^2$ depends on the number of interesting parameters being fit and the confidence level (Avni, 1976; Press et al., 1992; Wall et al., 2003). In this widely used method a confidence interval can be obtained independently of the value of $\chi^2_{\rm min}$ for the fit. Of course we must be careful as a high value of χ^2, or equivalently a small p-value is also indicating a poor quality fit, something that we must consider in our analysis.

For these reasons we decided to estimate the confidence intervals for the best fit value by using a Neyman construction (Beringer et al, 2012; James, 2006), combined with a Monte Carlo procedure in which we fit a large number of mock data sets of known and fixed power-law PSD to construct the confidence band. This requires that for each PSD fit we run a large number of fits to simulated data which increases the computational time. This procedure is feasible when fitting a single power-law index but it can be prohibitive when fitting a large number of parameters, and other methods have to be explored for those cases (something which is outside the scope of the current analysis).

An example of the application of this method is presented in Section 3.4.1.

3.4 Implementation

The method described above is implemented in Python and validated with simulated data sets with known PSDs and typical sampling patterns taken from the OVRO sample. This section starts with an example of the application of the method to a simulated light curve of known PSD. Four tests intended to validate the procedure by fitting a large number of simulated data with known PSD, using sampling patterns taken from the OVRO program and observational errors consistent with our data, are presented. This section ends with

a study of the effects of using a different number of simulated light curves (M as defined in Section 3.3.1) when fitting simulated data in one of them, and an example light curve from the OVRO program in the other. The idea is to get an indication of the associated uncertainties by changing M, as it can have a large impact on the computational time.

3.4.1 An example of the application of the method

An example fit to simulated data is presented to help the reader understand its application. A simulated light curve with a PSD with power-law exponent $\beta = 2.0$, no observational noise added and sampled in the same way as the source J1653+3945 is shown in Figure 3.6 along with the periodogram and best fit.

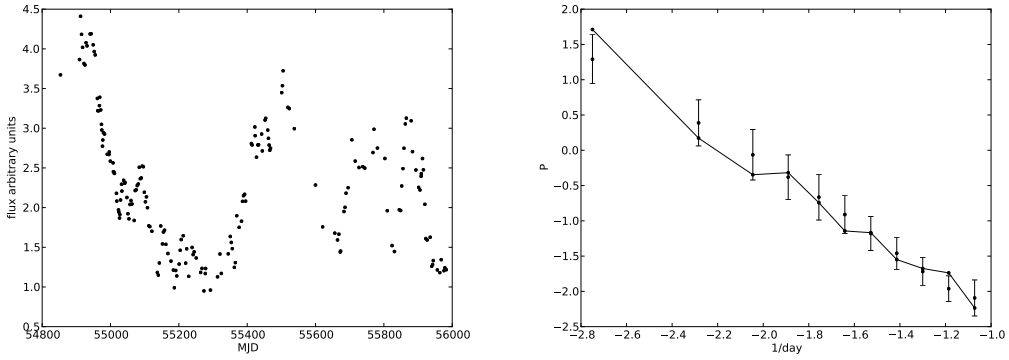

Figure 3.6: Example of the PSD fit method applied to simulated data. Left panel is the simulated light curve with a PSD $\propto 1/\nu^2$ and no noise. Right panel is the data periodogram binned in frequency (black line) and the mean PSD and scatter for the best fit with $\beta = 1.85 \pm 0.2$ (black dots and error bars).

The results of the fitting procedure are summarized by a plot of p vs β (Figure 3.7). The best fit corresponds to $\beta = 1.85 \pm 0.2$, where the errors where obtained with a Neyman construction whose resulting confidence band is also shown in the figure. The errors correspond to a 68% confidence interval obtained from the distribution of best fit values to these simulated light curves (Figure 3.7). In what follows all the errors are obtained in this way. This Monte Carlo error can be compared with the original error prescription which can be applied in this case and produces a value of ± 0.5, more than twice the value estimated from the simulations.

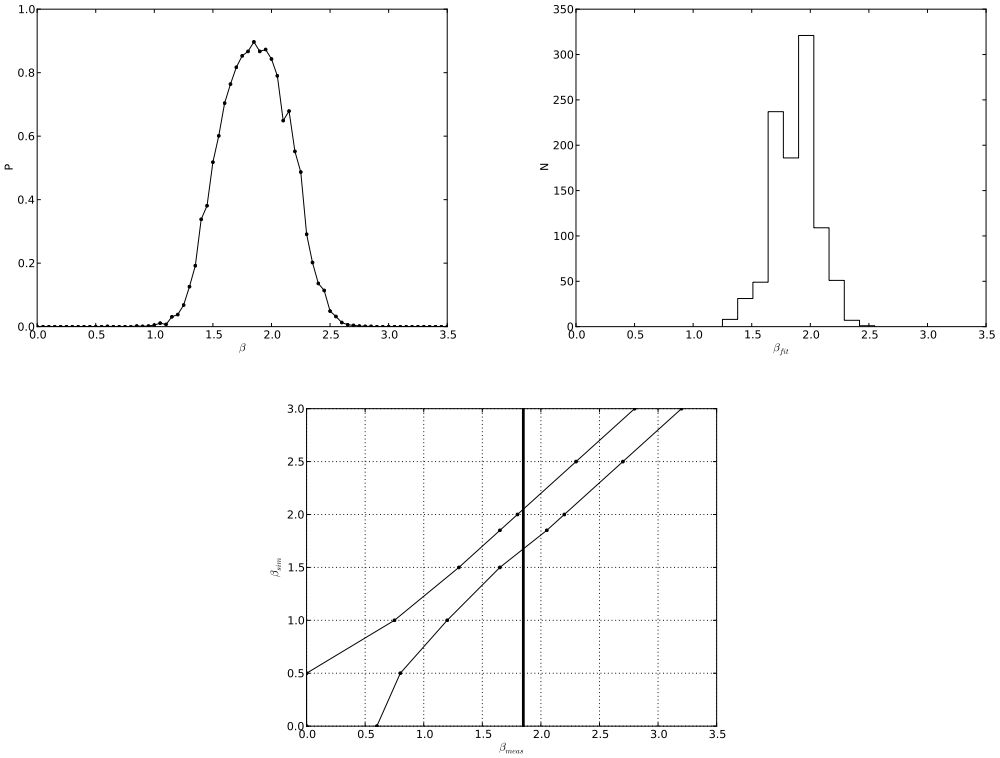

Figure 3.7: Example of the fitting method applied to simulated data of known PSD. Upper left panel is p versus β for the different power-laws tested. The peak at 1.85 indicates the best fit. Upper right panel is the distribution of best fits for 1000 simulated light curves with $\beta_{\rm sim} = 1.85$ and same sampling as data. The error on the fit is obtained from the confidence band which is shown in the lower panel. The intersection of the vertical line with the confidence band give us $\beta = 1.85 \pm 0.2$.

3.4.2 Validation of the implementation with simulated data sets

In order to validate the implementation we tested it with simulated data sets of known PSD. Typical sampling patterns and various relative amounts of noise are considered to investigate the behavior of the method under different conditions. In each of the tests we use $M = 1000$ to get the mean PSD and scatter at each trial value of β. We use trial values of β from 0.0 to 3.5 in steps of 0.05. As a last test we explore the effect of varying M, the number of simulated light curves, on the repeatability of the result in order to establish a criterion to select the number we will use for the data analysis and to get an idea of possible errors associated with that choice.

3.4.2.1 OVRO sampling pattern 1 and no noise

In this test we use the sampling pattern for the source J1653+3945. The OVRO data are shown in Figure 3.8 as reference, because the actual fitted data were simulated and we only use the sampling pattern of this light curve. This comment applies to all the other tests in this section. The results of the fit for simulated data as a distribution of best fit values are shown in Figure 3.8. We find that in all cases we are able to recover the true β with a typical uncertainty of 0.2.

3.4.2.2 OVRO sampling pattern 1 and noise

In this test we use the sampling pattern for the source J1653+3945 and error bars consistent with the noise in this source. The results of the fit for simulated data as a distribution of best fit values are shown in Figure 3.9. In this case the large measurement errors make recovering the PSD exponent very hard and the fitting procedure fails to yield a meaningful constraint.

3.4.2.3 OVRO sampling pattern 2 and noise

In this test we use the sampling pattern for the source J0423−0120 and error bars consistent with the noise in this source. The OVRO data are shown in Figure 3.10. The results of the fit for simulated data as a distribution of best fit values are shown in Figure 3.10.

In this case the procedure also provides good constraints on β except for the case of $\beta = 3.0$. If necessary this could be handled by the use of a different window function.

3.4.2.4 OVRO sampling pattern 3 and noise

In this test we use the sampling pattern for the source J2253+1608 and error bars consistent with the noise in this source. The OVRO data are shown in Figure 3.11. The results of the fit for simulated data as a distribution of best fit values are shown in Figure 3.11. In this last case we are also able to constrain β with an uncertainty of about 0.2.

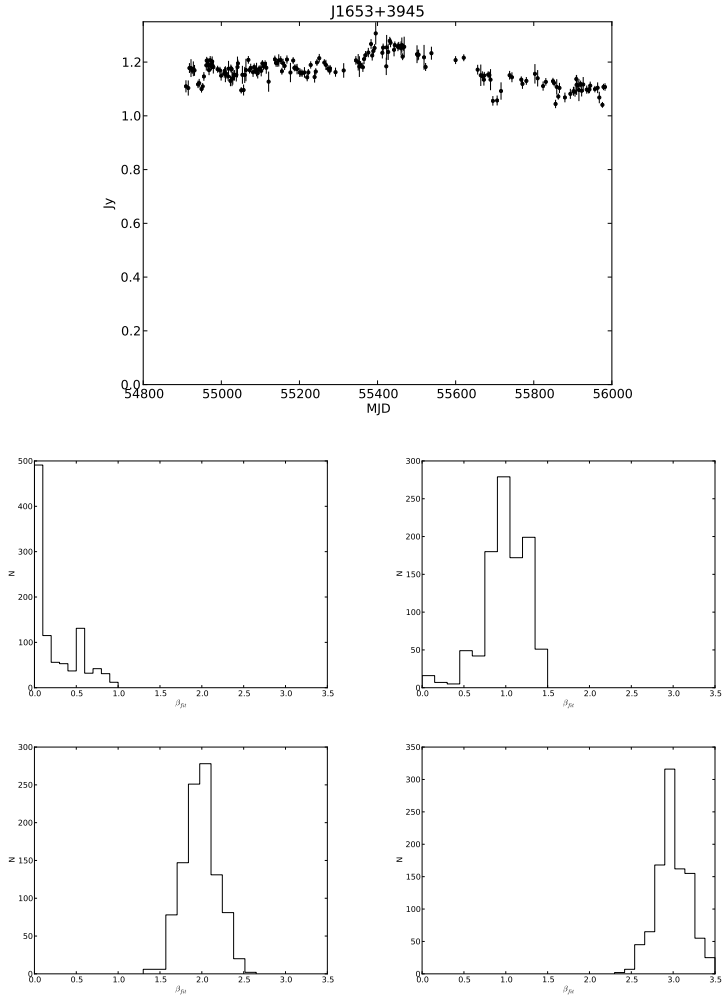

Figure 3.8: Upper panel shows the OVRO data used to get the time sampling. The error bars are not used in this test and we assume a perfect measurement. Four lower panels are the distribution of best fit values for 1000 simulated light curves in each case. In each case this distribution gives an estimation of the error on the fit and is used to construct the confidence band. Top left is for $\beta_{\rm sim} = 0.0$ and $\beta_{\rm fit} = 0.0^{+0.3}_{-0.0}$, top right is for $\beta_{\rm sim} = 1.0$ and $\beta_{\rm fit} = 1.0 \pm 0.2$, lower left is for $\beta_{\rm sim} = 2.0$ and $\beta_{\rm fit} = 2.0^{+0.15}_{-0.2}$, and lower right is for $\beta_{\rm sim} = 3.0$ and $\beta_{\rm fit} = 3.0^{+0.2}_{-0.15}$. In the case of $\beta_{\rm sim} = 0.0$ we report the mode and dispersion about that value. All the other cases use the median and dispersion.

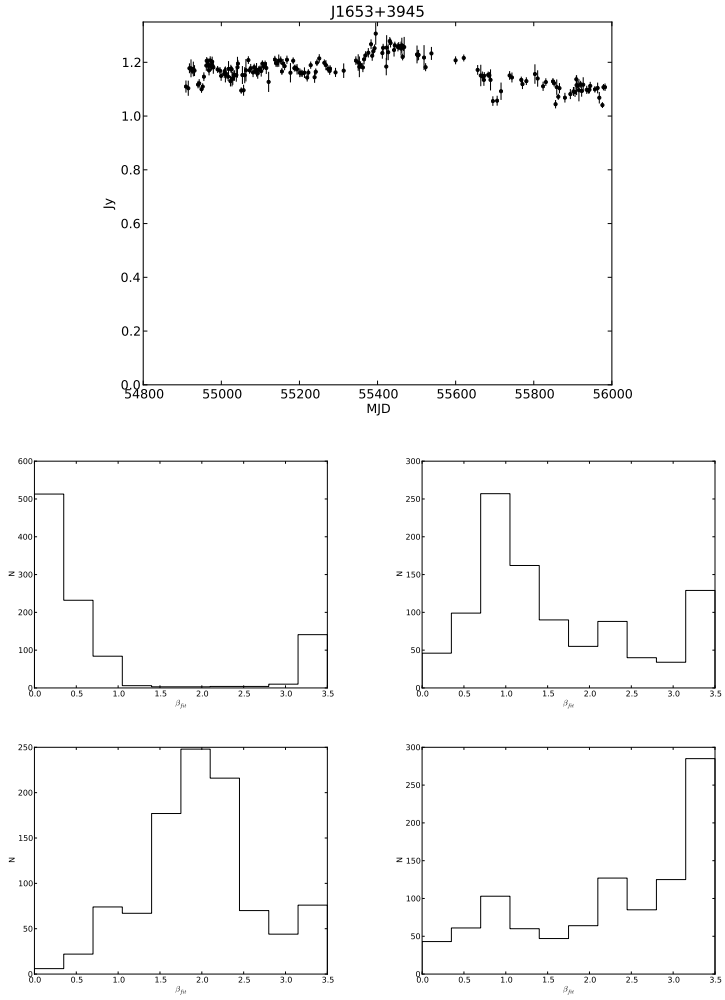

Figure 3.9: Upper panel shows the OVRO data used to get the time sampling and the error bars. Four lower panels are the distribution of best fit values for 1000 simulated light curves in each case. In each case this distribution gives an estimation of the error on the fit and is used to construct the confidence band. Top left is for $\beta_{\rm sim} = 0.0$ and $\beta_{\rm fit} = 0.05^{+0.55}_{-0.05}$, top right is for $\beta_{\rm sim} = 1.0$ and $\beta_{\rm fit} = 1.3^{+1.5}_{-0.55}$, lower left is for $\beta_{\rm sim} = 2.0$ and $\beta_{\rm fit} = 1.9^{+0.6}_{-0.55}$, and lower right is for $\beta_{\rm sim} = 3.0$ and $\beta_{\rm fit} = 3.0^{+0.4}_{-1.85}$. In the cases of $\beta_{\rm sim} = 0.0$ and 3.0 we report the mode and dispersion about that value. All the other cases use the median and dispersion.

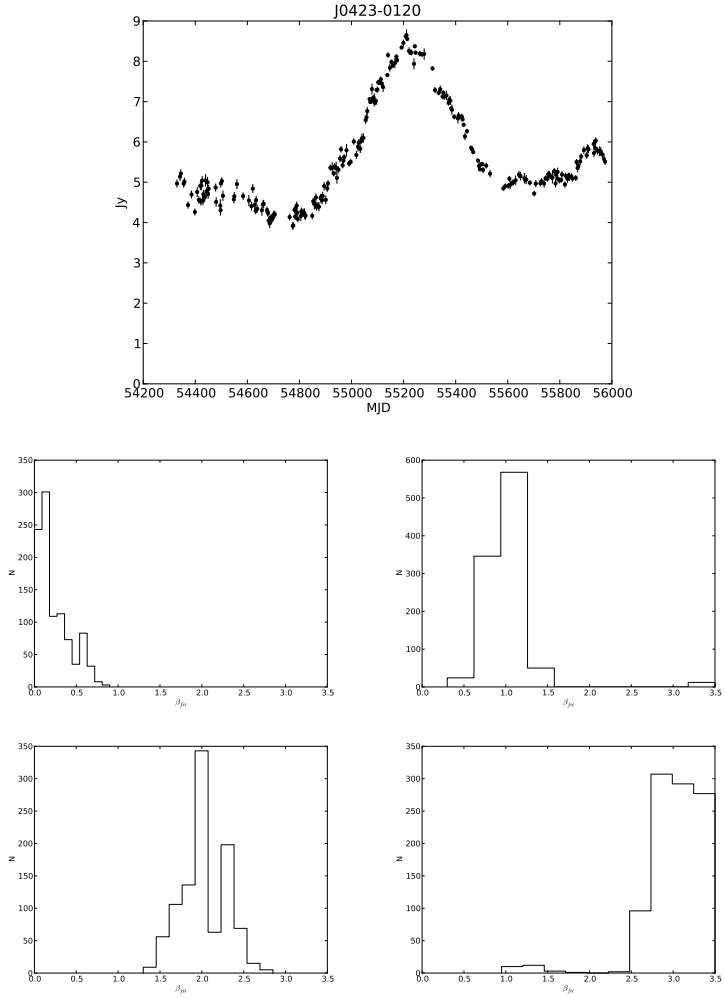

Figure 3.10: Upper panel shows the OVRO data used to get the time sampling and the error bars. Four lower panels are the distribution of best fit values for 1000 simulated light curves in each case. In each case this distribution gives an estimation of the error on the fit and is used to construct the confidence band. Top left is for $\beta_{\rm sim} = 0.0$ and $\beta_{\rm fit} = 0.15^{+0.25}_{-0.1}$, top right is for $\beta_{\rm sim} = 1.0$ and $\beta_{\rm fit} = 1.0 \pm 0.15$, lower left is for $\beta_{\rm sim} = 2.0$ and $\beta_{\rm fit} = 2.0 \pm 0.25$, and lower right is for $\beta_{\rm sim} = 3.0$ and $\beta_{\rm fit} = 3.05 \pm 0.3$. In the case of $\beta_{\rm sim} = 0.0$ we report the mode and dispersion about that value. All the other cases use the median and dispersion.

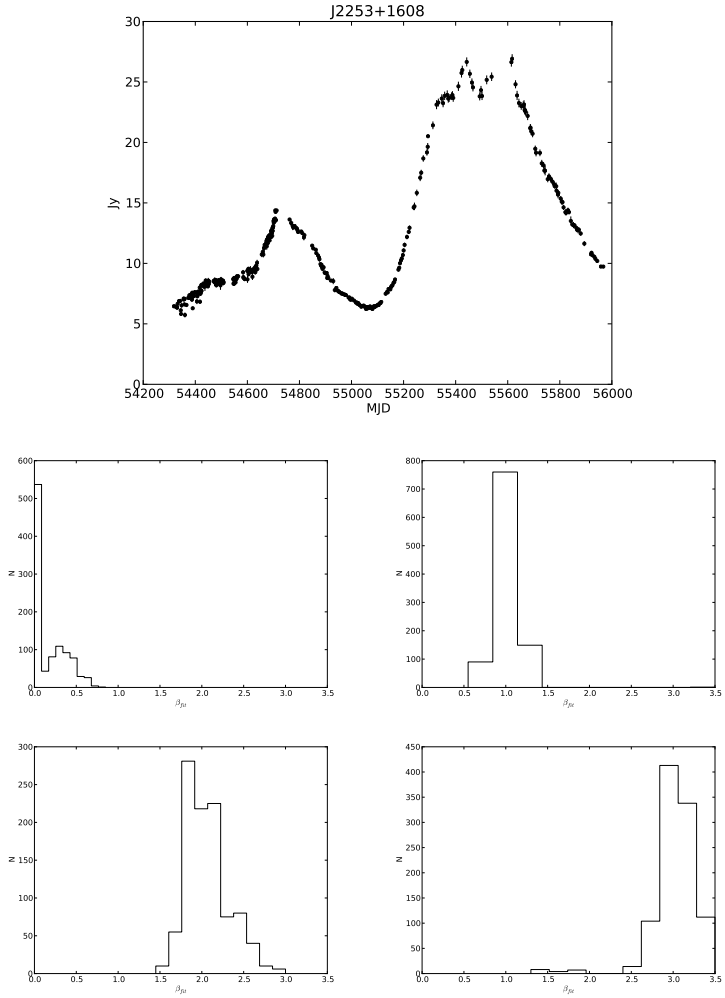

Figure 3.11: Upper panel shows the OVRO data used to get the time sampling and the error bars. Four lower panels are the distribution of best fit values for 1000 simulated light curves in each case. In each case this distribution gives an estimation of the error on the fit and is used to construct the confidence band. Top left is for $\beta_{\rm sim} = 0.0$ and $\beta_{\rm fit} = 0.05^{+0.25}_{-0.05}$, top right is for $\beta_{\rm sim} = 1.0$ and $\beta_{\rm fit} = 1.0^{+0.15}_{-0.1}$, lower left is for $\beta_{\rm sim} = 2.0$ and $\beta_{\rm fit} = 2.05 \pm 0.25$, and lower right is for $\beta_{\rm sim} = 3.0$ and $\beta_{\rm fit} = 3.0^{+0.2}_{-0.15}$. In the case of $\beta_{\rm sim} = 0.0$ we report the mode and dispersion about that value. All the other cases use the median and dispersion.

3.4.2.5 Effect of increasing the number of simulations

The original paper does not present a detailed discussion on the required number of simulations to get reliable results. They start by using M=1,000 for simple cases and move to M=100 for multi parameter fits, arguing that since the p as a function of fitted parameters contours of the fits looks well defined implies that M=100 is sufficient. This argument for the minimum number of simulations required to estimate the mean PSD is not compelling enough as it does not really test the repeatability of the process which can be a problem in any procedure using random numbers. In our opinion a better test is to run the fitting procedure for an example case a number of times and check its repeatability. This exercise is computer intensive, so we run the analysis with typical radio sampling for a couple of cases and assume that the results are representative for the rest of the sources. In any case, given the available computing power we do not exceed M=1,000 in order to get results in a reasonable time scale and appropriate accuracy when fitting all the radio sources (about 1500). We think that understanding the repeatability of the results is a key step that is missing in the original description of the method.

The first test consists of fitting the same simulated data set used in Section 3.4.1,100 times using M=100, M=1,000 and M=10,000 simulated light curves at each trial power-law exponent of the PSD. The distribution of best fit values is used to estimate the repeatability of the fitting process. The second test does the same but in this case it fits the OVRO data for J0423−0120 shown in Figure 3.10, and this time incorporating the observational noise in the fit. The results are summarized in Table 3.2 which shows that the repeatability of the results increases as M increases, as we would expect. The scatter is reduced by half by going from M=100 to M=10,000. We also note that in the case of the OVRO data we get a big increase in accuracy when going from M=100 to M=1,000, but a much smaller one by going to M=10,000. This information is encoded in the Monte Carlo error computation but it is very informative to know it more precisely in a couple of examples.

3.5 Summary

An implementation of the method presented by Uttley et al. (2002), is described. The method is modified to suit the available data sets. An improved way of dealing with the effects of red-noise leakage is implemented. This uses interpolation and windowing with the

Table 3.2: Repeatability of fitted parameters as a function of number of simulated light curves

Test	β for M=100	β for M=1,000	β for M=10,000
Simulated with known PSD	1.85 ± 0.08	1.85 ± 0.05	1.86 ± 0.03
OVRO data with noise	2.27 ± 0.13	2.30 ± 0.07	2.32 ± 0.06

Hanning window and provides the ability to fit steep PSDs as the ones found in our data sets. We demonstrate that windowing is essential to obtain an upper limit on the value of the PSD power-law index. An upper limit is a requisite for meaningful cross-correlation significance estimates which depend on the model used for the light curves. The method used for error estimation is modified for one which provides a more intuitive procedure along with indicating the presence of biases in the fitting procedure. The method is validated using simulated data sets and found to be accurate with a typical error in β of less than ± 0.3 for cases in which the signal power is large compared to observational noise. The performance of the method is degraded when fitting time series in which the signal power is comparable to the observational noise (Figure 3.9). In these cases the procedure fails to provide a reliable constraint on the shape of the PSD, a situation we can consider when analyzing our data set by using the Neyman construction to obtain confidence intervals. We also check the repeatability of the best fit value when running the procedure multiple times and find that it improves when using a large number of simulated light curves. For an example using the OVRO data set, we find that big improvements are expected when going from M=100 to M=1,000, but then the improvements are slow, and might not be worth the increased computational time.

Chapter 4

Characterization of the radio PSDs for a large sample of blazars

4.1 Introduction

In addition to our study of the location of the high energy emission region in blazars through correlated variability, another important goal of our program is to understand the characteristics of the variability in the radio band, and their possible variation for different classes of sources or cosmic evolution. Richards et al. (2011) present a study of the radio variability using the modulation index, and find that *Fermi* detected blazars are a more variable population than the sources not detected by *Fermi*. They also find some indications of a difference between the variability properties of BL Lac versus FSRQ sources but at lower statistical significance. The modulation index measures the variability without any regard for the time domain information. In this chapter we go a step further into the time domain and characterize the radio variability with the simplest power spectral density model of a single power-law as for the sources in the cross-correlation sample studied in Chapter 6. For this study we use all the 1593 blazars monitored with the OVRO 40 meter telescope blazar monitoring program as described in Chapter 2 and study the variation of the measured PSD power-law index for different source classes and redshifts. A detailed look at the properties of the radio PSDs for the sources in the cross-correlation sample is presented in Chapter 6.

Our sample is the largest blazar sample monitored in the radio band but our light curves are still short when compared to other radio monitoring programs with smaller sample sizes like the University of Michigan Radio Observatory (UMRAO, Hughes et al., 1992) and the Metsähovi Radio Observatory (Hovatta et al., 2007) which have been monitoring sources for

decades, although at a slower cadence. One interesting question concerns the time variation of the properties of the radio light curves as seen in X-ray binaries which show transitions between different states on short time scales (e.g. Remillard & McClintock, 2006). The similarity between the underlying emission mechanisms in these objects leads us to believe that similar transitions could be observed in blazars and other AGNs on time scales in proportion to the larger black hole masses (as has been claimed by Marscher et al., 2002, for 3C 120). The longer time series available from these programs might be able to probe the time scales of these transitions and allow us to explore changes in the characteristics of the jets. In order to study the variation of source properties when different time scales are considered, we characterize the PSDs for a sample of 51 sources observed at 14.5 GHz by the UMRAO program from the mid 1970s to early 1990s and published in Hughes et al. (1992). In their study the PSD power-law index is constrained indirectly by the use of structure functions which under certain assumptions can reveal the properties of the PSD for the simple power-law case. These conditions are not guaranteed to be valid in all cases of interest as discussed by Emmanoulopoulos et al. (2010), along with other problems related to the use of structure functions for short time series[1]. Here we reanalyze their data using the method described in Chapter 3 to characterize the power-law index of the PSD directly and compare the results with those from the structure function analysis. Because the two programs use observations at similar frequencies, we can compare the evolution of the PSD characteristics for these two non overlapping time periods in the sources with data in both programs, and thus learn about possible changes in the variability on decades time scales.

4.2 Characterization of the PSDs for the radio sample

The quality of our radio light curves allows us to obtain constraints on the PSD shape for a large number of sources. The PSDs are fitted with a single power-law model, but given the large number of sources we perform a coarser fit that takes one tenth of the time of the finer fits used for the cross-correlation sample discussed in Chapter 6. This allows us to get results for all of them in about a week. In each case we test a range of values of β in steps of $\Delta\beta = 0.1$ and use M=100 light curves for the determination of the mean and

[1]For example they describe its shortcomings as a tool to determine characteristic time scales for the variability in blazar light curves, a use that is often found in the blazar literature. A complete discussion of those problems is out of the scope of this investigation but we recommend reading Emmanoulopoulos et al. (2010) to anyone interested in using structure functions to characterize light curve variability.

scatter of the model PSD at each tested value. The confidence bands are constructed with a resolution of $\Delta\beta = 0.25$ and interpolated for intermediate values and for each case we simulate 100 light curves to determine the acceptance intervals. The search interval is taken to be $0.0 \leq \beta_{\rm radio} \leq 3.5$ as is done for the cross-correlation sample. In each case where a PSD is computed we bin it in frequency intervals of 1.3 dex if the bin contains at least 4 points. In bins with less than 4 points the width is increased in steps of 1.1 dex until it contains at least 4 points. Each simulated light curve has a time resolution of 1 day and a length of 20 years.

4.2.1 Possible outcomes of the PSD fitting procedure

Before presenting the results we briefly discuss the possible outcomes of the process and how the results would be used. There are 4 possible outcomes for the procedure, which are described below.

Successful fit: In this case proper upper and lower limits on β are obtained. In this case we can directly use the constraint on the evaluation of the significance.

Lower limit: In this case the procedure returns a proper lower limit, but the upper limit is equal to the maximum of the search interval and the procedure fails to return a proper upper limit for β so that the result cannot be used directly in the evaluation of the significance.

No constraint: The procedure cannot favor any particular interval in β or the goodness of fit was too low to consider the fit a good one. We consider a fit acceptable if the p-value is > 0.05. This result cannot be used directly in the evaluation of the significance.

No variation detected: In this case it is not possible to run the fitting procedure because no variation is detected and we cannot normalize the simulated light curves. This happens when Equation 3.8 does not have a real solution for A. The reason being that all the variance in the data can be explained by the observational noise, and no variance in the signal is required. In this case we do not get any direct constraint from the method, but the fact that no variance from the signal is needed to explain the variability means that we are not detecting any source variability so we cannot measure its PSD nor estimate the significance of correlations.

4.2.2 Results of the PSD fit

We have enough signal strength to test 1259 sources and the results of the successful fits are presented in Table C.1. At the level of 68.3% confidence intervals for the radio light curves we obtain successful fits for 424 sources. For the 82.6% confidence intervals required to combine both fitted values in the significance estimate[2], we find successful fits for the radio light curves for 238 sources. These sources have the highest quality fits and are the ones used in the following sections to explore statistical differences between source populations.

The distribution of best fit power-law index of the PSDs for the 238 highest quality fits is consistent ($p = 0.011$) with a single value equal to the sample mean of 2.25 ± 0.02 and can be described by a single Gaussian with parameters $\mu = 2.3$ and $\sigma = 0.4$. The distribution is shown in Figure 4.1.

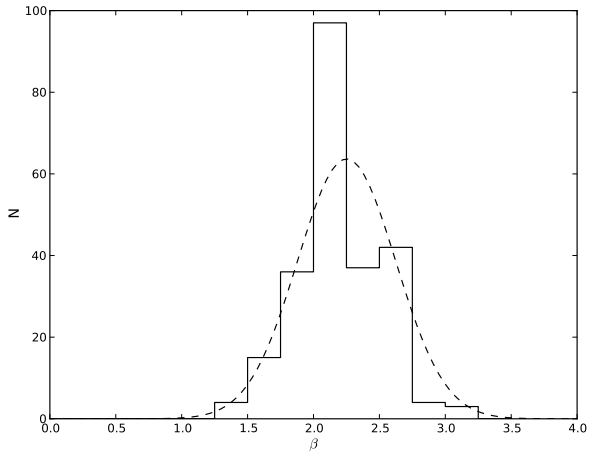

Figure 4.1: Distribution of power-law exponents of the radio light curve PSDs for the complete OVRO sample. The distribution is consistent with a single value equal to the sample mean and is described with a normal distribution with $\mu = 2.3$ and $\sigma = 0.4$, which is plotted with a dashed line.

[2]The details are discussed in the first part of Section 6.2

4.3 Variation of the power-law index distribution for different populations

Here we investigate possible differences between the distributions of the PSD shapes for different subclasses of blazars. We consider optical classes which divide them into two groups, BL Lac and FSRQ, and spectral energy density (SED) classes which separate them by the value of the synchrotron peak into low-synchrotron-peaked blazar (LSP, $\nu_{\rm peak}^{\rm Sy} < 10^{14}$ Hz), intermediate-synchrotron-peaked blazars (ISP, $10^{14}\,{\rm Hz} < \nu_{\rm peak}^{\rm Sy} < 10^{15}\,{\rm Hz}$) and high-synchrotron-peaked blazars (HSP, $10^{15}\,{\rm Hz} < \nu_{\rm peak}^{\rm Sy}$) (Abdo et al., 2010).

In this section we explore the relationship between these different classes and the properties of the radio PSD. We also explore possible variations with redshift which could indicate cosmic evolution in the variability properties.

Comparisons of the distributions of the power-law index of the radio PSD for different classes of object are presented in Figure 4.2 for the gamma-ray detected versus gamma-ray non-detected sources, Figure 4.3 for BL Lacs versus FSRQs, Figure 4.4 for LSPs versus ISPs (there are no HSP sources with high-quality PSD fits) and Figure 4.5 for the low-redshift sources ($z \leq 1$) versus high-redshift sources ($z > 1$).

From the figures it is clear that there are no obvious differences between the power-law index distributions for the different source classes. To make a quantitative statement about the comparison between the distributions we perform a two-sample Kolmogorov-Smirnov test of the null hypothesis that both samples come from the same parent distribution. In none of the cases we can reject the null hypothesis at the 0.01 significance level, thus we conclude that there is no difference in the distribution of the power-law index of the PSD for these different source classes. In the case of the gamma-ray-loud versus gamma-ray-quiet we get a p-value of 0.69, for the FSRQ versus BL Lac we get a p-value of 0.67, and for the high versus low redshift we get a p-value of 0.016. We also perform a K-S test for the case of ISP versus LSP and consistent distributions, but the small number of sources in the ISP category make this result less reliable.

In all cases the distributions are very similar, except for the case of the high versus low redshift sources which gives a small p-value, but not enough to reject the null hypothesis at the chosen significance level.

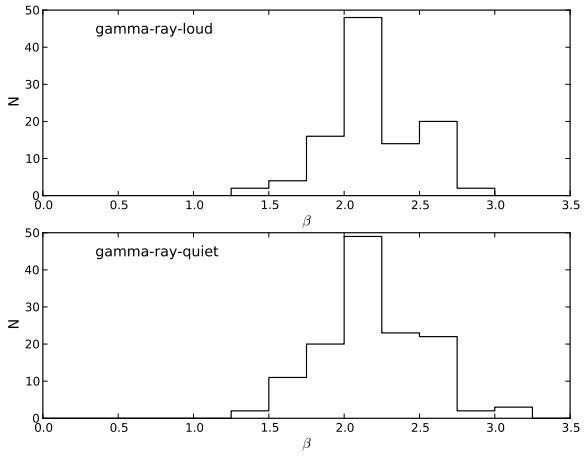

Figure 4.2: Distribution of power-law exponents of the radio light curve PSDs for gamma-ray-loud versus gamma-ray-quiet blazars

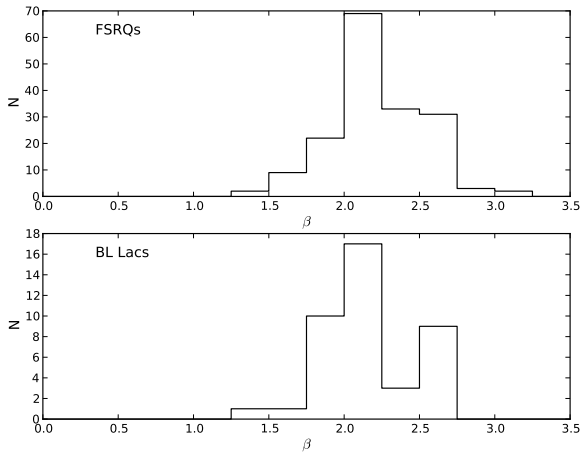

Figure 4.3: Distribution of power-law exponents of the radio light curve PSDs for FSRQ versus BL Lac blazars

4.4 Comparison of the radio PSD fits with historic light curves from the UMRAO program

The University of Michigan Radio Astronomy Observatory (UMRAO) carried out a blazar monitoring program from 1965 until early 2012. Many of those sources are in our monitoring program, so we can use them to study possible variations of the PSD in the radio band. With this purpose we take the 51 light curves published in Hughes et al. (1992) that have

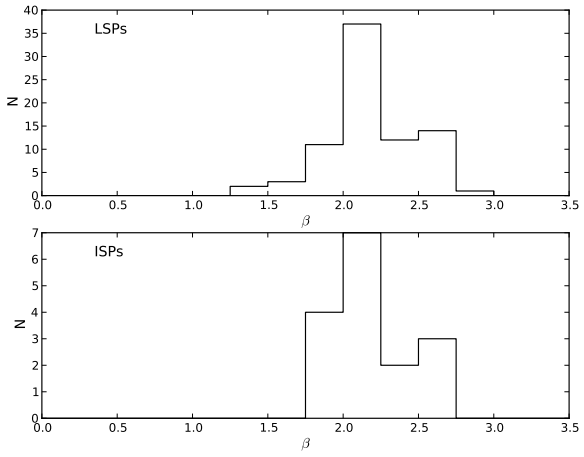

Figure 4.4: Distribution of power-law exponents of the radio light curve PSDs for LSPs versus ISPs. There are no HSP sources with high-quality PSD fits.

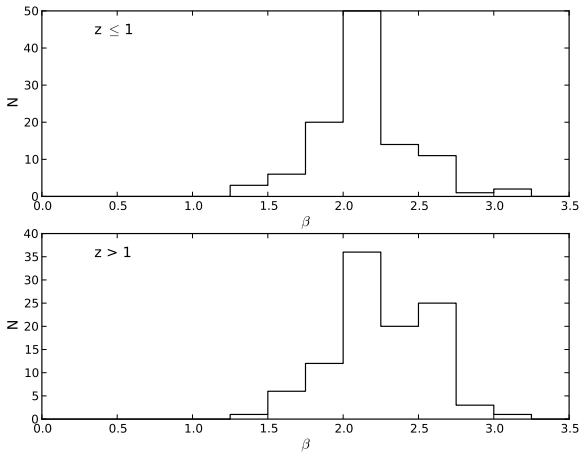

Figure 4.5: Distribution of power-law exponents of the radio light curve PSDs for low versus high-redshift sources

data at 4.8, 8.0 and 14.5 GHz, with a length and sampling interval that are different for each source. We fit the PSDs of the 14.5 GHz light curves using a simple power-law model as in the case of the OVRO sample. Only 47 light curves have their PSDs fitted, the other 4 have large gaps in their light curves and a good fit could not be obtained, so we dropped these from the sample.

4.4.1 Distribution of PSD power-law index for the UMRAO sample

In each case we test a range of values of β in steps of $\Delta\beta = 0.05$ and use M=100 light curves for the determination of the mean and scatter of the model PSD at each tested value. The confidence bands are constructed with a resolution of $\Delta\beta = 0.25$ and interpolated for intermediate values and for each case we simulate 100 light curves to determine the acceptance intervals. The search interval is taken to be $0.0 \leq \beta_{\rm radio} \leq 3.5$ as is done for the cross-correlation sample. In each case where a PSD is computed we bin it in frequency intervals of 1.3 dex if the bin contains at least 4 points. In bins with less than 4 points the width is increased in steps of 1.1 dex until it contains at least 4 points. Each simulated light curve has a time resolution of 1 day and a length of 50 years.

As with the case of the cross-correlation sample (Section 6.2.1), the fitting procedure does not provide a proper confidence interval in all cases. A summary of the results for all the sources is included in Table D.1. In the case of 68.3% confidence intervals we obtain successful fits for 27 sources, lower limits for 10 sources and no constraints for 10 sources. For the 82.6% confidence intervals required to combine with a gamma-ray PSD fit in the significance estimate, we find for the radio light curves successful fits for 24 sources, lower limits for 13 sources and no constraints for 10 sources. The 1σ errors on the PSD fits range from 0.03 to 1.3 with a median of 0.2.

As in the case of the cross-correlation sample, we examine the distribution and find that considering the best fits (24 sources with higher quality fits) the distribution is consistent with single value equal to the sample mean of 2.38 ± 0.06 and can be described with a single Gaussian with $\mu = 2.4$ and $\sigma = 0.3$ ($p = 0.16$). A K-S test reveals that this distribution is consistent with the distribution found for the complete radio sample with $p = 0.45$. This distribution is shown in Figure 4.6.

4.4.2 Comparison between the PSD fits for the UMRAO and OVRO light curves

There are 43 UMRAO sources in the OVRO monitoring program for which we can in principle compare the values of the PSD fits using the light curves from these two programs. This comparison is valid under the assumption that the 14.5 GHz frequency of the UMRAO observations and the 15 GHz of the OVRO program are close enough that any difference

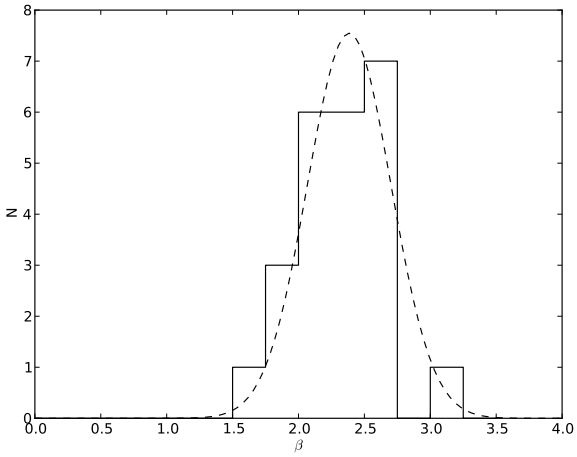

Figure 4.6: Distribution of power-law exponents of the radio light curve PSDs of the UMRAO sample. The distribution is consistent with single value equal to the sample mean and is described with a normal distribution with $\mu = 2.4$ and $\sigma = 0.3$, which is plotted with a dashed line.

between the PSDs is due to variations in the sources and not to the different frequency of the observations.

There is a significant overlap between the two samples as described below. If we consider only the 47 sources with good UMRAO data, there are 40 that are also in the OVRO program. Of these 40, only 21 have well constrained UMRAO PSDs, and 23 have well constrained OVRO PSDs.

In the current study we are mostly interested in the relation between the PSD power-law index obtained from the UMRAO and the OVRO data sets for the sources that are constrained in both data sets, as these could indicate the existence of changes in the variability characteristics in decades time scales. There are 12 sources in which we can do this and their results are shown in Table 4.1.

For these sources the error on the power-law index fit is generally smaller for the UMRAO light curves, with a mean ratio between the OVRO errors and UMRAO errors of 2.0 and a standard deviation of 1.5.

In 9 out of 12 cases the values we obtain are consistent within the error bars, so in this respect there is a general agreement between these measurements that use data for non-overlapping periods of time.

For two out of three sources in which the values are not consistent within the errors bars

Table 4.1: PSD fit results for sources in the UMRAO and OVRO data set with good quality fits in both programs. Left half of the table is for the UMRAO light curves and includes the exponent of the structure function b_s as reported in Hughes et al. (1992). The right half is for the OVRO light curves.

UMRAO name	β	β_{low}	β_{up}	b_s	OVRO name	β	β_{low}	β_{up}
0048−097	1.8	1.6	2.1	1.0	J0050−0929	2.3	2.0	2.5
0420−014	2.3	2.1	2.5	1.2	J0423−0120	2.5	2.2	2.7
3C120	2.5	2.5	2.6	1.0	J0433+0521	2.2	1.9	2.4
0607−157	2.7	2.6	2.8	1.3	J0609−1542	2.3	2.0	2.5
0754+100	2.2	1.8	2.7	1.6	J0757+0956	2.0	1.9	2.4
0814+425	2.0	0.9	3.1	1.2	J0818+4222	2.0	1.1	2.3
3C273	2.2	2.0	2.3	1.15	J1229+0203	2.2	1.9	2.5
3C279	2.2	2.1	2.4	1.1	J1256−0547	2.4	2.2	2.6
1335−127	2.3	2.1	2.5	1.1	J1337−1257	2.6	2.1	3.0
NRAO530	2.4	2.0	2.6	0.8	J1733−1304	2.0	1.7	2.2
2145+067	3.0	2.9	3.2	1.65	J2148+0657	2.2	2.0	2.5
3C454.3	2.5	2.5	2.6	1.55	J2253+1608	2.4	2.1	2.6

(3C 120 and 0607−157) the difference is within the repeatability error of about 0.1 we found in Section 3.4.2.5. In the case of 2145+067 the difference is larger, and therefore this is the only source in which we have evidence for a change in the value of PSD power-law index. Figure 4.7 shows a comparison of both measurements in which the horizontal axis is the source index as in Table 4.1 and the vertical one the value of the power-law index. Sources with discrepant measurements of β have been labeled to make them easier to identify.

4.4.3 Comparison of power-law indices estimated from the structure function and direct fits of the PSD

In the original analysis of the UMRAO data set (Hughes et al., 1992), structure functions were used to constrain the power-law index of the PSD. In the ideal case, the exponent of the structure function (b_s in Table D.1) is related to the power-law exponent of the PSD (β) by $\beta = b_s + 1$. Figure 4.8 presents a comparison of the power-law index obtained from the structure function and from the direct fit to the PSD for the 24 sources with better quality direct PSD fits.

There is agreement between the two measurements for 14 sources, which is about half the sample we use in this comparison. The difference is not large for the 10 sources in

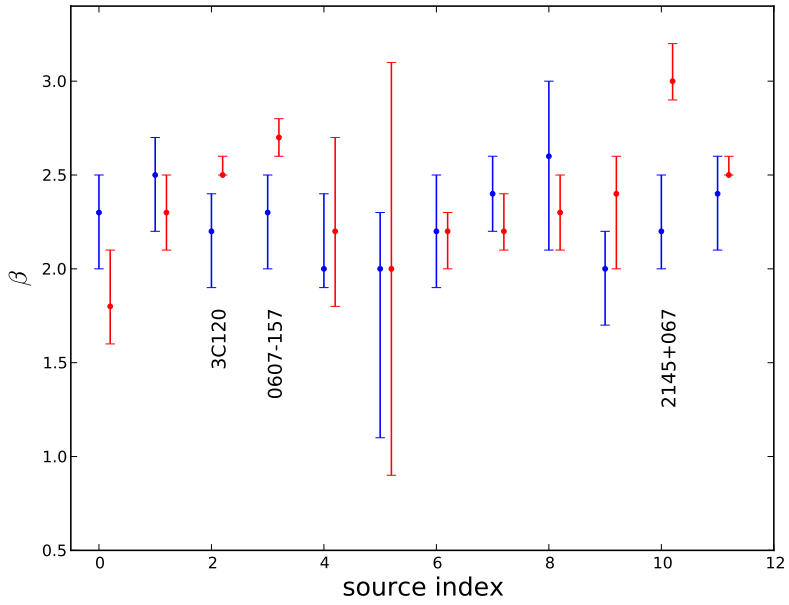

Figure 4.7: Comparison of the power-law index of the PSD measured for the OVRO light curve (blue) and for the UMRAO light curve (red). The horizontal axis is a label associated with the order in which the sources appear in Table 4.1 and the vertical one the value of the power-law index. Only the sources in which both measurements are not consistent are labeled.

which there is no agreement between the two methods but even in this case the direct PSD fit provides a way to estimate the uncertainty in the fit while this has not been provided for the structure function case. The direct PSD fit can also be generalized to study more complex PSD shapes which might become necessary for very long and well sampled light curves.

4.5 Summary

We have estimated the power-law index of the radio PSDs for all the sources in our monitoring program and we found that its distribution can be described by a normal distribution with $\mu = 2.3$ and $\sigma = 0.4$. We also investigated possible variations of the power-law index across different source populations but found no evidence for such a variation when dividing the sources by gamma-ray-loud versus gamma-ray-quiet, FSRQ versus BL Lac, SED class, and redshift.

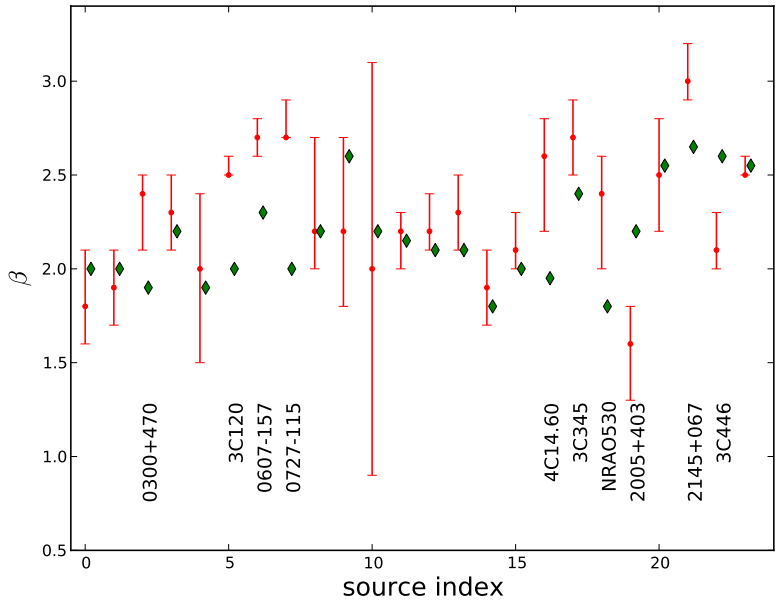

Figure 4.8: Comparison of the power-law index of the PSD as measured from the structure function (green diamonds, Hughes et al., 1992) and direct PSD fit (red symbols) for the 24 sources with better direct PSD fits are included. The sources are taken from Table D.1 and are labeled in the horizontal axis by the RA order used there. Only the sources in which the two measurements are not consistent are labeled.

An interesting question is the possible change of the PSD parameters with time. To investigate this we fitted the PSDs to historic data from the UMRAO program and compared them with our determination. It is found that for the 12 sources with good quality PSD fits in both programs, 9 have consistent PSDs, two are slightly different and in only one case is the difference large enough to be considered significant.

We also found that the distribution of the 24 UMRAO sources with good quality fits can be described with a normal distribution with $\mu = 2.4$ and $\sigma = 0.3$, which is in turn consistent with the distribution found in the OVRO population.

We also compared estimates of the power-law index of the PSD obtained indirectly by structure function fits (Hughes et al., 1992) and our direct fits of the PSDs. We found agreement in 58% of the cases and relatively small differences in the inconsistent cases. In spite of this agreement we still think that direct PSD fits should be the preferred method since it provides an uncertainty estimate and can also be generalized to more complex PSD shapes.

From these results we conclude that the distribution of radio PSDs for blazars is consistent with a single distribution and that the value for an individual source is stable in time for most sources on times scales of a few decades.

Chapter 5

Significance of cross-correlations between two wavebands

5.1 Introduction

The key goal of the OVRO 40 m telescope blazar monitoring program is to understand the relation between the radio and gamma-ray emission in blazars in order to constrain the location of the gamma-ray emission site with respect to the radio emitting region. This will help us constrain theoretical models for the blazar emission mechanism at high energies, furthering our understanding of the basic physics in this class of objects.

Our approach is to search for correlated variability between these two energy bands which would be a strong indication of co-spatial location of the emission regions. The study of cross-correlations between two energy bands presents a number of challenges from the data analysis and statistical point of view: Among these are uneven sampling, non-equal error bars and short length of the time series.

This chapter deals with the statistical problem of quantifying the significance of the cross-correlation between two time series in the case of uneven sampling and non-uniform measurement errors. The two time series are assumed to contain no upper or lower limits, a subject which is out of the scope of the current analysis.

Two alternative ways to estimate the cross-correlation coefficient are described in Section 5.2. Standard cross-correlation tests that assume that the data are uncorrelated are not applicable in this case, in which we have to explicitly consider the existence of long term correlations in the time series (i.e., flare like features). A description of the method we use to estimate the significance and a discussion motivating it are given in Section 5.3.

Different approaches have been used in the literature by different authors, but the criteria they have used to select an alternative do not consider the measurement of significance, which is our primary concern. In Section 5.4, we propose a way to choose the best method based on the significance levels of the correlation coefficients found in simulated data with known correlation properties. A series of tests comparing these alternatives is presented in Section 5.5. This is followed by a brief discussion of the dependence of the significance on the model used for the light curves (Section 5.6.1), the error of the significance estimates obtained using Monte Carlo methods (Section 5.6.2), and an estimation of the correction for multiple hypothesis tests to allow for the fact that a range of time lags is considered. These issues have been ignored in the literature, producing significance estimates that might not be repeatable due to the small number of simulations used or that might be less significant due to the broad time lag range used to search for cross-correlation peaks. The chapter concludes with a summary of our findings and general recommendations for studies using this or other methods based on Monte Carlo simulations.

5.2 The estimation of the cross-correlation function

Our basic data sets are two time series we call A and B. These time series are time ordered sequences of triplets $(t_{ai}, a_i, \sigma_{ai})$ with $i = 1, ..., N$ and $(t_{bj}, b_j, \sigma_{bj})$ with $j = 1, ..., P$. In both cases t_{xi} is the observation time, x_i is the measured value of a quantity of interest (e.g. flux density, photon flux, etc.) and σ_{xi} an estimate of the observational error associated with the measurement.

Since the time interval between successive samples is not uniform and the A and B time series are not sampled simultaneously we need to resort to some kind of time binning in order to measure the cross-correlation. The cross-correlation between two unevenly sampled time series can be measured using a number of different approaches. The usual approach is to generalize a standard method and use time binning to deal with the uneven sampling. Here we consider the discrete correlation function (Edelson & Krolik, 1988) and the local cross-correlation function (e.g., Welsh, 1999). These methods provide a way of estimating the cross-correlation coefficients, but do not provide an estimate of the associated statistical significance. This is discussed in Section 5.3.

The two most commonly found alternatives are presented below.

5.2.1 The Discrete Correlation Function (DCF)

The discrete correlation function was proposed by Edelson & Krolik (1988) and developed in the context of reverberation mapping studies. For two time series a_i and b_j, we first calculate the unbinned discrete correlation for each of the pairs formed by taking one data point from each time series

$$\mathrm{UDCF}_{ij} = \frac{(a_i - \bar{a})(b_j - \bar{b})}{\sigma_a \sigma_b} \tag{5.1}$$

where $\bar{a}$ and $\bar{b}$ are the mean values for the time series, and σ_a and σ_b are the corresponding standard deviations. This particular value, UDCF_{ij}, is associated with a time lag of $\Delta t_{ij} = t_{bj} - t_{ai}$. The discrete cross-correlation is estimated within independent time bins of width Δt, by averaging the unbinned values within each bin,

$$\mathrm{DCF}(\tau) = \frac{1}{M} \sum \mathrm{UDCF}_{ij}, \tag{5.2}$$

the uncertainty in the binned discrete cross-correlation is given by the scatter in the unbinned values for each time bin and is given by

$$\sigma_{\mathrm{DCF}}(\tau) = \frac{1}{M-1} \left(\sum [\mathrm{UDCF}_{ij} - \mathrm{DCF}(\tau)]^2 \right)^{1/2} \tag{5.3}$$

In the expressions above the sum is over the M pairs for which $\tau \leq \Delta t_{ij} < \tau + \Delta t$, where τ is the time lag, and all the bins have at least two data points in order to get a well-defined error. In practice it is recommended to choose M larger that 2 to reduce the effect of statistical fluctuations.

In this case the mean and standard deviation use all the data points in a given time series, but the DCF for a given time lag only includes overlapping samples. This particular choice for normalization produces values of the DCF which are not restricted to the usual $[-1, 1]$ interval of standard correlation statistics. This immediately challenges the interpretation of the amplitude of the DCF as a valid measure of the cross-correlation and invalidates the use of standard statistical tests developed for other correlation statistics, forcing us to find alternative ways to estimate the significance of correlations. A modification that corrects this normalization problem but not the significance evaluation issue is described below.

5.2.2 The Local Cross-Correlation Function (LCCF)

Motivated by the normalization problems presented by the DCF, some authors have proposed a different prescription (e.g., Welsh, 1999). In this case we only consider the samples that overlap with a certain coarse grain of the time delays, which is equivalent to the width of time bins Δt. In this case we have

$$\mathrm{LCCF}(\tau) = \frac{1}{M} \frac{\sum (a_i - \bar{a}_\tau)(b_j - \bar{b}_\tau)}{\sigma_{a\tau}\sigma_{b\tau}} \tag{5.4}$$

where the sum is over the M pairs of indices (i, j) such that $\tau \leq \Delta t_{ij} < \tau + \Delta t$. The averages ($a_\tau$ and b_τ) and standard deviations ($\sigma_{a\tau}$ and $\sigma_{b\tau}$) are also over the M overlapping samples only.

The main justification for using this expression instead of the DCF is that we recover cross-correlation coefficients that are bound to the $[-1, 1]$ interval. This latter property is a result of using only the overlapping samples to compute the means and standard deviations, which in effect reduces the problem to a standard cross-correlation, that is bounded to $[-1, 1]$ as a consequence of the Cauchy-Schwarz inequality. Additionally Welsh (1999) shows that the LCCF can determine time lags more accurately than the DCF in simulated data sets. These are certainly desirable properties, but as explained in Section 5.3 they do not solve the estimation of significance problem.

5.2.3 Other schemes

Any standard cross-correlation method can be generalized to unevenly sampled time series as follows. First we decide on a time binning interval, Δt. We then start delaying one of the time series by arbitrary amounts τ. Comparing the times for the delayed and unmodified time series we find the set of overlapping samples, as the ones for which $\Delta t_{ij} < \Delta t$. After this we have a set of data pairs (a_k, b_k) with $k = 1, ..., K$, where K is the number of overlapping samples. At this point we can forget about the time variable and treat these data pairs as time independent. The LCCF as described in Section 5.2.2 is naturally understood under this scheme. Any standard cross-correlation technique can be used on this new subset. In particular we can apply survival analysis techniques to allow for the use of upper limits in the time series, or other non-parametric tests that can give us more robust results. Likewise the DCF can also be interpreted in this way if we substitute the mean and standard deviations

from the overlapping samples by the values obtained for the complete time series.

A number of other alternatives have been proposed in the literature to handle the problem of measuring the correlation between unevenly sampled time series. Among them are the interpolated cross-correlation function (ICCF; Gaskell & Peterson, 1987), inverse Fourier transform of the cross-spectrum (Scargle, 1989) and the z-transformed cross-correlation function (Alexander, 1997). These are only mentioned here to guide the reader to other alternatives but are not explored in this work.

5.2.4 Estimation of the uncertainty in the location of the cross-correlation peak

A related issue is the estimation of the uncertainty in the location of the cross-correlation peaks. This is sometimes confused by some researchers with the estimation of the significance, but here we are assuming that we have already a significant correlation and attempt to estimate the error in the location of the peaks due to sampling and observational errors. The standard method used by the reverberation mapping community (Peterson et al., 1998) uses bootstrapping and randomization to generate slightly modified versions of the original data set to quantify the uncertainty in the location of the cross-correlation peak. A modified data set is constructed by the application of two procedures. First is "random subset selection" in which a bootstrapped light curve is constructed by randomly selecting with replacement samples from the original time series. Secondly we perturb the selected flux measurements by "flux randomization", in which normally distributed noise with a variance equal to the measured variance is added to the measured fluxes. Each of these modified data sets is cross-correlated using the method of our choice and a value for the cross-correlation peak of interest is measured. By repeating this for many randomized data sets, a distribution of measured time lags for the cross-correlation peaks is obtained. This distribution is used to construct a confidence interval for the position of the peak.

5.2.5 Light curve detrending

There has been some discussion in the literature about the effects of detrending the light curves in order to improve the accuracy of the time lag estimates. Welsh (1999) strongly recommended removing at least a linear trend from the light curves. His results are based

on simulations with even sampling and do not directly apply to uneven sampling as shown by Peterson et al. (2004), who find that detrending does not improve accuracy and produces large errors in some cases. Based on that we have decided not to detrend the light curves.

We warn the reader that care must be taken when correlating time series where long term trends are present as these are guaranteed to produce large values of the cross-correlation coefficient. Our studies are mostly concerned with the correlation between periods of high activity in different energy bands for light curves that appear to have a detectable "quiescent" level. This is generally true for gamma-ray light curves, but is not always true for radio light curves. Radio light curves showing a single dominant increasing or decreasing linear trend should be interpreted with care as they can produce spurious correlations. In our opinion the only remedy for those cases is to collect longer light curves.

5.3 The estimation of the significance

A complete quantification of the cross-correlation needs an estimate of the statistical significance of the given statistic. There are well defined procedures to do this using standard methods like the Pearson's correlation coefficient, Spearman's ρ and others. In our case we need to consider the intrinsic correlation between adjacent samples of a given time series which are produced by the presence of flare-like features which are a distinctive characteristic of blazar light curves. This behavior can be modeled statistically by red-noise stochastic processes (e.g., Hufnagel & Bregman (1992) in the radio and optical, Lawrence & Papadakis (1993) in the X-rays and Abdo et al. (2010) in gamma-rays). Red-noise processes are characterized by their power spectral density (PSD), show variability at all time scales and appear as time series in which flare like features are a common phenomenon. The frequent appearance of flares means that high correlation coefficients between any two energy bands are to be expected even in the absence of any relation between the processes responsible for their production. To illustrate this point Figure 5.1 shows simulated light curves with power-law power spectral densities (PSD $\propto 1/\nu^{\beta}$). These and all the simulated light curves used in this work are generated using the method described in Timmer & Koenig (1995) which randomizes both the amplitude and phase of the Fourier transform coefficients according to the statistical properties of the periodogram.

In fact, every time we cross-correlate two time series, each of which has a flare we

will get a peak in the cross-correlation at some time lag. The real question then is how to quantify the chances of that peak being just a random occurrence. The problem is further complicated by the uneven sampling and non-uniform errors, so the only feasible method is to use Monte Carlo simulations. Standard methods are not suitable for this analysis as they assume that the data are uncorrelated, and ignoring the correlations will lead to an overestimate of the significance of the cross-correlations and to erroneous physical interpretation.

In Figure 5.2 we show the results of cross-correlating the independently simulated light curves from Figure 5.1 which have different values of the power-law exponent for the power spectral density. It can be seen that correlating light curves with steep power spectral density, which show frequent flare-like features, can result in high cross-correlation coefficients that have nothing to do with a physical relation between the light curve pairs. The results illustrate how easy it is to get high cross-correlations for unrelated light curves with steep PSDs and the dangers of interpreting them as signs of a physical connection. Standard statistical tests that assume uncorrelated data are equivalent to the case of white noise time series (PSD $\propto 1/\nu^0$) which is illustrated in the upper panels of Figure 5.2. Since it is evident that blazar light curves are more similar to the simulated light curves with steep PSDs is easy to see how misleading is to use statistical tests that ignore the long term correlations in the individual time series.

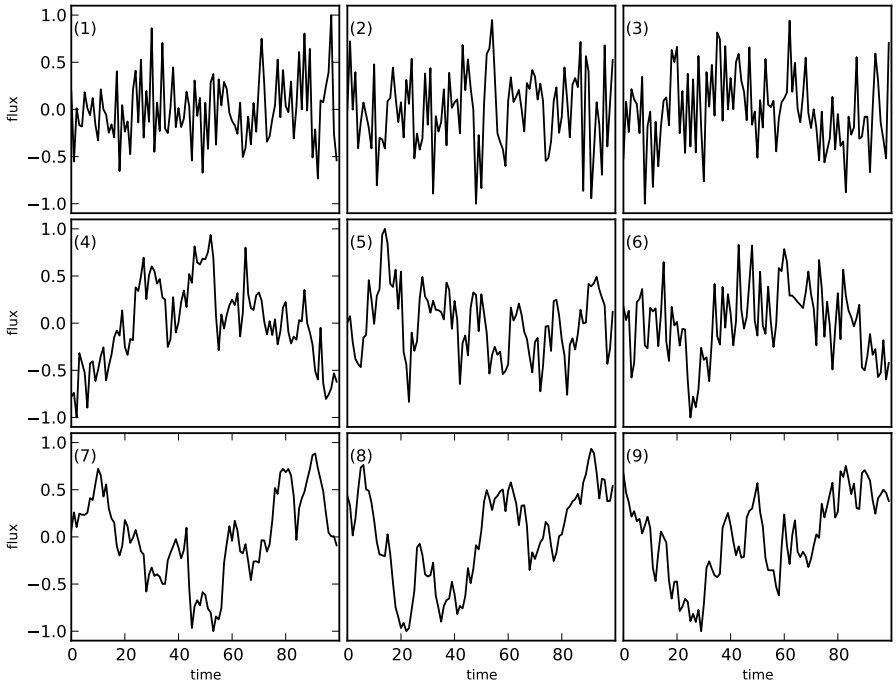

Figure 5.1: Illustration of the time domain characteristic of simulated light curves with different power-law power spectral density. In all panels the horizontal axis is time and the vertical one is amplitude, both in arbitrary units. Top panels 1, 2 and 3 for PSD $\propto 1/\nu^0$, central panels 4, 5 and 6 for $\propto 1/\nu^1$ and lower panels 7, 8 and 9 for $\propto 1/\nu^2$. The light curves with steeper PSD show more flare-like features that can induce high values of the cross-correlation coefficient as shown in Figure 5.2.

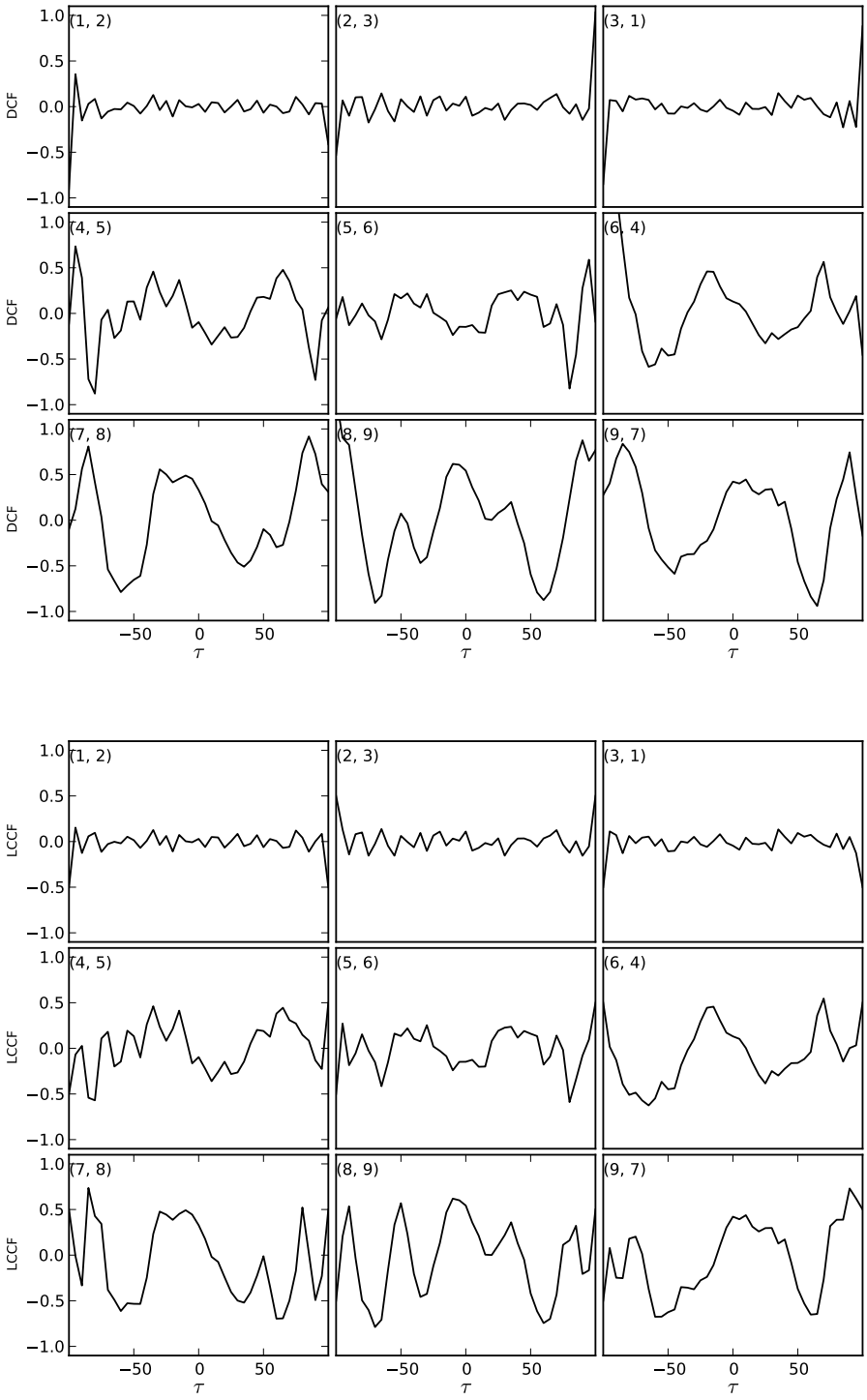

Figure 5.2: Examples of the cross-correlation of simulated light curves shown in Figure 5.1 using the DCF (upper figure) and LCCF (lower figure). In all panels the horizontal axis is time lag in arbitrary units and the vertical one is the amplitude of the cross-correlation. Upper panels, cross-correlation of independent $\beta = 0.0$ light curves. Central panels, cross-correlation of independent $\beta = 1.0$ light curves. Lower panels, cross-correlation of independent $\beta = 2.0$ light curves. The pair of numbers on the upper left corner of each panel are the light curve numbers from Figure 5.1 which are correlated in each case. The light curve pairs have been simulated independently and yet show large peaks in the discrete cross-correlation function for the cases of $\beta = 1.0$ and 2.0. The appearance and amplitude of peaks in the cross-correlation appears to increases for steeper power spectral densities.

5.3.1 Monte Carlo procedure for the estimation of the significance

In order to obtain a Monte Carlo estimate of the distribution of random cross-correlations we need a model for the light curves. A commonly used model for time variability in blazars and other AGNs is a simple power-law power spectral density (PSD $\propto 1/\nu^{\beta}$), as has been measured for small number of sources at different wavelengths. Of particular interest for this work are the results presented in Abdo et al. (2010) where they find a value of $\beta_{\gamma} = 1.4 \pm 0.1$ for bright BL Lacs and $\beta_{\gamma} = 1.7 \pm 0.3$ for the bright FSRQs in the gamma-ray band. In the radio band a number of publications have dealt with the issue. It has been found that $\beta_{\rm radio} = 2.3 \pm 0.5$ for 3C279 at 14.5 GHz (Chatterjee et al., 2008) using a fit to the power spectral density for an 11 year light curve. Additional indirect estimates for the power spectral density power-law index are obtained by Hufnagel & Bregman (1992) using structure function fits. For five sources, they obtain values of $\alpha = 0.4 \pm 0.2$ to 1.5 ± 0.1, where α is the exponent on the structure function ${\rm SF}(\tau) \propto \tau^{\alpha}$. The same method is used for 51 sources by Hughes et al. (1992) who found that most values of α are from 0.6 to 1.8, while a couple are closer to 0. However the often assumed relation between the exponents of the power spectral density and the structure function ($\beta = \alpha + 1$) is only valid under special conditions not necessarily found in real data sets (Paltani, 1999; Emmanoulopoulos et al., 2010). The structure function has been widely used in blazar variability studies but its interpretation is not straightforward as has been recently discussed by Emmanoulopoulos et al. (2010), who used simulations to demonstrate that many of the features are associated with the length and sampling patterns of the light curves. For these reasons, values obtained from the structure function can only be taken as a rough measure of the properties of the time series, and therefore we do not use them here. In this chapter we assume that $\beta_{\gamma} = 1.5$ and $\beta_{\rm radio} = 2.0$, and consider them as reference values that can be used to take a first look at the statistical significance of the peaks and to test the methods we develop. A proper characterization of the PSDs is presented in Chapters 3 and 6 in which we discuss the method we use and its application to our data set.

To estimate the significance of the cross-correlation coefficients, we use a Monte Carlo method to estimate the distribution of random cross-correlations by using simulated time series with statistical properties similar to the observations. These and related ideas have been applied by several authors (e.g., Edelson et al., 1995; Uttley et al., 2003; Arévalo et

al., 2008; Chatterjee et al., 2008). The details of the procedure vary from author to author so we provide a detailed description of our implementation to allow others to evaluate and reproduce our analysis.

The algorithmic description of the method we use to measure the significance of the time lags is as follows:

- We calculate the cross-correlation coefficients between the unevenly sampled time series using one of the methods described in Section 5.2.
- Using an appropriate model for the PSDs at each energy band we simulate time series with the given noise properties and sampled exactly as the data. The resulting flux densities are perturbed by adding noise according to the observational errors. We calculate the cross-correlation coefficients of the simulated light curve pairs using the same method as for the real data.
- We repeat the previous step for a large number of radio/gamma-ray simulated light curve pairs and accumulate the resulting cross-correlation coefficients for each time lag.
- For each time lag bin the distribution of the simulated cross-correlation coefficients is used to estimate the significance levels of the data cross-correlation coefficients.

An additional detail is that the gamma-ray time series are the result of long integrations so each simulated data point is generated by averaging the required number of samples to simulate the time binning. For the radio light curves the integrations are so short that the closest sample can be chosen. Figure 5.5 shows the application of the method for an example taken from our monitoring program using $\beta = 2$ in both bands with the DCF and the LCCF. In both cases the cross-correlation coefficient at each time lag is represented by the black dots and the distribution of random cross-correlations by the colored dotted lines. A time lag $\tau > 0$ means the gamma-ray emission lags the radio and $\tau < 0$ the opposite. The red lines contain 68.27% of the random cross-correlations so we refer to them as the 1σ lines, the orange lines contains 95.45% (2σ), and the green lines contains 99.73%(3σ)[1]. The colored contours provide a quick way to evaluate the results of the cross-correlation significance estimate and are used for this purpose throughout this thesis. In this case

[1]In what follows we refer to them as the 1, 2 and 3σ lines or significance levels

although the amplitudes are relatively high for both the DCF and LCCF, the significance is not even 2σ indicating only marginal evidence of a correlation.

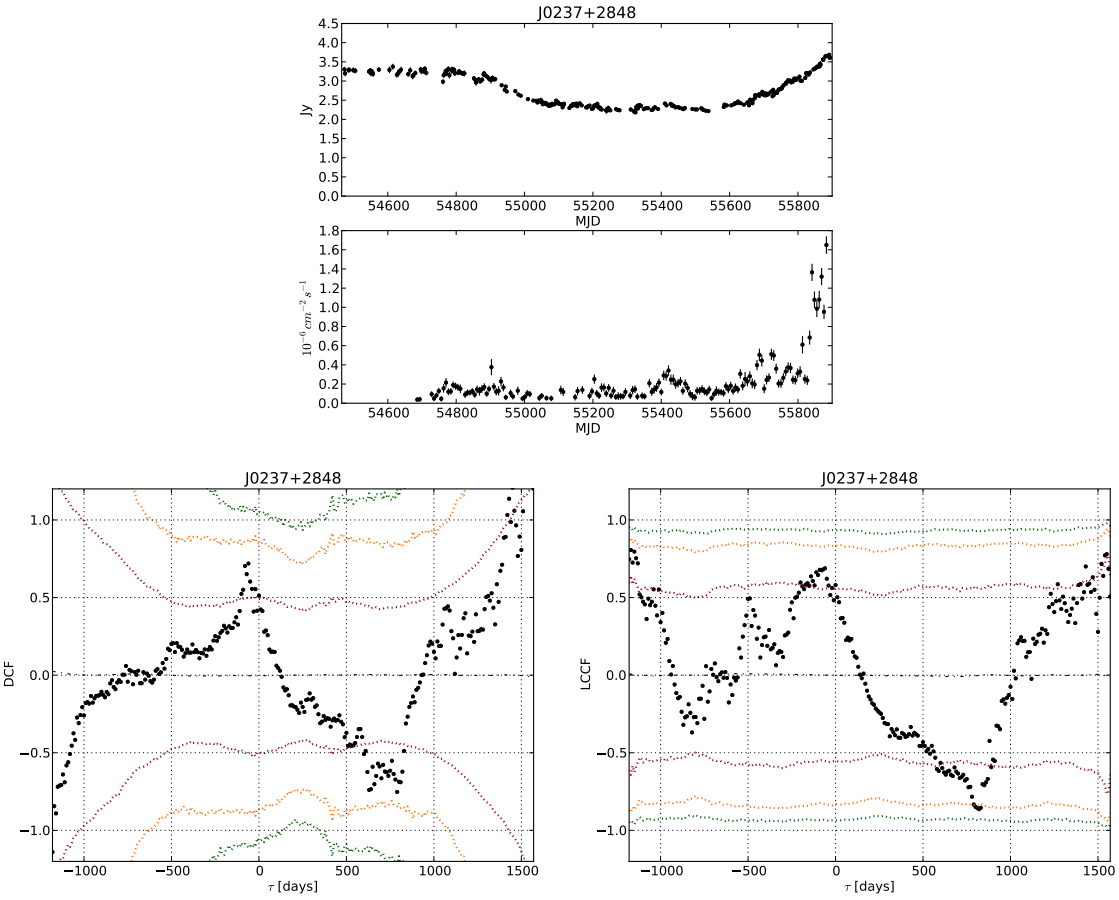

Figure 5.3: Example of cross-correlation significance results. Upper panel shows the radio (upper) and gamma-ray (lower) light curves for J0237+2848. Lower left panel is for the DCF and lower right panel for the LCCF. The black dots represent the cross-correlation for the data, while the color contours show the distribution of random cross-correlations obtained by the Monte Carlo simulation with red for 1σ, orange for 2σ and green for 3σ significance. A time lag $\tau > 0$ indicates the gamma-ray emission lags the radio and $\tau < 0$ the opposite.

5.4 Characterization of the methods

The method used to estimate the significance described in Section 5.3 can in principle be used with any of the different alternatives presented in Section 5.2, but ideally we would like to make a choice that is best suited to the problem we are facing. A couple of different

practices have been followed in the literature for reasons that are not always made explicit. Two examples where the choice is explicitly justified are White & Peterson (1994) who used the interpolated cross-correlation function and Welsh (1999) who recommended using the LCCF. In both cases the argument in favor of their chosen method is mostly to reduce the bias and error in the measured time lags with respect to the true one. Furthermore White & Peterson (1994) argue that for some time lags the DCF can become meaningless with values outside the $[-1, 1]$ interval for standard correlation tests. As we said before, this does not immediately invalidate the DCF but it invalidates the application of standard statistical tests to evaluate the significance of a given cross-correlation amplitude. The reduction of bias and error in the measurement of the time lags is obviously of concern, but in our case we are also interested in the quantification of the significance. This means that we need to compare the methods using a metric that specifically measures the detection efficiency of correlations within a chosen error tolerance for the recovered time lag. Ideally we would like to do this using a physical model for the correlation properties of the time series. Unfortunately such predictions are not currently available and we can only test the method using some ideal cases with simple and known correlation properties. The results of these tests are presented in Section 5.5.

Below we define a few basic concepts from hypothesis testing, describe the test we use to choose the best method and provide a simple algebraic relation between the DCF and LCCF that helps explain their differences.

5.4.1 A brief review of hypothesis testing

In what follows we provide definitions for some terms that are often used in the following chapters. The presentation is based on Beringer et al (2012), which can be consulted in case additional details or references are needed.

In a hypothesis test we have to decide between two alternative hypotheses to explain the outcome of an experiment; they are usually called H_0, the null hypothesis, and H_1, the alternative hypothesis.

In taking a decision we can make two kinds of errors:

- *Type-I error*: rejecting H_0 when it is in fact true
- *Type-II error*: accepting H_0 when it is in fact false

The chances of making those errors can be quantified by two numbers:

- α: the probability of making a *type-I error*, commonly known as the *significance level* of the test
- β: the probability of making a *type-II error*. We commonly talk about the *power* of the test which is defined as $1 - \beta$

In some cases we have a well defined null hypothesis but no explicit alternative hypothesis. In these cases we can define a statistic t whose value is related to the agreement of the data with the null hypothesis. The statistic t is a random variable under the null hypothesis with probability density function $g(t|H_0)$, which gives the probability of the outcome t under the null hypothesis H_0. The p-value is defined as the probability of finding t in a region of equal of lesser compatibility with H_0. For example if we take t to be a correlation coefficient (the DCF or LCCF at a given time lag in this case), a small value close to zero is more compatible with a null hypothesis of no correlation, while a large value is less compatible and hence has a larger chance of representing a real correlation. For this case the p-value is given by

$$p = \int_{t_{obs}}^{t_{max}} g(t|H_0)dt \tag{5.5}$$

where t_{obs} is the observed cross-correlation coefficient value and t_{max} is 1 for the LCCF and ∞ for the DCF. The null hypothesis is rejected if $p \leq \alpha$.

When quoting the results of a *significance test* we can use the p-value or an equivalent *significance* Z defined as $Z = \Phi^{-1}(1 - p)$, where Φ is the cumulative distribution of the standard normal distribution and Φ^{-1} is its inverse. This is the formal definition of significances quoted as $Z\sigma$ which is more common in astronomy than the p-values.

5.4.2 Application to our statistical test

The procedure described in Section 5.3 provides an estimate of the p-value of a given data set under a given null hypothesis defined by the model used to generate the Monte Carlo light curve pairs. The *significance level* of the test (α) is set by construction by simply rejecting the null hypothesis when $p \leq \alpha$. The case for the *power* of the test is harder because we have a well defined null hypothesis of uncorrelated time series with a given

PSD, but not a well defined alternative hypothesis as we have not specified a predictive physical model for the correlation between the two wavebands. Estimating the power of the test is not possible without a model for the correlation, but we can get some idea for it by testing the detection efficiency for simple cases in the way described below.

The procedure we use consists in generating simulated data sets with known correlation properties and similar sampling as the data. The simulated data sets are then run through the same procedures as the data and the fraction of cases where we can successfully detect the correlation is the *power* or *detection efficiency* of the test for the particular model. We can never test all the cases so only a few idealized models can be tested to at least compare different methods.

We test the properties of the method by using it in simulated identical time series with a time shift, sampled in the same way as the data. We test a few possible delays in the ranges we find in the data. This is the ideal case of the best possible correlation. Since this is not a physical model for the relation between the two energy bands, it only provides a relative indication of the detection efficiency. Its most useful feature is that it provides an objective way to compare different approaches to search for correlations, as we can choose between methods by comparing their detection efficiencies.

5.4.3 Relation between the DCF and LCCF

In Section 5.5 we perform a series of tests designed to help us compare the detection efficiency of the DCF and LCCF. In looking at these results is its useful to consider the relation between those two correlation measures.

From our previous discussions we can see that the only difference between the DCF and LCCF is in the values used for the means and standard deviations. In the case of the DCF the means and standard deviations are calculated from the complete time series ($\bar{a}, \bar{b}$ for the means and σ_a, σ_b for the standard deviations), while for the LCCF only the overlapping samples at each time lag are used ($\bar{a_\tau}, \bar{b_\tau}$ for the means and $\sigma_{a\tau}, \sigma_{b\tau}$ for the standard deviations). It can be shown that the two are related at a given time lag by

$$\mathrm{DCF}(\tau) = \mathrm{LCCF}(\tau)\frac{\sigma_{a\tau}\sigma_{b\tau}}{\sigma_a\sigma_b} + \frac{(\bar{a_\tau} - \bar{a})(\bar{b_\tau} - \bar{b})}{\sigma_a\sigma_b}. \tag{5.6}$$

This linear relation has coefficients that depend on the sampling pattern and the overlap

between the two time series at different time lags. For long stationary time series the means and variances of the overlapping and complete time series will be identical and the DCF will equal the LCCF. For short or non-stationary time series the coefficients will make the DCF different from the LCCF.

Deviations of the multiplicative coefficient ($\frac{\sigma_{a\tau}\sigma_{b\tau}}{\sigma_a\sigma_b}$) from 1 change the amplitude of the DCF, and deviations of the additive coefficient $\frac{(\bar{a_\tau}-\bar{a})(\bar{b_\tau}-\bar{b})}{\sigma_a\sigma_b}$ from 0 change the zero point of the DCF. The combination of these variations explains why the DCF is not bounded to the $[-1, 1]$ interval as the LCCF is, and can also explain why they have different detection efficiencies.

5.5 Comparison of the DCF and the LCCF

The two methods we consider are compared to determine quantitatively which is the best for the problem of detecting significant correlations between two time series. The comparison is made in terms of detection efficiency of correlations at a given significance level and a maximum time lag error. For the tests we simulate a time series with a very fine time resolution and make two copies, one for each band, in which the only difference is a known time lag and the different sampling pattern which is taken from example light curves from our monitoring program.

In all the cases we bin the cross-correlation with $\Delta t = 10$ days and model the time series with a PSD $\propto 1/\nu^2$, which is also used for the Monte Carlo evaluation of the significance. We use 1000 uncorrelated time series to estimate the distribution of random cross-correlations and significance. This same realization is then used to measure the significance of the peaks we find for 1000 correlated time series we use to test our detection algorithm.

This corresponds to the ideal case of a perfect intrinsic correlation which is only distorted by the time lag and different sampling of the two time series. The case is also ideal with respect to the significance evaluation as we perfectly know the model for the light curves. It is important to keep these points in mind and to realize that the actual detection efficiencies could be much lower than what we find through these tests.

5.5.1 Uniform and identical sampling for both time series, zero lag and no noise.

As a check of the method and to help the reader understand the results, we first test our ability to detect correlations in a very simple case. In this case a time series with a uniform sampling period of 3 days is correlated with a copy of itself without any delay or noise. An example of the simulated data set along with the results for the DCF and LCCF is shown in Figure 5.4. The results of the Monte Carlo significance analysis are shown in Figure 5.5. The same procedure is repeated for all simulated time series with known correlation and the fraction of detected lags at the known lag ($\pm\Delta t$) with a given significance level is reported as an efficiency in Figure 5.6.

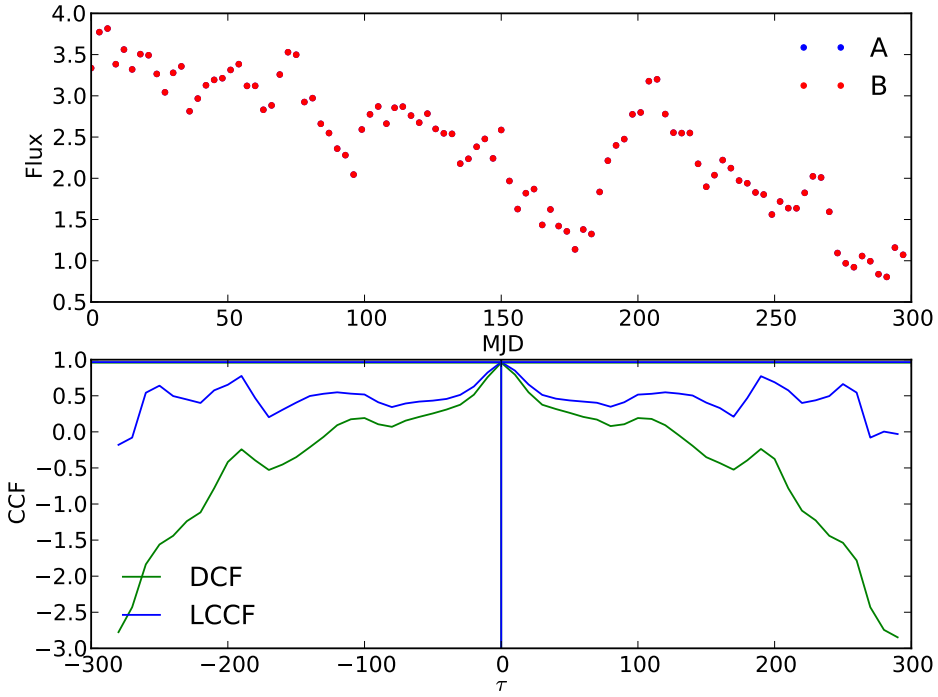

Figure 5.4: Example of simulated data with PSD $\propto 1/\nu^2$ and uniform sampling. The upper panel shows the two time series which overlap perfectly in this case. The lower panel has the results of the DCF and LCCF for this case. The vertical lines show the position of the most significant peak with color corresponding to the method used. Horizontal color lines mark the amplitude of the most significant peak for each method.

In this case, we recover most of the time lags at the right value and the behaviors of

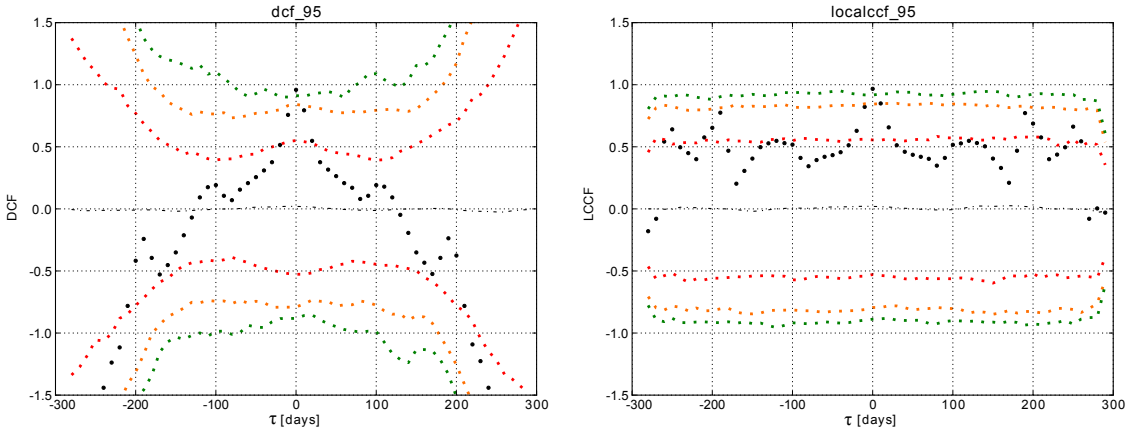

Figure 5.5: Cross-correlation significance results for the example shown in Figure 5.4. Left panel is for the DCF and right panel for the LCCF. The time lag at zero is recovered with high significance in both cases. The most striking difference between the two methods is the normalization which is not restricted to the $[-1, 1]$ interval in the case of the DCF.

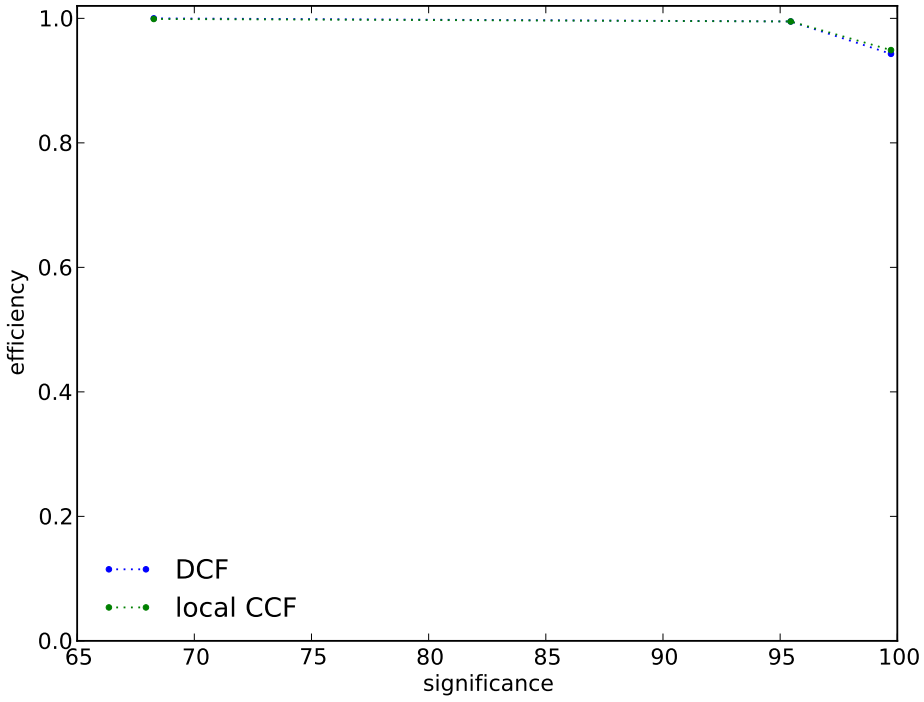

Figure 5.6: Detection efficiency versus significance for both methods. In this case close to 95% of the lags are recovered at the right value and 3σ significance.

the DCF and LCCF are very similar. The values of the coefficients of the linear relation for $\tau = 0$ (Equation 5.6), are very close to the case when the DCF and LCCF are equal (Figure 5.7).

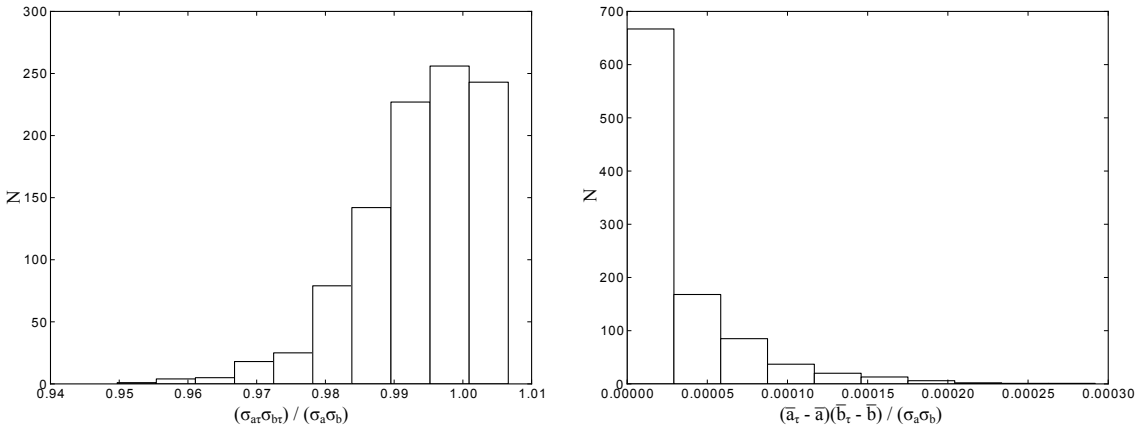

Figure 5.7: Distribution of the coefficients of the linear relation between DCF and LCCF for $\tau = 0$. Left panel is the multiplicative factor, which is very close to 1 in most cases. Right panel is the additive constant which is very close to 0. These values make DCF $\approx$ LCCF which makes the results of both methods very similar as can be seen in Figure 5.6.

5.5.2 Data sampling case 1, "short data set": 2 years of OVRO and 1 year of *Fermi*-LAT.

We now study a case with sampling taken from a preliminary OVRO 40 m blazar monitoring program/*Fermi*-LAT data set, again with no noise added to the simulations and zero lag between the two light curves, so the only difference is in the sampling pattern. In this case a source was observed for two years with the OVRO 40 m telescope at 15 GHz with a nearly twice per week sampling (Richards et al., 2011). The gamma-ray data for the same source has a cadence of about one observation per week and was observed for one year (Abdo et al., 2010). The cadence is not uniform due to periods of high wind, small distance to the Sun or bad weather for the radio data and non-detections in the high energy band. These non-detections are reported as upper limits and are not considered in the correlation analysis.

An example of simulated data with this sampling is shown in Figure 5.8 (upper panel), along with the results for the cross-correlation (lower panel). In this case the radio sampling (blue dots) covers a longer time span than the gamma-ray one (red dots). Figure 5.9 shows the results of the Monte Carlo significance analysis for this example using the DCF and LCCF.

Figure 5.10 shows that in this case we only recover a fraction of the time lags at a 3σ significance. To understand why this is happening Figure 5.11 has been included. The figure shows that for the case of the DCF we find that for a large number of cases the most significant peak in the correlation is at a lag different from zero. Moreover some of those spurious lags are of high statistical significance. We still get significant peaks at lags different from zero for the LCCF but at a much smaller rate.

To understand how we can get small values of the DCF at zero lag while still having large values of the LCCF, we can take a look at the distributions of the coefficients of the linear relation (Equation 5.6) which are shown in Figure 5.12. The multiplicative coefficient should be one in the ideal case but instead it has a broad distribution (left panel). The additive coefficient that should be zero in the ideal case also has a broad distribution (right panel). This can effectively reduce the value of the correlation coefficient or make its distribution broader reducing its discriminating power. This is exactly what we see in Figure 5.13, which shows the distribution of cross-correlation coefficients at $\tau = 0$ days. In the figure,

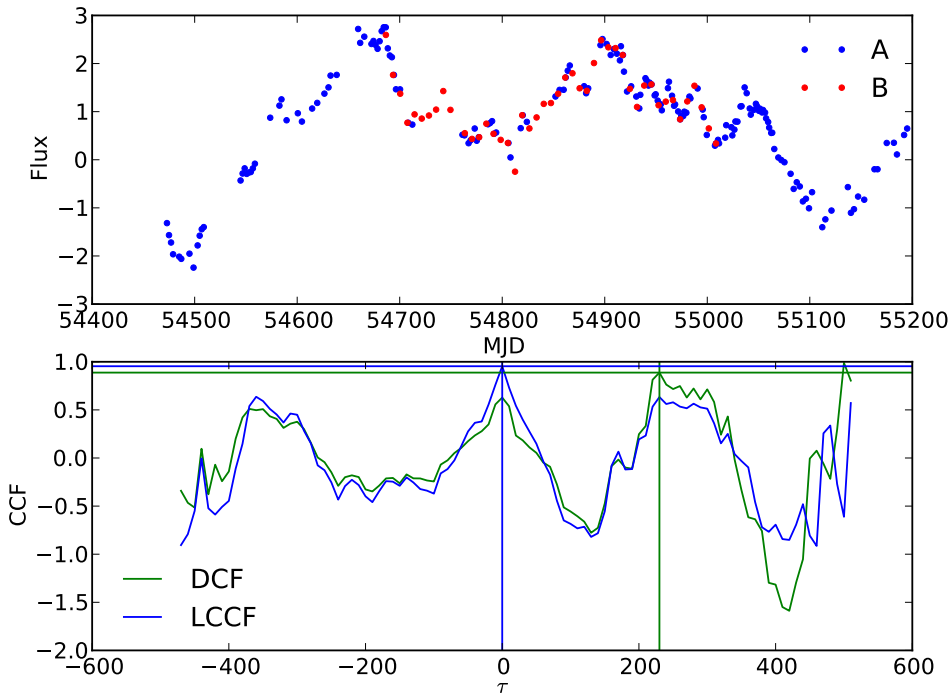

Figure 5.8: Example of simulated data with PSD $\propto 1/\nu^2$ for the "short data set" sampling. The upper panel shows the two time series which have some small differences produced by the different sampling at each waveband. The lower panel has the results of the DCF and LCCF for this case. The vertical lines show the position of the most significant peak with color corresponding to the method used. Horizontal color lines mark the amplitude of the most significant peak for each method. In this example the LCCF recovers the right time lag, but the DCF finds a spurious time lag.

the distribution of random cross-correlations is represented with a dotted line and the one for correlated data with a solid line. The upper panel is for the DCF and the lower panel for the LCCF. The vertical green line represents the 3σ significance threshold amplitude for cross-correlation coefficients. The fraction of correlated data cross-correlations (solid line) that is to the right of the green line is approximately equal to the detection efficiency [2]. It can be seen that this fraction is much larger for the LCCF as a result of increased scatter in the distribution of the DCF when compared to the LCCF of correlated data for the reasons presented at the beginning of this paragraph.

[2]The equality is only approximate because a peak with larger significance might have appeared in a lag different than $\tau = 0$. These cases are not excluded from the histogram.

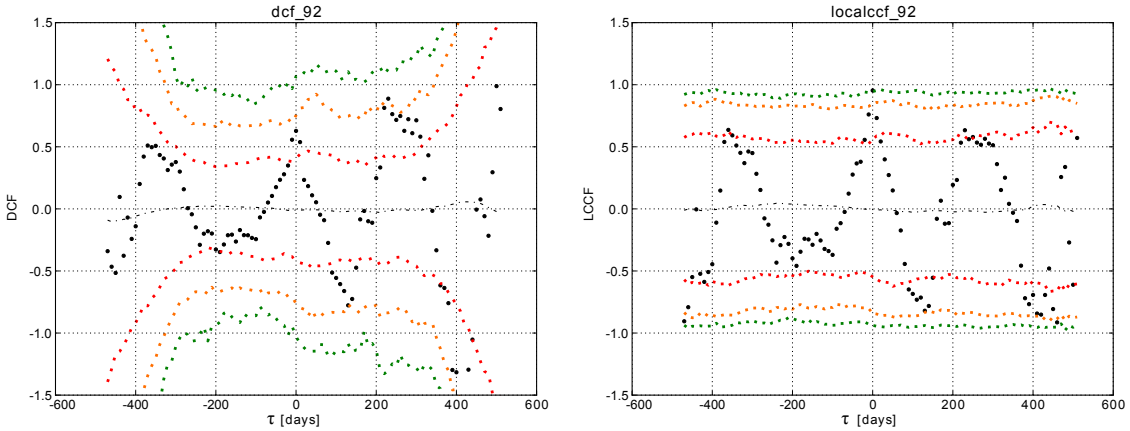

Figure 5.9: Cross-correlation significance results for the example shown in Figure 5.8. Left panel is for the DCF and right panel for the LCCF. In this example the time lag at zero is recovered with high significance with LCCF but not by the DCF, which has its most significant peak at a different time lag.

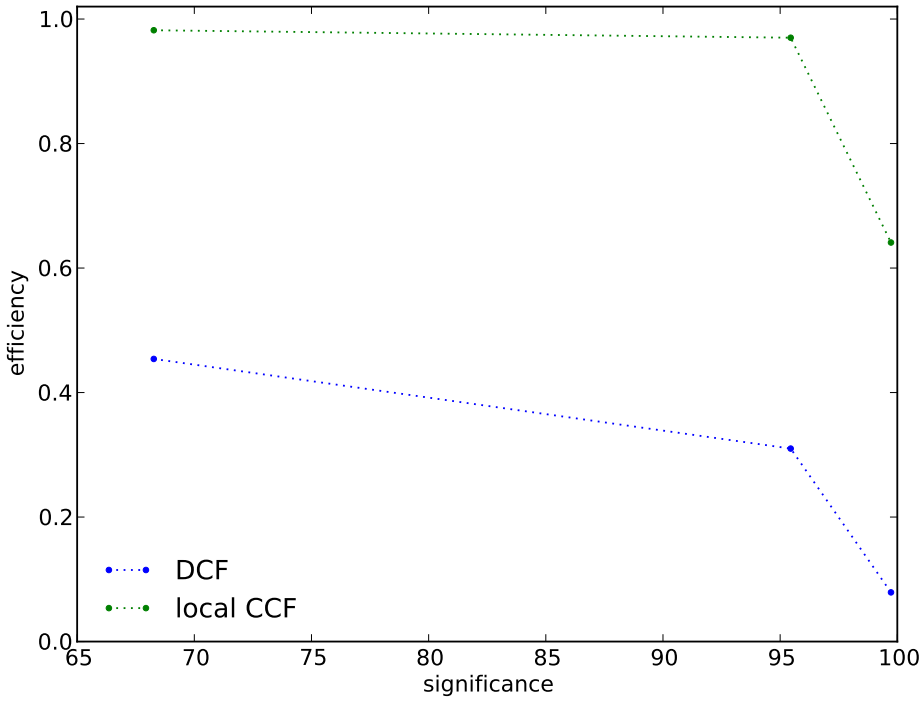

Figure 5.10: Detection efficiency versus significance for both methods. In this case the efficiencies differ significantly between both methods, with the LCCF being the more efficient.

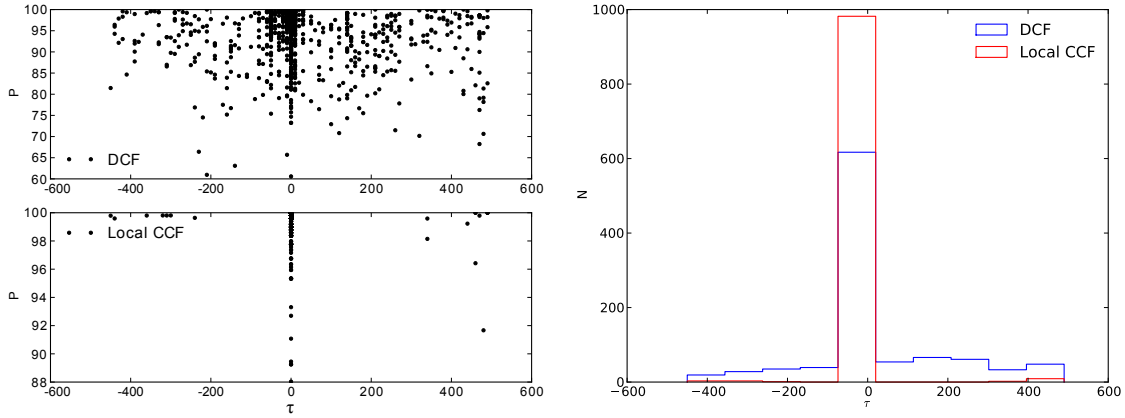

Figure 5.11: Distribution of most significant peaks in the correlation for both methods. Left panel shows the lag and significance of the most significant peak. Upper sub-panel for the DCF and lower sub-panel for the LCCF. The right panel is a histogram of the distribution of lags for the most significant peak.

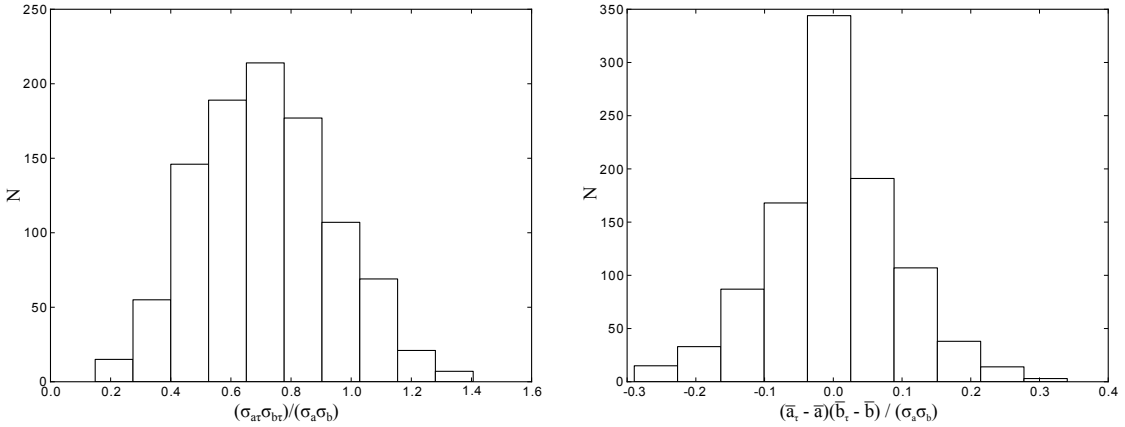

Figure 5.12: Distribution of the coefficients of the linear relation between DCF and LCCF for $\tau = 0$. Left panel is the multiplicative factor, which has a very broad distribution and is different from 1 in most cases. Right panel is the additive constant which also has a very broad distribution very different from the ideal case of 0. These values show the DCF to be different from the LCCF and have a role in producing spurious highly significant peaks in the correlation.

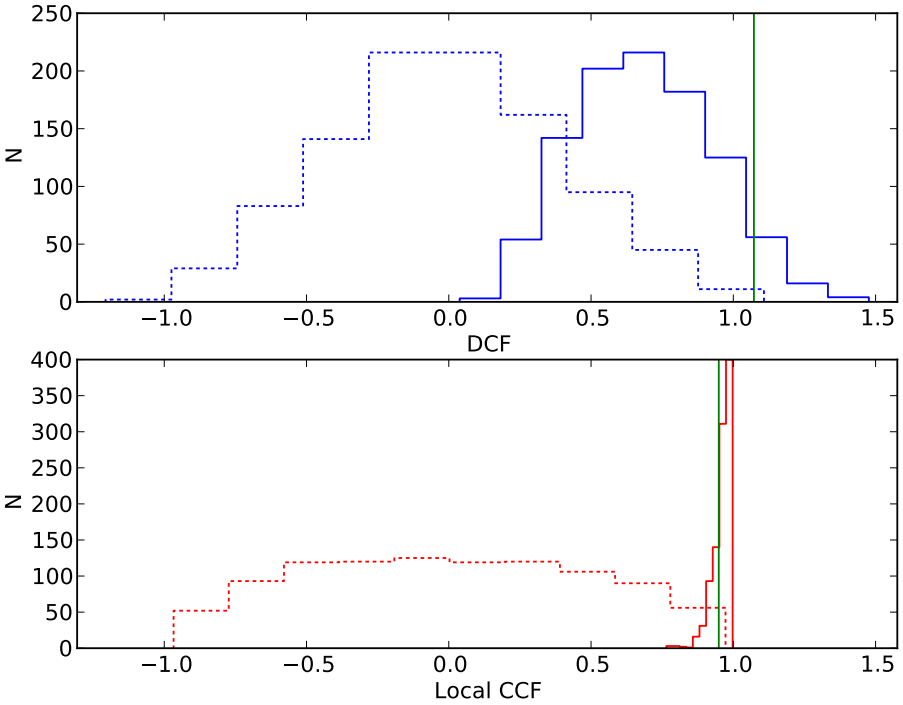

Figure 5.13: Distribution of the cross-correlation coefficient for both methods at $\tau = 0$ days. Both panels show the distribution of random cross-correlations with dotted line and the one for correlated data with solid line. Points with cross-correlation coefficient to the right of the vertical green line have a significance of at least 3σ. Upper panel is for the DCF and lower panel for the LCCF.

5.5.3 Data sampling case 2, "long data set": 4 years of OVRO and 3 years of *Fermi*-LAT.

We can make the same comparison using the best data set available at the moment which has radio light curves with a duration of 4 years sampled about twice a week and gamma-ray light curves for a 3 year duration and weekly sampling. We again consider the case with no noise added to the simulations and zero lag between the two light curves, so the only difference is in the sampling pattern. An example of a simulated data set with this sampling is shown in Figure 5.14 (upper panel), along with the results for the cross-correlation (lower panel). Figure 5.15 shows the results of the Monte Carlo significance analysis of this example using both methods. Comparison of the results of this section with the ones in Section 5.5.2 can give us an idea of the variation of the relative power to detect correlations in different data sets.

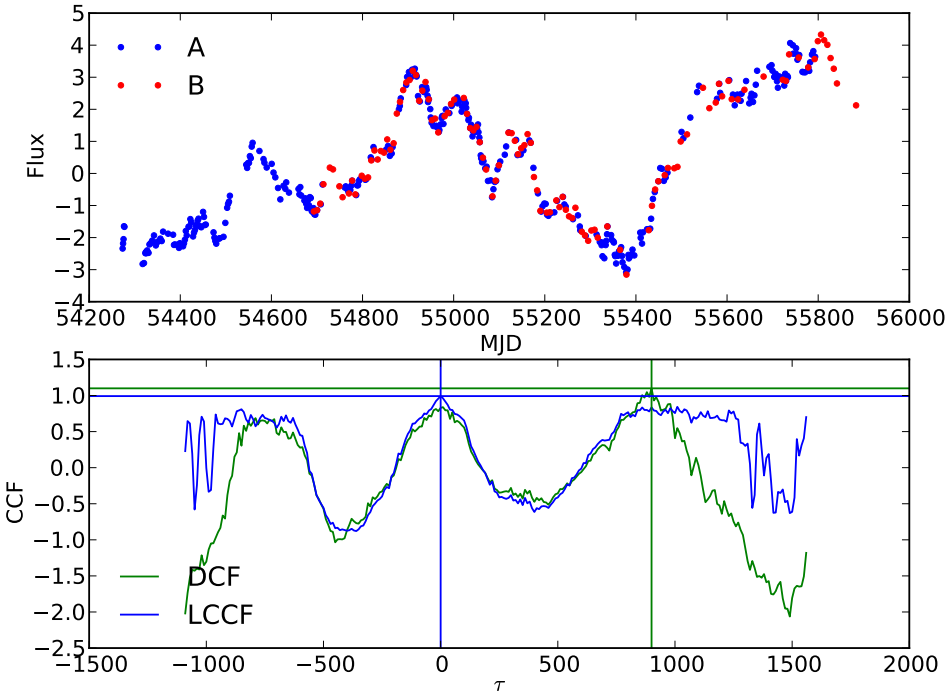

Figure 5.14: Example of simulated data for the "long data set". The upper panel shows the two time series which have some small differences produced by the different sampling at each waveband. The lower panel has the results of the DCF and LCCF for this case. The vertical lines show the position of the most significant peak. The LCCF recovers the right time lag, but the DCF finds an spurious time lag.

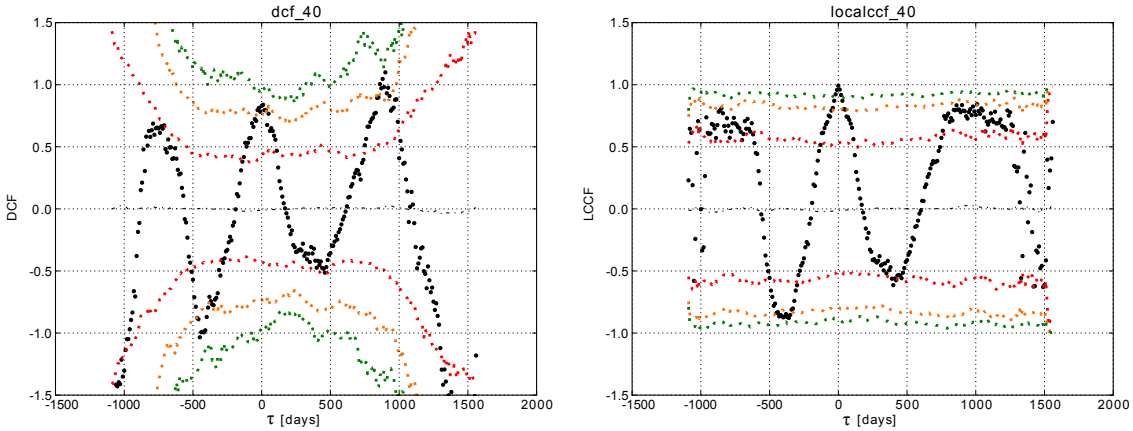

Figure 5.15: Cross-correlation significance results for the example shown in Figure 5.14. Left panel is for the DCF and right panel for the LCCF. The time lag at zero is recovered with high significance with the LCCF but not by the DCF, which has its most significant peak at a different time lag.

As in the case of the "short data set" we find that the efficiency of detection strongly depends on the method used. Figure 5.16 shows that the LCCF recovers the right time lag at high significance for all the cases, while the DCF does so in only about 15% of the cases. An examination of Figure 5.17 shows that the DCF produces spurious correlation peaks with a wide distribution. As in the case of the "short data set" some of those spurious peaks have high statistical significance.

A comparison of Figures 5.10 and 5.16 shows that the performance of both methods improves as expected when using longer time series. However, as can be seen from Figure 5.17, the performance of the DCF is still rather poor and produces a large fraction of spurious statistically significant correlation peaks, while the LCCF recovers a significant correlation at $\tau = 0$ in all cases.

Figure 5.18 shows the distribution of the coefficients for the linear relation between the DCF and LCCF (Equation 5.6). We again see that they significantly differ from the ideal case of a stationary time series. This provides an explanation for the difference between these two estimators of the correlation. As for the case of the "short data set" we also look at the distribution of cross-correlation coefficients for the uncorrelated and correlated data sets at $\tau = 0$ (Figure 5.19). We again see the broad distribution of correlation coefficients for the DCF of correlated data sets and the much narrower distribution for the LCCF. This

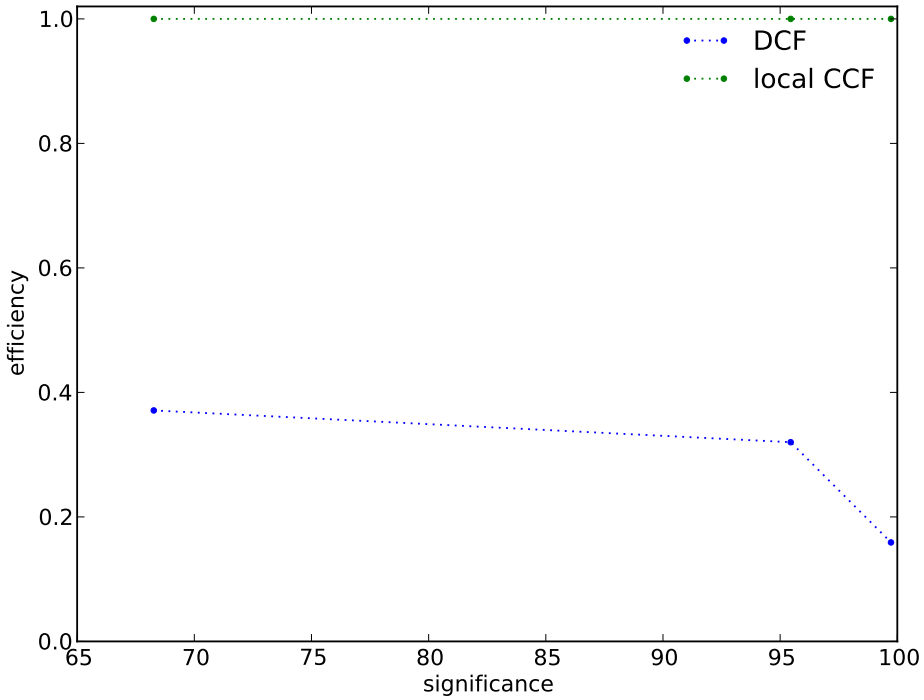

Figure 5.16: Detection efficiency versus significance for both methods. In this case the efficiencies differ significantly between both methods, with the LCCF being the more efficient.

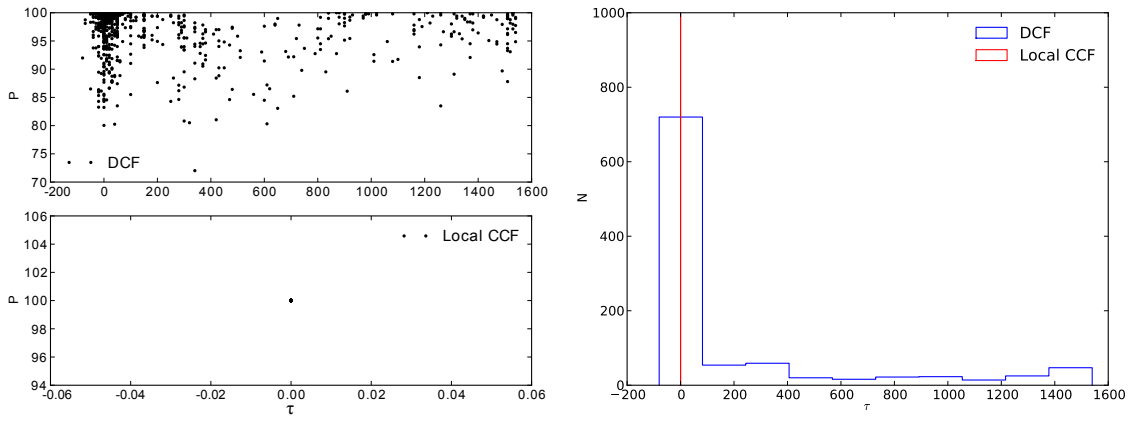

Figure 5.17: Distribution of most significant peaks in the correlation for both methods. Left panel shows the lag and significance of the most significant peak. Upper sub-panel for the DCF and lower sub-panel for the LCCF. The right panel is a histogram of the distribution of lags for the most significant peak.

explains the better discriminating power of the LCCF.

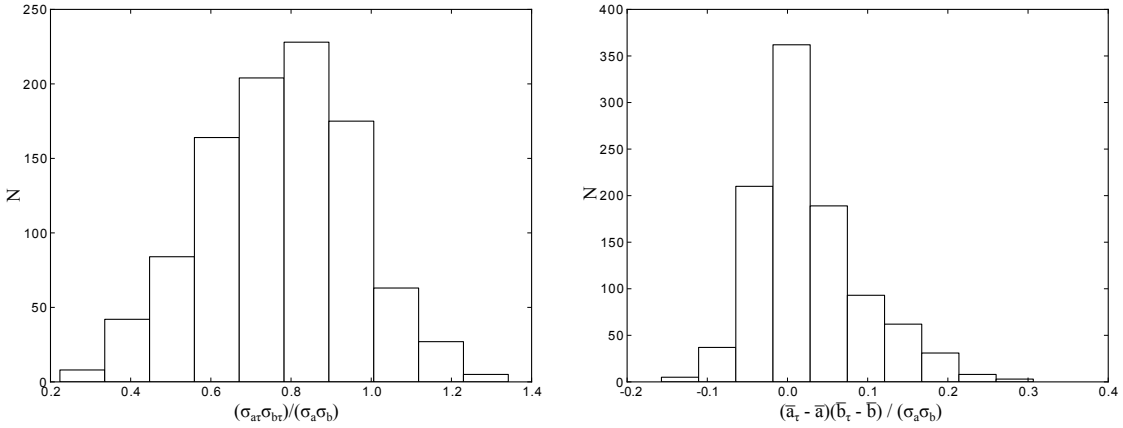

Figure 5.18: Distribution of the coefficients of the linear relation between DCF and LCCF for $\tau = 0$. Left panel is the multiplicative factor, which has a very broad distribution and is different from 1 in most cases. Right panel is the additive constant which also has a very broad distribution very different from the ideal case of 0. These values show the DCF to be different from the LCCF and have a role in producing spurious highly significant peaks in the correlation.

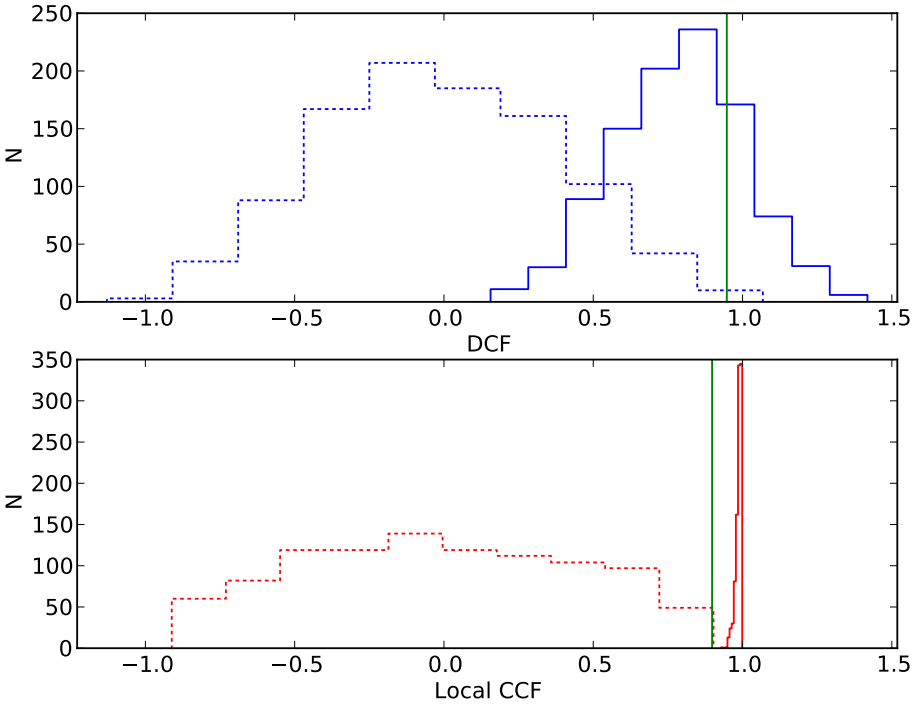

Figure 5.19: Distribution of the cross-correlation coefficient for both methods at $\tau = 0$ days. Both panels show the distribution of random cross-correlations with dotted line and the one for correlated data with solid line. Points with cross-correlation coefficient to the right of the vertical green line have a significance of at least 3σ. Upper panel is for the DCF and lower panel for the LCCF.

5.5.4 Additional tests

Additional tests were performed introducing time lags for the time series and measuring the efficiency of detection. They all show the same qualitative information so only the efficiency results are included below in order to compare the results for the "short" and "long" data sets. The results for zero time lag are repeated to allow for an easier comparison. In all cases the LCCF outperforms the DCF and the efficiency of detection improves when using the "long data set" when compared to the "short data set". These results demonstrate that the LCCF is the more efficient method for recovering time lags with high significance.

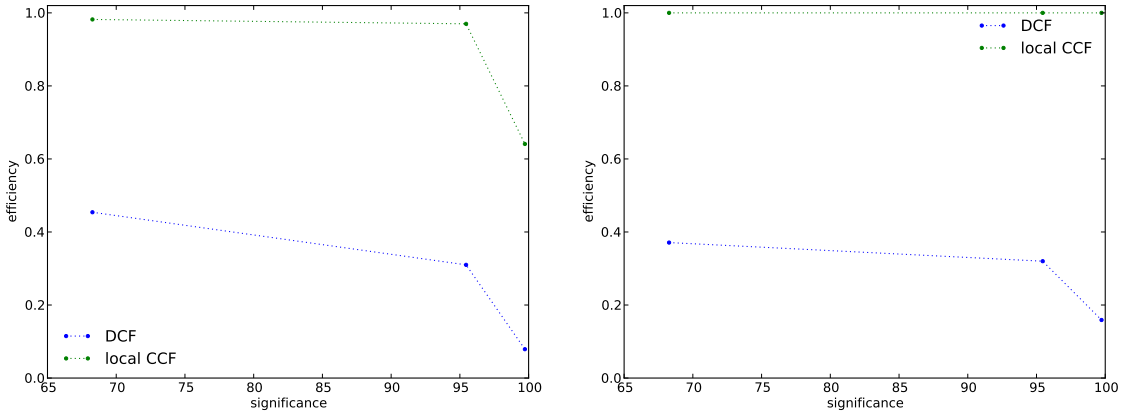

Figure 5.20: Efficiency versus significance comparison between the LCCF and DCF for a time lag $\tau = 0$ days. Left panel "short data set", right panel "long data set".

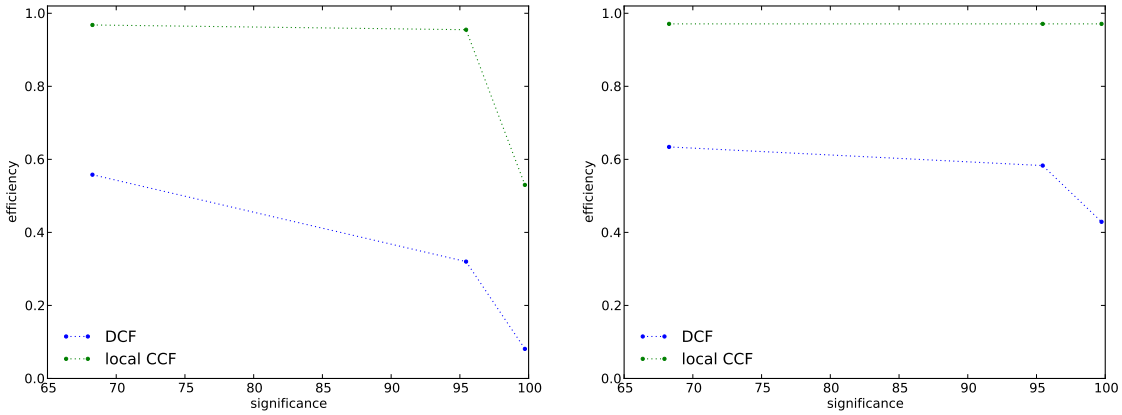

Figure 5.21: Efficiency versus significance comparison between the LCCF and DCF for a time lag $\tau = 100$ days. Left panel "short data set", right panel "long data set".

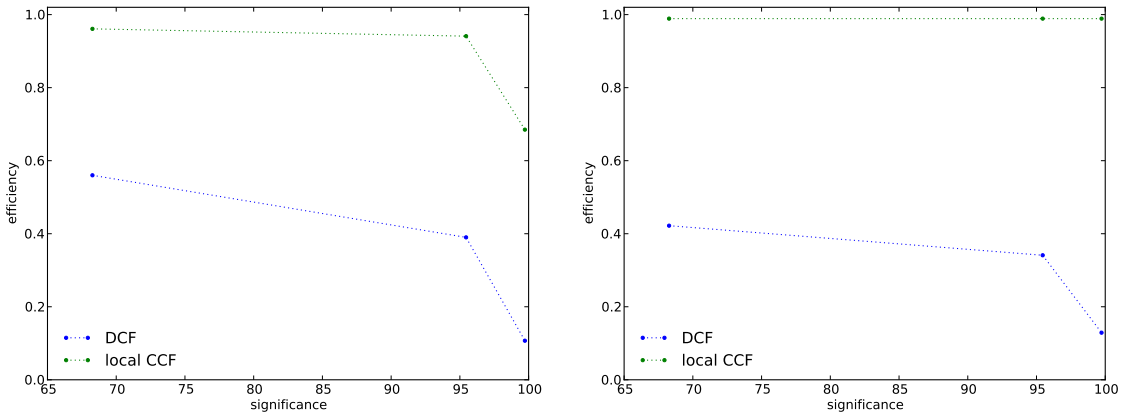

Figure 5.22: Efficiency versus significance comparison between the LCCF and DCF for a time lag $\tau = -100$ days. Left panel "short data set", right panel "long data set".

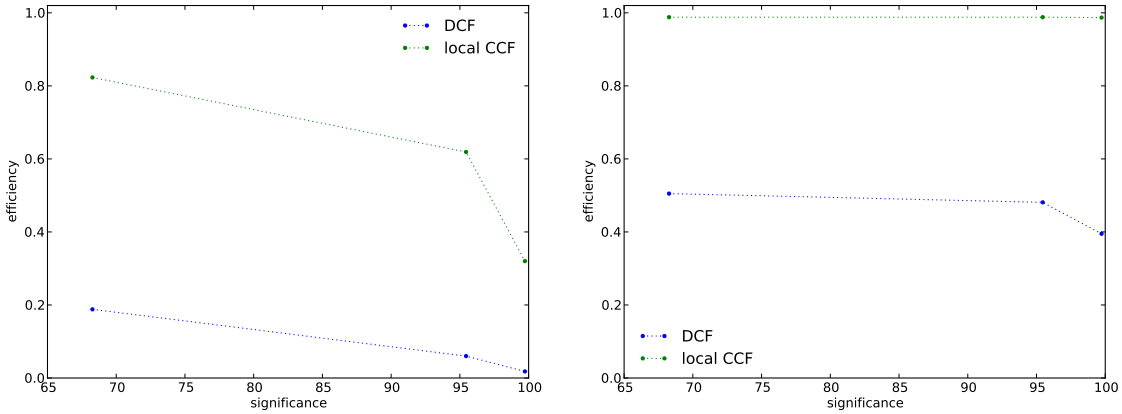

Figure 5.23: Efficiency versus significance comparison between the LCCF and DCF for a time lag $\tau = 200$ days. Left panel "short data set", right panel "long data set".

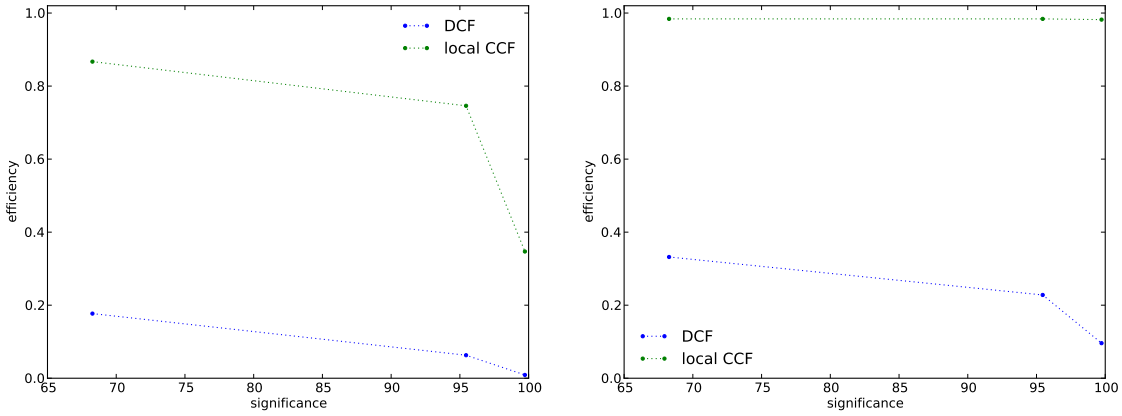

Figure 5.24: Efficiency versus significance comparison between the LCCF and DCF for a time lag $\tau = -200$ days. Left panel "short data set", right panel "long data set".

5.6 Additional considerations

In this section we describe some additional issues that should be considered when estimating the significance of cross-correlations using the Monte Carlo test we have described or similar methods. Two of these have been ignored in the literature (correction for multiple comparisons and the error on the significance estimate) while the other has not been fully appreciated and has led some authors to suggest tests that are not consistent with the basic statistical properties of blazar light curves.

5.6.1 The dependence of the significance estimate on the model light curves

As illustrated in Figure 5.2, the distribution of random cross-correlation coefficients will depend on the model used for the simulated light curves. In order to better appreciate that dependence, we have estimated the significance of cross-correlations between the radio and gamma-ray emission using the LCCF on 4 years of radio data and 3 years of gamma-ray data for J0237+2848. We have used 10,000 simulated light curves with PSD $\propto 1/\nu^{\beta}$ for $\beta = 0$, 1 and 2. Figure 5.25 presents the results in the form introduced in Figure 5.3. As in Figure 5.2 we observe an increase in the amplitude of the random cross-correlation when steeper power spectral densities are used in the simulations. This manifests as increased scatter in the distribution of random cross-correlations and a lower significance estimate for the cross-correlations. The dependence of the results on the particular model of the light curves illustrates the importance of a proper characterization of the variability of the light curves, a subject which is discussed in Chapter 3.

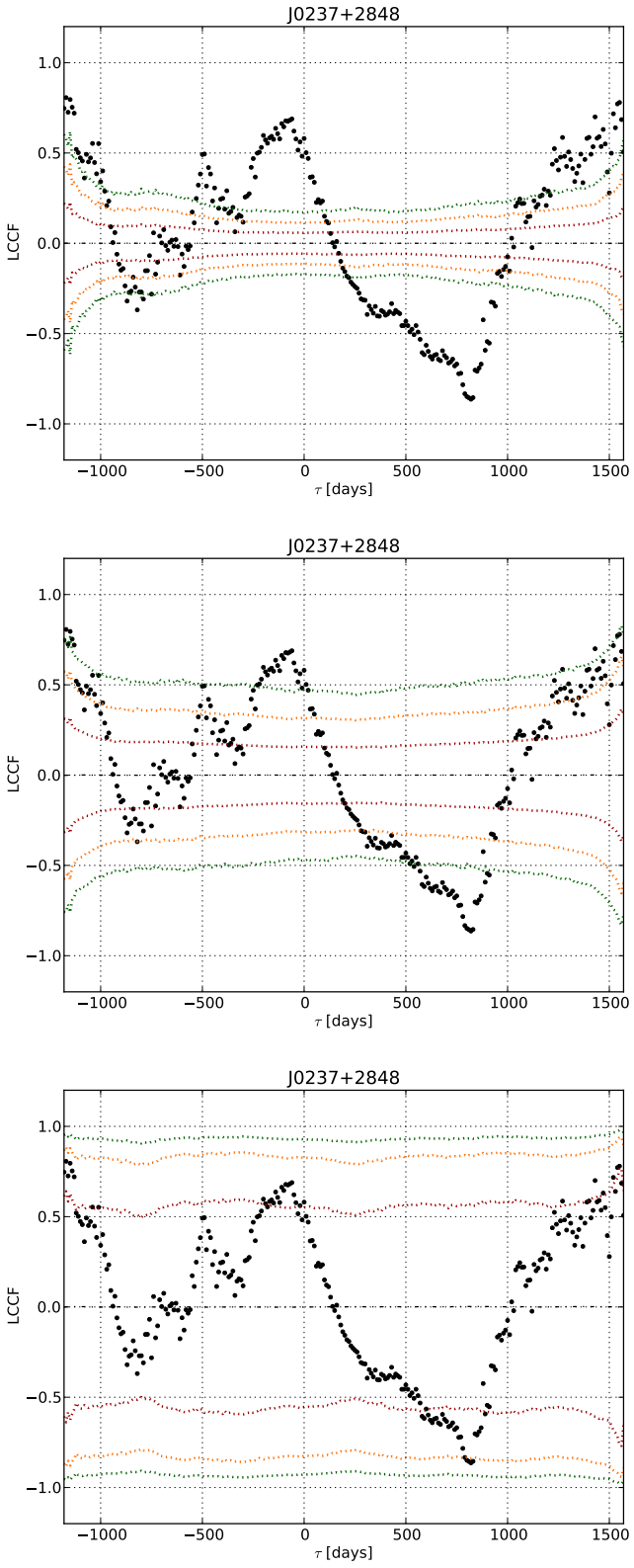

Figure 5.25: Example of cross-correlation significance results for J0237+2848 using $\beta = 0$ (upper panel), $\beta = 1$ (central panel) and $\beta = 2$ (lower panel). The black dots represent the LCCF for the data, while the color contours the distribution of random cross-correlations obtained by the Monte Carlo simulation with red for 1σ, orange for 2σ and green for 3σ. The increased amplitude of random cross-correlations is evident for steeper PSDs.

This dependence on the model used for the light curves has motivated some researchers to search for model-independent significance estimates. This is certainly desirable but in principle not much easier than actually determining an appropriate model for the light curves. Care must be taken to ensure that the assumptions that these methods use are consistent with the basic properties of blazar light curves. One example of a randomization technique that people sometimes suggest in informal conversations is to shuffle the time of the data samples to generate data sets with equal sampling and properties as the observations. These data could then be used to get an estimate of the distribution of random cross-correlations in a model independent way. This suggestion is fundamentally flawed for the blazar case as it destroys the feature that produces spurious correlations, the flares. In fact this will most probably produce white noise time series providing a very optimistic significance estimate. Others propose to use light curves for other sources in place of simulated light curves. Although promising this will only work if the sampling pattern and statistical properties of the other sources are similar to the source in question, something that has not been rigorously proved.

5.6.2 Error on the significance estimate and minimum number of simulations

It is expected that the accuracy of the significance estimates will increase as the number of simulated light curve pairs increases. In order to get an estimate on the expected error in our significance estimate due to the finite number of simulations we have divided a full simulation with 100,000 simulated light curve pairs into independent subsets and provide estimates for each of them. The idea is to observe the scatter when a small number of simulations is used and compare its variation as more simulations are used. The original simulation is divided in two halves which are subsequently divided into two. The process is repeated until the number of simulations in each subset is small enough that results have a very large scatter and do not give us reliable significance estimates. For all the sources we find that the individual results of smaller simulations are less accurate than the final one. In all cases the average gives the result of the complete simulation which is not surprising as together they encode the same information. As expected the scatter is much smaller when a large number of simulations is used. An example is presented in Figure 5.26, which clearly shows the reduction in the scatter as the number of simulated light curve pairs is

increased. With less than 1,000 simulations the scatter is of a few percentage points, and gets to about 0.2% for more than 10,000 simulations.

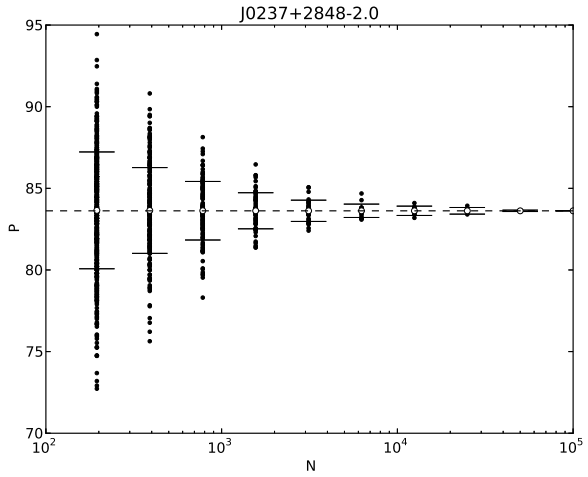

Figure 5.26: Example of scatter in the significance estimate for independent subsets of the full simulation using different numbers of light curve pairs. The horizontal axis shows the number of simulations used to get each estimate and the vertical the significance. Black dots represent each of the independent subsets of the full simulation. The empty circles and error bars represent the mean and standard deviation for subsets of a given number of simulations. The horizontal segmented line corresponds to the results using the whole simulation. As expected the scatter of the estimates obtained using smaller number of simulations is larger.

The process described above could in principle be used to obtain an error estimate but we have instead computed a more conventional bootstrap estimate of the standard error following the procedure described below. For the time lag of interests, we have N values of the random cross-correlations, from these 1,000 bootstrap samples have been obtained and the sample standard deviation of bootstrap replications of the significance is used as the error estimate. An example of the distribution of bootstrapped estimates is shown in Figure 5.27. We think this error estimate is a required step of any Monte Carlo estimate of the significance and recommend the adoption of this or equivalent procedures, an issue that has surprisingly been up to now ignored by all authors.

5.6.3 Correction for multiple hypothesis tests

Our observational problem is to search for a correlation and measure its significance at a time lag which is not specified in advance. The distribution for the cross-correlation coefficient

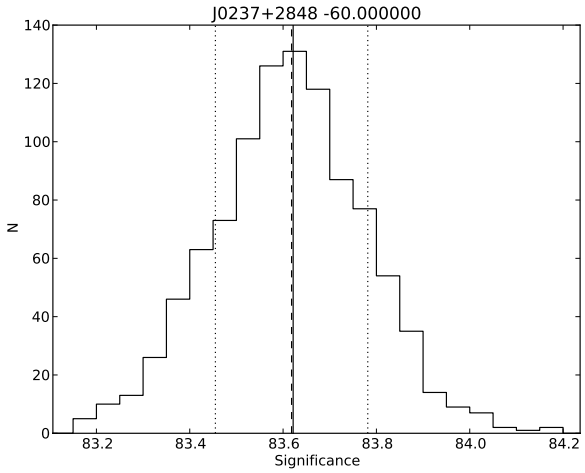

Figure 5.27: The distribution of the significance estimates for the bootstrap samples is represented as a histogram. The solid line represents the value obtained using the whole simulation. The segmented line is the mean of the distribution and the dotted lines the one standard deviation upper and lower limits.

for uncorrelated data is constructed at each time lag, and in our procedure we compute the data cross-correlation, find the peaks and check the significance of those choosing the most significant as the one to report. This is effectively equivalent to performing multiple hypothesis tests.

Performing multiple hypothesis tests at a given per test significance level, reduces the significance of the composite test. In this case the significances we directly obtain at a given time lag are for an individual test and we must adjust them to incorporate the fact that we are simultaneously searching for a peak at a nonspecific time lag. Although this is a recognized problem in high energy physics and known as the "look-elsewhere effect" (Beringer et al, 2012, and references therein), we are not aware of a solution for the case of cross-correlations between two time series as applies to our particular problem. In what follows we describe an approximate way to account for this effect, that can at least give us a bound on the required correction to the significances.

A conservative correction for multiple comparisons can be made for independent tests and is often referred as the Bonferroni correction when used in approximate form for a small significance level α. The derivation of the correction is straightforward and is a useful illustration of the problem so it is included below. For an individual test the probability of rejecting the null hypothesis when true (*type-I error*) is the significance level α. The

probability of not rejecting the null hypothesis when true is then $(1-\alpha)$. If we perform N independent tests, the probability of not rejecting the null hypothesis when true for all of them is $(1-\alpha)^N$, and its complement, the probability of rejecting a true null hypothesis in at least one test is $\alpha_{comb} = 1-(1-\alpha)^N$. This α_{comb} is the significance of the combined test and is larger than α, meaning that by performing multiple statistical tests, we are in fact increasing the chances of rejecting a true null hypothesis. In our case we are increasing the chances of concluding that the time series are correlated by not specifying in advance the time lag at which correlation is expected.

From the discussion above it follows that if we know N, the number of independent tests we are performing, in this case independent time lags, we can easily correct our p-values and significance levels of the tests. This is not trivial in our case as the time lag bins are not completely independent as a consequence of autocorrelations in the individual time series, and all we have is an upper limit for N which could be too conservative. Fortunately we can look at a typical case and estimate a correction based on a simulated experiment using our Monte Carlo method, in which we search for significant time lags in uncorrelated time series. By repeating this many times we can estimate the rate at which significant correlations are obtained with a given p-value under the null hypothesis, but in this case for the composite test in which we search for a correlation at a nonspecific time lag. The correction we propose uses the fact that by definition the distribution of p-values under the null hypothesis is uniform in the interval $[0,1]$. We compare the cumulative distribution of measured p-values at a given p and correct it with a p dependent coefficient that makes the distribution consistent with a uniform on $[0,1]$ for p-values smaller than the given p. Multiplying the measured p-values by this correction factor adjusts them for the effect of multiple comparisons. In this way, we can look at the corrected p-values and interpret them in the usual sense of a probability of an extreme result under the null hypothesis, which in this case is no correlation in all the time lags we have explored.

The correction could in principle depend on the search range for time lags, the time length and sampling of the light curves and the model used for the light curves in the null hypothesis which in this case are uncorrelated time series with PSD $\propto 1/\nu^{\beta}$. To explore this, a series of tests using different search ranges and PSD power-law exponents were performed. We use a sampling pattern typical of the data set we call "long data set" which is the one used in the study of cross-correlations. In particular we use the sampling

pattern for J0237+2848 that is shown in Figure 5.3. Some results for the case of $\beta = 2.0$ are presented in Figures 5.28 and 5.29 to illustrate the procedure. For the other cases we simply report a summary in Table 5.1.

Figure 5.28 (left panel) is the cumulative distribution of p-values (upper plot) along with the correction factor (lower plot). It shows that the significances have to be corrected by a factor of about 127 to 14 for the range of interest ($p < 0.045$ or about 2σ significance level). The right panel of the figure shows the distribution of time lags for spurious cross-correlation peaks and makes evident the increased rate of spurious peaks at the edges of the search range. These spurious peaks are the result of the very small overlap between the time series and the fact that it is much easier to get simple linear trends on both light curves when a short time period is considered for time series with steep PSD. These linear trends will always produce correlations of very high amplitude. In consequence we can conclude that these extremes have to be excluded so we have an approximately constant distribution for the time lag of spurious peaks.

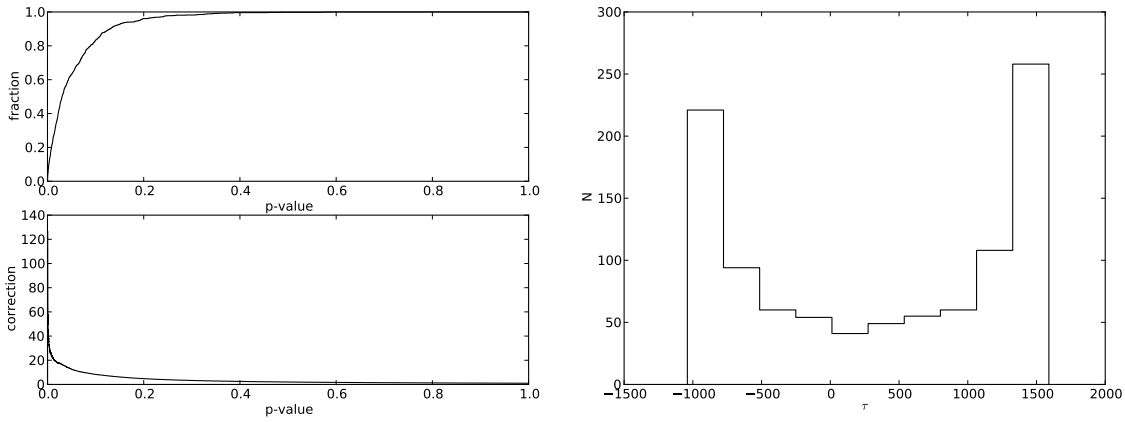

Figure 5.28: Correction for multiple hypothesis tests for PSD $\propto 1/\nu^2$ using the whole range of time lags obtained from cross-correlations. Upper left panel is the cumulative distribution of p-values for spurious peaks, while lower left panel is the correction factor that makes the distribution uniform as explained in the text. Right panel is the time lag distribution of spurious peaks. The peaks at the edges of the time range are produced by the small time overlap of the time series and the frequent presence of trends in time series with steep PSDs.

Figure 5.29 shows the same information for the search interval $[-550, 550]$ days which corresponds to approximately one and a half years. In this case the correction factor goes

from about 8 to 4 and the distribution of time lags for spurious peaks is closer to uniform but still somewhat biased towards the edges of the interval. Given the large fraction of spurious correlations found at the edges of the search range when using the whole search range (Figure 5.28), we have decided to restrict the search of cross-correlations to a range of approximately $[-550, 550]$ days, or half the length of the gamma-ray light curves which are the shortest in this case. By doing this we also reduce the correction by a factor of about 10, making the effect of multiple comparisons much less serious.

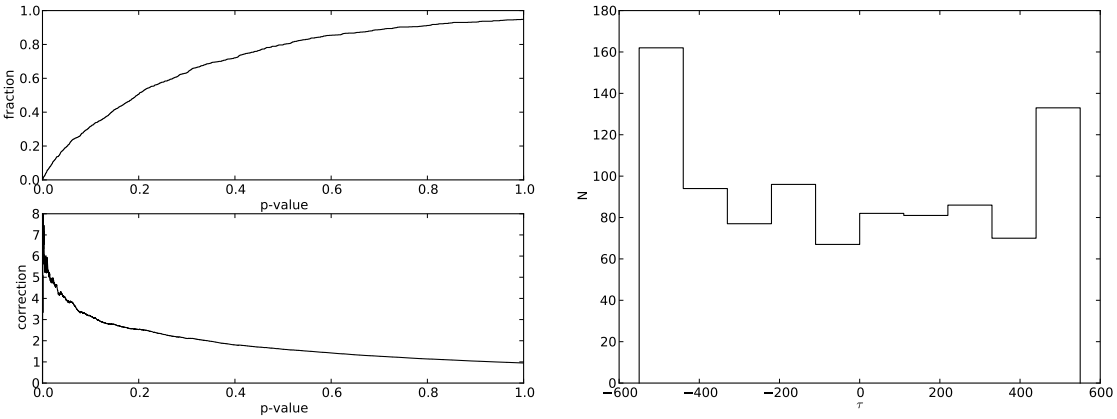

Figure 5.29: Correction for multiple hypothesis tests for PSD $\propto 1/\nu^2$ using a range of time lags from -550 days to 550 days, approximately a year and a half. Upper left panel is the cumulative distribution of p-values for spurious peaks, while lower left panel is the correction factor that makes the distribution uniform as explained in the text. Right panel is the time lag distribution of spurious peaks. Reducing the search range reduces the magnitude of the correction and makes the distribution of spurious time lags closer to uniform when compared to Figure 5.28.

We also compute the correction for the cases of $\beta = 0$, 1 and 3, to get a quantitative estimate for different cases. These results are presented in Table 5.1, which shows the correction factors for all of the cases we tried. For each β and time lag search range, three values are given, the first one is the maximum value of the correction, the second one for an originally 3σ significance, and the last one for a 2σ one. The effect of these corrections can be approximately read out of Figure 5.30. To help the reader appreciate the effect of the corrections we also show the equivalent significance in units of σ which are more familiar than p-values. The results have some uncertainty but are a good indication of the increased rate of spurious correlations when the search range is broader.

Table 5.1: Correction factors for multiple hypothesis tests. For each β and time lag search range, three values are given, the first one is the maximum value of the correction, the second one for an originally 3σ significance, and the last one for a 2σ one. The effect of these corrections can be approximately read out of Figure 5.30.

β	Correction whole range	Correction $[-550, 550]$ days	Correction $[-365, 365]$ days	Correction $[-60, 60]$ days
0.0	185, 107, 22	98, 45, 20	78, 34, 18	10, 6, 5
1.0	161, 55, 20	44, 19, 10	35, 13, 7	3, 3, 2
2.0	127, 36, 14	8, 7, 4	15, 5, 3	5, 2, 1
3.0	74, 27, 10	30, 8, 3	20, 4, 2	3, 1, 1

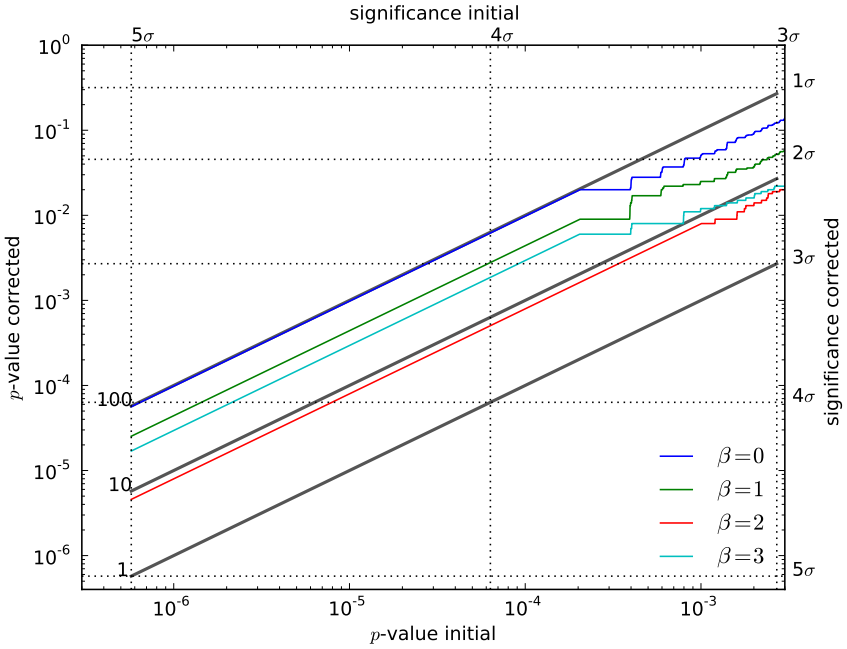

Figure 5.30: Correction of p-values for multiple hypothesis tests. Given an initial p-value obtained using the Monte Carlo significance test and a correction factor the corrected value can be read of the horizontal axis. Color lines represent the corrections obtained with a time lag search interval of $[-550, 550]$ days for $\beta = 0, 1, 2, 3$ as indicated in the figure. Solid lines are correction curves with the correction factor indicated on the left end of the line. Doted lines represent the significances as integer factors of σ, which have been included as they might be more familiar than p-values. The appropriate correcting factor can be obtained from Table 5.1.

Due to the uncertainty in the derived correction factors, we have decided not to implement this correction and only indicate the approximate magnitude and the existence of the effect. The advantages of narrowing the search range are obvious in terms of the smaller

correction factors for the significances and the reduced rate of spurious correlations at the edges of the search range where little overlap between the time series is obtained. Figure 5.30 illustrates the effect of correction factors in the range found in Table 5.1. A few constant corrections factors have been included for reference and the actual correction factors versus p-values for the search range $[-550, 550]$ days and $\beta = 0, 1, 2$ and 3 are included. Due to the limited number of simulations used there is a minimum p-value obtained in the simulations, below which the value of the correction is assumed constant and appears as a straight line parallel to the reference correction factors.

The solution we have presented gives a rough idea of the magnitude of the problem but further investigation is certainly needed as application of this method requires a large computational time. Possible ideas are to explore simulations like those we have presented here or the possibility of finding some simple rules to estimate the corrections. Exploring how to use the ideas developed by the high energy physics community for the "look-elsewhere effect" problem is another possible direction for future studies.

5.7 Conclusions

A description of the problem of estimating the cross-correlation for unevenly sampled time series has been given. We have shown through a graphical example that high values of the cross-correlation coefficients for red-noise time series are ubiquitous and that any method that aims at quantifying the significance of correlation coefficients for light curves having flare-like features needs to take this into account. We have described a general Monte Carlo method to estimate the significance of cross-correlation coefficients between two wavebands. A number of tests aimed at measuring the effectiveness of a particular cross-correlation method have been performed to compare the LCCF and the DCF. Given the absence of a physical model for the expected correlations, the method cannot be used to give a definitive value of the detection efficiency but it can be used to compare different alternatives. The main result is that the LCCF has a much larger detection efficiency than the DCF when trying to recover a linear correlation. The CCF has the additional problem of producing a large fraction of spurious high significance time correlations which could be mistaken as real correlations; this problem is less important for the LCCF especially when long time series are used.

The origin of the difference and the lack of discriminating power for the DCF seems to originate in the short duration or non-stationarity of the time series involved. It was found that when correlating evenly sampled time series the differences were small, and we could expect this would be the case for very long time series, which are rare in real applications. In conclusion, we recommend the use of the LCCF as a tool to search for correlations.

We also show that the significance of the cross-correlation coefficients is strongly dependent on the power-law slope of the PSD. This makes characterization of the light curves very important and the method we use to characterize the PSDs is presented in Chapter 3. We investigate the error on the estimated significance by repeating the analysis using different numbers of simulations. This is a serious concern that has been overlooked by many authors who use small numbers of simulations in order to reduce the computational time. We suggest using a bootstrap estimate of the error on the significance and reporting its value as part of the analysis results, especially in cases where high significances are claimed. We also present an estimation of the effect of multiple hypothesis tests that is introduced by searching for cross-correlations at a nonspecific time lag, and show that in general the significance estimates have to be reduced to account for this effect. Estimates for the correction are obtained to illustrate the magnitude of the effect but are not applied as they are quite uncertain. It is also found that the probability of finding spurious cross-correlation peaks is very large when the light curves have small overlap, specially for steep PSDs. Based on this observation and the smaller correction factors required to correct for multiple hypothesis tests, we have decided to restrict the time lag search range to the interval $[-550, 550]$ days, which is about half the length of the gamma-ray light curves in our data set. The results of the application of this method to our data set are presented in Chapter 6.

Chapter 6

Radio/gamma-ray time lags

6.1 Introduction

In this chapter we use the methods developed in the previous chapters to investigate the existence of correlated variability between the radio and gamma-ray light curves and thus throw light on the location of the gamma-ray emission site in blazars. We present the results of the PSD fits to the radio and gamma-ray light curves for 86 sources with good quality sampling in both bands. These results provide constraints on the values of the power-law exponent of the PSDs and allow us to obtain a confidence interval for the value of the significance of the cross-correlations between those two energy bands. A detailed study of the significance of the correlations is obtained for a few sources in which we obtain simultaneous constraints for the radio and gamma-ray PSDs. For the rest of the sources we estimate the significance using an average value of the PSD taken from published results and from our own study of the gamma-ray PSD. We also present the results of including the recent active period in the blazar Mrk 421, which reveal correlated variability in a source for which none was detected in the data set used in our uniform study of all the sources. We close this chapter with a brief discussion of our findings. The physical implications are discussed in Chapter 7.

6.2 Characterization of the PSD

A first step in the study of the significance of the cross-correlation between the radio and gamma-ray bands is the characterization of the light curves using the method described in Chapter 3 which provides the exponent of the simple power-law PSD model we use in this

investigation. The model parameters are used to obtain the simulated light curves we use in the estimation of the significance of cross-correlations as described in Chapter 5.

From the discussion in the first part of Section 4.2.1, we can see that there is a clear procedure for two out of four possible outcomes of the PSD fitting. For the cases of a lower limit and no upper constraint we have to define an appropriate procedure that uses the information we obtain in the other cases. As we discussed in Section 5.6.1, the significance of the cross-correlation depends on the value of the power-law exponent β, with the largest significance for $\beta = 0$ and smaller for larger values. In this sense the most conservative estimate of the significance is one that uses the upper limit on β. Given that for the non-constrained cases we do not have more information than the one for the population of sources, we derive a reasonable significance estimate by adopting an average β estimated from the population with successful fits. This is a safe procedure except for light curves that show strong linear trends or high noise in at least one of the bands. These cases will be indicated and treated with caution when discussing the results of the cross-correlation analysis, but are included here as they could point to interesting cases for follow up studies.

Before discussing the results of the PSD fits, we make a brief note on the confidence intervals of the power-law indices required when combining the results of the radio and gamma-ray PSD fits. If the individual confidence intervals for $\beta_{\rm radio}$ and β_γ have a probability of $\delta = 0.683$ as required for a 1σ constraint, we have by definition that the probabilities of the intervals containing the true values are $P(\beta^{\rm low}_{\rm radio} \leq \beta_{\rm radio} \leq \beta^{\rm up}_{\rm radio}) = \delta$ for the radio band and $P(\beta^{\rm low}_{\gamma} \leq \beta_{\gamma} \leq \beta^{\rm up}_{\gamma}) = \delta$ for the gamma-ray band. When we combine those intervals using the fact that the measurements are independent we obtain $P([\beta^{\rm low}_{\rm radio} \leq \beta_{\rm radio} \leq \beta^{\rm up}_{\rm radio}]\, and\, [\beta^{\rm low}_{\gamma} \leq \beta_{\gamma} \leq \beta^{\rm up}_{\gamma}]) = \delta^2$, thus the probability of the combined interval is smaller than 0.683. In order to correct for this and obtain the appropriate coverage we need to obtain confidence intervals with a coverage of $\sqrt{0.683} \approx 0.826$ for β in each band. These two confidence intervals are reported as results of the PSD fitting.

6.2.1 Characterization of the radio and gamma-ray light curves

The PSDs for the radio and gamma-ray light curves are each fitted with a single power-law model. For each band we test a range of values of β in steps of $\Delta\beta = 0.05$ and use $M = 1000$ light curves for the determination of the mean and scatter of the model PSD at each tested value. The confidence bands are constructed with a resolution of $\Delta\beta = 0.25$

and interpolated for intermediate values and for each case we simulate 1000 light curves for the acceptance intervals at each β. The search interval for the radio data is taken to be $0.0 \leq \beta_{\rm radio} \leq 3.5$ and for gamma-ray $0.0 \leq \beta_{\gamma} \leq 2.5$. This choice is based in preliminary fits that showed that most best fit values lie in those intervals, and by the observation that not many light curves show the characteristic low frequency trends with little variability shown by simulated light curves with very steep PSDs. Another factor is the ability to suppress the effects of red-noise leakage which is determined by the window function. This stops being effective for values of $\beta \gtrsim 4.0$ as can be seen in Figure 3.2 and its associated discussion. In each case where a PSD is computed we bin it in frequency intervals of 1.3 dex if the bin contains at least 4 points. In bins with less than 4 points the width is increased in steps of 1.1 dex until it contains at least 4 points. Each simulated light curve has a time resolution of 1 day and a length of 20 years.

The results of applying the method described in Chapter 3 to the 86 sources with radio and gamma-ray light curves (see Section 2.9 for details on the sample selection) are presented in Table E.1 for the radio light curves and Table E.2 for the gamma-ray ones. These tables contain the best fit, confidence interval, p-value of the best fit and other important parameters of the light curves. We also include summary figures for the PSD fit for each source in Appendix E.2 for the radio light curves and Appendix E.3 for the gamma-ray ones. Some basic statistics of the results are given below.

The fitting procedure does not provide a proper confidence interval in all cases. At the level of 68.3% confidence intervals for the radio light curves we obtain successful fits for 43 sources, lower limits for 8 sources, and no constraints for 30 sources and are not able to run the procedure for 5 sources because of the absence of measured variability (Section 4.2.1). For the gamma-ray light curves we obtain successful fits for 29 sources, lower limits for 19 sources, and no constraints for 20 sources and are not able to run the procedure for 18 sources.

For the 82.6% confidence intervals required to combine both fitted values in the significance estimate, we find for the radio light curves successful fits for 33 sources, lower limits for 13 sources, and no constraints for 35 sources and are not able to run the procedure for 5 sources. For the gamma-ray light curves we obtain successful fits for 23 sources, lower limits for 10 sources, and no constraints for 35 sources and are not able to run the procedure for 18 sources.

The 1σ errors on the PSD fits for the radio light curves range from 0.2 to 1.0 with a median of 0.4. For the gamma-ray light curves the errors range from 0.2 to 0.8 with a median of 0.4.

Even though the errors are similar in both cases, the radio PSD fits are of much better quality than those of the gamma-ray light curves. In the later case we sometimes see little discrimination between models and low quality of fits. This could be a consequence of short and noisier light curves when compared to the radio light curves, or an indication of the inadequacy of the simple power-law PSD as a model for the gamma-ray light curves. We expect the situation to improve as longer gamma-ray light curves are collected by the *Fermi*-LAT.

6.2.2 Distribution of the fitted values of the PSD for the radio and gamma-ray light curves

We study the distribution of the PSD power-law indices for the sources in which the procedure provides a proper constraint. The histogram in Figure 6.1 shows that there is a preferred value for the power-law exponent of the radio PSD with all the values distributed around a peak in the distribution. A χ^2 test shows that the measured values of β including their measurement errors are consistent with a single value equal to the sample mean of 2.29 ± 0.06 ($p = 0.27$). We use the weighted mean and standard deviations to characterize the distribution of measured values obtaining a normal model with $\mu = 2.3$ and $\sigma = 0.4$. This result is consistent to what we find for the complete OVRO sample in Section 4.2 and is the distribution we use to constrain the values for the sources in which the fitting procedure could not measure the slope of the radio PSD.

The same is done for the gamma-ray light curves and the histogram shown in Figure 6.2. We see a larger fraction of sources with β_γ of about 0.5, but the distribution is broad and shows a second peak about 1.6. For the weighted average we obtain a normal distribution with parameters $\mu = 0.7$ and $\sigma = 0.6$, but as suggested by the shape of the distribution in Figure 6.2 a χ^2 test shows that the measured values are not consistent with a single value equal to the sample mean of 0.7 ± 0.1 ($p < 10^{-6}$).

The presence of two peaks in the distribution could indicate the existence of different source classes with different properties or simply be the result of a systematic effect of the PSD fitting process. We first examine two possible systematic effects, one related to the

gamma-ray brightness of the source and one related to the ratio of signal power to noise power in the light curves. By separating the sources in two brightness groups of about equal size and applying a Kolmorov-Smirnov test (K-S test), no significant difference is found between the distribution the bright and dim populations ($p = 0.33$). The same is found when dividing the sources into groups with low noise ($\sigma^2_{\rm noise}/\sigma^2_{\rm data} < 0.1$) and high noise ($\sigma^2_{\rm noise}/\sigma^2_{\rm data} \geq 0.1$), in this case we find $p = 0.99$ for the K-S test. These two tests rule out the most probable systematic problem due to the presence of noise in the light curves which makes the PSD fit less certain.

The second and more interesting possibility of a difference between source populations is also examined. A comparison of the distribution of the power-law indices between sources with different optical classes reveals consistent distributions for the BL Lacs and FSRQs, with $p = 0.76$ for the K-S test. The case of the spectral energy distribution class is similar, and in this case we find consistent distributions for the LSP and ISP blazars with $p = 0.46$ for the K-S test. No HSP blazars have good quality fits.

Given the small number of sources, we think that a reasonable assumption for the PSD shape for sources in which no direct constraint is obtained is to use an average value of the gamma-ray PSD. We recognize this is a crude assumption that would need to be revised when longer gamma-ray light curves become available. As an alternative to the average power-law index of the PSD we obtain, we can use the ensemble average PSD obtained in Abdo et al. (2010). Their method provides an estimation of the average PSD shape but cannot tell us much about the variability of the PSD shape between different sources, so it has to be used with caution.

6.3 Significance of the cross-correlations

Ideally we would like to determine the significance of the cross-correlations for each source using the best fit values for the power-law index of the PSDs at the radio and gamma-ray band for each particular source, but this is currently possible for only 17 sources. For the rest all we can do is to get a best guess significance estimate by using an average value taken from the objects for which we can obtain good fits in both the gamma-ray and radio wavebands.

For the radio band we can use an average value of $\beta_{\rm radio} = 2.3$, which is consistent with

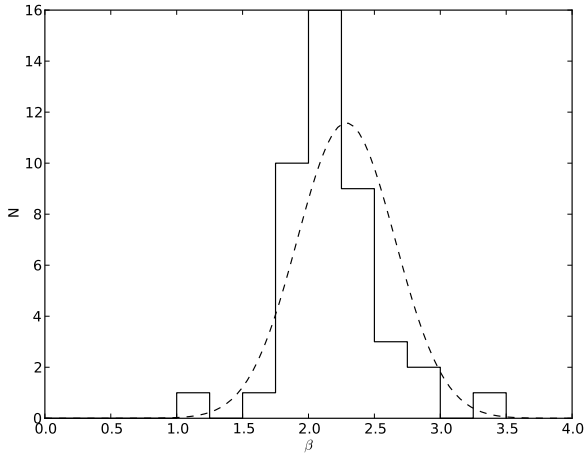

Figure 6.1: Distribution of power-law exponents of the radio light curve PSDs. The distribution is consistent with a single value equal to the sample mean and can be described by a normal with $\mu = 2.3$ and $\sigma = 0.4$ represented by the dashed line.

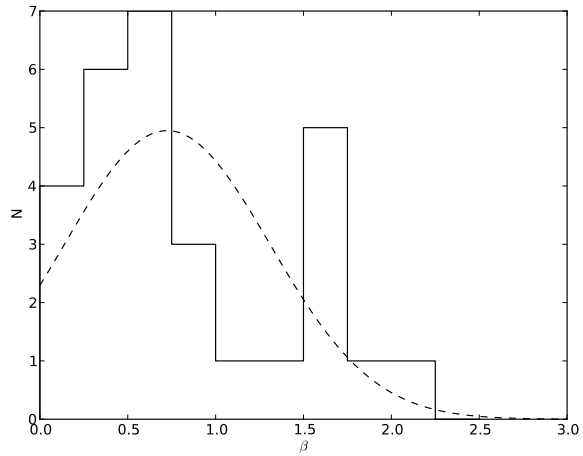

Figure 6.2: Distribution of power-law exponent of the gamma-ray light curve PSDs. The distribution shows some concentration about 0.5 with hints of a second peak about 1.6. A weighted average estimate of a normal distribution gives $\mu = 0.7$ and $\sigma = 0.6$ and is represented by the dashed line. The distribution is not consistent with a single value equal to the sample mean ($p < 10^{-6}$).

the distribution shown in Figure 6.1 and discussed in Section 6.2.2.

For the gamma-ray band there is more uncertainty as we can only constrain the PSD for a small number of sources (29 out of 86) and not all the fits are of high quality. One possibility is to use the sample mean of the good fits which is found to be 0.7 ± 0.1, that

is obtained from a distribution which presents large scatter with values going from 0 to 2.0 and typical errors of 0.4 (Figure 6.2 and associated discussion). A second option is to use the average gamma-ray PSD reported in Abdo et al. (2010). In their study they find a value of $\beta_\gamma = 1.4 \pm 0.1$ for the average PSD of the nine brightest FSRQs and $\beta_\gamma = 1.7 \pm 0.3$ for the average PSD of the six brightest BL Lacs. We take a conservative approach and adopt a single value equal to the average of $\beta_\gamma = 1.6$ for all the sources regardless of their class. The advantage of this choice are its simplicity and a uniform treatment of all the sources. A drawback of this particular choice is that it is hard to assess the real variance between the individual PSD shapes, so we think this value can only provide an approximate estimate for the significance. More data are required to settle the issue of the appropriate value of the power-law index of the gamma-ray light curves. Ideally we would like to characterize the PSDs for many individual gamma-ray light curves to understand the variability between sources, which is hidden when using ensemble averages as the one in Abdo et al. (2010). This program requires longer gamma-ray light curves which will be available later in the *Fermi* mission.

We can obtain a conservative estimate by using $\beta_{\rm radio} = 2.3$ and $\beta_\gamma = 1.6$, but we also study the case of $\beta_{\rm radio} = 2.3$ and $\beta_\gamma = 0.7$ to get an idea of the results under this more aggressive assumption and point to interesting sources for more detailed studies.

In order to reduce the chances of getting spurious results due to our rather short light curves, we have restricted the search for correlations to a range between plus and minus half the length of the shortest light curve. We have also excluded 23 sources in which there is no variability at the 3σ level detected in at least one of the bands as determined with a χ^2 test of the hypothesis of a constant source. For these cases there is not enough variability relative to the observational noise and a meaningful cross-correlation analysis is not possible. Figures for each of these non-variable sources are included in Appendix F. Even with this cautious approach, it is still possible to get misleadingly high values of the correlation coefficient due to slow trends in the light curves. Some authors (e.g. Welsh, 1999) suggest subtracting these trends before performing a correlation analysis but our light curves are not long enough to perform the subtraction with confidence, so instead we report these results with a warning in the tables (*tr* and *tg* for trends in the radio and gamma-ray light curve respectively). These trends are determined not in the complete light curves, but on the overlapping sections included in the cross-correlation for the most significant peak

in each source. To quantify the presence of trends we first fitted the light curve segments with a linear function that represents a slow trend in the light curve. This linear trend was subtracted and the residuals were tested for variability with a χ^2 test for the null hypothesis of constant residuals. To get an estimate that is robust to single residuals of large magnitude, we used the average p-value of 1000 bootstrap samples of the residuals. Sources in which the residuals are consistent to being constant at the 3σ level were flagged as having trends and not considered as reliable correlations.

Another problematic situation is faced when correlating light curves with a high noise content in which the variability is hard to trace. Sources in which the noise power is at least 1/3 of the total power were flagged as noisy in the results table (*nr* for noisy in radio and *ng* for noisy in gamma-rays). Sources with any of these flags will produce unreliable results and are not included in the discussions of significant results. Nonetheless they were still included in the analysis as they can provide objects for further study.

A final flag indicates sources with cross-correlation functions with two peaks of comparable significance, or a broad peak with the same characteristics (*dt* for double time lag). In these cases we report the values obtained by the data reduction script in each case, so it is important to note that those are not mistakes in the analysis, but an ambiguity produced by our data set and measurement errors in the significance estimate. Sources with this flag are included in the discussions of significant results.

For the significance estimate of each source we simulate 20,000 light curve pairs. Each light curve has a time resolution of 1 day and a length of 10 years. The cross-correlations are binned with a 10 day interval.

The results of the cross-correlation significance analysis for each one of the alternatives discussed above are presented in Table 6.1. Table 6.2 has the results for the sources with constrained PSDs. Notice that in the case of the sources with constrained PSDs we have also included four sources with poor radio or gamma-ray PSD fit which are indicated with the flags *pfr* or *pfg*. In these cases we have a p-value of the best fit between 0.01 and 0.05, below the original threshold, but still excluding very poor quality PSD fits. The last column in each table contains flags indicating possible problems with the light curves as discussed above. The distribution of time lags and significances is shown in Figures 6.3, 6.4 and 6.5 for all the sources in the cases we have described. Figures showing the light curves and results of the cross-correlation analysis for all the sources in all the cases described here

are presented in Appendix F. A negative time lag indicates that the variability in the radio light curve lags the one of the gamma-ray band, while the opposite is true for a positive time lag.

Table 6.1: Cross-correlation significance results using populations values for the PSDs in both bands
Columns are: τ time lag; CCF cross-correlation; Sig. significance for time lag; Unc. uncertainty in significance, Trends for radio *tr* and gamma-rays *tg*, and Flags are flags describing possible problems with the light curves, *dt* for cross-correlations with two peaks with almost equal significance or a broad peak, *nr* and *ng* for sources with noisy light curves in radio or gamma-rays respectively. See text for more details.

	$\beta_{\rm radio} = 2.3$, $\beta_\gamma = 1.6$					$\beta_{\rm radio} = 2.3$, $\beta_\gamma = 0.7$					
Name	τ	CCF	Sig.	Unc.	Trends	τ	CCF	Sig.	Unc.	Trends	Flags
OVRO	[day]		%	%		[day]		%	%		
J0108+0135	-340 ± 16	0.33	58.64	0.49	...	-340 ± 16	0.33	84.15	0.36	...	ng
J0112+2244	-380 ± 14	0.24	39.83	0.52	...	-380 ± 13	0.24	65.0	0.46	...	...
J0112+3208	190 ± 12	0.36	54.65	0.5	tg	190 ± 12	0.36	76.81	0.41	tg	...
J0136+4751	-230 ± 13	0.62	89.06	0.31	...	-230 ± 14	0.62	99.58	0.07	...	...
J0217+0144	-60 ± 15	0.38	65.75	0.46	...	-60 ± 15	0.38	90.04	0.3	...	...
J0221+3556	190 ± 12	0.51	93.08	0.25	...	-300 ± 15	0.55	99.67	0.06	...	dt, ng
3C66A	460 ± 16	0.27	50.35	0.5	...	460 ± 15	0.27	76.76	0.42	...	...
J0237+2848	-140 ± 12	0.63	86.72	0.34	...	-140 ± 12	0.63	99.56	0.07	...	...
J0238+1636	-30 ± 8	0.93	99.88	0.04	...	-30 ± 9	0.93	99.99	0.0	...	dt
J0319+4130	-420 ± 13	0.59	82.39	0.39	...	-420 ± 13	0.59	98.7	0.12	...	...
J0423−0120	-20 ± 16	0.49	78.0	0.42	...	-20 ± 16	0.49	97.17	0.16	...	...
J0442−0017	420 ± 29	0.22	36.75	0.48	...	420 ± 30	0.22	59.38	0.5	...	...
J0509+0541	450 ± 14	0.25	62.87	0.5	tg	450 ± 15	0.25	81.94	0.39	tg	ng
C0719+3307	140 ± 8	0.61	90.05	0.31	...	140 ± 8	0.61	99.26	0.09	...	...
J0721+7120	-200 ± 12	0.37	51.04	0.5	...	-200 ± 12	0.37	83.64	0.37	...	...
J0725+1425	150 ± 13	0.19	31.45	0.48	...	150 ± 13	0.19	53.45	0.51	...	...
J0739+0137	-360 ± 15	0.5	79.7	0.39	...	-360 ± 14	0.5	96.91	0.17	...	ng

Continues

Table 6.1

Name	τ	CCF	Sig.	Unc.	Trends	τ	CCF	Sig.	Unc.	Trends	Flags
OVRO	[day]		%	%		[day]		%	%		
J0742+5444	-190 ± 9	0.69	87.9	0.33	...	-190 ± 9	0.69	99.61	0.06	...	...
J0808−0751	-150 ± 15	0.59	77.62	0.43	...	-150 ± 15	0.59	98.54	0.12	...	...
J0831+0429	150 ± 16	0.42	75.92	0.44	...	110 ± 16	0.4	94.3	0.23	...	dt, ng
0836+710	210 ± 11	0.63	91.74	0.28	tg	210 ± 11	0.63	98.81	0.11	tg	ng
J0854+2006	-70 ± 16	0.38	62.48	0.48	...	-70 ± 16	0.38	87.09	0.33	...	ng
J0909+0121	510 ± 16	0.39	68.85	0.48	...	-210 ± 11	0.43	92.16	0.27	...	dt
J0920+4441	-460 ± 13	0.49	71.14	0.45	...	-290 ± 12	0.47	94.53	0.23	...	dt
C1012+2439	490 ± 49	0.57	99.51	0.07	tr, tg	490 ± 47	0.57	99.69	0.06	tr, tg	nr, ng
J1058+0133	510 ± 15	0.6	93.42	0.25	...	510 ± 15	0.6	99.62	0.06	...	ng
J1104+3812	-500 ± 10	0.39	73.78	0.43	...	-500 ± 11	0.39	93.99	0.24	...	ng
J1127−1857	10 ± 11	0.76	96.67	0.18	...	10 ± 11	0.76	99.99	0.0	...	...
J1159+2914	-70 ± 17	0.42	58.74	0.51	...	-40 ± 15	0.42	89.46	0.31	...	dt
J1217+3007	120 ± 9	0.5	91.88	0.27	...	120 ± 10	0.5	99.47	0.07	...	ng
C1224+2122	-380 ± 10	0.59	74.7	0.43	...	-380 ± 9	0.59	97.31	0.16	...	...
J1229+0203	-270 ± 16	0.41	55.83	0.48	...	-240 ± 15	0.41	87.75	0.34	...	dt
C1239+0443	-50 ± 15	0.67	89.01	0.3	...	-50 ± 15	0.67	99.47	0.07	...	...
J1256−0547	190 ± 10	0.47	67.79	0.47	...	190 ± 9	0.47	94.5	0.23	...	...
J1310+3220	500 ± 56	0.32	48.74	0.52	...	500 ± 57	0.32	71.22	0.45	...	...
J1312+4828	-350 ± 16	0.36	62.38	0.51	...	-350 ± 15	0.36	85.28	0.34	...	...
J1332−0509	-90 ± 15	0.51	68.12	0.46	...	-90 ± 15	0.51	94.66	0.22	...	...
C1345+4452	30 ± 14	0.51	65.4	0.47	...	30 ± 14	0.51	91.31	0.28	...	...
CR1427+2347	110 ± 13	0.45	95.59	0.2	tr, tg	-330 ± 12	0.45	99.58	0.07	tr	dt, nr, ng

Continues

Table 6.1

Name	τ	CCF	Sig.	Unc.	Trends	τ	CCF	Sig.	Unc.	Trends	Flags
OVRO	[day]		%	%		[day]		%	%		
J1504+1029	-40 ± 13	0.87	98.47	0.12	...	-40 ± 13	0.87	99.99	0.0	...	...
PKS1510−089	-60 ± 6	0.65	83.02	0.38	...	-60 ± 6	0.65	99.24	0.09	...	...
J1522+3144	350 ± 9	0.45	75.09	0.44	...	350 ± 9	0.45	96.03	0.19	...	...
CR1542+6129	360 ± 16	0.38	78.75	0.41	tg	360 ± 17	0.38	92.15	0.27	tg	ng
J1555+1111	530 ± 17	0.43	99.69	0.06	tr, tg	530 ± 17	0.43	99.95	0.02	tr, tg	nr, ng
J1635+3808	500 ± 9	0.79	95.06	0.22	...	500 ± 9	0.79	99.89	0.03	...	...
J1653+3945	-480 ± 12	0.5	98.11	0.13	tg	-480 ± 13	0.5	99.88	0.03	tg	ng
J1709+4318	-50 ± 12	0.59	80.86	0.39	...	-50 ± 12	0.59	98.29	0.13	...	...
J1733−1304	-260 ± 14	0.5	69.14	0.46	tg	-140 ± 11	0.5	94.97	0.22	...	dt
J1748+7005	230 ± 10	0.55	77.32	0.43	...	230 ± 10	0.55	97.47	0.16	...	...
J1800+7828	500 ± 10	0.52	79.11	0.42	tg	500 ± 10	0.52	94.07	0.24	tg	...
J1824+5651	-240 ± 12	0.46	76.82	0.43	tg	-240 ± 11	0.46	95.6	0.2	tg	ng
J1848+3219	-300 ± 12	0.53	64.71	0.48	...	-300 ± 11	0.53	91.95	0.28	...	...
J1849+6705	-40 ± 9	0.38	53.86	0.5	...	-40 ± 10	0.38	84.58	0.36	...	...
J1959+6508	-80 ± 13	0.41	90.97	0.3	tg	-80 ± 13	0.41	99.29	0.08	tg	ng
C2025−0735	130 ± 12	0.55	72.89	0.44	...	130 ± 9	0.55	93.36	0.25	...	...
J2143+1743	-320 ± 11	0.34	54.4	0.5	...	-320 ± 11	0.34	83.4	0.38	...	...
BLLacertae	-160 ± 13	0.71	89.33	0.32	...	-160 ± 14	0.71	99.84	0.04	...	...
J2203+1725	530 ± 9	0.58	92.61	0.26	...	530 ± 9	0.58	99.5	0.07	...	ng
J2229−0832	310 ± 13	0.55	90.47	0.3	...	310 ± 13	0.55	98.42	0.13	...	ng
2230+114	-430 ± 10	0.42	54.75	0.49	...	-430 ± 9	0.42	85.47	0.35	...	...
J2236+2828	110 ± 14	0.35	58.37	0.49	...	110 ± 13	0.35	85.39	0.35	...	...

Continues

Table 6.1

Name	τ	CCF	Sig.	Unc.	Trends	τ	CCF	Sig.	Unc.	Trends	Flags
OVRO	[day]		%	%		[day]		%	%		
J2253+1608	-80 ± 17	0.55	73.28	0.44	...	-80 ± 17	0.55	97.6	0.15	...	...
C2311+3425	-120 ± 14	0.73	91.24	0.27	...	-120 ± 14	0.73	99.89	0.03	...	...

Table 6.2: Cross-correlation significance results for sources with constrained PSDs
Columns are: τ time lag; CCF cross-correlation; Sig best fit. significance of correlation for best fit PSD; Sig lower and upper limit limits on significance of correlations; Unc. uncertainty in the significance and Flags are flags as in Table 6.1 plus *pfr* and *pfg* for poor PSD fit in radio or gamma-rays respectively. None of the sources in this sample is affected by trends so that column is not included. See text for more details.

Name	τ	CCF	Sig.	Sig.	Sig.	Sig Unc.	
OVRO	[day]		best fit	lower limit	upper limit	best fit	
			%	%	%	%	Flags
J0112+2244	-380 ± 13	0.24	59.63	36.05	94.45	0.48	...
3C66A	460 ± 14	0.27	81.16	60.78	99.96	0.39	...
J0238+1636	-30 ± 9	0.93	99.99	99.99	99.99	0.0	dt, pfr
J0721+7120	-200 ± 11	0.37	49.48	40.5	66.05	0.49	pfr
J0808−0751	-150 ± 16	0.59	99.52	88.86	99.99	0.07	...
J1159+2914	-70 ± 18	0.42	79.05	55.61	95.39	0.39	dt
C1224+2122	-380 ± 10	0.59	99.78	96.51	99.99	0.05	...
J1229+0203	-240 ± 16	0.41	86.32	68.08	99.99	0.33	dt

Continues

Table 6.2

Name OVRO	τ [day]	CCF	Sig. best fit %	Sig. lower limit %	Sig. upper limit %	Sig Unc. best fit %	Flags
J1256−0547	190 ± 10	0.47	65.03	54.86	80.94	0.48	...
J1332−0509	−90 ± 15	0.51	99.56	90.36	99.98	0.07	...
PKS1510−089	−60 ± 6	0.65	76.99	66.28	92.41	0.44	pfg
J1635+3808	500 ± 8	0.79	96.28	90.24	99.99	0.2	...
J1748+7005	230 ± 10	0.55	99.48	87.86	99.99	0.07	...
J1849+6705	−40 ± 10	0.38	90.61	61.42	99.91	0.3	...
J2143+1743	−320 ± 11	0.34	99.03	90.25	99.48	0.1	pfr
BLLacertae	−160 ± 14	0.71	85.27	72.37	99.99	0.36	...
C2311+3425	−120 ± 14	0.73	99.99	99.33	99.99	0.0	...

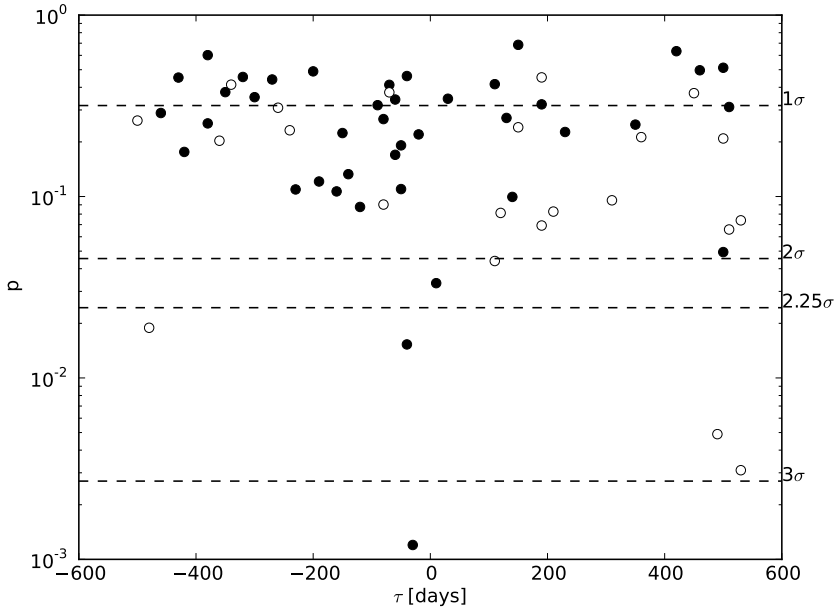

Figure 6.3: Time lag and significance of most significant peak on the radio/gamma-ray cross-correlation for the case of $\beta_{\rm radio} = 2.3$ and $\beta_\gamma = 1.6$. Filled circles are for sources with no flags and empty circles for flagged sources. The vertical axis is the p-value associated with the fit with values indicated in the vertical axis on the left. The horizontal dashed lines are some reference equivalent significances as labeled on the right end of the lines. See Section 6.3.1.1 for more details.

6.3.1 The significance of the cross-correlations

The significances of the cross-correlations coefficients depend on the values used for the power-law PSD at both bands, so we give a separate discussion for each case below. As mentioned earlier, a negative time lag indicates the radio light curve lags the gamma-ray one, while a positive time lag corresponds to the opposite case.

6.3.1.1 Estimates with $\beta_{\rm radio} = 2.3$ and $\beta_\gamma = 1.6$

Of the 63 sources with significant variability in both bands only 41 have none of the flags described in the first part of Section 6.3 and are thus included in the discussion below.

Only 1 out of 41 sources is found to have a $\geq 3\sigma$ significant correlation which is considered a highly significant correlation as we expect none to be present by chance in a sample of 41. We extend the search for significant correlations by setting a threshold such that at

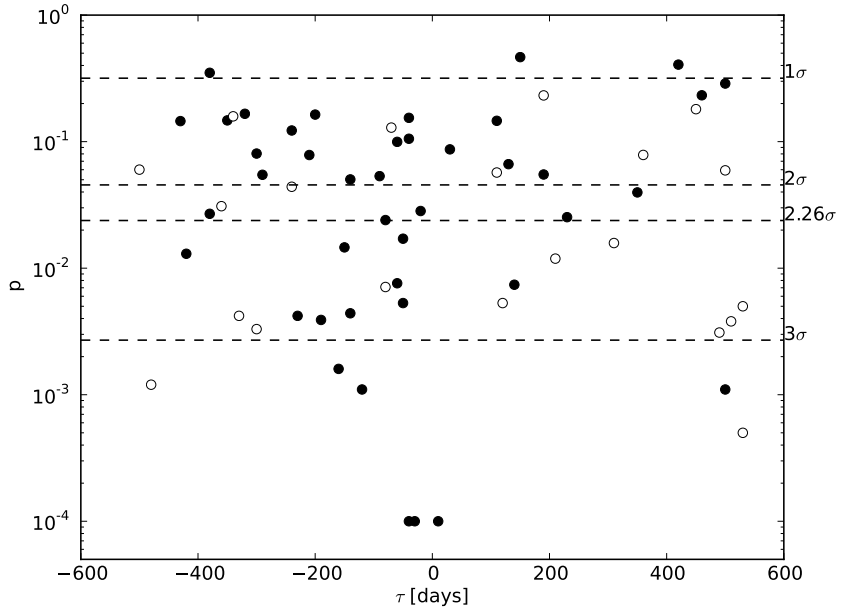

Figure 6.4: Time lag and significance of most significant peak on the radio/gamma-ray cross-correlation for the case of $\beta_{\rm radio} = 2.3$ and $\beta_\gamma = 0.7$. Filled circles are for sources with no flags and empty circles for flagged sources. The vertical axis is the p-value associated with the fit with values indicated in the vertical axis on the left. The horizontal dashed lines are some reference equivalent significances as labeled on the right end of the lines. See Section 6.3.1.2 for more details.

most one source is expected to have a chance high cross-correlation coefficient in a sample of 41, that is 2.25σ (97.56%). The cases above the threshold are: J0238+1636 (AO 0235+164) with a time lag of -30 ± 8 day and 99.88% significance, and J1504+1029 (PKS 1502+106) with a time lag of -40 ± 13 day and 98.47% significance. The results for these cases are presented in Figures 6.6 and 6.7, which show the radio and gamma-ray light curves on the left panel, the cross-correlations with color contours for the significance levels for each case in the middle panel (red for 1σ, orange for 2σ and green for 3σ) and p-values with equivalent significances in the right panel. Notice that in the right panel the p-values are for positive and negative correlations, thus some of the troughs could represent anti-correlations that are not considered in this discussion. The ambiguity can easily be resolved by looking at the cross-correlation plot on the middle panel.

We note that the cross-correlation peaks are broad in both cases and that for AO 0235+164, a second peak of comparable significance is seen at $\tau = -150 \pm 20$ day. This will be con-

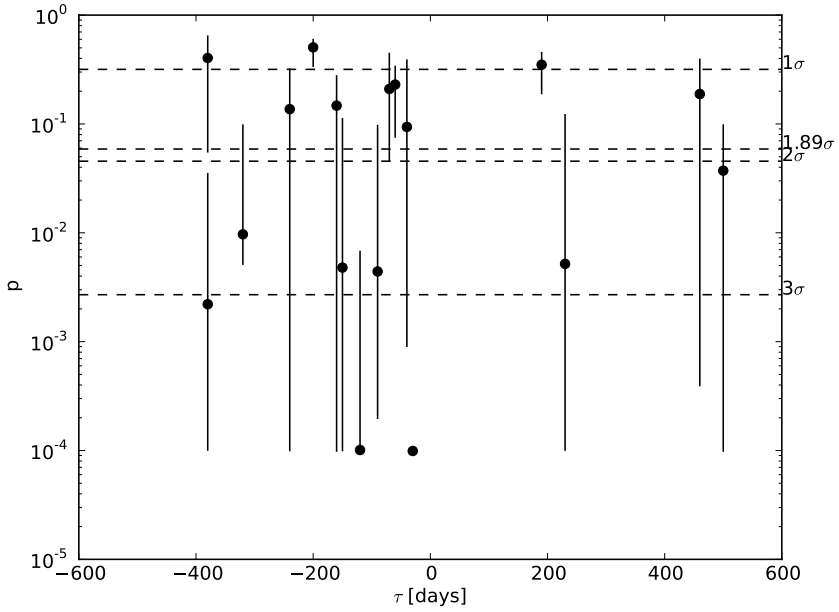

Figure 6.5: Time lag and significance of most significant peak on the radio/gamma-ray cross-correlation for the cases in which the PSD at both bands is constrained. The vertical axis is the p-value associated with the fit with values indicated in the vertical axis on the left. The horizontal dashed lines are some reference equivalent significances as labeled on the right end of the lines. See Section 6.3.1.3 for more details.

sidered when discussing the interpretation of the results in Chapter 7. The same comment applies to all the other instances in which we discuss this source.

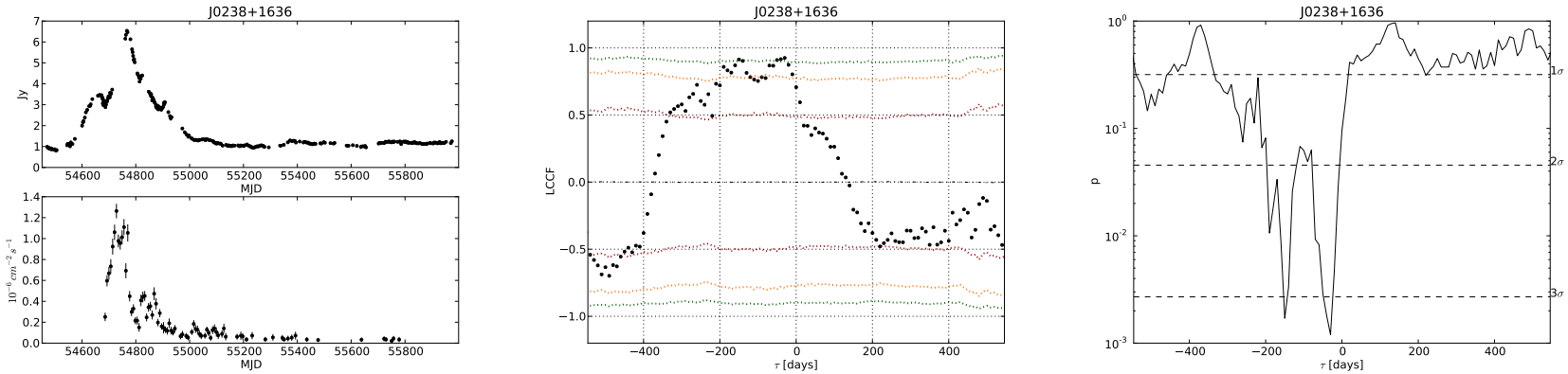

Figure 6.6: Light curves and cross-correlation significance for J0238+1636 in the case of $\beta_{\rm radio} = 2.3$ and $\beta_\gamma = 1.6$. The most significant cross-correlation is at -30 ± 8 day with 99.88% significance.

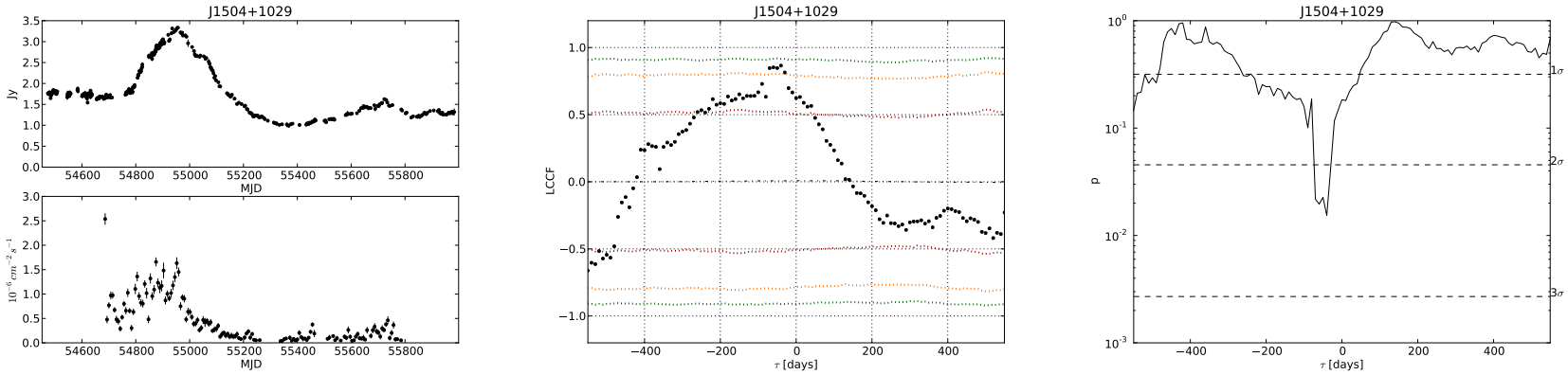

Figure 6.7: Light curves and cross-correlation significance for J1504+1029 in the case of $\beta_{\rm radio} = 2.3$ and $\beta_\gamma = 1.6$. The most significant cross-correlation is at -40 ± 13 day with 98.47% significance.

6.3.1.2 Estimates with $\beta_{\rm radio} = 2.3$ and $\beta_\gamma = 0.7$

In this case 42 sources have no flags and are thus included in the discussion of significant cross-correlations. The threshold for one expected chance correlation in a sample of 42 sources is 2.26σ (97.62%). In this case we find 6 sources with $\geq 3\sigma$ significant correlations and 15 at the $\geq 2.26\sigma$ level. The larger number of sources with significant correlations is a consequence of using a flatter PSD for the gamma-rays which gives less frequent and smaller amplitude chance cross-correlations as discussed in Section 5.6.1.

The cases with $\geq 3\sigma$ significance are J0238+1636 (AO 0235+164), J1127−1857 (PKS 1124−186), J1504+1029 (PKS 1502+106), C2311+3425 (B2 2308+34), J1635+3808 (4C +38.41) and BL Lacertae. These are shown in Figures 6.8, 6.9, 6.10, 6.11, 6.12 and 6.13.

For the case of the $\geq 2.26\sigma$ significances (not included in the list above) we have 9 additional cases which in order of significance are: J0742+5444, J0136+4751, J0237+2848, C1239+0443, C0719+3307, PKS1510−089, J0319+4130, J0808−0751 and J1709+4318. Given that in the case of $\beta_\gamma = 0.7$ we are making an aggressive guess of the significance estimate, we do not give further consideration to these cases beyond noting that they could be interesting objects for further study. In spite of this, it is interesting to note that in most cases the radio emission lags the gamma-ray one, with only two cases with gamma-ray emission lagging the radio activity and one in which the variations are simultaneous. Figures for these sources can be found in Appendix F.2.

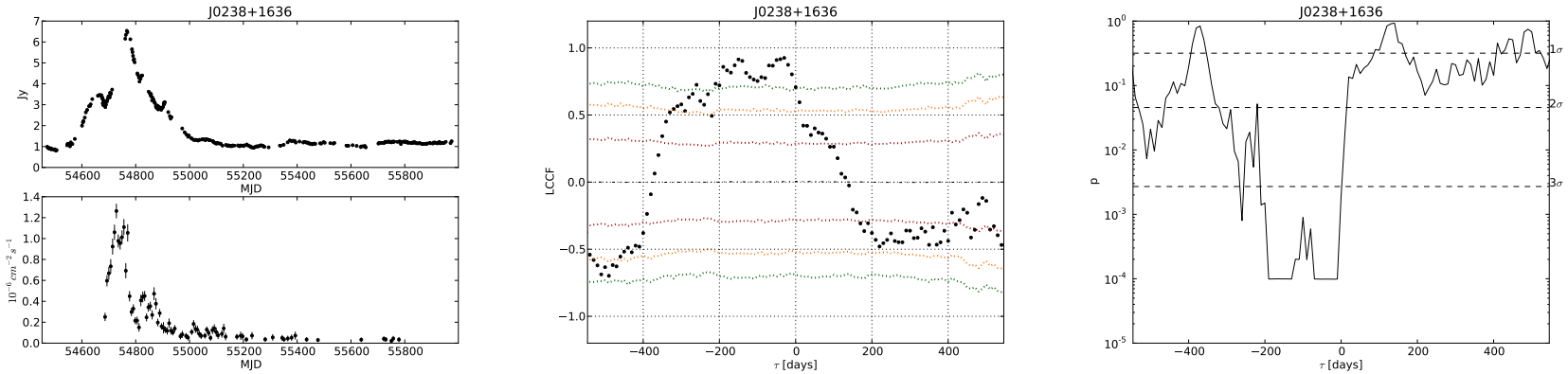

Figure 6.8: Light curves and cross-correlation significance for J0238+1636 in the case of $\beta_{\rm radio} = 2.3$ and $\beta_\gamma = 0.7$. The most significant cross-correlation is at -30 ± 9 day with 99.99% significance.

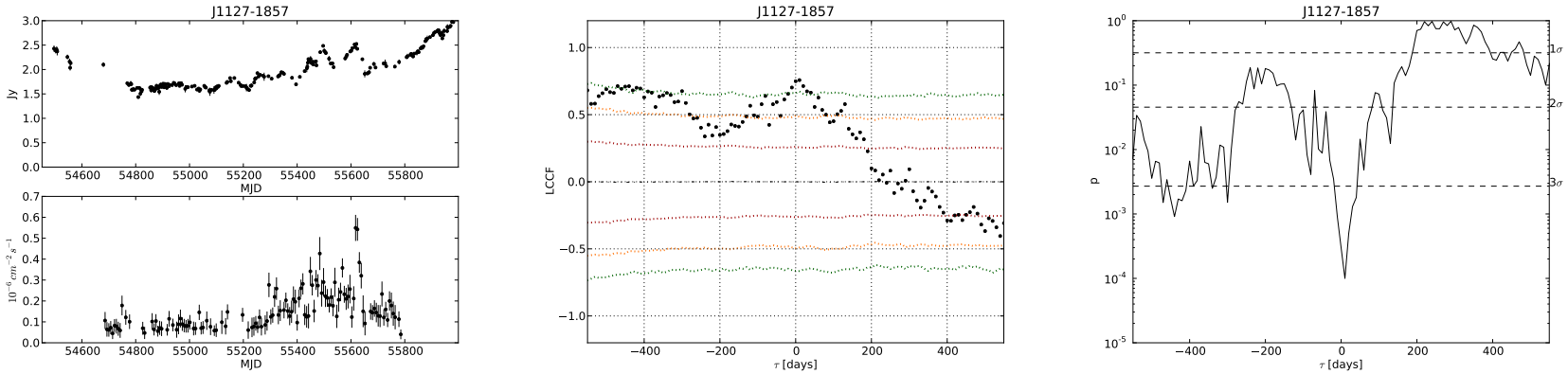

Figure 6.9: Light curves and cross-correlation significance for J1127-1857 in the case of $\beta_{\rm radio} = 2.3$ and $\beta_\gamma = 0.7$. The most significant cross-correlation is at 10 ± 11 day with 99.99% significance.

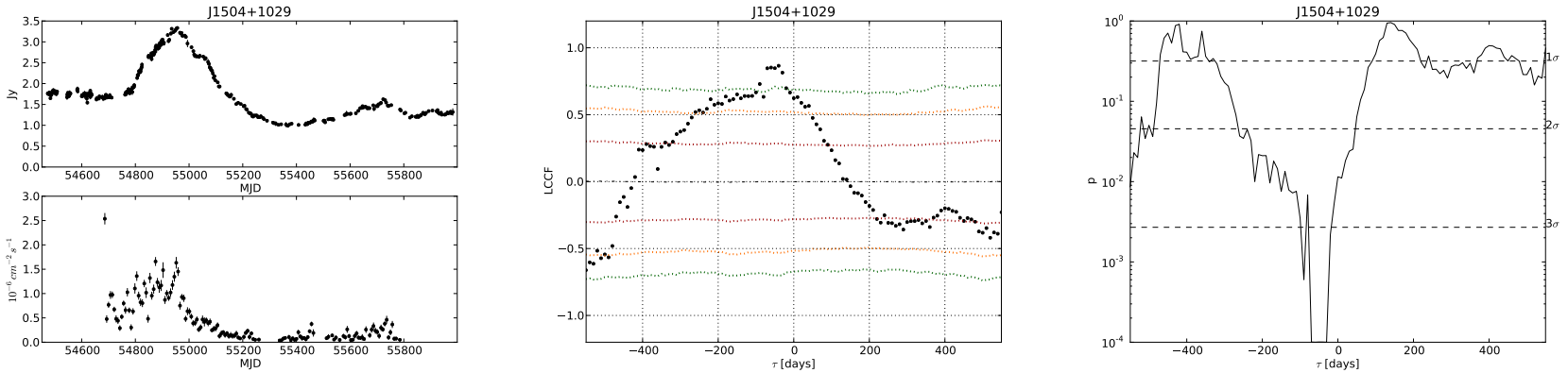

Figure 6.10: Light curves and cross-correlation significance for J1504+1029 in the case of $\beta_{\rm radio} = 2.3$ and $\beta_\gamma = 0.7$. The most significant cross-correlation is at -40 ± 13 day with 99.99% significance.

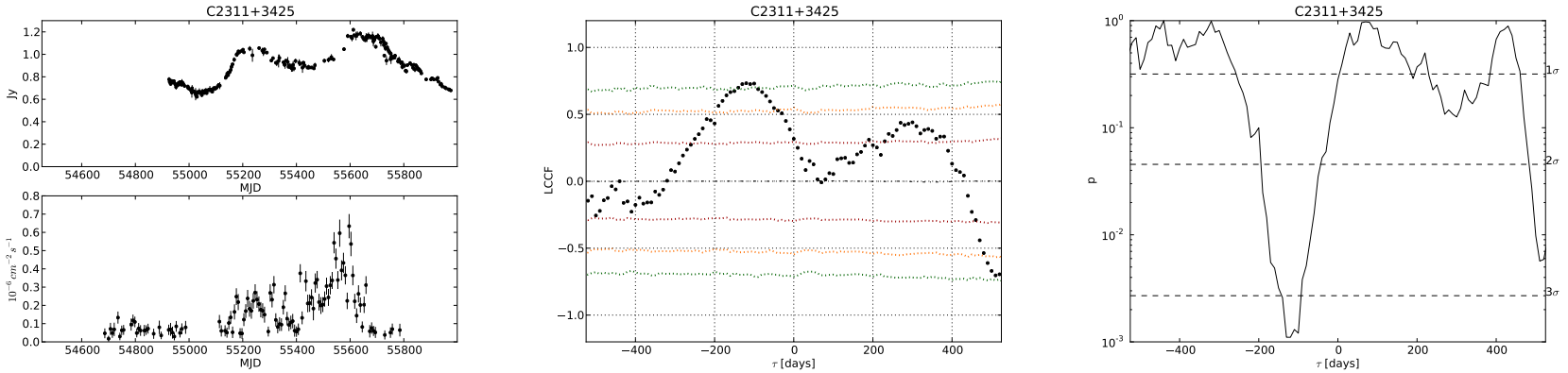

Figure 6.11: Light curves and cross-correlation significance for C2311+3425 in the case of $\beta_{\rm radio} = 2.3$ and $\beta_\gamma = 0.7$. The most significant cross-correlation is at -120 ± 14 day with 99.89% significance.

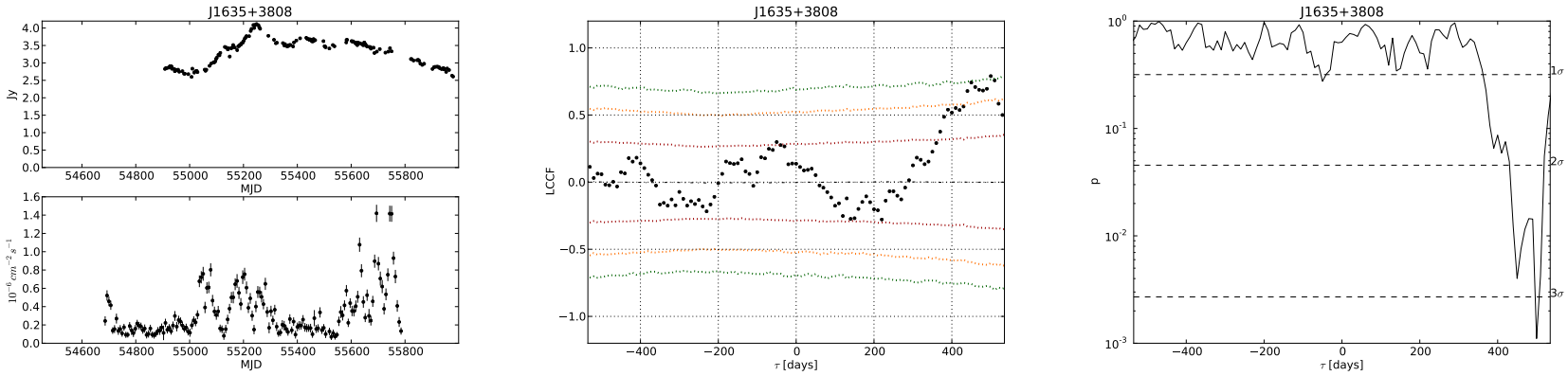

Figure 6.12: Light curves and cross-correlation significance for J1635+3808 in the case of $\beta_{\text{radio}} = 2.3$ and $\beta_\gamma = 0.7$. The most significant cross-correlation is at 500 ± 9 day with 99.89% significance.

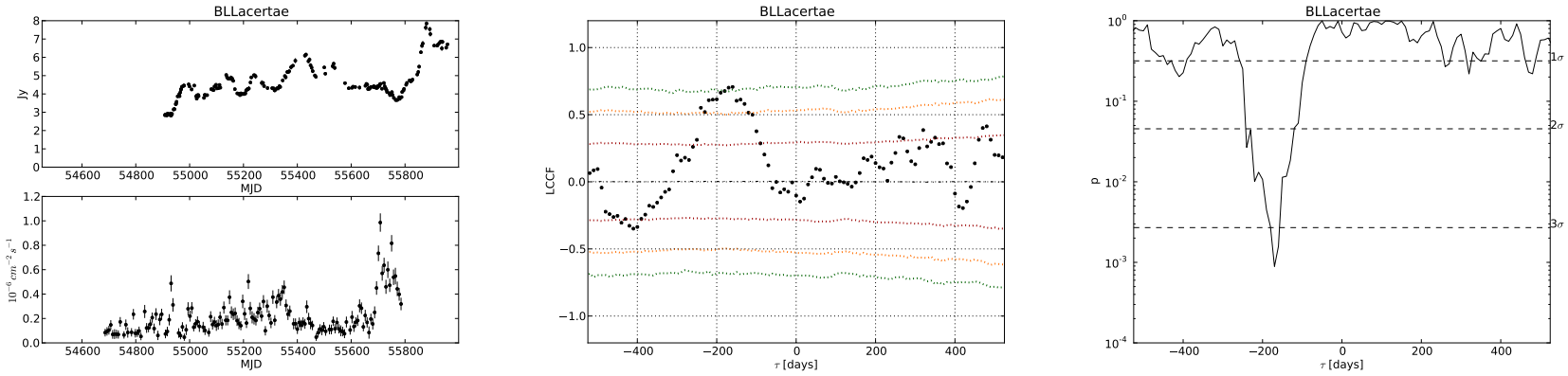

Figure 6.13: Light curves and cross-correlation significance for BLLacertae in the case of $\beta_{\text{radio}} = 2.3$ and $\beta_\gamma = 0.7$. The most significant cross-correlation is at -160 ± 14 day with 99.84% significance.

6.3.1.3 Estimates using the best fit values of the PSDs

We now look at the 17 highest quality cases in which the PSD can be constrained in both bands. For these cases we estimate the significance using the best fit value of the PSD at each band, the flattest PSDs to get an upper limit on the significance and the steepest PSDs to get a lower limit on the significance. Only the cases with no flags besides the *dt*, *pfr* or *pfg* are described below. No column indicating a trends flag is included in Table 6.2, because none of the sources presented that particular problem.

There is 1 case in which the significance is $\geq 3\sigma$ even for the lower limit: J0238+1636 (AO 0235+164, $\tau = -30 \pm 9$). Figure 6.14 summarizes the result for this source. In this and all the figures for the best fit case the panel with the p-values and significances shows the estimate obtained with the best fit PSD as a solid line and 1σ confidence limits as the shaded area.

There is an additional case C2311+3425 (B2 2308+34, $\tau = -120 \pm 14$) for which the best fit value of the PSDs gives a $\geq 3\sigma$ significance but the lower limit is below the 3σ level still at a high level of 99.93%. Figure 6.15 summarizes the result for this source.

There is another case C1224+2122 (4C +21.35, $\tau = -380 \pm 10$) for which the best fit value of the PSDs gives a $\geq 3\sigma$ significance but the lower limit is below the 3σ level but only at a moderately high level of 96.51%. The results are shown in Figure 6.16. The not so high level of significance for the low limit, and the presence of a long term trend in the radio light curve for this source cast some doubt into the interpretation of this correlation as significance.

There are 5 additional cases in which the significance is $\geq 1.89\sigma$ (94.12% for which we expect 1 significant case by chance) when the best fit PSDs are used, but in all of them the lower limit is below 1.89σ so they are not significant. These cases are in order of significance: J1332−0509 (PKS 1329−049 , $\tau = -90 \pm 15$), J0808−0751 (PKS 0805−07, $\tau = -150 \pm 16$), J1748+7005 (S4 1749+70, $\tau = 230 \pm 10$), J2143+1743 (OX 169, $\tau = -320 \pm 11$) and J1635+3808 (4C +38.41, $\tau = 500 \pm 8$). All but one of them are consistent with being 3σ significant if the flatter allowed PSDs are used, the exception is J2143+1743. We cannot confirm a correlation in these sources, but instead we identify them as interesting candidates for further study. The figures for these cases can be found in Appendix F.

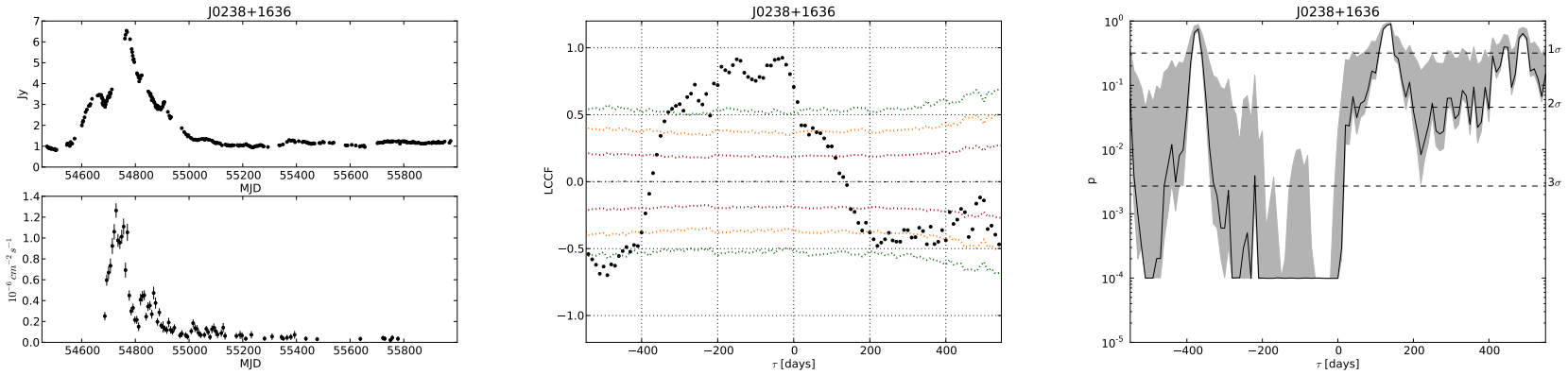

Figure 6.14: Light curves and cross-correlation significance for J0238+1636 for the best fit PSD and limits at each band (shaded area on the right panel). The most significant cross-correlation is at -30 ± 9 day with 99.99% significance.

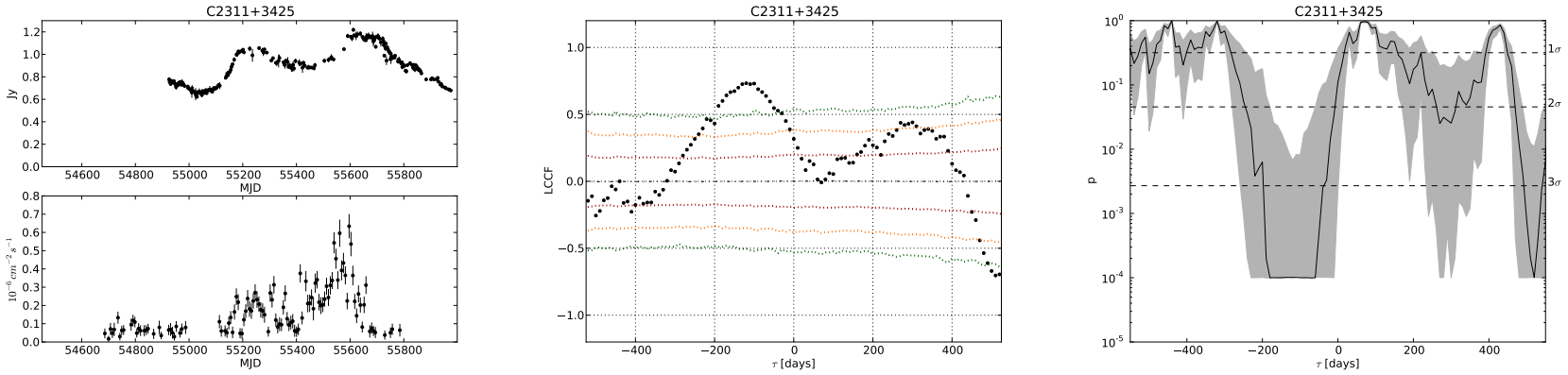

Figure 6.15: Light curves and cross-correlation significance for C2311+3425 for the best fit PSD and limits at each band (shaded area on the right panel). The most significant cross-correlation is at -120 ± 14 day with 99.99% significance.

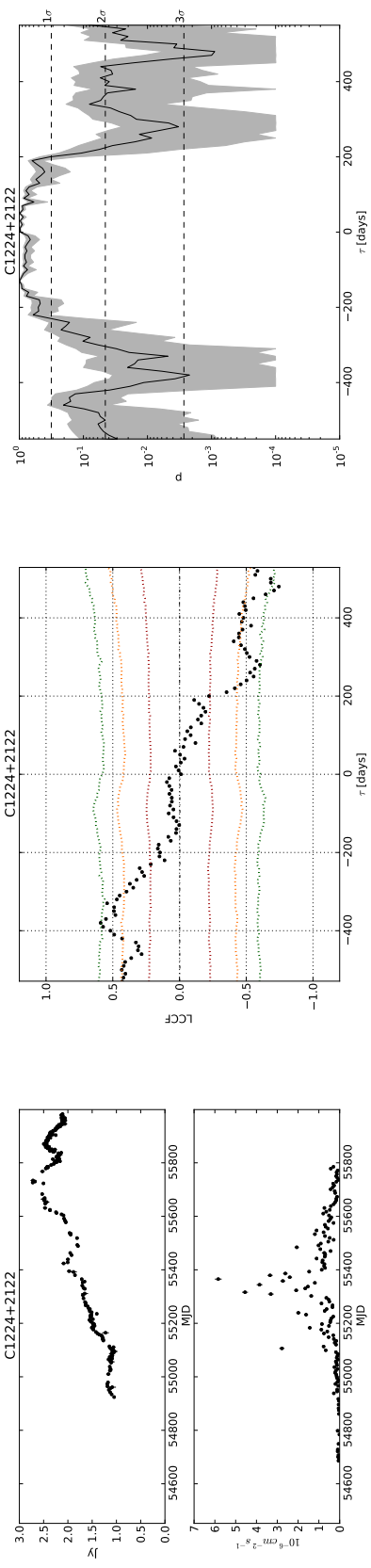

Figure 6.16: Light curves and cross-correlation significance for C1224+2122 for the best fit PSD and limits at each band (shaded area on the right panel). The most significant cross-correlation is at -380 ± 10 day with 99.78% significance.

6.4 The big flare in Mrk 421

A major radio flare was observed from Mrk 421 in which its flux density reached 1.11 ± 0.03 Jy, approximately 2.5 times its previous median flux density and 1.5 times its previous maximum observed flux density at OVRO (Hovatta et al., 2012). Comparison to University of Michigan Radio Astronomy Observatory (UMRAO) 14.5 GHz long-term monitoring since 1980 shows that this is the highest flux density ever observed in this source. On 16 July 2012 the source was detected at its highest level to date by *Fermi*-LAT. Its integrated photon flux for E $>$ 100 MeV was $1.4 \pm 0.2 \times 10^{-6}$ ph cm^{-2}s^{-1}, a factor of 8 greater than the average flux reported in the second *Fermi* LAT catalog (D'Ammando & Orienti, 2012).

We extended the analysis for Mrk 421 to include the major flare and fitted its PSDs at both bands. The radio light curve is found to have $\beta_{\rm radio}$ between 0.6 and 2.0 with a best fit of 1.8. For the gamma-ray light curve β_γ is between 1.6 and 2.1 with a best fit of 1.6.

With these values we find a peak in the cross-correlation at -40 ± 9 days with a significance between 96.16% and 99.99% depending on the PSD model. Using the best fit values the significance is 98.96% (Figure 6.17). Nonetheless the significance obtained using only 3 years of gamma-ray and 4 years of radio data for the case $\beta_{\rm radio} = 2.3$ and $\beta_\gamma = 1.6$ is only 43.3% for a correlation at -40 days and a maximum at -500 days with a 73.8% significance (see Figure 6.18 for a comparison). *By extending the data set after the observation of the flare we are in fact doing "a posteriori" statistics, so this result should be treated with caution until we have extended the whole sample to cover this time period.*

Before the flare Mrk 421 was not very active and weak in gamma-rays, with only small amplitude variations in the radio and gamma-ray bands (Figure 6.18). We also notice that without including the recent flare we were not able to constrain the radio or the gamma-ray PSDs for this source, while this become possible using the extended light curves. A number of sources in our sample show similar low variability characteristics, so they could potentially flare and show interesting correlations. The longer light curves being obtained with our monitoring program and *Fermi* will also allow us to obtain better constraints on the PSDs.

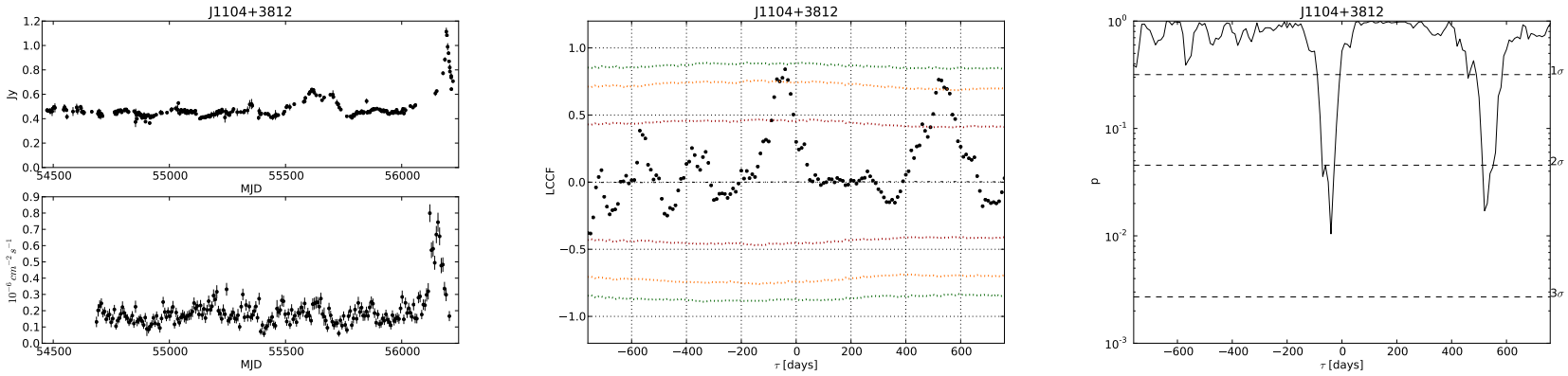

Figure 6.17: Light curves and cross-correlation results for J1104+3812 (Mrk 421) using the extended light curves and best fits values of the PSD. The most significant peak is at -40 ± 9 days and has a 98.96% significance.

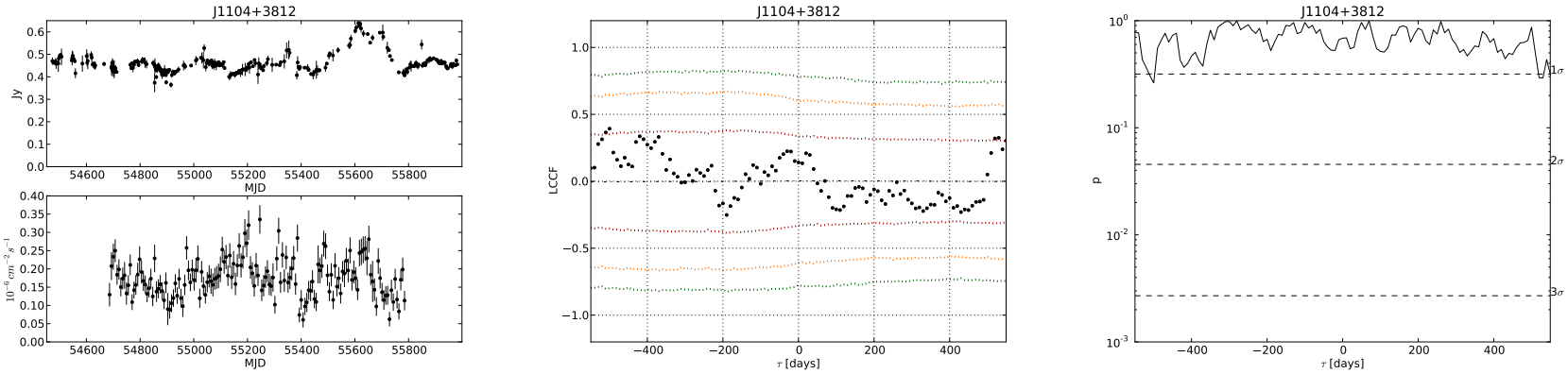

Figure 6.18: Light curves and cross-correlation significance for J1104+3812 (Mrk 421) for $\beta_{\text{radio}} = 2.3$ and $\beta_\gamma = 1.6$ and time range for the uniform data set. The most significant cross-correlation is at -500 ± 10 day with 73.78% significance.

6.5 Summary

We have characterized the power spectral density and estimated the significance of cross-correlations between the radio and gamma-ray bands for a sample of 86 sources with good sampling properties in both bands. We find 1σ constraints for the PSD power-law index for 43 sources in the radio band and 29 sources in the gamma-ray band. These constraints are used to characterize the distribution of PSD power-law indices in both bands.

When we adopt a population value from our results of the PSD characterization of $\beta_{\rm radio} = 2.3$ in the radio band and a published ensemble average for the gamma-ray band of $\beta_\gamma = 1.6$, we put constraints on the significance of cross-correlations between the radio and gamma-ray bands for 41 sources that present significant variability simultaneously in both bands and are not flagged as having noisy light curves or trends. We find that 1 out of 41 sources have correlations with $\geq 3\sigma$ significance, and 2 when considering all the $\geq 2.25\sigma$ significant cases for which we expect one chance high cross-correlation.

We also estimate the significance using our own average of the gamma-ray PSD power-law index ($\beta_\gamma = 0.7$) and in this case we find that out of 42 sources 6 have $\geq 3\sigma$ significant correlations, and 15 when considering all the cases at $\geq 2.26\sigma$ level for which we expect one chance high cross-correlation. This case uses a more aggressive assumption for the power-law index of the gamma-ray band, which is the larger uncertainty in this analysis, and it is therefore used only to point to interesting objects for further study.

For 17 sources in which we can simultaneously constrain the radio and gamma-ray PSDs we compute best fit and limits for the significances and find that 1 source has a $\geq 3\sigma$ significance even when the lower limits are considered. An additional case has $\geq 3\sigma$ significance for the best fit and a high value of the significance for the lower limit and it is therefore considered significant. There a number of cases in which the significance goes above 3σ if extremes values of the PSDs are used, but with best fit values below the 3σ threshold. These results indicate that we can only confirm the existence of correlated variability for a handful of sources using the current data set.

We find that by including data with the recent major flare in Mrk 421, we are able to constrain the radio and gamma-ray PSDs and find significant correlated variability for a source that did not show any indication for this in the data set analyzed here. This is a clear indication that in order to fully understand the multi-wavelength behavior of blazars long

term unbiased campaigns are required. Long light curves increase the chances of observing the sources on all the relevant time scales, facilitate the modeling of their variability and decrease the statistical variation inherent in finite length light curves.

We end this chapter with a note on the interpretation of the measured delays. The time delays we measure for these sources are determined solely by the position of the peak in the cross-correlation function. This peak is in most cases somewhat noisy and sits on a broad base, as in AO 0235+164 where a second peak located at $\tau = -150 \pm 20$ day is clearly visible. The quoted uncertainty in the position of the peak is obtained by accounting for the effects of sampling and noise in the light curves, but it does not explicitly consider the width of the cross-correlation peak, which is determined by the time scales of the correlated light curves. This width, which is much larger than the reported error, adds significant uncertainty to the interpretation of our results. Another caveat is that the time lag and error we report only indicate the uncertainty in the position of this cross-correlation peak and does not consider other effects, such as the response times to the perturbations that start the flares in the emission regions. These response times, possibly dependent on the energy of the emission, could change the interpretation of our measurement, not only adding more uncertainty but systematically changing the relevant time delays. To account for these effects we would need to model the response of the emission regions at different energy bands

A discussion of the physical implications of the correlations and measured time lags is presented in Chapter 7.

Chapter 7

Interpretation of the time lags for blazars with significant cross-correlation: The location of the gamma-ray emission site

In this chapter we discuss the implications of the measured time lags for sources with significant cross-correlations, that were found in Chapter 6. In particular, we use these time lags and the physical properties of the jets to estimate the distance of the gamma-ray emission zone from the black hole/accretion disk system.

7.1 Significance of the cross-correlations between the radio and gamma-ray bands

In Chapter 6 we studied the significance of the correlations between the radio and gamma-ray bands and found that significant correlations are only present in a few blazars. A detailed study of 17 sources, in which we can simultaneously constrain the radio and gamma-ray power-law index of the PSDs, showed that only 2 blazars have highly significant correlations, with the radio emission lagging the gamma-ray variations: AO 0235+164 ($\tau = -30 \pm 9$ day) and B2 2308+34 ($\tau = -120 \pm 14$ day). We remind the reader that in the case of AO 0235+164 there is significant uncertainty as there is a second peak of comparable significance at $\tau = -150 \pm 20$ day that we will discuss along with the more significant one. For the rest of our sample we used $\beta_{\rm radio} = 2.3$ and $\beta_{\gamma} = 1.6$, to constrain the significance as discussed in Chapter 6. Employing this procedure, we found an additional significant case,

where the radio emission also lags the gamma-ray variations: PKS 1502+106 ($\tau = -40 \pm 13$ day). In addition to the uniform sample described above, we explored the case of a big gamma-ray/radio flare in Mrk 421 and found that by extending the light curves to include the flare, we could constrain the power-law index of the PSD in both bands. This allows us to find a significant correlation for this source, again with radio emission lagging the gamma-ray variations with $\tau = -40 \pm 9$ day.

7.1.1 Interpretation of the time delays

The observed time delays between the radio and gamma-ray emission are interpreted in the context of a model in which a moving emission region, confined to the jet, is responsible for the observed radio and gamma-ray activity. This region moves away from the black hole/accretion disk system at a speed β in units of the speed of light, and corresponds to the moving disturbances observed with VLBI. In this picture, for which a schematic is provided in Figure 7.1, the flare in gamma-rays becomes observable at a distance d_γ from the base of the jet in the black hole/accretion disk, which we will refer as the central engine. Nonetheless, the gamma-ray flare can start closer to the black hole than d_γ, but it will only be visible to an observer once it crosses the surface of unity gamma-ray opacity. This surface corresponds to the gamma-spheres in the Blandford & Levinson (1995) model, described in Chapter 1. Likewise, the radio flare only becomes visible to an observer once it moves beyond the surface of unity radio opacity, which is frequency dependent as described in Blandford & Königl (1979). In what follows, we refer to this surface of unit opacity in the jet as the radio core, whose distance to the central engine is labeled in Figure 7.1 as $d_{\rm core}$.

Our measurement of the time lag between these two bands gives us an estimate of the time interval between the emergence of gamma-ray and radio radiation from the jet, $t_{\rm r} - t_\gamma$ in the source frame. The distance traveled by the emission region between the peaks in the gamma-ray and radio emission can be estimated as

$$d = \frac{\Gamma D \beta c \Delta t}{(1+z)} \tag{7.1}$$

where Γ is the bulk Lorentz factor, D is the Doppler factor, β is the bulk jet speed in units of the speed of light c, Δt is the measured time lag and z is the redshift (Pushkarev et al., 2010). In order to obtain d, we need to measure all the jet physical properties involved in

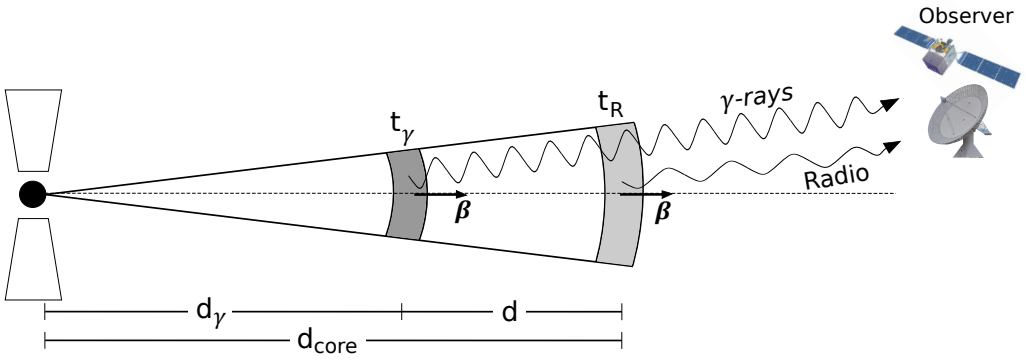

Figure 7.1: Schematic of the model used in the interpretation of the time lag between the radio and gamma-ray emission. The central engine in the far right launches a jet in which moving disturbances propagate away at speed β. A moving disturbance (shaded area) is depicted at two times: t_γ at which gamma-ray emission peaks and t_r for the peak of the radio emission when crossing the radio core. All the relevant distances have been indicated.

Equation 7.1. The procedure to obtain each one of them is described in detail in Section 7.1.1.1.

An estimate of d is not enough to determine the distance from the central engine, d_γ, at which the gamma-ray flare becomes visible to an observer, but this can be done indirectly by determining the distance between the surface of the radio core and the central engine, combined with d,

$$d_\gamma = d_{\rm core} - d \tag{7.2}$$

An estimate of $d_{\rm core}$ can be obtained from VLBI observations, in which the angular diameter of the radio core can be determined directly, $\theta_{\rm core}$ in Figure 7.2. This, combined with an estimate of the intrinsic jet opening angle, $\alpha_{\rm int}$, and the source redshift, allows us to estimate $d_{\rm core}$. The intrinsic opening angle is determined in two steps. First, a determination of the apparent opening angle ($\alpha_{\rm app}$) is made from a direct fit to the jet width as a function of distance to the core, or by multiple component fittings in the (u, v) plane (Pushkarev et al., 2009). Then, this apparent opening angle is deprojected using a measurement of the jet viewing angle (Equation 7.11), and is given by $\alpha_{\rm int} = \alpha_{\rm app} \sin(\theta)$.

The expression for $d_{\rm core}$, under the assumption of a conical jet with a constant opening

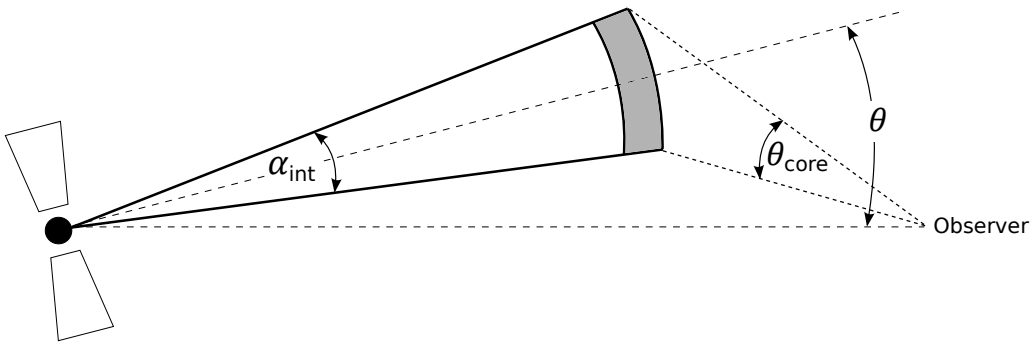

Figure 7.2: Geometry of the jet parameters measured with VLBI observations, with the radio represented as the shaded area. $\alpha_{\rm int}$ is the opening angle of the radio, θ is the viewing angle of the jet and $\theta_{\rm core}$ the angular diameter of the core. All the angles have been exaggerated for clarity.

angle with vertex at the central engine, is

$$d_{\rm core} \sim \frac{(\theta_{\rm core}/2) d_{\rm A}}{\tan(\alpha_{\rm int}/2)} \tag{7.3}$$

where $d_{\rm A}$ is the angular diameter distance, which we obtain by adopting a ΛCDM cosmology with $H_0 = 70$ km s^{-1} Mpc^{-1}, $\Omega_{\rm m} = 0.27$ and $\Omega_\Lambda = 0.73$ (Komatsu et al., 2011).

Equation 7.3 is only valid if the jet is a cone of constant opening angle. However, there is observational evidence for collimation in the jet of M87, as described in Asada & Nakamura (2012) and references therein. These authors characterized the streamlines of the M87 jet, and found a parabolic shape for the inner region that transitions to a conical outer jet. Given the radius of the jet cross-section r, and the distance between the central engine and the jet surface z, illustrated in Figure 7.3, the Asada & Nakamura (2012) model for the jet profile is characterized as $z \propto r^a$. For $z \lesssim 2.5 \times 10^5\ r_s$, where r_s is the Schwarzschild radius, they found $a = 1.73 \pm 0.05$, while at further distances $a = 0.96 \pm 0.1$, consistent with a cone of constant opening angle. Since it is plausible to expect collimation in every AGN jet, we estimate its effect on the derived distance from the central engine to the surface of the radio core. The difference between the estimated distance assuming a constant opening angle ($d_{\rm core}$(cone)) and the case including collimation ($d_{\rm core}$(coll)) is illustrated in Figure 7.3.

Assuming the radio core is in the collimation zone, which has a power-law collimation

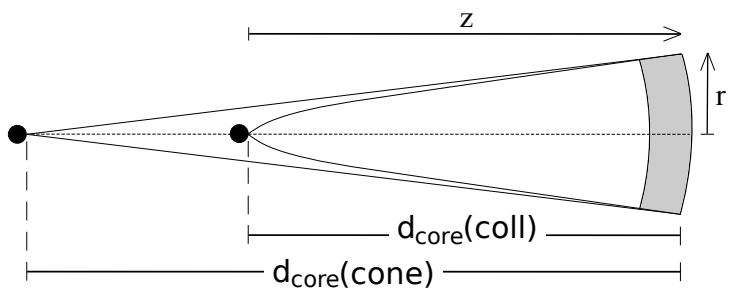

Figure 7.3: Comparison of the estimated distance between the surface of the radio core (shaded region) and central engine (black circles) for the parabolical ($d_{\rm core}$(coll)) and conical ($d_{\rm core}$(cone)) jet profiles. In general $d_{\rm core}$(coll) $< d_{\rm core}$(cone).

($d_{\rm core} \propto r_{\rm core}^{a}$, $a > 1$), we have

$$d_{\rm core}({\rm coll}) = \frac{1}{a} d_{\rm core}({\rm cone}) \tag{7.4}$$

Therefore, if we assume the same collimation model as in M87, our estimate of $d_{\rm core}$ is reduced by a factor of 1.73. If the radio core is downstream of the collimation zone, we would obtain a value in between the ones from the collimated and conical jet. In our estimations we quote the results of using both a jet with collimation and a conical jet, in order to provide a lower and upper limit to $d_{\rm core}$.

7.1.1.1 Estimation of the jet physical properties

The estimation of the distance traveled by the emission region between the peaks in the gamma-ray and radio emission (Equation 7.1), requires the values for a number of other physical properties. Here we only present the basic relations required in this investigation, and refer the interested reader to more comprehensive reviews of the theory of jets (e.g., Begelman et al., 1984).

The bulk Lorentz factor (Γ) and the Doppler factor (D) are given by

$$\Gamma = \frac{1}{\sqrt{1-\beta^2}} \tag{7.5}$$

$$D = \frac{1}{\Gamma(1-\beta\cos(\theta))} \tag{7.6}$$

where θ is the angle between the jet and the line of sight, often called the jet viewing angle (see Figure 7.2). Another important quantity is the apparent jet speed, $\beta_{\rm app}$, which is also in units of the speed of light and is given by

$$\beta_{\rm app} = \frac{\beta \sin(\theta)}{1 - \beta \cos(\theta)} \tag{7.7}$$

Values of D are estimated from the variability time scale ($t_{\rm var}$). These are obtained from Hovatta et al. (2009) and have a typical 27% scatter for individual flares in a given source. This scatter is considered as the uncertainty in D for our calculations. The variability time scale is measured as the e-folding time scale of flares that are fitted to the light curve. This time scale is used to estimate the size of the emission region, which is determined by light travel time effects to have a radius of order $ct_{\rm var}/(1+z)$. The factor of $(1+z)$ accounts for cosmological time dilation. The amplitude of the fitted exponential components is the flux density change associated with the flare (ΔS_ν). The observed brightness temperature of the flaring region is given by

$$T_{\rm b,var} = 1.47 \times 10^{19} \Delta S_\nu \nu^{-2} t_{\rm var}^{-2} d_{\rm A}^2 (1+z)^3 \ {\rm K} \tag{7.8}$$

where ΔS_ν is in Jy, ν is the observing frequency in GHz, $t_{\rm var}$ is in days and $d_{\rm A}$ is the angular diameter distance in Gpc. The $(1+z)^3$ factor comes from cosmological time dilation and black-body temperature transformation due to frequency redshifting. In this model we assume that the very high observed brightness temperatures are produced by beaming, and thus the source has a much lower intrinsic temperature. The intrinsic brightness temperature is assumed to be equal to the equipartition brightness temperature, $T_{\rm b,int} = 5 \times 10^{10}$ K (Readhead, 1994). The final step is to use the relations between beamed and unbeamed quantities, which are $\nu_{\rm rec} = D\nu_{\rm em}$, $t_{\rm rec} = t_{\rm em}/D$ and $S_{\nu,{\rm rec}} = D^3 S_{\nu,{\rm em}}$. This finally leads to

$$D_{\rm var} = \left(\frac{T_{\rm b,var}}{T_{\rm b,int}} \right)^{1/3}, \tag{7.9}$$

making $D_{\rm var}$ a weak function of the assumed $T_{\rm b,int}$.

The apparent jet speed, $\beta_{\rm app}$, can be measured using VLBI observations (e.g., Lister et al., 2009). With a knowledge of D and $\beta_{\rm app}$, it is possible to obtain Γ and the jet viewing angle θ, using the following relationships which can be derived from Equations 7.6 and 7.7

$$\Gamma = \frac{\beta_{\rm app}^2 + D^2 + 1}{2D} \tag{7.10}$$

$$\theta = \arctan\left(\frac{2\beta_{\rm app}}{\beta_{\rm app}^2 + D^2 - 1}\right) \tag{7.11}$$

The errors in the derived quantities, presented in the following sections, are computed considering the measured uncertainties of the time lags and jet physical properties. These uncertainties are propagated using a Monte Carlo method with the assumption of normal errors.

7.1.1.2 Estimation of d

We can now use these expressions to estimate the distance traveled by the emission region between the observed peaks of the radio and gamma-ray emission.

For AO 0235+164 we have $D_{\rm var} = 24$ (Hovatta et al., 2009) but no measurement of $\beta_{\rm app}$ since its jet is unresolved in VLBA observations at 15 GHz (Lister et al., 2009). In this case we assume the source is seen at the critical angle, for which the apparent speed is maximum for a given value of β. This angle is given by $\cos(\theta_{\rm cr}) = \beta$ and produces a maximum apparent speed of $\beta_{\rm app} = \Gamma\beta$. In this special case we have $D = \Gamma$, so using the measurement of $D_{\rm var}$ we can obtain β and thus the critical angle, which in this case is $\theta_{\rm cr} = \theta = 2.4^\circ$. We can finally use Equation 7.1 to obtain a distance between the radio and gamma-ray emission region for the most significant time lag ($\tau = -30 \pm 9$ day) and the other significant peak ($\tau = -150 \pm 20$ day). We obtain $d = 7.5 \pm 5.3$ pc for the peak at -30 day, and $d = 37.3 \pm 24.0$ pc for the peak at -150 day in AO 0235+164. The critical angle is the maximum angle for which we can solve for β given the value of D we assume. To test the dependence of d on this assumption we use $\theta = \theta_{\rm cr}/2$ and obtain in this case 3.9 ± 3.2 pc for the peak at -30 day, and 20 ± 15 pc for the one at -150 day. If we instead assume the jet is directly pointing at us we get 3.7 ± 2.6 pc for the peak at -30 day, and 19 ± 12 pc for the one at -150 day.

For PKS 1502+106 we have $D_{\rm var} = 12$ (Hovatta et al., 2009) and $\beta_{\rm app} = (14.8 \pm 1.2)c$ (Lister et al., 2009), so we can use Equations 7.10 and 7.11 to obtain $\Gamma = 15.2 \pm 11.5$ and $\theta = (4.7 \pm 1.1)^\circ$. Since $\Gamma \to \infty$ when $\beta \to 1$, its numerical determination is problematic, making its uncertainty large when $\beta \sim 1$. On the other hand, β is very well determined

with $\beta = 0.9978 \pm 0.0006$. With these values we get a distance of $d = 2.1 \pm 0.9$ pc for PKS 1502+106. If we had used the critical angle assumption as in the case of AO 0235+164, then $\theta_{\rm cr} = 4.78^\circ$ for PKS 1502+106, and together with the value of $D_{\rm var}$ we would have obtained a distance of about 1.7 ± 1.2 pc.

The case of B2 2308+34 is more uncertain as there are no published VLBI results, although the source has been recently added to the MOJAVE program. Preliminary analysis using the OVRO light curves indicates a variability Doppler factor of about 20. A detailed estimation of the variability Doppler factors for the blazars in the OVRO 40 m monitoring program will be presented in Hovatta et al. (in preparation). In consequence, a constraint on the distance traveled by the emission region between the radio and gamma-ray emission peaks is not possible for this object.

In the case of Mrk 421 there is also uncertainty, and we provide an estimation only to get an indication of what might be happening in the source. We use a preliminary variability Doppler factor for the recent flare of $D = 4$ (Richards et al., in preparation). The value of $\beta_{\rm app}$ is uncertain, since the jet components are consistent with being stationary as reported by Lico et al. (2012). These authors argue for an scenario in which the jet has a velocity structure with $\Gamma_{\rm radio} \sim 1.8$ and $\Gamma_\gamma \sim 20$, with a viewing angle between 2°and 5°. Assuming a representative value of 4° for the viewing angle and our measured variability Doppler factor, we obtain a $\Gamma \sim 2.2$ and a distance of about 0.2 pc between the location of the start of the gamma-ray flare and the crossing of the radio core. No uncertainties have been provided in this case, because the limited knowledge of the properties of this jet makes such estimation difficult. Upcoming results from VLBA observations, triggered by the observation of this extreme event, will improve this constraint (Richards et al., in preparation).

7.1.1.3 Estimation of $d_{\rm core}$

We can estimate the distance between the central engine and the surface of the radio core with a measurement of the core angular size and the intrinsic opening angle of the jet. Core angular sizes (FWHM) have been measured in Lister et al. (2009) for AO 0235+164 ($\theta_{\rm core} = 0.21 \pm 0.06$ mas) and PKS 1502+106 ($\theta_{\rm core} = 0.15 \pm 0.05$ mas). In all these cases we have used the average of multiple epochs with uncertainties given by the scatter in the measurements. For Mrk 421, Kovalev et al. (2005) report a value of $\theta_{\rm core} = 0.16$ mas for

which no error estimate is given, however the angular resolution of the observations is about 0.05 mas.

For the intrinsic opening angles we use $\alpha_{\rm int} \lesssim 2.4^\circ$ for AO 0235+164, which is the critical angle upper limit we find in Section 7.1.1.2 and consistent to what is used in Agudo et al. (2011b). For PKS 1502+106 we use $\alpha_{\rm int} = 3.11^\circ$ (Pushkarev et al., 2009), while for Mrk 421 we use $\alpha_{\rm int} = 2.4^\circ$, which is the mean value for BL Lacs found by Pushkarev et al. (2009). No uncertainties are quoted for the apparent and intrinsic opening angle measurements, but we can estimate them at least for PKS 1502+106. For the apparent opening angle of 37.9°, we assume a 5°uncertainty estimated from the observed variation in one example presented in Pushkarev et al. (2009). Using the apparent opening angle and the viewing angle we found in Section 7.1.1.2 ($\theta = 4.7^\circ \pm 1.1^\circ$) we obtain $\alpha_{\rm int} = 3.11^\circ \pm 0.83^\circ$.

The estimates of $d_{\rm core}$ for the conical jet model are $\gtrsim 40 \pm 11$ pc for AO 0235+164, 24 ± 15 pc for PKS 1502+106, and about 2.4 pc for Mrk 421.

The uncertainty in the case of PKS 1502+106 has been derived using $\theta_{\rm core} = 0.15 \pm 0.05$ mas and $\alpha_{\rm int} = 3.11 \pm 0.83^\circ$, and restricting the value of $\alpha_{\rm int} > 0.1^\circ$, which is about the smaller intrinsic opening angle measured by Pushkarev et al. (2009). This avoids the rapid divergence of $d_{\rm core}$ for small values of $\alpha_{\rm int}$, which greatly increases the scatter in the resulting $d_{\rm core}$. Considering a larger threshold of 1° reduces the uncertainty to 12 pc. The minimum error is 8 pc and is obtained by only including the uncertainty in $\theta_{\rm core}$.

In the case of the collimated jet, these are corrected using Equation 7.4 and we obtain values of $d_{\rm core} \gtrsim 23 \pm 6$ pc for AO 0235+164, 14 ± 9 pc for PKS 1502+106, and about 1.4 pc for Mrk 421.

7.1.1.4 Estimation of d_γ

We can finally estimate d_γ, the distance between the central engine and the region where the gamma-ray flare has its peak (Figure 7.1 and Equation 7.2). A summary of these results is presented in Table 7.1, in which the two peaks found in AO 0235+164 are included.

7.2 Conclusions

Our results indicate that the region at which the observed gamma-ray flare peaks is outside the broad line region (∼1 pc) for PKS 1502+106. However, the case of AO 0235+164 is

Table 7.1: Estimate of the distance between the region of the gamma-ray flare peak and the central engine. All distances are in parsec and time lags in day.

Source	d	$d_{\rm core}$(coll)	$d_{\rm core}$(cone)	d_γ(coll)	d_γ(cone)
AO 0235+164, $\tau = -30 \pm 9$	8 ± 5	$\gtrsim 23 \pm 6$	$\gtrsim 40 \pm 11$	$\gtrsim 15 \pm 8$	$\gtrsim 32 \pm 12$
AO 0235+164, $\tau = -150 \pm 20$	37 ± 24	$\gtrsim 23 \pm 6$	$\gtrsim 40 \pm 11$	$\gtrsim -14 \pm 25$	$\gtrsim 3 \pm 26$
PKS 1502+106	2 ± 1	14 ± 9	24 ± 15	12 ± 9	22 ± 15

uncertain because of the broad correlation peak, and we cannot reject a location of the gamma-ray emission site close to the central engine. The location for Mrk 421 is on the scale of the broad line region, but this result needs to be confirmed with high quality VLBI observations, in order to better constrain the properties of the jet.

We mentioned before that the gamma-ray flare could start at a closer distance than d_γ, but be unobservable due to gamma-ray opacity (Blandford & Levinson, 1995). In their paper the radius of the gamma-sphere, at which the opacity at gamma-rays is unity for energies of up to 10 GeV, is estimated to be $\sim 3 \times 10^{-4} - 0.3$ pc, depending on the AGN luminosity. Thus, it seems improbable that the gamma-ray flare occurs inside the gamma-sphere for PKS 1502+106, in which this is much smaller than the distance we have obtained. However, further observations would be required to discard this scenario. One approach would be to measure the expected time delay between different parts of the gamma-ray band, that is predicted by the energy dependent radius of the gamma-spheres.

Therefore, our results for these blazars with highly significant correlations, disfavor the model of Blandford & Levinson (1995) only for PKS 1502+106, although with large uncertainties, and are inconclusive for the other two sources. In the case of a location far from the central engine for PKS 1502+106, the favored mechanism for production of the high energy peak in blazars is inverse Compton. The source of the seed photons for inverse Compton could originate in the same jet (synchrotron photons, e.g., Jones et al., 1974) or in an external region present at this large distance from the nucleus (e.g., infrared photons form the dust torus as proposed by Błażejowski et al., 2000).

Chapter 8

Summary

We have presented the results of a major effort aimed at constraining the location of the gamma-ray emission site in blazars, by the study of correlated variability between the radio and gamma-ray bands for a large sample of blazars. The main observational effort required for this program is the high cadence monitoring of a large sample of blazars at 15 GHz with the Owens Valley Radio Observatory 40 meter telescope (Chapter 2). This monitoring program started in 2008 and is currently looking at 1593 blazars, most of them candidate gamma-ray emitters and including all the *Fermi* detected sources associated with radio blazars visible from Owens Valley. The continuous monitoring and operation of the OVRO 40 m telescope required a complete automation of the observing procedures. To accomplish this, we developed an observing scheme that takes into account astronomical and technical constraints, enabling a high cadence 3-day cycle for all our sources and allowing for appropriate calibrations, as described in detail in Chapter 2. To achieve the goals of this program we also needed to analyze the gamma-ray data obtained by the Large Area Telescope on board the *Fermi* Gamma-ray Space Telescope, a subject that is also discussed in Chapter 2, where the basics of gamma-ray data reduction were presented.

The nature of the available data sets, that are unevenly sampled light curves of short duration and non-uniform errors, required the development of custom statistical techniques that make extensive use of simulated data sets. The techniques we developed for this investigation were described in detail in Chapters 3 and 5. A number of advances with respect to the original implementations described in the literature were developed. In particular, the power spectral density fit method of Uttley et al. (2002) was reformulated to use data that has a more uniform cadence, although still unevenly sampled. This required the use of interpolation and a sampling window function to control the negative effects of

red-noise leakage, which is a serious problem when fitting steep power spectral densities. Improvements in the computation of the uncertainties are discussed, along with estimates for the repeatability of the fitting results, which set a lower limit on the precision we can achieve with the method. A refinement of the method used to estimate the significance of cross-correlation for unevenly sampled light curves was also developed. We found that when compared to the discrete cross-correlation function (DCF, Edelson & Krolik, 1988) the local cross-correlation function (LCCF, Welsh, 1999) reduced the number of spurious peaks and increased the detection efficiency in simulated data with known correlations properties. Therefore, we recommend its use for cross-correlations studies using unevenly sampled light curves. We demonstrated the strong effect that the model used for the power spectral density has on the significance estimates, thus highlighting the importance of a proper characterization of the variability. We also developed a method to estimate the uncertainty in the significance estimates and discussed the problem of multiple hypothesis testing. These last two issues had been completely ignored by previous authors.

We studied the variability properties through the characterization of the power spectral density for all the blazars in the OVRO 40 m monitoring program (Chapter 4). We modeled their power spectral densities with a single power-law ($P(\nu) \propto 1/\nu^{\beta_{\rm radio}}$) and found that the distribution of their slopes is consistent with a single value equal to the sample mean of $\beta_{\rm radio} \sim 2.3$. No variation in the distribution of $\beta_{\rm radio}$ was found when dividing the sources by gamma-ray-loud versus gamma-ray-quiet, FSRQ versus BL Lac, SED class, and redshift. We used data from the UMRAO program for 51 blazars observed from the late 1970s to the early 1990s (Hughes et al., 1992), and found that the distribution of their PSD power-law index is consistent with the one found for the OVRO sample. Out of 12 sources with good quality PSD fits in both programs, we find consistent values for $\beta_{\rm radio}$ in 11, indicating that the variability properties of most sources are constant on time scales of decades. We also compared the determinations of β_{radio} using structure functions (Hughes et al., 1992) and our PSD fits and found consistent results or small differences in the majority of cases. However, we recommend the use of our method for power spectral density measurements, as it provides an uncertainty estimate and can be generalized for more complex PSDs.

In Chapter 6 we studied the existence of statistically significant correlations and measured the time lags for the significant cases. Using 4 years of radio data and 3 years of gamma-ray data, we studied the significance of correlations for a sample of 86 sources with

good cadence in the radio and gamma-ray bands. A detailed study of 17 sources in which we can simultaneously constrain the radio and gamma-ray PSDs showed that only 2 blazars have highly significant correlations. In these blazars the radio emission lags the gamma-ray variations: AO 0235+164 ($\tau = -30 \pm 9$ day and $\tau = -150 \pm 20$ day) and B2 2308+34 ($\tau = -120 \pm 14$ day). For the rest of the blazars we used the distributions of power-law indices of the PSDs in the radio and gamma-ray bands ($\beta_{\rm radio} = 2.3$ and $\beta_\gamma = 1.6$), to constrain the significance and find an additional significant case, also with radio emission lagging the gamma-ray variations: PKS 1502+106 ($\tau = -40 \pm 13$ day).

In addition to the study of correlations for the uniform sample described above, we studied Mrk 421 using data that includes its recent gamma-ray and radio flare. After including the additional data, we were able to constrain the radio and gamma-ray PSDs and found significant correlated variability. In Mrk 421 again the radio emission lags the gamma-ray variations with $\tau = -40 \pm 9$ day.

Our findings demonstrate that in order to fully understand the multi-wavelength behavior of blazars long term unbiased campaigns are required. Extended light curves increase the chances of observing the sources in all the relevant time scales, facilitate the modeling of their variability, and decrease the statistical variation inherent in finite length light curves.

The observations and analysis presented here are consistent with a close relation between the regions producing the radio and gamma-ray emission in a handful of the sources. Nonetheless, the relation between these regions is still uncertain for the majority of the sources in our sample, and extended light curves are required to better understand their properties. We also constrained the location of the peak of the flaring episode, from which gamma-rays are emitted, to be tens of parsecs away from the black hole for PKS 1502+106, although with large uncertainty. Our results are inconclusive regarding the location of the gamma-ray emission site for AO 0235+164 because of the broad correlation peak, and we cannot reject a location close to the central engine. The location for Mrk 421 is on the scale of the broad line region (typically less than 1 pc), but this result needs to be confirmed with high quality VLBI observations, in order to better constrain the properties of the jet. These results disfavor the Blandford & Levinson (1995) mechanism as the origin of the gamma-ray emission for PKS 1502+106, and are inconclusive for the other sources. We note that the uncertainties in the estimated distances are large, mostly due to the difficulties in characterizing the properties of the radio jets in these sources and the broad peaks in the

cross-correlation function.

A definitive solution to the problem of the existence of correlated variability between radio (or other bands) and the gamma-ray emission requires the study of large samples of objects, observed independently of their state for long periods of time, ideally decades, and their analysis using well defined statistical methods like the ones we have developed in this thesis. The majority of the light curves studied in this work have few events at radio and gamma-rays, which complicates an unambiguous and statistically significant time lag determination. Longer radio and gamma-ray light curves are being obtained through continuous monitoring with the OVRO 40 m telescope and *Fermi*. These extended light curves will improve our ability to characterize the PSDs and estimate the significance of correlations, as demonstrated by the case of Mrk 421. This will allow us to set stricter constraints for the significance of correlations in larger samples of sources, thus improving our knowledge of the location of the gamma-ray emission site in the whole blazar population.

Appendix A

Sources Table

Table A.1 contains the list of sources monitored in radio along with associated gamma-ray sources for gamma-ray detected sources. The redshift, optical class and SED class are taken from CGRaBS (Healey et al., 2008), 1LAC (Abdo et al., 2010) or 2LAC (Ackermann et al., 2011). For each source the most recent reported properties are listed. The source names are the internal ones used in the radio monitoring program, for convenience we provide them for the 86 sources included in the cross-correlation sample in Table A.1. For the rest of the sources more common names can be found using NED[1].

Table A.2 contains the same basic information for all the sources in the blazar monitoring program.

In both tables a value of the redshift equal to zero means that redshift measurement was not possible even though and optical spectrum was available (Ackermann et al., 2011).

[1] `http://ned.ipac.caltech.edu/`

Table A.1: OVRO blazar monitoring program source in cross-correlation sample

OVRO name	Common name	2FGL name	RA	DEC	z	Optical Class	SED class
RBS76	KUV 00311-1938	J0033.5-1921	00:33:34.30	-19:21:34.0	0.61	BLL	HSP
J0108+0135	4C +01.02	J0108.6+0135	01:08:38.77	+01:35:00.3	2.099	FSRQ	LSP
J0112+2244	S2 0109+22	J0112.1+2245	01:12:05.82	+22:44:38.8	0.265	BLL	ISP
J0112+3208	4C 31.03	J0112.8+3208	01:12:50.33	+32:08:17.6	0.603	FSRQ	LSP
BBJ0136+3905	B3 0133+388	J0136.5+3905	01:36:32.40	+39:05:59.0	0.0	BLL	HSP
J0136+4751	OC 457	J0136.9+4751	01:36:58.59	+47:51:29.1	0.859	FSRQ	LSP
C0144+2705	TXS 0141+268	J0144.6+2704	01:44:33.56	+27:05:03.1	0.0	BLL	LSP
J0217+0144	PKS 0215+015	J0217.9+0143	02:17:48.96	+01:44:49.7	1.721	FSRQ	LSP
J0221+3556	S4 0218+35	J0221.0+3555	02:21:05.47	+35:56:13.7	0.944	FSRQ	...
3C66A	3C 66A	J0222.6+4302	02:22:39.60	+43:02:07.0	0.0	BLL	ISP
J0237+2848	4C +28.07	J0237.8+2846	02:37:52.41	+28:48:09.0	1.206	FSRQ	LSP
J0238+1636	AO 0235+164	J0238.7+1637	02:38:38.93	+16:36:59.3	0.94	BLL	LSP
J0319+4130	NGC 1275	J0319.8+4130	03:19:48.16	+41:30:42.1	0.018	Radio Gal	...
J0423-0120	PKS 0420-01	J0423.2-0120	04:23:15.80	-01:20:33.1	0.916	FSRQ	LSP
J0442-0017	PKS 0440-00	J0442.7-0017	04:42:38.66	-00:17:43.4	0.844	FSRQ	LSP
J0509+0541	TXS 0506+056	J0509.4+0542	05:09:25.96	+05:41:35.3	0.0	BLL	ISP
J0612+4122	B3 0609+413	J0612.8+4122	06:12:51.19	+41:22:37.4	0.0	BLL	...
C0719+3307	B2 0716+33	J0719.3+3306	07:19:19.42	+33:07:09.7	0.779	FSRQ	LSP
J0721+7120	S5 0716+71	J0721.9+7120	07:21:53.45	+71:20:36.4	0.0	BLL	ISP
J0725+1425	4C +14.23	J0725.3+1426	07:25:16.81	+14:25:13.7	1.038	FSRQ	LSP
J0738+1742	PKS 0735+17	J0738.0+1742	07:38:07.39	+17:42:19.0	0.424	BLL	LSP
J0739+0137	PKS 0736+01	J0739.2+0138	07:39:18.03	+01:37:04.6	0.189	FSRQ	LSP
J0742+5444	GB6 J0742+5444	J0742.6+5442	07:42:39.79	+54:44:24.7	0.723	FSRQ	LSP
J0808-0751	PKS 0805-07	J0808.2-0750	08:08:15.54	-07:51:09.9	1.837	FSRQ	LSP
J0831+0429	PKS 0829+046	J0831.9+0429	08:31:48.88	+04:29:39.1	0.174	BLL	LSP
0836+710	4C +71.07	J0841.6+7052	08:41:24.37	+70:53:42.2	2.218	FSRQ	LSP
J0854+2006	OJ 287	J0854.8+2005	08:54:48.87	+20:06:30.6	0.306	BLL	ISP
J0856-1105	CRATES J0856-1105	J0856.6-1105	08:56:41.80	-11:05:14.5	0.0	BLL	LSP
J0909+0121	PKS 0906+01	J0909.1+0121	09:09:10.09	+01:21:35.6	1.026	FSRQ	LSP
J0915+2933	B2 0912+29	J0915.8+2932	09:15:52.40	+29:33:24.0	0.0	BLL	HSP
J0920+4441	S4 0917+44	J0920.9+4441	09:20:58.46	+44:41:54.0	2.189	FSRQ	LSP
C0957+5522	4C +55.17	J0957.7+5522	09:57:38.18	+55:22:57.7	0.899	FSRQ	LSP
C1012+2439	MG2 J101241+2439	J1012.6+2440	10:12:41.38	+24:39:23.4	1.805	FSRQ	...
J1015+4926	1H 1013+498	J1015.1+4925	10:15:04.13	+49:26:00.7	0.212	BLL	HSP
C1037+5711	GB6 J1037+5711	J1037.6+5712	10:37:44.31	+57:11:55.6	0.0	BLL	ISP
J1058+0133	4C +01.28	J1058.4+0133	10:58:29.60	+01:33:58.8	0.888	BLL	LSP
J1058+5628	TXS 1055+567	J1058.6+5628	10:58:37.73	+56:28:11.2	0.143	BLL	HSP
J1104+3812	Mkn 421	J1104.4+3812	11:04:27.31	+38:12:31.8	0.031	BLL	HSP
J1127-1857	PKS 1124-186	J1126.6-1856	11:27:04.39	-18:57:17.4	1.048	FSRQ	LSP
BBJ1150+4154	RBS 1040	J1150.5+4154	11:50:34.65	+41:54:40.8	0.0	BLL	HSP
J1159+2914	Ton 599	J1159.5+2914	11:59:31.83	+29:14:43.8	0.725	FSRQ	LSP
J1217+3007	1ES 1215+303	J1217.8+3006	12:17:52.08	+30:07:00.6	0.13	BLL	HSP
J1221+2813	W Comae	J1221.4+2814	12:21:31.69	+28:13:58.5	0.103	BLL	ISP
C1224+2122	4C +21.35	J1224.9+2122	12:24:54.46	+21:22:46.4	0.434	FSRQ	LSP
J1229+0203	3C 273	J1229.1+0202	12:29:06.70	+02:03:08.6	0.158	FSRQ	LSP
J1231+2847	B2 1229+29	J1231.7+2848	12:31:43.58	+28:47:49.8	0.236	BLL	HSP
C1239+0443	MG1 J123931+0443	J1239.5+0443	12:39:32.76	+04:43:05.2	1.761	FSRQ	LSP
J1248+5820	PG 1246+586	J1248.2+5820	12:48:18.78	+58:20:28.7	0.0	BLL	ISP
C1253+5301	S4 1250+53	J1253.1+5302	12:53:11.92	+53:01:11.7	0.0	BLL	ISP
J1256-0547	3C 279	J1256.1-0547	12:56:11.17	-05:47:21.5	0.536	FSRQ	LSP
J1310+3220	OP 313	J1310.6+3222	13:10:28.66	+32:20:43.8	0.997	FSRQ	LSP
J1312+4828	GB 1310+487	J1312.8+4828	13:12:43.35	+48:28:30.9	0.501	FSRQ	LSP
J1332-0509	PKS 1329-049	J1332.0-0508	13:32:04.46	-05:09:43.3	2.15	FSRQ	LSP
J1344-1723	PMN J1344-1723	J1344.2-1723	13:44:14.40	-17:23:40.4	2.506	FSRQ	...

Continues

Table A.1

OVRO name	Common name	2FGL name	RA	DEC	z	Optical Class	SED class
C1345+4452	B3 1343+451	J1345.4+4453	13:45:33.17	+44:52:59.6	2.534	FSRQ	LSP
CR1427+2347	PKS 1424+240	J1427.0+2347	14:27:00.39	+23:48:00.0	0.0	BLL	HSP
J1504+1029	PKS 1502+106	J1504.3+1029	15:04:24.98	+10:29:39.2	1.839	FSRQ	LSP
PKS1510-089	PKS 1510-08	J1512.8-0906	15:12:50.53	-09:05:59.8	0.36	FSRQ	LSP
J1522+3144	B2 1520+31	J1522.1+3144	15:22:09.99	+31:44:14.4	1.484	FSRQ	LSP
CR1542+6129	GB6 J1542+6129	J1542.9+6129	15:42:56.95	+61:29:55.4	0.0	BLL	ISP
J1555+1111	PG 1553+113	J1555.7+1111	15:55:43.04	+11:11:24.4	0.0	BLL	HSP
J1635+3808	4C +38.41	J1635.2+3810	16:35:15.49	+38:08:04.5	1.813	FSRQ	LSP
J1653+3945	Mkn 501	J1653.9+3945	16:53:52.22	+39:45:36.6	0.034	BLL	HSP
J1709+4318	B3 1708+433	J1709.7+4319	17:09:41.09	+43:18:44.5	1.027	FSRQ	LSP
J1725+1152	1H 1720+117	J1725.0+1151	17:25:04.34	+11:52:15.5	0.0	BLL	HSP
J1733-1304	PKS 1730-13	J1733.1-1307	17:33:02.71	-13:04:49.5	0.902	FSRQ	LSP
J1748+7005	S4 1749+70	J1748.8+7006	17:48:32.84	+70:05:50.8	0.77	BLL	ISP
J1800+7828	S5 1803+784	J1800.5+7829	18:00:45.68	+78:28:04.0	0.68	BLL	LSP
J1806+6949	3C 371	J1806.7+6948	18:06:50.68	+69:49:28.1	0.051	BLL	ISP
J1824+5651	4C +56.27	J1824.0+5650	18:24:07.07	+56:51:01.5	0.664	BLL	LSP
J1848+3219	B2 1846+32A	J1848.5+3216	18:48:22.10	+32:19:02.6	0.798	FSRQ	LSP
J1849+6705	S4 1849+67	J1849.4+6706	18:49:16.08	+67:05:41.7	0.657	FSRQ	LSP
CR1903+5540	TXS 1902+556	J1903.3+5539	19:03:11.61	+55:40:38.4	0.0	BLL	ISP
J1959+6508	1ES 1959+650	J2000.0+6509	19:59:59.85	+65:08:54.7	0.047	BLL	HSP
C2025-0735	PKS 2023-07	J2025.6-0736	20:25:40.66	-07:35:52.7	1.388	FSRQ	LSP
C2121+1901	OX 131	J2121.0+1901	21:21:00.61	+19:01:28.3	2.18	FSRQ	LSP
J2143+1743	OX 169	J2143.5+1743	21:43:35.54	+17:43:48.7	0.211	FSRQ	LSP
BLLacertae	BL Lacertae	J2202.8+4216	22:02:43.30	+42:16:40.0	0.069	BLL	ISP
J2203+1725	PKS 2201+171	J2203.4+1726	22:03:26.89	+17:25:48.3	1.076	FSRQ	LSP
C2225-0457	3C 446	J2225.6-0454	22:25:47.26	-04:57:01.4	1.404	FSRQ	LSP
J2229-0832	PKS 2227-08	J2229.7-0832	22:29:40.08	-08:32:54.4	1.56	FSRQ	LSP
2230+114	CTA 102	J2232.4+1143	22:32:36.41	+11:43:50.9	1.037	FSRQ	LSP
J2236+2828	B2 2234+28A	J2236.4+2828	22:36:22.47	+28:28:57.4	0.795	BLL	LSP
CR2243+2021	RGB J2243+203	J2243.9+2021	22:43:54.74	+20:21:03.8	0.0	BLL	HSP
J2253+1608	3C 454.3	J2253.9+1609	22:53:57.75	+16:08:53.6	0.859	FSRQ	LSP
C2311+3425	B2 2308+34	J2311.0+3425	23:11:05.33	+34:25:10.9	1.817	FSRQ	LSP

Table A.2: OVRO blazar monitoring program source list

OVRO name	RA	DEC	CGRaBS name	1FGL name	2FGL name	z	Optical Class	SED class
J0001-1551	00:01:05.33	-15:51:07.1	J0001-1551			2.044	FSRQ	...
J0001+1914	00:01:08.62	+19:14:33.8	J0001+1914			3.1	FSRQ	...
CRJ0001-0746	00:01:18.03	-07:46:27.0		J0000.9-0745	J0000.9-0748	0.0	BLL	ISP
J0003+2129	00:03:19.35	+21:29:44.4	J0003+2129			0.45	AGN	...
J0004-1148	00:04:04.92	-11:48:58.4	J0004-1148			...	BLL	...
J0004+4615	00:04:16.13	+46:15:18.0	J0004+4615			1.81	FSRQ	...
J0004+2019	00:04:35.76	+20:19:42.2	J0004+2019			0.677	BLL	...
J0005-1648	00:05:17.93	-16:48:04.7	J0005-1648			...	...	...
J0005+0524	00:05:20.21	+05:24:10.7	J0005+0524			1.9	FSRQ	...
J0005+3820	00:05:57.18	+38:20:15.2	J0005+3820	J0005.7+3815	J0006.1+3821	0.229	FSRQ	LSP
J0006-0623	00:06:13.89	-06:23:35.3	J0006-0623			0.347	BLL	...
J0006+2422	00:06:48.79	+24:22:36.5	J0006+2422			1.684	FSRQ	...
MG4J000800+4712	00:07:59.80	+47:12:07.5			J0007.8+4713	0.28	BLL	LSP
J0009+0628	00:09:03.93	+06:28:21.2		J0008.9+0635		...	BLL	LSP
NVSSJ000922+503028	00:09:22.60	+50:30:28.8			J0009.1+5030	...	AGU	...
J0010+2047	00:10:28.74	+20:47:49.7	J0010+2047			0.6	FSRQ	...
J0010+1058	00:10:31.01	+10:58:29.5	J0010+1058			0.089	AGN	...
J0010+1724	00:10:33.99	+17:24:18.8	J0010+1724			1.601	FSRQ	...
J0011+0057	00:11:30.40	+00:57:51.8	J0011+0057	J0011.1+0050		1.492	FSRQ	LSP
J0012+3353	00:12:47.38	+33:53:38.5	J0012+3353			1.682	FSRQ	...
J0013-1513	00:13:20.71	-15:13:47.9	J0013-1513			1.838	FSRQ	...
J0013-0423	00:13:54.13	-04:23:52.3	J0013-0423			1.075	FSRQ	...
J0013+1910	00:13:56.38	+19:10:41.9	J0013+1910		J0013.8+1907	0.473	BLL	...
J0015-1812	00:15:02.49	-18:12:50.9	J0015-1812			0.743	FSRQ	...
J0016-0015	00:16:11.09	-00:15:12.5	J0016-0015		J0017.4-0018	1.574	FSRQ	LSP
J0017+8135	00:17:08.48	+81:35:08.1	J0017+8135			3.387	FSRQ	...
J0017-0512	00:17:35.82	-05:12:41.7	J0017-0512	J0017.4-0510	J0017.6-0510	0.226	FSRQ	LSP
BBJ0018+2947	00:18:27.75	+29:47:30.4		J0018.6+2945	J0018.5+2945	0.0	BLL	HSP
J0019+2021	00:19:37.85	+20:21:45.6	J0019+2021	J0019.3+2017		...	BLL	LSP
J0019+2602	00:19:39.78	+26:02:52.3	J0019+2602			0.284	FSRQ	...
J0019+7327	00:19:45.79	+73:27:30.0	J0019+7327			1.781	FSRQ	...
J0022+4525	00:22:06.61	+45:25:33.8	J0022+4525			1.897	FSRQ	...
1RXS002209.2-185333	00:22:09.10	-18:53:32.8			J0022.2-1853	...	AGU	HSP
J0022+0608	00:22:32.44	+06:08:04.2	J0022+0608	J0022.5+0607	J0022.5+0607	0.0	BLL	LSP
J0023+4456	00:23:35.44	+44:56:35.8	J0023+4456	J0023.0+4453	J0023.2+4454	1.062	FSRQ	...

Continues

Table A.2

OVRO name	RA	DEC	CGRaBS name	1FGL name	2FGL name	z	Optical Class	SED class
J0024+2439	00:24:27.33	+24:39:26.3	J0024+2439			1.444	FSRQ	...
CLJ0024+0349	00:24:45.22	+03:49:03.6			J0024.5+0346	0.545	FSRQ	...
J0027+2241	00:27:15.37	+22:41:58.2	J0027+2241			1.108	FSRQ	...
J0028+2408	00:28:34.21	+24:08:08.1	J0028+2408			0.373	BLL	...
J0029+0554	00:29:45.90	+05:54:40.7	J0029+0554			1.317	FSRQ	...
RBS76	00:33:34.30	-19:21:34.0		J0033.5-1921	J0033.5-1921	0.61	BLL	HSP
RXJ0035.2+15	00:35:14.70	+15:15:04.0		J0035.1+1516	J0035.2+1515	0.0	BLL	HSP
J0035-1305	00:35:47.77	-13:05:11.3	J0035-1305			...	...	...
J0037+2141	00:37:23.54	+21:41:53.2	J0037+2141			0.598	BLL	...
J0037+1109	00:37:26.04	+11:09:50.9	J0037+1109			...	...	...
J0037+0808	00:37:32.20	+08:08:13.0	J0037+0808			...	...	...
NVSSJ003750+123818	00:37:50.80	+12:38:18.6			J0037.8+1238	0.0	BLL	HSP
BZBJ0038+0013	00:38:08.50	+00:13:36.0			J0038.1+0015	0.0	BLL	...
J0038-0329	00:38:20.79	-03:29:59.0	J0038-0329			1.858	FSRQ	...
J0038+4137	00:38:24.84	+41:37:06.0	J0038+4137			1.353	FSRQ	...
J0038+1856	00:38:28.89	+18:56:17.7	J0038+1856			1.193	FSRQ	...
J0039+1411	00:39:39.62	+14:11:57.5	J0039+1411			1.738	BLL	...
J0040-0146	00:40:57.61	-01:46:32.1	J0040-0146			1.176	FSRQ	...
J0042+2320	00:42:04.55	+23:20:01.2	J0042+2320	J0041.9+2318		1.426	FSRQ	...
J0042+1009	00:42:44.37	+10:09:49.2	J0042+1009			1.657	FSRQ	...
CLJ0043+3426	00:43:48.85	+34:26:26.1			J0043.7+3426	0.966	FSRQ	...
BBJ0045+2127	00:45:19.20	+21:27:42.0		J0045.3+2127	J0045.3+2127	0.0	BLL	HSP
GB6J0045+1217	00:45:43.30	+12:17:09.9			J0045.5+1218	...	AGU	HSP
J0046+3900	00:46:47.58	+39:00:47.2	J0046+3900			0.958	FSRQ	...
J0047+2435	00:47:43.88	+24:35:16.1	J0047+2435			0.62	FSRQ	...
CLJ0048+2235	00:48:02.62	+22:35:24.2			J0047.9+2232	1.161	FSRQ	LSP
J0048+3157	00:48:47.14	+31:57:25.1	J0048+3157			0.014	AGN	...
J0049+5128	00:49:37.99	+51:28:13.7	J0049+5128			0.87	FSRQ	...
J0049+0237	00:49:43.24	+02:37:03.8	J0049+0237	J0050.2+0235	J0050.2+0234	0.0	BLL	...
J0050-0452	00:50:21.53	-04:52:20.7	J0050-0452	J0050.0-0446	J0050.1-0452	0.922	FSRQ	...
J0050-0929	00:50:41.32	-09:29:05.2	J0050-0929	J0050.6-0928	J0050.6-0929	0.635	BLL	ISP
J0051-0650	00:51:08.21	-06:50:02.2	J0051-0650	J0051.1-0649	J0051.0-0648	1.975	FSRQ	LSP
J0052+4402	00:52:27.83	+44:02:54.5	J0052+4402			2.624	FSRQ	...
J0056+1625	00:56:55.29	+16:25:13.3	J0056+1625			0.206	BLL	...
J0057+2218	00:57:33.32	+22:18:41.3	J0057+2218			...	BLL	...
J0057+3021	00:57:48.89	+30:21:08.8	J0057+3021			0.016	AGN	...

Continues

Table A.2

OVRO name	RA	DEC	CGRaBS name	1FGL name	2FGL name	z	Optical Class	SED class
C0058+3311	00:58:32.07	+33:11:17.2		J0058.0+3314	J0057.9+3311	1.369	FSRQ	...
J0058+0620	00:58:33.81	+06:20:06.1	J0058+0620			0.592	FSRQ	...
1RXS005916.3-015030	00:59:16.80	-01:50:17.5			J0059.2-0151	...	AGU	HSP
C0100+0745	01:00:20.79	+07:45:51.4		J0100.2+0747	J0100.2+0746	0.0	BLL	...
J0100+3345	01:00:38.29	+33:45:06.2	J0100+3345			2.144	FSRQ	...
J0102+4214	01:02:27.15	+42:14:19.0		J0102.2+4223	J0102.3+4216	0.874	FSRQ	...
CLJ0105+3928	01:05:09.20	+39:28:15.3			J0105.3+3930	0.44	BLL	...
J0105+4819	01:05:49.93	+48:19:03.2	J0105+4819			...	...	...
J0106+3402	01:06:00.29	+34:02:03.0	J0106+3402			0.579	BLL	...
J0106+2539	01:06:10.97	+25:39:30.5	J0106+2539			0.199	NLRG	...
J0106+1300	01:06:33.36	+13:00:02.6	J0106+1300			...	...	...
J0106-0315	01:06:42.58	-03:15:19.9	J0106-0315			...	...	...
J0107+2611	01:07:47.88	+26:11:08.6	J0107+2611			0.522	FSRQ	...
J0108+0135	01:08:38.77	+01:35:00.3	J0108+0135	J0108.6+0135	J0108.6+0135	2.099	FSRQ	LSP
J0109+1816	01:09:08.18	+18:16:07.5		J0109.0+1816	J0109.0+1817	0.443	BLL	HSP
J0110-0415	01:10:30.26	-04:15:14.5	J0110-0415			...	...	...
J0110-0741	01:10:50.02	-07:41:41.2	J0110-0741			1.776	FSRQ	...
J0111+3906	01:11:37.31	+39:06:28.1	J0111+3906			0.669	NLRG	...
J0111-1317	01:11:56.86	-13:17:01.1	J0111-1317			2.42	FSRQ	...
J0112+2244	01:12:05.82	+22:44:38.8	J0112+2244	J0112.0+2247	J0112.1+2245	0.265	BLL	ISP
J0112+3522	01:12:12.94	+35:22:19.3	J0112+3522			0.45	FSRQ	...
J0112+3208	01:12:50.33	+32:08:17.6		J0112.9+3207	J0112.8+3208	0.603	FSRQ	LSP
J0113+4948	01:13:27.01	+49:48:24.1	J0113+4948	J0113.8+4945	J0113.7+4948	0.395	FSRQ	LSP
J0113+0222	01:13:43.14	+02:22:17.3	J0113+0222			0.047	BLL	...
J0115-0127	01:15:17.10	-01:27:04.6	J0115-0127			1.365	FSRQ	...
CLJ0115+0356	01:15:40.51	+03:56:43.3			J0115.4+0358	0.0	BLL	...
BBJ0115+2519	01:15:46.10	+25:19:53.0		J0115.5+2519	J0115.7+2518	0.0	BLL	HSP
J0116-1136	01:16:12.52	-11:36:15.4	J0116-1136	J0115.5-1132	J0116.0-1134	0.671	FSRQ	LSP
J0116+2422	01:16:38.07	+24:22:53.7	J0116+2422			...	...	...
J0117+1418	01:17:25.20	+14:18:12.4	J0117+1418			0.839	FSRQ	...
J0121+1127	01:21:29.00	+11:27:00.5	J0121+1127			2.465	FSRQ	...
J0121+1149	01:21:41.60	+11:49:50.4	J0121+1149			0.57	FSRQ	...
J0121+0422	01:21:56.77	+04:22:27.5	J0121+0422			0.637	FSRQ	...
J0122+2502	01:22:38.81	+25:02:31.8	J0122+2502			2.025	FSRQ	...
J0123+2615	01:23:43.04	+26:15:22.4	J0123+2615			0.849	FSRQ	...
PMNJ0124-0624	01:24:50.40	-06:25:01.8			J0124.5-0621	...	BLL	...

Continues

Table A.2

OVRO name	RA	DEC	CGRaBS name	1FGL name	2FGL name	z	Optical Class	SED class
J0124+2805	01:24:55.88	+28:05:11.4	J0124+2805			0.71	FSRQ	...
J0125-0005	01:25:28.84	-00:05:56.0	J0125-0005			1.077	FSRQ	...
J0126+2559	01:26:42.79	+25:59:01.3	J0126+2559			2.37	FSRQ	...
NVSSJ012713+032259	01:27:13.90	+03:22:58.9			J0127.2+0324	...	AGU	HSP
J0127-0821	01:27:16.31	-08:21:29.0	J0127-0821			0.362	BLL	...
J0128+4901	01:28:08.06	+49:01:06.0	J0128+4901			0.067	AGN	...
CLJ0128+4439	01:28:41.34	+44:39:18.0		J0128.6+4439		0.228	FSRQ	...
J0130+0842	01:30:27.64	+08:42:46.2	J0130+0842			0.725	FSRQ	...
J0131+3834	01:31:26.71	+38:34:39.2	J0131+3834			1.277	FSRQ	...
J0132-1654	01:32:43.49	-16:54:48.5	J0132-1654	J0132.6-1655	J0132.8-1654	1.02	FSRQ	LSP
J0132+4325	01:32:44.13	+43:25:32.7	J0132+4325			...	...	...
1RXS013427.2+263846	01:34:27.90	+26:38:42.2			J0134.4+2636	...	AGU	HSP
BBJ0136+3905	01:36:32.40	+39:05:59.0		J0136.5+3905	J0136.5+3905	0.0	BLL	HSP
J0136+4751	01:36:58.59	+47:51:29.1	J0136+4751	J0137.0+4751	J0136.9+4751	0.859	FSRQ	LSP
J0137+3122	01:37:08.73	+31:22:35.8	J0137+3122			1.716	FSRQ	...
J0140-1532	01:40:04.44	-15:32:55.7	J0140-1532			0.819	FSRQ	...
J0141-0928	01:41:25.83	-09:28:43.7	J0141-0928	J0141.7-0929	J0141.5-0928	0.733	BLL	ISP
J0141-0202	01:41:33.79	-02:02:21.5	J0141-0202			1.281	FSRQ	...
J0143+4129	01:43:03.18	+41:29:20.4	J0143+4129			0.825	FSRQ	...
C0144+2705	01:44:33.56	+27:05:03.1		J0144.6+2703	J0144.6+2704	0.0	BLL	LSP
J0148+3854	01:48:24.38	+38:54:05.2	J0148+3854			1.442	FSRQ	...
PMNJ0148+0129	01:48:33.70	+01:29:00.8			J0148.6+0127	...	AGU	...
J0148+4215	01:48:44.58	+42:15:19.4	J0148+4215			3.242	FSRQ	...
J0149+0555	01:49:22.37	+05:55:53.6	J0149+0555			2.345	FSRQ	...
J0149+1857	01:49:49.72	+18:57:20.6	J0149+1857			0.584	FSRQ	...
J0151-1732	01:51:06.08	-17:32:44.7	J0151-1732			...	...	...
J0151+2744	01:51:27.15	+27:44:41.8	J0151+2744			1.26	FSRQ	...
J0152+2207	01:52:18.06	+22:07:07.7	J0152+2207			1.32	FSRQ	...
PMNJ0152+0146	01:52:39.40	+01:47:16.9			J0152.6+0148	0.08	BLL	HSP
CR0154+0823	01:54:02.77	+08:23:51.1		J0154.1+0823	J0153.9+0823	0.0	BLL	ISP
BBJ0154+4433	01:54:54.50	+44:33:36.0		J0155.0+4433	J0154.9+4434	0.0	BLL	...
J0154+4743	01:54:56.29	+47:43:26.5	J0154+4743			1.026	FSRQ	...
J0155+2230	01:55:58.94	+22:30:11.9	J0155+2230			1.456	FSRQ	...
MG4J015630+3913	01:56:31.30	+39:14:31.4			J0156.4+3909	...	AGU	...
BBJ0159+1047	01:59:34.30	+10:47:05.0		J0159.5+1047	J0159.5+1046	0.195	BLL	HSP
J0200-1542	02:00:51.15	-15:42:36.9	J0200-1542			...	...	...

Continues

Table A.2

OVRO name	RA	DEC	CGRaBS name	1FGL name	2FGL name	z	Optical Class	SED class
J0200-1356	02:00:58.32	-13:56:18.0	J0200-1356			...	...	...
J0202+3943	02:02:01.66	+39:43:21.6	J0202+3943			0.78	FSRQ	...
J0202-0559	02:02:06.87	-05:59:00.3	J0202-0559			0.189	FSRQ	...
J0202-1948	02:02:13.85	-19:48:19.5	J0202-1948			0.493	FSRQ	...
RXJ0202.4+08	02:02:26.40	+08:49:13.0		J0202.1+0849		...	BLL	LSP
J0202+4205	02:02:43.65	+42:05:16.3	J0202+4205			...	BLL	...
J0203+7232	02:03:33.39	+72:32:53.7	J0203+7232	J0203.5+7234	J0203.6+7235	0.0	BLL	LSP
B20200+30	02:03:45.36	+30:41:29.1		J0203.5+3044		...	...	...
J0203+1134	02:03:46.66	+11:34:45.4	J0203+1134			3.61	FSRQ	...
J0204+4005	02:04:05.20	+40:05:03.5	J0204+4005			0.072	NLRG	...
J0204+1514	02:04:50.41	+15:14:11.0	J0204+1514	J0204.5+1516	J0205.0+1514	0.405	AGN	...
J0204-1701	02:04:57.67	-17:01:19.8	J0204-1701	J0205.0-1702	J0205.3-1657	1.739	FSRQ	LSP
J0205+3212	02:05:04.93	+32:12:30.1	J0205+3212	J0205.3+3217	J0205.4+3211	1.466	FSRQ	LSP
J0205+3932	02:05:14.00	+39:32:57.0	J0205+3932			0.454	FSRQ	...
J0206-1150	02:06:26.08	-11:50:39.7	J0206-1150		J0206.5-1149	1.663	FSRQ	LSP
BBJ0208+3523	02:08:38.19	+35:23:12.7		J0208.6+3522		0.318	BLL	HSP
J0209+1352	02:09:36.00	+13:52:00.7	J0209+1352			0.631	FSRQ	...
J0209+7229	02:09:51.79	+72:29:26.7	J0209+7229			0.895	FSRQ	...
J0210-1444	02:10:23.18	-14:44:59.0	J0210-1444			...	...	...
J0211+1051	02:11:13.18	+10:51:34.8	J0211+1051	J0211.2+1049	J0211.2+1050	0.0	BLL	ISP
J0211-1558	02:11:49.76	-15:58:18.9	J0211-1558			0.177	FSRQ	...
CLJ0212+2244	02:12:52.84	+22:44:52.2		J0213.2+2244	J0213.1+2245	0.459	BLL	HSP
J0213+1820	02:13:10.53	+18:20:25.4	J0213+1820			1.818	FSRQ	...
J0213+8717	02:13:57.85	+87:17:28.8	J0213+8717			...	...	...
J0215-0222	02:15:42.02	-02:22:56.8	J0215-0222			1.178	FSRQ	...
PKS0214-085	02:17:02.66	-08:20:52.3		J0217.0-0829	J0217.5-0813	0.607	FSRQ	LSP
J0217+0837	02:17:17.13	+08:37:03.9	J0217+0837	J0217.2+0834	J0217.4+0836	0.085	BLL	ISP
J0217+7349	02:17:30.82	+73:49:32.6	J0217+7349			2.367	FSRQ	...
J0217+0144	02:17:48.96	+01:44:49.7	J0217+0144	J0217.9+0144	J0217.9+0143	1.721	FSRQ	LSP
1RXSJ021905.8-17250	02:19:05.50	-17:25:13.6			J0219.1-1725	0.128	BLL	HSP
J0219+0120	02:19:07.03	+01:20:59.7	J0219+0120			1.623	FSRQ	...
J0219-1842	02:19:21.16	-18:42:38.8	J0219-1842			...	BLL	...
J0219+4727	02:19:23.36	+47:27:40.0	J0219+4727			...	...	...
J0220-1305	02:20:28.22	-13:05:19.1	J0220-1305			1.445	FSRQ	...
J0221+3556	02:21:05.47	+35:56:13.7	J0221+3556	J0221.0+3555	J0221.0+3555	0.944	FSRQ	...
J0222-1615	02:22:00.73	-16:15:16.6	J0222-1615	J0222.1-1618	J0222.0-1615	0.7	FSRQ	LSP

Continues

Table A.2

OVRO name	RA	DEC	CGRaBS name	1FGL name	2FGL name	z	Optical Class	SED class
3C66A	02:22:39.60	+43:02:07.0		J0222.6+4302	J0222.6+4302	0.0	BLL	ISP
1RXS022314.6-111741	02:23:14.10	-11:17:37.7			J0223.0-1118	0.042	AGU	HSP
J0224+0659	02:24:28.43	+06:59:23.3	J0224+0659			0.511	FSRQ	...
J0225+1846	02:25:04.67	+18:46:48.8	J0225+1846			2.69	FSRQ	...
J0226-1843	02:26:47.63	-18:43:39.2	J0226-1843			...	...	...
RXJ0227.2+0201	02:27:16.40	+02:01:58.7			J0227.3+0203	0.456	BLL	HSP
J0230+4032	02:30:45.71	+40:32:53.1	J0230+4032	J0230.8+4031	J0230.8+4031	1.019	FSRQ	...
J0231+1322	02:31:45.89	+13:22:54.7	J0231+1322			2.065	FSRQ	...
J0237+0526	02:37:14.04	+05:26:49.9	J0237+0526			0.562	FSRQ	...
J0237+3022	02:37:21.84	+30:22:59.8	J0237+3022			...	...	...
J0237+2848	02:37:52.41	+28:48:09.0	J0237+2848	J0237.9+2848	J0237.8+2846	1.206	FSRQ	LSP
J0238+1636	02:38:38.93	+16:36:59.3	J0238+1636	J0238.6+1637	J0238.7+1637	0.94	BLL	LSP
J0239-0234	02:39:45.47	-02:34:41.0	J0239-0234			1.116	FSRQ	...
J0239+0416	02:39:51.27	+04:16:21.4	J0239+0416			0.978	FSRQ	...
J0240+4216	02:40:05.25	+42:16:22.5	J0240+4216			1.701	FSRQ	...
J0240+1848	02:40:42.82	+18:48:00.1	J0240+1848			1.297	FSRQ	...
J0241-0815	02:41:04.80	-08:15:20.8	J0241-0815			0.0050	AGN	...
J0242+2653	02:42:20.83	+26:53:37.7	J0242+2653			1.851	FSRQ	...
J0242+1742	02:42:24.27	+17:42:58.8	J0242+1742			...	...	...
J0242+1101	02:42:29.17	+11:01:00.7	J0242+1101			2.68	FSRQ	...
NGC1068	02:42:40.60	-00:00:47.6			J0242.5+0006	0.0040	starburst	...
J0243-0550	02:43:12.47	-05:50:55.3	J0243-0550			1.801	FSRQ	...
J0243+7120	02:43:30.89	+71:20:17.9		J0243.5+7116	J0242.9+7118	0.0	BLL	LSP
B20242+23	02:45:16.86	+24:05:35.2		J0245.4+2413	J0245.1+2406	2.247	FSRQ	LSP
J0245-1107	02:45:24.95	-11:07:16.8	J0245-1107			0.099	GALAXY	...
J0246-1236	02:46:58.47	-12:36:30.9	J0246-1236			2.201	FSRQ	...
J0249+0619	02:49:18.02	+06:19:52.0	J0249+0619			1.881	FSRQ	...
NVSSJ024948+843556	02:49:48.40	+84:35:56.2			J0248.6+8440	...	AGU	...
J0251+4315	02:51:34.54	+43:15:15.8	J0251+4315			1.31	FSRQ	...
J0251+7226	02:51:37.35	+72:26:55.8	J0251+7226			...	...	...
J0251+3734	02:51:59.17	+37:34:18.1	J0251+3734			1.818	FSRQ	...
MG3J025334+3217	02:53:33.40	+32:17:21.3			J0253.4+3218	...	AGU	...
J0254+2343	02:54:24.72	+23:43:26.5	J0254+2343			1.988	FSRQ	...
J0254+3931	02:54:42.63	+39:31:34.7	J0254+3931			0.291	FSRQ	...
J0256+1542	02:56:54.92	+15:42:43.2	J0256+1542			...	...	...
J0257-1212	02:57:41.00	-12:12:01.5	J0257-1212	J0257.8-1204	J0257.7-1213	1.391	FSRQ	...

Continues

Table A.2

OVRO name	RA	DEC	CGRaBS name	1FGL name	2FGL name	z	Optical Class	SED class
J0257+1847	02:57:45.63	+18:47:05.4	J0257+1847			0.427	FSRQ	...
J0257+7843	02:57:52.57	+78:43:47.1	J0257+7843			...	...	...
J0258+0541	02:58:50.53	+05:41:08.0	J0258+0541			1.381	FSRQ	...
J0259+0747	02:59:27.08	+07:47:39.6		J0259.5+0743	J0259.5+0740	0.893	FSRQ	LSP
J0259-0018	02:59:28.51	-00:18:00.0	J0259-0018			...	...	...
CRJ0305-0607	03:05:00.57	-06:07:41.5		J0305.0-0601		...	BLL	...
J0305+0523	03:05:48.19	+05:23:31.5	J0305+0523			...	...	...
NGC1218	03:08:26.24	+04:06:39.9		J0308.3+0403		0.029	AGN	...
J0309+1029	03:09:03.62	+10:29:16.3	J0309+1029		J0309.1+1027	0.863	FSRQ	LSP
J0309-0559	03:09:23.29	-05:59:20.4	J0309-0559			0.745	FSRQ	...
NVSSJ030943-074427	03:09:43.10	-07:44:27.3			J0309.3-0743	...	AGU	HSP
J0310+3814	03:10:49.88	+38:14:53.8	J0310+3814	J0310.6+3812	J0310.7+3813	0.816	FSRQ	LSP
J0312+0133	03:12:43.60	+01:33:17.5	J0312+0133	J0312.6+0131	J0312.6+0132	0.664	FSRQ	...
J0313+4120	03:13:01.96	+41:20:01.2	J0313+4120			0.136	AGN	...
J0315-1656	03:15:27.68	-16:56:29.7	J0315-1656			...	...	...
J0315-1031	03:15:56.87	-10:31:39.4		J0315.9-1033	J0315.8-1024	1.565	FSRQ	...
BBJ0316+0904	03:16:12.70	+09:04:44.0		J0316.1+0904	J0316.1+0904	0.0	BLL	HSP
J0318-0029	03:18:14.43	-00:29:48.9	J0318-0029			...	...	...
J0319-1613	03:19:05.53	-16:13:47.0	J0319-1613			1.618	FSRQ	...
J0319+6949	03:19:22.07	+69:49:25.6	J0319+6949			...	...	...
J0319+4130	03:19:48.16	+41:30:42.1	J0319+4130	J0319.7+4130	J0319.8+4130	0.018	Radio Gal	...
J0319+1901	03:19:51.26	+19:01:31.3	J0319+1901			0.296	FSRQ	...
0317+185	03:19:51.80	+18:45:34.2		J0319.7+1847	J0319.6+1849	0.19	BLL	HSP
BBJ0321+2326	03:21:59.90	+23:36:11.0		J0322.1+2336	J0322.0+2336	0.0	BLL	HSP
J0322+3948	03:22:51.83	+39:48:02.3	J0322+3948			...	...	...
J0323+0145	03:23:09.87	+01:45:50.5	J0323+0145			...	...	...
B20321+33	03:24:41.20	+34:10:45.0		J0325.0+3403	J0324.8+3408	0.061	NLSyI	...
J0325+2224	03:25:36.81	+22:24:00.4	J0325+2224	J0325.9+2219	J0326.1+2226	2.066	FSRQ	LSP
RBS421	03:25:41.20	-16:46:16.0		J0325.9-1649	J0325.6-1650	0.291	BLL	HSP
BBJ0326+0225	03:26:13.90	+02:25:14.0		J0326.2+0222	J0326.1+0224	0.147	BLL	HSP
J0327+0044	03:27:59.22	+00:44:22.7	J0327+0044			1.357	FSRQ	...
J0329+3510	03:29:15.36	+35:10:06.0	J0329+3510			...	...	...
NVSSJ033223-111951	03:32:23.20	-11:19:51.4			J0332.5-1118	...	AGU	HSP
TXS0330+291	03:33:49.00	+29:16:31.4			J0333.7+2918	...	AGU	ISP
J0334+0800	03:34:53.32	+08:00:14.5	J0334+0800			1.982	FSRQ	...
J0336-1302	03:36:35.03	-13:02:04.8	J0336-1302			1.303	FSRQ	...

Continues

Table A.2

OVRO name	RA	DEC	CGRaBS name	1FGL name	2FGL name	z	Optical Class	SED class
J0338+3106	03:38:00.34	+31:06:09.7	J0338+3106			1.662	FSRQ	...
PKS0336-177	03:39:13.71	-17:36:00.8		J0339.1-1734	J0339.2-1734	0.065	AGN	...
J0339-0146	03:39:30.94	-01:46:35.8	J0339-0146		J0339.4-0144	0.852	FSRQ	LSP
J0341+3352	03:41:09.98	+33:52:21.6	J0341+3352			0.725	FSRQ	...
CLJ0342+3859	03:42:16.27	+38:59:06.3			J0342.4+3859	0.945	FSRQ	...
J0343+3622	03:43:28.95	+36:22:12.4	J0343+3622			1.484	FSRQ	...
J0345+1453	03:45:06.42	+14:53:49.6	J0345+1453			1.557	FSRQ	...
J0348-1610	03:48:39.27	-16:10:17.8	J0348-1610			...	BLL	...
J0351-1153	03:51:10.96	-11:53:22.8	J0351-1153			1.52	FSRQ	...
J0354+8009	03:54:46.13	+80:09:28.8		J0354.6+8009	J0354.1+8010	0.0	BLL	LSP
J0357+2319	03:57:21.61	+23:19:53.8	J0357+2319			...	...	...
J0357+0542	03:57:46.13	+05:42:31.3	J0357+0542			2.164	FSRQ	...
J0359+2758	03:59:27.94	+27:58:24.0	J0359+2758			...	...	...
J0359+3220	03:59:44.91	+32:20:47.1	J0359+3220			1.332	FSRQ	...
J0400+0550	04:00:11.74	+05:50:43.1	J0400+0550			0.761	FSRQ	...
J0401-1606	04:01:06.64	-16:06:39.0	J0401-1606			0.031	FSRQ	...
J0401+0413	04:01:19.91	+04:13:34.4	J0401+0413			0.306	GALAXY	...
J0401+2110	04:01:45.16	+21:10:28.6	J0401+2110			0.834	FSRQ	...
J0403+2600	04:03:05.59	+26:00:01.5	J0403+2600			2.109	FSRQ	...
J0405-0739	04:05:00.86	-07:39:21.9	J0405-0739			2.817	FSRQ	...
J0405-1308	04:05:33.97	-13:08:14.6			J0405.8-1309	0.571	FSRQ	LSP
J0406+0637	04:06:34.31	+06:37:15.0	J0406+0637			0.666	FSRQ	...
J0407+0742	04:07:29.09	+07:42:07.5	J0407+0742		J0407.7+0740	1.133	FSRQ	LSP
J0408-0122	04:08:19.63	-01:22:30.8	J0408-0122			...	...	...
J0409-1238	04:09:05.77	-12:38:48.1	J0409-1238			1.563	FSRQ	...
J0409+1217	04:09:22.01	+12:17:39.8	J0409+1217			1.02	BLL	...
J0412+0010	04:12:33.46	+00:10:48.5	J0412+0010			1.13	FSRQ	...
J0412+0438	04:12:38.19	+04:38:06.1	J0412+0438			1.081	FSRQ	...
J0412+1856	04:12:45.95	+18:56:37.1	J0412+1856			...	...	...
J0414+3418	04:14:37.26	+34:18:51.1	J0414+3418			...	...	...
J0416-1851	04:16:36.54	-18:51:08.3	J0416-1851	J0416.5-1851	J0416.7-1849	1.536	FSRQ	LSP
J0416+0105	04:16:52.49	+01:05:23.9		J0416.8+0107	J0416.8+0105	0.287	BLL	HSP
J0422-0643	04:22:10.80	-06:43:45.3		J0422.0-0647	J0422.1-0645	0.242	FSRQ	LSP
J0422+0219	04:22:52.21	+02:19:26.9	J0422+0219	J0422.1+0211		2.277	FSRQ	LSP
J0423-0120	04:23:15.80	-01:20:33.1	J0423-0120	J0423.2-0118	J0423.2-0120	0.916	FSRQ	LSP
C0424+0036	04:24:46.84	+00:36:06.3		J0424.8+0036	J0424.7+0034	0.0	BLL	LSP

Continues

Table A.2

OVRO name	RA	DEC	CGRaBS name	1FGL name	2FGL name	z	Optical Class	SED class
J0424+0805	04:24:57.60	+08:05:17.3	J0424+0805			3.086	FSRQ	...
J0426+2327	04:26:55.74	+23:27:39.7	J0426+2327			0.55	NLRG	...
J0426+2350	04:26:55.97	+23:50:26.6	J0426+2350			...	...	...
J0428+3259	04:28:05.81	+32:59:52.0	J0428+3259			0.476	FSRQ	...
J0428+1732	04:28:35.63	+17:32:23.6	J0428+1732			3.317	FSRQ	...
J0432-1614	04:32:29.08	-16:14:05.7	J0432-1614			...	...	...
J0433+0521	04:33:11.10	+05:21:15.6	J0433+0521			0.033	AGN	...
J0433+2905	04:33:37.83	+29:05:55.5	J0433+2905	J0433.5+2905	J0433.5+2905	0.0	BLL	LSP
J0434-1442	04:34:19.02	-14:42:55.3	J0434-1442			1.899	FSRQ	...
J0435+2923	04:35:58.37	+29:23:36.4	J0435+2923			2.336	FSRQ	...
J0437-1844	04:37:01.48	-18:44:48.6	J0437-1844			2.702	FSRQ	...
GB6J0437+6757	04:37:32.50	+67:57:15.9			J0436.2+6759	...	AGU	...
J0438+3004	04:38:04.95	+30:04:45.5	J0438+3004			1.454	FSRQ	...
J0438-1251	04:38:35.02	-12:51:03.5	J0438-1251	J0438.8-1250	J0439.0-1252	1.285	FSRQ	...
J0439+0520	04:39:02.26	+05:20:43.7	J0439+0520			0.202	FSRQ	...
J0439+3045	04:39:17.78	+30:45:07.5	J0439+3045			...	...	...
J0440+1437	04:40:21.14	+14:37:57.0			J0440.4+1433	...	AGU	...
B20437+27B	04:40:50.37	+27:50:46.8		J0440.6+2748	J0440.9+2749	0.0	BLL	...
J0442-0017	04:42:38.66	-00:17:43.4	J0442-0017		J0442.7-0017	0.844	FSRQ	LSP
BBJ0448-1632	04:48:37.64	-16:32:42.8		J0448.5-1633	J0448.5-1633	0.0	BLL	HSP
J0449+1121	04:49:07.67	+11:21:28.6	J0449+1121			1.207	FSRQ	...
J0449-1814	04:49:16.21	-18:14:47.4	J0449-1814			...	...	...
J0449+6332	04:49:23.31	+63:32:09.5	J0449+6332			0.781	FSRQ	...
J0452+1236	04:52:42.60	+12:36:24.6	J0452+1236			1.177	FSRQ	...
J0455+0655	04:55:20.71	+06:55:38.9	J0455+0655			...	...	...
MG2J045613+2702	04:56:17.20	+27:02:21.0			J0456.5+2658	...	AGU	...
J0456+0400	04:56:47.17	+04:00:52.9	J0456+0400			1.349	FSRQ	...
J0457+0645	04:57:07.71	+06:45:07.3	J0457+0645	J0457.9+0649		0.405	FSRQ	LSP
J0457-1819	04:57:54.32	-18:19:16.1	J0457-1819			...	...	...
J0501-0159	05:01:12.81	-01:59:14.3	J0501-0159	J0501.0-0200	J0501.2-0155	2.291	FSRQ	LSP
J0501+1356	05:01:45.27	+13:56:07.2	J0501+1356			...	...	...
J0501+7128	05:01:45.78	+71:28:34.0	J0501+7128			...	...	...
PKS0459+060	05:02:15.40	+06:09:07.9			J0502.5+0607	1.106	FSRQ	...
J0502+1338	05:02:33.22	+13:38:10.9	J0502+1338			...	BLL	...
J0503+6600	05:03:56.44	+66:00:31.5	J0503+6600			1.696	FSRQ	...
J0505+0459	05:05:23.19	+04:59:42.7	J0505+0459		J0505.5+0501	0.954	FSRQ	LSP

Continues

Table A.2

OVRO name	RA	DEC	CGRaBS name	1FGL name	2FGL name	z	Optical Class	SED class
CRJ0505+0415	05:05:34.77	+04:15:54.6		J0505.2+0420		...	BLL	HSP
CRJ0505-0419	05:05:51.23	-04:19:26.7		J0505.8-0416	J0505.8-0411	1.481	FSRQ	LSP
NVSSJ050558+611336	05:05:58.60	+61:13:36.0			J0505.9+6116	...	AGU	HSP
1WGAJ0506.6-0857	05:06:39.70	-08:58:01.5			J0506.5-0901	0.0	BLL	HSP
0502+675	05:07:56.25	+67:37:24.4		J0507.9+6738	J0508.0+6737	0.416	BLL	HSP
PMNJ0508-1936	05:08:19.00	-19:35:56.5			J0508.1-1936	...	AGU	...
J0508+8432	05:08:42.36	+84:32:04.5	J0508+8432			1.34	BLL	...
J0509+0541	05:09:25.96	+05:41:35.3	J0509+0541	J0509.3+0540	J0509.4+0542	0.0	BLL	ISP
C0509+1011	05:09:27.46	+10:11:44.6		J0509.2+1015	J0509.2+1013	0.621	FSRQ	...
J0510+1800	05:10:02.37	+18:00:41.6	J0510+1800			0.416	AGN	...
J0511+1357	05:11:38.32	+13:57:19.2	J0511+1357			1.696	FSRQ	...
GB6J0515+1527	05:15:47.40	+15:27:16.8			J0515.9+1528	0.0	BLL	...
CLJ0516+7351	05:16:31.18	+73:51:08.7			J0515.5+7355	0.249	BLL	HSP
J0517+0648	05:17:51.34	+06:48:03.2	J0517+0648			0.84	FSRQ	...
J0521-1737	05:21:23.56	-17:37:30.3	J0521-1737			...	...	...
PKS0519+01	05:22:17.50	+01:13:31.5			J0521.9+0108	2.941	FSRQ	...
J0522-0725	05:22:23.19	-07:25:13.5	J0522-0725			0.164	FSRQ	...
GB6J0526+6317	05:26:06.50	+63:17:28.7			J0526.8+6326	...	AGU	...
J0527+0106	05:27:16.32	+01:06:00.1	J0527+0106			...	...	...
J0527+0331	05:27:32.71	+03:31:31.5	J0527+0331			...	BLL	...
J0529-0519	05:29:53.53	-05:19:41.6	J0529-0519			0.685	FSRQ	...
J0530+1331	05:30:56.42	+13:31:55.1	J0530+1331	J0531.0+1331	J0530.8+1333	2.07	FSRQ	LSP
J0532+0732	05:32:39.00	+07:32:43.3	J0532+0732	J0532.9+0733	J0532.7+0733	1.254	FSRQ	LSP
J0538+5107	05:38:54.79	+51:07:23.4	J0538+5107			...	...	...
GB6J0540+5823	05:40:29.80	+58:23:39.4			J0540.4+5822	...	AGU	HSP
J0541+5312	05:41:16.17	+53:12:24.8	J0541+5312			1.275	FSRQ	...
J0541-0541	05:41:38.08	-05:41:49.4	J0541-0541			0.839	FSRQ	...
J0542-0913	05:42:55.88	-09:13:31.1	J0542-0913			...	...	...
J0551-1909	05:51:55.26	-19:09:21.0	J0551-1909			0.73	FSRQ	...
J0552+0313	05:52:50.10	+03:13:27.3	J0552+0313			...	...	...
J0554+6857	05:54:00.81	+68:57:54.5	J0554+6857			1.373	FSRQ	...
J0558-1317	05:58:02.55	-13:17:41.2	J0558-1317			1.725	FSRQ	...
J0559+5804	05:59:13.39	+58:04:03.4	J0559+5804			0.904	FSRQ	...
J0559-1817	05:59:46.40	-18:17:47.5	J0559-1817			...	...	...
GB6J0601+5315	06:02:00.20	+53:16:00.1			J0602.3+5315	...	AGU	HSP
CLJ0604+0000	06:04:58.42	+00:00:43.4			J0605.0+0001	...	AGU	...

Continues

Table A.2

OVRO name	RA	DEC	CGRaBS name	1FGL name	2FGL name	z	Optical Class	SED class
J0606-0724	06:06:43.55	-07:24:30.2	J0606-0724			1.227	FSRQ	...
J0607+4739	06:07:23.25	+47:39:47.0	J0607+4739	J0607.2+4739	J0607.4+4739	0.0	BLL	ISP
J0607+6720	06:07:52.67	+67:20:55.4	J0607+6720			1.97	FSRQ	...
J0607-0834	06:07:59.70	-08:34:50.0	J0607-0834	J0608.2-0837	J0608.0-0836	0.87	FSRQ	LSP
C0608-1520	06:08:01.53	-15:20:37.0		J0608.0-1521	J0608.0-1521	1.094	FSRQ	LSP
NVSSJ060915-024754	06:09:15.00	-02:47:54.2			J0609.4-0248	...	AGU	HSP
J0609-1542	06:09:40.95	-15:42:40.7	J0609-1542			0.324	FSRQ	...
J0610-1847	06:10:17.89	-18:47:40.1	J0610-1847		J0609.6-1847	0.0	BLL	LSP
B30607+434	06:11:07.00	+43:24:04.7			J0611.0+4321	...	AGU	...
J0612+4122	06:12:51.19	+41:22:37.4	J0612+4122	J0612.7+4120	J0612.8+4122	0.0	BLL	...
J0616-1041	06:16:41.81	-10:41:08.5	J0616-1041			...	...	...
J0617+5701	06:17:16.92	+57:01:16.4		J0616.9+5701	J0616.9+5701	0.0	BLL	ISP
J0617-1715	06:17:33.42	-17:15:25.1		J0617.7-1718	J0617.6-1716	0.098	BLL	LSP
J0617+7816	06:17:56.93	+78:16:07.4	J0617+7816			1.43	FSRQ	...
J0618+4620	06:18:08.20	+46:20:16.2	J0618+4620			0.607	FSRQ	...
J0619-1140	06:19:04.10	-11:40:55.0	J0619-1140			0.97	FSRQ	...
CLJ0621+3750	06:21:57.64	+37:50:57.0			J0621.9+3750	...	AGU	...
J0623+3830	06:23:28.94	+38:30:49.8	J0623+3830			0.421	NLRG	...
J0624+3856	06:24:19.02	+38:56:48.7	J0624+3856			3.469	FSRQ	...
J0625+4440	06:25:18.26	+44:40:01.6	J0625+4440	J0625.4+4440	J0625.2+4441	0.0	BLL	...
J0626+8202	06:26:03.01	+82:02:25.6	J0626+8202			0.71	FSRQ	...
J0629-1959	06:29:23.76	-19:59:19.7	J0629-1959	J0629.6-2000	J0629.3-2001	0.0	BLL	...
J0630-1323	06:30:53.90	-13:23:34.5	J0630-1323			1.021	FSRQ	...
J0631-1410	06:31:20.23	-14:10:31.8	J0631-1410			1.017	FSRQ	...
J0632+3200	06:32:30.79	+32:00:53.7	J0632+3200			1.832	FSRQ	...
GB6J0636+7138	06:36:42.70	+71:38:43.1			J0633.8+7132	...	AGU	LSP
J0637+3322	06:37:55.94	+33:22:06.3	J0637+3322			...	...	...
J0638+5933	06:38:02.87	+59:33:22.2	J0638+5933			...	...	...
J0639+7324	06:39:21.96	+73:24:58.0	J0639+7324	J0639.9+7325		1.854	FSRQ	LSP
J0642+6758	06:42:04.25	+67:58:35.6	J0642+6758			3.177	FSRQ	...
J0642+8811	06:42:06.15	+88:11:55.0	J0642+8811			...	...	...
J0642+3509	06:42:58.14	+35:09:18.4	J0642+3509			0.269	NLRG	...
J0644+3914	06:44:53.71	+39:14:47.5	J0644+3914			1.266	FSRQ	...
BUJ0645+6024	06:45:01.37	+60:24:42.3		J0645.5+6033		0.832	AGN	...
J0646+4451	06:46:32.03	+44:51:16.6	J0646+4451			3.408	FSRQ	...
J0650+6001	06:50:31.25	+60:01:44.5	J0650+6001			0.455	FSRQ	...

Continues

Table A.2

OVRO name	RA	DEC	CGRaBS name	1FGL name	2FGL name	z	Optical Class	SED class
BL0647+250	06:50:46.60	+25:03:00.0		J0650.7+2503	J0650.7+2505	0.0	BLL	HSP
J0650+5616	06:50:48.19	+56:16:34.5	J0650+5616			1.428	FSRQ	...
NVSSJ065345+282010	06:53:45.70	+28:20:10.2			J0653.7+2818	...	AGU	...
J0653+3705	06:53:58.28	+37:05:40.6	J0653+3705			1.982	FSRQ	...
J0654+5042	06:54:22.09	+50:42:23.9	J0654+5042	J0654.4+5042	J0654.5+5043	1.253	FSRQ	LSP
J0654+4514	06:54:23.71	+45:14:23.5	J0654+4514	J0654.3+4514	J0654.2+4514	0.928	FSRQ	LSP
J0655+4100	06:55:10.02	+41:00:10.2	J0655+4100			0.022	NLRG	...
J0657+2423	06:57:05.67	+24:23:55.4	J0657+2423			1.926	FSRQ	...
J0702+2644	07:02:31.79	+26:44:11.1	J0702+2644			...	...	...
J0702+8549	07:02:32.83	+85:49:52.5	J0702+8549			1.059	FSRQ	...
CLJ0706+3744	07:06:31.70	+37:44:36.4			J0706.5+3744	0.0	BLL	HSP
NVSSJ070651+774137	07:06:51.10	+77:41:36.4			J0706.5+7741	...	AGU	ISP
BBJ0710+5908	07:10:30.00	+59:08:19.0		J0710.6+5911	J0710.5+5908	0.125	BLL	HSP
B30707+476	07:10:46.11	+47:32:11.1		J0711.4+4731	J0710.8+4733	1.292	BLL	ISP
J0712+5033	07:12:43.64	+50:33:22.7	J0712+5033	J0712.7+5033	J0712.9+5032	0.0	BLL	LSP
CLJ0713+1935	07:13:55.68	+19:35:00.4		J0714.0+1935	J0714.0+1933	0.54	FSRQ	LSP
J0717+4538	07:17:51.85	+45:38:03.2	J0717+4538			0.94	FSRQ	...
C0719+3307	07:19:19.42	+33:07:09.7		J0719.3+3306	J0719.3+3306	0.779	FSRQ	LSP
J0720+4737	07:20:21.50	+47:37:44.1	J0720+4737			...	...	...
J0721+7120	07:21:53.45	+71:20:36.4	J0721+7120	J0721.9+7120	J0721.9+7120	0.0	BLL	ISP
J0722+3722	07:22:01.26	+37:22:28.6	J0722+3722			1.629	FSRQ	...
BBJ0723+5841	07:23:13.96	+58:41:18.4		J0722.3+5837		...	BLL	HSP
J0725+1425	07:25:16.81	+14:25:13.7	J0725+1425	J0725.3+1431	J0725.3+1426	1.038	FSRQ	LSP
J0726+7911	07:26:11.75	+79:11:31.0	J0726+7911			...	...	...
J0726+2153	07:26:14.26	+21:53:20.1	J0726+2153			1.857	FSRQ	...
J0726+0636	07:26:36.37	+06:36:42.9	J0726+0636			1.95	FSRQ	...
J0728+2153	07:28:20.61	+21:53:06.4	J0728+2153			...	...	...
J0728+5701	07:28:49.63	+57:01:24.4	J0728+5701			0.424	FSRQ	...
BBJ0730+3307	07:30:26.05	+33:07:22.7		J0730.0+3305	J0729.9+3304	0.112	BLL	HSP
J0730+4049	07:30:51.35	+40:49:50.8	J0730+4049			2.501	FSRQ	...
J0731+2451	07:31:33.74	+24:51:58.6	J0731+2451			1.089	FSRQ	...
J0732+2548	07:32:56.28	+25:48:38.7	J0732+2548			1.443	FSRQ	...
J0733+5022	07:33:52.52	+50:22:09.1	J0733+5022		J0733.9+5023	0.718	FSRQ	LSP
J0733+0456	07:33:57.46	+04:56:14.5	J0733+0456			3.01	FSRQ	...
J0735+4750	07:35:02.31	+47:50:08.4	J0735+4750			0.782	FSRQ	...
J0736+2604	07:36:58.07	+26:04:49.9	J0736+2604			0.997	FSRQ	...

Continues

Table A.2

OVRO name	RA	DEC	CGRaBS name	1FGL name	2FGL name	z	Optical Class	SED class
J0738+1742	07:38:07.39	+17:42:19.0	J0738+1742	J0738.2+1741	J0738.0+1742	0.424	BLL	LSP
J0739+0137	07:39:18.03	+01:37:04.6	J0739+0137	J0739.1+0138	J0739.2+0138	0.189	FSRQ	LSP
J0740+2852	07:40:33.54	+28:52:47.3	J0740+2852			0.711	FSRQ	...
J0741+3112	07:41:10.70	+31:12:00.2	J0741+3112			0.631	FSRQ	...
J0742+4900	07:42:02.75	+49:00:15.6	J0742+4900			2.305	FSRQ	...
J0742+5444	07:42:39.79	+54:44:24.7		J0742.2+5443	J0742.6+5442	0.723	FSRQ	LSP
J0743+1714	07:43:05.11	+17:14:24.4	J0743+1714			...	BLL	...
1ES0737+746	07:44:05.26	+74:33:57.6		J0745.2+7438	J0745.0+7436	0.315	BLL	HSP
J0745+1011	07:45:33.06	+10:11:12.7	J0745+1011			2.624	FSRQ	...
J0745-0044	07:45:54.08	-00:44:17.5	J0745-0044			0.994	FSRQ	...
J0745+3313	07:45:59.33	+33:13:34.1	J0745+3313			0.61	FSRQ	...
J0746+2549	07:46:25.88	+25:49:02.1		J0746.6+2548	J0746.6+2549	2.979	FSRQ	LSP
J0746+2734	07:46:40.43	+27:34:59.1	J0746+2734			...	...	...
J0747+7639	07:47:14.63	+76:39:17.3	J0747+7639			...	...	...
NVSSJ074715+851208	07:47:15.40	+85:12:07.9			J0745.9+8512	...	AGU	HSP
J0748+2400	07:48:36.11	+24:00:24.1	J0748+2400			0.409	FSRQ	...
B30745+453	07:49:06.40	+45:10:33.7			J0747.7+4501	0.192	FSRQ	ISP
J0749+7420	07:49:22.46	+74:20:41.6	J0749+7420			1.629	FSRQ	...
J0750+1823	07:50:00.33	+18:23:11.4	J0750+1823			1.16	FSRQ	...
J0750+4814	07:50:20.44	+48:14:53.6	J0750+4814			1.956	FSRQ	...
J0750+1021	07:50:32.88	+10:21:26.8	J0750+1021			1.117	FSRQ	...
J0750+1231	07:50:52.05	+12:31:04.8	J0750+1231	J0750.6+1235	J0750.6+1230	0.889	FSRQ	LSP
J0751+3313	07:51:53.67	+33:13:19.8	J0751+3313			1.932	FSRQ	...
J0752+3730	07:52:40.91	+37:30:24.3	J0752+3730			0.44	AGN	...
J0753+5352	07:53:01.38	+53:52:59.6	J0753+5352	J0752.8+5353	J0753.0+5352	0.73	BLL	LSP
GB10751+485	07:54:45.50	+48:23:50.0			J0754.8+4824	0.0	BLL	ISP
J0754+3033	07:54:48.86	+30:33:55.0	J0754+3033			0.796	FSRQ	...
J0756+6347	07:56:54.61	+63:47:59.0	J0756+6347			...	...	...
J0757+0956	07:57:06.64	+09:56:34.9	J0757+0956	J0757.2+0956	J0757.1+0957	0.266	BLL	ISP
B30757+441	08:01:08.27	+44:01:10.2		J0800.5+4407	J0801.5+4401	0.0	BLL	...
J0802+1809	08:02:48.03	+18:09:49.3	J0802+1809			1.586	FSRQ	...
J0805-0111	08:05:12.89	-01:11:13.8	J0805-0111		J0805.2-0121	1.394	FSRQ	...
J0805+6144	08:05:18.18	+61:44:23.7	J0805+6144	J0806.2+6148	J0805.5+6145	3.033	FSRQ	LSP
RXJ0805.4+75	08:05:26.50	+75:34:25.0		J0804.7+7534	J0805.3+7535	0.121	BLL	HSP
J0806+4504	08:06:33.47	+45:04:32.3	J0806+4504			2.102	FSRQ	...
J0807+5117	08:07:01.01	+51:17:38.7	J0807+5117			1.136	FSRQ	...

Continues

Table A.2

OVRO name	RA	DEC	CGRaBS name	1FGL name	2FGL name	z	Optical Class	SED class
J0807-0541	08:07:09.62	-05:41:13.9		J0807.0-0544	J0807.1-0543	0.0	BLL	...
J0808-0751	08:08:15.54	-07:51:09.9	J0808-0751	J0808.2-0750	J0808.2-0750	1.837	FSRQ	LSP
J0808+7315	08:08:16.49	+73:15:12.0	J0808+7315			0.496	FSRQ	...
J0808+4950	08:08:39.67	+49:50:36.5	J0808+4950			1.436	FSRQ	...
J0808+4052	08:08:56.65	+40:52:44.9	J0808+4052			1.418	FSRQ	...
J0809+3455	08:09:38.89	+34:55:37.2		J0809.4+3455		0.082	BLL	HSP
J0809+5341	08:09:41.73	+53:41:25.1	J0809+5341			2.133	FSRQ	...
1ES0806+524	08:09:49.20	+52:18:58.0		J0809.5+5219	J0809.8+5218	0.137	BLL	HSP
J0810+4134	08:10:58.99	+41:34:02.8	J0810+4134			0.507	FSRQ	...
J0811+4533	08:11:08.78	+45:33:49.0	J0811+4533			1.017	FSRQ	...
J0811+0146	08:11:26.71	+01:46:52.2	J0811+0146	J0811.2+0148	J0811.4+0149	1.148	BLL	LSP
J0813+2542	08:13:03.84	+25:42:11.1	J0813+2542			2.024	FSRQ	...
ATJ0814-1012	08:14:11.71	-10:12:10.8			J0814.0-1006	0.0	BLL	HSP
J0814+6431	08:14:39.19	+64:31:22.0	J0814+6431	J0815.0+6434	J0814.7+6429	0.0	BLL	ISP
J0815+3635	08:15:25.94	+36:35:15.1	J0815+3635			1.028	FSRQ	...
BBJ0816+5739	08:16:22.70	+57:39:09.0		J0816.7+5739	J0816.5+5739	0.0	BLL	HSP
BBJ0816-1311	08:16:27.10	-13:11:52.0		J0816.4-1311	J0816.4-1311	0.0	BLL	HSP
BZBJ0816+2051	08:16:49.90	+20:51:05.0			J0816.9+2049	0.0	BLL	...
J0817+3227	08:17:28.55	+32:27:02.9	J0817+3227			...	...	...
J0817-0933	08:17:49.75	-09:33:30.5	J0817-0933	J0818.0-0938	J0818.2-0935	0.0	BLL	...
RXJ0817.9+3243	08:17:50.70	+32:43:39.6			J0817.9+3238	0.0	BLL	HSP
J0818+4222	08:18:16.00	+42:22:45.4	J0818+4222	J0818.2+4222		...	BLL	LSP
J0818+4754	08:18:22.47	+47:54:34.8	J0818+4754			...	...	...
J0819+3226	08:19:02.33	+32:26:37.2	J0819+3226			0.651	FSRQ	...
RXJ0819.2-0756	08:19:17.50	-07:56:28.2			J0819.6-0803	0.0	BLL	HSP
5C07.119	08:19:18.70	+27:47:30.8			J0819.3+2750	0.0	BLL	...
B30819+408	08:22:57.40	+40:41:49.7			J0823.0+4041	...	AGU	LSP
J0823+2928	08:23:41.13	+29:28:28.2	J0823+2928			2.368	FSRQ	...
J0824-1827	08:24:04.07	-18:27:40.8	J0824-1827			...	...	...
J0824+5552	08:24:47.24	+55:52:42.7	J0824+5552	J0825.0+5555	J0824.9+5552	1.418	FSRQ	LSP
J0824-1527	08:24:51.63	-15:27:45.9	J0824-1527			1.289	FSRQ	...
J0824+3916	08:24:55.48	+39:16:41.9	J0824+3916		J0824.7+3914	1.216	FSRQ	LSP
J0825+1332	08:25:11.89	+13:32:32.5	J0825+1332			1.143	FSRQ	...
J0825+6157	08:25:38.61	+61:57:28.6	J0825+6157			0.542	FSRQ	...
J0825+0309	08:25:50.34	+03:09:24.5	J0825+0309	J0825.9+0309	J0825.9+0308	0.506	BLL	ISP
J0827+3525	08:27:38.59	+35:25:05.1	J0827+3525			2.249	FSRQ	...

Continues

Table A.2

OVRO name	RA	DEC	CGRaBS name	1FGL name	2FGL name	z	Optical Class	SED class
J0830+2410	08:30:52.09	+24:10:59.8	J0830+2410	J0830.5+2407	J0830.5+2407	0.942	FSRQ	LSP
J0831+0429	08:31:48.88	+04:29:39.1	J0831+0429	J0831.6+0429	J0831.9+0429	0.174	BLL	LSP
J0831+0847	08:31:55.10	+08:47:43.7	J0831+0847			0.941	FSRQ	...
J0833+0350	08:33:18.91	+03:50:32.4	J0833+0350			0.903	FSRQ	...
J0833+4224	08:33:53.89	+42:24:01.9	J0833+4224	J0834.4+4221	J0834.3+4221	0.249	FSRQ	...
J0834+6019	08:34:17.54	+60:19:47.1	J0834+6019			0.72	FSRQ	...
B30831+442	08:34:58.10	+44:03:37.9			J0834.3+4400	0.0	BLL	...
C0835+0937	08:35:43.22	+09:37:18.0		J0835.4+0936		...	BLL	...
J0835+6835	08:35:47.59	+68:35:11.5	J0835+6835			1.414	FSRQ	...
J0836+0052	08:36:15.79	+00:53:00.0	J0836+0052			1.826	FSRQ	...
J0836+2728	08:36:22.89	+27:28:52.5	J0836+2728			0.765	FSRQ	...
J0837+5825	08:37:22.41	+58:25:01.8	J0837+5825			2.101	FSRQ	...
J0837+2454	08:37:40.25	+24:54:23.1	J0837+2454			1.122	FSRQ	...
FIRSTJ083943.3+3540	08:39:43.30	+35:40:00.9			J0839.7+3541	0.0	BLL	...
J0839+0319	08:39:49.20	+03:19:53.9	J0839+0319			1.57	FSRQ	...
J0839+0104	08:39:49.61	+01:04:26.7	J0839+0104	J0839.5+0059	J0839.6+0059	1.123	FSRQ	...
3C207	08:40:47.59	+13:12:23.6			J0840.7+1310	0.68	SSRQ	...
0836+710	08:41:24.37	+70:53:42.2		J0842.2+7054	J0841.6+7052	2.218	FSRQ	LSP
J0842+1835	08:42:05.09	+18:35:41.0	J0842+1835			1.272	FSRQ	...
BBJ0842+0252	08:42:25.51	+02:52:52.7		J0842.2+0251		0.425	BLL	HSP
BBJ0844+5312	08:44:11.60	+53:12:50.0		J0844.0+5314	J0843.9+5312	0.0	BLL	ISP
BBJ0847+1133	08:47:12.93	+11:33:50.3		J0847.2+1134	J0847.2+1134	0.198	BLL	HSP
J0847-0703	08:47:56.74	-07:03:16.9	J0847-0703		J0848.1-0703	0.0	BLL	ISP
CLJ0848+6606	08:48:54.62	+66:06:09.5			J0849.2+6606	0.0	BLL	...
TXS0846+051	08:49:32.40	+04:55:06.8			J0849.0+0455	0.0	BLL	...
J0849+5108	08:49:57.98	+51:08:29.0	J0849+5108			0.584	FSRQ	...
C0850+4854	08:50:00.53	+48:54:52.6		J0849.9+4852	J0849.8+4852	0.0	BLL	ISP
J0850-1213	08:50:09.63	-12:13:35.6	J0850-1213	J0850.0-1213	J0850.2-1212	0.566	FSRQ	LSP
RXJ0850.6+34	08:50:36.20	+34:55:23.0		J0850.2+3457		0.149	BLL	ISP
J0851+0845	08:51:28.43	+08:45:15.3	J0851+0845			...	...	...
J0853-0150	08:53:01.33	-01:50:48.2	J0853-0150			1.498	FSRQ	...
J0854+5757	08:54:42.00	+57:57:29.9	J0854+5757			1.318	FSRQ	...
J0854+2006	08:54:48.87	+20:06:30.6	J0854+2006	J0854.8+2006	J0854.8+2005	0.306	BLL	ISP
3C209	08:55:09.40	-07:15:02.9			J0855.1-0712	...	AGU	...
TXS0853+211	08:56:39.70	+20:57:44.2			J0856.3+2058	0.0	BLL	...
J0856-1105	08:56:41.80	-11:05:14.5	J0856-1105	J0856.6-1105	J0856.6-1105	0.0	BLL	LSP

Continues

Table A.2

OVRO name	RA	DEC	CGRaBS name	1FGL name	2FGL name	z	Optical Class	SED class
GB6J0856+7146	08:56:54.70	+71:46:24.7			J0856.0+7136	...	AGU	LSP
J0856+1739	08:56:56.69	+17:39:47.8	J0856+1739			0.516	FSRQ	...
J0856+2111	08:56:57.24	+21:11:43.6	J0856+2111			2.098	FSRQ	...
PKS0855-19	08:58:05.20	-19:50:36.3			J0858.1-1952	...	AGU	LSP
J0900+4108	09:00:21.43	+41:08:23.0	J0900+4108			1.629	FSRQ	...
J0900-1242	09:00:39.77	-12:42:32.6	J0900-1242			...	...	...
J0901+0448	09:01:11.86	+04:48:58.8	J0901+0448			1.863	FSRQ	...
J0902+5402	09:02:19.29	+54:02:57.3	J0902+5402			1.682	FSRQ	...
NVSSJ090226+205045	09:02:26.80	+20:50:45.6			J0902.4+2050	0.0	BLL	ISP
J0902+4310	09:02:30.92	+43:10:14.2	J0902+4310			2.41	FSRQ	...
J0903-1721	09:03:00.02	-17:21:05.2	J0903-1721			0.872	FSRQ	...
S40859+47	09:03:04.00	+46:51:04.6			J0903.4+4651	1.466	FSRQ	LSP
J0903+6757	09:03:53.16	+67:57:22.7	J0903+6757			1.499	FSRQ	...
J0905+1358	09:05:34.99	+13:58:06.3		J0905.5+1356	J0905.6+1357	0.0	BLL	...
J0905+2849	09:05:41.77	+28:49:28.3	J0905+2849			1.219	FSRQ	...
PMNJ0906-0905	09:06:17.90	-09:05:44.0			J0906.2-0906	...	AGU	...
J0906+6930	09:06:30.75	+69:30:30.8	J0906+6930			5.47	FSRQ	...
J0908+1609	09:08:55.92	+16:09:54.8	J0908+1609			...	...	...
RXJ0909.0+23	09:09:00.60	+23:11:14.0		J0909.2+2310	J0909.2+2308	0.223	BLL	HSP
J0909+0121	09:09:10.09	+01:21:35.6	J0909+0121	J0909.0+0126	J0909.1+0121	1.026	FSRQ	LSP
J0909+0200	09:09:39.85	+02:00:05.3	J0909+0200			...	BLL	...
C0909-0231	09:09:44.92	-02:31:30.4		J0909.6-0229	J0909.7-0229	0.957	FSRQ	...
J0910+3329	09:10:37.04	+33:29:24.4		J0910.7+3332	J0910.6+3329	0.0	BLL	HSP
J0910+2248	09:10:42.13	+22:48:35.6	J0910+2248	J0911.0+2247	J0910.9+2246	2.661	FSRQ	LSP
1RXSJ091211.9+27595	09:12:11.20	+27:59:27.8			J0912.5+2758	0.0	BLL	HSP
B30908+416B	09:12:11.62	+41:26:09.4		J0912.3+4127	J0912.1+4126	2.563	FSRQ	LSP
J0914+0245	09:14:38.28	+02:45:37.8	J0914+0245			...	...	...
J0915+2933	09:15:52.40	+29:33:24.0		J0915.7+2931	J0915.8+2932	0.0	BLL	HSP
S40913+39	09:16:48.90	+38:54:28.4			J0917.0+3900	1.267	FSRQ	LSP
J0917-1345	09:17:39.00	-13:45:42.2	J0917-1345			...	...	...
J0919+3324	09:19:08.79	+33:24:42.0	J0919+3324			...	...	...
J0920+4441	09:20:58.46	+44:41:54.0	J0920+4441	J0920.9+4441	J0920.9+4441	2.189	FSRQ	LSP
J0921+6215	09:21:36.23	+62:15:52.2	J0921+6215	J0919.6+6216	J0921.9+6216	1.453	FSRQ	LSP
J0922-0529	09:22:23.68	-05:29:07.2	J0922-0529			0.974	NLRG	...
GB6J0922+0433	09:22:27.00	+04:33:37.5			J0922.7+0435	...	AGU	...
J0923+3849	09:23:14.45	+38:49:39.9	J0923+3849			...	...	...

Continues

Table A.2

OVRO name	RA	DEC	CGRaBS name	1FGL name	2FGL name	z	Optical Class	SED class
J0923+4125	09:23:31.30	+41:25:27.4	J0923+4125	J0923.2+4121	J0923.2+4125	1.732	FSRQ	...
J0923+2815	09:23:51.52	+28:15:25.0		J0924.2+2812	J0924.0+2819	0.744	FSRQ	...
J0925+1658	09:25:49.96	+16:58:12.2	J0925+1658			1.545	FSRQ	...
J0926+4029	09:26:00.43	+40:29:49.7	J0926+4029			1.879	FSRQ	...
J0927+3902	09:27:03.01	+39:02:20.9	J0927+3902			0.695	FSRQ	...
J0928+4446	09:28:24.14	+44:46:04.8	J0928+4446			1.904	FSRQ	...
J0929+5013	09:29:15.44	+50:13:36.0	J0929+5013		J0929.5+5009	0.0	BLL	ISP
J0929+8612	09:29:43.02	+86:12:21.3	J0929+8612			...	BLL	...
J0930+7420	09:30:53.78	+74:20:05.9	J0930+7420			...	...	...
J0932+5306	09:32:41.15	+53:06:33.8	J0932+5306			0.597	FSRQ	...
J0933-0819	09:33:17.10	-08:19:10.9	J0933-0819			0.903	FSRQ	...
J0933-1139	09:33:34.46	-11:39:25.6	J0933-1139			...	...	...
J0934+3926	09:34:06.67	+39:26:32.1	J0934+3926	J0934.5+3929	J0934.7+3932	0.0	BLL	...
J0935-1939	09:35:15.62	-19:39:08.8	J0935-1939			...	...	...
J0936-0535	09:36:36.67	-05:35:52.5	J0936-0535			...	...	...
J0937+5008	09:37:12.33	+50:08:52.1	J0937+5008	J0937.7+5005	J0937.6+5009	0.276	FSRQ	LSP
J0938-0708	09:38:56.11	-07:08:00.7	J0938-0708			1.281	FSRQ	...
TXS0936-173	09:39:19.20	-17:31:35.5			J0939.1-1734	...	AGU	...
J0939+4141	09:39:49.62	+41:41:54.2	J0939+4141			1.224	FSRQ	...
J0940+2603	09:40:14.72	+26:03:29.9	J0940+2603			0.498	FSRQ	...
BBJ0940+6148	09:40:22.45	+61:48:26.2		J0941.2+6149	J0941.4+6148	0.211	BLL	HSP
J0941-1335	09:41:02.55	-13:35:51.0	J0941-1335			0.551	FSRQ	...
J0941+2728	09:41:48.11	+27:28:38.8	J0941+2728	J0941.2+2722		1.306	FSRQ	...
J0942+6403	09:42:03.91	+64:03:11.3	J0942+6403			0.952	FSRQ	...
J0942-0759	09:42:21.47	-07:59:53.2	J0942-0759			...	...	...
J0943+1702	09:43:17.23	+17:02:19.0	J0943+1702			1.598	FSRQ	...
J0943+3614	09:43:19.15	+36:14:52.1	J0943+3614			0.022	AGN	...
J0945+4636	09:45:42.09	+46:36:50.6	J0945+4636			0.639	FSRQ	...
J0945+5757	09:45:42.24	+57:57:47.7		J0945.6+5754	J0945.9+5751	0.229	BLL	...
RXSJ094620.5+010459	09:46:19.90	+01:04:53.1			J0946.2+0104	0.557	BLL	HSP
J0946+1017	09:46:35.07	+10:17:06.1		J0946.6+1012	J0946.5+1015	1.006	FSRQ	...
J0948+4039	09:48:55.34	+40:39:44.6	J0948+4039		J0948.8+4040	1.249	FSRQ	LSP
J0948+0022	09:48:57.32	+00:22:25.6	J0948+0022	J0949.0+0021	J0948.8+0020	0.585	NLSyI	...
US1015	09:50:11.80	+45:53:19.1			J0950.1+4554	0.399	BLL	ISP
BBJ0952+3936	09:52:14.71	+39:36:15.9		J0952.2+3926		...	BLL	HSP
J0952+5048	09:52:27.31	+50:48:50.7	J0952+5048			1.091	FSRQ	...

Continues

Table A.2

OVRO name	RA	DEC	CGRaBS name	1FGL name	2FGL name	z	Optical Class	SED class
J0952+3512	09:52:32.03	+35:12:52.4	J0952+3512			1.876	FSRQ	...
C0953-0840	09:53:02.72	-08:40:18.4		J0953.0-0838	J0953.1-0839	0.0	BLL	HSP
J0953+3225	09:53:27.95	+32:25:51.5	J0953+3225			1.574	FSRQ	...
J0954+2639	09:54:39.80	+26:39:24.5	J0954+2639			...	...	...
M82	09:55:52.73	+69:40:45.8		J0956.5+6938	J0955.9+6936	0.0010	starburst	...
J0956+2515	09:56:49.87	+25:15:16.0	J0956+2515	J0956.9+2513	J0956.9+2516	0.708	FSRQ	LSP
J0957-1350	09:57:18.19	-13:50:01.3	J0957-1350		J0957.6-1350	1.323	FSRQ	...
J0957-0156	09:57:27.21	-01:56:54.6	J0957-0156			0.86	FSRQ	...
C0957+5522	09:57:38.18	+55:22:57.7		J0957.7+5523	J0957.7+5522	0.899	FSRQ	LSP
J0958+4725	09:58:19.67	+47:25:07.8	J0958+4725			1.882	FSRQ	...
J0958+5039	09:58:37.81	+50:39:57.5	J0958+5039			1.154	FSRQ	...
J0958+6533	09:58:47.25	+65:33:54.8	J0958+6533	J1000.1+6539	J0958.6+6533	0.367	BLL	ISP
J1001+2911	10:01:10.21	+29:11:37.5	J1001+2911	J1000.9+2915	J1001.0+2913	0.558	BLL	ISP
J1001+3424	10:01:11.94	+34:24:50.4	J1001+3424			0.948	FSRQ	...
J1001+1015	10:01:57.73	+10:15:49.7	J1001+1015			1.533	FSRQ	...
1RXSJ100235.8+22160	10:02:34.60	+22:16:15.2			J1003.0+2219	0.0	BLL	HSP
J1002+1216	10:02:52.85	+12:16:14.6	J1002+1216			0.861	FSRQ	...
BBJ1006+3454	10:06:56.46	+34:54:45.2		J1007.0+3454		...	BLL	HSP
J1007-0207	10:07:04.35	-02:07:10.9	J1007-0207			1.214	FSRQ	...
J1007+1356	10:07:41.50	+13:56:29.6	J1007+1356			2.707	FSRQ	...
J1008+0621	10:08:00.82	+06:21:21.2	J1008+0621	J1007.9+0619	J1007.7+0621	0.0	BLL	LSP
PKS1005+007	10:08:11.50	+00:29:59.6			J1008.6+0028	...	AGU	ISP
J1010+8250	10:10:15.78	+82:50:14.4	J1010+8250			0.322	FSRQ	...
J1010-0200	10:10:51.67	-02:00:19.6		J1011.0-0156	J1010.8-0158	0.887	FSRQ	...
J1010+3330	10:10:51.83	+33:30:17.7	J1010+3330			2.068	FSRQ	...
CRJ1012+0630	10:12:13.35	+06:30:57.2		J1012.2+0634	J1012.1+0631	0.727	BLL	ISP
J1012+2312	10:12:16.39	+23:12:14.6	J1012+2312			0.749	FSRQ	...
C1012+2439	10:12:41.38	+24:39:23.4		J1012.7+2440	J1012.6+2440	1.805	FSRQ	...
B31009+427	10:12:44.20	+42:29:56.5			J1012.5+4227	0.365	BLL	HSP
J1013+3445	10:13:49.62	+34:45:50.8	J1013+3445			1.414	FSRQ	...
J1013+2449	10:13:53.43	+24:49:16.4	J1013+2449			1.636	FSRQ	...
J1014+2301	10:14:47.07	+23:01:16.6	J1014+2301		J1014.1+2306	0.566	FSRQ	LSP
J1015+4926	10:15:04.13	+49:26:00.7	J1015+4926	J1015.1+4927	J1015.1+4925	0.212	BLL	HSP
PMNJ1015-0626	10:15:35.50	-06:26:48.1			J1016.2-0638	...	AGU	...
J1015+6728	10:15:38.02	+67:28:44.4	J1015+6728			...	...	...
J1015+1227	10:15:44.02	+12:27:07.1	J1015+1227			...	BLL	...

Continues

Table A.2

OVRO name	RA	DEC	CGRaBS name	1FGL name	2FGL name	z	Optical Class	SED class
CR1016+0513	10:16:03.14	+05:13:02.3		J1016.1+0514	J1016.0+0513	1.714	FSRQ	...
J1016+2037	10:16:44.33	+20:37:47.3	J1016+2037			3.11	FSRQ	...
J1017+6116	10:17:25.89	+61:16:27.5	J1017+6116			2.805	FSRQ	...
J1018+3542	10:18:10.99	+35:42:39.4	J1018+3542		J1017.0+3531	1.228	FSRQ	LSP
J1018+0530	10:18:27.85	+05:30:29.9	J1018+0530			1.938	FSRQ	...
TXS1015+594	10:18:58.60	+59:11:27.7			J1019.0+5915	0.0	BLL	ISP
J1019+6320	10:19:50.87	+63:20:01.6	J1019+6320		J1019.8+6322	0.0	BLL	...
J1021+3437	10:21:17.48	+34:37:21.6	J1021+3437			1.4	FSRQ	...
WNB1016.6+8038	10:22:01.90	+80:23:50.4			J1021.6+8021	...	AGU	...
J1022+4239	10:22:13.13	+42:39:25.6	J1022+4239			0.991	FSRQ	...
BBJ1022-0113	10:22:43.73	-01:13:02.5		J1022.8-0115	J1023.1-0115	0.0	BLL	HSP
J1023+3948	10:23:11.57	+39:48:15.4	J1023+3948			1.254	FSRQ	...
J1023+2856	10:23:24.05	+28:56:51.0	J1023+2856			0.671	FSRQ	...
RXJ1023.6+3001	10:23:39.70	+30:00:55.2			J1023.6+2959	0.433	BLL	HSP
J1024+1912	10:24:44.81	+19:12:20.4	J1024+1912			0.828	FSRQ	...
J1025-0509	10:25:45.42	-05:09:54.1	J1025-0509			...	...	...
J1025+1253	10:25:56.29	+12:53:49.0	J1025+1253			0.663	FSRQ	...
BBJ1026-1748	10:26:58.52	-17:48:58.5		J1027.1-1747	J1026.7-1749	0.114	BLL	HSP
J1028+0255	10:28:20.40	+02:55:22.5	J1028+0255			0.715	FSRQ	...
J1029-1852	10:29:33.10	-18:52:50.3	J1029-1852			1.784	FSRQ	...
BBJ1031+5053	10:31:18.50	+50:53:35.0		J1031.0+5051	J1031.0+5053	0.0	BLL	HSP
S51027+74	10:31:22.50	+74:41:57.9			J1029.9+7437	...	AGU	ISP
TXS1029+378	10:32:40.70	+37:38:26.0		J1032.7+3737	J1032.6+3733	0.0	BLL	...
J1033+4116	10:33:03.71	+41:16:06.2	J1033+4116	J1033.2+4116	J1033.2+4117	1.117	FSRQ	LSP
J1033+3935	10:33:22.06	+39:35:51.1	J1033+3935			1.095	FSRQ	...
J1033+0711	10:33:34.02	+07:11:26.1	J1033+0711			1.535	FSRQ	...
J1033+6051	10:33:51.43	+60:51:07.3	J1033+6051			1.401	FSRQ	...
J1036+1440	10:36:03.71	+14:40:45.0	J1036+1440			1.373	FSRQ	...
J1036+2203	10:36:32.98	+22:03:12.2	J1036+2203			0.595	FSRQ	...
J1036-0605	10:36:47.57	-06:05:41.2	J1036-0605			...	...	...
C1037+5711	10:37:44.31	+57:11:55.6		J1037.7+5711	J1037.6+5712	0.0	BLL	ISP
J1038+0512	10:38:46.78	+05:12:29.1	J1038+0512			0.473	FSRQ	...
J1039-1541	10:39:06.71	-15:41:06.7	J1039-1541			0.525	FSRQ	...
J1041+0610	10:41:17.16	+06:10:16.9	J1041+0610		J1040.7+0614	1.264	FSRQ	LSP
J1041+5233	10:41:46.78	+52:33:28.2	J1041+5233			0.678	FSRQ	...
J1043+2408	10:43:09.03	+24:08:35.4	J1043+2408	J1043.1+2404	J1043.1+2404	0.559	BLL	ISP

Continues

Table A.2

OVRO name	RA	DEC	CGRaBS name	1FGL name	2FGL name	z	Optical Class	SED class
J1044+2959	10:44:06.34	+29:59:01.0	J1044+2959			2.983	FSRQ	...
J1044+5322	10:44:10.67	+53:22:20.5	J1044+5322			1.901	FSRQ	...
J1044+8054	10:44:23.07	+80:54:39.4	J1044+8054	J1048.7+8054	J1042.6+8053	1.26	FSRQ	LSP
J1045+0624	10:45:52.73	+06:24:36.5	J1045+0624			1.509	FSRQ	...
J1046+5354	10:46:24.04	+53:54:26.2	J1046+5354			1.71	FSRQ	...
J1047-1308	10:47:03.93	-13:08:32.4	J1047-1308			1.288	FSRQ	...
J1047+2635	10:47:36.69	+26:35:27.5	J1047+2635			0.99	FSRQ	...
C1047+7238	10:47:47.52	+72:38:13.0		J1048.5+7239	J1049.7+7240	0.0	BLL	...
J1048-1909	10:48:06.62	-19:09:35.7	J1048-1909			0.595	FSRQ	...
J1048+7143	10:48:27.62	+71:43:35.9	J1048+7143	J1048.8+7145	J1048.3+7144	1.15	FSRQ	LSP
CLJ1049+2338	10:49:00.25	+23:38:19.9			J1048.6+2336	0.319	BLL	...
GB6J1049+1548	10:49:39.10	+15:48:38.0			J1049.4+1551	...	AGU	...
J1051+2027	10:51:01.37	+20:27:20.0	J1051+2027			1.036	FSRQ	...
PB00667	10:51:25.30	+39:43:25.5			J1051.3+3938	0.498	BLL	HSP
J1051+2119	10:51:48.79	+21:19:52.3	J1051+2119			1.3	FSRQ	...
BBJ1051+0103	10:51:51.84	+01:03:10.8		J1051.9+0106	J1051.8+0107	0.265	BLL	ISP
BBJ1053+4929	10:53:44.10	+49:29:56.0		J1053.6+4927	J1053.6+4928	0.14	BLL	HSP
CLJ1054+2210	10:54:30.62	+22:10:54.8		J1054.5+2212	J1054.5+2212	0.0	BLL	ISP
J1054-0713	10:54:41.01	-07:13:26.2	J1054-0713			1.618	FSRQ	...
J1056+7011	10:56:53.62	+70:11:45.9	J1056+7011		J1057.1+7001	2.492	FSRQ	LSP
J1058+8114	10:58:11.53	+81:14:32.7	J1058+8114		J1059.4+8113	0.706	FSRQ	LSP
J1058+1951	10:58:17.90	+19:51:50.9	J1058+1951			1.11	FSRQ	...
J1058+0133	10:58:29.60	+01:33:58.8	J1058+0133	J1058.4+0134	J1058.4+0133	0.888	BLL	LSP
J1058+5628	10:58:37.73	+56:28:11.2	J1058+5628	J1058.6+5628	J1058.6+5628	0.143	BLL	HSP
CR1059-1134	10:59:12.43	-11:34:22.7		J1059.3-1132	J1059.3-1132	0.0	BLL	LSP
J1059+2057	10:59:39.04	+20:57:22.0	J1059+2057			0.4	AGN	...
J1102+2757	11:02:14.29	+27:57:08.7	J1102+2757			1.861	FSRQ	...
J1103+3014	11:03:13.30	+30:14:42.7	J1103+3014			0.387	FSRQ	...
J1104+0730	11:04:24.07	+07:30:53.2		J1104.4+0734	J1104.3+0729	0.0	BLL	...
J1104+3812	11:04:27.31	+38:12:31.8	J1104+3812	J1104.4+3812	J1104.4+3812	0.031	BLL	HSP
J1106+2812	11:06:07.26	+28:12:47.0		J1106.5+2809	J1106.1+2814	0.843	FSRQ	LSP
BZBJ1107+0222	11:07:35.80	+02:22:25.4			J1107.5+0223	0.0	BLL	...
BBJ1107+1502	11:07:48.06	+15:02:10.5		J1107.8+1502	J1107.8+1505	0.0	BLL	HSP
J1108+4330	11:08:23.48	+43:30:53.6	J1108+4330			1.226	FSRQ	...
J1108+0811	11:08:37.50	+08:11:01.6	J1108+0811			1.123	FSRQ	...
1ES1106+244	11:09:16.20	+24:11:20.2			J1109.3+2414	0.482	BLL	...

Continues

Table A.2

OVRO name	RA	DEC	CGRaBS name	1FGL name	2FGL name	z	Optical Class	SED class
J1110-1835	11:10:27.77	-18:35:52.8		J1110.2-1839	J1110.1-1835	0.0	BLL	LSP
BBJ1110+7133	11:10:37.60	+71:33:56.6		J1109.9+7134	J1110.2+7134	0.0	BLL	HSP
J1110+4403	11:10:46.34	+44:03:25.9	J1110+4403			1.693	FSRQ	...
C1112+3446	11:12:38.77	+34:46:39.1		J1112.8+3444	J1112.4+3450	1.956	FSRQ	...
J1113+1442	11:13:58.70	+14:42:27.0	J1113+1442			0.866	FSRQ	...
J1114-0816	11:14:32.55	-08:16:39.0	J1114-0816			2.078	FSRQ	...
J1116+0829	11:16:09.97	+08:29:22.0	J1116+0829			0.486	AGN	...
C1117+2014	11:17:06.26	+20:14:07.4		J1117.1+2013	J1117.2+2013	0.138	BLL	HSP
BBJ1117+5355	11:17:57.43	+53:55:54.8		J1118.0+5354	J1118.0+5354	0.0	BLL	HSP
J1118+1234	11:18:57.30	+12:34:41.7	J1118+1234			2.129	FSRQ	...
J1119+0410	11:19:42.83	+04:10:27.9	J1119+0410			0.736	FSRQ	...
J1119+1656	11:19:52.43	+16:56:56.9	J1119+1656			0.949	FSRQ	...
J1120+0704	11:20:38.44	+07:04:47.2			J1120.4+0710	1.336	FSRQ	LSP
BBJ1120+4212	11:20:48.00	+42:12:12.0		J1121.0+4209	J1121.0+4211	0.0	BLL	HSP
J1120-1420	11:20:55.56	-14:20:29.9	J1120-1420			1.114	FSRQ	...
J1121-1722	11:21:20.81	-17:22:40.8	J1121-1722			0.986	FSRQ	...
J1121-0553	11:21:25.11	-05:53:56.4		J1121.5-0554		1.297	FSRQ	LSP
J1121-0711	11:21:42.12	-07:11:06.3	J1121-0711			...	BLL	...
J1122+1805	11:22:29.71	+18:05:26.4	J1122+1805			1.04	FSRQ	...
J1124+2336	11:24:02.71	+23:36:45.9	J1124+2336	J1123.9+2339	J1124.2+2338	1.549	FSRQ	...
GB6J1124+4933	11:24:53.60	+49:34:11.0			J1125.2+4933	0.0	BLL	HSP
J1125+0001	11:25:42.30	+00:01:01.4	J1125+0001			1.696	FSRQ	...
BBJ1125-0742	11:25:51.99	-07:42:21.1		J1126.0-0741	J1126.0-0743	0.279	BLL	HSP
J1125+2610	11:25:53.71	+26:10:20.0	J1125+2610			2.341	FSRQ	...
J1126+4516	11:26:57.66	+45:16:06.3	J1126+4516			1.811	FSRQ	...
J1127-1857	11:27:04.39	-18:57:17.4	J1127-1857	J1126.8-1854	J1126.6-1856	1.048	FSRQ	LSP
J1127+0555	11:27:36.53	+05:55:32.1	J1127+0555			2.217	FSRQ	...
J1127+5650	11:27:40.14	+56:50:14.8	J1127+5650			2.89	FSRQ	...
J1127+3620	11:27:58.87	+36:20:28.4	J1127+3620		J1127.6+3622	0.884	FSRQ	...
J1128+5925	11:28:13.34	+59:25:14.8	J1128+5925			1.795	FSRQ	...
J1128+1039	11:28:45.55	+10:39:07.0	J1128+1039			...	...	...
J1129-0240	11:29:52.92	-02:40:07.7	J1129-0240			2.093	FSRQ	...
C1130-1449	11:30:07.05	-14:49:27.4			J1130.3-1448	1.184	FSRQ	LSP
J1130+3815	11:30:53.28	+38:15:18.5	J1130+3815			1.733	FSRQ	...
BZBJ1131+5809	11:31:18.70	+58:08:56.9			J1130.9+5809	0.36	BLL	ISP
J1131-0500	11:31:30.52	-05:00:19.7	J1131-0500			0.266	AGN	...

Continues

Table A.2

OVRO name	RA	DEC	CGRaBS name	1FGL name	2FGL name	z	Optical Class	SED class
J1132+0034	11:32:45.62	+00:34:27.8			J1132.9+0033	0.678	BLL	ISP
J1133+0040	11:33:20.06	+00:40:52.8	J1133+0040			1.633	FSRQ	...
J1135-0428	11:35:58.23	-04:28:27.9	J1135-0428			0.273	FSRQ	...
J1136-0330	11:36:23.65	-03:30:29.5	J1136-0330			1.648	FSRQ	...
J1136+7009	11:36:26.41	+70:09:27.3	J1136+7009	J1136.6+7009	J1136.7+7009	0.046	BLL	HSP
J1136+3407	11:36:27.34	+34:07:39.5	J1136+3407			1.332	FSRQ	...
BBJ1136+6737	11:36:30.09	+67:37:04.3		J1136.2+6739	J1136.3+6736	0.134	BLL	HSP
BBJ1136+2550	11:36:50.11	+25:50:52.4		J1136.9+2551	J1137.0+2553	0.156	BLL	HSP
J1141+6410	11:41:12.23	+64:10:05.5	J1141+6410			...	...	...
CRJ1142+1547	11:42:07.74	+15:47:54.2		J1141.8+1549	J1141.9+1550	0.299	BLL	...
87GB114026.7+613850	11:43:12.10	+61:22:10.9			J1143.1+6119	0.0	BLL	...
J1143+6633	11:43:41.61	+66:33:31.2	J1143+6633			2.328	FSRQ	...
J1145+0455	11:45:21.32	+04:55:26.7	J1145+0455			1.342	FSRQ	...
J1146+5848	11:46:26.91	+58:48:34.2	J1146+5848			1.982	FSRQ	...
J1146+5356	11:46:44.21	+53:56:43.1	J1146+5356			2.201	FSRQ	...
J1146+3958	11:46:58.30	+39:58:34.3	J1146+3958	J1146.8+4004	J1146.9+4000	1.088	FSRQ	...
J1147+3501	11:47:22.13	+35:01:07.5	J1147+3501			0.063	AGN	...
J1147-0724	11:47:51.55	-07:24:41.1	J1147-0724	J1147.7-0722	J1147.7-0724	1.342	FSRQ	LSP
J1147+2635	11:47:59.77	+26:35:42.3	J1147+2635			0.867	FSRQ	...
J1148+5924	11:48:50.36	+59:24:56.4	J1148+5924			0.011	AGN	...
J1148-0404	11:48:55.89	-04:04:09.5	J1148-0404			0.341	FSRQ	...
J1148+5254	11:48:56.57	+52:54:25.3	J1148+5254			1.633	FSRQ	...
J1150+4332	11:50:16.61	+43:32:05.9	J1150+4332			3.037	FSRQ	...
J1150+2417	11:50:19.21	+24:17:53.9	J1150+2417	J1150.2+2419	J1150.1+2419	0.2	BLL	LSP
J1150-0640	11:50:23.98	-06:40:26.6	J1150-0640			...	...	...
BBJ1150+4154	11:50:34.65	+41:54:40.8		J1150.5+4152	J1150.5+4154	0.0	BLL	HSP
CRJ1151+5859	11:51:24.66	+58:59:17.6		J1151.6+5857	J1151.5+5857	0.0	BLL	ISP
CRJ1151-1347	11:51:29.97	-13:47:50.8		J1151.4-1345	J1151.5-1347	0.838	BLL	...
J1152-0841	11:52:16.46	-08:41:03.3	J1152-0841	J1152.2-0836	J1152.4-0840	2.367	FSRQ	...
J1152+4939	11:52:32.87	+49:39:38.8	J1152+4939			1.093	FSRQ	...
J1152-0519	11:52:55.49	-05:19:48.5	J1152-0519			1.983	FSRQ	...
J1153+8058	11:53:12.50	+80:58:29.1	J1153+8058			1.25	FSRQ	...
J1154+5934	11:54:01.37	+59:34:54.2	J1154+5934			0.871	FSRQ	...
J1154+6022	11:54:04.53	+60:22:20.8			J1154.4+6019	1.12	FSRQ	LSP
BBJ1154-0010	11:54:04.56	-00:10:09.8		J1154.0-0008	J1154.0-0010	0.254	BLL	HSP
J1154+1225	11:54:10.40	+12:25:09.8	J1154+1225			0.081	FSRQ	...

Continues

Table A.2

OVRO name	RA	DEC	CGRaBS name	1FGL name	2FGL name	z	Optical Class	SED class
J1157+5527	11:57:56.13	+55:27:12.9	J1157+5527			0.0040	AGN	...
J1158+2450	11:58:25.79	+24:50:18.0	J1158+2450			0.202	FSRQ	...
J1158+4825	11:58:26.77	+48:25:16.2	J1158+4825			2.028	FSRQ	...
GB6J1158+0937	11:58:54.10	+09:37:10.3			J1158.8+0939	0.0	BLL	...
J1159+2914	11:59:31.83	+29:14:43.8	J1159+2914	J1159.4+2914	J1159.5+2914	0.725	FSRQ	LSP
GB6J1200+0202	12:00:12.40	+02:02:09.3			J1200.0+0159	...	AGU	...
J1201+1431	12:01:44.27	+14:31:36.5	J1201+1431			...	...	...
J1202-0528	12:02:35.63	-05:28:02.5	J1202-0528			...	...	...
J1203+6031	12:03:03.51	+60:31:19.1		J1202.9+6032	J1203.2+6030	0.065	BLL	ISP
J1203+4803	12:03:29.86	+48:03:13.6	J1203+4803			0.817	FSRQ	...
BBJ1204+1145	12:04:12.12	+11:45:55.4		J1204.4+1139	J1204.2+1144	0.296	BLL	HSP
CRJ1204-0710	12:04:16.66	-07:10:09.0		J1204.3-0714	J1204.3-0711	0.184	BLL	ISP
J1207+1211	12:07:12.62	+12:11:45.9	J1207+1211			0.89	FSRQ	...
J1207+2754	12:07:27.90	+27:54:58.8	J1207+2754			2.177	FSRQ	...
CR1208+5441	12:08:54.26	+54:41:58.2		J1209.3+5444	J1208.8+5441	1.344	FSRQ	...
J1209+4119	12:09:22.78	+41:19:41.4	J1209+4119	J1209.4+4119	J1209.6+4121	0.0	BLL	LSP
J1209+2547	12:09:45.09	+25:47:03.8	J1209+2547			1.436	FSRQ	...
J1209+1810	12:09:51.76	+18:10:06.8		J1209.7+1806	J1209.7+1807	0.845	FSRQ	...
J1210-1218	12:10:06.00	-12:18:08.8	J1210-1218			...	...	...
4C+13.46	12:13:32.00	+13:07:20.3			J1214.6+1309	1.139	FSRQ	LSP
J1214+0829	12:14:59.91	+08:29:22.5	J1214+0829			2.359	FSRQ	...
BBJ1215+5002	12:15:00.78	+50:02:15.6		J1214.9+5004	J1214.9+5004	0.0	BLL	...
J1215+1654	12:15:03.98	+16:54:37.9	J1215+1654		J1214.8+1653	1.132	FSRQ	LSP
J1215-1731	12:15:46.75	-17:31:45.4	J1215-1731			...	...	...
J1217+5835	12:17:11.02	+58:35:26.2	J1217+5835			2.552	FSRQ	...
J1217+3007	12:17:52.08	+30:07:00.6	J1217+3007	J1217.7+3007	J1217.8+3006	0.13	BLL	HSP
CR1218-0119	12:18:34.93	-01:19:54.4			J1218.5-0122	0.0	BLL	...
J1219+4829	12:19:06.42	+48:29:56.2	J1219+4829			1.076	FSRQ	...
J1219+6344	12:19:10.59	+63:44:10.7	J1219+6344			...	...	...
J1219+6600	12:19:35.80	+66:00:31.9	J1219+6600			1.266	FSRQ	...
FRBAJ1219-03	12:19:45.70	-03:14:24.0		J1219.8-0309	J1219.8-0310	0.299	BLL	HSP
CRJ1220+7105	12:20:03.63	+71:05:31.1		J1221.5+7106	J1219.2+7107	0.451	FSRQ	...
J1220+3431	12:20:08.29	+34:31:21.7	J1220+3431	J1220.2+3432		...	BLL	ISP
PKS1217+02	12:20:12.30	+02:03:41.5			J1219.7+0201	0.241	FSRQ	ISP
J1220+3808	12:20:59.23	+38:08:55.7	J1220+3808			...	...	...
1ES1218+304	12:21:21.90	+30:10:37.0		J1221.3+3008	J1221.3+3010	0.184	BLL	HSP

Continues

Table A.2

OVRO name	RA	DEC	CGRaBS name	1FGL name	2FGL name	z	Optical Class	SED class
J1221+4411	12:21:27.04	+44:11:29.7	J1221+4411			1.344	FSRQ	...
J1221+2813	12:21:31.69	+28:13:58.5	J1221+2813	J1221.5+2814	J1221.4+2814	0.103	BLL	ISP
J1222+0413	12:22:22.55	+04:13:15.8	J1222+0413	J1222.5+0415	J1222.4+0413	0.966	FSRQ	LSP
J1223+8040	12:23:40.50	+80:40:04.3		J1224.8+8044	J1223.9+8043	0.0	BLL	LSP
MS1221.8+2452	12:24:24.20	+24:36:23.6			J1224.4+2436	0.218	BLL	HSP
J1224+4335	12:24:51.51	+43:35:19.3			J1225.0+4335	0.0	BLL	...
C1224+2122	12:24:54.46	+21:22:46.4		J1224.7+2121	J1224.9+2122	0.434	FSRQ	LSP
BBJ1226+0638	12:26:44.23	+06:38:53.2		J1226.8+0638		...	BLL	HSP
J1226-1328	12:26:54.42	-13:28:39.1	J1226-1328	J1226.7-1332	J1226.7-1331	0.456	BLL	...
J1227+4932	12:27:55.73	+49:32:56.0	J1227+4932			1.348	FSRQ	...
J1228+3128	12:28:24.96	+31:28:37.6	J1228+3128			2.195	FSRQ	...
J1228+3706	12:28:47.42	+37:06:12.1	J1228+3706			1.515	FSRQ	...
C1228+4858	12:28:51.77	+48:58:01.3		J1228.2+4855	J1228.6+4857	1.722	FSRQ	LSP
J1229+0203	12:29:06.70	+02:03:08.6	J1229+0203	J1229.1+0203	J1229.1+0202	0.158	FSRQ	LSP
J1230+2518	12:30:14.09	+25:18:07.1	J1230+2518	J1230.4+2520	J1230.2+2517	0.135	BLL	ISP
3C274	12:30:49.42	+12:23:28.0		J1230.8+1223	J1230.8+1224	0.0040	Radio Gal	...
J1231+0418	12:31:27.58	+04:18:01.9	J1231+0418			1.03	FSRQ	...
J1231+2847	12:31:43.58	+28:47:49.8		J1231.6+2850	J1231.7+2848	0.236	BLL	HSP
J1232+4821	12:32:34.79	+48:21:33.0	J1232+4821			1.588	FSRQ	...
BBJ1233-0144	12:33:41.33	-01:44:23.7		J1233.6-0146	J1233.7-0145	0.0	BLL	...
J1235+3621	12:35:05.81	+36:21:19.3	J1235+3621			1.598	FSRQ	...
J1238+0723	12:38:02.45	+07:23:21.8	J1238+0723			1.172	FSRQ	...
PMNJ1238-1959	12:38:24.20	-19:59:13.4			J1238.1-1953	...	AGU	ISP
J1239+0730	12:39:24.59	+07:30:17.2	J1239+0730		J1239.5+0728	0.4	AGU	LSP
C1239+0443	12:39:32.76	+04:43:05.2		J1239.5+0443	J1239.5+0443	1.761	FSRQ	LSP
J1239-1023	12:39:43.06	-10:23:28.7	J1239-1023			0.75	FSRQ	...
RXJ1241.8-1455	12:41:49.30	-14:55:59.0			J1241.6-1457	0.0	BLL	HSP
J1242+3750	12:42:51.37	+37:51:00.0	J1242+3750			1.316	FSRQ	...
C1243+3627	12:43:12.74	+36:27:44.0		J1243.1+3627	J1243.1+3627	0.0	BLL	HSP
J1243+7442	12:43:45.03	+74:42:37.2	J1243+7442			0.782	FSRQ	...
J1243-0218	12:43:52.49	-02:18:38.4	J1243-0218			...	...	...
1RXSJ124510.5+57102	12:45:09.80	+57:09:54.6			J1245.1+5708	0.0	BLL	ISP
J1245-1617	12:45:53.09	-16:17:15.6	J1245-1617			...	...	...
J1247+1022	12:47:47.34	+10:22:31.6	J1247+1022			1.37	FSRQ	...
J1248+5820	12:48:18.78	+58:20:28.7	J1248+5820	J1248.2+5820	J1248.2+5820	0.0	BLL	ISP
J1248-0632	12:48:22.98	-06:32:09.8	J1248-0632			0.762	FSRQ	...

Continues

Table A.2

OVRO name	RA	DEC	CGRaBS name	1FGL name	2FGL name	z	Optical Class	SED class
RXJ1249.8+3708	12:49:46.60	+37:07:50.9			J1249.9+3705	0.0	BLL	HSP
J1251-1717	12:51:14.48	-17:17:13.2	J1251-1717			0.606	FSRQ	...
1RXS125117.4+103914	12:51:17.80	+10:39:05.1			J1251.2+1045	0.245	BLL	HSP
C1253+5301	12:53:11.92	+53:01:11.7			J1253.1+5302	0.0	BLL	ISP
J1253+0326	12:53:47.01	+03:26:30.4		J1253.7+0326		0.065	BLL	HSP
BBJ1253+6242	12:53:59.30	+62:42:57.6		J1254.0+6236	J1254.1+6237	0.0	BLL	HSP
J1254-1317	12:54:31.47	-13:17:16.3	J1254-1317			...	...	...
TXS1252+224	12:54:33.10	+22:11:02.9			J1254.4+2209	0.0	BLL	...
J1254+1141	12:54:38.26	+11:41:05.9	J1254+1141			0.87	FSRQ	...
J1255+1817	12:55:31.76	+18:17:50.9	J1255+1817			1.367	FSRQ	...
J1256-0547	12:56:11.17	-05:47:21.5	J1256-0547	J1256.2-0547	J1256.1-0547	0.536	FSRQ	LSP
J1256-1146	12:56:15.95	-11:46:37.4		J1256.5-1148	J1256.5-1145	0.058	AGN	...
1RXS125716.0+364713	12:57:16.50	+36:47:14.8			J1257.0+3650	0.531	BLL	HSP
J1257+3229	12:57:57.23	+32:29:29.3	J1257+3229	J1258.3+3227	J1258.2+3231	0.806	FSRQ	LSP
BQJ1258-1800	12:58:38.30	-18:00:03.0		J1258.4-1802	J1258.4-1801	1.956	FSRQ	...
J1300+1206	13:00:01.94	+12:06:22.1	J1300+1206			...	...	...
J1300+2830	13:00:28.53	+28:30:10.2	J1300+2830			0.645	FSRQ	...
J1300+5029	13:00:41.25	+50:29:36.8	J1300+5029			1.561	FSRQ	...
5C12.170	13:01:29.10	+33:37:00.8			J1301.6+3331	1.009	AGU	...
J1301+4634	13:01:32.60	+46:34:02.9	J1301+4634			0.205	GALAXY	...
J1302+5748	13:02:52.46	+57:48:37.6	J1302+5748			1.088	FSRQ	...
C1303+2433	13:03:03.21	+24:33:55.7		J1303.0+2433	J1303.1+2435	0.993	BLL	...
J1303-1051	13:03:13.87	-10:51:17.1	J1303-1051			...	BLL	...
CRJ1305+7854	13:05:00.02	+78:54:35.7		J1306.0+7852	J1305.7+7854	0.0	BLL	...
J1305-1033	13:05:33.02	-10:33:19.4	J1305-1033			0.286	FSRQ	...
J1306+5529	13:06:03.35	+55:29:43.8	J1306+5529			1.601	FSRQ	...
J1306-1718	13:06:32.65	-17:18:58.7	J1306-1718			...	...	...
J1308+3546	13:08:23.71	+35:46:37.2	J1308+3546	J1308.5+3550	J1308.5+3547	1.055	FSRQ	LSP
J1309+5557	13:09:09.75	+55:57:38.2	J1309+5557			1.629	FSRQ	...
BBJ1309+4305	13:09:25.50	+43:05:05.0		J1309.5+4304	J1309.4+4304	0.691	BLL	HSP
J1309+1154	13:09:33.93	+11:54:24.6	J1309+1154	J1309.2+1156	J1309.3+1154	0.0	BLL	...
J1310+0044	13:10:28.50	+00:44:08.9	J1310+0044			1.603	FSRQ	...
J1310+3220	13:10:28.66	+32:20:43.8	J1310+3220	J1310.6+3222	J1310.6+3222	0.997	FSRQ	LSP
J1310+4653	13:10:53.59	+46:53:52.2	J1310+4653			0.972	FSRQ	...
J1310+3233	13:10:59.40	+32:33:34.4	J1310+3233			1.65	FSRQ	...
J1311+5513	13:11:03.21	+55:13:54.3	J1311+5513			0.924	FSRQ	...

Continues

Table A.2

OVRO name	RA	DEC	CGRaBS name	1FGL name	2FGL name	z	Optical Class	SED class
RXJ1311.1+0035	13:11:06.40	+00:35:09.7			J1310.9+0036	0.0	BLL	HSP
J1312+4828	13:12:43.35	+48:28:30.9	J1312+4828	J1312.4+4827	J1312.8+4828	0.501	FSRQ	LSP
J1312-0424	13:12:50.90	-04:24:49.9	J1312-0424		J1313.0-0425	0.825	FSRQ	LSP
J1313+1027	13:13:41.65	+10:27:14.4	J1313+1027			2.901	FSRQ	...
J1314+2348	13:14:43.80	+23:48:26.7		J1314.7+2346	J1314.6+2348	0.0	BLL	ISP
J1314+5306	13:14:43.83	+53:06:27.7	J1314+5306			...	...	...
J1317+3425	13:17:36.49	+34:25:15.9	J1317+3425	J1317.8+3425	J1317.9+3426	1.055	FSRQ	LSP
J1317-1345	13:17:36.54	-13:45:32.7	J1317-1345			...	...	...
J1318-0607	13:18:33.71	-06:07:23.8	J1318-0607			2.734	FSRQ	...
PMNJ1318-1235	13:18:42.90	-12:35:03.6			J1318.9-1228	...	AGU	...
J1319-1217	13:19:12.07	-12:17:32.1	J1319-1217			0.86	FSRQ	...
J1319-1239	13:19:31.67	-12:39:25.1	J1319-1239			0.0080	AGN	...
J1321+2216	13:21:11.20	+22:16:12.1	J1321+2216	J1321.1+2214	J1321.1+2215	0.943	FSRQ	...
CRJ1321+8316	13:21:45.59	+83:16:13.4		J1321.3+8310		...	...	...
J1322-0937	13:22:36.91	-09:37:37.8	J1322-0937	J1322.7-0943		1.864	FSRQ	...
J1322+3912	13:22:55.66	+39:12:08.0	J1322+3912			2.985	FSRQ	...
4C+29.48	13:23:04.00	+29:41:14.7			J1323.0+2941	...	AGU	...
J1323+7942	13:23:51.57	+79:42:51.9	J1323+7942			1.97	FSRQ	...
J1324-1049	13:24:25.79	-10:49:23.2	J1324-1049			0.872	FSRQ	...
J1324+4743	13:24:29.35	+47:43:20.6	J1324+4743			2.26	FSRQ	...
J1325-0804	13:25:09.62	-08:04:48.4	J1325-0804			2.354	FSRQ	...
J1326-0500	13:26:54.61	-05:00:59.0	J1326-0500			1.882	FSRQ	...
J1327+2210	13:27:00.86	+22:10:50.2	J1327+2210	J1326.6+2213	J1326.8+2210	1.403	FSRQ	LSP
J1327+5008	13:27:25.12	+50:08:49.2	J1327+5008			1.012	FSRQ	...
J1327-1336	13:27:42.02	-13:36:00.2	J1327-1336			1.33	FSRQ	...
J1327+1223	13:27:54.68	+12:23:09.2	J1327+1223			0.95	FSRQ	...
1RXS132928.0-053132	13:29:28.00	-05:31:32.4			J1329.3-0528	0.576	AGN	...
J1329+3154	13:29:52.86	+31:54:11.0	J1329+3154			...	BLL	...
NVSSJ133025+700141	13:30:25.60	+70:01:40.9			J1330.9+7001	0.0	BLL	HSP
J1330+5202	13:30:42.60	+52:02:15.4	J1330+5202	J1331.0+5202		0.688	AGN	...
J1332-0509	13:32:04.46	-05:09:43.3	J1332-0509	J1331.9-0506	J1332.0-0508	2.15	FSRQ	LSP
J1332-1256	13:32:39.25	-12:56:15.3		J1332.6-1255	J1332.5-1255	1.492	FSRQ	...
J1332+4722	13:32:45.24	+47:22:22.7	J1332+4722	J1332.9+4728	J1332.7+4725	0.668	FSRQ	LSP
J1333+2725	13:33:07.49	+27:25:18.4	J1333+2725		J1332.7+2726	2.126	FSRQ	...
J1333+1649	13:33:35.78	+16:49:04.0	J1333+1649			2.097	FSRQ	...
J1333-1950	13:33:45.17	-19:50:42.4	J1333-1950			...	...	...

Continues

Table A.2

OVRO name	RA	DEC	CGRaBS name	1FGL name	2FGL name	z	Optical Class	SED class
CLJ1333+5057	13:33:53.78	+50:57:35.9		J1333.2+5056	J1333.5+5058	1.362	FSRQ	LSP
J1334-1150	13:34:04.19	-11:50:14.3	J1334-1150			1.402	FSRQ	...
J1335+4542	13:35:21.96	+45:42:38.2	J1335+4542			2.452	FSRQ	...
J1335+5844	13:35:25.93	+58:44:00.3	J1335+5844			...	...	...
J1336-0829	13:36:08.51	-08:29:51.8	J1336-0829			0.023	GALAXY	...
J1337+6532	13:37:16.06	+65:32:46.3	J1337+6532			0.946	FSRQ	...
J1337-1257	13:37:39.78	-12:57:24.7	J1337-1257	J1337.7-1255	J1337.7-1257	0.539	FSRQ	LSP
J1337+5501	13:37:49.64	+55:01:02.1	J1337+5501			1.099	FSRQ	...
FRBAJ1338+11	13:38:58.91	+11:53:17.6		J1338.9+1153	J1338.9+1152	0.0	BLL	...
BBJ1340+4410	13:40:29.79	+44:10:03.9		J1340.6+4406	J1340.5+4407	0.546	BLL	HSP
BBJ1341+3959	13:41:05.10	+39:59:45.4		J1341.3+3951		0.172	BLL	HSP
J1341+2816	13:41:15.28	+28:16:05.1	J1341+2816			1.275	FSRQ	...
J1342+2709	13:42:08.38	+27:09:30.6	J1342+2709			1.185	FSRQ	...
J1343+6602	13:43:45.96	+66:02:25.7	J1343+6602			0.766	FSRQ	...
J1344+6606	13:44:08.68	+66:06:11.6	J1344+6606			1.351	FSRQ	...
J1344-1723	13:44:14.40	-17:23:40.4	J1344-1723	J1344.2-1723	J1344.2-1723	2.506	FSRQ	...
C1345+4452	13:45:33.17	+44:52:59.6		J1345.4+4453	J1345.4+4453	2.534	FSRQ	LSP
J1345+0706	13:45:49.31	+07:06:31.1		J1346.0+0703	J1345.9+0706	1.095	FSRQ	LSP
J1347+1835	13:47:23.49	+18:35:37.6	J1347+1835			2.169	FSRQ	...
J1349-1110	13:49:03.19	-11:10:00.8	J1349-1110			0.141	FSRQ	...
J1349-1132	13:49:31.44	-11:32:53.9	J1349-1132			0.341	FSRQ	...
J1349+5341	13:49:34.66	+53:41:17.0	J1349+5341			0.979	FSRQ	...
J1350+0940	13:50:22.13	+09:40:10.6	J1350+0940			0.132	AGN	...
J1350-1634	13:50:36.15	-16:34:49.5	J1350-1634			0.086	FSRQ	...
J1350+3034	13:50:52.73	+30:34:53.6	J1350+3034	J1351.0+3035		0.714	FSRQ	LSP
J1350+6428	13:50:55.71	+64:28:56.8	J1350+6428			...	...	...
PKS1348+007	13:51:04.30	+00:31:19.8			J1351.1+0032	2.084	FSRQ	...
J1351+0830	13:51:16.92	+08:30:39.9	J1351+0830			1.429	FSRQ	...
BBJ1351+1114	13:51:20.90	+11:14:52.0		J1351.5+1115	J1351.4+1115	0.0	BLL	HSP
J1351+5542	13:51:58.20	+55:42:10.9	J1351+5542			0.389	FSRQ	...
J1353+1435	13:53:22.84	+14:35:39.3		J1353.3+1434	J1353.3+1435	0.0	BLL	LSP
J1353+7532	13:53:23.16	+75:32:57.7	J1353+7532			1.619	FSRQ	...
FIRSTJ135426.6+3706	13:54:26.70	+37:06:54.2			J1354.5+3703	0.0	BLL	...
CR1354-1041	13:54:46.52	-10:41:02.7		J1354.9-1041	J1354.7-1047	0.332	FSRQ	LSP
J1357-1527	13:57:11.24	-15:27:28.8	J1357-1527			1.89	FSRQ	...
RXJ1357.6+0128	13:57:38.50	+01:28:13.4			J1358.0+0137	0.0	BLL	HSP

Continues

Table A.2

OVRO name	RA	DEC	CGRaBS name	1FGL name	2FGL name	z	Optical Class	SED class
J1357+7643	13:57:55.37	+76:43:21.0	J1357+7643	J1358.1+7646	J1358.1+7644	1.585	FSRQ	LSP
J1359+5544	13:59:05.74	+55:44:29.4		J1359.1+5539	J1359.4+5541	1.014	FSRQ	...
J1359+4011	13:59:38.10	+40:11:38.3	J1359+4011			0.407	FSRQ	...
J1400-1858	14:00:03.87	-18:58:11.0	J1400-1858			0.114	FSRQ	...
J1401+5835	14:01:45.70	+58:35:42.3	J1401+5835			1.924	FSRQ	...
J1405+0415	14:05:01.12	+04:15:35.8	J1405+0415			3.215	FSRQ	...
J1405-1440	14:05:32.88	-14:40:18.2	J1405-1440			1.096	FSRQ	...
J1406+3433	14:06:53.84	+34:33:37.3	J1406+3433			2.56	FSRQ	...
J1407+2827	14:07:00.39	+28:27:14.6	J1407+2827			0.077	AGN	...
J1408+6854	14:08:19.07	+68:54:50.8	J1408+6854			1.272	FSRQ	...
1406-076	14:08:56.48	-07:52:26.7		J1408.9-0751	J1408.8-0751	1.494	FSRQ	LSP
BZBJ1410+2820	14:10:29.40	+28:20:55.2			J1410.3+2811	0.0	BLL	HSP
J1410+0731	14:10:35.08	+07:31:21.5	J1410+0731			0.901	FSRQ	...
J1412+1334	14:12:36.37	+13:34:38.2	J1412+1334			...	...	...
J1415+0832	14:15:09.92	+08:32:05.4	J1415+0832			0.327	FSRQ	...
J1415+1320	14:15:58.82	+13:20:23.7	J1415+1320		J1416.0+1323	0.247	AGU	LSP
J1416-1705	14:16:34.38	-17:05:45.6	J1416-1705			...	...	...
2E1415+2557	14:17:56.64	+25:43:24.5		J1417.8+2541	J1418.1+2539	0.237	BLL	HSP
SDSSJ141826.	14:18:26.30	-02:33:34.0		J1418.3-0235	J1418.4-0234	0.0	BLL	...
1RXS141901.8+773229	14:19:00.40	+77:32:26.1			J1419.4+7730	...	AGU	HSP
CT_1419-0838	14:19:22.43	-08:38:30.4			J1419.4-0835	...	AGU	LSP
J1419+5423	14:19:46.60	+54:23:14.8	J1419+5423		J1420.2+5422	0.153	BLL	LSP
J1419+3821	14:19:46.62	+38:21:48.5	J1419+3821		J1419.4+3820	1.831	FSRQ	LSP
J1419+2706	14:19:59.30	+27:06:25.6	J1419+2706			0.536	FSRQ	...
J1420+1703	14:20:20.89	+17:03:29.2	J1420+1703			1.854	FSRQ	...
PMNJ1420-1118	14:21:00.10	-11:18:19.9			J1421.1-1117	...	AGU	...
J1421+4645	14:21:23.07	+46:45:48.0	J1421+4645			1.668	FSRQ	...
J1421-1931	14:21:36.98	-19:31:18.7	J1421-1931			...	...	...
J1422+3223	14:22:30.38	+32:23:10.4	J1422+3223			0.685	FSRQ	...
1ES1421+582	14:22:38.89	+58:01:55.5		J1422.2+5757		...	BLL	HSP
CLJ1423+3737	14:23:04.61	+37:37:30.6		J1422.7+3743		...	BLL	...
J1423+4802	14:23:06.16	+48:02:10.8	J1423+4802			2.22	FSRQ	...
J1423+5055	14:23:14.19	+50:55:37.3	J1423+5055			0.276	FSRQ	...
J1424+2256	14:24:38.09	+22:56:00.6	J1424+2256			3.62	FSRQ	...
CLJ1424+3615	14:24:55.51	+36:15:36.1		J1425.0+3614	J1425.1+3615	0.0	BLL	ISP
J1425+1424	14:25:49.02	+14:24:56.9	J1425+1424			0.78	FSRQ	...

Continues

Table A.2

OVRO name	RA	DEC	CGRaBS name	1FGL name	2FGL name	z	Optical Class	SED class
BBJ1426+3404	14:26:07.70	+34:04:26.0		J1426.0+3403	J1426.1+3406	0.0	BLL	ISP
J1426+3625	14:26:37.09	+36:25:09.6	J1426+3625			1.091	FSRQ	...
CR1427+2347	14:27:00.39	+23:48:00.0		J1426.9+2347	J1427.0+2347	0.0	BLL	HSP
J1428+2724	14:28:31.76	+27:24:32.2	J1428+2724			0.014	AGN	...
H1426+428	14:28:32.70	+42:40:20.0		J1428.7+4239	J1428.6+4240	0.129	BLL	HSP
J1430+1043	14:30:09.74	+10:43:26.9	J1430+1043			1.71	FSRQ	...
J1430+3649	14:30:40.58	+36:49:03.9	J1430+3649			0.566	BLL	...
J1431+3952	14:31:20.54	+39:52:41.5	J1431+3952			1.215	FSRQ	...
J1433-1548	14:33:21.47	-15:48:44.6	J1433-1548			1.573	FSRQ	...
J1434+4203	14:34:05.70	+42:03:16.0	J1434+4203	J1433.9+4204	J1433.8+4205	1.24	FSRQ	...
J1434+1952	14:34:39.80	+19:52:00.8	J1434+1952			1.382	FSRQ	...
J1435+2021	14:35:21.95	+20:21:17.9			J1435.1+2022	0.748	BLL	...
J1435+3012	14:35:35.40	+30:12:24.5	J1435+3012			1.568	FSRQ	...
J1436+2321	14:36:40.99	+23:21:03.3	J1436+2321	J1436.9+2314	J1436.9+2319	1.548	FSRQ	LSP
J1436+6336	14:36:45.80	+63:36:37.9	J1436+6336			2.066	FSRQ	...
J1436-1846	14:36:56.77	-18:46:34.2	J1436-1846			...	...	...
BBJ1436+5639	14:36:57.72	+56:39:24.9		J1437.0+5640	J1437.1+5640	0.0	BLL	HSP
J1437+0405	14:37:08.19	+04:05:34.3	J1437+0405			2.025	FSRQ	...
J1437+3119	14:37:39.50	+31:19:01.0	J1437+3119			1.357	FSRQ	...
J1438+3710	14:38:53.61	+37:10:35.4	J1438+3710			2.401	FSRQ	...
J1439+2114	14:39:08.90	+21:14:50.8	J1439+2114			...	...	...
PG1437+398	14:39:17.50	+39:32:42.0		J1439.2+3930	J1439.2+3932	0.349	BLL	HSP
J1439+4958	14:39:46.98	+49:58:05.5	J1439+4958		J1440.3+4948	0.0	BLL	ISP
J1439-1531	14:39:56.88	-15:31:50.5	J1439-1531			...	BLL	...
C1440+0610	14:40:52.94	+06:10:16.2		J1440.9+0613	J1440.9+0611	0.0	BLL	ISP
J1442+3234	14:42:00.14	+32:34:20.3	J1442+3234			2.12	FSRQ	...
CLJ1442+4348	14:42:07.15	+43:48:36.7		J1442.1+4348	J1442.0+4352	0.0	BLL	...
BBJ1442+1200	14:42:48.20	+12:00:40.0		J1442.8+1158	J1442.7+1159	0.163	BLL	HSP
J1443+2501	14:43:56.89	+25:01:44.5		J1443.8+2457	J1444.1+2500	0.939	FSRQ	LSP
J1445-1614	14:45:09.58	-16:14:10.7	J1445-1614			1.195	FSRQ	...
J1445-1629	14:45:53.39	-16:29:01.6	J1445-1629			...	...	...
J1446+1721	14:46:35.35	+17:21:07.6	J1446+1721			1.026	FSRQ	...
RXJ1448.0+36	14:48:00.60	+36:08:31.0		J1447.9+3608	J1448.0+3608	0.0	BLL	HSP
J1448+7601	14:48:28.78	+76:01:11.6	J1448+7601			0.899	FSRQ	...
J1450+0910	14:50:31.17	+09:10:28.0	J1450+0910			2.612	FSRQ	...
CLJ1450+5201	14:50:59.99	+52:01:11.7		J1451.0+5204		...	BLL	...

Continues

Table A.2

OVRO name	RA	DEC	CGRaBS name	1FGL name	2FGL name	z	Optical Class	SED class
J1451-0127	14:51:47.41	-01:27:35.3	J1451-0127			1.314	FSRQ	...
J1453+1036	14:53:01.49	+10:36:17.2	J1453+1036			2.27	FSRQ	...
J1453+3505	14:53:18.55	+35:05:39.4	J1453+3505			0.721	FSRQ	...
J1453+2648	14:53:53.61	+26:48:33.5	J1453+2648			...	BLL	...
C1454+5124	14:54:27.12	+51:24:33.7		J1454.6+5125	J1454.4+5123	0.0	BLL	ISP
J1456+5048	14:56:08.12	+50:48:36.3	J1456+5048			...	...	...
J1457+0749	14:57:38.13	+07:49:54.7	J1457+0749			...	...	...
J1458+3720	14:58:44.80	+37:20:21.6	J1458+3720			0.333	BLL	...
J1459-1810	14:59:28.76	-18:10:45.2	J1459-1810			0.235	FSRQ	...
J1459+4442	14:59:35.46	+44:42:07.9	J1459+4442			3.402	FSRQ	...
J1500+4751	15:00:48.66	+47:51:15.5	J1500+4751			...	BLL	...
MS14588+2249	15:01:01.90	+22:38:06.0		J1501.1+2237	J1501.0+2238	0.235	BLL	HSP
J1502-1508	15:02:25.02	-15:08:52.5	J1502-1508			...	...	...
BBJ1503-1541	15:03:40.60	-15:41:13.9		J1503.5-1544	J1503.7-1541	0.0	BLL	...
CLJ1503+4759	15:03:48.00	+47:59:31.0		J1503.3+4759		...	BLL	LSP
J1504+0813	15:04:24.12	+08:13:39.6	J1504+0813			2.832	FSRQ	...
J1504+1029	15:04:24.98	+10:29:39.2	J1504+1029	J1504.4+1029	J1504.3+1029	1.839	FSRQ	LSP
J1505+0326	15:05:06.48	+03:26:30.8	J1505+0326	J1505.0+0328	J1505.1+0324	0.409	NLSyI	...
J1506+3730	15:06:09.53	+37:30:51.1	J1506+3730	J1505.8+3725	J1506.0+3729	0.674	FSRQ	...
J1506+8319	15:06:24.75	+83:19:28.1	J1506+8319			2.577	FSRQ	...
J1506+4933	15:06:44.11	+49:33:55.8	J1506+4933			1.395	FSRQ	...
PMNJ1506+0814	15:06:44.40	+08:13:58.5			J1506.6+0806	0.0	BLL	HSP
J1506+4239	15:06:53.04	+42:39:23.0	J1506+4239			0.587	FSRQ	...
J1507-1652	15:07:04.79	-16:52:30.3	J1507-1652			0.876	FSRQ	...
J1508-1548	15:08:35.70	-15:48:31.5	J1508-1548			2.499	FSRQ	...
RBS1467	15:08:42.50	+27:09:08.3			J1508.5+2709	0.27	BLL	HSP
SBS1508+561	15:09:47.80	+55:56:16.9			J1509.7+5556	0.0	BLL	HSP
J1510-1121	15:10:44.44	-11:21:39.7	J1510-1121			...	...	...
PKS1508-05	15:10:53.59	-05:43:07.4		J1511.1-0545	J1510.9-0545	1.185	FSRQ	LSP
J1511+0518	15:11:41.26	+05:18:09.3	J1511+0518			0.084	AGN	...
PKS1509+022	15:12:15.75	+02:03:17.0		J1512.3+0201	J1512.2+0201	0.219	FSRQ	LSP
PKS1510-089	15:12:50.53	-09:05:59.8		J1512.8-0906	J1512.8-0906	0.36	FSRQ	LSP
J1513-1012	15:13:44.89	-10:12:00.3	J1513-1012			1.513	FSRQ	...
BQJ1514+4450	15:14:36.60	+44:50:04.0		J1514.7+4447	J1514.6+4449	0.57	FSRQ	ISP
J1516+0015	15:16:40.22	+00:15:01.9	J1516+0015			0.052	NLRG	...
J1516+1932	15:16:56.80	+19:32:13.0	J1516+1932	J1516.9+1928	J1516.9+1925	0.0	BLL	...

Continues

Table A.2

OVRO name	RA	DEC	CGRaBS name	1FGL name	2FGL name	z	Optical Class	SED class
J1517+1332	15:17:17.15	+13:32:24.5	J1517+1332			1.499	FSRQ	...
BBJ1517+6525	15:17:47.60	+65:25:23.0		J1517.8+6530	J1518.0+6526	0.702	BLL	HSP
B31518+423	15:20:39.72	+42:11:11.5		J1519.7+4216		0.484	FSRQ	...
NVSSJ152048-034850	15:20:48.70	-03:48:50.1			J1520.8-0349	0.0	BLL	HSP
J1521+4336	15:21:49.61	+43:36:39.3	J1521+4336		J1522.0+4348	2.171	FSRQ	LSP
J1522+3144	15:22:09.99	+31:44:14.4	J1522+3144	J1522.1+3143	J1522.1+3144	1.484	FSRQ	LSP
J1526-0425	15:26:15.02	-04:25:10.0	J1526-0425			1.492	FSRQ	...
J1526+6650	15:26:42.87	+66:50:54.6	J1526+6650			3.02	FSRQ	...
87GB152947.5+574636	15:30:58.30	+57:36:24.9			J1531.0+5725	0.0	BLL	...
BUJ1532+3016	15:32:02.23	+30:16:28.8		J1531.8+3018		0.065	BLL	HSP
J1532-1319	15:32:45.37	-13:19:10.0	J1532-1319			...	...	...
J1533-0421	15:33:14.22	-04:21:16.6	J1533-0421			0.84	FSRQ	...
RGBJ1534+372	15:34:47.20	+37:15:53.8			J1535.4+3720	0.143	BLL	ISP
J1534+0131	15:34:52.45	+01:31:04.2	J1534+0131			1.42	FSRQ	...
J1535+4957	15:35:52.04	+49:57:39.1	J1535+4957			1.119	FSRQ	...
CLJ1537+8154	15:37:00.09	+81:54:31.0		J1536.6+8200		...	...	...
J1537-1527	15:37:41.57	-15:27:12.5	J1537-1527			1.766	FSRQ	...
J1538+1444	15:38:03.42	+14:44:07.5	J1538+1444			...	...	...
J1538-1655	15:38:50.94	-16:55:27.0	J1538-1655			...	...	...
J1539+3104	15:39:16.17	+31:04:07.7	J1539+3104			1.211	FSRQ	...
J1539+2744	15:39:39.14	+27:44:38.3	J1539+2744	J1539.7+2747	J1539.5+2747	2.191	FSRQ	LSP
1544+820	15:40:16.01	+81:55:05.5			J1538.1+8159	0.0	BLL	HSP
J1540+1447	15:40:49.49	+14:47:45.9	J1540+1447		J1540.4+1438	0.605	BLL	LSP
CR1542+6129	15:42:56.95	+61:29:55.4		J1542.9+6129	J1542.9+6129	0.0	BLL	ISP
J1544+3240	15:44:05.66	+32:40:48.3	J1544+3240			1.05	FSRQ	...
J1545+5135	15:45:02.82	+51:35:00.9	J1545+5135			1.93	FSRQ	...
1RXSJ154604.6+08191	15:46:04.20	+08:19:14.9			J1546.1+0820	0.0	BLL	HSP
J1548+1727	15:48:55.10	+17:27:41.0	J1548+1727			1.874	FSRQ	...
J1549+5038	15:49:17.47	+50:38:05.8	J1549+5038			2.175	FSRQ	...
J1549+0237	15:49:29.44	+02:37:01.2	J1549+0237	J1549.3+0235	J1549.5+0237	0.414	FSRQ	LSP
J1550+0527	15:50:35.27	+05:27:10.5	J1550+0527	J1550.7+0527	J1550.7+0526	1.417	FSRQ	LSP
J1551+5806	15:51:58.21	+58:06:44.5	J1551+5806			1.32	FSRQ	...
J1552+0850	15:52:03.26	+08:50:47.3			J1551.9+0855	0.0	BLL	...
CR1553+1256	15:53:32.70	+12:56:51.7		J1553.4+1255	J1553.5+1255	1.308	FSRQ	...
J1555+1111	15:55:43.04	+11:11:24.4	J1555+1111	J1555.7+1111	J1555.7+1111	0.0	BLL	HSP
J1557-0001	15:57:51.44	-00:01:50.4	J1557-0001			1.772	FSRQ	...

Continues

Table A.2

OVRO name	RA	DEC	CGRaBS name	1FGL name	2FGL name	z	Optical Class	SED class
J1558-1409	15:58:21.96	-14:09:59.0	J1558-1409			0.097	AGN	...
J1558+5625	15:58:48.29	+56:25:14.1		J1558.9+5627	J1559.0+5627	0.3	BLL	ISP
J1559+0304	15:59:30.98	+03:04:48.3	J1559+0304			3.891	FSRQ	...
WNB1609.6+8517	16:00:31.30	+85:09:48.4			J1558.3+8513	...	AGU	LSP
J1602+3326	16:02:07.26	+33:26:53.1	J1602+3326			1.1	NLRG	...
J1602+2646	16:02:39.63	+26:46:06.0	J1602+2646			0.373	FSRQ	...
J1603-1007	16:03:18.79	-10:07:21.3	J1603-1007			0.959	FSRQ	...
J1603+1554	16:03:38.06	+15:54:02.4	J1603+1554			0.109	FSRQ	...
J1603+1105	16:03:41.93	+11:05:48.7	J1603+1105			0.143	BLL	...
J1603+5730	16:03:55.93	+57:30:54.4	J1603+5730			2.858	FSRQ	...
J1604+5714	16:04:37.36	+57:14:36.7	J1604+5714	J1604.3+5710	J1604.6+5710	0.72	FSRQ	LSP
J1605-1139	16:05:18.22	-11:39:50.0	J1605-1139			...	...	...
J1605+3001	16:05:33.04	+30:01:29.7	J1605+3001			2.404	FSRQ	...
J1606+3124	16:06:08.52	+31:24:46.5	J1606+3124			4.56	FSRQ	...
J1606+2717	16:06:58.30	+27:17:05.6	J1606+2717			0.934	FSRQ	...
C1607+1551	16:07:06.43	+15:51:34.5		J1607.1+1552	J1607.0+1552	0.496	BLL	LSP
J1608+1029	16:08:46.20	+10:29:07.8	J1608+1029	J1609.0+1031	J1608.5+1029	1.232	FSRQ	LSP
J1610+2414	16:10:42.03	+24:14:49.0	J1610+2414			1.449	FSRQ	...
J1611+1856	16:11:49.04	+18:56:38.1	J1611+1856			1.776	FSRQ	...
J1613+4223	16:13:04.80	+42:23:18.9	J1613+4223			...	...	...
J1613+3412	16:13:41.06	+34:12:47.9	J1613+3412	J1613.5+3411	J1613.4+3409	1.4	FSRQ	LSP
J1616+4632	16:16:03.77	+46:32:25.2		J1616.1+4637		0.95	FSRQ	...
J1616+0459	16:16:37.56	+04:59:32.7	J1616+0459			3.199	FSRQ	...
J1617-1122	16:17:06.01	-11:22:38.6	J1617-1122			...	...	...
J1617-1941	16:17:27.09	-19:41:32.0	J1617-1941			...	...	...
J1617+0246	16:17:49.91	+02:46:43.1	J1617+0246			1.341	FSRQ	...
J1618+0819	16:18:26.93	+08:19:50.7	J1618+0819			0.445	FSRQ	...
J1619+2247	16:19:14.83	+22:47:47.9	J1619+2247			1.987	FSRQ	...
J1619-1817	16:19:16.68	-18:17:21.8	J1619-1817			...	...	...
J1620+4901	16:20:31.22	+49:01:53.3	J1620+4901			1.513	FSRQ	...
J1623+6624	16:23:04.52	+66:24:01.1	J1623+6624			0.203	FSRQ	...
J1623+3909	16:23:07.62	+39:09:32.4	J1623+3909			1.975	FSRQ	...
J1623+0741	16:23:58.25	+07:41:30.5	J1623+0741			1.301	FSRQ	...
J1624+5741	16:24:24.81	+57:41:16.3	J1624+5741			0.789	FSRQ	...
J1624+5652	16:24:32.18	+56:52:28.0	J1624+5652			...	BLL	...
4C-06.46	16:24:32.92	-06:49:49.7		J1624.7-0642		...	...	...

Continues

Table A.2

OVRO name	RA	DEC	CGRaBS name	1FGL name	2FGL name	z	Optical Class	SED class
J1624+2748	16:24:35.72	+27:48:57.7	J1624+2748			...	...	...
J1625+4134	16:25:57.67	+41:34:40.6	J1625+4134			2.55	FSRQ	...
J1628-1415	16:28:46.62	-14:15:42.1	J1628-1415			1.026	FSRQ	...
J1630+0701	16:30:41.82	+07:01:09.1	J1630+0701			0.736	FSRQ	...
J1630+5221	16:30:43.15	+52:21:38.6		J1630.2+5220	J1630.4+5218	0.0	BLL	ISP
J1631+4927	16:31:16.54	+49:27:39.5	J1631+4927			0.52	FSRQ	...
J1632+8232	16:32:31.98	+82:32:16.4	J1632+8232	J1635.4+8228		0.025	AGN	...
J1635+3808	16:35:15.49	+38:08:04.5	J1635+3808	J1635.0+3808	J1635.2+3810	1.813	FSRQ	LSP
J1636+2112	16:36:38.19	+21:12:55.7	J1636+2112			1.802	FSRQ	...
J1637+4717	16:37:45.13	+47:17:33.8	J1637+4717		J1637.7+4714	0.735	FSRQ	LSP
J1638+5720	16:38:13.46	+57:20:24.0	J1638+5720			0.751	FSRQ	...
J1639+5357	16:39:39.84	+53:57:47.1	J1639+5357			1.977	FSRQ	...
J1639+1632	16:39:42.14	+16:32:21.8	J1639+1632			...	...	...
J1640-0011	16:40:10.59	-00:11:47.5	J1640-0011			0.651	FSRQ	...
J1640+3946	16:40:29.63	+39:46:46.0	J1640+3946		J1640.7+3945	1.66	FSRQ	LSP
J1640+1144	16:40:58.89	+11:44:04.2		J1641.0+1143	J1641.0+1141	0.078	AGN	...
J1641+2257	16:41:25.23	+22:57:04.1	J1641+2257			2.063	FSRQ	...
J1642-0621	16:42:02.18	-06:21:23.6	J1642-0621		J1641.6-0614	0.0	BLL	...
J1642+6856	16:42:07.85	+68:56:39.7	J1642+6856			0.751	FSRQ	...
J1642+3948	16:42:58.81	+39:48:37.0	J1642+3948			0.593	FSRQ	...
J1644-1804	16:44:35.74	-18:04:32.5	J1644-1804			...	...	...
J1644-0743	16:44:52.06	-07:43:43.1	J1644-0743			0.139	NLRG	...
J1646+4059	16:46:56.86	+40:59:17.2	J1646+4059			0.835	FSRQ	...
J1647+4950	16:47:34.91	+49:50:00.6	J1647+4950	J1647.4+4948	J1647.5+4950	0.047	AGN	...
J1648+2224	16:48:01.54	+22:24:33.1	J1648+2224			...	...	...
CLJ1649+5235	16:49:24.99	+52:35:15.0			J1649.6+5238	0.0	BLL	...
J1649+0412	16:49:27.67	+04:12:04.0	J1649+0412			...	...	...
J1650+0824	16:50:37.56	+08:24:52.2	J1650+0824		J1650.8+0830	1.965	FSRQ	...
J1651+0129	16:51:03.66	+01:29:23.5	J1651+0129			...	...	...
J1652+0618	16:52:01.40	+06:18:55.3	J1652+0618			...	...	...
J1652+3902	16:52:58.51	+39:02:49.8	J1652+3902			1.299	FSRQ	...
J1653+3107	16:53:29.91	+31:07:56.9	J1653+3107			1.298	FSRQ	...
J1653-1551	16:53:34.20	-15:51:29.9	J1653-1551			...	...	...
J1653+3945	16:53:52.22	+39:45:36.6	J1653+3945	J1653.9+3945	J1653.9+3945	0.034	BLL	HSP
J1655+4233	16:55:18.79	+42:33:39.8	J1655+4233			...	...	...
J1656+1826	16:56:34.09	+18:26:26.4	J1656+1826			2.551	FSRQ	...

Continues

Table A.2

OVRO name	RA	DEC	CGRaBS name	1FGL name	2FGL name	z	Optical Class	SED class
J1656+6012	16:56:48.25	+60:12:16.5		J1656.9+6017		0.623	FSRQ	LSP
PMNJ1657-1021	16:57:32.60	-10:21:16.3			J1657.1-1027	...	AGU	...
J1657+4808	16:57:46.88	+48:08:33.0	J1657+4808		J1657.9+4809	1.669	FSRQ	LSP
J1658+3443	16:58:01.42	+34:43:28.4	J1658+3443			1.939	FSRQ	...
J1658+4737	16:58:02.78	+47:37:49.3	J1658+4737			1.622	FSRQ	...
J1658+0515	16:58:33.45	+05:15:16.4	J1658+0515			0.879	FSRQ	...
J1658-0739	16:58:44.06	-07:39:17.7	J1658-0739			3.742	FSRQ	...
J1700+6830	17:00:09.30	+68:30:07.0	J1700+6830	J1700.1+6830	J1700.2+6831	0.301	FSRQ	LSP
J1701+3954	17:01:24.64	+39:54:37.1	J1701+3954			0.507	BLL	...
J1701-1903	17:01:26.89	-19:03:31.6	J1701-1903			...	...	...
J1702+1502	17:02:21.72	+15:02:06.1	J1702+1502			1.041	FSRQ	...
J1707-1415	17:07:20.39	-14:15:23.1	J1707-1415			...	...	...
J1707+1122	17:07:32.48	+11:22:00.7	J1707+1122			2.406	FSRQ	...
J1707+0148	17:07:34.42	+01:48:45.7	J1707+0148			2.576	FSRQ	...
J1707+1331	17:07:45.63	+13:31:05.2	J1707+1331			0.936	FSRQ	...
J1709-1728	17:09:34.35	-17:28:53.4	J1709-1728			...	...	...
J1709+4318	17:09:41.09	+43:18:44.5	J1709+4318	J1709.6+4320	J1709.7+4319	1.027	FSRQ	LSP
J1712+6053	17:12:12.38	+60:53:28.9	J1712+6053			1.684	FSRQ	...
J1712-1820	17:12:31.70	-18:20:02.8	J1712-1820			...	...	...
J1713+4916	17:13:35.15	+49:16:32.6	J1713+4916			1.552	FSRQ	...
J1716+2152	17:16:11.19	+21:52:13.6	J1716+2152			0.359	FSRQ	...
J1716+6836	17:16:13.94	+68:36:38.7	J1716+6836		J1714.8+6836	0.777	FSRQ	LSP
J1716-0452	17:16:26.49	-04:52:11.9	J1716-0452			1.026	FSRQ	...
J1719-1420	17:19:02.02	-14:20:19.0	J1719-1420			0.64	FSRQ	...
J1719+1745	17:19:13.05	+17:45:06.4	J1719+1745	J1719.2+1745	J1719.3+1744	0.137	BLL	LSP
J1719+4858	17:19:14.49	+48:58:49.4	J1719+4858			0.025	AGN	...
J1719+4804	17:19:38.26	+48:04:12.3	J1719+4804			1.083	FSRQ	...
J1719+0817	17:19:52.21	+08:17:03.5	J1719+0817			1.185	FSRQ	...
J1721+3542	17:21:09.49	+35:42:16.1	J1721+3542			0.283	FSRQ	...
J1722+5856	17:22:36.73	+58:56:22.3	J1722+5856			1.979	FSRQ	...
J1722+6105	17:22:40.06	+61:05:59.8	J1722+6105			2.058	FSRQ	...
J1722+2815	17:22:42.16	+28:15:00.0	J1722+2815			0.945	FSRQ	...
J1722+1013	17:22:44.58	+10:13:35.8		J1722.5+1012	J1722.7+1013	0.732	FSRQ	LSP
C1724+4004	17:24:05.43	+40:04:36.5		J1724.0+4002	J1724.0+4003	1.049	FSRQ	...
J1724+3303	17:24:14.19	+33:03:04.0	J1724+3303			1.87	FSRQ	...
J1724+1648	17:24:21.40	+16:48:19.0	J1724+1648			...	...	...

Continues

Table A.2

OVRO name	RA	DEC	CGRaBS name	1FGL name	2FGL name	z	Optical Class	SED class
J1724-1443	17:24:46.97	-14:43:59.5	J1724-1443			0.899	FSRQ	...
J1725+1152	17:25:04.34	+11:52:15.5	J1725+1152	J1725.0+1151	J1725.0+1151	0.0	BLL	HSP
J1725+3026	17:25:17.50	+30:26:40.9	J1725+3026			0.978	FSRQ	...
BBJ1725+5851	17:25:35.00	+58:51:39.0		J1725.5+5854	J1725.2+5853	0.0	BLL	ISP
J1726+3213	17:26:35.12	+32:13:23.0	J1726+3213			1.094	FSRQ	...
J1726+2717	17:26:53.42	+27:17:16.4	J1726+2717			0.535	FSRQ	...
J1727+5510	17:27:23.47	+55:10:53.5	J1727+5510			0.247	FSRQ	...
J1727+4530	17:27:27.65	+45:30:39.7	J1727+4530	J1727.3+4525	J1727.1+4531	0.717	FSRQ	LSP
J1728+1215	17:28:07.05	+12:15:39.5	J1728+1215		J1727.9+1220	0.583	FSRQ	...
J1728+5013	17:28:18.62	+50:13:10.5	J1728+5013		J1728.2+5015	0.055	BLL	HSP
J1728+0427	17:28:24.95	+04:27:04.9	J1728+0427	J1728.2+0431	J1728.2+0429	0.293	FSRQ	LSP
PKS1728+004	17:30:35.00	+00:24:38.7		J1730.4+0008	J1730.7+0023	1.335	FSRQ	...
CRJ1730+3714	17:30:47.05	+37:14:55.1		J1730.8+3716	J1731.3+3718	0.204	BLL	ISP
J1733-1304	17:33:02.71	-13:04:49.5	J1733-1304	J1733.0-1308	J1733.1-1307	0.902	FSRQ	LSP
J1733-0456	17:33:33.01	-04:56:02.0	J1733-0456			...	...	...
J1734+3857	17:34:20.58	+38:57:51.4	J1734+3857	J1734.4+3859	J1734.3+3858	0.975	FSRQ	LSP
J1735-1117	17:35:27.18	-11:17:34.5		J1735.4-1118		...	...	...
J1735+3616	17:35:48.09	+36:16:45.6	J1735+3616			0.893	FSRQ	...
J1735+5049	17:35:49.01	+50:49:11.6	J1735+5049			...	...	...
NVSSJ173605+203301	17:36:05.20	+20:33:00.7			J1735.9+2033	0.0	BLL	HSP
J1736+0631	17:36:28.59	+06:31:47.5	J1736+0631			2.388	FSRQ	...
J1738+4008	17:38:19.12	+40:08:18.2	J1738+4008			3.591	FSRQ	...
J1738+3224	17:38:40.50	+32:24:09.1	J1738+3224			0.126	FSRQ	...
J1739+4955	17:39:27.40	+49:55:03.4	J1739+4955		J1739.5+4955	1.545	FSRQ	LSP
J1739+3358	17:39:35.36	+33:58:08.2	J1739+3358			1.626	FSRQ	...
J1739+4737	17:39:57.13	+47:37:58.4	J1739+4737		J1740.3+4738	0.954	FSRQ	...
J1740-0811	17:40:01.57	-08:11:14.8	J1740-0811			...	...	...
J1740+2211	17:40:05.87	+22:11:01.0	J1740+2211			1.406	FSRQ	...
J1740+4506	17:40:06.37	+45:06:50.4	J1740+4506			2.788	FSRQ	...
J1740+5211	17:40:36.98	+52:11:43.4	J1740+5211		J1740.2+5212	1.379	FSRQ	LSP
J1740+4348	17:40:48.96	+43:48:16.2	J1740+4348			2.246	FSRQ	...
J1741+4751	17:41:34.82	+47:51:32.6	J1741+4751			...	...	...
J1742+5945	17:42:32.01	+59:45:06.7		J1742.1+5947	J1742.1+5948	0.0	BLL	ISP
J1743+3747	17:43:47.64	+37:47:53.8	J1743+3747			1.958	FSRQ	...
C1743+1935	17:43:57.83	+19:35:09.0		J1744.2+1934	J1744.1+1934	0.083	BLL	HSP
J1743-0350	17:43:58.86	-03:50:04.6	J1743-0350			1.057	FSRQ	...

Continues

Table A.2

OVRO name	RA	DEC	CGRaBS name	1FGL name	2FGL name	z	Optical Class	SED class
J1745+2252	17:45:04.66	+22:52:48.0	J1745+2252			1.884	FSRQ	...
J1745-0753	17:45:27.10	-07:53:03.8	J1745-0753	J1745.6-0751	J1745.5-0751	0.0	BLL	LSP
J1745+1720	17:45:35.21	+17:20:01.4	J1745+1720			1.702	FSRQ	...
J1747+4658	17:47:26.65	+46:58:50.9	J1747+4658			1.484	BLL	...
J1748+3404	17:48:05.82	+34:04:01.2	J1748+3404			2.764	FSRQ	...
J1748+7005	17:48:32.84	+70:05:50.8	J1748+7005	J1748.5+7004	J1748.8+7006	0.77	BLL	ISP
J1749+4321	17:49:00.36	+43:21:51.3	J1749+4321	J1749.0+4323	J1749.1+4323	0.0	BLL	LSP
J1751+0939	17:51:32.82	+09:39:00.7	J1751+0939	J1751.5+0937	J1751.5+0938	0.322	BLL	LSP
J1752+1734	17:52:46.01	+17:34:20.3	J1752+1734			0.507	FSRQ	...
J1753+4409	17:53:22.65	+44:09:45.7	J1753+4409			0.871	FSRQ	...
J1753+2848	17:53:42.48	+28:48:04.9	J1753+2848			1.118	FSRQ	...
J1754+6452	17:54:07.59	+64:52:02.6	J1754+6452			0.977	FSRQ	...
CLJ1754+3212	17:54:11.80	+32:12:23.1			J1754.3+3212	0.0	BLL	HSP
1RXSJ175615.5+55221	17:56:15.90	+55:22:17.6			J1756.5+5523	0.0	BLL	HSP
J1756+1553	17:56:33.72	+15:53:43.8	J1756+1553			0.547	FSRQ	...
J1756+3046	17:56:49.23	+30:46:47.5	J1756+3046			1.983	FSRQ	...
J1756+1535	17:56:53.11	+15:35:20.8	J1756+1535			...	...	...
J1759+2343	17:59:00.36	+23:43:47.0	J1759+2343			1.721	FSRQ	...
J1800+3848	18:00:24.76	+38:48:30.7	J1800+3848			2.092	FSRQ	...
J1800+7828	18:00:45.68	+78:28:04.0	J1800+7828	J1800.4+7827	J1800.5+7829	0.68	BLL	LSP
J1801+4404	18:01:32.31	+44:04:21.9	J1801+4404		J1801.7+4405	0.663	FSRQ	LSP
J1803+0934	18:03:33.65	+09:34:25.9	J1803+0934			0.683	FSRQ	...
CRJ1803+0341	18:03:56.28	+03:41:07.6		J1804.1+0336		1.42	FSRQ	...
J1804+0042	18:04:08.88	+00:42:22.1	J1804+0042			0.07	GALAXY	...
J1804+0101	18:04:15.99	+01:01:32.4	J1804+0101			1.522	FSRQ	...
J1805+1714	18:05:47.44	+17:14:55.9	J1805+1714			...	...	...
J1806+6949	18:06:50.68	+69:49:28.1	J1806+6949	J1807.0+6945	J1806.7+6948	0.051	BLL	ISP
J1807+2204	18:07:38.81	+22:04:56.4	J1807+2204			0.798	FSRQ	...
J1808+4542	18:08:21.88	+45:42:20.9	J1808+4542			0.83	FSRQ	...
J1809+1849	18:09:45.34	+18:49:03.1	J1809+1849			0.928	FSRQ	...
J1809+2910	18:09:45.39	+29:10:19.9		J1809.6+2908	J1809.7+2909	0.0	BLL	...
CLJ1810+1608	18:10:50.17	+16:08:20.8			J1810.8+1606	0.0	BLL	...
87GB181007.0+533142	18:11:11.20	+53:32:25.1			J1811.0+5340	...	AGU	...
NVSSJ181118+034113	18:11:17.90	+03:41:14.1			J1811.3+0339	0.0	BLL	HSP
J1811+1704	18:11:43.19	+17:04:57.3	J1811+1704			...	BLL	...
J1813+0615	18:13:33.41	+06:15:42.0	J1813+0615		J1813.7+0617	0.0	BLL	...

Continues

Table A.2

OVRO name	RA	DEC	CGRaBS name	1FGL name	2FGL name	z	Optical Class	SED class
J1813+3144	18:13:35.21	+31:44:17.6		J1813.4+3141	J1813.5+3143	0.117	BLL	ISP
J1813+2952	18:13:37.27	+29:52:37.9	J1813+2952			1.351	FSRQ	...
J1815+1623	18:15:14.85	+16:23:46.3	J1815+1623			0.742	FSRQ	...
J1816+5307	18:16:57.07	+53:07:44.5	J1816+5307			...	...	...
J1818+5017	18:18:30.52	+50:17:19.7	J1818+5017			1.395	FSRQ	...
J1818+0903	18:18:40.06	+09:03:46.2		J1818.1+0905	J1818.6+0903	0.354	FSRQ	...
MG2J181902+2132	18:19:05.20	+21:32:35.0			J1818.7+2138	...	AGU	...
NVSSJ182021+362343	18:20:20.90	+36:23:43.1			J1820.6+3625	...	AGU	HSP
J1823+7938	18:23:14.10	+79:38:49.0	J1823+7938			0.224	FSRQ	...
7C1823+6856	18:23:32.80	+68:57:51.9			J1823.7+6856	0.0	BLL	LSP
J1824+1044	18:24:02.86	+10:44:23.8	J1824+1044			1.364	FSRQ	...
J1824+5651	18:24:07.07	+56:51:01.5	J1824+5651	J1824.0+5651	J1824.0+5650	0.664	BLL	LSP
1RXS182418.7+430954	18:24:19.10	+43:09:49.5			J1823.8+4312	0.487	AGU	HSP
J1827+2658	18:27:55.43	+26:58:05.9	J1827+2658			...	...	...
87GB182712.0+272717	18:29:13.90	+27:29:03.0			J1829.1+2725	...	AGU	...
BBJ1829+5402	18:29:24.29	+54:02:59.8		J1829.8+5404	J1829.2+5402	0.0	BLL	HSP
3C380	18:29:31.78	+48:44:46.2		J1829.8+4845	J1829.7+4846	0.692	SSRQ	...
MG1J183001+1323	18:30:00.70	+13:24:13.8			J1830.0+1325	...	AGU	...
J1832+1357	18:32:43.48	+13:57:44.4	J1832+1357			2.83	FSRQ	...
J1835+3241	18:35:03.39	+32:41:46.8	J1835+3241			0.058	AGN	...
J1835+6119	18:35:19.67	+61:19:40.0	J1835+6119			2.274	FSRQ	...
J1835+2506	18:35:58.38	+25:06:45.4	J1835+2506			1.973	FSRQ	...
RXJ1836.2+3136	18:36:21.10	+31:36:25.4			J1836.2+3137	0.0	BLL	HSP
BBJ1838+4802	18:38:49.10	+48:02:34.0		J1838.6+4756	J1838.7+4759	0.0	BLL	HSP
J1840+2457	18:40:03.44	+24:57:41.2	J1840+2457			1.635	FSRQ	...
J1840+3900	18:40:57.16	+39:00:45.7	J1840+3900			3.095	FSRQ	...
RXJ1841.7+3218	18:41:47.10	+32:18:38.4			J1841.7+3221	0.0	BLL	HSP
J1842+6809	18:42:33.64	+68:09:25.2	J1842+6809			0.475	FSRQ	...
J1846+3747	18:46:31.93	+37:47:17.3	J1846+3747			2.441	FSRQ	...
J1848+3219	18:48:22.10	+32:19:02.6	J1848+3219	J1848.5+3224	J1848.5+3216	0.798	FSRQ	LSP
J1849+6705	18:49:16.08	+67:05:41.7	J1849+6705	J1849.3+6705	J1849.4+6706	0.657	FSRQ	LSP
J1849+3024	18:49:20.11	+30:24:14.2	J1849+3024			0.672	FSRQ	...
MG2J184929+2748	18:49:31.60	+27:48:00.7			J1849.5+2744	0.0	BLL	...
J1850+2825	18:50:27.59	+28:25:13.1	J1850+2825			2.56	FSRQ	...
J1852+4855	18:52:28.55	+48:55:47.5	J1852+4855	J1852.5+4853	J1852.5+4856	1.25	FSRQ	LSP
J1852+4019	18:52:30.37	+40:19:06.6	J1852+4019			2.12	FSRQ	...

Continues

Table A.2

OVRO name	RA	DEC	CGRaBS name	1FGL name	2FGL name	z	Optical Class	SED class
J1854+7351	18:54:57.30	+73:51:19.9	J1854+7351			0.46	FSRQ	...
J1855+3742	18:55:27.71	+37:42:57.0	J1855+3742			1.12	FSRQ	...
J1900+2722	19:00:34.68	+27:22:30.9	J1900+2722			...	...	...
J1900+2701	19:00:48.51	+27:01:57.5	J1900+2701			...	...	...
CR1903+5540	19:03:11.61	+55:40:38.4		J1903.0+5539	J1903.3+5539	0.0	BLL	ISP
PMNJ1911-1908	19:11:29.60	-19:08:23.6			J1911.5-1908	...	AGU	...
J1912+3740	19:12:25.13	+37:40:36.7	J1912+3740			1.104	FSRQ	...
1RXS191401.9+443849	19:14:01.70	+44:38:33.5			J1913.4+4440	...	AGU	HSP
J1916-1519	19:16:52.51	-15:19:00.1	J1916-1519			...	...	...
J1917-1921	19:17:44.82	-19:21:31.6	J1917-1921	J1917.7-1922	J1917.6-1921	0.137	BLL	HSP
J1918+5520	19:18:10.74	+55:20:38.6	J1918+5520			1.734	FSRQ	...
J1918+4937	19:18:45.58	+49:37:56.1	J1918+4937			0.926	FSRQ	...
J1921-1231	19:21:23.92	-12:31:54.4		J1921.1-1234	J1921.3-1231	0.0	BLL	...
J1921-1607	19:21:51.53	-16:07:12.6		J1922.0-1608	J1921.9-1608	0.0	BLL	...
J1923+3941	19:23:48.70	+39:41:06.7	J1923+3941			...	...	...
CRJ1925-1018	19:25:03.20	-10:18:12.4		J1925.1-1018		...	BLL	...
CLJ1926+6154	19:26:49.89	+61:54:42.4			J1927.0+6153	0.0	BLL	HSP
J1927+6117	19:27:30.45	+61:17:32.9	J1927+6117			...	BLL	...
J1927+7358	19:27:48.49	+73:58:01.6	J1927+7358			0.303	FSRQ	...
J1933+6540	19:33:57.33	+65:40:16.9	J1933+6540			1.687	FSRQ	...
J1934+6138	19:34:40.68	+61:38:41.6	J1934+6138			1.749	FSRQ	...
J1935+8130	19:35:22.69	+81:30:14.6	J1935+8130			...	...	...
J1936+7131	19:36:03.56	+71:31:31.8	J1936+7131			1.864	FSRQ	...
J1936-0402	19:36:53.74	-04:02:45.5	J1936-0402			0.49	FSRQ	...
6CB194425+834912	19:37:39.70	+83:56:29.5			J1936.9+8402	...	AGU	...
J1938-1749	19:38:04.96	-17:49:20.4	J1938-1749			0.903	FSRQ	...
J1939-1525	19:39:26.66	-15:25:43.1	J1939-1525			1.657	FSRQ	...
J1939-1002	19:39:57.25	-10:02:41.6	J1939-1002			3.787	FSRQ	...
J1941-0211	19:41:18.94	-02:11:45.4	J1941-0211			0.202	FSRQ	...
J1941+7221	19:41:26.98	+72:21:42.2		J1941.6+7214	J1941.6+7218	...	AGU	...
NGC6814	19:42:40.40	-10:19:19.8			J1942.5-1024	0.0050	Seyfert	...
J1947-0103	19:47:43.78	-01:03:24.6	J1947-0103			...	...	...
J1949+5041	19:49:43.49	+50:41:32.0	J1949+5041			1.927	FSRQ	...
J1949-1957	19:49:53.42	-19:57:13.2	J1949-1957			2.652	FSRQ	...
J1951+0134	19:51:36.02	+01:34:42.7	J1951+0134			4.114	FSRQ	...
J1951-0509	19:51:47.46	-05:09:44.0	J1951-0509			1.083	FSRQ	...

Continues

Table A.2

OVRO name	RA	DEC	CGRaBS name	1FGL name	2FGL name	z	Optical Class	SED class
J1954-1123	19:54:41.15	-11:23:22.7	J1954-1123	J1954.8-1124	J1954.6-1122	0.683	FSRQ	LSP
J1954+6153	19:54:55.99	+61:53:58.3	J1954+6153			...	...	...
1RXS195500.6-160328	19:55:00.40	-16:03:37.9			J1954.4-1607	...	AGU	HSP
J1955+5131	19:55:42.73	+51:31:48.5	J1955+5131			1.223	FSRQ	...
J1955+0618	19:55:55.27	+06:18:12.2	J1955+0618			...	...	...
J1959+6508	19:59:59.85	+65:08:54.7	J1959+6508	J2000.0+6508	J2000.0+6509	0.047	BLL	HSP
J2000-1325	20:00:42.14	-13:25:33.6	J2000-1325			0.222	FSRQ	...
J2000-1748	20:00:57.09	-17:48:57.7	J2000-1748	J2000.9-1749	J2000.8-1751	0.652	FSRQ	LSP
CRJ2001+7040	20:01:33.95	+70:40:25.8		J2001.9+7040	J2001.7+7042	0.254	BLL	LSP
J2003-0421	20:03:24.97	-04:21:38.5	J2003-0421			...	...	...
J2004+7355	20:04:17.13	+73:55:06.0	J2004+7355			...	...	...
J2005+7752	20:05:31.00	+77:52:43.2	J2005+7752	J2006.0+7751	J2004.5+7754	0.342	BLL	ISP
J2006+6424	20:06:17.70	+64:24:45.4	J2006+6424			1.574	FSRQ	...
J2007+0636	20:07:11.91	+06:36:44.6	J2007+0636			2.864	FSRQ	...
J2007+6607	20:07:28.77	+66:07:22.6	J2007+6607			1.325	FSRQ	...
3C407	20:08:24.39	-04:18:29.3		J2008.6-0419		0.589	AGN	...
J2009+7229	20:09:52.30	+72:29:19.4	J2009+7229	J2009.1+7228	J2009.7+7225	0.0	BLL	LSP
J2009+0727	20:09:55.51	+07:27:13.7	J2009+0727			0.763	FSRQ	...
J2010+6116	20:10:49.29	+61:16:15.2	J2010+6116			0.87	FSRQ	...
J2011-1546	20:11:15.71	-15:46:40.3	J2011-1546			1.18	FSRQ	...
NVSSJ201431+064849	20:14:31.00	+06:48:49.7			J2014.7+0646	...	AGU	HSP
J2015-1252	20:15:13.70	-12:52:57.0	J2015-1252			0.614	FSRQ	...
J2015-0137	20:15:15.16	-01:37:32.5		J2015.3-0129	J2015.1-0137	0.0	BLL	LSP
J2015+6554	20:15:55.37	+65:54:52.7	J2015+6554			2.845	FSRQ	...
J2016+1632	20:16:13.86	+16:32:34.1	J2016+1632			...	...	...
PMNJ2016-0903	20:16:24.00	-09:03:33.0			J2016.3-0904	0.367	BLL	ISP
J2018-1109	20:18:28.01	-11:09:55.5	J2018-1109			0.9	FSRQ	...
J2018-0509	20:18:57.76	-05:09:29.4	J2018-0509			0.905	FSRQ	...
J2020+6747	20:20:18.91	+67:47:06.4	J2020+6747			2.571	FSRQ	...
J2021+0515	20:21:35.27	+05:15:04.8	J2021+0515			...	...	...
J2022+6136	20:22:06.67	+61:36:58.8	J2022+6136			0.227	AGN	...
J2022+7611	20:22:35.59	+76:11:26.2	J2022+7611	J2020.4+7608	J2022.5+7614	0.594	BLL	ISP
J2023-0123	20:23:32.82	-01:23:42.2	J2023-0123			...	...	...
J2023-1139	20:23:36.70	-11:39:58.3		J2023.7-1141	J2023.4-1137	0.698	FSRQ	...
J2024+1718	20:24:56.56	+17:18:13.2	J2024+1718			1.05	FSRQ	...
J2025+0316	20:25:09.63	+03:16:44.4	J2025+0316			2.21	FSRQ	...

Continues

Table A.2

OVRO name	RA	DEC	CGRaBS name	1FGL name	2FGL name	z	Optical Class	SED class
C2025-0735	20:25:40.66	-07:35:52.7		J2025.6-0735	J2025.6-0736	1.388	FSRQ	LSP
J2027-0831	20:27:52.60	-08:31:56.0	J2027-0831			1.697	FSRQ	...
J2030-0622	20:30:15.13	-06:22:15.0		J2030.3-0617	J2030.3-0622	0.671	FSRQ	...
J2030-0503	20:30:22.42	-05:03:12.8	J2030-0503			0.543	FSRQ	...
RXJ2030.8+1935	20:30:57.10	+19:36:13.2			J2031.0+1938	...	AGU	HSP
J2031+0239	20:31:47.25	+02:39:37.3	J2031+0239			0.858	FSRQ	...
J2031+1219	20:31:55.00	+12:19:41.3	J2031+1219	J2031.5+1219	J2031.7+1223	1.213	BLL	ISP
J2033+2146	20:33:32.03	+21:46:22.4	J2033+2146			0.173	FSRQ	...
J2035+1056	20:35:22.34	+10:56:06.8		J2035.4+1100	J2035.4+1058	0.601	FSRQ	LSP
87GB203539.4+654245	20:36:19.90	+65:53:14.7			J2036.6+6551	0.0	BLL	ISP
J2036-0629	20:36:40.71	-06:29:03.9	J2036-0629			1.636	FSRQ	...
J2037-1522	20:37:27.93	-15:22:00.5	J2037-1522			1.802	FSRQ	...
J2039-1046	20:39:00.70	-10:46:41.9		J2039.0-1047	J2039.1-1046	0.0	BLL	LSP
MG2J204208+2426	20:42:05.90	+24:26:52.1			J2042.1+2428	0.104	BLL	HSP
J2042+7508	20:42:37.32	+75:08:02.4	J2042+7508			0.104	FSRQ	...
J2043+1255	20:43:10.21	+12:55:13.6	J2043+1255			3.277	FSRQ	...
J2045-1858	20:45:23.73	-18:58:53.5	J2045-1858			...	...	...
J2049+1003	20:49:45.86	+10:03:14.4	J2049+1003		J2049.8+1001	...	AGU	...
J2050+0407	20:50:06.24	+04:07:48.9	J2050+0407	J2050.1+0407	J2050.0+0408	0.0	BLL	...
J2051+1743	20:51:35.58	+17:43:36.9	J2051+1743			0.195	AGN	...
SDSSJ205528.	20:55:28.20	-00:21:17.0		J2055.5-0023	J2055.4-0023	0.0	BLL	HSP
J2101+0341	21:01:38.84	+03:41:31.3	J2101+0341			1.015	FSRQ	...
J2102+6758	21:02:43.81	+67:58:19.8	J2102+6758			...	...	...
J2106+2135	21:06:10.82	+21:35:36.1	J2106+2135			0.647	FSRQ	...
J2106+0231	21:06:28.15	+02:31:37.8	J2106+0231			2.942	FSRQ	...
J2108+1430	21:08:41.03	+14:30:27.0	J2108+1430			2.017	FSRQ	...
CRJ2108-0250	21:08:44.73	-02:50:34.3		J2108.5-0249	J2108.7-0246	0.149	BLL	...
J2110-1020	21:10:00.98	-10:20:57.4	J2110-1020			...	...	...
J2110+0809	21:10:09.68	+08:09:55.4		J2110.0+0811	J2109.9+0807	1.58	FSRQ	...
1RXS211242.5+081831	21:12:42.80	+08:18:36.1			J2112.5+0818	...	AGU	HSP
J2114+1714	21:14:40.64	+17:14:22.3	J2114+1714			...	...	...
J2114+2832	21:14:58.34	+28:32:57.2	J2114+2832			2.345	FSRQ	...
J2115-1416	21:15:18.43	-14:16:43.4	J2115-1416			1.7	FSRQ	...
J2115+2933	21:15:29.42	+29:33:38.4	J2115+2933	J2115.5+2937	J2115.3+2932	1.514	FSRQ	LSP
C2116+3339	21:16:14.52	+33:39:20.4		J2116.1+3338	J2116.2+3339	0.35	BLL	ISP
J2117+0503	21:17:20.76	+05:03:04.1	J2117+0503			1.794	FSRQ	...

Continues

Table A.2

OVRO name	RA	DEC	CGRaBS name	1FGL name	2FGL name	z	Optical Class	SED class
J2118+0013	21:18:17.40	+00:13:16.8		J2117.8+0016		0.463	FSRQ	...
J2118-0636	21:18:43.24	-06:36:18.0	J2118-0636			0.328	FSRQ	...
NVSSJ212035-125443	21:20:35.80	-12:54:43.5			J2120.6-1301	...	AGU	...
J2120+0533	21:20:41.19	+05:33:45.0	J2120+0533			0.535	NLRG	...
C2121+1901	21:21:00.61	+19:01:28.3		J2120.9+1901	J2121.0+1901	2.18	FSRQ	LSP
J2123+0535	21:23:44.51	+05:35:22.1	J2123+0535			1.941	FSRQ	...
J2124-1941	21:24:44.64	-19:41:43.5	J2124-1941			...	...	...
J2125+0441	21:25:29.26	+04:41:35.5	J2125+0441			1.394	FSRQ	...
B22125+35	21:27:43.00	+36:13:04.9			J2127.8+3614	0.0	BLL	ISP
J2128-0244	21:28:22.22	-02:44:32.8	J2128-0244			1.812	FSRQ	...
J2129-1538	21:29:12.18	-15:38:41.0	J2129-1538			3.28	FSRQ	...
J2130-0927	21:30:19.09	-09:27:37.4	J2130-0927			0.78	FSRQ	...
J2131-1207	21:31:35.26	-12:07:04.8	J2131-1207			0.501	FSRQ	...
RBS1752	21:31:35.50	-09:15:22.0		J2131.7-0914	J2131.6-0914	0.449	BLL	HSP
J2133+1443	21:33:37.39	+14:43:46.5	J2133+1443			...	...	...
J2134-0153	21:34:10.31	-01:53:17.2	J2134-0153	J2134.0-0203	J2133.8-0154	1.284	BLL	LSP
J2136+0041	21:36:38.58	+00:41:54.2	J2136+0041			1.941	FSRQ	...
J2139+1423	21:39:01.31	+14:23:36.0	J2139+1423			2.427	FSRQ	...
J2139+0122	21:39:42.51	+01:22:27.1	J2139+0122			1.401	FSRQ	...
J2142-0437	21:42:36.90	-04:37:43.6	J2142-0437			0.344	FSRQ	...
J2143+1743	21:43:35.54	+17:43:48.7	J2143+1743	J2143.4+1742	J2143.5+1743	0.211	FSRQ	LSP
J2145+1115	21:45:18.78	+11:15:27.3	J2145+1115			0.548	FSRQ	...
J2146-1525	21:46:22.98	-15:25:43.9	J2146-1525		J2146.5-1530	0.698	FSRQ	LSP
NVSSJ214637-134359	21:46:37.00	-13:43:59.9			J2146.6-1345	0.0	BLL	HSP
J2147+0929	21:47:10.17	+09:29:46.7	J2147+0929	J2147.2+0929	J2147.3+0930	1.113	FSRQ	LSP
J2148+0657	21:48:05.46	+06:57:38.6	J2148+0657	J2148.5+0654	J2148.2+0659	0.999	FSRQ	LSP
J2148-1723	21:48:36.80	-17:23:44.0	J2148-1723			2.13	FSRQ	...
J2148+0211	21:48:39.88	+02:11:26.8	J2148+0211			...	...	...
J2149+0322	21:49:41.87	+03:22:51.4		J2149.7+0327	J2149.6+0326	0.0	BLL	...
BBJ2150-1410	21:50:15.50	-14:10:50.1		J2150.3-1410		0.229	BLL	HSP
J2151+0709	21:51:31.43	+07:09:26.8	J2151+0709			1.364	FSRQ	...
J2151+0552	21:51:37.88	+05:52:13.0	J2151+0552			0.74	FSRQ	...
J2152+1734	21:52:24.82	+17:34:37.8	J2152+1734	J2152.5+1734	J2152.4+1735	0.871	BLL	LSP
J2153-1136	21:53:50.24	-11:36:14.1	J2153-1136		J2154.0-1138	1.582	FSRQ	...
J2156-0037	21:56:14.76	-00:37:04.6	J2156-0037			0.495	BLL	...
J2157+3127	21:57:28.82	+31:27:01.4	J2157+3127	J2157.4+3129	J2157.4+3129	1.488	FSRQ	LSP

Continues

Table A.2

OVRO name	RA	DEC	CGRaBS name	1FGL name	2FGL name	z	Optical Class	SED class
J2158-1501	21:58:06.28	-15:01:09.3	J2158-1501	J2157.9-1503	J2157.9-1501	0.672	FSRQ	LSP
TXS2157+102	22:00:07.90	+10:30:07.7			J2159.9+1023	0.0	BLL	...
J2200+2137	22:00:14.20	+21:37:57.0	J2200+2137			...	BLL	...
J2200+0234	22:00:49.41	+02:34:30.1	J2200+0234			1.323	FSRQ	...
BLLacertae	22:02:43.30	+42:16:40.0		J2202.8+4216	J2202.8+4216	0.069	BLL	ISP
J2203+3145	22:03:14.98	+31:45:38.3	J2203+3145			0.298	FSRQ	...
J2203+1725	22:03:26.89	+17:25:48.3	J2203+1725	J2203.5+1726	J2203.4+1726	1.076	FSRQ	LSP
J2203+1007	22:03:30.95	+10:07:42.6	J2203+1007			1.005	NLRG	...
J2204+0440	22:04:17.66	+04:40:02.0		J2204.6+0442	J2204.6+0442	0.027	BLL	ISP
J2204+3632	22:04:21.10	+36:32:37.1	J2204+3632			0.073	GALAXY	...
J2206-0031	22:06:43.29	-00:31:02.5	J2206-0031		J2206.6-0029	0.0	BLL	...
J2207+1652	22:07:52.87	+16:52:17.8	J2207+1652			1.639	FSRQ	...
J2210+2013	22:10:51.66	+20:13:24.0	J2210+2013			0.282	FSRQ	...
J2211+1841	22:11:53.89	+18:41:49.9	J2211+1841			0.07	AGN	...
J2212+2355	22:12:05.97	+23:55:40.6	J2212+2355	J2212.1+2358	J2211.9+2355	1.125	FSRQ	LSP
J2212+2843	22:12:10.25	+28:43:00.6	J2212+2843			...	...	...
J2214+3739	22:14:05.69	+37:39:09.2	J2214+3739			2.249	FSRQ	...
J2216+3518	22:16:20.01	+35:18:14.2	J2216+3518			0.51	FSRQ	...
J2216+3102	22:16:42.72	+31:02:35.4	J2216+3102			2.462	FSRQ	...
J2217+2421	22:17:00.83	+24:21:46.0	J2217+2421	J2217.1+2423	J2217.1+2422	0.505	BLL	LSP
J2218+1520	22:18:10.91	+15:20:35.7	J2218+1520			2.335	FSRQ	...
J2218-0335	22:18:52.04	-03:35:36.9	J2218-0335			0.901	FSRQ	...
J2219+1806	22:19:14.09	+18:06:35.6	J2219+1806	J2219.3+1804	J2219.1+1805	1.071	FSRQ	...
J2219+2613	22:19:49.74	+26:13:28.0	J2219+2613			0.085	AGN	...
NVSSJ222329+010226	22:23:29.50	+01:02:26.4			J2223.4+0104	...	AGU	...
J2225+2118	22:25:38.05	+21:18:06.5	J2225+2118			1.953	FSRQ	...
C2225-0457	22:25:47.26	-04:57:01.4		J2225.8-0457	J2225.6-0454	1.404	FSRQ	LSP
J2226+0052	22:26:46.53	+00:52:11.3	J2226+0052			2.248	FSRQ	...
J2228+2503	22:28:01.55	+25:03:03.1	J2228+2503			0.558	FSRQ	...
J2229-0832	22:29:40.08	-08:32:54.4	J2229-0832	J2229.7-0832	J2229.7-0832	1.56	FSRQ	LSP
J2230-1325	22:30:15.31	-13:25:42.9	J2230-1325			1.42	FSRQ	...
J2230+6946	22:30:36.47	+69:46:28.1	J2230+6946			1.426	FSRQ	...
2230+114	22:32:36.41	+11:43:50.9		J2232.5+1144	J2232.4+1143	1.037	FSRQ	LSP
J2235-1826	22:35:56.12	-18:26:09.5	J2235-1826			2.153	FSRQ	...
J2236+2828	22:36:22.47	+28:28:57.4	J2236+2828	J2236.2+2828	J2236.4+2828	0.795	BLL	LSP
J2236-1433	22:36:34.09	-14:33:22.2	J2236-1433	J2236.4-1432	J2236.5-1431	0.0	BLL	LSP

Continues

Table A.2

OVRO name	RA	DEC	CGRaBS name	1FGL name	2FGL name	z	Optical Class	SED class
J2236+7322	22:36:38.60	+73:22:52.7	J2236+7322			1.345	FSRQ	...
J2238+0724	22:38:10.40	+07:24:14.0	J2238+0724			1.012	FSRQ	...
J2238+2749	22:38:12.87	+27:49:52.8	J2238+2749			0.836	FSRQ	...
J2241+4120	22:41:07.21	+41:20:11.6	J2241+4120			...	BLL	...
J2241+0953	22:41:49.72	+09:53:52.4	J2241+0953			1.707	FSRQ	...
CR2243+2021	22:43:54.74	+20:21:03.8		J2244.0+2021	J2243.9+2021	0.0	BLL	HSP
J2244+4057	22:44:12.73	+40:57:13.6			J2244.1+4059	1.171	BLL	ISP
J2244+2600	22:44:35.15	+26:00:20.7	J2244+2600			2.043	FSRQ	...
J2245+0324	22:45:28.28	+03:24:08.9	J2245+0324			1.34	FSRQ	...
J2245+0500	22:45:53.65	+05:00:57.0	J2245+0500			1.091	FSRQ	...
J2246-1206	22:46:18.23	-12:06:51.3	J2246-1206			0.63	FSRQ	...
BBJ2247+0000	22:47:30.20	+00:00:06.0		J2247.3+0000	J2247.2-0002	0.949	BLL	ISP
J2247-1237	22:47:52.64	-12:37:19.7	J2247-1237			1.892	FSRQ	...
J2247+0310	22:47:58.68	+03:10:42.3	J2247+0310			1.571	FSRQ	...
J2249+2107	22:49:00.57	+21:07:02.9	J2249+2107			1.274	FSRQ	...
J2250+3824	22:50:05.75	+38:24:37.2		J2250.1+3825	J2250.0+3825	0.119	BLL	HSP
J2251+4030	22:51:59.77	+40:30:58.2		J2251.7+4030	J2251.9+4032	0.229	BLL	...
J2253+1942	22:53:07.37	+19:42:34.6	J2253+1942			0.284	FSRQ	...
J2253+1608	22:53:57.75	+16:08:53.6	J2253+1608	J2253.9+1608	J2253.9+1609	0.859	FSRQ	LSP
CT_2255+2410	22:55:15.36	+24:10:11.2			J2255.2+2408	0.0	BLL	HSP
J2257+0243	22:57:17.56	+02:43:17.6	J2257+0243			2.089	FSRQ	...
J2259-0811	22:59:00.69	-08:11:03.0	J2259-0811			1.376	FSRQ	...
CLJ2300+3137	23:00:22.84	+31:37:04.4			J2300.6+3139	0.0	BLL	...
J2300+1655	23:00:42.99	+16:55:14.4	J2300+1655			1.283	FSRQ	...
J2301-0158	23:01:07.98	-01:58:04.6	J2301-0158			0.778	FSRQ	...
J2303+3853	23:03:04.06	+38:53:48.4	J2303+3853			...	...	...
FRBAJ2304+37	23:04:36.60	+37:05:08.0		J2304.3+3709	J2304.7+3703	0.0	BLL	HSP
J2305+8242	23:05:17.54	+82:42:49.2	J2305+8242			...	BLL	...
J2307+3230	23:07:15.92	+32:30:31.9	J2307+3230			1.937	FSRQ	...
J2307+1450	23:07:34.00	+14:50:18.0	J2307+1450	J2307.3+1452	J2308.0+1457	0.503	BLL	...
J2308+2008	23:08:11.64	+20:08:42.2	J2308+2008			0.25	FSRQ	...
J2310+1055	23:10:28.51	+10:55:30.7	J2310+1055			0.494	FSRQ	...
NVSSJ231101+020504	23:11:01.20	+02:05:06.6			J2310.9+0204	0.0	BLL	...
C2311+3425	23:11:05.33	+34:25:10.9		J2311.0+3425	J2311.0+3425	1.817	FSRQ	LSP
J2311+4543	23:11:47.41	+45:43:56.0	J2311+4543			1.447	FSRQ	...
BUJ2313+1444	23:13:57.36	+14:44:23.8		J2314.1+1444	J2314.0+1446	0.163	BLL	HSP

Continues

Table A.2

OVRO name	RA	DEC	CGRaBS name	1FGL name	2FGL name	z	Optical Class	SED class
J2321+3204	23:21:54.95	+32:04:07.6		J2322.0+3208	J2322.2+3206	1.489	FSRQ	LSP
J2321+2732	23:21:59.86	+27:32:46.4		J2321.6+2726	J2321.0+2737	1.253	FSRQ	LSP
J2322+4445	23:22:20.35	+44:45:42.4	J2322+4445			...	...	...
J2322+1843	23:22:28.56	+18:43:24.9	J2322+1843			1.725	FSRQ	...
CRJ2322+3436	23:22:44.01	+34:36:13.9		J2322.6+3435	J2322.6+3435	0.098	BLL	HSP
PKS2320-021	23:23:04.63	-01:50:48.1		J2322.3-0153		1.774	FSRQ	...
J2323-0317	23:23:31.95	-03:17:05.0	J2323-0317	J2323.5-0315	J2323.6-0316	1.41	FSRQ	LSP
1ES2321+419	23:23:52.10	+42:10:58.7		J2323.5+4211	J2323.8+4212	0.059	BLL	HSP
PMNJ2324+0801	23:24:45.30	+08:02:05.7			J2324.6+0801	...	AGU	...
C2325+3957	23:25:17.87	+39:57:36.5		J2325.2+3957	J2325.3+3957	0.0	BLL	LSP
NVSSJ232538+164641	23:25:38.10	+16:46:41.4			J2325.4+1650	...	AGU	ISP
J2327+1524	23:27:21.97	+15:24:37.3	J2327+1524			0.046	FSRQ	...
J2327+0940	23:27:33.58	+09:40:09.5	J2327+0940	J2327.7+0943	J2327.5+0940	1.841	FSRQ	LSP
J2327+1533	23:27:35.98	+15:33:09.6	J2327+1533			0.989	FSRQ	...
J2329+0834	23:29:05.79	+08:34:15.8	J2329+0834			0.948	FSRQ	...
NVSSJ232914+375414	23:29:14.20	+37:54:14.6			J2329.2+3755	0.264	BLL	HSP
J2330+3348	23:30:13.74	+33:48:36.4	J2330+3348			1.809	FSRQ	...
J2330+1100	23:30:40.85	+11:00:18.7	J2330+1100			1.489	FSRQ	...
J2331-1556	23:31:38.65	-15:56:57.0	J2331-1556		J2331.8-1607	1.153	FSRQ	LSP
J2334+0736	23:34:12.82	+07:36:27.5	J2334+0736	J2334.3+0735	J2334.3+0734	0.401	FSRQ	LSP
BBJ2334+1408	23:34:53.80	+14:32:14.0		J2334.7+1429	J2334.8+1431	0.0	BLL	...
J2335-0131	23:35:20.41	-01:31:09.6	J2335-0131			1.184	FSRQ	...
J2336-1451	23:36:57.70	-14:51:21.6	J2336-1451			...	...	...
J2337+2617	23:37:30.08	+26:17:47.7	J2337+2617			...	...	...
J2337-0230	23:37:57.34	-02:30:57.6	J2337-0230	J2338.3-0231	J2338.1-0229	1.072	FSRQ	LSP
BBJ2338+2124	23:38:56.30	+21:24:41.0		J2339.0+2123	J2339.0+2125	0.291	BLL	HSP
J2339-1206	23:39:47.04	-12:06:45.8	J2339-1206			...	...	...
J2340+2641	23:40:29.04	+26:41:56.8	J2340+2641			0.372	BLL	...
FRBAJ2340+80	23:40:54.28	+80:15:16.1		J2341.6+8015	J2341.7+8016	0.274	BLL	HSP
J2343+2339	23:43:12.38	+23:39:45.7	J2343+2339			1.328	FSRQ	...
1RXSJ234332.5+34395	23:43:33.70	+34:40:00.5			J2343.6+3437	0.366	BLL	HSP
J2343+1543	23:43:42.75	+15:43:03.0	J2343+1543			1.445	FSRQ	...
J2345-1555	23:45:12.46	-15:55:07.8	J2345-1555	J2344.6-1554	J2345.0-1553	0.621	FSRQ	LSP
J2346+8007	23:46:25.58	+80:07:55.2	J2346+8007			...	BLL	...
J2346+0930	23:46:36.83	+09:30:45.5	J2346+0930			0.677	FSRQ	...
J2348-1631	23:48:02.61	-16:31:12.0	J2348-1631	J2348.0-1629	J2347.9-1629	0.576	FSRQ	LSP

Continues

Table A.2

OVRO name	RA	DEC	CGRaBS name	1FGL name	2FGL name	z	Optical Class	SED class
J2348-0425	23:48:11.76	-04:25:56.4	J2348-0425			1.106	FSRQ	...
J2350+1106	23:50:02.03	+11:06:36.7	J2350+1106			0.921	FSRQ	...
CLJ2352+1749	23:52:05.84	+17:49:13.8			J2352.0+1753	0.0	BLL	...
J2352+3947	23:52:48.91	+39:47:56.2	J2352+3947			0.858	FSRQ	...
J2354-1513	23:54:30.20	-15:13:11.2	J2354-1513			2.675	FSRQ	...
NVSSJ235612+403648	23:56:12.50	+40:36:48.3			J2356.1+4034	0.331	BLL	HSP
J2357-0152	23:57:25.14	-01:52:15.5	J2357-0152			0.812	BLL	...
J2357-1125	23:57:31.20	-11:25:39.2	J2357-1125			0.96	FSRQ	...
J2358-1020	23:58:10.88	-10:20:08.6	J2358-1020			1.639	FSRQ	...
J2358+1955	23:58:46.09	+19:55:20.3	J2358+1955			1.066	FSRQ	...

Appendix B

Telescope calibration summary

This appendix summarizes the results of the periodic calibration runs performed during the course of the radio monitoring program from November 2008 to December 2011.

B.1 Receiver noise temperature

The receiver temperature is measured with the hot/cold test method in which matched loads of known temperatures are connected to the receiver (e.g. Rohlfs & Wilson, 2004). A hot load at temperature $T_{\rm H}$ and a cold one at $T_{\rm C}$ produce outputs given by

$$P_{\rm C} = G(T_{\rm L} + T_{\rm rx}) \tag{B.1}$$

$$P_{\rm H} = G(T_{\rm H} + T_{\rm rx}) \tag{B.2}$$

Where G is the gain of the receiver. Defining the Y-factor by $Y \equiv P_{\rm H}/P_{\rm C}$, the receiver noise temperature is given by

$$T_{\rm rx} = \frac{T_{\rm H} - YT_{\rm C}}{Y - 1} \tag{B.3}$$

Figure B.1 presents historic data for the receiver noise temperature, showcasing the stability of the receiver noise temperature except for one high measurement in February 2010. Excluding that point the mean value is $T_{\rm rx} = 29.4 \pm 0.2$ K.

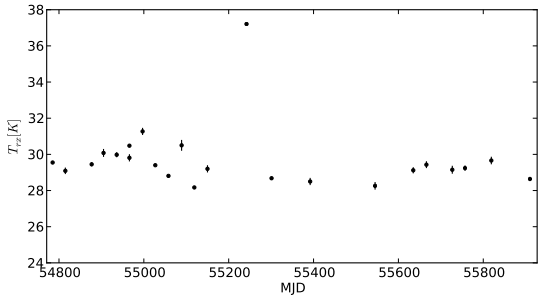

Figure B.1: Receiver noise temperature measured with a hot/cold test. Excluding the February 2010 outlier the mean value is $T_{\rm rx} = 29.4 \pm 0.2$ K.

B.2 Calibration and noise diode temperature

During the hot/cold test we also measure the noise temperature of the noise diode. In this case the noise diode is fired during the cold load stage, and we solve for $T_{\rm noise}$ in an analogous way as for $T_{\rm rx}$. The noise temperature of the calibration diode is measured indirectly by determining the ratio between the power outputs for the noise and calibration diodes. The historic results are shown in Figure B.2.

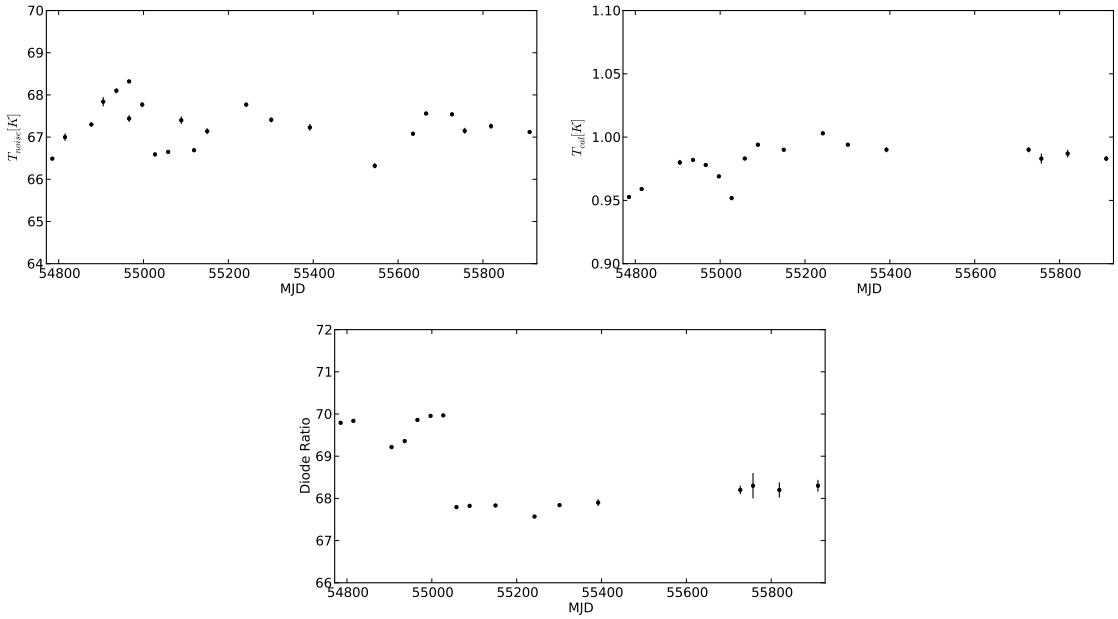

Figure B.2: Noise and calibration diode noise temperature. Upper left panel is the noise diode noise temperature, upper right panel is the calibration diode noise temperature and lower panel is the ratio between the noise and calibration diodes output power.

B.3 Focus curve

The focus curve corrects for variations of the optimum focus position with zenith angle, solar elongation and Sun zenith angle, as explained in 2.5.2. Here we give the mathematical expressions and historic values for the model coefficients.

B.3.1 Simple focus model

In this model the only dependence is with the zenith angle. The model is given by

$$z = \alpha_2 ZA^2 + \alpha_1 ZA + \alpha_0 \tag{B.4}$$

where z is the focus position in mm, and ZA is the zenith angle in degrees.

Date	Parameters $[\alpha_2, \alpha_1, \alpha_0]$
Feb 07 A	[-4.787e-03, 7.471e-02, 2.270e+00]
Feb 07 B	[-5.897e-03, 1.571e-01, 1.389e+00]
Jul 08	[-2.500e-03, -1.106e-01, 5.001e+00]
Oct 08	[-3.401e-03, 4.587e-03, 1.701e+00]
Jun 09	[-3.822e-03, 3.792e-02, 1.827e-01]
Jul 09	[-1.897e-03, -1.593e-01, 3.189e+00]
Dec 09	[-3.707e-03, 4.209e-02, -1.614e+00]
Apr 10	[-2.469e-03, -9.092e-02, -6.698e+00]
Jul 10	[-2.860e-03, -8.070e-02, -5.973e+00]
Oct 11	[-8.761e-03 , 4.361e-01, -1.709e+01]

Table B.1: Focus curve model parameters for the simple model

B.3.2 Complete focus model

This model takes into account the dependence with solar elongation and Sun zenith angle and is defined as

$$z = c_1 ZA^2 + c_2 ZA + c_3 + c_4 SA^2 + c_5 SA + c_6 SZA^2 + c_7 SZA \tag{B.5}$$

where SA is the solar elongation and SZA is the Sun zenith angle.

Date	$[c_1, c_2, c_3, c_4, c_5, c_6, c_7]$
Oct 2008	[-3.659e-03, 1.018e-02, 7.015, 1.894e-04, -3.552e-02, 2.085e-04, -6.770e-2]
Jun 2009	[-3.818e-03, 3.122e-02, 3.974e+00, 2.736e-04, -4.315e-02, 6.112e-05, -3.031e-02]
Dec 2009	[-3.717e-03, 4.304e-02, 6.1251e+00, -3.934e-05, 7.645e-03, 5.408e-04, -1.387e-01]
Apr 2010	[-3.268e-03, -2.415e-02, -1.991e+00, 2.445e-04, -5.208e-02, 1.555e-04, -6.103e-02]
Jul 2010	[-3.567e-03, -1.138e-02, -2.070e+00, 2.186e-04, -4.466e-02, 2.261e-04, -6.4414e-02]
Oct 2011	[-5.030e-03, 1.246e-01, -2.272e+00, 1.371e-04, -3.327e-02, 4.992e-04, -1.276e-01]

Table B.2: Focus curve model coefficients

B.3.3 Focus error correction model

The difference between the actual and best focus prescription is then feed into the out of focus gain formula reproduced below. This fit was obtained on December 2009 but it is very similar to the others as can be seen from Figure B.3

$$f(z) = -1.10679320 \times 10^{-3} z^2 - 7.37326817 \times 10^{-5} z + 1.0 \tag{B.6}$$

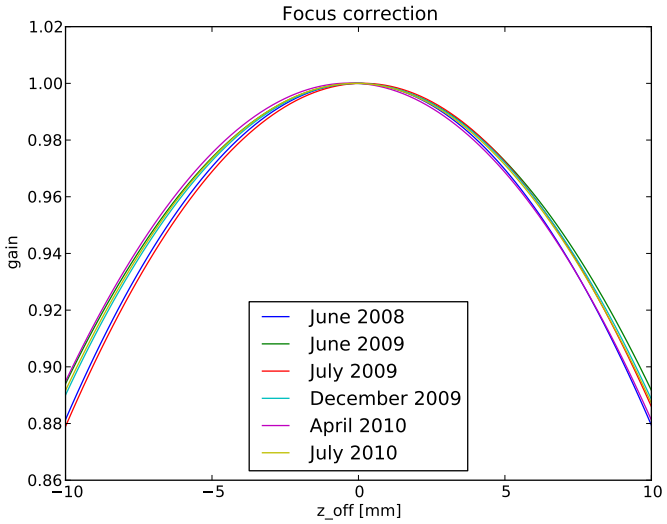

Figure B.3: Focus error model correction for various epochs. The correction is very stable even after larger changes in the focus model itself.

B.4 Gain curve

The gain curve model and historic values of its coefficients are given for future reference. Experience has shown that the gain curve is very stable and big changes only happen after major receiver maintenance. Table B.3 shows the parameters of the best measurements and Figure B.4 the gain curves for different epochs.

The gain curve model is a polynomial of five degrees on the zenith angle and is given by

$$g = c_5 ZA^5 + c_4 ZA^4 + c_3 ZA^3 + c_2 ZA^2 + c_1 ZA + c_0 \tag{B.7}$$

Date	Source	$[c_5, c_4, c_3, c_2, c_1, c_0]$
Feb 2007	DR 21	[-1.689e-09, 3.752e-07, -2.912e-05, 7.457e-04, 4.123e-03, 7.158e-01]
Dec 2008	3C 84	[-3.432e-10, 5.545e-08, 4.111e-08, -5.071e-04, 2.917e-02, 5.325e-01]
Aug 2010	3C 84	[1.654e-09, -4.763e-07, 5.198e-05, -2.829e-03, 7.493e-02, 2.391e-01]
Mar 2011	3C 286	[-4.106e-09, 8.270e-07, -6.030e-05, 1.744e-03, -1.210e-02, 8.464e-01]
Nov 2011	3C 386	[-2.138e-09, 4.779e-07, -3.858e-05, 1.210e-03, -8.936e-03, 8.798e-01]

Table B.3: Gain curve model coefficients

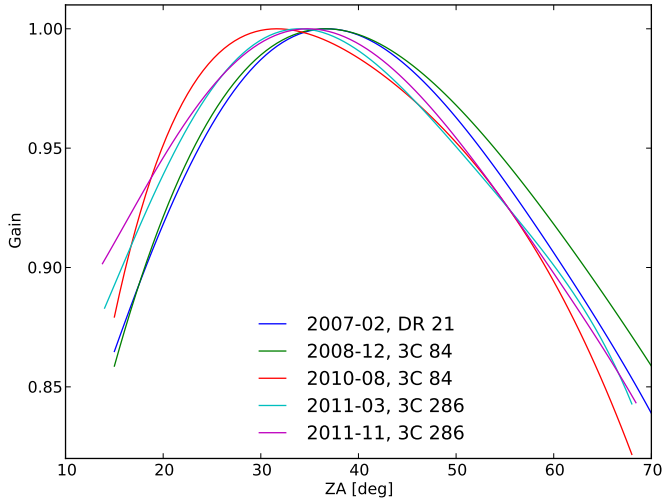

Figure B.4: Comparison of historic gain curves for different epochs. The date and source used are indicated in the figure.

B.5 Nonlinearity correction

Ideal amplifiers have a linear response to an input signal that is given by their gain. A real amplifier deviates from this simple behavior and show gain compression, in which the gain is smaller for high input values. Small nonlinearities are modeled following Herbig (1994) and Leitch (1998). In this model the nonlinearity is given by any of the two equivalent expressions below

$$P_{\rm out} = G(1 + bP_{\rm out})P_{\rm in} \tag{B.8}$$

$$P_{\rm out} = \frac{GP_{\rm in}}{(1 - bP_{\rm in})} \tag{B.9}$$

where $P_{\rm out}$ is the observer output power, $P_{\rm in}$ is the input power level, G is the gain of the element and b is the nonlinearity parameter. A negative value of b reduces the gain and can be used to model gain compression.

Flux density measurements are differential measurements. To find the differential gain we take the derivative $dP_{\rm out}/dP_{\rm in}$ at a given background level, $P_{\rm in,0}$ at the input and $P_{\rm out,0}$ in the output

$$\left.\frac{dP_{\rm out}}{dP_{\rm in}}\right|_{P_{\rm in,0}} = \frac{G}{(1 - bGP_{\rm in,0})^2} = G(1 + bP_{\rm out,0})^2 \tag{B.10}$$

This is the expression we have to use when correcting flux density measurements or noise diodes powers. The value of b can be estimated by firing the calibration or noise diode with different background levels ($P_{\rm in,0}$). This can be achieved by performing the measurement of the diode at different elevations during an sky dip and also during hot/cold test. Since the nonlinearity parameter as well as the gain depend in all the elements in the signal path, the value of b depends on the particular value of the variable attenuator in the OVRO 40 meter telescope receiver. During normal observations this is set to a value of 5 or 4 dB, and to 9 dB during hot/cold test measurements to avoid saturation during the hot load stage. Values for the nonlinearity during a hot/cold test and skydips are given in Figure B.5.

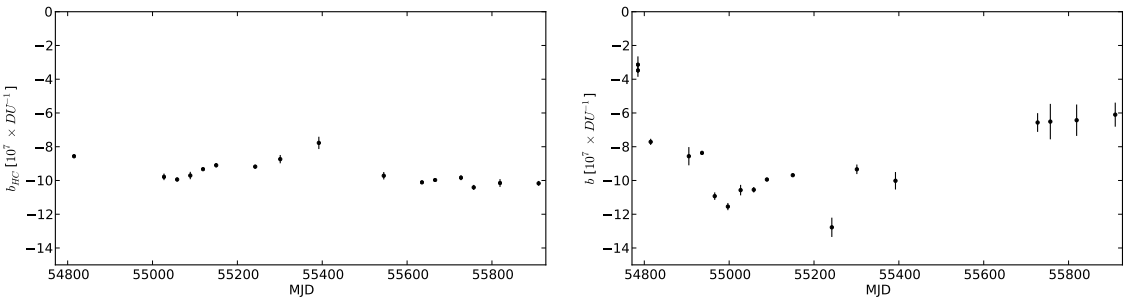

Figure B.5: Nonlinearity correction for the hot/cold test (left panel) and skydip (right panel). During the hot/cold test the variable attenuator is at 9 dB. For the skydip is it at is normal value of 5 dB for measurements until December 2008 and to 4 dB after that.

B.6 Sydips

Skydips are performed at most calibration runs (see Section 2.5.4 for a detailed explanation). A summary of the historical results is presented in Figure B.6.

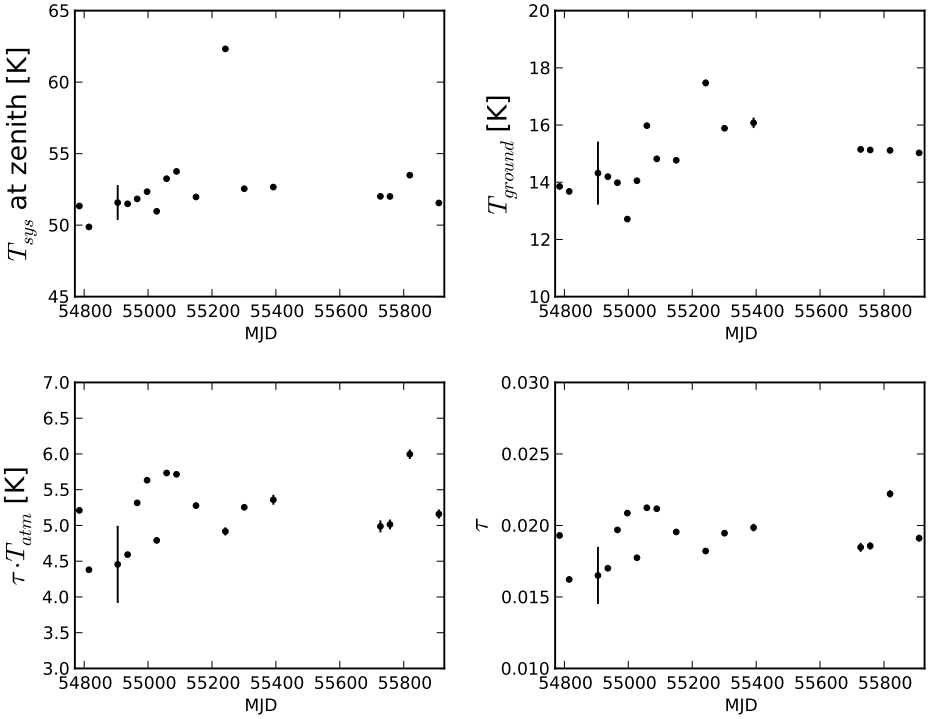

Figure B.6: Skydip parameters. The parameters are defined in 2.5.4. Upper left panel is $T_{\rm sys}$ at zenith. Upper right is $T_{\rm ground}$. Lower left panel is $\tau T_{\rm atm}$ and lower right panel is for τ assuming that $T_{\rm atm} = 270$ K.

The mean values of the parameters are given for reference: $T_{\rm sys}(ZA = 0) = 52.6 \pm 0.6$ K; $T_{\rm ground} = 14.8 \pm 0.3$ K; $\tau \cdot T_{\rm atm} = 5.2 \pm 0.1$ K and $\tau = 0.0191 \pm 0.0004$.

Appendix C

Results of the PSD characterization of the complete radio sample

This table contains the PSD fit information for 424 sources with 1σ constraints on the PSD power-law index and that have more than 100 data points in their light curves. In all the analyses comparing population properties only the 238 sources with well defined 82.6% confidence intervals are used. The results for the sources in the cross-correlation sample (Table E.1) are repeated in this table.

The columns contain the following information:

OVRO name: Name of the source in the OVRO 40 m blazar monitoring program

N points: Number of data points in the light curve

T: Time span of the light curve in days

$\langle \Delta t \rangle$**:** Mean sampling interval in days

$\sigma^2_{\rm noise}/\sigma^2_{\rm data}$**:** Ratio of estimated noise variance to total variance

p**-value:** p-value of the best fit power-law index of the PSD

β**:** Best fit value for the power-law index of the PSD

$\beta_{\rm low}$**:** 68.3% lower limit for the power-law index of the PSD

$\beta_{\rm up}$**:** 68.3% upper limit for the power-law index of the PSD

$\beta^{\rm comb}_{\rm low}$**:** 82.6% lower limit for the power-law index of the PSD

$\beta^{\rm comb}_{\rm up}$**:** 82.6% upper limit for the power-law index of the PSD

Table C.1: Radio band PSD characterization for all the OVRO blazar sample

OVRO name	N points	T	$\langle\Delta t\rangle$	$\sigma^2_{\rm noise}/\sigma^2_{\rm data}$	p-value	β	$\beta_{\rm low}$	$\beta_{\rm up}$	$\beta^{\rm comb}_{\rm low}$	$\beta^{\rm comb}_{\rm up}$
2230+114	211	1054.1	5.0	0.0026	0.62	2.4	2.0	2.6	1.7	2.8
3C66A	339	1494.9	4.4	0.061	0.65	1.9	0.6	2.4	0.4	2.5
BBJ2247+0000	141	932.3	6.7	0.064	0.65	2.1	0.4	3.4	0.0	...
BLLacertae	189	1049.1	5.6	0.0066	0.22	2.1	0.9	2.4	0.9	2.7
BQJ1258-1800	118	923.5	7.9	0.012	0.95	2.2	0.9	2.5	0.9	...
C0424+0036	164	1050.2	6.4	0.019	0.06	2.4	0.9	2.9	0.6	...
C0509+1011	159	1048.1	6.6	0.024	0.81	2.7	0.9	3.2	0.7	...
C1130-1449	147	1057.1	7.2	0.0046	0.47	3.0	1.2	3.3	1.2	...
C1224+2122	234	1058.1	4.5	0.0048	0.79	2.4	2.0	2.7	0.9	2.7
C1239+0443	134	1058.2	8.0	0.029	0.086	2.0	0.6	2.6	0.0	...
C1345+4452	175	1056.8	6.1	0.013	0.65	2.1	0.9	2.6	0.6	2.6
C2311+3425	215	1049.4	4.9	0.017	0.89	2.1	0.6	2.5	0.6	2.7
CLJ0048+2235	165	928.5	5.7	0.025	1.0	2.5	0.7	2.8	0.7	3.2
CR1553+1256	179	1057.4	5.9	0.043	0.17	2.0	0.6	3.4	0.1	...
J0004+2019	285	1504.1	5.3	0.068	0.63	1.5	1.1	2.3	0.6	...
J0004+4615	270	1493.9	5.6	0.061	0.33	1.9	0.6	2.6	0.6	2.7
J0004-1148	233	1203.6	5.2	0.0068	0.67	2.7	2.2	3.0	1.5	3.0
J0005+3820	285	1493.9	5.3	0.043	0.1	2.0	1.5	2.5	0.6	...
J0006-0623	197	1124.9	5.7	0.057	0.93	1.8	1.2	2.9	0.6	3.2
J0013-0423	206	1124.9	5.5	0.012	0.95	2.6	2.3	3.0	1.2	3.1
J0013-1513	278	1506.8	5.4	0.1	0.05	2.4	0.6	3.4	0.4	...
J0019+2021	286	1504.1	5.3	0.05	0.29	2.4	0.7	3.0	0.6	...
J0019+2602	218	1213.9	5.6	0.017	0.46	2.6	0.7	2.8	0.7	3.3
J0038+1856	268	1482.2	5.6	0.077	0.98	2.2	0.6	2.6	0.6	...
J0038+4137	289	1493.9	5.2	0.23	0.28	2.1	0.4	3.4	0.0	...
J0046+3900	322	1495.9	4.7	0.15	0.17	1.9	0.7	2.2	0.4	...
J0048+3157	316	1495.9	4.7	0.0093	0.93	2.1	1.8	2.3	1.8	2.5
J0049+0237	200	1474.0	7.4	0.12	0.93	1.7	0.6	3.1	0.6	...
J0049+5128	236	1058.8	4.5	0.061	0.92	2.2	0.4	2.8	0.4	2.8
J0050-0452	164	1051.2	6.4	0.069	0.08	1.9	0.0	2.4	0.0	...
J0050-0929	243	1488.0	6.1	0.0038	0.8	2.3	2.0	2.5	1.9	2.7
J0056+1625	296	1504.1	5.1	0.031	0.78	2.3	2.1	2.6	2.0	...
J0057+3021	263	1262.6	4.8	0.14	0.64	1.4	0.1	2.0	0.0	3.4
J0105+4819	329	1494.9	4.6	0.26	0.52	1.9	0.4	2.2	0.4	3.2
J0106+3402	301	1495.9	5.0	0.022	0.37	2.7	2.3	3.0	0.9	3.0
J0107+2611	254	1262.6	5.0	0.51	0.78	0.2	0.0	3.4	0.0	...
J0108+0135	157	1051.2	6.7	0.012	0.66	2.3	0.9	2.8	0.9	...
J0110-0741	238	1481.0	6.2	0.013	0.55	2.4	2.1	2.6	2.1	2.8
J0111-1317	252	1506.8	6.0	0.061	0.37	2.2	0.4	2.6	0.4	...
J0112+2244	318	1504.1	4.7	0.011	0.36	2.0	1.7	2.4	1.4	2.4
J0112+3208	204	1113.0	5.5	0.038	0.9	1.9	0.6	2.4	0.4	...

Continues

Table C.1

OVRO name	N points	T	$\langle\Delta t\rangle$	$\sigma^2_{\rm noise}/\sigma^2_{\rm data}$	p-value	β	$\beta_{\rm low}$	$\beta_{\rm up}$	$\beta^{\rm comb}_{\rm low}$	$\beta^{\rm comb}_{\rm up}$
J0112+3522	328	1488.9	4.6	0.01	0.66	2.3	2.0	2.5	2.0	2.5
J0113+4948	329	1510.8	4.6	0.048	0.72	2.4	0.6	2.7	0.6	3.0
J0116-1136	250	1497.9	6.0	0.042	0.84	1.9	1.4	2.2	0.6	2.5
J0117+1418	292	1481.0	5.1	0.042	0.21	1.9	0.6	2.5	0.6	2.8
J0121+1149	293	1481.0	5.1	0.0042	0.56	2.2	2.0	2.5	2.0	2.6
J0122+2502	360	1497.9	4.2	0.24	0.64	1.2	0.3	3.4	0.3	...
J0123+2615	363	1497.9	4.1	0.13	0.95	1.6	0.3	1.8	0.3	...
J0127-0821	239	1506.9	6.3	0.092	0.81	2.1	0.6	2.5	0.6	...
J0128+4901	332	1510.8	4.6	0.0072	0.06	2.0	1.8	2.2	1.8	2.4
J0132+4325	328	1494.9	4.6	0.03	0.05	2.1	1.8	2.5	0.6	2.5
J0132-1654	226	1503.8	6.7	0.0035	0.13	2.4	2.0	2.8	1.8	2.8
J0136+4751	331	1510.8	4.6	0.0065	0.82	1.6	1.4	1.9	1.4	1.9
J0140-1532	223	1506.8	6.8	0.12	0.71	2.0	0.9	2.4	0.4	...
J0141-0202	255	1506.9	5.9	0.08	0.72	1.7	0.6	2.2	0.3	2.5
J0141-0928	250	1503.9	6.0	0.036	0.06	1.8	0.6	2.3	0.4	2.9
J0143+4129	322	1494.9	4.7	0.19	0.81	1.7	0.4	2.2	0.0	...
J0149+0555	240	1481.0	6.2	0.13	0.44	1.8	0.4	2.5	0.1	...
J0154+4743	324	1494.9	4.6	0.021	0.81	2.9	2.5	3.2	2.5	...
J0202+3943	323	1467.0	4.6	0.11	0.66	2.2	1.9	2.8	0.9	3.0
J0202+4205	318	1485.0	4.7	0.049	0.38	1.6	0.3	1.9	0.3	1.9
J0203+1134	308	1503.1	4.9	0.022	0.39	2.4	2.2	2.8	0.9	2.8
J0203+7232	206	1494.0	7.3	0.056	0.53	2.3	0.9	2.7	0.9	...
J0204+4005	313	1485.0	4.8	0.2	0.67	1.8	0.4	2.2	0.0	...
J0204-1701	244	1487.8	6.1	0.11	0.08	1.6	0.1	2.1	0.0	...
J0205+3212	323	1495.9	4.6	0.0039	0.65	2.7	2.6	2.9	2.6	3.1
J0206-1150	251	1500.9	6.0	0.021	0.21	2.1	1.7	2.5	1.5	2.5
J0217+7349	214	1494.0	7.0	0.017	0.57	1.5	1.3	1.7	0.8	2.1
J0219-1842	219	1497.8	6.9	0.045	0.58	2.0	0.6	2.4	0.6	2.6
J0222-1615	184	1327.3	7.3	0.13	0.15	1.4	0.3	2.3	0.0	...
J0224+0659	191	1214.7	6.4	0.0069	1.0	2.0	1.8	2.3	1.3	2.7
J0225+1846	294	1499.1	5.1	0.0070	0.58	2.5	2.3	2.8	1.2	2.8
J0231+1322	295	1503.1	5.1	0.019	0.6	2.9	2.8	3.3	2.7	3.4
J0237+0526	212	1215.7	5.8	0.089	0.14	2.0	0.4	3.0	0.1	...
J0237+2848	296	1494.9	5.1	0.011	0.38	2.7	2.5	3.0	2.5	3.0
J0239-0234	204	1505.9	7.4	0.016	0.72	2.4	1.8	2.8	1.4	...
J0241-0815	247	1505.9	6.1	0.031	0.6	2.0	1.7	2.2	0.6	2.5
J0242+1742	258	1501.1	5.8	0.064	0.31	1.9	1.2	2.4	0.6	...
J0243-0550	187	1505.9	8.1	0.065	0.36	2.0	0.6	2.7	0.6	2.7
J0251+7226	196	1489.4	7.6	0.07	0.51	2.2	0.6	2.9	0.4	...
J0254+3931	316	1492.9	4.7	0.045	0.9	2.0	1.6	2.2	0.6	2.2
J0257+7843	207	1494.0	7.3	0.49	0.24	1.4	0.0	3.0	0.0	...
J0258+0541	209	1215.7	5.8	0.15	0.62	1.6	0.3	3.4	0.0	...

Continues

Table C.1

OVRO name	N points	T	$\langle\Delta t\rangle$	$\sigma^2_{\rm noise}/\sigma^2_{\rm data}$	p-value	β	$\beta_{\rm low}$	$\beta_{\rm up}$	$\beta^{\rm comb}_{\rm low}$	$\beta^{\rm comb}_{\rm up}$
J0259+0747	152	932.3	6.2	0.025	0.96	2.3	0.9	3.0	0.7	...
J0309+1029	328	1506.9	4.6	0.02	0.91	2.0	0.9	2.5	0.9	2.5
J0312+0133	232	1505.9	6.5	0.087	0.91	1.9	0.6	2.5	0.6	...
J0313+4120	334	1496.9	4.5	0.019	0.77	2.1	1.8	2.3	0.6	2.9
J0319+4130	337	1496.9	4.5	0.0058	0.9	2.8	2.5	3.0	2.5	3.0
J0319-1613	187	1476.0	7.9	0.044	0.64	2.2	1.2	2.6	0.6	3.3
J0325+2224	317	1510.9	4.8	0.01	0.47	2.3	2.0	2.5	2.0	2.8
J0329+3510	316	1496.9	4.8	0.022	0.53	2.2	1.5	2.5	1.1	2.5
J0339-0146	251	1502.9	6.0	0.0076	1.0	2.7	2.4	3.0	2.4	3.0
J0345+1453	212	1510.9	7.2	0.066	0.13	1.9	0.6	2.4	0.6	...
J0354+8009	137	917.5	6.7	0.17	0.49	1.6	0.0	3.4	0.0	...
J0357+2319	300	1510.9	5.1	0.02	0.34	2.0	1.7	2.2	1.4	2.4
J0401+0413	239	1505.9	6.3	0.028	0.93	1.6	1.1	2.0	0.6	2.2
J0403+2600	304	1504.1	5.0	0.017	0.97	2.2	1.9	2.4	1.9	2.5
J0406+0637	231	1506.0	6.5	0.048	1.0	2.2	0.6	2.8	0.6	...
J0407+0742	225	1506.0	6.7	0.019	0.14	1.9	1.4	2.3	1.4	2.4
J0409-1238	216	1494.0	6.9	0.089	0.29	1.8	0.6	2.7	0.6	...
J0414+3418	262	1502.2	5.8	0.074	1.0	1.8	1.4	2.2	1.1	...
J0416-1851	153	1051.1	6.9	0.025	0.46	2.0	0.9	2.3	0.6	2.3
J0423-0120	229	1496.0	6.6	0.0058	0.63	2.5	2.2	2.7	2.2	2.8
J0433+0521	242	1500.9	6.2	0.0087	0.52	2.2	1.9	2.4	1.8	2.5
J0442-0017	220	1500.9	6.9	0.02	0.48	1.8	1.3	2.1	0.8	...
J0449+1121	265	1500.9	5.7	0.013	0.88	2.4	2.2	2.8	2.0	3.0
J0449+6332	247	1061.1	4.3	0.0044	0.69	2.4	2.2	2.6	1.9	3.0
J0501-0159	211	1500.9	7.1	0.021	0.66	2.4	1.9	2.7	0.9	...
J0502+1338	238	1501.9	6.3	0.041	0.96	2.5	2.2	3.0	1.2	...
J0505+0459	233	1500.9	6.5	0.017	0.52	2.2	1.5	2.8	0.6	2.8
J0508+8432	213	1489.5	7.0	0.047	0.63	2.5	0.4	2.8	0.4	3.4
J0509+0541	228	1501.0	6.6	0.043	0.59	2.2	1.9	2.7	0.6	2.7
J0510+1800	230	1491.9	6.5	0.014	0.53	3.0	2.8	3.2	2.6	3.2
J0527+0331	218	1501.0	6.9	0.035	0.57	2.1	0.9	2.5	0.9	2.8
J0541-0541	166	1220.7	7.4	0.025	0.93	2.4	1.2	2.8	1.1	2.9
J0542-0913	162	1343.4	8.3	0.027	0.87	2.4	0.9	3.0	0.9	...
J0558-1317	243	1508.9	6.2	0.14	0.31	2.3	0.6	3.1	0.6	...
J0607-0834	238	1502.9	6.3	0.0048	0.06	1.3	1.2	1.5	1.1	1.6
J0609-1542	158	1076.1	6.9	0.0075	0.16	2.3	2.0	2.5	1.4	2.7
J0616-1041	224	1506.9	6.8	0.093	0.07	1.5	0.6	2.0	0.5	2.8
J0618+4620	238	1494.9	6.3	0.1	0.63	1.7	0.9	2.2	0.3	...
J0625+4440	238	1505.0	6.4	0.051	0.99	2.0	0.6	2.5	0.6	3.4
J0626+8202	202	1501.7	7.5	0.049	0.57	2.3	1.2	3.4	0.9	...
J0629-1959	156	1070.1	6.9	0.025	0.53	1.9	0.8	2.4	0.6	...
J0630-1323	234	1502.9	6.5	0.11	0.9	2.0	0.6	3.4	0.6	...

Continues

Table C.1

OVRO name	N points	T	$\langle\Delta t\rangle$	$\sigma^2_{\rm noise}/\sigma^2_{\rm data}$	p-value	β	$\beta_{\rm low}$	$\beta_{\rm up}$	$\beta^{\rm comb}_{\rm low}$	$\beta^{\rm comb}_{\rm up}$
J0639+7324	169	1203.1	7.2	0.0074	0.96	2.6	1.4	3.0	1.4	3.1
J0642+8811	205	1495.5	7.3	0.047	1.0	2.0	0.6	3.0	0.4	...
J0646+4451	237	1508.9	6.4	0.019	0.91	2.6	2.2	2.8	0.9	2.9
J0654+4514	242	1508.9	6.3	0.0052	0.57	2.2	1.9	2.5	1.7	2.6
J0717+4538	233	1499.0	6.5	0.037	0.11	2.3	1.9	2.8	0.6	3.5
J0725+1425	211	1504.0	7.2	0.036	0.94	1.1	0.5	1.5	0.5	...
J0728+5701	246	1505.0	6.1	0.039	0.49	2.0	1.2	2.2	0.9	2.4
J0733+5022	252	1508.9	6.0	0.063	0.34	1.7	0.8	2.1	0.6	...
J0739+0137	167	1067.9	6.4	0.019	0.47	2.0	0.9	2.5	0.6	...
J0741+3112	182	1475.0	8.1	0.042	0.63	2.2	0.9	2.8	0.6	3.2
J0742+4900	248	1508.9	6.1	0.11	0.23	1.7	0.6	3.4	0.6	...
J0742+5444	159	1016.3	6.4	0.013	0.095	1.9	0.8	2.5	0.6	2.9
J0746+2549	134	934.5	7.0	0.037	0.05	2.0	0.6	3.4	0.6	...
J0746+2734	197	1508.9	7.7	0.039	0.44	1.8	0.6	2.6	0.6	...
J0748+2400	151	1348.3	9.0	0.014	0.79	2.3	1.4	2.8	1.1	...
J0750+1021	198	1503.9	7.6	0.087	0.58	2.1	0.6	2.8	0.6	...
J0750+1231	182	1503.9	8.3	0.022	0.48	2.1	0.9	2.5	0.9	2.9
J0750+1823	155	1505.0	9.8	0.06	0.4	2.3	0.6	3.0	0.6	3.2
J0750+4814	265	1509.0	5.7	0.057	0.78	1.8	1.4	2.1	0.6	3.4
J0752+3730	192	1502.9	7.9	0.21	0.35	1.8	0.6	2.7	0.0	3.4
J0753+5352	246	1508.9	6.2	0.021	0.08	2.1	1.1	2.4	0.9	2.5
J0757+0956	193	1503.9	7.8	0.018	0.44	2.0	1.9	2.4	1.6	2.6
J0805+6144	262	1503.2	5.8	0.031	0.17	2.3	0.9	2.7	0.9	...
J0805-0111	236	1502.9	6.4	0.033	0.85	2.2	0.9	2.6	0.9	2.6
J0808+4052	206	1508.9	7.4	0.041	0.69	2.2	1.2	2.9	1.1	...
J0808+4950	202	1509.0	7.5	0.037	0.46	2.3	0.9	2.8	0.6	...
J0808-0751	241	1502.9	6.3	0.0042	0.08	2.0	1.6	2.2	1.6	2.5
J0811+0146	215	1500.0	7.0	0.015	0.5	1.9	1.4	2.2	1.3	...
J0811+4533	195	1509.0	7.8	0.032	0.95	2.1	1.2	2.5	1.2	2.8
J0818+4222	207	1509.0	7.3	0.013	0.14	2.0	1.1	2.3	1.1	2.6
J0824+3916	212	1508.9	7.2	0.02	0.33	2.4	1.5	2.9	0.9	3.2
J0825+0309	243	1502.9	6.2	0.0059	0.36	2.5	2.4	2.7	2.2	2.9
J0831+0429	245	1502.9	6.2	0.014	0.55	1.9	0.8	2.1	0.6	2.3
J0833+4224	202	1509.0	7.5	0.063	0.76	2.0	0.6	2.4	0.1	...
J0837+5825	198	1501.0	7.6	0.013	0.71	2.4	2.2	2.8	2.0	2.8
J0839+0104	223	1500.0	6.8	0.038	0.47	2.7	2.2	3.0	2.0	...
J0847-0703	223	1502.9	6.8	0.013	0.47	2.4	2.1	2.5	2.1	2.6
J0902+4310	160	1066.1	6.7	0.011	0.51	1.9	0.6	2.8	0.6	2.8
J0909+0121	237	1507.9	6.4	0.013	0.53	2.3	1.8	2.6	1.4	...
J0921+6215	230	1508.9	6.6	0.039	1.0	2.0	0.6	3.4	0.6	...
J0929+5013	239	1508.9	6.3	0.076	0.22	1.8	0.9	2.6	0.6	...
J0929+8612	215	1501.7	7.0	0.052	0.82	2.7	1.2	3.3	0.9	...

Continues

Table C.1

OVRO name	N points	T	$\langle\Delta t\rangle$	$\sigma^2_{\rm noise}/\sigma^2_{\rm data}$	p-value	β	$\beta_{\rm low}$	$\beta_{\rm up}$	$\beta^{\rm comb}_{\rm low}$	$\beta^{\rm comb}_{\rm up}$
J0933-0819	220	1502.9	6.9	0.082	0.78	1.8	0.8	3.1	0.6	...
J0948+0022	211	1498.9	7.1	0.02	0.13	2.1	1.3	2.4	1.1	3.4
J0948+4039	214	1282.5	6.0	0.012	0.47	2.8	0.9	3.2	0.9	...
J0956+2515	307	1507.9	4.9	0.019	0.52	2.0	1.4	2.2	0.9	3.4
J0958+4725	209	1289.5	6.2	0.015	0.86	2.4	2.2	3.0	0.9	3.0
J0958+5039	195	1289.5	6.6	0.12	0.95	2.2	0.0	3.3	0.0	...
J0958+6533	261	1509.2	5.8	0.0093	0.37	1.9	1.6	2.1	0.8	2.2
J1007-0207	218	1502.9	6.9	0.08	0.75	2.2	0.6	2.8	0.6	3.4
J1012+2312	289	1508.9	5.2	0.074	0.29	2.0	0.6	2.6	0.4	...
J1013+3445	213	1288.9	6.1	0.13	0.83	1.5	0.1	2.2	0.1	...
J1014+2301	271	1508.2	5.6	0.091	0.1	2.0	1.8	2.6	0.9	2.8
J1018+0530	211	1507.9	7.2	0.098	0.05	1.6	0.6	3.4	0.3	...
J1024+1912	277	1504.9	5.5	0.068	1.0	2.6	2.1	3.2	0.7	...
J1025+1253	229	1503.0	6.6	0.041	0.1	2.1	0.6	2.4	0.6	...
J1025-0509	209	1506.0	7.2	0.047	0.9	1.8	0.8	2.1	0.8	...
J1033+3935	199	1288.9	6.5	0.88	0.19	3.1	0.0	3.4	0.0	...
J1033+4116	204	1288.9	6.3	0.0032	0.13	2.4	2.0	2.8	1.4	2.9
J1033+6051	167	1128.2	6.8	0.014	0.19	2.5	0.9	2.9	0.9	...
J1036+2203	271	1508.2	5.6	0.072	0.19	1.8	0.6	3.3	0.6	...
J1038+0512	201	1507.9	7.5	0.021	0.15	2.0	1.1	2.5	1.1	2.6
J1044+8054	229	1501.7	6.6	0.021	0.85	2.8	0.9	3.2	0.9	...
J1048+7143	250	1507.7	6.1	0.014	0.31	2.0	1.4	2.2	1.1	2.6
J1048-1909	150	1073.0	7.2	0.012	0.13	2.4	1.8	2.8	0.9	...
J1056+7011	167	1073.3	6.5	0.0026	0.77	2.6	2.4	2.9	2.4	3.0
J1058+8114	226	1501.7	6.7	0.011	0.73	1.9	1.6	2.5	1.3	2.7
J1059+2057	293	1508.9	5.2	0.089	0.08	1.6	1.3	2.1	0.3	3.3
J1104+3812	276	1508.2	5.5	0.13	0.34	1.8	0.4	2.2	0.0	...
J1108+4330	244	1508.2	6.2	0.13	0.58	1.9	0.4	3.3	0.1	...
J1113+1442	277	1508.9	5.5	0.05	0.72	1.9	1.5	2.7	1.0	...
J1118+1234	324	1504.9	4.7	0.049	0.54	2.4	0.7	3.0	0.7	3.2
J1124+2336	282	1504.9	5.4	0.0094	0.96	3.2	2.9	3.4	2.8	...
J1125+2610	324	1507.9	4.7	0.024	0.88	2.7	2.4	3.0	1.0	3.0
J1127+0555	204	1503.0	7.4	0.015	0.55	1.9	1.4	2.2	0.8	2.5
J1127+5650	247	1504.9	6.1	0.056	0.16	2.0	0.6	2.7	0.6	...
J1127-1857	197	1483.9	7.6	0.0079	0.22	2.0	1.7	2.3	1.6	2.4
J1128+5925	238	1502.9	6.3	0.028	0.97	2.1	0.9	2.6	0.6	3.4
J1130+3815	265	1504.9	5.7	0.032	0.51	2.3	1.8	2.8	0.9	...
J1135-0428	197	1503.0	7.7	0.025	0.98	2.1	1.4	2.4	1.1	...
J1146+3958	243	1508.2	6.2	0.0077	0.89	2.5	2.0	2.8	1.9	3.0
J1146+5356	243	1504.9	6.2	0.045	0.8	1.7	0.6	2.4	0.6	...
J1146+5848	232	1504.9	6.5	0.0099	0.78	2.7	2.4	2.9	1.2	3.0
J1147+2635	335	1504.9	4.5	0.066	0.89	2.6	0.4	3.2	0.4	...

Continues

Table C.1

OVRO name	N points	T	$\langle\Delta t\rangle$	$\sigma^2_{\rm noise}/\sigma^2_{\rm data}$	p-value	β	$\beta_{\rm low}$	$\beta_{\rm up}$	$\beta^{\rm comb}_{\rm low}$	$\beta^{\rm comb}_{\rm up}$
J1150-0640	205	1507.0	7.4	0.033	0.8	2.5	0.9	2.8	0.9	2.8
J1152-0841	205	1507.0	7.4	0.0074	0.9	2.7	2.2	3.0	1.2	3.2
J1157+5527	251	1504.9	6.0	0.028	0.94	2.1	1.7	2.5	0.9	2.7
J1159+2914	275	1504.9	5.5	0.0038	0.22	2.1	1.9	2.4	1.8	2.6
J1202-0528	199	1507.0	7.6	0.031	0.57	2.4	0.7	2.8	0.7	3.0
J1203+4803	272	1508.2	5.6	0.049	0.14	2.1	1.5	2.8	0.6	...
J1207+1211	246	1507.1	6.2	0.058	0.72	2.2	0.6	2.5	0.6	3.4
J1207+2754	342	1504.9	4.4	0.047	0.43	2.7	0.9	3.3	0.7	...
J1215+1654	347	1508.9	4.4	0.061	0.6	1.6	0.8	3.3	0.8	...
J1219+4829	273	1505.0	5.5	0.015	0.05	2.4	2.2	2.9	2.1	2.9
J1220+3808	268	1508.2	5.6	0.072	0.87	1.9	0.6	2.2	0.6	...
J1222+0413	180	1502.9	8.4	0.021	0.05	1.9	1.6	2.6	1.4	2.6
J1226-1328	219	1507.0	6.9	0.04	0.08	2.1	1.6	2.7	0.9	2.8
J1228+3706	270	1508.2	5.6	0.045	0.46	2.1	1.9	2.6	1.8	2.6
J1229+0203	334	1503.9	4.5	0.019	0.39	2.2	1.9	2.5	0.6	2.8
J1230+2518	304	1508.9	5.0	0.0083	0.71	2.2	1.1	2.4	1.1	2.9
J1235+3621	257	1502.2	5.9	0.31	0.36	2.4	0.0	3.4	0.0	...
J1238+0723	202	1503.0	7.5	0.067	0.35	2.1	0.9	2.5	0.6	...
J1239+0730	210	1507.0	7.2	0.039	0.62	1.6	1.0	2.0	0.8	...
J1254+1141	386	1508.8	3.9	0.0082	0.3	2.5	2.3	2.6	2.3	2.9
J1254-1317	202	1505.0	7.5	0.066	0.77	1.8	0.6	3.4	0.6	...
J1256-0547	283	1508.0	5.3	0.0064	0.91	2.4	2.2	2.6	2.0	2.7
J1257+3229	414	1508.9	3.7	0.028	0.12	2.0	1.7	2.2	1.2	2.2
J1300+1206	316	1504.0	4.8	0.1	0.19	2.2	1.0	3.0	0.6	...
J1300+2830	404	1508.9	3.7	0.08	0.98	2.1	1.8	2.8	1.6	2.8
J1302+5748	212	1495.3	7.1	0.018	0.63	2.7	2.4	3.2	1.2	3.3
J1305-1033	199	1506.9	7.6	0.016	0.07	2.4	2.2	3.0	1.1	3.4
J1306+5529	214	1495.3	7.0	0.083	1.0	1.9	0.6	3.3	0.4	3.4
J1308+3546	399	1502.9	3.8	0.07	0.85	2.0	0.6	2.6	0.6	...
J1310+3220	413	1502.9	3.6	0.0065	0.2	2.2	1.9	2.4	1.9	2.4
J1310+3233	389	1508.9	3.9	0.034	0.29	1.7	0.6	2.0	0.6	2.4
J1317+3425	407	1502.9	3.7	0.063	0.91	2.0	0.6	2.2	0.6	2.2
J1322-0937	211	1506.9	7.2	0.027	0.64	2.1	1.5	2.8	1.2	2.8
J1323+7942	156	1067.2	6.9	0.033	0.69	1.9	0.9	2.8	0.9	...
J1326-0500	204	1504.9	7.4	0.078	0.97	2.1	1.4	3.4	0.6	...
J1327+1223	319	1489.0	4.7	0.036	0.33	2.3	0.7	3.0	0.6	3.0
J1327+2210	466	1508.8	3.2	0.014	0.16	2.1	1.9	2.5	1.9	2.5
J1332-0509	212	1503.0	7.1	0.0089	0.45	2.2	1.7	2.7	1.4	2.9
J1333+2725	495	1508.9	3.1	0.02	0.6	2.1	1.6	2.4	1.1	2.4
J1335+4542	249	1503.0	6.1	0.18	0.8	1.4	0.3	3.1	0.0	3.1
J1337+5501	198	1482.3	7.5	0.048	0.7	2.2	0.9	2.8	0.9	...
J1337-1257	136	1074.1	8.0	0.0070	0.67	2.6	2.1	3.0	2.1	3.0

Continues

Table C.1

OVRO name	N points	T	$\langle\Delta t\rangle$	$\sigma^2_{\rm noise}/\sigma^2_{\rm data}$	p-value	β	$\beta_{\rm low}$	$\beta_{\rm up}$	$\beta^{\rm comb}_{\rm low}$	$\beta^{\rm comb}_{\rm up}$
J1342+2709	487	1508.9	3.1	0.044	0.95	2.5	2.2	2.8	2.2	3.0
J1344+6606	166	1073.2	6.5	0.063	0.99	2.4	0.7	3.0	0.4	3.5
J1345+0706	131	922.5	7.1	0.028	0.9	2.1	0.9	2.5	0.4	2.6
J1349+5341	207	1489.2	7.2	0.056	0.32	1.5	1.1	2.1	0.6	2.1
J1349-1132	141	1074.1	7.7	0.028	0.34	2.0	0.8	2.7	0.6	...
J1357+7643	197	1503.0	7.7	0.0087	0.92	2.5	2.0	3.0	2.0	3.0
J1405-1440	138	1075.1	7.8	0.64	1.0	0.9	0.0	1.1	0.0	...
J1410+0731	229	1503.0	6.6	0.066	0.45	2.0	0.6	2.6	0.6	...
J1415+0832	237	1508.0	6.4	0.056	0.14	1.9	0.6	2.3	0.6	...
J1420+1703	189	1502.9	8.0	0.037	0.96	2.0	1.5	2.5	0.8	...
J1426+3625	211	1281.6	6.1	0.026	0.34	2.3	0.9	2.8	0.6	2.9
J1436+6336	250	1505.2	6.0	0.082	0.99	2.1	1.5	2.8	0.6	3.2
J1445-1629	135	1067.0	8.0	0.053	0.3	2.0	0.4	3.3	0.4	...
J1446+1721	318	1499.9	4.7	0.012	0.98	2.6	2.4	2.9	2.3	2.9
J1448+7601	146	1067.2	7.4	0.023	0.76	2.0	0.6	2.8	0.6	2.9
J1450+0910	309	1508.9	4.9	0.02	0.85	2.3	1.1	2.9	0.9	2.9
J1453+2648	153	1070.3	7.0	0.022	0.82	2.2	1.9	2.7	0.9	...
J1504+1029	328	1508.9	4.6	0.0037	0.084	2.5	2.3	2.7	2.2	2.8
J1513-1012	218	1508.9	7.0	0.044	0.16	2.2	0.6	3.4	0.6	3.4
J1516+1932	369	1508.1	4.1	0.0081	0.61	2.6	2.3	2.9	2.2	2.9
J1534+0131	250	1508.1	6.1	0.041	0.2	2.1	1.1	2.5	0.9	2.7
J1539+2744	304	1508.2	5.0	0.045	0.33	1.6	0.6	3.1	0.6	3.1
J1540+1447	220	1288.7	5.9	0.036	0.08	2.2	0.9	2.4	0.9	...
J1549+0237	259	1508.1	5.8	0.0089	0.39	2.5	2.2	2.8	2.0	2.8
J1551+5806	228	1508.8	6.6	0.32	0.53	1.4	0.0	3.3	0.0	...
J1552+0850	140	938.6	6.8	0.044	0.12	1.9	0.6	2.3	0.3	...
J1557-0001	252	1508.0	6.0	0.054	0.11	2.4	0.7	2.8	0.7	...
J1602+2646	276	1504.9	5.5	0.37	0.98	0.6	0.0	0.9	0.0	...
J1603+1105	228	1288.7	5.7	0.029	0.95	2.5	0.9	3.0	0.9	...
J1605+3001	203	1504.9	7.5	0.079	0.74	1.6	0.8	3.0	0.0	...
J1610+2414	192	1281.5	6.7	0.1	0.69	2.1	0.6	2.9	0.1	...
J1613+3412	201	1500.9	7.5	0.018	0.51	2.7	2.4	2.9	2.3	3.1
J1616+4632	143	925.8	6.5	0.056	0.15	2.0	0.6	3.4	0.6	...
J1617+0246	266	1508.1	5.7	0.15	0.59	1.6	0.6	3.4	0.3	3.4
J1625+4134	206	1508.2	7.4	0.026	0.27	2.4	2.1	2.9	2.1	2.9
J1630+0701	260	1500.9	5.8	0.1	0.94	2.0	0.6	2.7	0.4	3.4
J1635+3808	162	1070.0	6.6	0.0069	0.98	2.1	1.6	2.5	1.4	2.9
J1637+4717	177	1505.0	8.6	0.042	0.69	2.0	1.7	3.4	0.9	3.4
J1638+5720	178	1504.9	8.5	0.012	0.64	2.2	1.7	2.5	0.9	2.7
J1640+3946	178	1073.1	6.1	0.0090	0.39	2.0	0.8	2.4	0.8	3.4
J1642+3948	169	1067.1	6.4	0.015	0.91	2.5	0.9	3.0	0.9	...
J1642+6856	166	1073.4	6.5	0.0012	0.64	3.1	2.9	3.2	2.8	3.2

Continues

Table C.1

OVRO name	N points	T	$\langle\Delta t\rangle$	$\sigma^2_{\rm noise}/\sigma^2_{\rm data}$	p-value	β	$\beta_{\rm low}$	$\beta_{\rm up}$	$\beta^{\rm comb}_{\rm low}$	$\beta^{\rm comb}_{\rm up}$
J1642-0621	185	1074.2	5.8	0.0044	0.44	2.6	2.4	2.8	1.2	2.9
J1648+2224	190	1288.8	6.8	0.21	0.17	1.7	0.1	3.4	0.0	...
J1649+0412	264	1500.9	5.7	0.058	0.31	2.0	0.4	2.2	0.4	2.6
J1651+0129	275	1500.9	5.5	0.047	0.55	1.8	1.5	2.4	0.8	2.6
J1652+3902	183	1073.1	5.9	0.037	1.0	1.5	0.6	2.3	0.6	...
J1657+4808	224	1503.9	6.7	0.022	0.09	2.0	1.6	2.4	0.9	2.7
J1707+0148	288	1504.0	5.2	0.025	0.43	2.5	2.2	3.0	1.5	3.0
J1707-1415	250	1509.9	6.1	0.14	0.16	2.1	0.4	2.6	0.4	...
J1719+1745	315	1508.1	4.8	0.061	0.15	1.3	1.1	1.6	0.8	2.6
J1722+2815	248	1493.9	6.0	0.027	0.78	2.2	2.0	2.5	2.0	2.7
J1722+6105	207	1501.2	7.3	0.027	0.51	2.0	1.1	2.5	0.9	2.5
J1728+0427	285	1508.0	5.3	0.013	0.36	1.9	1.8	2.1	1.6	2.2
J1733-0456	188	1074.1	5.7	0.2	0.43	1.7	0.4	2.9	0.0	...
J1733-1304	273	1510.8	5.6	0.02	0.91	2.0	1.7	2.2	1.5	2.4
J1734+3857	185	1073.1	5.8	0.032	0.19	2.0	0.9	3.0	0.1	...
J1736+0631	253	1502.0	6.0	0.069	0.07	1.9	0.6	2.4	0.6	2.6
J1738+4008	256	1507.8	5.9	0.15	0.53	1.9	0.4	2.6	0.0	...
J1739+4955	229	1503.9	6.6	0.03	0.14	2.0	1.6	2.6	1.1	2.6
J1740+5211	223	1503.9	6.8	0.0086	0.17	2.5	2.2	2.9	1.8	3.0
J1740-0811	187	1074.1	5.8	0.093	0.71	2.0	0.0	3.2	0.0	...
J1743+3747	261	1507.8	5.8	0.036	0.73	3.0	2.8	3.2	2.5	...
J1743-0350	168	1184.8	7.1	0.0090	0.93	3.1	1.2	3.2	1.2	3.4
J1745-0753	190	1074.1	5.7	0.0064	0.41	2.2	2.0	2.5	1.4	2.5
J1748+3404	254	1493.9	5.9	0.15	0.33	1.5	0.3	1.8	0.1	...
J1748+7005	250	1508.0	6.1	0.022	0.92	2.2	1.5	2.5	1.4	2.7
J1749+4321	254	1503.9	5.9	0.14	0.96	1.7	0.6	2.1	0.4	...
J1752+1734	325	1502.0	4.6	0.061	0.5	2.0	0.1	3.3	0.1	...
J1753+2848	265	1493.9	5.7	0.0070	0.76	2.8	2.5	3.0	2.5	3.0
J1754+6452	236	1508.0	6.4	0.05	0.68	2.7	2.2	3.0	0.7	...
J1759+2343	334	1487.9	4.5	0.077	0.92	2.5	0.9	3.2	0.7	3.5
J1800+3848	260	1493.9	5.8	0.047	0.89	2.4	2.0	2.8	0.9	2.9
J1801+4404	248	1503.9	6.1	0.0043	0.49	2.6	2.4	2.8	2.4	3.0
J1806+6949	246	1508.0	6.2	0.072	0.22	1.9	1.5	2.7	0.6	...
J1808+4542	245	1503.9	6.2	0.078	0.21	2.0	1.7	2.4	0.9	...
J1809+1849	328	1508.9	4.6	0.11	0.96	2.1	1.9	2.4	0.9	3.2
J1811+1704	335	1502.0	4.5	0.014	0.35	2.5	2.2	2.8	1.2	2.8
J1813+2952	257	1493.9	5.8	0.14	0.09	1.9	0.4	2.7	0.4	...
J1815+1623	340	1508.9	4.5	0.019	0.96	2.3	2.2	2.6	2.1	2.8
J1824+1044	336	1501.9	4.5	0.15	0.78	1.5	0.4	2.6	0.1	...
J1824+5651	240	1503.9	6.3	0.062	0.4	1.9	0.6	2.2	0.4	2.9
J1832+1357	336	1494.9	4.5	0.031	0.19	2.1	1.2	2.4	0.9	3.4
J1842+6809	241	1508.0	6.3	0.0053	0.91	2.7	2.5	2.9	2.4	3.0

Continues

Table C.1

OVRO name	N points	T	$\langle\Delta t\rangle$	$\sigma^2_{\rm noise}/\sigma^2_{\rm data}$	p-value	β	$\beta_{\rm low}$	$\beta_{\rm up}$	$\beta^{\rm comb}_{\rm low}$	$\beta^{\rm comb}_{\rm up}$
J1848+3219	265	1503.9	5.7	0.024	0.58	2.2	1.9	2.6	1.9	2.7
J1849+6705	242	1508.0	6.3	0.017	0.31	1.9	1.5	2.3	0.8	2.5
J1854+7351	219	1508.0	6.9	0.11	0.72	1.9	0.8	2.9	0.4	...
J1912+3740	253	1503.8	6.0	0.058	0.71	2.6	2.3	3.1	0.7	...
J1918+5520	251	1503.9	6.0	0.12	0.77	2.0	0.6	2.5	0.6	...
J1927+6117	251	1494.0	6.0	0.025	0.12	2.2	2.0	2.4	0.9	2.7
J1927+7358	216	1494.2	6.9	0.015	0.76	1.8	1.6	2.2	1.4	2.5
J1933+6540	246	1507.9	6.2	0.12	0.55	2.2	0.4	2.8	0.2	3.2
J1936+7131	163	1073.1	6.6	0.11	0.97	1.0	0.3	3.4	0.3	...
J1939-1525	207	1209.6	5.9	0.065	0.39	1.6	0.8	2.4	0.6	...
J1951-0509	235	1509.9	6.5	0.094	0.21	2.1	0.4	2.6	0.4	...
J1954-1123	197	1076.0	5.5	0.0062	0.07	2.2	1.8	2.6	0.9	2.7
J1955+5131	247	1501.9	6.1	0.056	0.8	2.2	2.0	2.8	0.6	...
J2000-1748	236	1221.6	5.2	0.0026	0.57	2.3	2.0	2.6	1.8	2.8
J2005+7752	263	1506.9	5.8	0.0083	0.07	2.0	1.8	2.2	0.8	2.2
J2006+6424	252	1507.9	6.0	0.028	0.9	2.3	2.1	2.6	1.2	2.7
J2011-1546	249	1486.8	6.0	0.039	0.76	2.5	1.2	3.0	0.7	3.0
J2015+6554	257	1507.9	5.9	0.029	0.75	1.8	1.5	2.1	1.4	2.1
J2022+7611	171	1074.7	6.3	0.0075	0.77	2.6	2.2	3.0	1.5	3.0
J2024+1718	261	1502.8	5.8	0.11	0.97	2.2	0.2	2.7	0.1	3.2
J2031+1219	346	1504.0	4.4	0.017	0.93	1.9	1.5	2.0	1.4	2.1
J2036-0629	287	1513.0	5.3	0.18	0.68	2.2	0.4	3.0	0.0	...
J2049+1003	221	1070.0	4.9	0.096	0.4	1.7	0.4	2.0	0.0	3.4
J2051+1743	372	1504.0	4.1	0.063	1.0	1.7	0.6	2.0	0.4	2.3
J2101+0341	300	1506.9	5.0	0.035	0.93	2.1	1.9	3.4	0.9	...
J2102+6758	264	1495.3	5.7	0.22	0.46	1.2	0.8	1.5	0.6	...
J2106+2135	337	1508.9	4.5	0.19	0.08	1.8	0.6	3.2	0.1	...
J2108+1430	376	1492.2	4.0	0.096	0.51	2.2	0.7	2.6	0.4	...
J2115+2933	258	1284.4	5.0	0.058	0.89	2.0	1.2	2.2	0.6	...
J2125+0441	308	1506.9	4.9	0.16	0.84	2.5	0.7	2.8	0.4	...
J2128-0244	298	1485.0	5.0	0.13	0.37	1.8	1.0	2.4	0.4	2.5
J2130-0927	263	1512.9	5.8	0.017	0.98	2.7	2.5	3.3	0.9	...
J2131-1207	193	1076.1	5.6	0.031	0.71	2.7	2.2	3.2	0.7	...
J2133+1443	396	1508.9	3.8	0.044	0.78	2.7	2.4	3.1	0.7	3.4
J2134-0153	294	1506.9	5.1	0.026	0.39	2.1	1.8	2.6	1.8	2.9
J2136+0041	308	1506.9	4.9	0.075	0.35	1.7	1.1	1.9	0.9	...
J2139+1423	341	1511.9	4.4	0.076	0.77	1.8	1.4	2.1	1.2	...
J2142-0437	279	1495.0	5.4	0.064	0.54	1.6	1.2	1.8	0.8	2.6
J2145+1115	359	1507.1	4.2	0.22	0.91	2.1	0.7	3.0	0.4	...
J2148+0657	305	1506.9	5.0	0.03	0.06	2.2	2.0	2.5	2.0	2.6
J2148-1723	213	1258.5	5.9	0.04	0.93	2.0	0.9	2.2	0.9	2.4
J2151+0709	300	1507.0	5.0	0.06	0.25	2.6	2.0	3.0	0.7	...

Continues

Table C.1

OVRO name	N points	T	$\langle\Delta t\rangle$	$\sigma^2_{\rm noise}/\sigma^2_{\rm data}$	p-value	β	$\beta_{\rm low}$	$\beta_{\rm up}$	$\beta^{\rm comb}_{\rm low}$	$\beta^{\rm comb}_{\rm up}$
J2152+1734	329	1505.8	4.6	0.33	0.98	1.7	0.4	2.6	0.0	...
J2156-0037	282	1506.9	5.4	0.045	0.27	1.8	1.5	2.0	0.9	2.0
J2200+2137	376	1508.9	4.0	0.98	0.23	2.4	0.0	3.4	0.0	...
J2203+1725	358	1507.8	4.2	0.023	0.23	2.0	1.7	2.2	1.5	2.3
J2203+3145	237	1270.5	5.4	0.021	0.76	2.1	1.8	2.4	1.8	2.6
J2206-0031	270	1506.9	5.6	0.04	0.67	1.8	1.5	2.3	0.6	2.3
J2207+1652	364	1508.9	4.2	0.063	0.41	2.4	0.7	3.0	0.6	...
J2211+1841	391	1511.9	3.9	0.017	0.31	1.9	1.5	2.2	1.5	2.2
J2212+2355	371	1508.9	4.1	0.041	0.77	1.7	1.4	2.0	1.4	2.2
J2216+3518	214	1074.1	5.0	0.081	0.36	2.0	0.4	2.6	0.1	...
J2217+2421	369	1511.9	4.1	0.048	0.24	2.0	1.2	2.2	0.6	2.4
J2218+1520	367	1504.1	4.1	0.055	0.5	1.7	0.6	2.2	0.6	...
J2218-0335	242	1495.0	6.2	0.05	0.62	1.8	1.4	2.3	1.1	2.6
J2225+2118	373	1507.9	4.1	0.014	0.18	2.5	2.3	2.7	2.1	2.8
J2226+0052	246	1504.0	6.1	0.023	0.67	2.5	0.9	2.8	0.7	3.4
J2229-0832	212	1101.0	5.2	0.0063	0.91	2.8	2.5	3.0	2.4	3.1
J2230+6946	228	1495.2	6.6	0.24	0.58	2.0	0.0	3.0	0.0	...
J2236+2828	321	1509.8	4.7	0.035	0.089	1.9	0.6	2.1	0.6	2.3
J2236-1433	221	1203.7	5.5	0.029	0.28	2.4	0.9	3.0	0.7	3.3
J2241+0953	349	1507.0	4.3	0.058	0.07	2.0	0.6	2.6	0.4	...
J2244+4057	178	927.4	5.2	0.0068	0.96	2.5	1.1	2.8	0.9	3.1
J2245+0324	240	1504.0	6.3	0.32	0.7	1.7	0.1	3.3	0.0	...
J2249+2107	356	1484.0	4.2	0.074	0.51	1.7	1.5	3.4	0.6	...
J2253+1608	323	1496.1	4.6	0.0015	0.072	2.4	2.1	2.6	1.9	2.6
J2253+1942	309	1496.1	4.9	0.031	0.63	2.0	1.8	2.2	1.5	2.5
J2300+1655	317	1494.1	4.7	0.11	0.08	1.9	0.6	2.2	0.6	2.5
J2301-0158	165	1112.0	6.8	0.021	0.98	2.0	0.9	2.4	0.9	2.6
J2310+1055	305	1496.1	4.9	0.12	0.3	1.8	0.1	2.4	0.0	...
J2311+4543	311	1500.1	4.8	0.019	0.85	2.3	1.9	2.5	1.2	2.7
J2321+2732	177	921.7	5.2	0.042	0.99	2.3	0.4	2.6	0.0	...
J2321+3204	150	929.7	6.2	0.18	0.38	1.5	0.1	2.2	0.0	...
J2322+1843	322	1496.1	4.7	0.25	0.21	2.8	0.4	3.4	0.0	...
J2322+4445	303	1500.1	5.0	0.18	0.47	1.5	0.3	3.0	0.1	...
J2329+0834	233	1504.0	6.5	0.037	0.29	2.1	0.6	2.9	0.6	...
J2331-1556	242	1496.9	6.2	0.041	0.65	1.9	1.4	2.4	0.8	...
J2335-0131	192	1212.7	6.3	0.028	0.15	2.2	0.6	2.8	0.4	...
J2337+2617	250	1500.2	6.0	0.12	0.92	2.5	0.7	2.8	0.4	...
J2337-0230	178	1198.7	6.8	0.15	0.12	1.3	0.0	3.4	0.0	...
J2343+2339	248	1502.1	6.1	0.065	0.89	1.9	1.2	2.3	1.2	2.3
J2345-1555	266	1497.9	5.7	0.012	0.72	1.9	1.7	2.3	1.5	2.3
J2346+0930	258	1495.0	5.8	0.048	0.38	1.9	1.2	2.2	0.4	2.2
J2346+8007	199	1508.9	7.6	0.032	0.57	2.3	1.2	2.8	1.1	...

Continues

Table C.1

OVRO name	N points	T	$\langle \Delta t \rangle$	$\sigma^2_{\rm noise}/\sigma^2_{\rm data}$	p-value	β	$\beta_{\rm low}$	$\beta_{\rm up}$	$\beta^{\rm comb}_{\rm low}$	$\beta^{\rm comb}_{\rm up}$
J2348-1631	267	1506.8	5.7	0.017	0.46	2.1	1.8	2.5	1.8	2.5
J2354-1513	281	1491.9	5.3	0.054	0.78	2.4	1.2	2.8	0.9	...
J2358+1955	280	1496.2	5.4	0.032	0.8	2.2	1.8	2.6	0.9	2.6
J2358-1020	278	1506.8	5.4	0.0088	0.49	2.3	2.0	2.5	2.0	2.8
PKS1510-089	134	1059.1	8.0	0.0021	0.18	2.3	1.6	2.9	1.6	2.9

Appendix D

Results of the PSD characterization of the UMRAO sources

This table contains the PSD fit information of the 14.5 GHz light curves for the sources in the University of Michigan Radio Observatory program as published in Hughes et al. (1992).

The columns contain the following information:

Source name: Name of the source as used in Hughes et al. (1992)

B1950 name: Name of the source in B1950 coordinates

RA: J2000 Right Ascension of the source

Dec: J2000 declination of the source

N points: Number of data points in the light curve

T: Time span of the light curve in days

$\langle \Delta t \rangle$**:** Mean sampling interval in days

$\sigma^2_{\rm noise}/\sigma^2_{\rm data}$**:** Ratio of estimated noise variance to total variance

p**-value:** p-value of the best fit power-law index of the PSD

β**:** Best fit value for the power-law index of the PSD

$\beta_{\rm low}$**:** 68.3% lower limit for the power-law index of the PSD

$\beta_{\rm up}$**:** 68.3% upper limit for the power-law index of the PSD

$\beta^{\rm comb}_{\rm low}$**:** 82.6% lower limit for the power-law index of the PSD

$\beta^{\rm comb}_{\rm up}$**:** 82.6% upper limit for the power-law index of the PSD

$b_{\rm s}$**:** Fitted slope of the structure function from Hughes et al. (1992)

Table D.1: Radio band PSD characterization for sources in the UMRAO sample

Source name	B1950 name	RA	Dec	N points	T	$\langle\Delta t\rangle$	$\sigma^2_{\rm noise}/\sigma^2_{\rm data}$	p-value	β	$\beta_{\rm low}$	$\beta_{\rm up}$	$\beta^{\rm comb}_{\rm low}$	$\beta^{\rm comb}_{\rm up}$	$b_{\rm s}$
IIIZW2	0007+106	00:10:31.0	+10:58:30	511	9924.9	19.5	0.0092	...	...	...	...	...	...	1.0
0048−097	0048−097	00:50:41.3	−09:29:05	227	4492.7	19.9	0.028	1.4e−01	1.8	1.6	2.1	1.4	2.9	1.0
DA55	0133+476	01:36:58.6	+47:51:29	401	5238.7	13.1	0.033	2.0e−02	1.9	1.7	...	1.2	...	0.9
0235+164	0235+164	02:38:38.9	+16:36:59	551	5930.0	10.8	0.0043	1.9e−01	1.9	1.7	2.1	1.7	2.2	1.0
0300+470	0300+470	03:03:35.2	+47:16:16	386	4985.4	12.9	0.023	1.1e−01	2.4	2.1	2.5	2.1	2.6	0.9
OE110	0306+102	03:09:03.6	+10:29:16	190	4492.7	23.8	0.05	5.1e−01	2.0	0.9	3.4	0.6	...	0.9
3C84	0316+413	03:19:48.2	+41:30:42	501	6516.1	13.0	0.0064	1.0e−01	3.5	3.1	...	3.1	...	1.6
NRAO140	0333+321	03:36:30.1	+32:18:29	270	4347.1	16.2	0.021	7.0e−01	2.9	2.5	3.2	2.5	...	1.6
CTA26	0336−019	03:39:30.9	−01:46:36	292	4601.3	15.8	0.033	9.2e−01	1.6	1.4	2.3	1.2	...	0.85
NRAO150	0355+508	03:59:29.7	+50:57:50	398	6337.0	16.0	0.0014	3.4e−01	3.5	3.4	...	3.4	...	1.55
3C111	0415+379	04:18:21.3	+38:01:36	201	4608.5	23.0	0.052	9.3e−01	1.9	1.1	...	0.8	...	1.0
0420−014	0420−014	04:23:15.8	−01:20:33	425	4787.9	11.3	0.0099	9.6e−01	2.3	2.1	2.5	1.2	2.5	1.2
OF038	0422+004	04:24:46.8	+00:36:06	286	4495.6	15.8	0.025	5.8e−01	2.0	1.5	2.4	0.9	2.9	0.9
3C120	0430+052	04:33:11.1	+05:21:16	563	6375.0	11.3	0.0030	1.0e+00	2.5	2.5	2.6	2.4	2.8	1.0
0528+134	0528+134	05:30:56.4	+13:31:55	92	3701.8	40.7	0.0082	...	...	...	...	...	...	1.2
0607−157	0607−157	06:09:40.9	−15:42:41	458	4638.3	10.1	0.0019	7.8e−01	2.7	2.6	2.8	2.5	2.9	1.3
0727−115	0727−115	07:30:19.1	−11:41:13	422	6365.0	15.1	0.0050	3.7e−01	2.7	2.7	2.9	2.5	2.9	1.0
0735+178	0735+178	07:38:07.4	+17:42:19	395	4636.2	11.8	0.0090	9.9e−01	2.2	2.0	2.7	2.0	2.7	1.2
0754+100	0754+100	07:57:06.6	+09:56:35	221	4784.9	21.7	0.011	3.3e−01	2.2	1.8	2.7	1.5	2.7	1.6
0814+425	0814+425	08:18:16.0	+42:22:45	191	4635.3	24.4	0.034	5.2e−01	2.0	0.9	3.1	0.9	3.4	1.2
OJ287	0851+202	08:54:48.9	+20:06:31	553	6397.0	11.6	0.0051	2.0e−02	1.7	1.6	2.0	1.6	2.0	1.0
4C39.25	0923+392	09:27:03.0	+39:02:21	434	5212.8	12.0	0.0044	1.3e−01	3.5	3.5	...	3.2	...	1.5
1055+018	1055+018	10:58:29.6	+01:33:59	203	3424.6	17.0	0.032	1.0e+00	1.5	0.8	...	0.8	...	1.0
1127−145	1127−145	11:30:07.1	−14:49:27	408	4637.3	11.4	0.11	6.2e−01	1.9	0.6	...	0.6	...	0.9
1156+295	1156+295	11:59:31.8	+29:14:44	331	4199.5	12.7	0.011	0.0e+00	0.0	0.0	0.2	0.0	0.5	1.0
3C273	1226+023	12:29:06.7	+02:03:09	510	6440.0	12.7	0.0031	5.1e−01	2.2	2.0	2.3	2.0	2.4	1.15

Continues

Table D.1

Source name	B1950 name	RA	Dec	N points	T	$\langle\Delta t\rangle$	$\sigma^2_{\rm noise}/\sigma^2_{\rm data}$	p-value	β	$\beta_{\rm low}$	$\beta_{\rm up}$	$\beta^{\rm comb}_{\rm low}$	$\beta^{\rm comb}_{\rm up}$	$b_{\rm s}$
3C279	1253−055	12:56:11.2	−05:47:22	504	6433.0	12.8	0.012	5.8e−01	2.2	2.1	2.4	2.0	2.5	1.1
1308+326	1308+326	13:10:28.7	+32:20:44	543	5614.6	10.4	0.0075	4.0e−02	2.1	1.9	2.2	1.7	2.3	1.05
1335−127	1335−127	13:37:39.8	−12:57:25	322	4514.6	14.1	0.0033	5.3e−01	2.3	2.1	2.5	2.0	2.7	1.1
1413+135	1413+135	14:15:58.8	+13:20:24	373	4231.5	11.4	0.0079	3.1e−01	1.9	1.7	2.1	1.6	2.2	0.8
1418+546	1418+546	14:19:46.6	+54:23:15	449	4637.3	10.4	0.013	6.0e−01	2.1	2.0	2.3	1.8	2.3	1.0
1510−089	1510−089	15:12:50.5	−09:06:00	442	4694.2	10.6	0.0062	3.0e−02	1.9	1.7	2.1	1.7	2.2	0.95
4C14.60	1538+149	15:40:49.5	+14:47:46	221	4494.6	20.4	0.023	2.8e−01	2.6	2.2	2.8	2.2	3.2	0.95
3C345	1641+399	16:42:58.8	+39:48:37	513	6439.9	12.6	0.0031	6.9e−01	2.7	2.5	2.9	2.5	2.9	1.4
MK501	1652+398	16:53:52.2	+39:45:37	151	4635.2	30.9	0.51	9.8e−01	1.4	0.0	...	0.0	...	0.0
NRAO530	1730−130	17:33:02.7	−13:04:50	332	6262.9	18.9	0.0084	9.3e−01	2.4	2.0	2.6	2.0	2.6	0.8
1749+701	1749+701	17:48:32.8	+70:05:51	167	4206.4	25.3	0.041	9.9e−01	2.2	1.1	...	0.9	...	1.1
OT081	1749+096	17:51:32.8	+09:39:01	453	4785.9	10.6	0.0057	4.0e−02	1.9	1.8	2.0	1.6	2.2	0.8
3C371	1807+698	18:06:50.7	+69:49:28	203	4494.6	22.3	0.13	4.3e−01	1.6	0.8	...	0.6	...	0.0
OV−236	1921−293	19:24:51.1	−29:14:30	447	5902.0	13.2	0.0031	3.0e−02	2.3	2.1	2.5	1.9	2.5	1.1
OV−198	1958−179	20:00:57.1	−17:48:58	104	3317.8	32.2	0.023	...	...	...	...	...	...	1.15
2005+403	2005+403	20:07:44.9	+40:29:49	376	5241.7	14.0	0.031	6.4e−01	1.6	1.3	1.8	1.3	2.0	1.2
3C418	2037+511	20:38:37.0	+51:19:13	124	6317.1	51.4	0.022	...	...	...	...	...	...	...
OX036	2121+053	21:23:44.5	+05:35:22	323	4544.6	14.1	0.0042	7.8e−01	2.5	2.2	2.8	2.2	2.8	1.55
2131−021	2131−021	21:34:10.3	−01:53:17	219	4281.2	19.6	0.0060	6.0e−01	3.2	2.8	...	2.6	...	1.35
2134+004	2134+004	21:36:38.6	+00:41:54	277	5197.8	18.8	0.018	9.7e−01	3.4	2.9	...	2.9	...	1.1
2145+067	2145+067	21:48:05.5	+06:57:39	385	4633.2	12.1	0.0037	8.4e−01	3.0	2.9	3.2	2.7	3.2	1.65
BLLAC	2200+420	22:02:43.3	+42:16:40	716	6382.0	8.9	9.6E−4	0.0e+00	0.0	0.0	0.2	0.0	0.2	1.0
3C446	2223−052	22:25:47.3	−04:57:01	354	4446.8	12.6	0.0025	8.1e−01	2.1	2.0	2.3	1.9	2.4	1.6
CTA102	2230+114	22:32:36.4	+11:43:51	444	4436.8	10.0	0.022	4.0e−02	1.2	1.1	1.2	1.1	1.3	0.7
3C454.3	2251+158	22:53:57.7	+16:08:54	549	6513.0	11.9	0.0018	3.2e−01	2.5	2.5	2.6	2.2	2.8	1.55

Table D.2: Radio band PSD characterization for OVRO sources in the UMRAO sample

Source name	OVRO name	N points	T	$\langle\Delta t\rangle$	$\sigma^2_{\rm noise}/\sigma^2_{\rm data}$	p-value	β	$\beta_{\rm low}$	$\beta_{\rm up}$	$\beta^{\rm comb}_{\rm low}$	$\beta^{\rm comb}_{\rm up}$
IIIZW2	J0010+1058	...	...	...	...	...	...	...	...	...	...
0048−097	J0050−0929	243	1488.0	6.1	0.0038	0.8	2.3	2.0	2.5	1.9	2.7
DA55	J0136+4751	331	1510.8	4.6	0.0065	0.82	1.6	1.4	1.9	1.4	1.9
0235+164	J0238+1636	...	...	...	...	...	...	...	...	...	...
OE110	J0309+1029	328	1506.9	4.6	0.02	0.91	2.0	0.9	2.5	0.9	2.5
3C84	J0319+4130	337	1496.9	4.5	0.0058	0.9	2.8	2.5	3.0	2.5	3.0
CTA26	J0339−0146	251	1502.9	6.0	0.0076	1.0	2.7	2.4	3.0	2.4	3.0
0420−014	J0423−0120	229	1496.0	6.6	0.0058	0.63	2.5	2.2	2.7	2.2	2.8
OF038	C0424+0036	164	1050.2	6.4	0.019	0.06	2.4	0.9	2.9	0.6	...
3C120	J0433+0521	242	1500.9	6.2	0.0087	0.52	2.2	1.9	2.4	1.8	2.5
0528+134	J0530+1331	...	...	...	...	...	...	...	...	...	...
0607−157	J0609−1542	158	1076.1	6.9	0.0075	0.16	2.3	2.0	2.5	1.4	2.7
0735+178	J0738+1742	...	...	...	...	...	...	...	...	...	...
0754+100	J0757+0956	193	1503.9	7.8	0.018	0.44	2.0	1.9	2.4	1.6	2.6
0814+425	J0818+4222	207	1509.0	7.3	0.013	0.14	2.0	1.1	2.3	1.1	2.6
OJ287	J0854+2006	...	...	...	...	...	...	...	...	...	...
4C39.25	J0927+3902	...	...	...	...	...	...	...	...	...	...
1055+018	J1058+0133	...	...	...	...	...	...	...	...	...	...
1127−145	C1130−1449	147	1057.1	7.2	0.0046	0.47	3.0	1.2	3.3	1.2	...
1156+295	J1159+2914	275	1504.9	5.5	0.0038	0.22	2.1	1.9	2.4	1.8	2.6
3C273	J1229+0203	334	1503.9	4.5	0.019	0.39	2.2	1.9	2.5	0.6	2.8
3C279	J1256−0547	283	1508.0	5.3	0.0064	0.91	2.4	2.2	2.6	2.0	2.7
1308+326	J1310+3220	413	1502.9	3.6	0.0065	0.2	2.2	1.9	2.4	1.9	2.4
1335−127	J1337−1257	136	1074.1	8.0	0.0070	0.67	2.6	2.1	3.0	2.1	3.0
1413+135	J1415+1320	...	...	...	...	...	...	...	...	...	...
1418+546	J1419+5423	...	...	...	...	...	...	...	...	...	...

Continues

Table D.2

Source name	OVRO name	N points	T	$\langle\Delta t\rangle$	$\sigma^2_{\rm noise}/\sigma^2_{\rm data}$	p-value	β	$\beta_{\rm low}$	$\beta_{\rm up}$	$\beta^{\rm comb}_{\rm low}$	$\beta^{\rm comb}_{\rm up}$
1510−089	PKS1510−089	134	1059.1	8.0	0.0021	0.18	2.3	1.6	2.9	1.6	2.9
4C14.60	J1540+1447	220	1288.7	5.9	0.036	0.08	2.2	0.9	2.4	0.9	...
3C345	J1642+3948	169	1067.1	6.4	0.015	0.91	2.5	0.9	3.0	0.9	...
MK501	J1653+3945	...	...	...	...	...	...	...	...	...	...
NRAO530	J1733−1304	273	1510.8	5.6	0.02	0.91	2.0	1.7	2.2	1.5	2.4
1749+701	J1748+7005	250	1508.0	6.1	0.022	0.92	2.2	1.5	2.5	1.4	2.7
OT081	J1751+0939	...	...	...	...	...	...	...	...	...	...
3C371	J1806+6949	246	1508.0	6.2	0.072	0.22	1.9	1.5	2.7	0.6	...
OV−198	J2000−1748	236	1221.6	5.2	0.0026	0.57	2.3	2.0	2.6	1.8	2.8
OX036	J2123+0535	...	...	...	...	...	...	...	...	...	...
2131−021	J2134−0153	294	1506.9	5.1	0.026	0.39	2.1	1.8	2.6	1.8	2.9
2134+004	J2136+0041	308	1506.9	4.9	0.075	0.35	1.7	1.1	1.9	0.9	...
2145+067	J2148+0657	305	1506.9	5.0	0.03	0.06	2.2	2.0	2.5	2.0	2.6
BLLAC	BLLacertae	189	1049.1	5.6	0.0066	0.22	2.1	0.9	2.4	0.9	2.7
3C446	C2225−0457	...	...	...	...	...	...	...	...	...	...
CTA102	2230+114	211	1054.1	5.0	0.0026	0.62	2.4	2.0	2.6	1.7	2.8
3C454.3	J2253+1608	323	1496.1	4.6	0.0015	0.072	2.4	2.1	2.6	1.9	2.6

Appendix E

Results of the PSD characterization for sources in the cross-correlation sample

The results of the PSD characterization for the sources in the cross-correlation sample as discussed in 6.2.1 are presented below. Each table contains the OVRO source names, basic properties of the light curves and the results of the constraint on the power-law index of the PSD. Summary figures for all the PSD fits are included too.

E.1 Tables with results of the PSD fit

Each table contains the following information,

OVRO name: Name of the source in the OVRO 40 m blazar monitoring program

N points: Number of data points in the light curve

T: Time span of the light curve in days

$\langle \Delta t \rangle$**:** Mean sampling interval in days

$\sigma^2_{noise}/\sigma^2_{data}$**:** Ratio of estimated noise variance to total variance

p**-value:** p-value of the best fit power-law index of the PSD

β**:** Best fit value for the power-law index of the PSD

β_{low}**:** 68.3% lower limit for the power-law index of the PSD

β_{up}**:** 68.3% upper limit for the power-law index of the PSD

β^{comb}_{low}**:** 82.6% lower limit for the power-law index of the PSD

β^{comb}_{up}**:** 82.6% upper limit for the power-law index of the PSD

Table E.1: Radio band PSD characterization of gamma-ray detected sources

OVRO name	N points	T	$\langle\Delta t\rangle$	$\sigma^2_{noise}/\sigma^2_{data}$	p-value	β	β_{low}	β_{up}	β^{comb}_{low}	β^{comb}_{up}
RBS76	96	647.2	6.8	1.0	9.9e−1	1.0	0.0	...	0.0	...
J0108+0135	157	1051.2	6.7	0.012	6.6e−1	2.3	0.9	2.8	0.9	...
J0112+2244	318	1504.1	4.7	0.011	3.6e−1	2.0	1.7	2.4	1.4	2.4
J0112+3208	204	1113.0	5.5	0.038	9.0e−1	1.9	0.6	2.4	0.4	...
BBJ0136+3905	186	922.5	5.0	2.2	...	...	...	...	...	...
J0136+4751	331	1510.8	4.6	0.0065	8.2e−1	1.6	1.4	1.9	1.4	1.9
C0144+2705	233	1035.2	4.5	0.057	3.1e−2	1.8	0.6	...	0.3	...
J0217+0144	250	1505.9	6.0	0.032	1.5e−2	1.9	1.4	2.1	1.1	...
J0221+3556	327	1494.9	4.6	0.063	2.5e−2	1.7	1.2	2.0	0.8	2.2
3C66A	339	1494.9	4.4	0.061	6.5e−1	1.9	0.6	2.4	0.4	2.5
J0237+2848	296	1494.9	5.1	0.011	3.8e−1	2.7	2.5	3.0	2.5	3.0
J0238+1636	294	1503.1	5.1	0.0011	4.3e−2	2.4	2.0	2.5	1.9	2.7
J0319+4130	337	1496.9	4.5	0.0058	9.0e−1	2.8	2.5	3.0	2.5	3.0
J0423−0120	229	1496.0	6.6	0.0058	6.3e−1	2.5	2.2	2.7	2.2	2.8
J0442−0017	220	1500.9	6.9	0.02	4.8e−1	1.8	1.3	2.1	0.8	...
J0509+0541	228	1501.0	6.6	0.043	5.9e−1	2.2	1.9	2.7	0.6	2.7
J0612+4122	160	1069.1	6.7	0.023	1.6e−1	2.1	0.6	...	0.4	...
C0719+3307	158	1051.8	6.7	0.03	5.6e−1	1.4	0.3	...	0.3	...
J0721+7120	276	1503.3	5.5	0.0028	1.4e−2	1.9	1.7	2.2	1.6	2.3
J0725+1425	211	1504.0	7.2	0.036	9.4e−1	1.1	0.5	1.5	0.5	...
J0738+1742	155	1070.0	6.9	0.24	2.7e−1	2.1	0.0	...	0.0	...
J0739+0137	167	1067.9	6.4	0.019	4.7e−1	2.0	0.9	2.5	0.6	...
J0742+5444	159	1016.3	6.4	0.013	9.5e−2	1.9	0.8	2.5	0.6	2.9
J0808−0751	241	1502.9	6.3	0.0042	8.0e−2	2.0	1.6	2.2	1.6	2.5
J0831+0429	245	1502.9	6.2	0.014	5.5e−1	1.9	0.8	2.1	0.6	2.3
0836+710	147	1036.3	7.1	0.0023	9.9e−1	3.3	2.9	...	1.5	...
J0854+2006	295	1504.9	5.1	0.0019	1.0e−3	2.1	1.8	2.3	1.6	2.4
J0856−1105	196	1498.9	7.7	0.11	6.0e−3	1.8	0.1	2.5	0.0	...
J0909+0121	237	1507.9	6.4	0.013	5.3e−1	2.3	1.8	2.6	1.4	...
J0915+2933	150	930.4	6.2	0.53	1.0e+00	3.4	0.4	...	0.0	...
J0920+4441	167	1073.1	6.5	0.11	2.9e−1	1.8	0.3	...	0.0	...
C0957+5522	148	1041.9	7.1	0.63	8.8e−1	1.4	0.0	...	0.0	...
C1012+2439	162	1053.4	6.5	0.79	6.8e−1	2.1	0.0	...	0.0	...
J1015+4926	197	1285.6	6.6	0.4	7.7e−1	2.0	0.0	...	0.0	...
C1037+5711	147	1052.9	7.2	0.08	4.7e−1	1.9	0.0	...	0.0	...

Continues

Table E.1

OVRO name	N points	T	$\langle\Delta t\rangle$	$\sigma^2_{noise}/\sigma^2_{data}$	p-value	β	β_{low}	β_{up}	β^{comb}_{low}	β^{comb}_{up}
J1058+0133	184	1484.1	8.1	0.066	8.2e−1	2.0	0.6	...	0.4	...
J1058+5628	155	1068.8	6.9	0.98	5.3e−1	2.5	0.0	...	0.0	...
J1104+3812	276	1508.2	5.5	0.13	3.4e−1	1.8	0.4	2.2	0.0	...
J1127−1857	197	1483.9	7.6	0.0079	2.2e−1	2.0	1.7	2.3	1.6	2.4
BBJ1150+4154	95	709.4	7.5	1.4	...	...	...	...	...	...
J1159+2914	275	1504.9	5.5	0.0038	2.2e−1	2.1	1.9	2.4	1.8	2.6
J1217+3007	250	1504.9	6.0	0.25	1.3e−2	1.8	0.0	...	0.0	...
J1221+2813	261	1504.9	5.8	0.11	1.1e−2	1.8	0.6	...	0.3	...
C1224+2122	234	1058.1	4.5	0.0048	7.9e−1	2.4	2.0	2.7	0.9	2.7
J1229+0203	334	1503.9	4.5	0.019	3.9e−1	2.2	1.9	2.5	0.6	2.8
J1231+2847	159	925.5	5.9	0.72	9.0e−2	1.9	0.0	...	0.0	...
C1239+0443	134	1058.2	8.0	0.029	8.6e−2	2.0	0.6	2.6	0.0	...
J1248+5820	190	1495.3	7.9	0.19	6.6e−1	1.6	0.1	...	0.0	...
C1253+5301	127	1040.5	8.3	0.92	6.1e−1	2.0	0.0	...	0.0	...
J1256−0547	283	1508.0	5.3	0.0064	9.1e−1	2.4	2.2	2.6	2.0	2.7
J1310+3220	413	1502.9	3.6	0.0065	2.0e−1	2.2	1.9	2.4	1.9	2.4
J1312+4828	210	1489.3	7.1	0.093	3.3e−2	1.8	0.6	...	0.6	...
J1332−0509	212	1503.0	7.1	0.0089	4.5e−1	2.2	1.7	2.7	1.4	2.9
J1344−1723	143	1075.1	7.6	0.021	5.2e−2	1.9	0.6	...	0.6	...
C1345+4452	175	1056.8	6.1	0.013	6.5e−1	2.1	0.9	2.6	0.6	2.6
CR1427+2347	150	1056.8	7.1	0.41	1.4e−1	1.7	0.0	...	0.0	...
J1504+1029	328	1508.9	4.6	0.0037	8.4e−2	2.5	2.3	2.7	2.2	2.8
PKS1510−089	134	1059.1	8.0	0.0021	1.8e−1	2.3	1.6	2.9	1.6	2.9
J1522+3144	200	1505.1	7.6	0.21	3.0e−3	1.6	0.3	...	0.0	...
CR1542+6129	168	1057.3	6.3	0.098	5.2e−1	2.0	0.0	...	0.0	...
J1555+1111	222	1284.7	5.8	0.5	3.9e−2	1.9	0.0	...	0.0	...
J1635+3808	162	1070.0	6.6	0.0069	9.8e−1	2.1	1.6	2.5	1.4	2.9
J1653+3945	184	1128.9	6.2	0.22	7.2e−1	1.7	0.0	...	0.0	...
J1709+4318	186	1073.1	5.8	0.053	1.0e−3	1.6	0.0	...	0.0	...
J1725+1152	240	1508.1	6.3	1.2	...	...	...	...	...	...
J1733−1304	273	1510.8	5.6	0.02	9.1e−1	2.0	1.7	2.2	1.5	2.4
J1748+7005	250	1508.0	6.1	0.022	9.2e−1	2.2	1.5	2.5	1.4	2.7
J1800+7828	166	1074.8	6.5	0.037	2.1e−2	1.7	0.6	2.6	0.6	...
J1806+6949	246	1508.0	6.2	0.072	2.2e−1	1.9	1.5	2.7	0.6	...
J1824+5651	240	1503.9	6.3	0.062	4.0e−1	1.9	0.6	2.2	0.4	2.9
J1848+3219	265	1503.9	5.7	0.024	5.8e−1	2.2	1.9	2.6	1.9	2.7

Continues

Table E.1

OVRO name	N points	T	$\langle\Delta t\rangle$	$\sigma^2_{noise}/\sigma^2_{data}$	p-value	β	β_{low}	β_{up}	β^{comb}_{low}	β^{comb}_{up}
J1849+6705	242	1508.0	6.3	0.017	3.1e−1	1.9	1.5	2.3	0.8	2.5
CR1903+5540	163	1050.2	6.5	0.33	6.4e−1	1.7	0.0	...	0.0	...
J1959+6508	256	1507.9	5.9	0.28	1.2e−1	1.8	0.0	...	0.0	...
C2025−0735	211	1060.1	5.0	0.018	8.0e−3	2.2	0.9	2.5	0.6	2.8
C2121+1901	231	1055.8	4.6	1.5	...	...	...	...	...	...
J2143+1743	362	1502.9	4.2	0.016	3.0e−2	1.9	1.5	2.0	1.4	2.2
BLLacertae	189	1049.1	5.6	0.0066	2.2e−1	2.1	0.9	2.4	0.9	2.7
J2203+1725	358	1507.8	4.2	0.023	2.3e−1	2.0	1.7	2.2	1.5	2.3
C2225−0457	191	1042.2	5.5	0.0034	9.8e−1	3.2	2.9	3.5	2.7	...
J2229−0832	212	1101.0	5.2	0.0063	9.1e−1	2.8	2.5	3.0	2.4	3.1
2230+114	211	1054.1	5.0	0.0026	6.2e−1	2.4	2.0	2.6	1.7	2.8
J2236+2828	321	1509.8	4.7	0.035	8.9e−2	1.9	0.6	2.1	0.6	2.3
CR2243+2021	196	1030.9	5.3	2.1	...	...	...	...	...	...
J2253+1608	323	1496.1	4.6	0.0015	7.2e−2	2.4	2.1	2.6	1.9	2.6
C2311+3425	215	1049.4	4.9	0.017	8.9e−1	2.1	0.6	2.5	0.6	2.7

Table E.2: Gamma-ray band PSD characterization of gamma-ray detected sources

OVRO name	N points	T	$\langle\Delta t\rangle$	$\sigma^2_{noise}/\sigma^2_{data}$	p-value	β	β_{low}	β_{up}	β^{comb}_{low}	β^{comb}_{up}
RBS76	98	1190.0	12.3	1.7	...	...	...	...	...	...
J0108+0135	146	1092.0	7.5	0.4	8.7e−1	0.8	0.4	...	0.2	...
J0112+2244	132	1099.0	8.4	0.25	8.8e−2	0.9	0.4	1.5	0.0	1.8
J0112+3208	102	1029.0	10.2	0.14	8.9e−1	2.2	1.5	...	0.5	...
BBJ0136+3905	125	1148.0	9.3	1.4	...	...	...	...	...	...
J0136+4751	117	1099.0	9.5	0.25	9.4e−1	2.1	1.4	...	0.0	...
C0144+2705	112	1099.0	9.9	0.87	5.5e−1	0.8	0.0	...	0.0	...
J0217+0144	92	1071.0	11.8	0.32	7.6e−1	2.5	0.0	...	0.0	...
J0221+3556	107	1085.0	10.2	0.53	9.9e−1	1.6	0.0	...	0.0	...
3C66A	158	1099.0	7.0	0.16	4.9e−1	0.6	0.3	1.0	0.2	1.2
J0237+2848	132	1099.0	8.4	0.19	7.9e−1	2.4	1.6	...	0.7	...
J0238+1636	79	1092.0	14.0	0.019	5.8e−01	0.1	0.0	0.8	0.0	1.0
J0319+4130	155	1099.0	7.1	0.2	7.6e−1	1.6	1.2	2.0	1.1	2.2
J0423−0120	110	1092.0	10.0	0.31	1.1e−1	1.2	0.1	...	0.0	...
J0442−0017	106	1099.0	10.5	0.14	9.7e−1	0.7	0.3	1.2	0.1	2.3
J0509+0541	124	1099.0	8.9	0.58	8.1e−1	2.5	1.5	...	0.0	...
J0612+4122	120	1169.0	9.8	1.3	...	...	...	...	...	...
C0719+3307	114	1099.0	9.7	0.2	4.8e−1	0.8	0.2	1.2	0.0	...
J0721+7120	154	1099.0	7.2	0.086	4.0e−1	1.9	1.6	2.2	1.4	2.3
J0725+1425	112	1085.0	9.8	0.04	7.3e−1	0.5	0.2	0.8	0.1	1.0
J0738+1742	146	1197.0	8.3	1.2	...	...	...	...	...	...
J0739+0137	96	1043.0	11.0	0.38	8.2e−1	2.5	0.5	...	0.0	...
J0742+5444	85	1092.0	13.0	0.085	9.9e−1	0.6	0.3	1.1	0.0	...
J0808−0751	111	1071.0	9.7	0.075	6.8e−1	0.5	0.2	0.9	0.1	1.1
J0831+0429	95	1085.0	11.5	0.46	9.3e−1	0.7	0.0	...	0.0	...
0836+710	77	1064.0	14.0	0.36	5.0e−1	2.4	0.0	...	0.0	...
J0854+2006	99	1099.0	11.2	0.37	1.0e−3	0.2	0.0	...	0.0	...
J0856−1105	81	1190.0	14.9	1.8	...	...	...	...	...	...
J0909+0121	99	1071.0	10.9	0.27	5.8e−1	0.4	0.0	...	0.0	...
J0915+2933	75	1190.0	16.1	2.1	...	...	...	...	...	...
J0920+4441	128	1092.0	8.6	0.091	8.3e−1	1.6	1.0	2.0	0.8	2.1
C0957+5522	172	1197.0	7.0	1.2	...	...	...	...	...	...
C1012+2439	84	1001.0	12.1	0.37	9.6e−1	1.1	0.0	...	0.0	...
J1015+4926	142	1099.0	7.8	0.96	7.3e−1	1.6	0.0	...	0.0	...
C1037+5711	110	1183.0	10.9	1.6	...	...	...	...	...	...

Continues

Table E.2

OVRO name	N points	T	$\langle\Delta t\rangle$	$\sigma^2_{noise}/\sigma^2_{data}$	p-value	β	β_{low}	β_{up}	β^{comb}_{low}	β^{comb}_{up}
J1058+0133	120	1099.0	9.2	0.42	9.7e−1	1.9	0.2	...	0.0	...
J1058+5628	115	1099.0	9.6	0.99	2.1e−1	1.8	0.0	...	0.0	...
J1104+3812	158	1099.0	7.0	0.35	9.6e−1	1.4	0.7	2.0	0.7	...
J1127−1857	120	1099.0	9.2	0.23	6.0e−1	2.4	0.7	...	0.0	...
BBJ1150+4154	88	1190.0	13.7	2.2	...	...	...	...	...	...
J1159+2914	135	1078.0	8.0	0.066	1.8e−1	1.0	0.7	1.4	0.5	1.6
J1217+3007	128	1092.0	8.6	0.35	7.8e−1	2.5	1.8	...	0.2	...
J1221+2813	120	1078.0	9.1	0.72	9.3e−1	2.3	0.0	...	0.0	...
C1224+2122	135	1099.0	8.2	0.0053	5.9e−2	0.4	0.2	0.8	0.2	0.8
J1229+0203	148	1099.0	7.5	0.015	8.9e−1	0.8	0.5	1.0	0.4	1.1
J1231+2847	94	1183.0	12.7	1.2	...	...	...	...	...	...
C1239+0443	106	1057.0	10.1	0.16	1.0e+00	1.7	0.8	2.3	0.0	...
J1248+5820	136	1176.0	8.7	1.5	...	...	...	...	...	...
C1253+5301	131	1190.0	9.2	1.1	...	...	...	...	...	...
J1256−0547	153	1099.0	7.2	0.033	9.1e−01	1.6	1.4	1.9	1.2	2.0
J1310+3220	96	1099.0	11.6	0.22	5.7e−1	0.2	0.1	...	0.0	...
J1312+4828	70	1050.0	15.2	0.02	1.0e+00	0.3	0.0	1.0	0.0	1.0
J1332−0509	110	1043.0	9.6	0.033	5.3e−1	0.3	0.2	0.6	0.1	0.8
J1344−1723	87	1190.0	13.8	1.1	...	...	...	...	...	...
C1345+4452	90	1099.0	12.3	0.15	9.7e−1	0.3	0.0	...	0.0	...
CR1427+2347	154	1092.0	7.1	0.59	9.6e−1	0.7	0.0	...	0.0	...
J1504+1029	134	1099.0	8.3	0.021	8.6e−1	2.3	2.0	...	1.9	...
PKS1510−089	157	1099.0	7.0	0.0096	9.0e−3	1.9	1.7	2.1	1.7	2.1
J1522+3144	158	1099.0	7.0	0.074	9.9e−1	0.7	0.4	0.9	0.4	1.0
CR1542+6129	129	1092.0	8.5	0.51	3.4e−1	0.7	0.2	...	0.0	...
J1555+1111	155	1099.0	7.1	0.75	1.5e−1	1.4	0.0	...	0.0	...
J1635+3808	157	1099.0	7.0	0.043	1.0e−1	1.5	1.2	1.8	1.1	1.8
J1653+3945	145	1092.0	7.6	0.76	6.9e−1	0.9	0.0	...	0.0	...
J1709+4318	74	966.0	13.2	0.062	9.8e−1	0.7	0.3	1.3	0.1	...
J1725+1152	82	1190.0	14.7	1.5	...	...	...	...	...	...
J1733−1304	95	1078.0	11.5	0.16	4.9e−1	0.5	0.0	...	0.0	...
J1748+7005	84	1092.0	13.2	0.044	9.6e−1	0.4	0.2	1.0	0.0	1.1
J1800+7828	125	1099.0	8.9	0.15	7.6e−1	0.4	0.2	0.7	0.0	0.9
J1806+6949	104	1057.0	10.3	0.83	2.1e−1	1.4	0.0	...	0.0	...
J1824+5651	77	1099.0	14.5	0.39	1.0e+00	0.5	0.0	...	0.0	...
J1848+3219	57	1085.0	19.4	0.11	3.6e−1	0.0	0.0	...	0.0	...

Continues

Table E.2

OVRO name	N points	T	$\langle\Delta t\rangle$	$\sigma^2_{noise}/\sigma^2_{data}$	p-value	β	β_{low}	β_{up}	β^{comb}_{low}	β^{comb}_{up}
J1849+6705	104	1099.0	10.7	0.051	5.3e−1	0.6	0.2	1.0	0.2	1.2
CR1903+5540	124	1176.0	9.6	1.3	...	...	...	...	...	...
J1959+6508	132	1099.0	8.4	0.61	9.7e−1	2.5	1.7	...	0.2	...
C2025−0735	97	1085.0	11.3	0.065	1.0e+00	0.1	0.0	0.8	0.0	...
C2121+1901	78	1197.0	15.5	1.8	...	...	...	...	...	...
J2143+1743	133	1092.0	8.3	0.27	9.9e−1	0.0	0.0	0.5	0.0	0.5
BLLacertae	146	1099.0	7.6	0.087	4.7e−1	2.0	1.5	2.3	1.5	2.4
J2203+1725	119	1099.0	9.3	0.38	5.4e−1	0.7	0.1	...	0.0	...
C2225−0457	78	1183.0	15.4	1.4	...	...	...	...	...	...
J2229−0832	125	1099.0	8.9	0.38	7.5e−01	0.8	0.0	...	0.0	...
2230+114	109	1099.0	10.2	0.059	7.8e−1	2.5	1.8	...	1.0	...
J2236+2828	101	1036.0	10.4	0.23	7.4e−1	2.0	0.0	...	0.0	...
CR2243+2021	123	1197.0	9.8	1.8	...	...	...	...	...	...
J2253+1608	157	1099.0	7.0	8.0E−4	0.0e+00	0.0	0.0	0.2	0.0	0.2
C2311+3425	113	1099.0	9.8	0.094	9.2e−1	0.2	0.0	0.7	0.0	0.9

E.2 PSD characterization figures for the radio light curves

We include summary figures for the fits of the radio PSDs for the sources in the cross-correlation sample. Each figure is made out of 4 panels described below:

Upper left Radio light curve. Flux units are Janskys and time is MJD.

Upper right The periodogram estimate in arbitrary units of power and 1/day for frequency. Periodogram for the light curve is represented by black dots joined by a solid black line.

The mean and dispersion in the PSD of simulated light curves for the best fit value of β are represented by the black dots with error bars. The best fit value is indicated in the caption.

Lower left Lower left is the p-value for each value of β tested in the model PSD ($\propto \nu^{-\beta}$). A high p-value indicates a model consistent with the observed periodogram. The best fit is the maximum and is indicated in the caption.

Lower right Confidence belt and best fit value (solid black horizontal line). The lower and upper limits for β obtained are indicated in the caption. Vertical axis is for the simulated value of β and horizontal axis for the fitted one.

The 81 cases in which there is enough signal to run the procedure are included here. Only 43 sources have a well defined 68.3% constraint and 33 a well defined 82.6% constraint. For the details see Chapter 6.

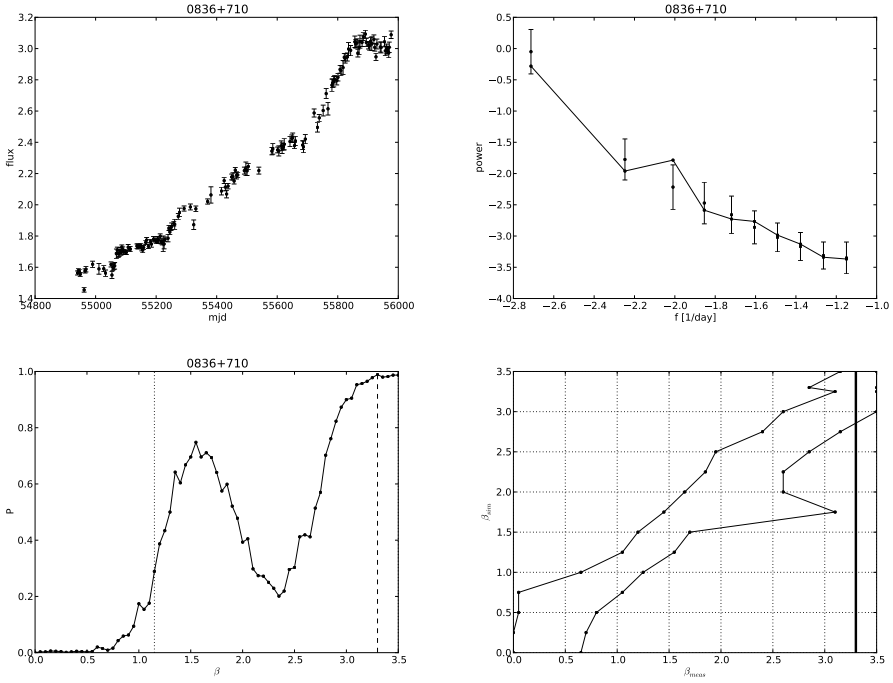

Figure E.1: PSD fit summary for 0836+710. The best fit is $\beta = 3.3$ with 1σ limits $\beta^{lower} = 2.9$ and an undetermined upper limit.

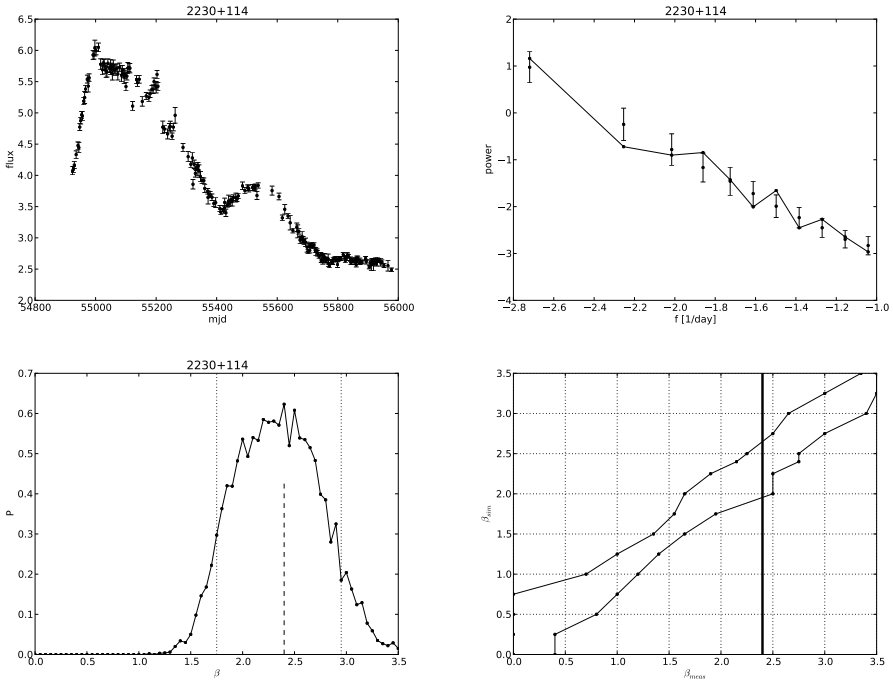

Figure E.2: PSD fit summary for 2230+114. The best fit is $\beta = 2.4$ with 1σ limits $\beta^{lower} = 2.0$ and $\beta^{upper} = 2.6$.

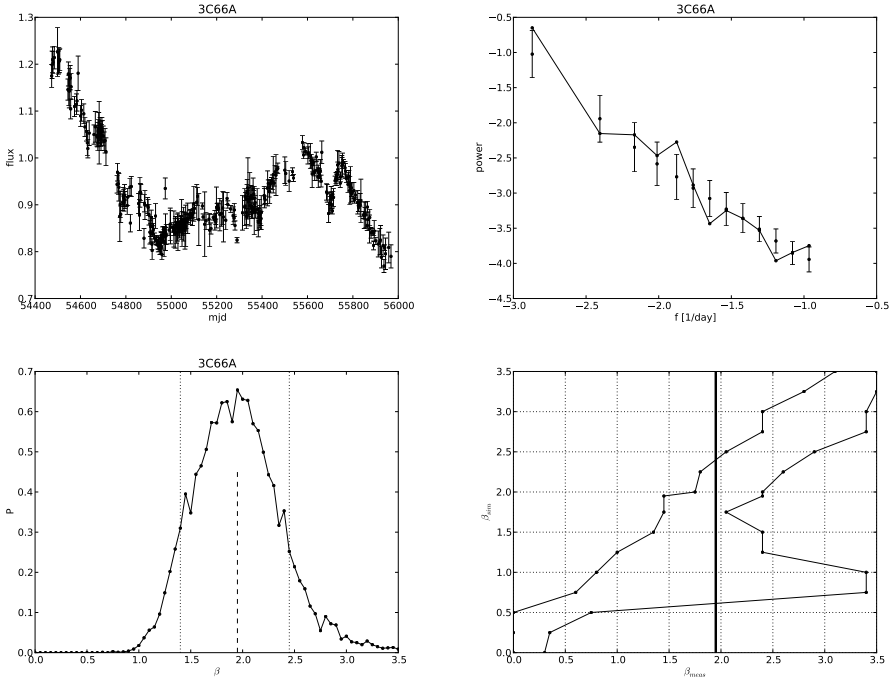

Figure E.3: PSD fit summary for 3C66A. The best fit is $\beta = 1.9$ with 1σ limits $\beta^{lower} = 0.6$ and $\beta^{upper} = 2.4$.

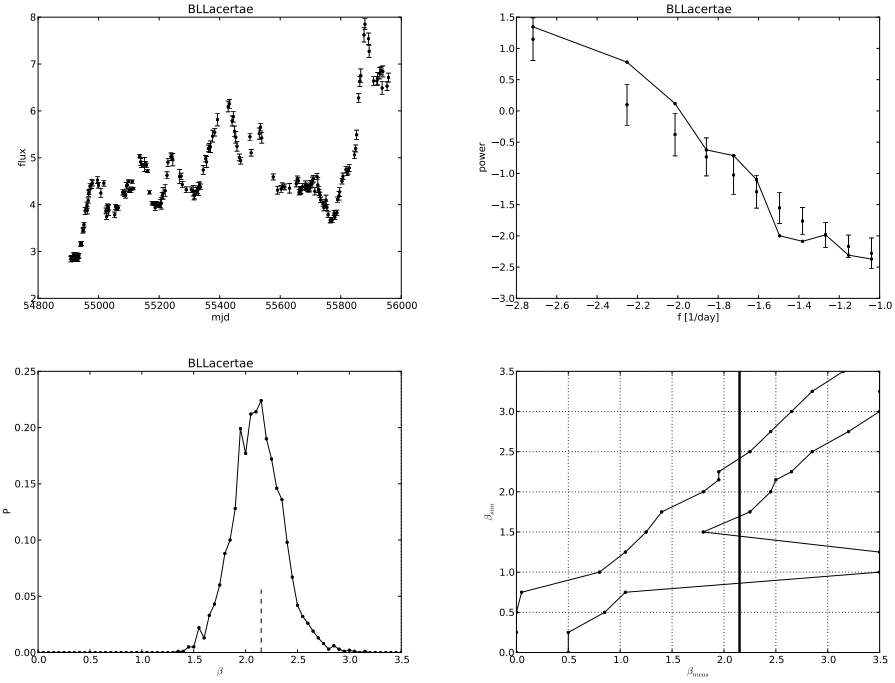

Figure E.4: PSD fit summary for BLLacertae. The best fit is $\beta = 2.1$ with 1σ limits $\beta^{lower} = 0.9$ and $\beta^{upper} = 2.4$.

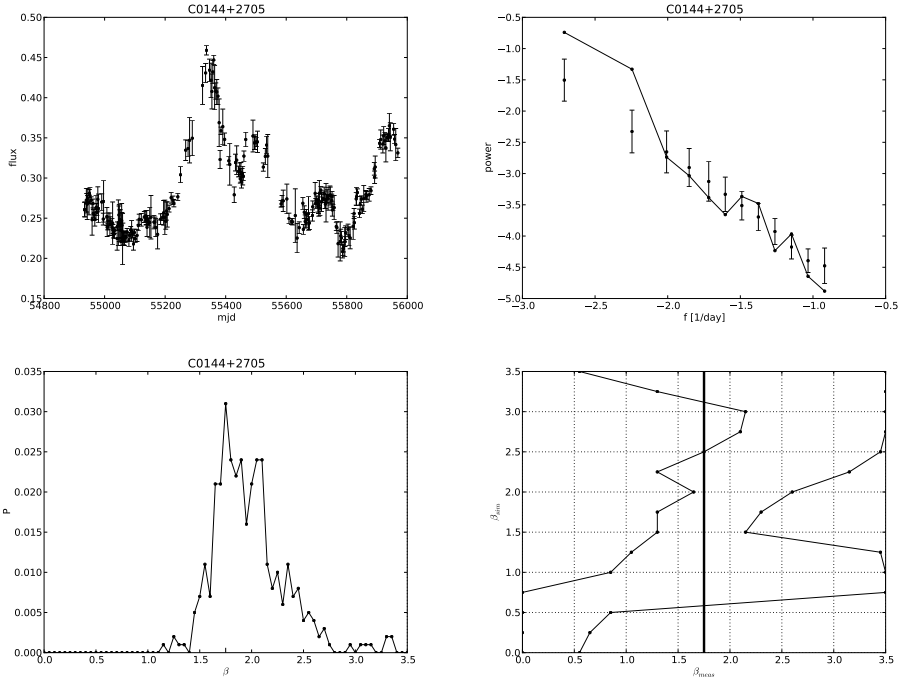

Figure E.5: PSD fit summary for C0144+2705. The best fit is $\beta = 1.8$ with 1σ limits $\beta^{lower} = 0.6$ and an undetermined upper limit.

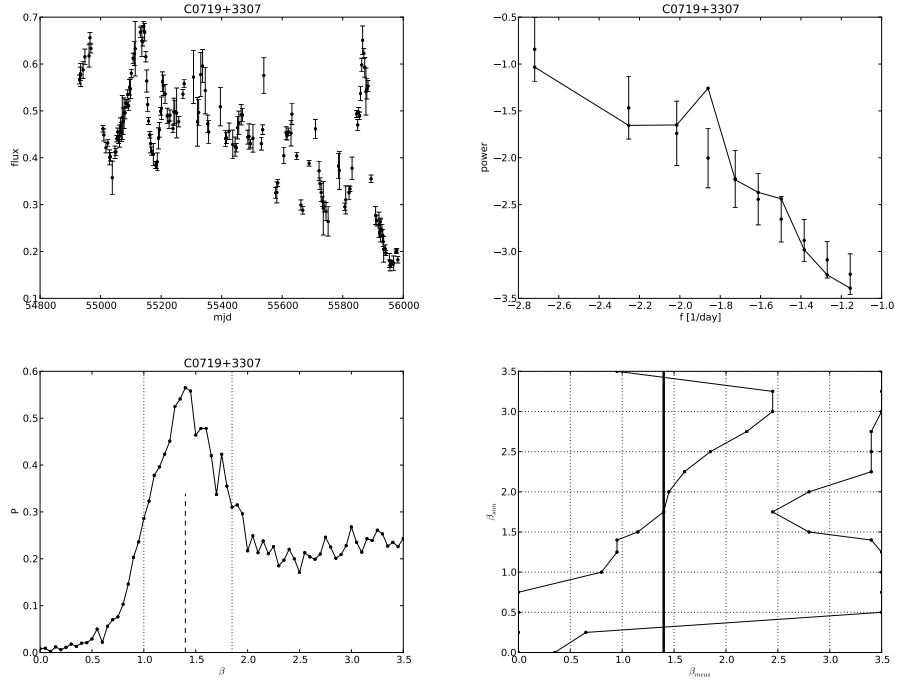

Figure E.6: PSD fit summary for C0719+3307. The best fit is $\beta = 1.4$ with 1σ limits $\beta^{lower} = 0.3$ and an undetermined upper limit.

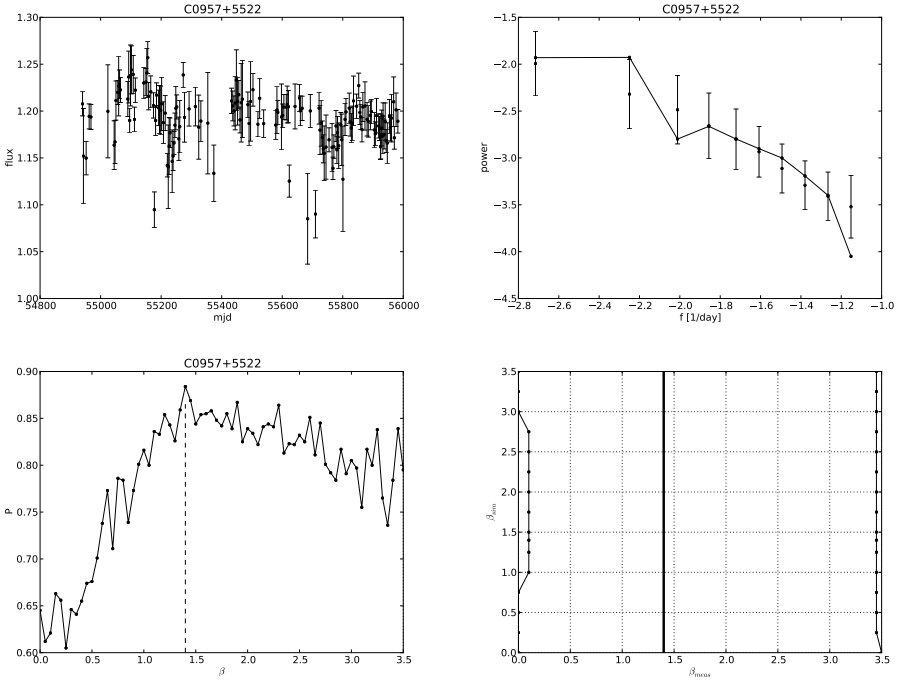

Figure E.7: PSD fit summary for C0957+5522. The best fit is $\beta = 1.4$ with 1σ limits $\beta^{lower} = 0.0$ and an undetermined upper limit.

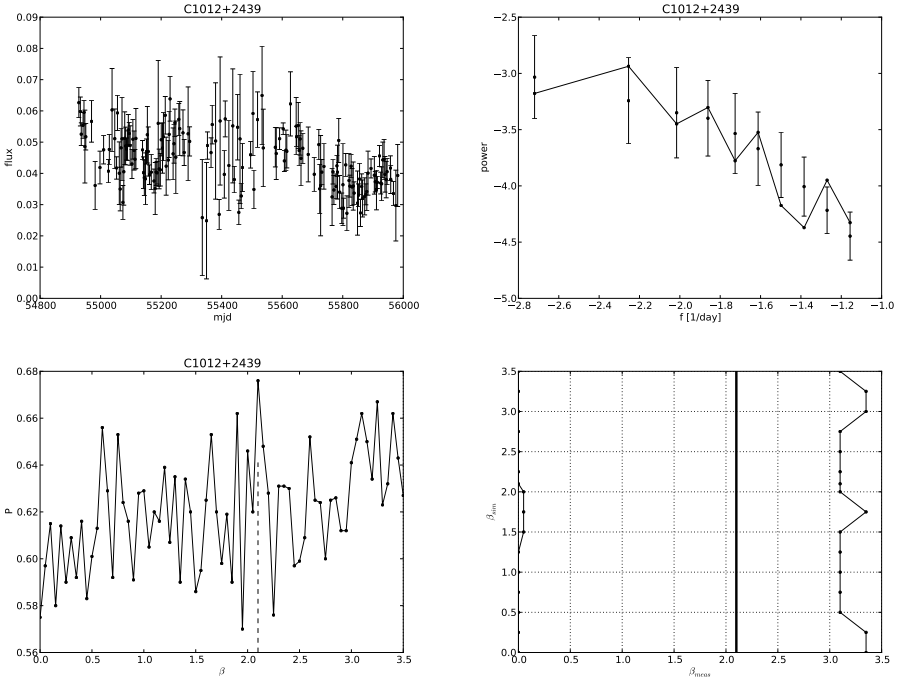

Figure E.8: PSD fit summary for C1012+2439. The best fit is $\beta = 2.1$ with 1σ limits $\beta^{lower} = 0.0$ and an undetermined upper limit.

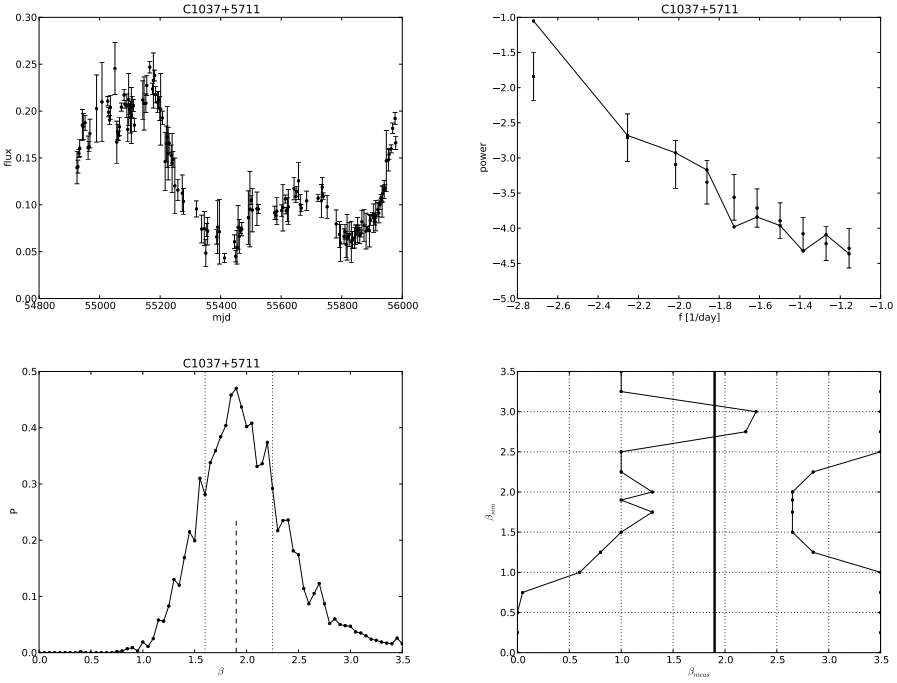

Figure E.9: PSD fit summary for C1037+5711. The best fit is $\beta = 1.9$ with 1σ limits $\beta^{lower} = 0.0$ and an undetermined upper limit.

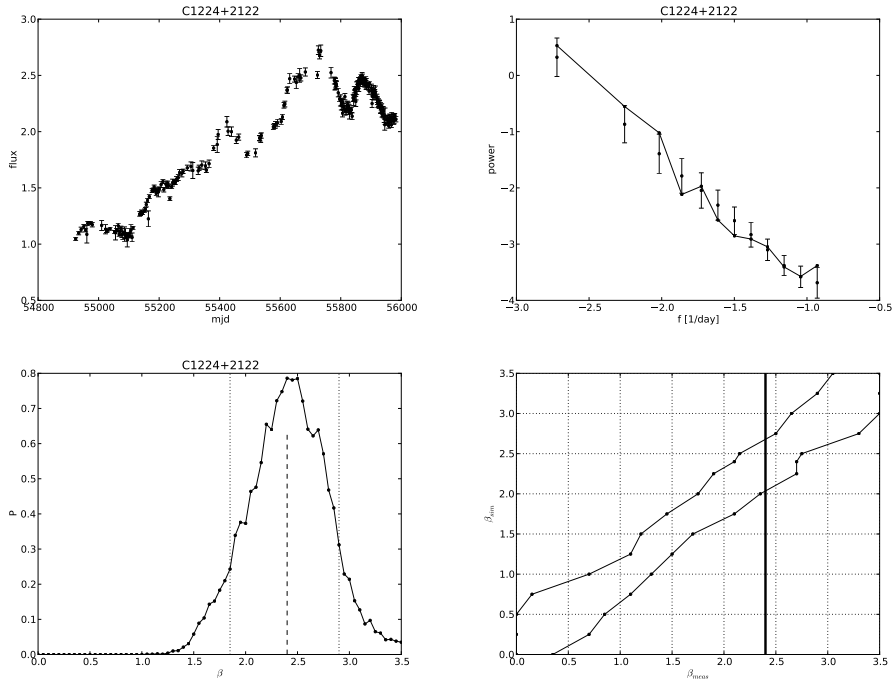

Figure E.10: PSD fit summary for C1224+2122. The best fit is $\beta = 2.4$ with 1σ limits $\beta^{lower} = 2.0$ and $\beta^{upper} = 2.7$.

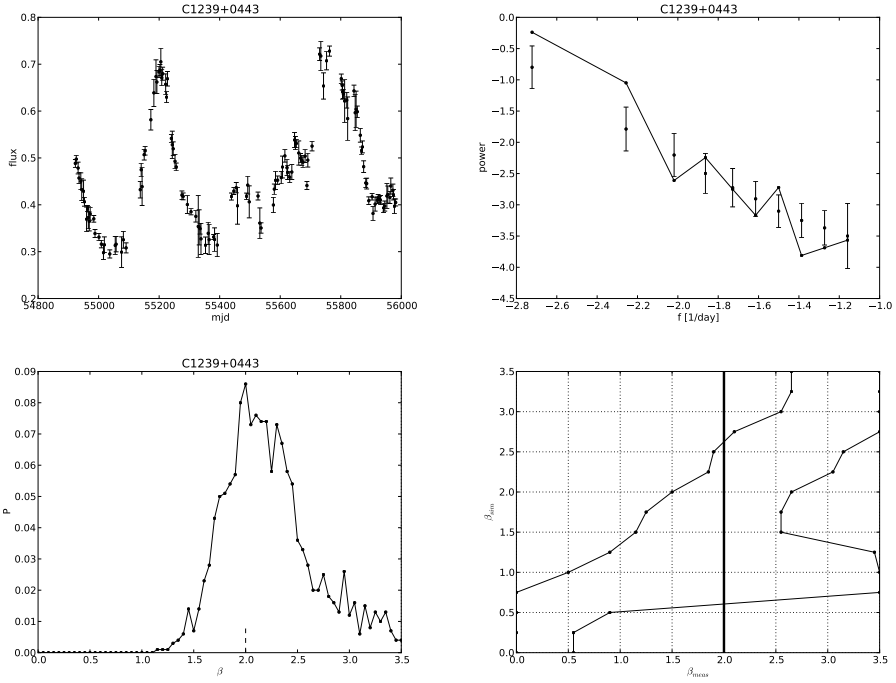

Figure E.11: PSD fit summary for C1239+0443. The best fit is $\beta = 2.0$ with 1σ limits $\beta^{lower} = 0.6$ and $\beta^{upper} = 2.6$.

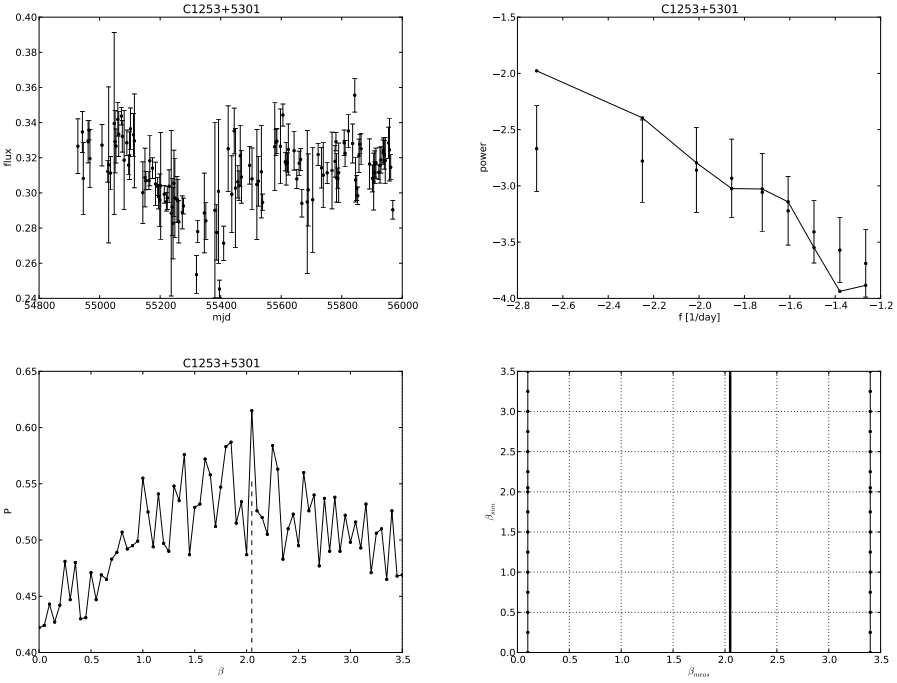

Figure E.12: PSD fit summary for C1253+5301. The best fit is $\beta = 2.0$ with 1σ limits $\beta^{lower} = 0.0$ and an undetermined upper limit.

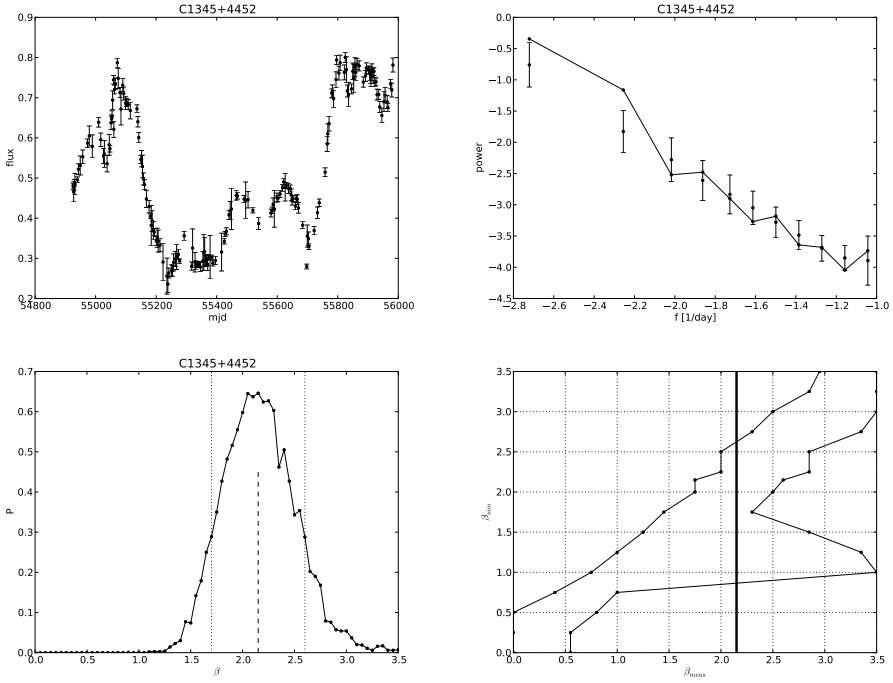

Figure E.13: PSD fit summary for C1345+4452. The best fit is $\beta = 2.1$ with 1σ limits $\beta^{lower} = 0.9$ and $\beta^{upper} = 2.6$.

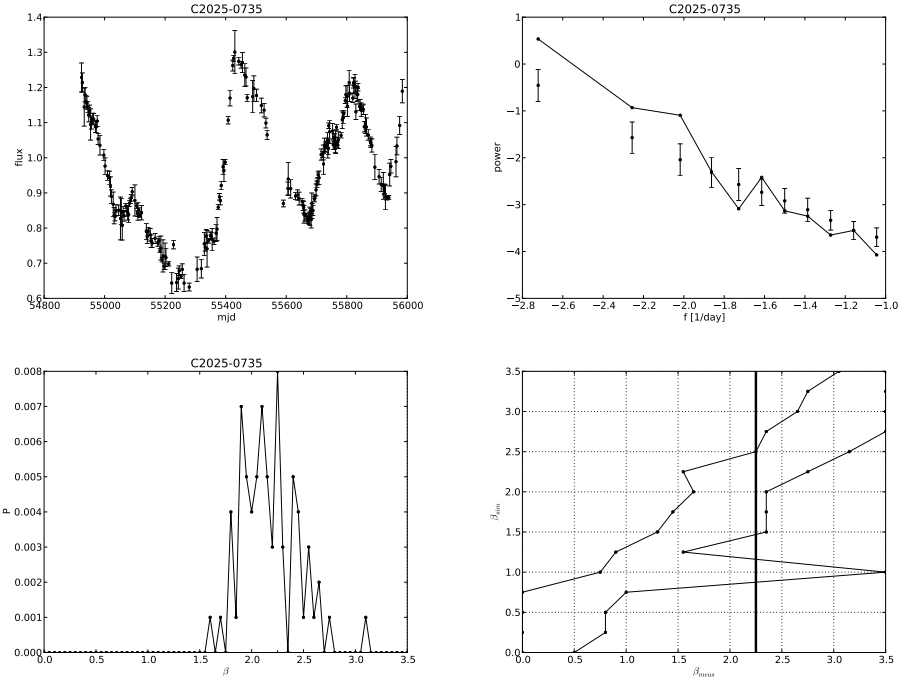

Figure E.14: PSD fit summary for C2025-0735. The best fit is $\beta = 2.2$ with 1σ limits $\beta^{lower} = 0.9$ and $\beta^{upper} = 2.5$.

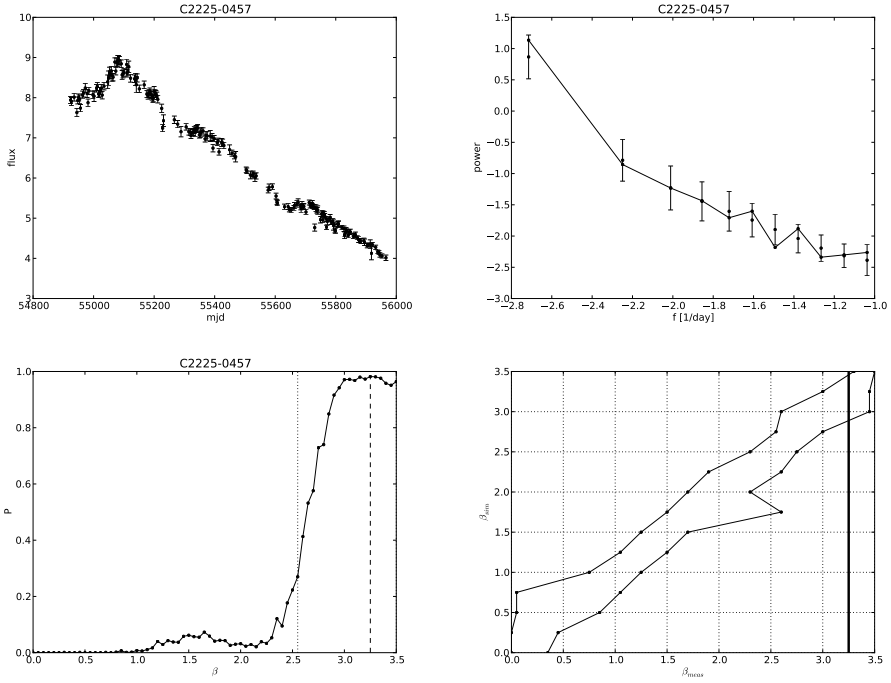

Figure E.15: PSD fit summary for C2225-0457. The best fit is $\beta = 3.2$ with 1σ limits $\beta^{lower} = 2.9$ and an undetermined upper limit.

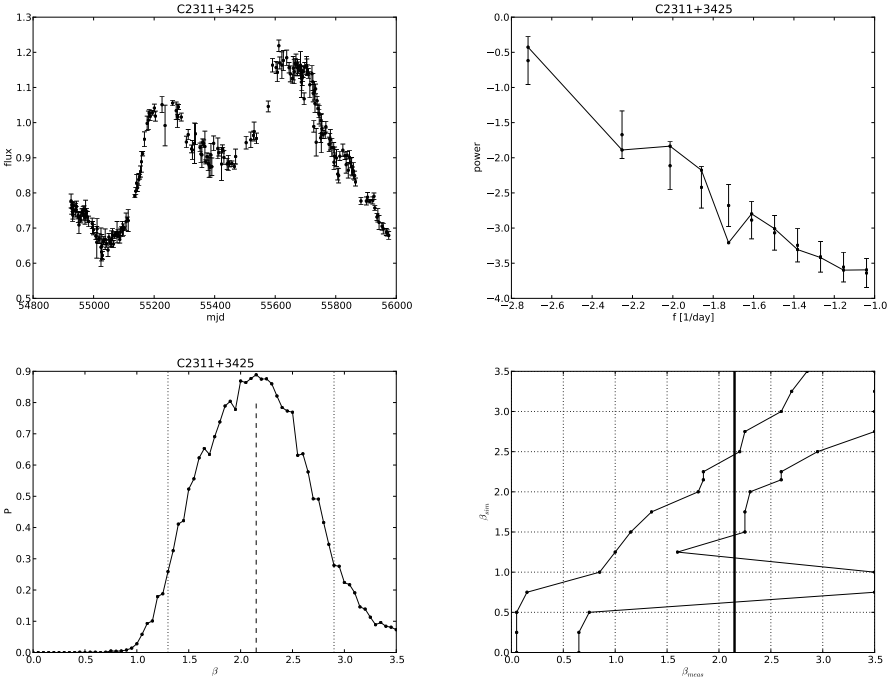

Figure E.16: PSD fit summary for C2311+3425. The best fit is $\beta = 2.1$ with 1σ limits $\beta^{lower} = 0.6$ and $\beta^{upper} = 2.5$.

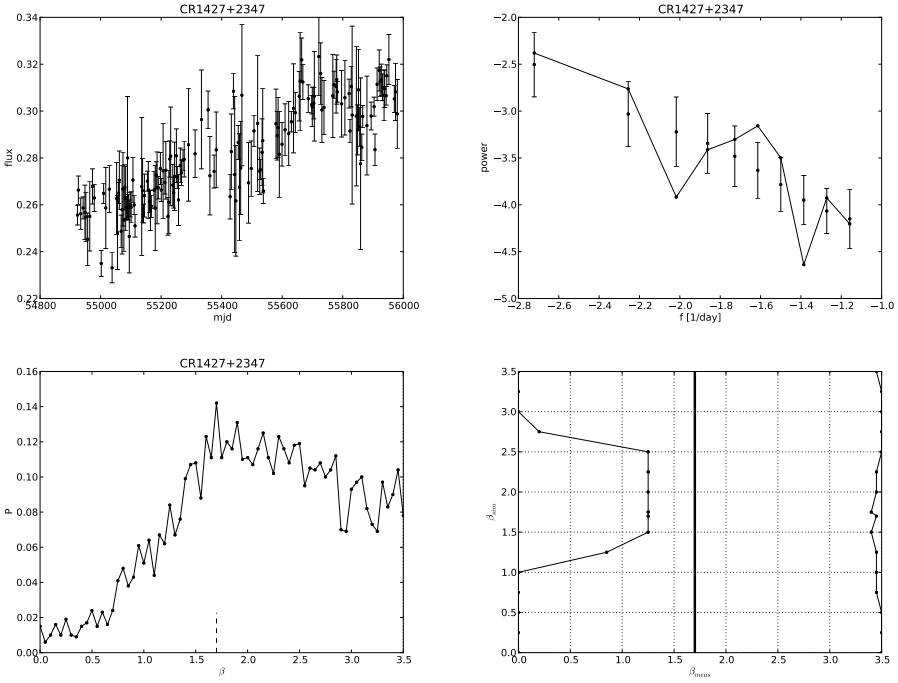

Figure E.17: PSD fit summary for CR1427+2347. The best fit is $\beta = 1.7$ with 1σ limits $\beta^{lower} = 0.0$ and an undetermined upper limit.

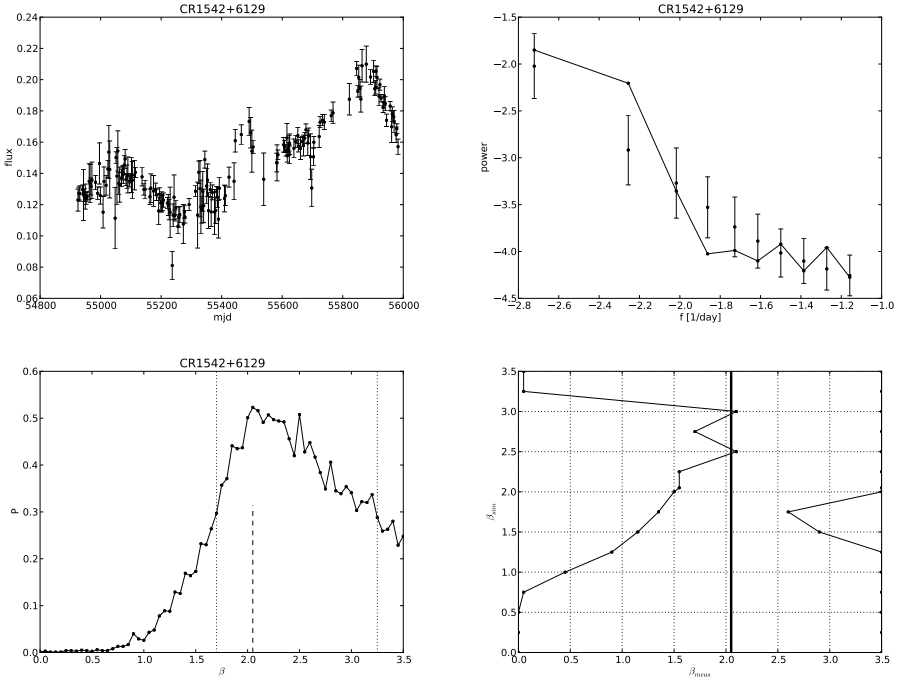

Figure E.18: PSD fit summary for CR1542+6129. The best fit is $\beta = 2.0$ with 1σ limits $\beta^{lower} = 0.0$ and an undetermined upper limit.

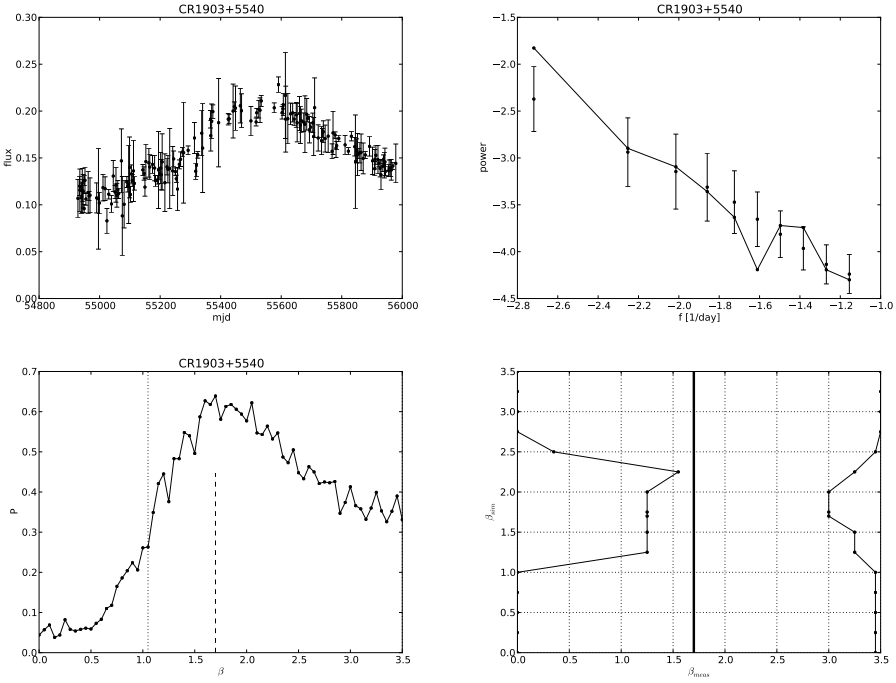

Figure E.19: PSD fit summary for CR1903+5540. The best fit is $\beta = 1.7$ with 1σ limits $\beta^{lower} = 0.0$ and an undetermined upper limit.

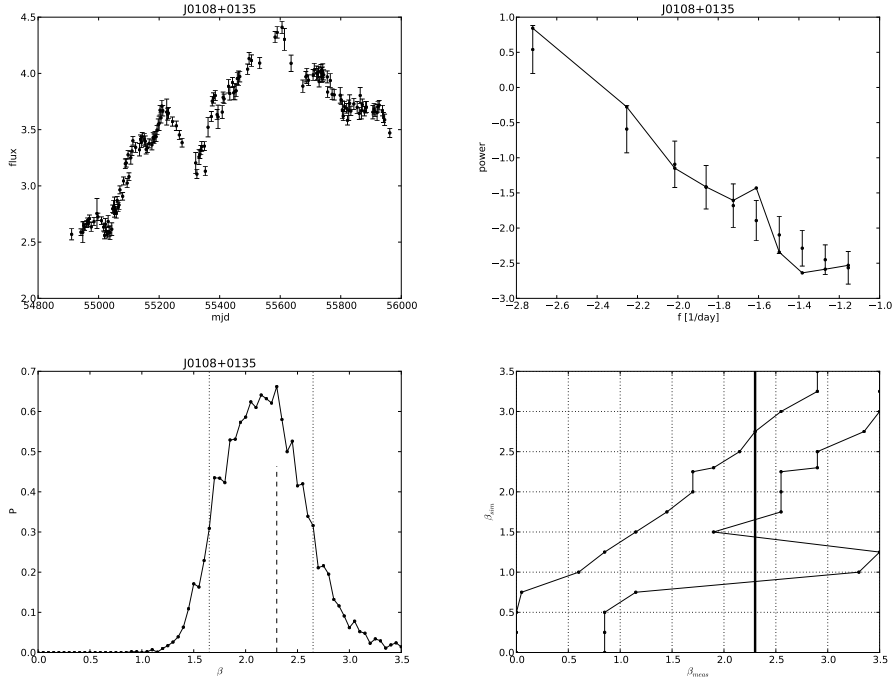

Figure E.20: PSD fit summary for J0108+0135. The best fit is $\beta = 2.3$ with 1σ limits $\beta^{lower} = 0.9$ and $\beta^{upper} = 2.8$.

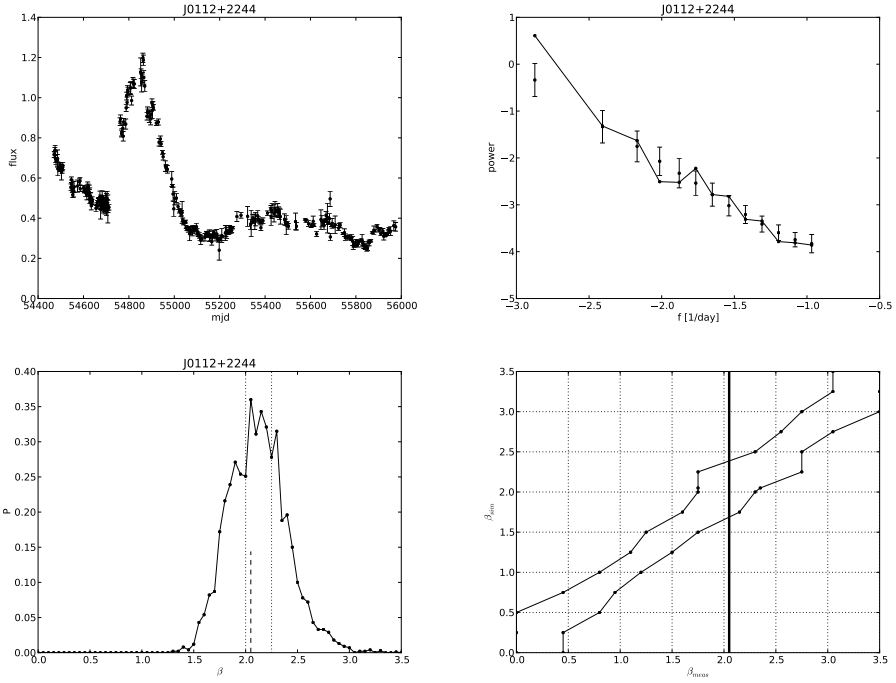

Figure E.21: PSD fit summary for J0112+2244. The best fit is $\beta = 2.0$ with 1σ limits $\beta^{lower} = 1.7$ and $\beta^{upper} = 2.4$.

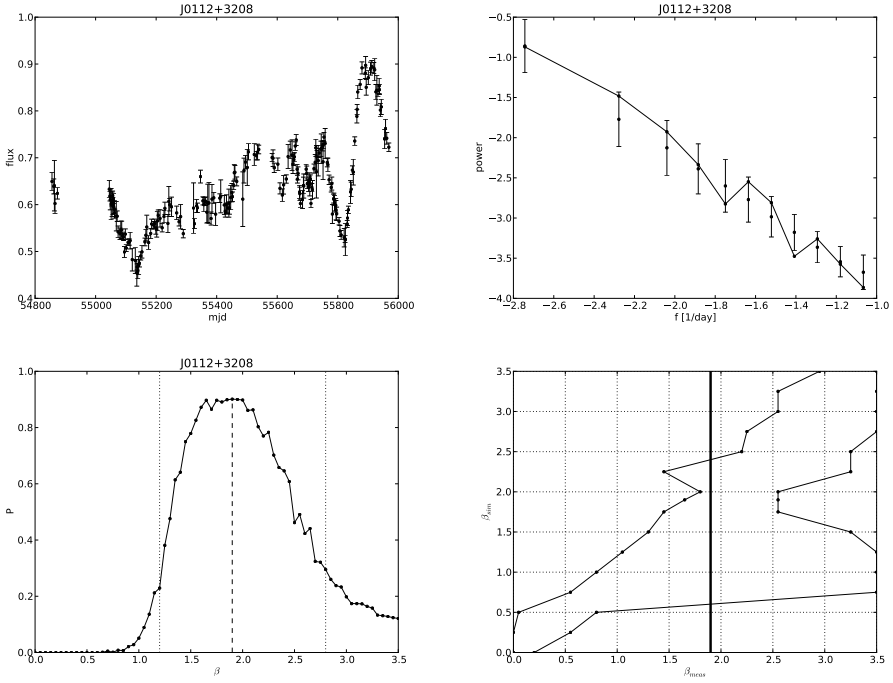

Figure E.22: PSD fit summary for J0112+3208. The best fit is $\beta = 1.9$ with 1σ limits $\beta^{lower} = 0.6$ and $\beta^{upper} = 2.4$.

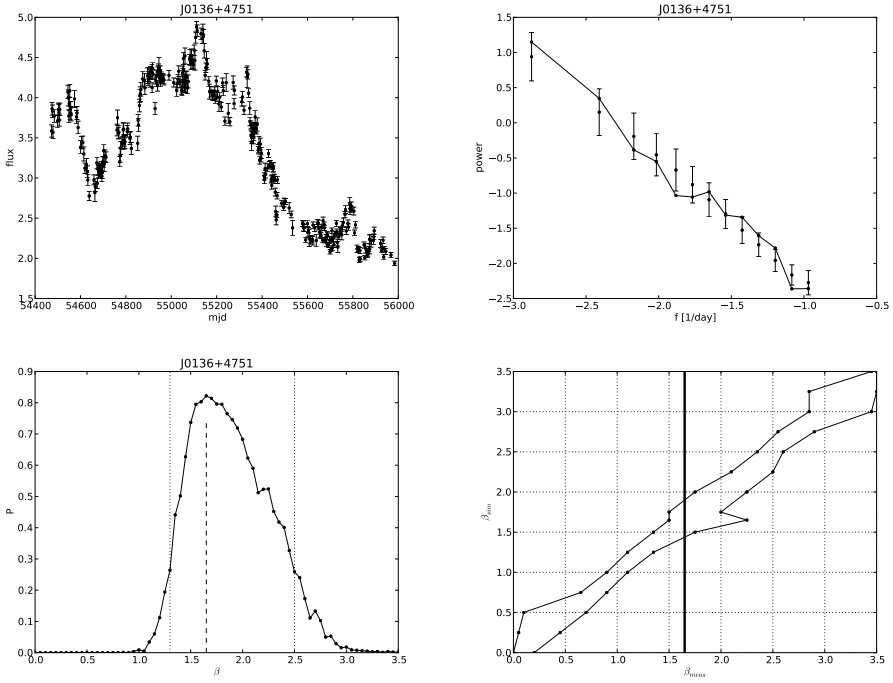

Figure E.23: PSD fit summary for J0136+4751. The best fit is $\beta = 1.6$ with 1σ limits $\beta^{lower} = 1.4$ and $\beta^{upper} = 1.9$.

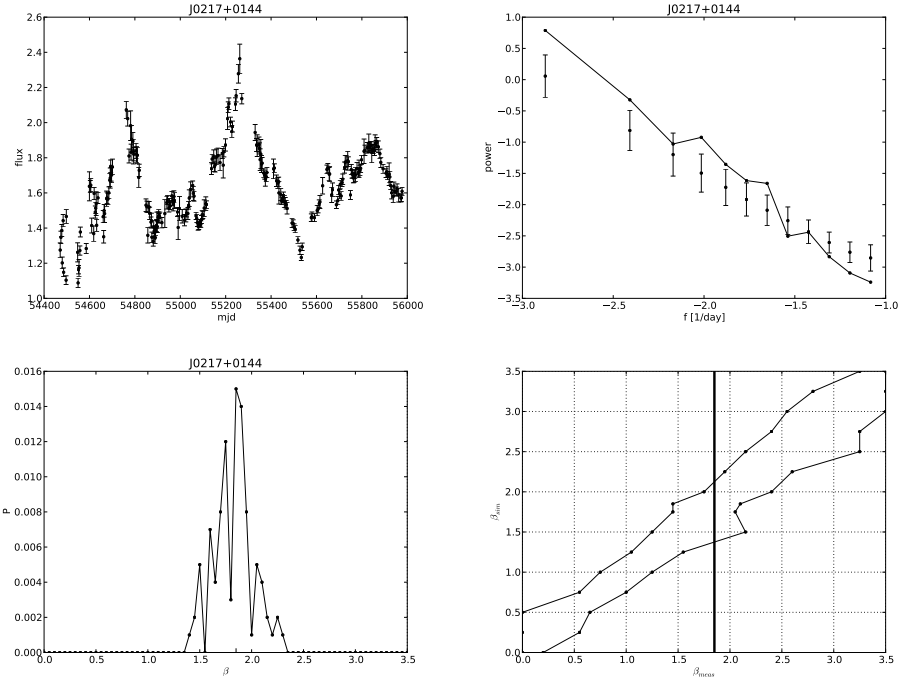

Figure E.24: PSD fit summary for J0217+0144. The best fit is $\beta = 1.9$ with 1σ limits $\beta^{lower} = 1.4$ and $\beta^{upper} = 2.1$.

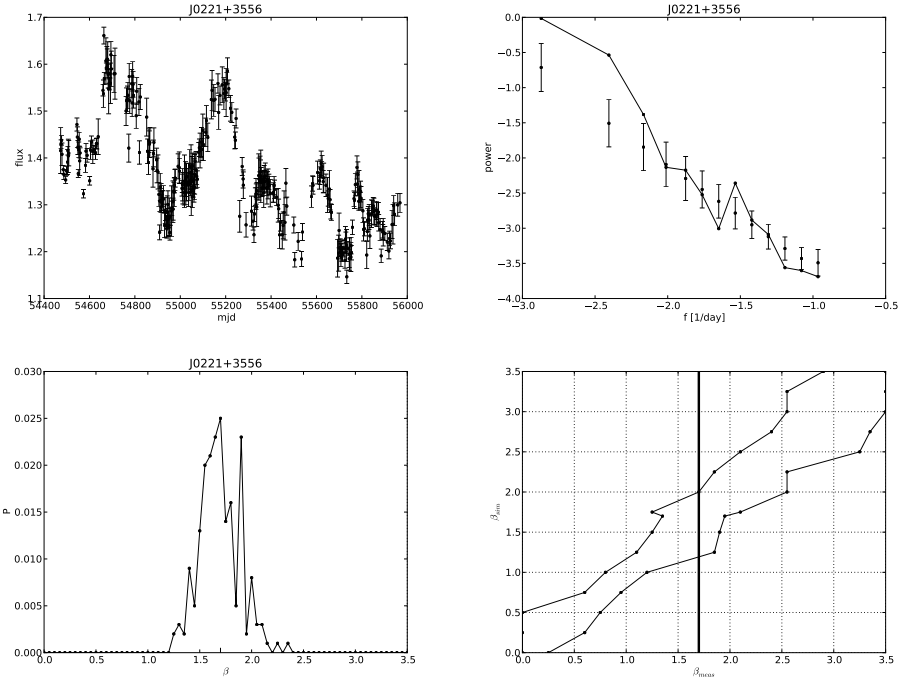

Figure E.25: PSD fit summary for J0221+3556. The best fit is $\beta = 1.7$ with 1σ limits $\beta^{lower} = 1.2$ and $\beta^{upper} = 2.0$.

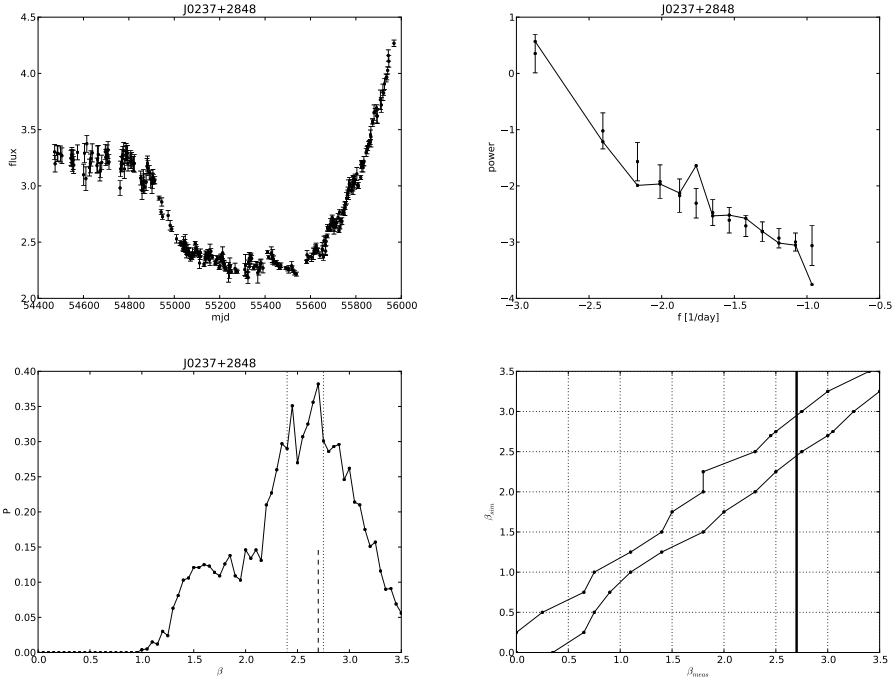

Figure E.26: PSD fit summary for J0237+2848. The best fit is $\beta = 2.7$ with 1σ limits $\beta^{lower} = 2.5$ and $\beta^{upper} = 3.0$.

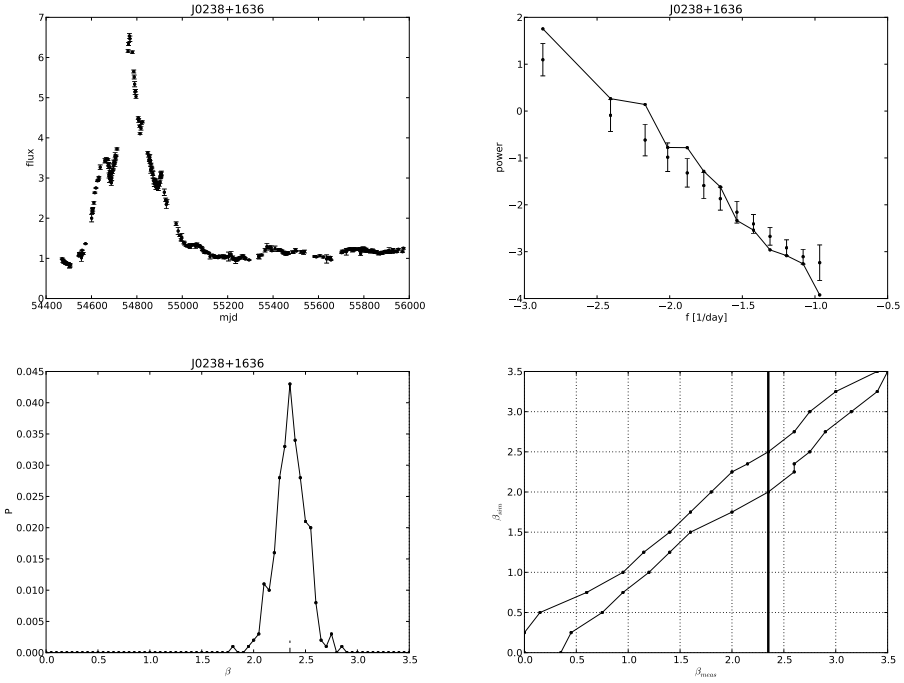

Figure E.27: PSD fit summary for J0238+1636. The best fit is $\beta = 2.4$ with 1σ limits $\beta^{lower} = 2.0$ and $\beta^{upper} = 2.5$.

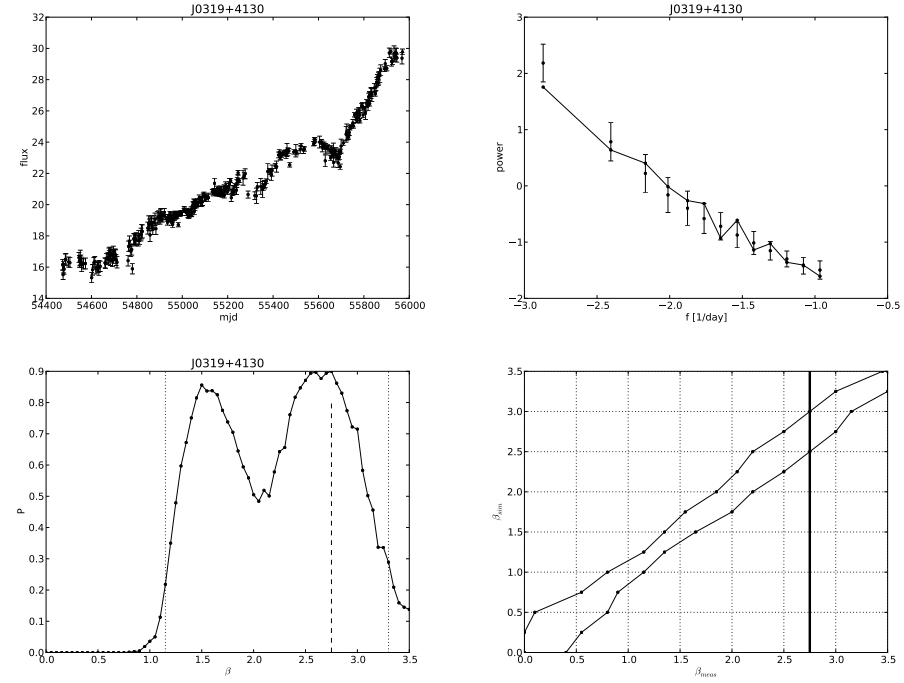

Figure E.28: PSD fit summary for J0319+4130. The best fit is $\beta = 2.8$ with 1σ limits $\beta^{lower} = 2.5$ and $\beta^{upper} = 3.0$.

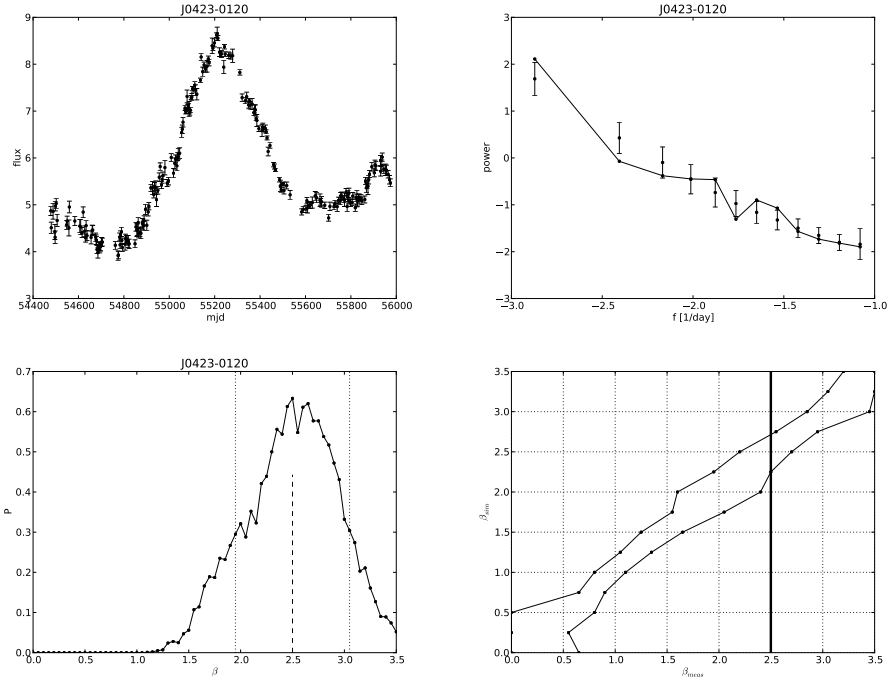

Figure E.29: PSD fit summary for J0423-0120. The best fit is $\beta = 2.5$ with 1σ limits $\beta^{lower} = 2.2$ and $\beta^{upper} = 2.7$.

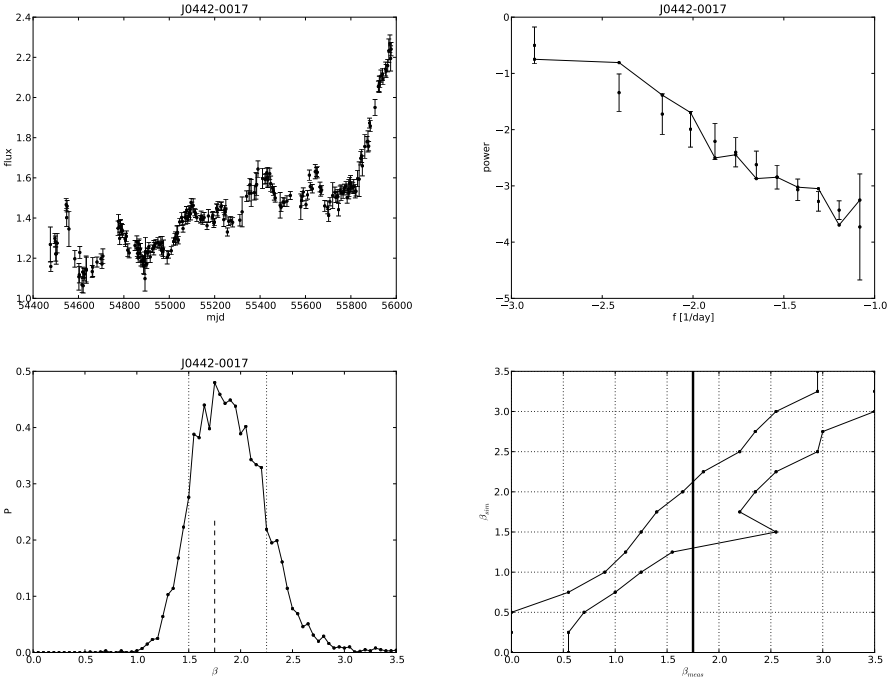

Figure E.30: PSD fit summary for J0442-0017. The best fit is $\beta = 1.8$ with 1σ limits $\beta^{lower} = 1.3$ and $\beta^{upper} = 2.1$.

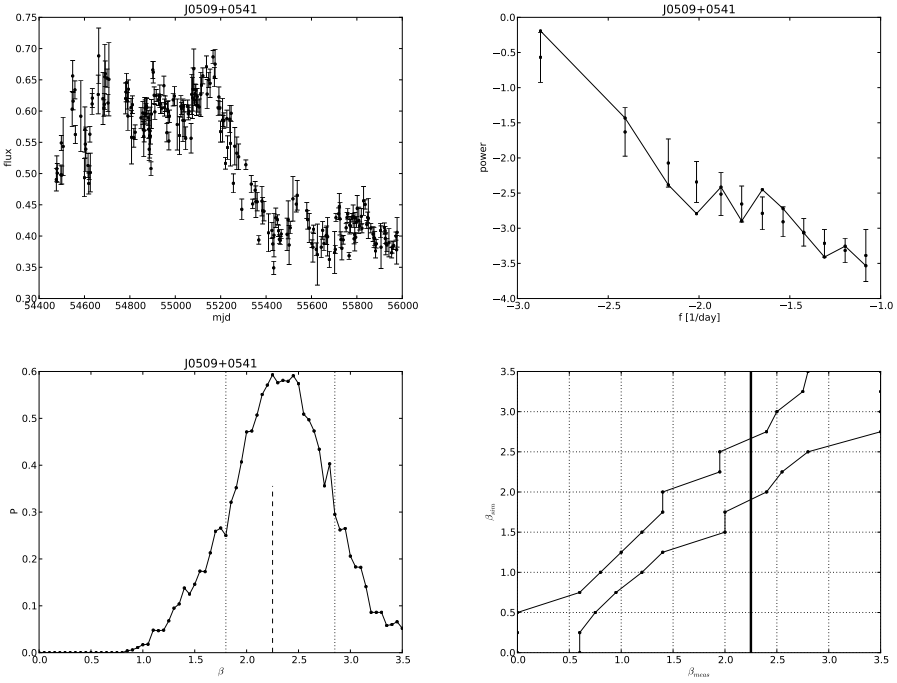

Figure E.31: PSD fit summary for J0509+0541. The best fit is $\beta = 2.2$ with 1σ limits $\beta^{lower} = 1.9$ and $\beta^{upper} = 2.7$.

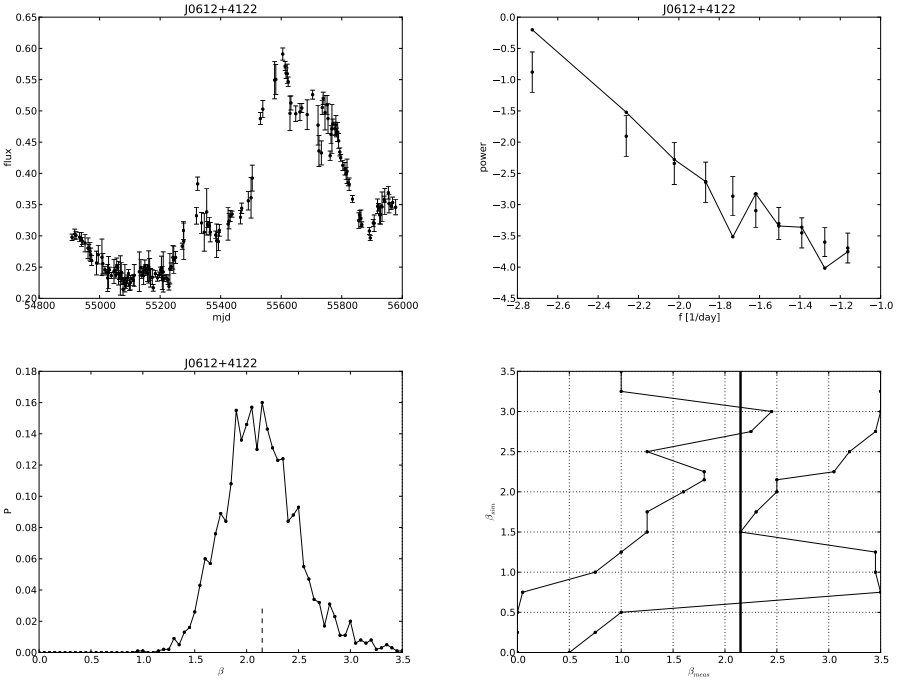

Figure E.32: PSD fit summary for J0612+4122. The best fit is $\beta = 2.1$ with 1σ limits $\beta^{lower} = 0.6$ and an undetermined upper limit.

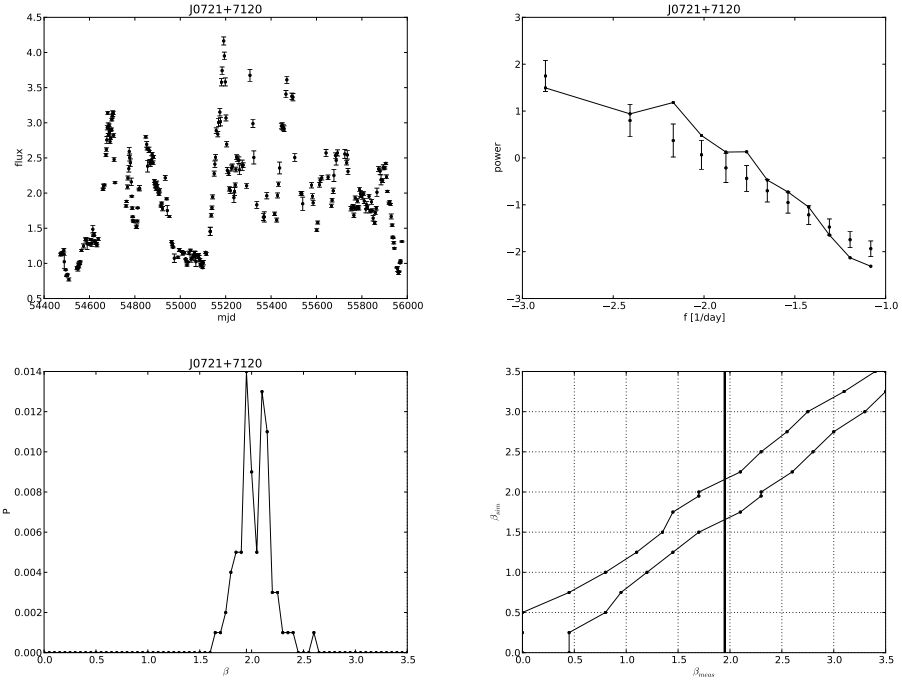

Figure E.33: PSD fit summary for J0721+7120. The best fit is $\beta = 1.9$ with 1σ limits $\beta^{lower} = 1.7$ and $\beta^{upper} = 2.2$.

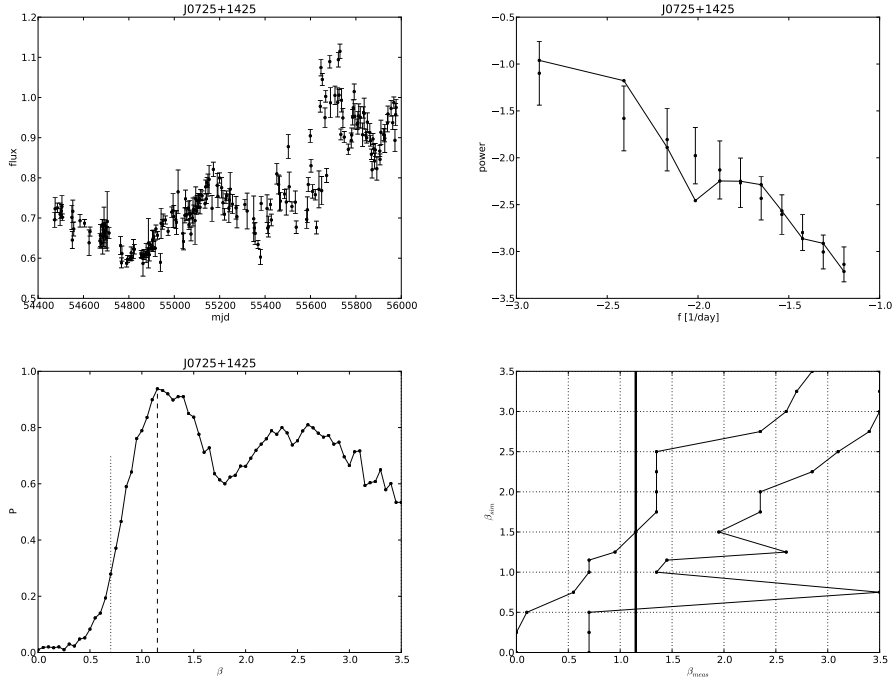

Figure E.34: PSD fit summary for J0725+1425. The best fit is $\beta = 1.1$ with 1σ limits $\beta^{lower} = 0.5$ and $\beta^{upper} = 1.5$.

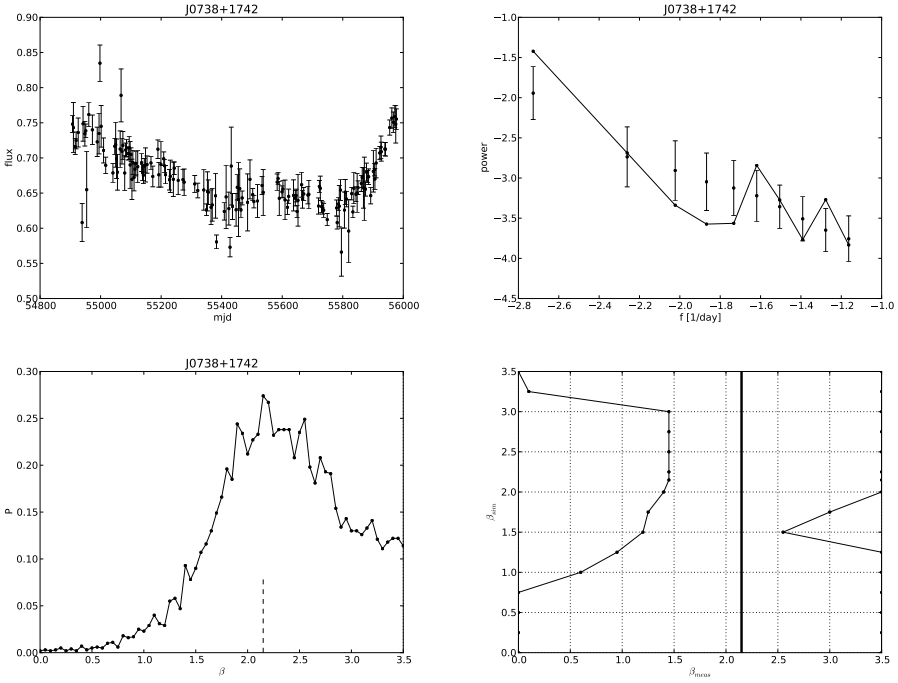

Figure E.35: PSD fit summary for J0738+1742. The best fit is $\beta = 2.1$ with 1σ limits $\beta^{lower} = 0.0$ and an undetermined upper limit.

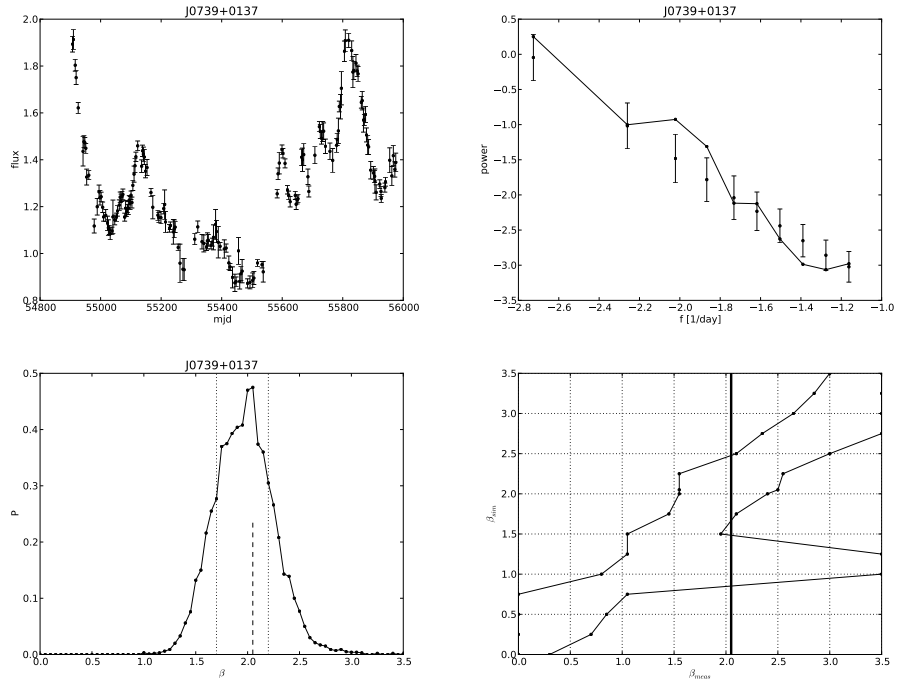

Figure E.36: PSD fit summary for J0739+0137. The best fit is $\beta = 2.0$ with 1σ limits $\beta^{lower} = 0.9$ and $\beta^{upper} = 2.5$.

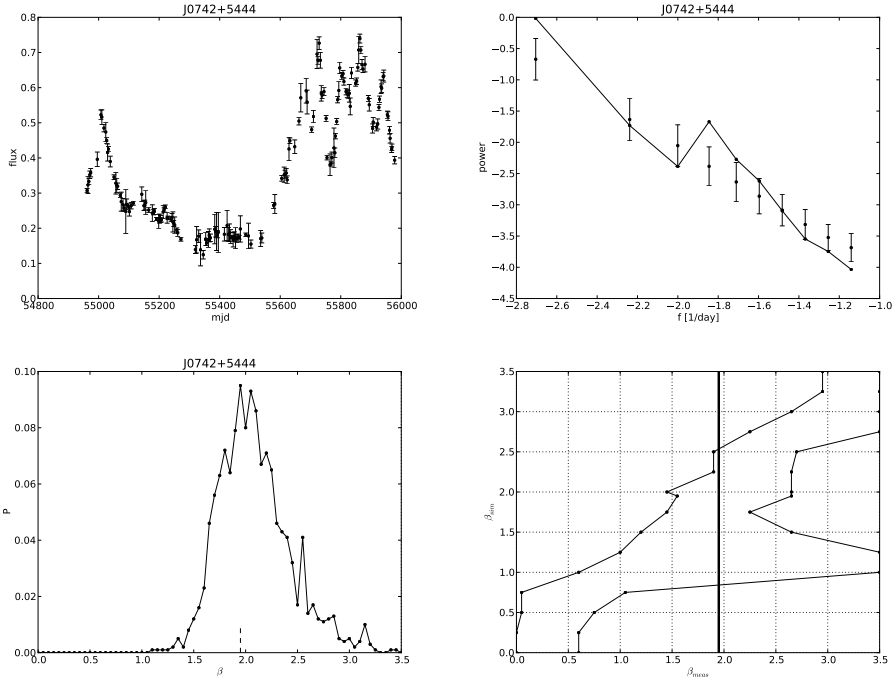

Figure E.37: PSD fit summary for J0742+5444. The best fit is $\beta = 1.9$ with 1σ limits $\beta^{lower} = 0.8$ and $\beta^{upper} = 2.5$.

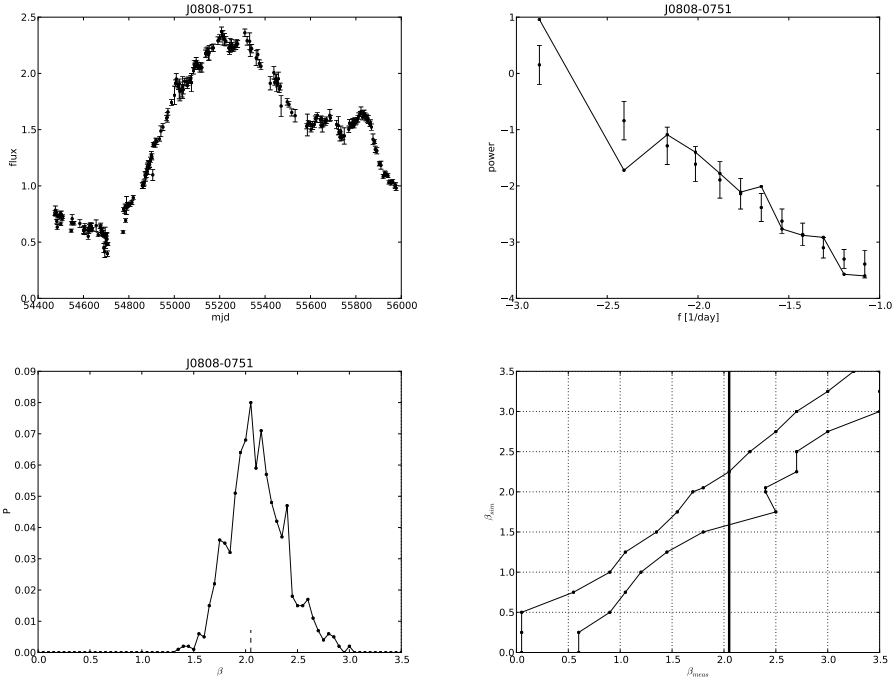

Figure E.38: PSD fit summary for J0808-0751. The best fit is $\beta = 2.0$ with 1σ limits $\beta^{lower} = 1.6$ and $\beta^{upper} = 2.2$.

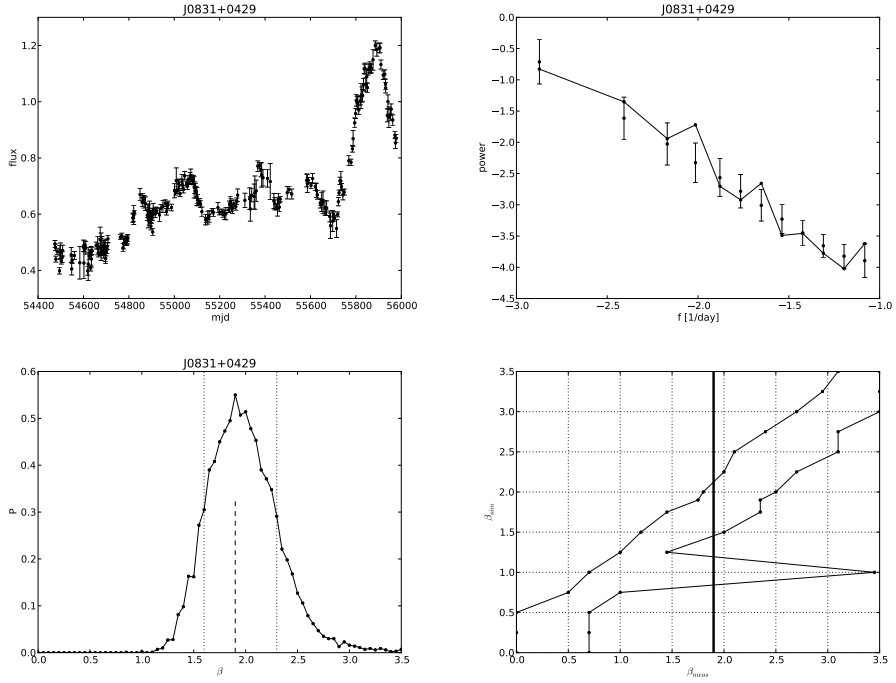

Figure E.39: PSD fit summary for J0831+0429. The best fit is $\beta = 1.9$ with 1σ limits $\beta^{lower} = 0.8$ and $\beta^{upper} = 2.1$.

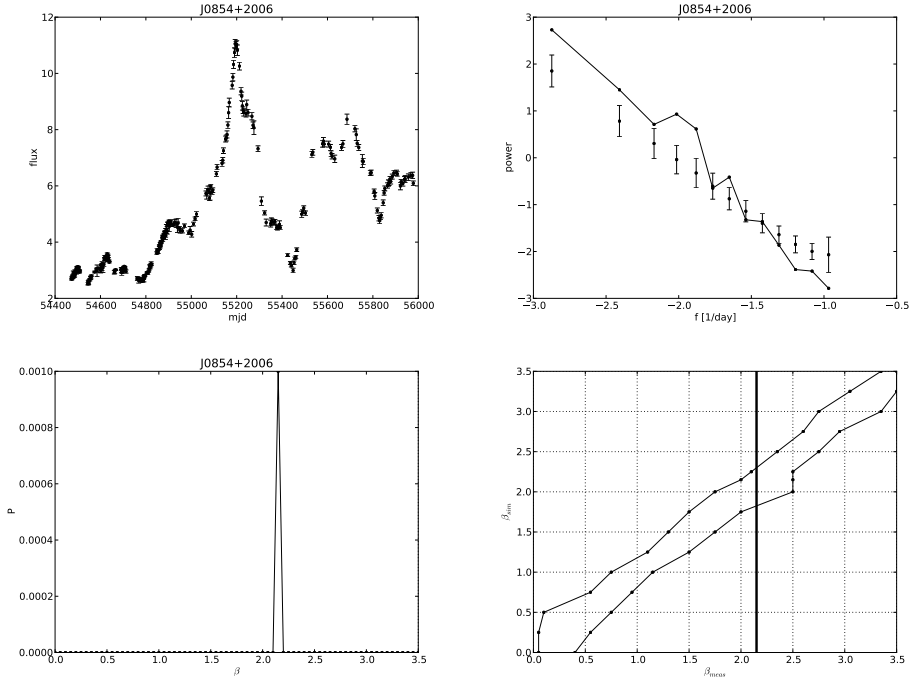

Figure E.40: PSD fit summary for J0854+2006. The best fit is $\beta = 2.1$ with 1σ limits $\beta^{lower} = 1.8$ and $\beta^{upper} = 2.3$.

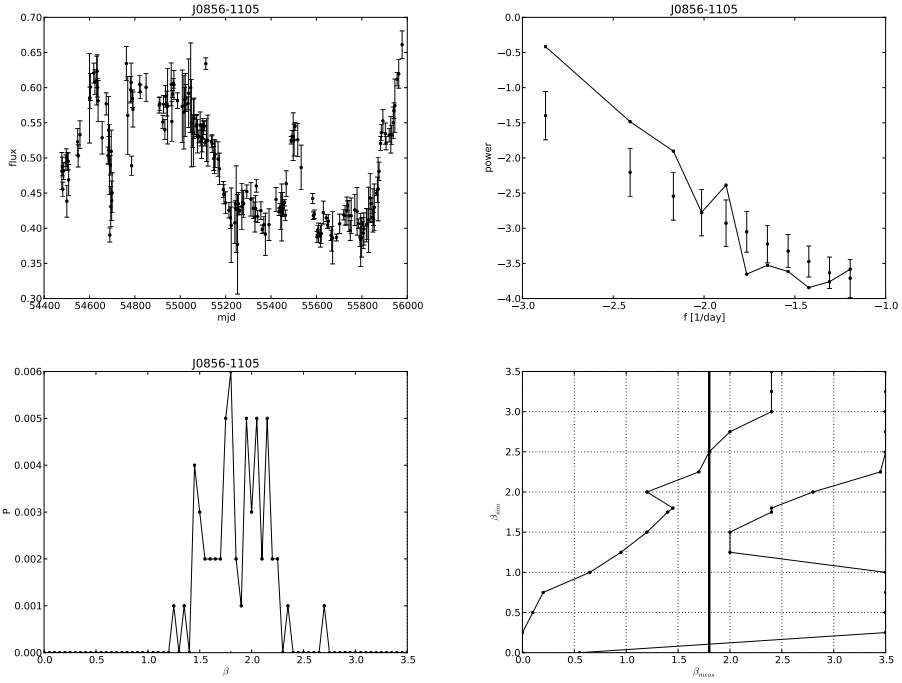

Figure E.41: PSD fit summary for J0856-1105. The best fit is $\beta = 1.8$ with 1σ limits $\beta^{lower} = 0.1$ and $\beta^{upper} = 2.5$.

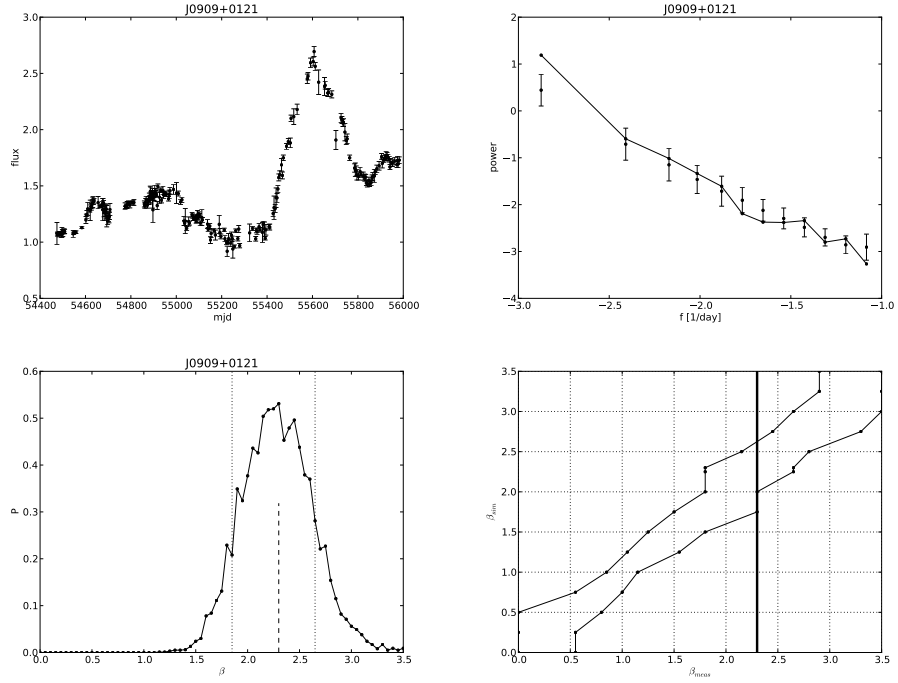

Figure E.42: PSD fit summary for J0909+0121. The best fit is $\beta = 2.3$ with 1σ limits $\beta^{lower} = 1.8$ and $\beta^{upper} = 2.6$.

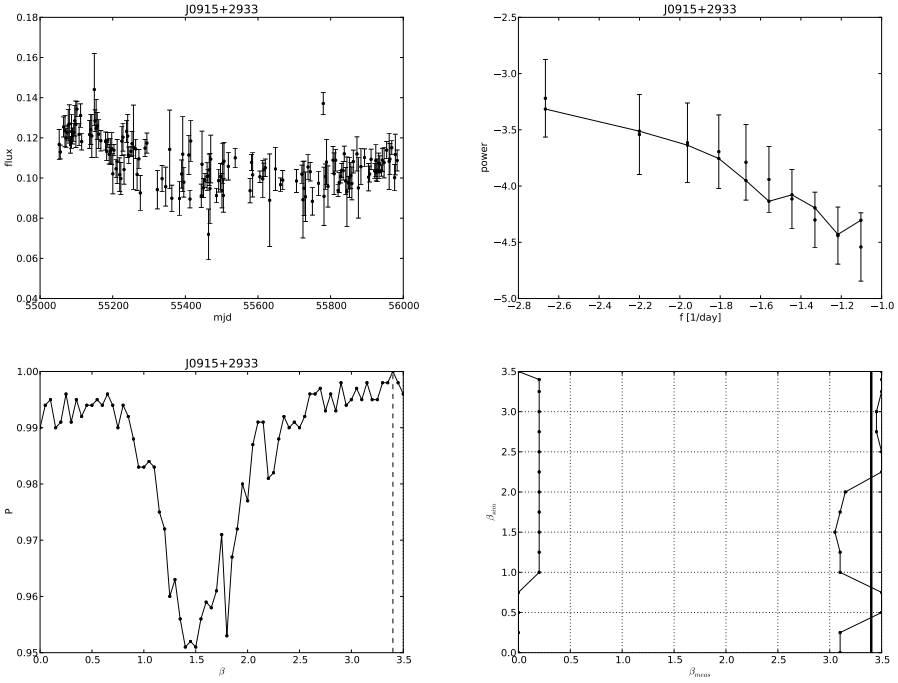

Figure E.43: PSD fit summary for J0915+2933. The best fit is $\beta = 3.4$ with 1σ limits $\beta^{lower} = 0.4$ and an undetermined upper limit.

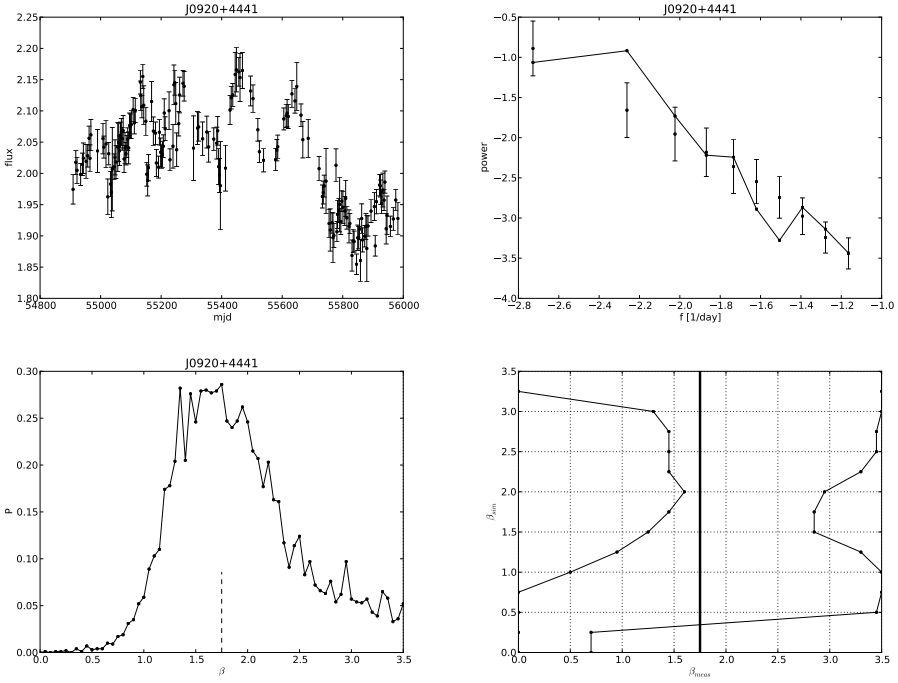

Figure E.44: PSD fit summary for J0920+4441. The best fit is $\beta = 1.8$ with 1σ limits $\beta^{lower} = 0.3$ and an undetermined upper limit.

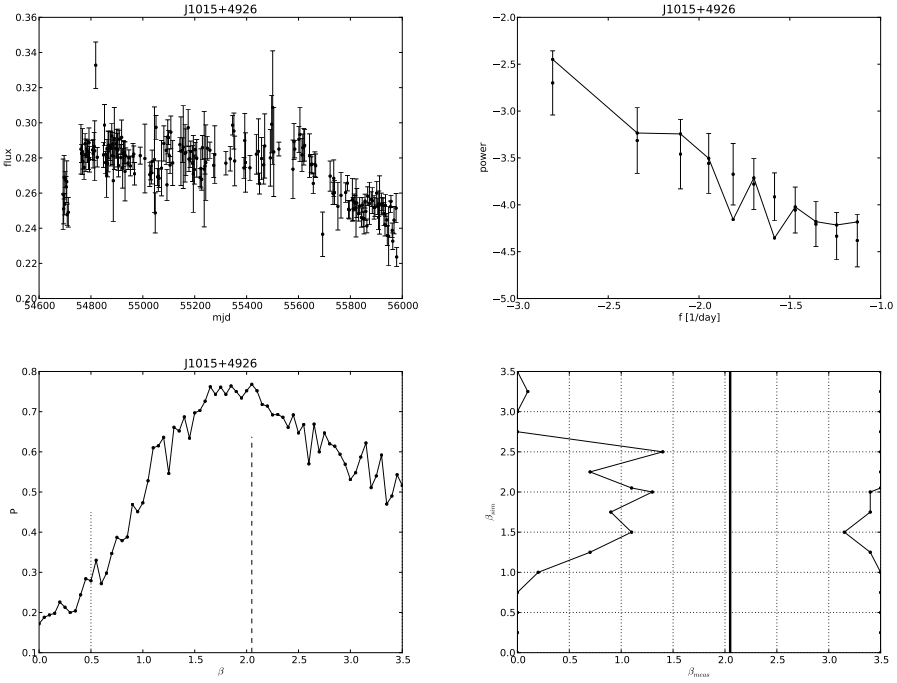

Figure E.45: PSD fit summary for J1015+4926. The best fit is $\beta = 2.0$ with 1σ limits $\beta^{lower} = 0.0$ and an undetermined upper limit.

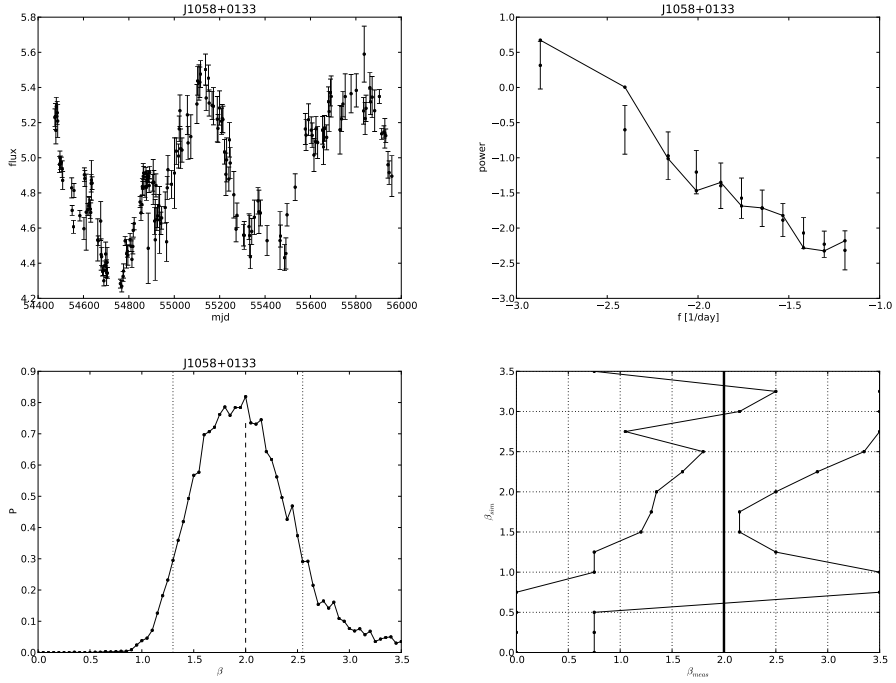

Figure E.46: PSD fit summary for J1058+0133. The best fit is $\beta = 2.0$ with 1σ limits $\beta^{lower} = 0.6$ and an undetermined upper limit.

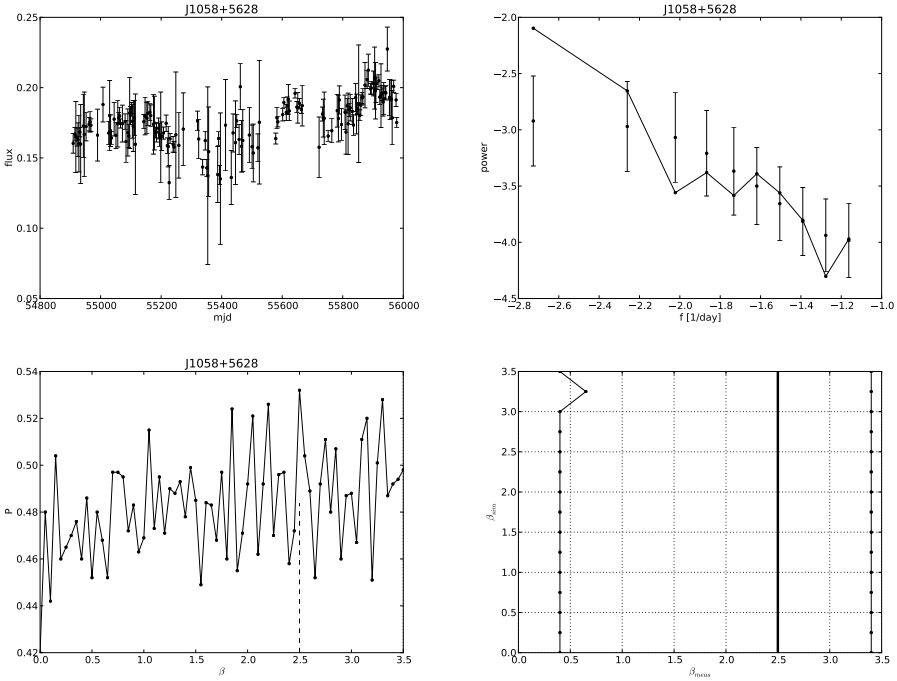

Figure E.47: PSD fit summary for J1058+5628. The best fit is $\beta = 2.5$ with 1σ limits $\beta^{lower} = 0.0$ and an undetermined upper limit.

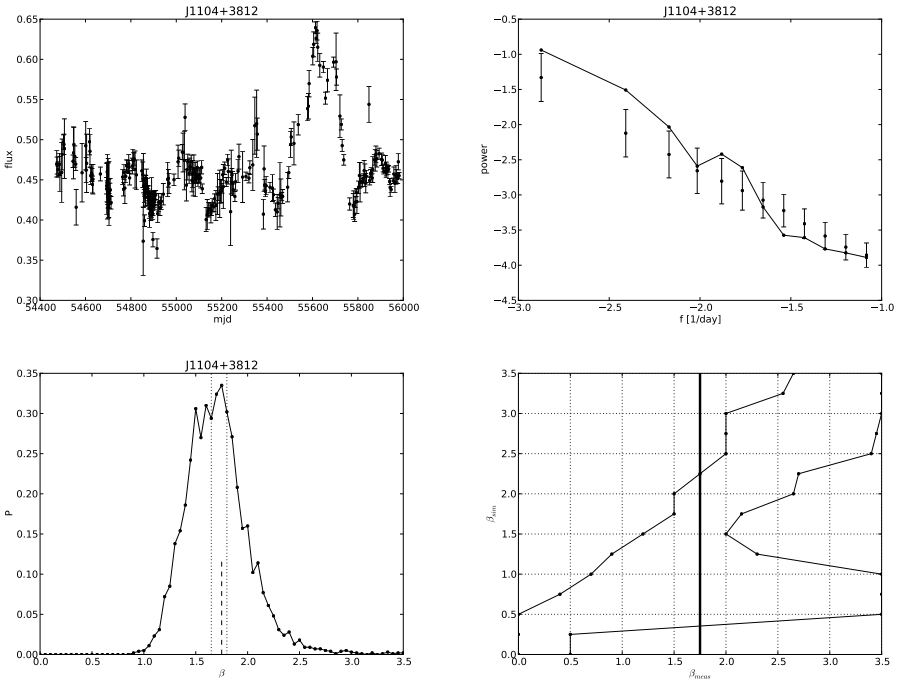

Figure E.48: PSD fit summary for J1104+3812. The best fit is $\beta = 1.8$ with 1σ limits $\beta^{lower} = 0.4$ and $\beta^{upper} = 2.2$.

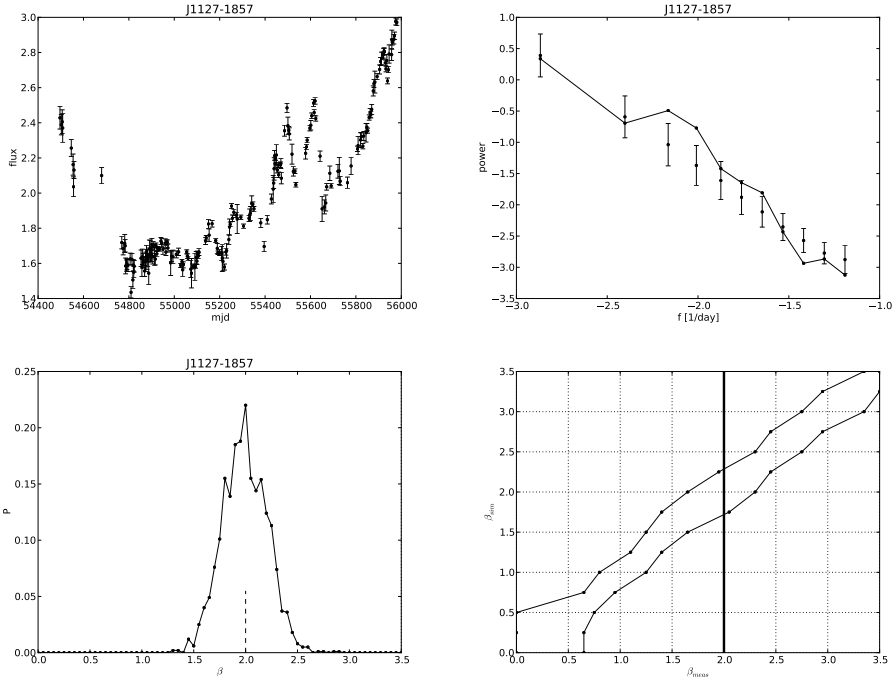

Figure E.49: PSD fit summary for J1127-1857. The best fit is $\beta = 2.0$ with 1σ limits $\beta^{lower} = 1.7$ and $\beta^{upper} = 2.3$.

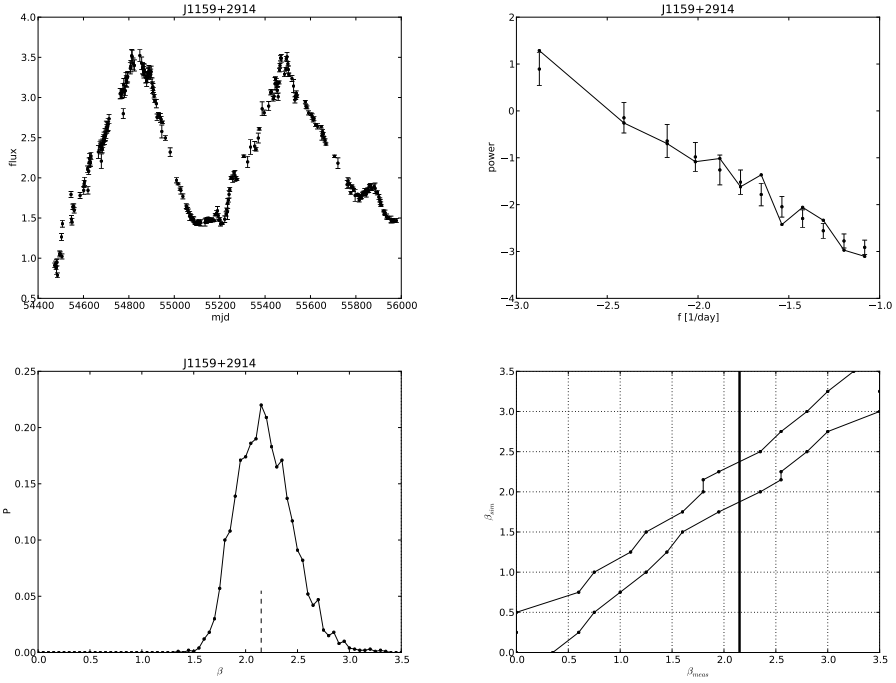

Figure E.50: PSD fit summary for J1159+2914. The best fit is $\beta = 2.1$ with 1σ limits $\beta^{lower} = 1.9$ and $\beta^{upper} = 2.4$.

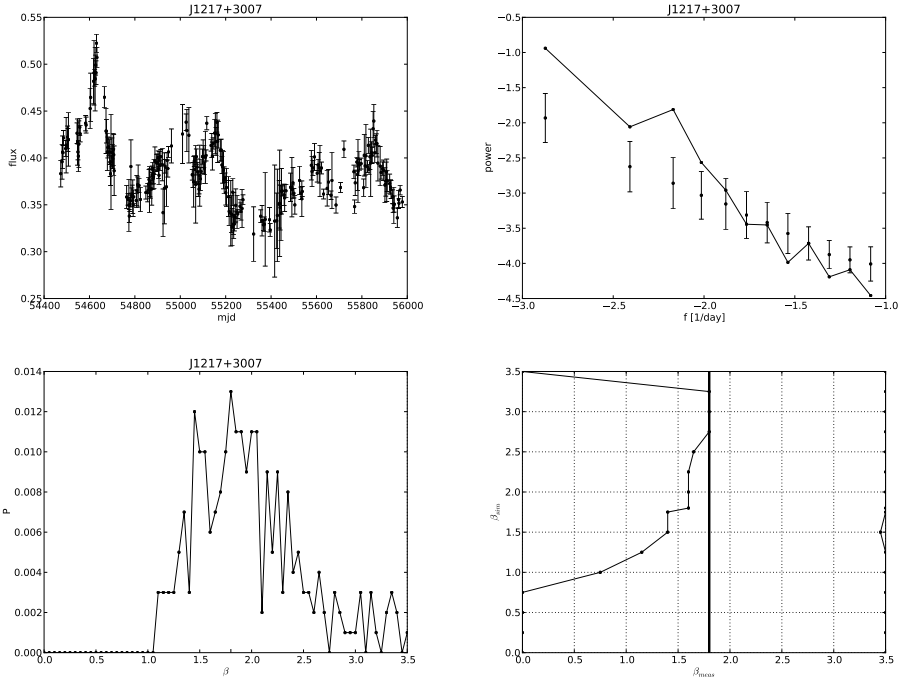

Figure E.51: PSD fit summary for J1217+3007. The best fit is $\beta = 1.8$ with 1σ limits $\beta^{lower} = 0.0$ and an undetermined upper limit.

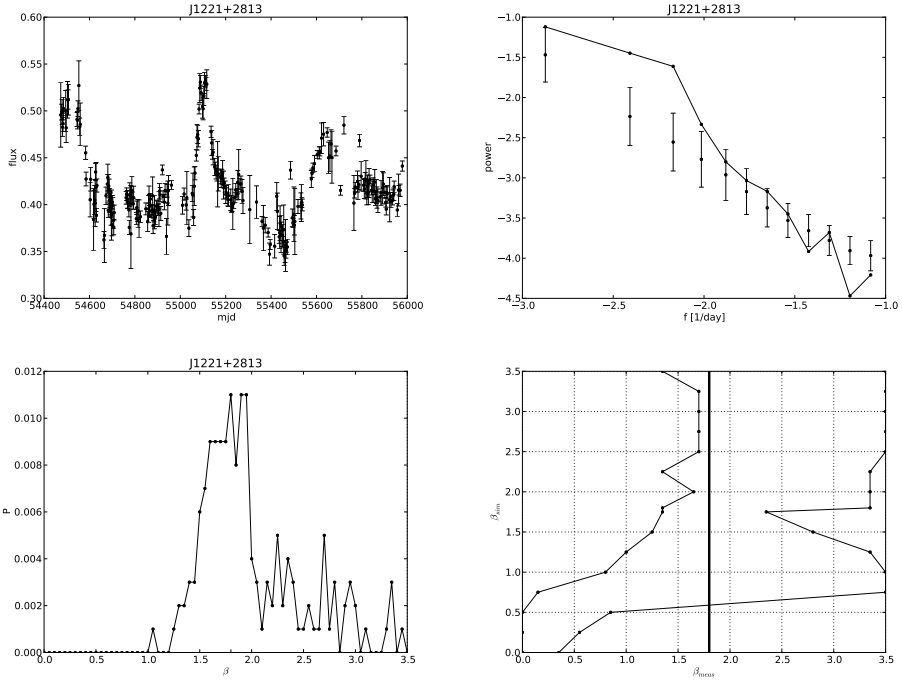

Figure E.52: PSD fit summary for J1221+2813. The best fit is $\beta = 1.8$ with 1σ limits $\beta^{lower} = 0.6$ and an undetermined upper limit.

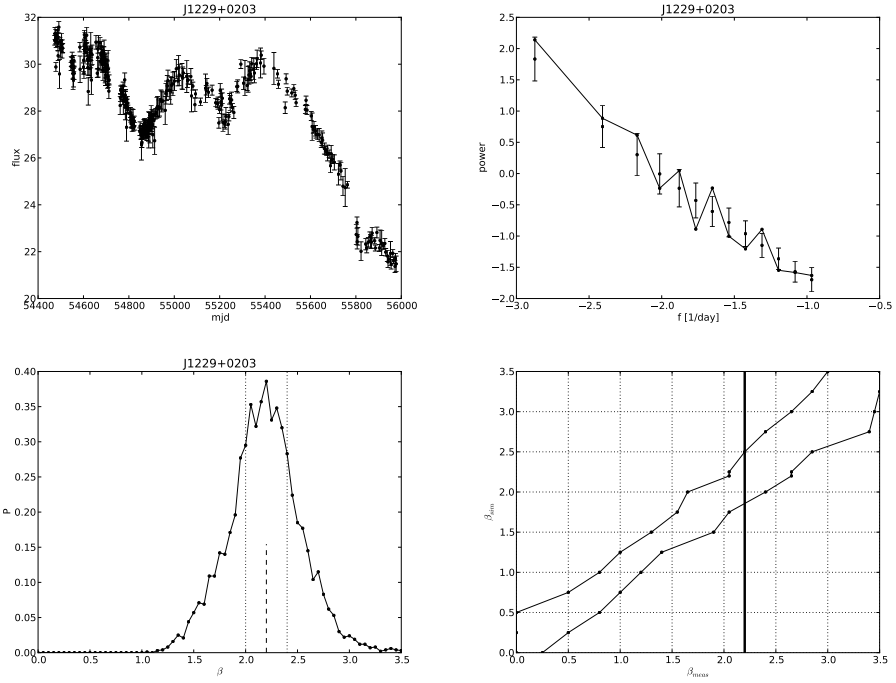

Figure E.53: PSD fit summary for J1229+0203. The best fit is $\beta = 2.2$ with 1σ limits $\beta^{lower} = 1.9$ and $\beta^{upper} = 2.5$.

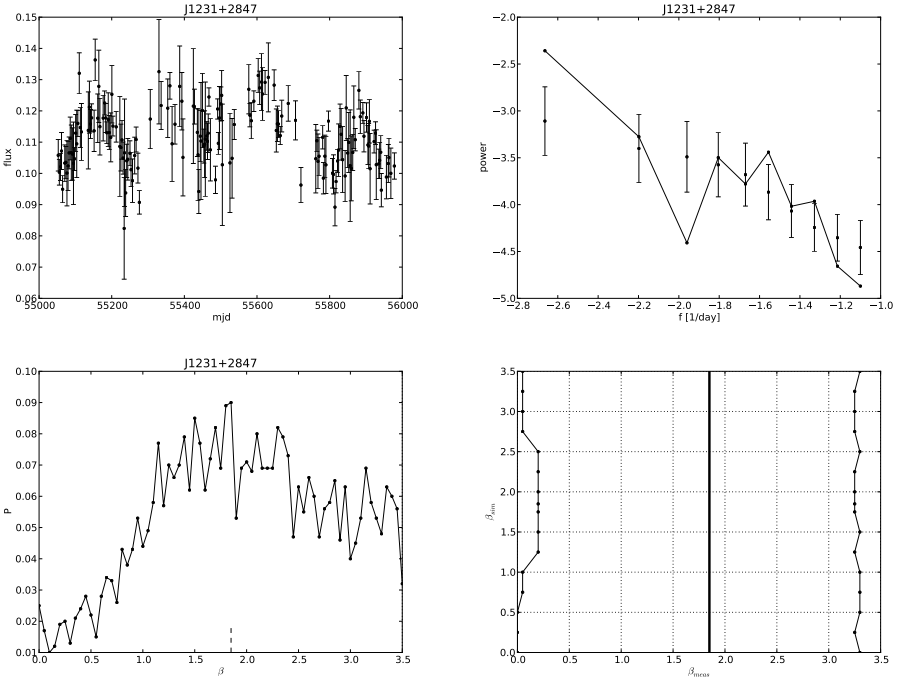

Figure E.54: PSD fit summary for J1231+2847. The best fit is $\beta = 1.9$ with 1σ limits $\beta^{lower} = 0.0$ and an undetermined upper limit.

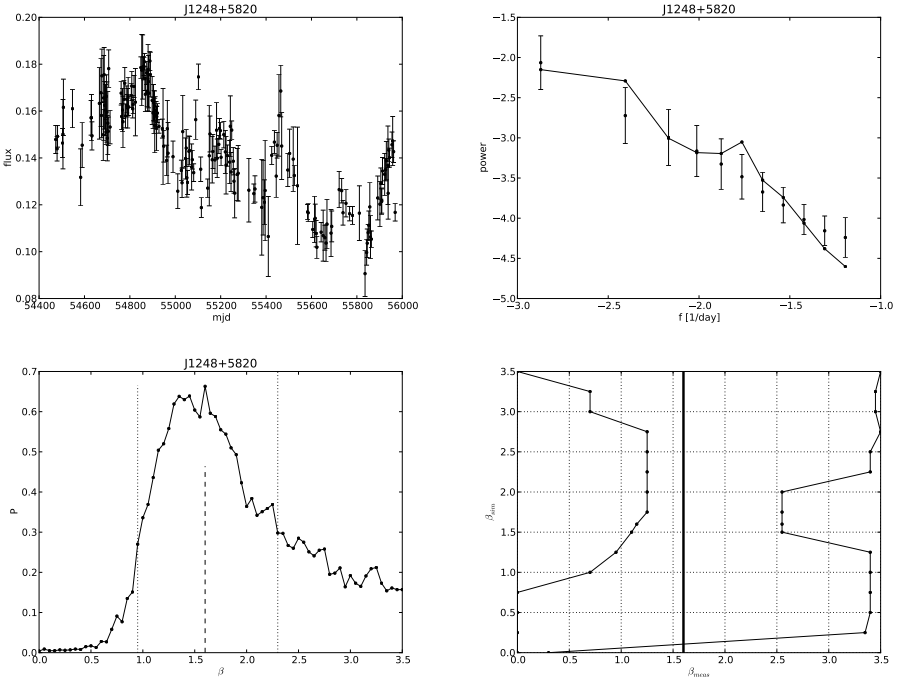

Figure E.55: PSD fit summary for J1248+5820. The best fit is $\beta = 1.6$ with 1σ limits $\beta^{lower} = 0.1$ and an undetermined upper limit.

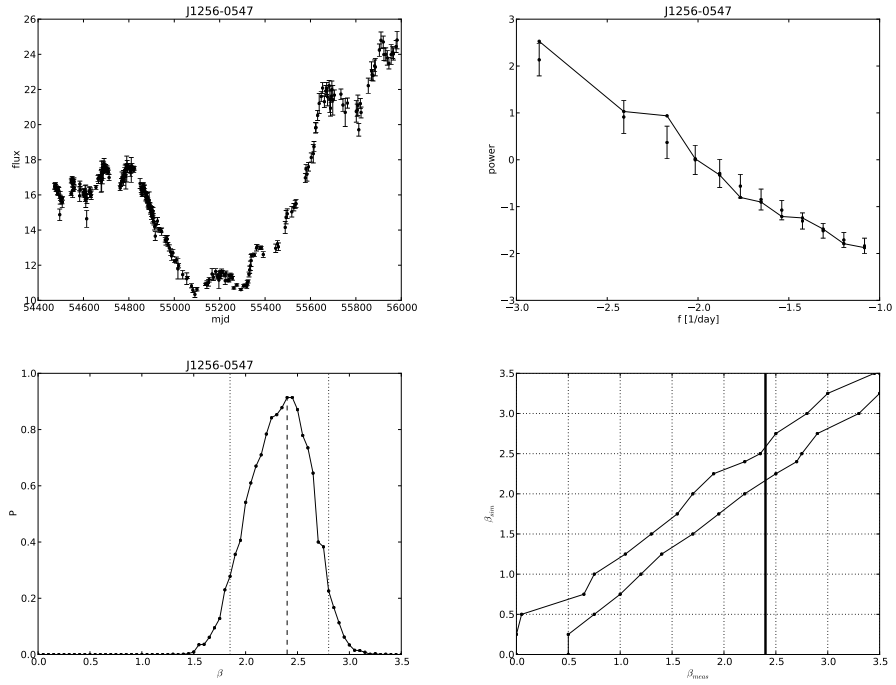

Figure E.56: PSD fit summary for J1256-0547. The best fit is $\beta = 2.4$ with 1σ limits $\beta^{lower} = 2.2$ and $\beta^{upper} = 2.6$.

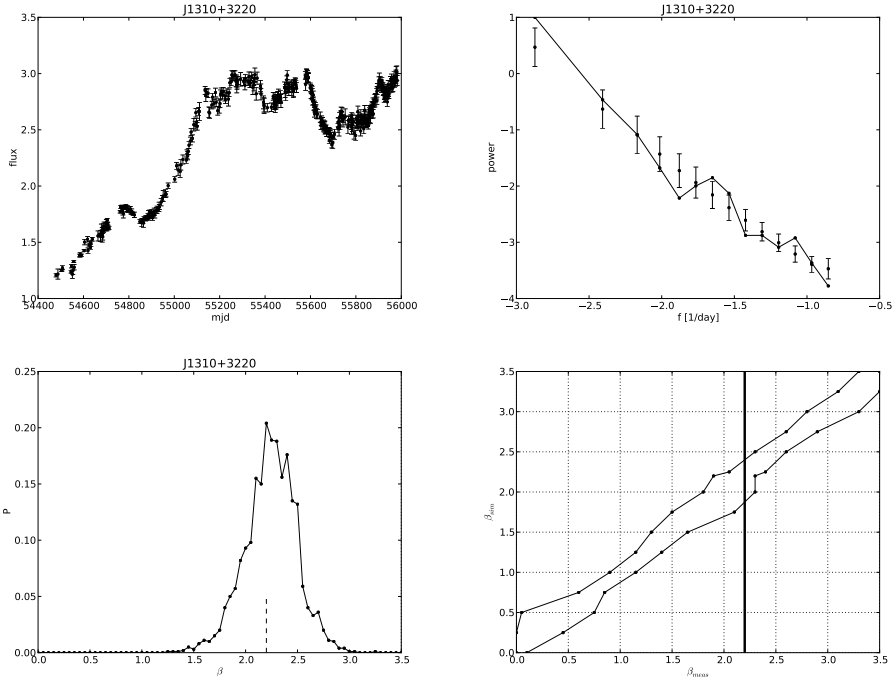

Figure E.57: PSD fit summary for J1310+3220. The best fit is $\beta = 2.2$ with 1σ limits $\beta^{lower} = 1.9$ and $\beta^{upper} = 2.4$.

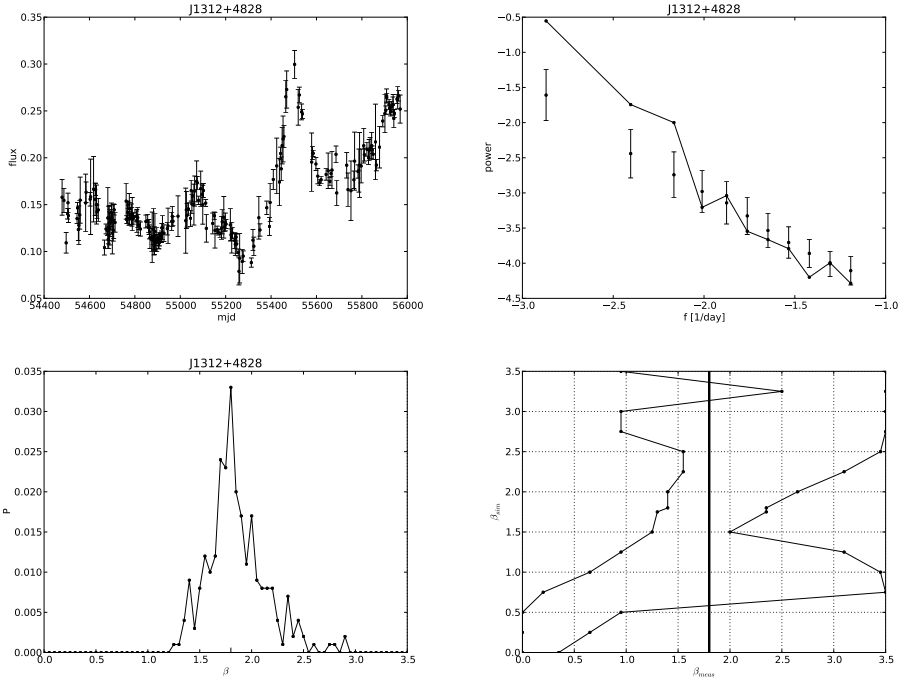

Figure E.58: PSD fit summary for J1312+4828. The best fit is $\beta = 1.8$ with 1σ limits $\beta^{lower} = 0.6$ and an undetermined upper limit.

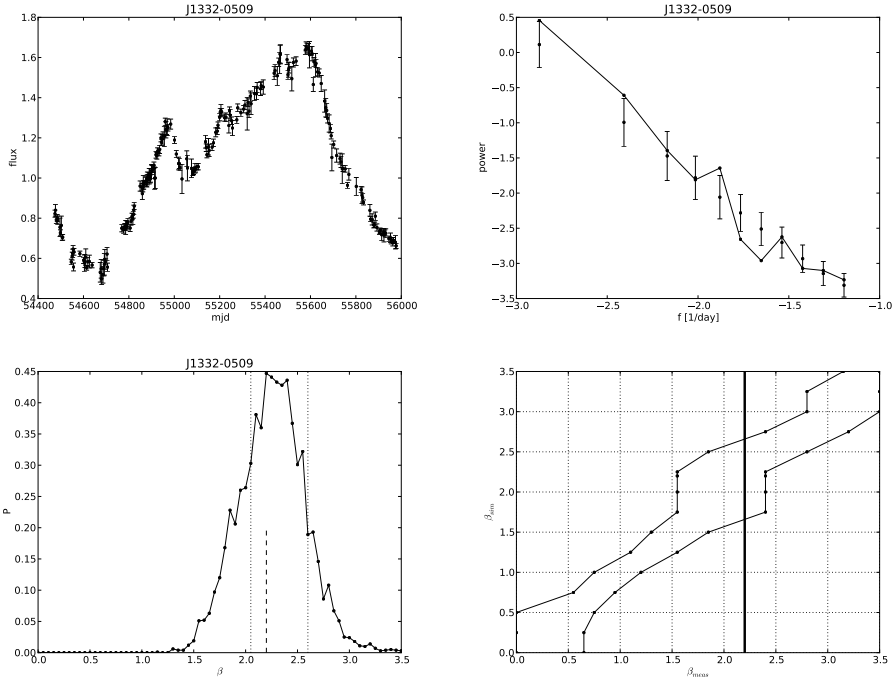

Figure E.59: PSD fit summary for J1332-0509. The best fit is $\beta = 2.2$ with 1σ limits $\beta^{lower} = 1.7$ and $\beta^{upper} = 2.7$.

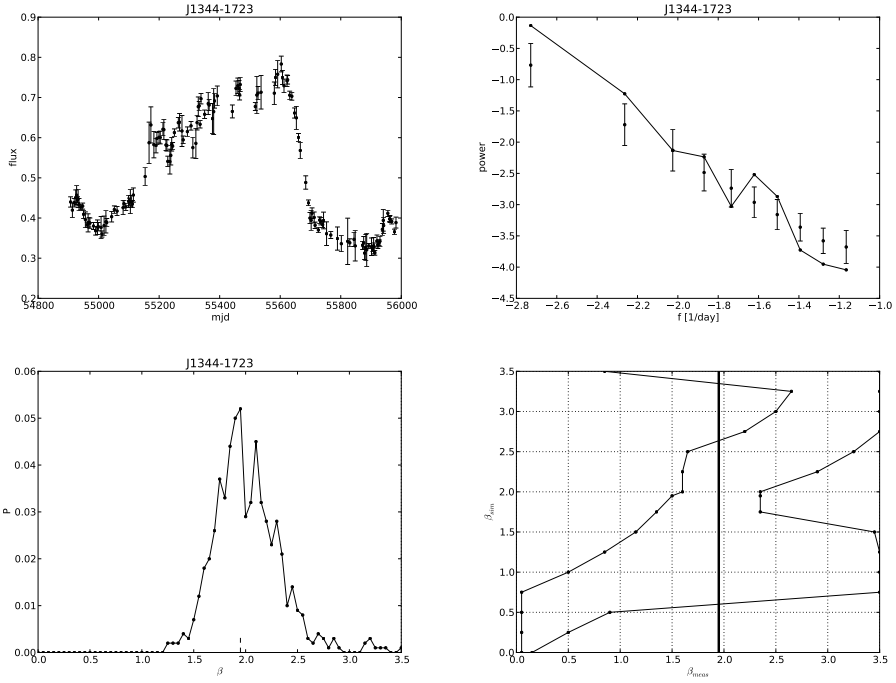

Figure E.60: PSD fit summary for J1344-1723. The best fit is $\beta = 1.9$ with 1σ limits $\beta^{lower} = 0.6$ and an undetermined upper limit.

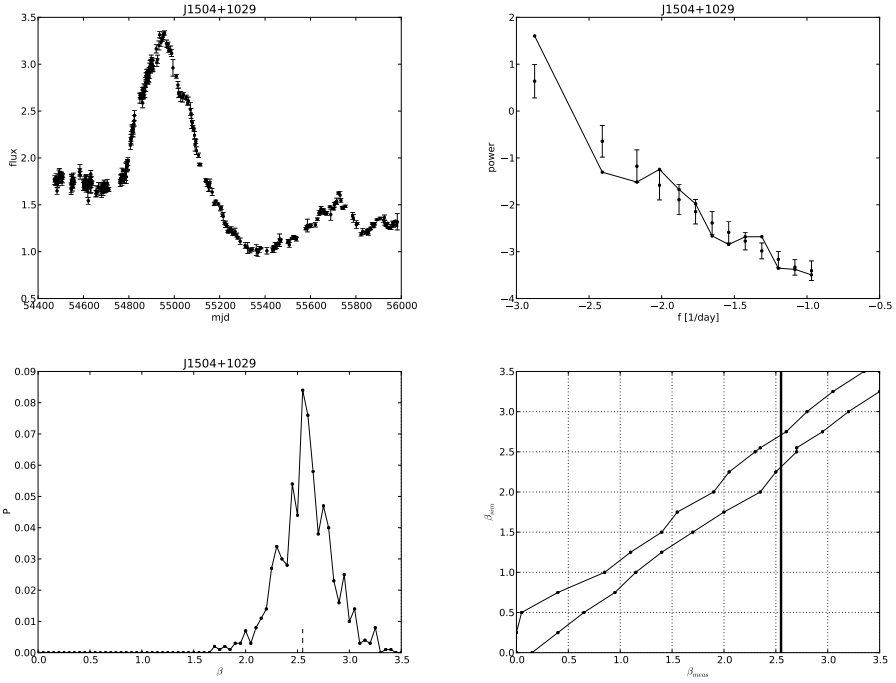

Figure E.61: PSD fit summary for J1504+1029. The best fit is $\beta = 2.5$ with 1σ limits $\beta^{lower} = 2.3$ and $\beta^{upper} = 2.7$.

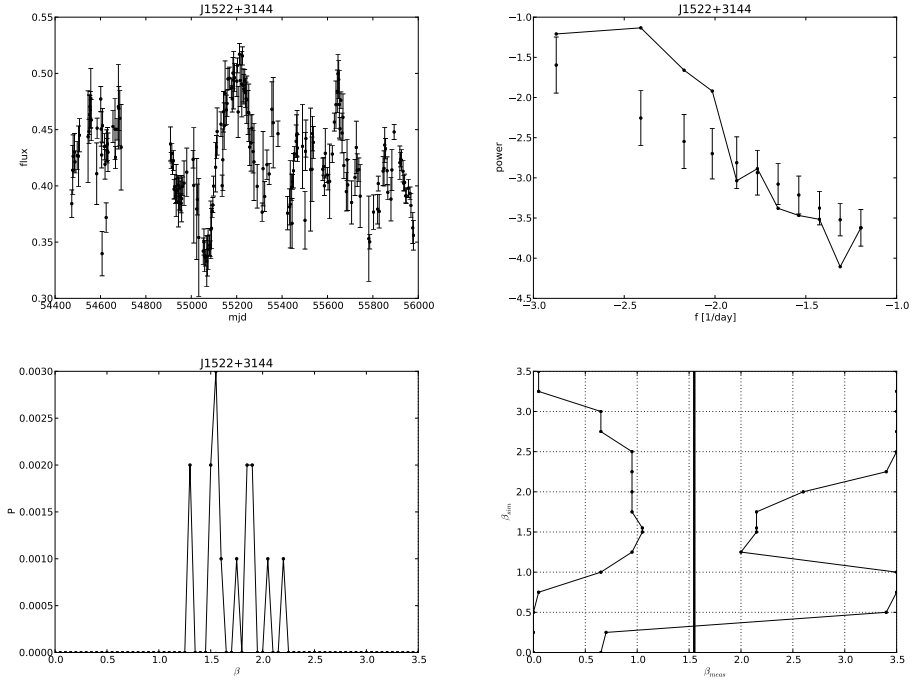

Figure E.62: PSD fit summary for J1522+3144. The best fit is $\beta = 1.6$ with 1σ limits $\beta^{lower} = 0.3$ and an undetermined upper limit.

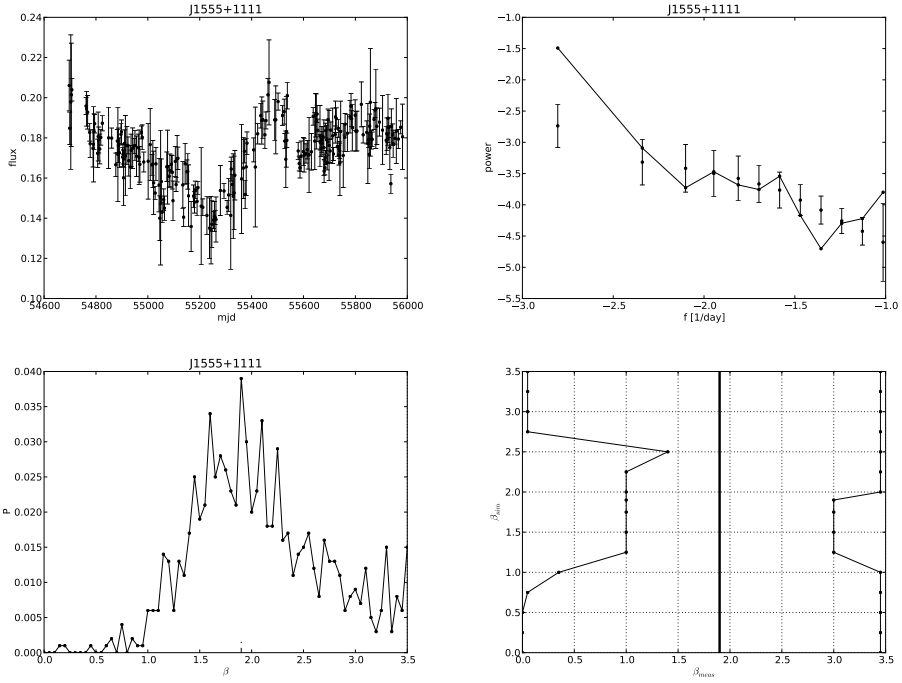

Figure E.63: PSD fit summary for J1555+1111. The best fit is $\beta = 1.9$ with 1σ limits $\beta^{lower} = 0.0$ and an undetermined upper limit.

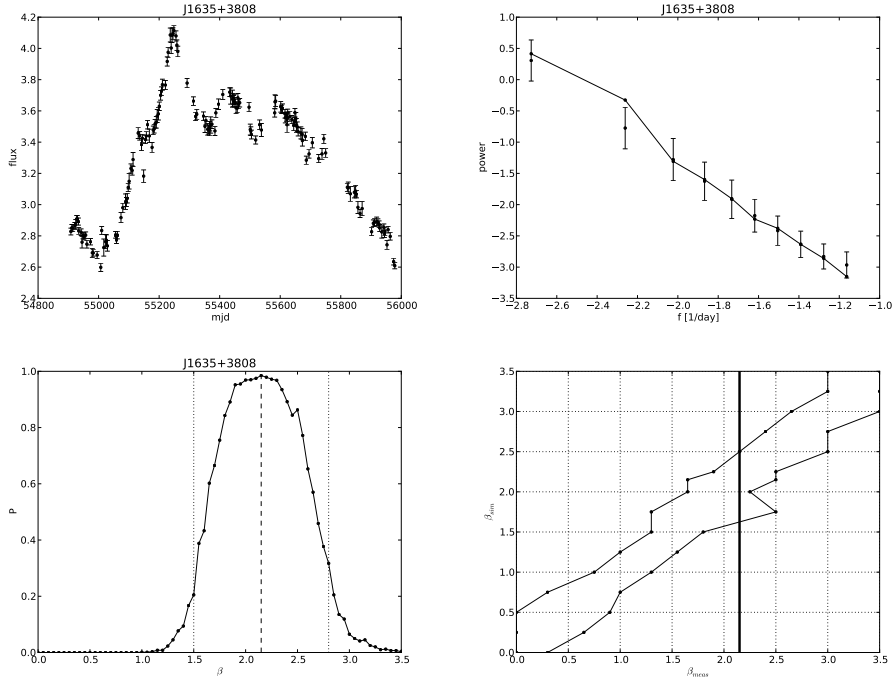

Figure E.64: PSD fit summary for J1635+3808. The best fit is $\beta = 2.1$ with 1σ limits $\beta^{lower} = 1.6$ and $\beta^{upper} = 2.5$.

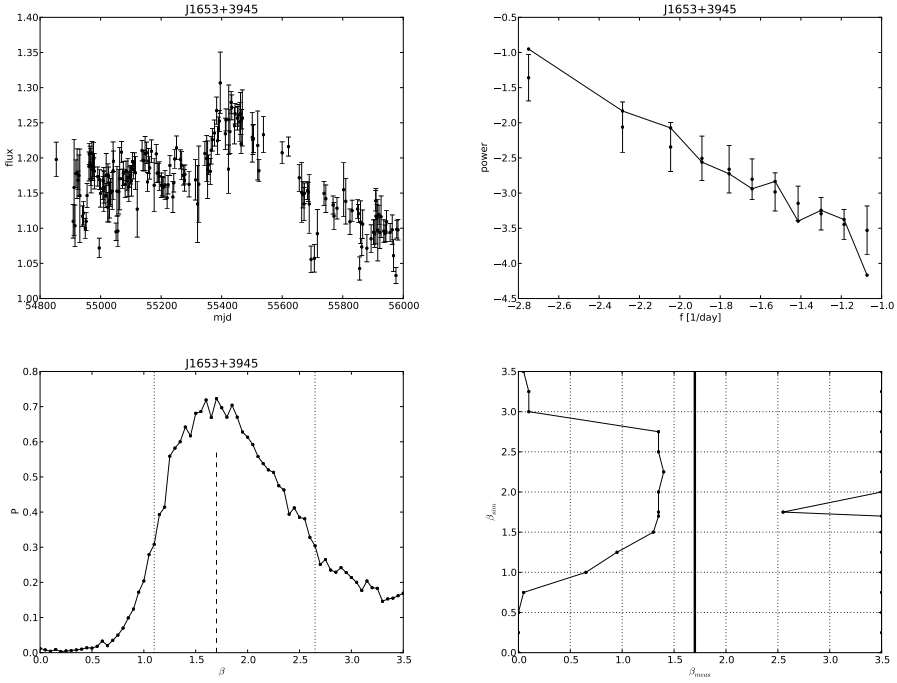

Figure E.65: PSD fit summary for J1653+3945. The best fit is $\beta = 1.7$ with 1σ limits $\beta^{lower} = 0.0$ and an undetermined upper limit.

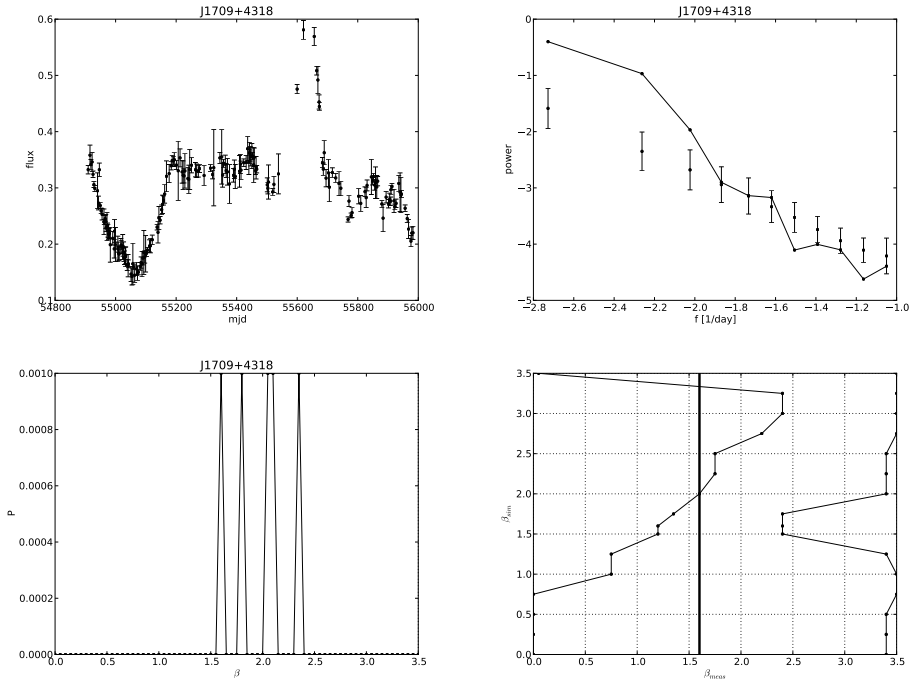

Figure E.66: PSD fit summary for J1709+4318. The best fit is $\beta = 1.6$ with 1σ limits $\beta^{lower} = 0.0$ and an undetermined upper limit.

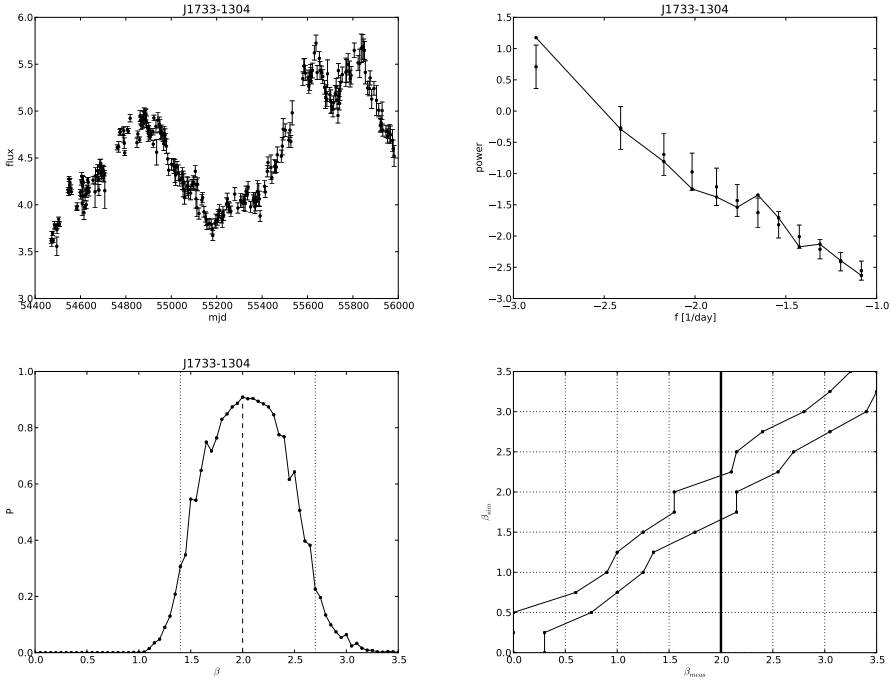

Figure E.67: PSD fit summary for J1733-1304. The best fit is $\beta = 2.0$ with 1σ limits $\beta^{lower} = 1.7$ and $\beta^{upper} = 2.2$.

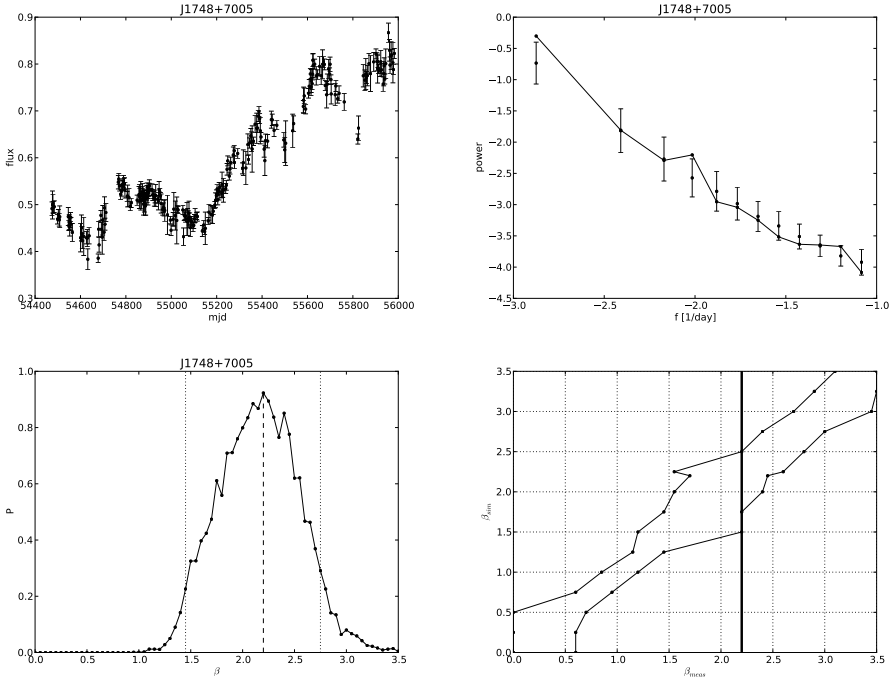

Figure E.68: PSD fit summary for J1748+7005. The best fit is $\beta = 2.2$ with 1σ limits $\beta^{lower} = 1.5$ and $\beta^{upper} = 2.5$.

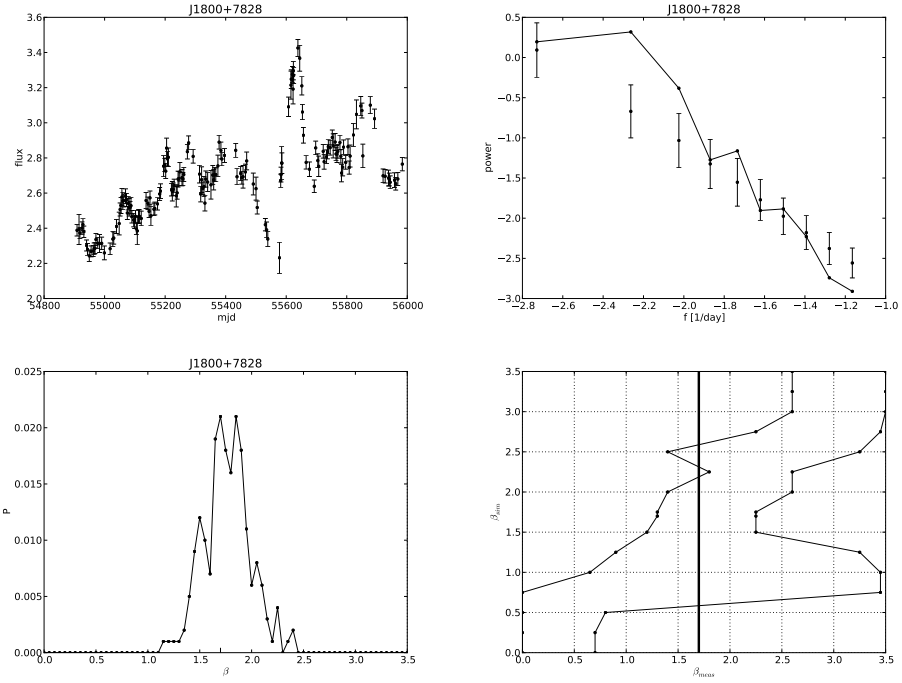

Figure E.69: PSD fit summary for J1800+7828. The best fit is $\beta = 1.7$ with 1σ limits $\beta^{lower} = 0.6$ and $\beta^{upper} = 2.6$.

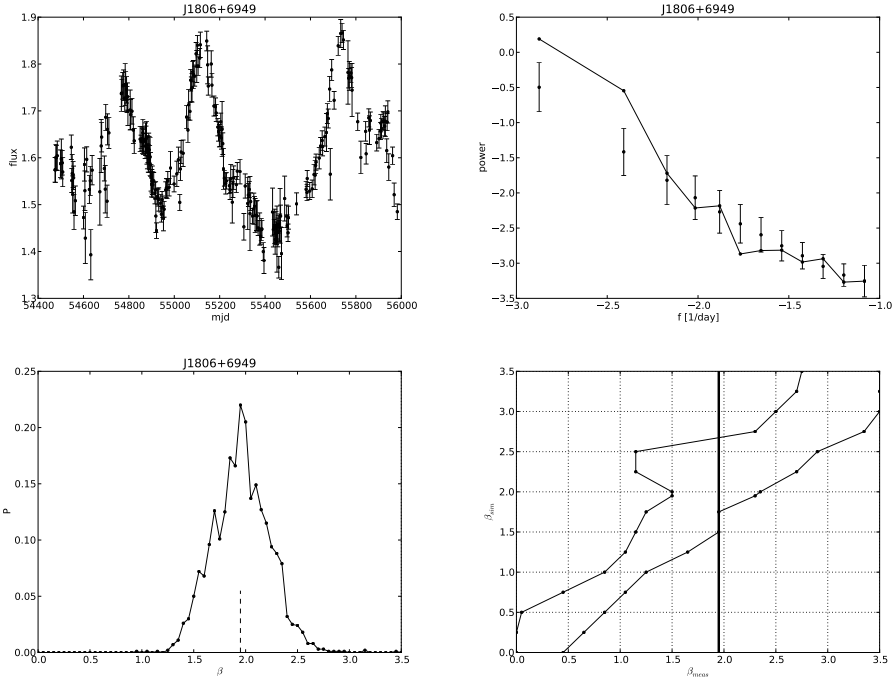

Figure E.70: PSD fit summary for J1806+6949. The best fit is $\beta = 1.9$ with 1σ limits $\beta^{lower} = 1.5$ and $\beta^{upper} = 2.7$.

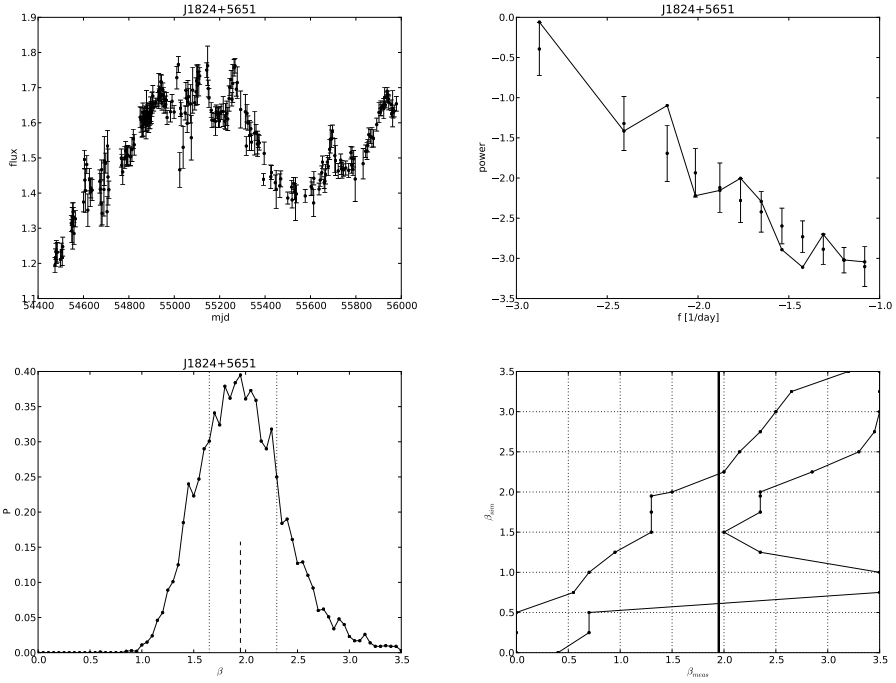

Figure E.71: PSD fit summary for J1824+5651. The best fit is $\beta = 1.9$ with 1σ limits $\beta^{lower} = 0.6$ and $\beta^{upper} = 2.2$.

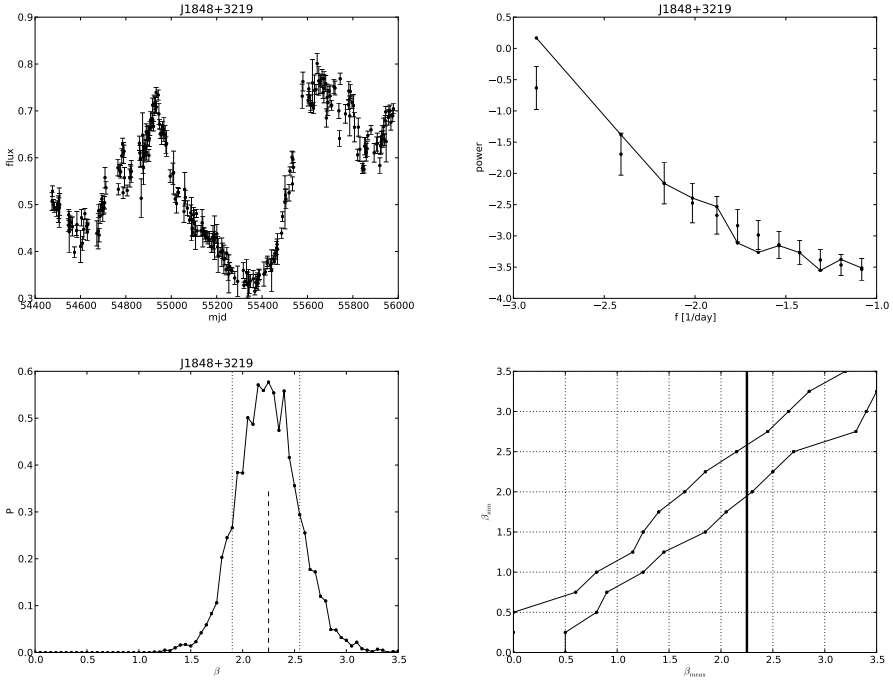

Figure E.72: PSD fit summary for J1848+3219. The best fit is $\beta = 2.2$ with 1σ limits $\beta^{lower} = 1.9$ and $\beta^{upper} = 2.6$.

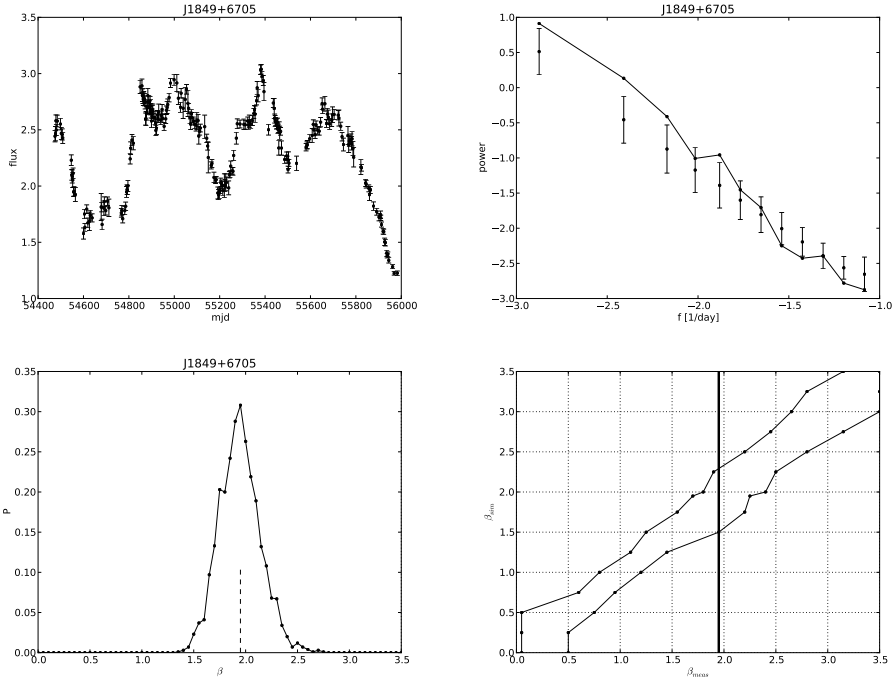

Figure E.73: PSD fit summary for J1849+6705. The best fit is $\beta = 1.9$ with 1σ limits $\beta^{lower} = 1.5$ and $\beta^{upper} = 2.3$.

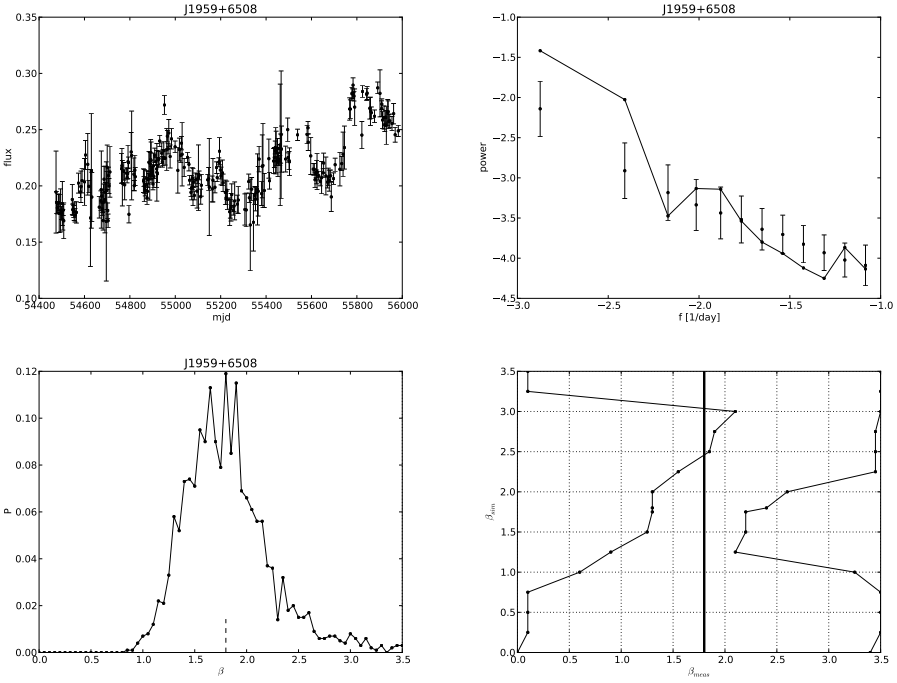

Figure E.74: PSD fit summary for J1959+6508. The best fit is $\beta = 1.8$ with 1σ limits $\beta^{lower} = 0.0$ and an undetermined upper limit.

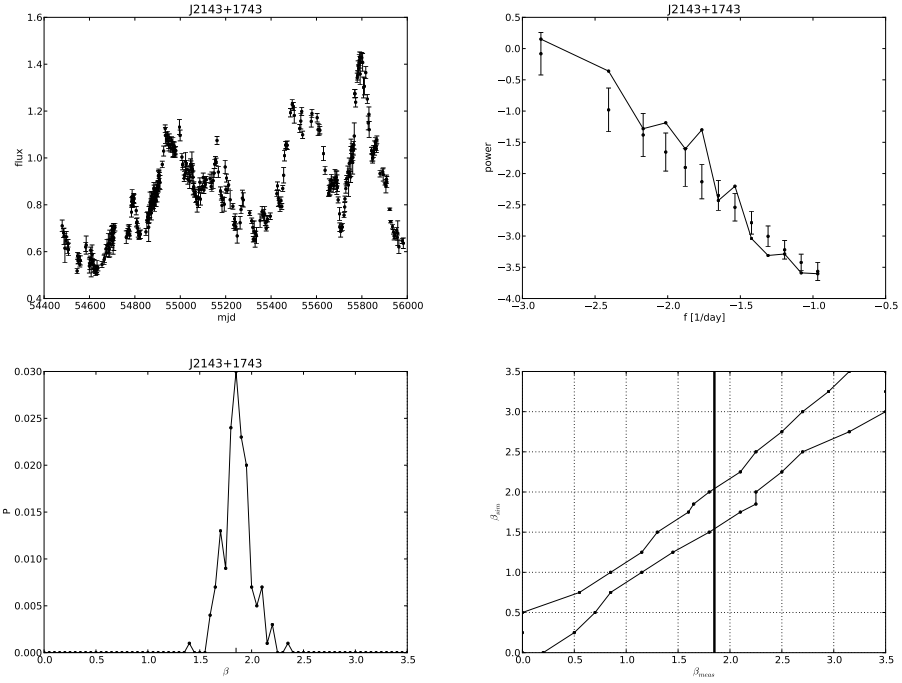

Figure E.75: PSD fit summary for J2143+1743. The best fit is $\beta = 1.9$ with 1σ limits $\beta^{lower} = 1.5$ and $\beta^{upper} = 2.0$.

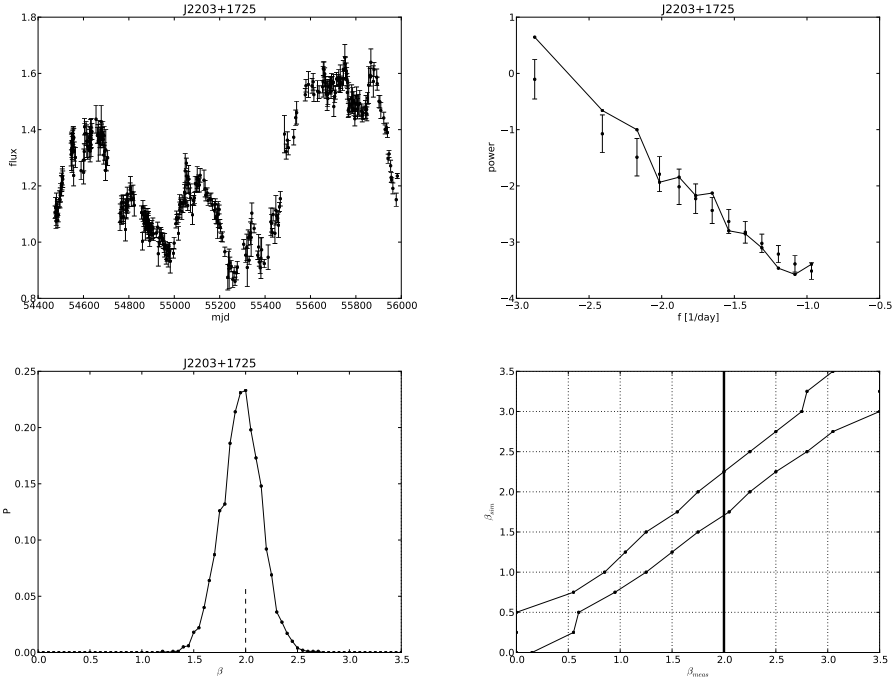

Figure E.76: PSD fit summary for J2203+1725. The best fit is $\beta = 2.0$ with 1σ limits $\beta^{lower} = 1.7$ and $\beta^{upper} = 2.2$.

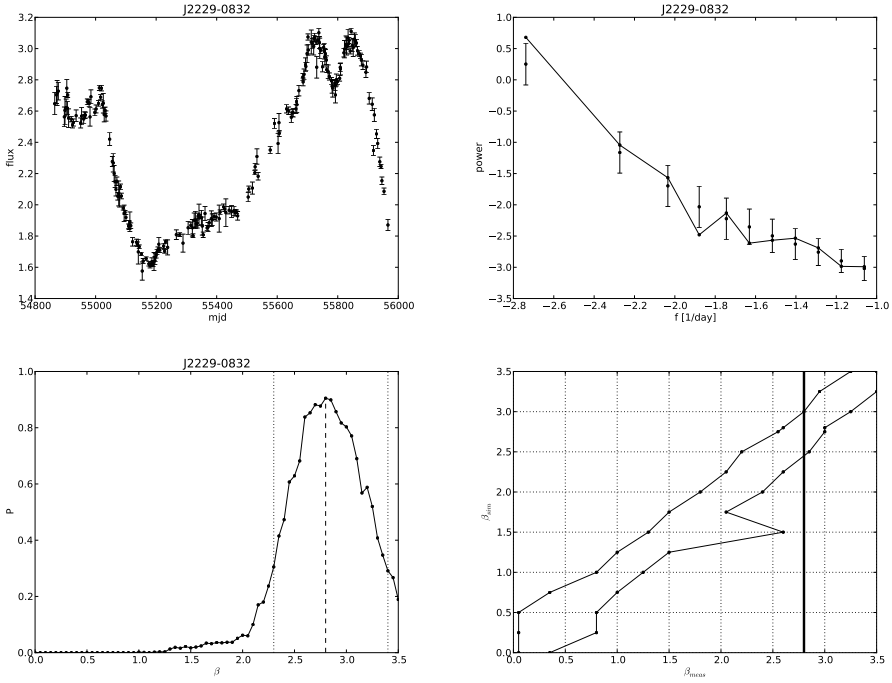

Figure E.77: PSD fit summary for J2229-0832. The best fit is $\beta = 2.8$ with 1σ limits $\beta^{lower} = 2.5$ and $\beta^{upper} = 3.0$.

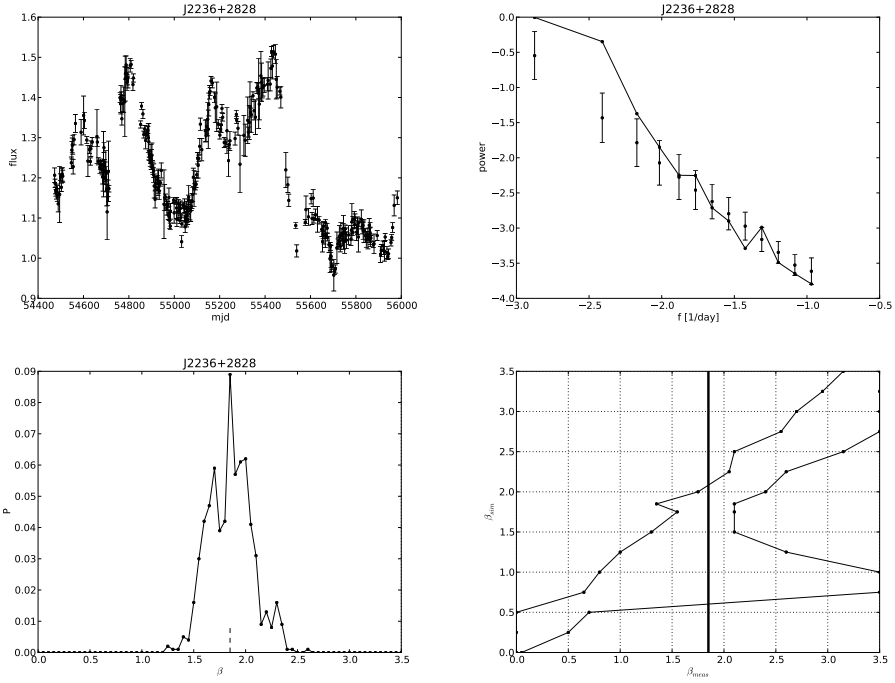

Figure E.78: PSD fit summary for J2236+2828. The best fit is $\beta = 1.9$ with 1σ limits $\beta^{lower} = 0.6$ and $\beta^{upper} = 2.1$.

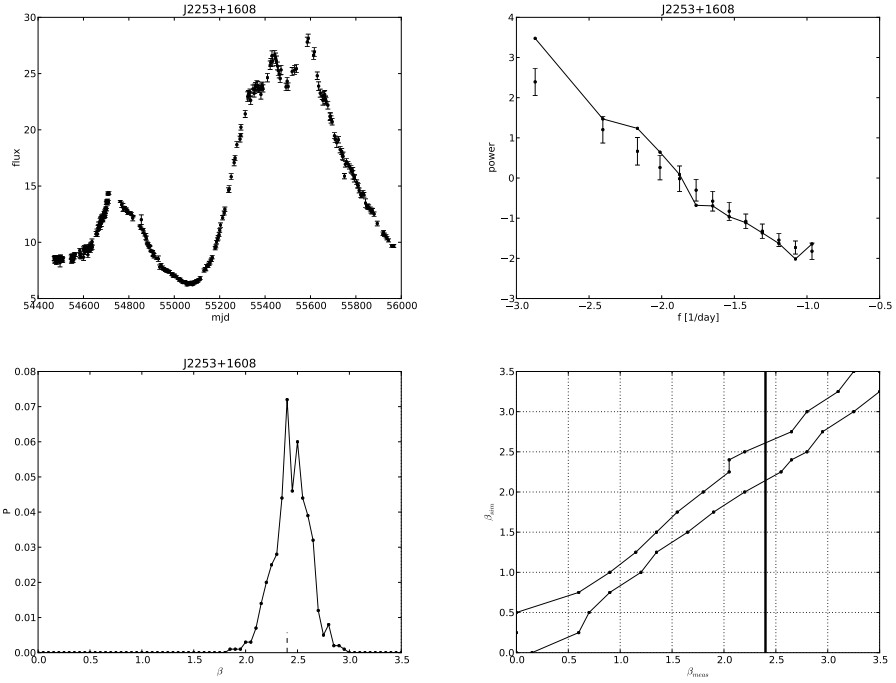

Figure E.79: PSD fit summary for J2253+1608. The best fit is $\beta = 2.4$ with 1σ limits $\beta^{lower} = 2.1$ and $\beta^{upper} = 2.6$.

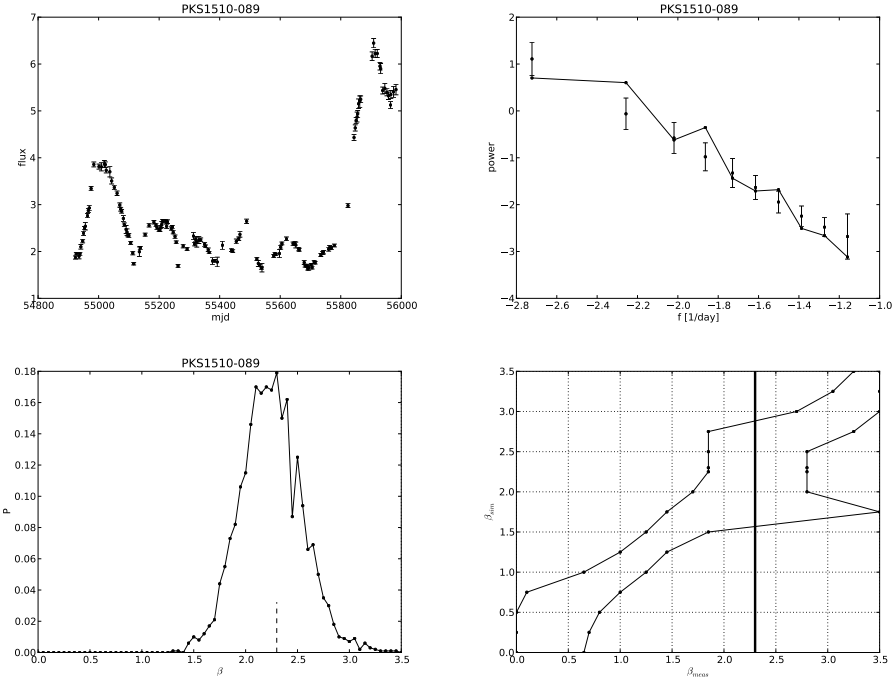

Figure E.80: PSD fit summary for PKS1510-089. The best fit is $\beta = 2.3$ with 1σ limits $\beta^{lower} = 1.6$ and $\beta^{upper} = 2.9$.

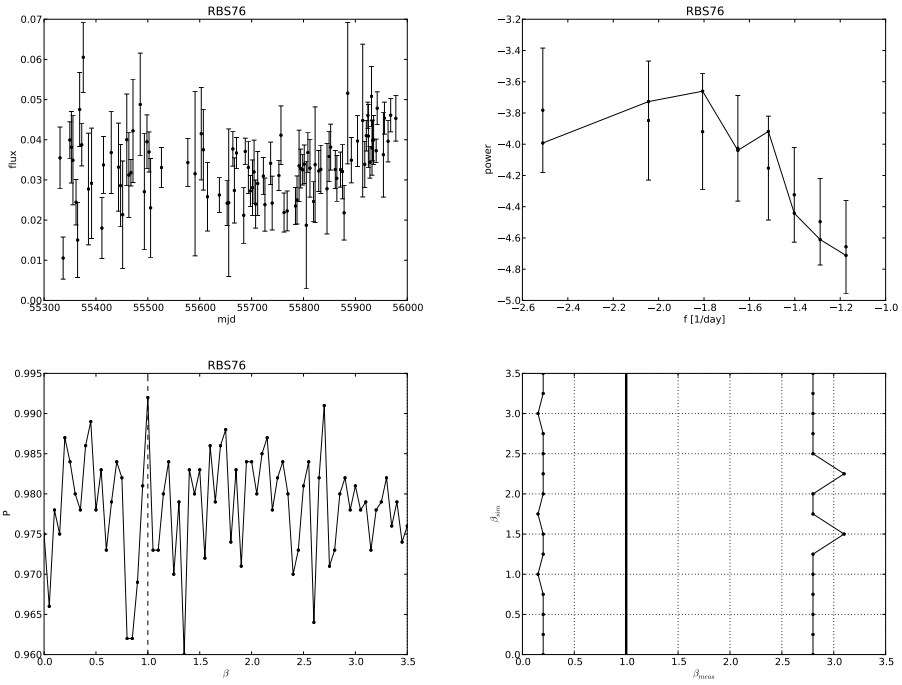

Figure E.81: PSD fit summary for RBS76. The best fit is $\beta = 1.0$ with 1σ limits $\beta^{lower} = 0.0$ and an undetermined upper limit.

E.3 PSD characterization figures for the gamma-ray light curves

We include summary figures for the fits of the gamma-ray PSDs for the sources in the cross-correlation sample. Each figure is made out of 4 panels described below:

Upper left Gamma-ray light curve. Flux units are 10^{-6} ph cm^{-2} s^{-1} integrated for energies between 100 MeV and 200 GeV.

Upper right The periodogram estimate in arbitrary units of power and 1/day for frequency. Periodogram for the light curve is represented by black dots joined by a solid black line.

The mean and dispersion in the PSD of simulated light curves for the best fit value of β are represented by the black dots with error bars. The best fit value is indicated in the caption.

Lower left Lower left is the p-value for each value of β tested in the model PSD ($\propto \nu^{-\beta}$). A high p-value indicates a model consistent with the observed periodogram. The best fit is the maximum and is indicated in the caption.

Lower right Confidence belt and best fit value (solid black horizontal line). The lower and upper limits for β obtained are indicated in the caption. Vertical axis is for the simulated value of β and horizontal axis for the fitted one.

The 68 cases in which there is enough signal to run the procedure are included here. Only 29 sources have a well defined 68.3% constraint and 23 a well defined 82.6% constraint. For the details see Chapter 6.

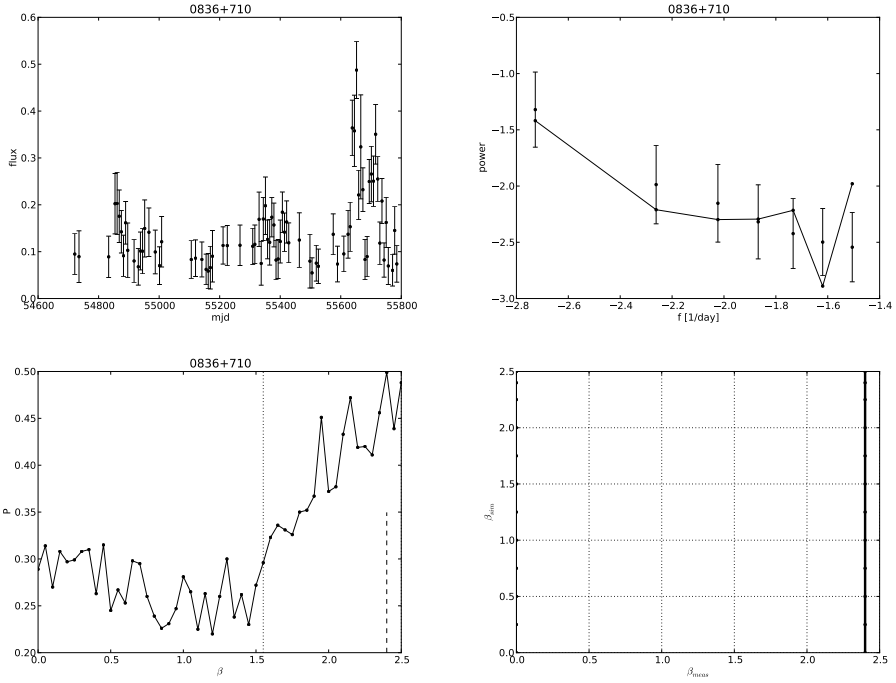

Figure E.82: PSD fit summary for 0836+710. The best fit is $\beta = 2.4$ with 1σ limits $\beta^{lower} = 0.0$ and an undetermined upper limit.

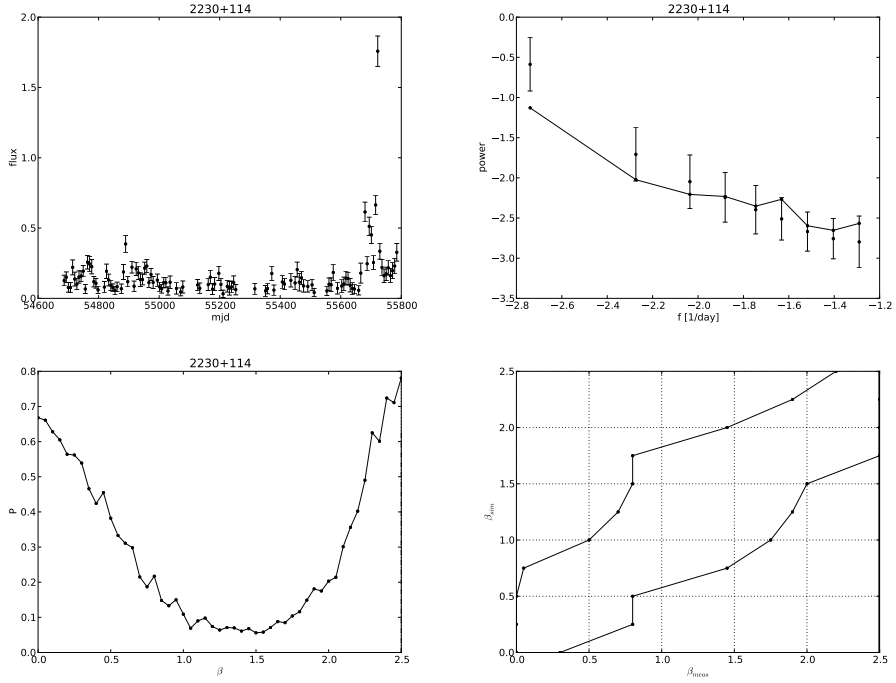

Figure E.83: PSD fit summary for 2230+114. The best fit is $\beta = 2.5$ with 1σ limits $\beta^{lower} = 1.8$ and an undetermined upper limit.

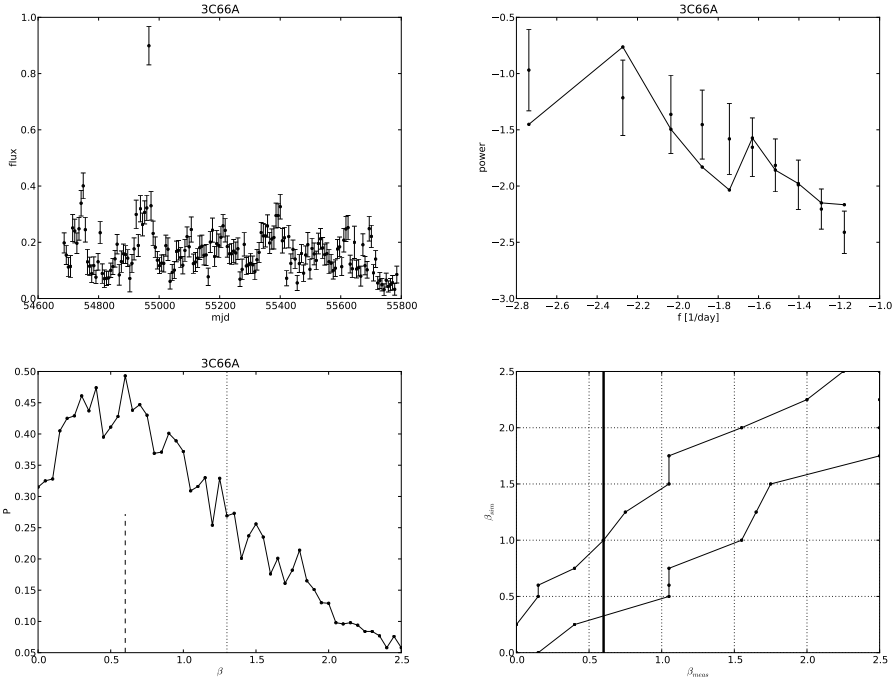

Figure E.84: PSD fit summary for 3C66A. The best fit is $\beta = 0.6$ with 1σ limits $\beta^{lower} = 0.3$ and $\beta^{upper} = 1.0$.

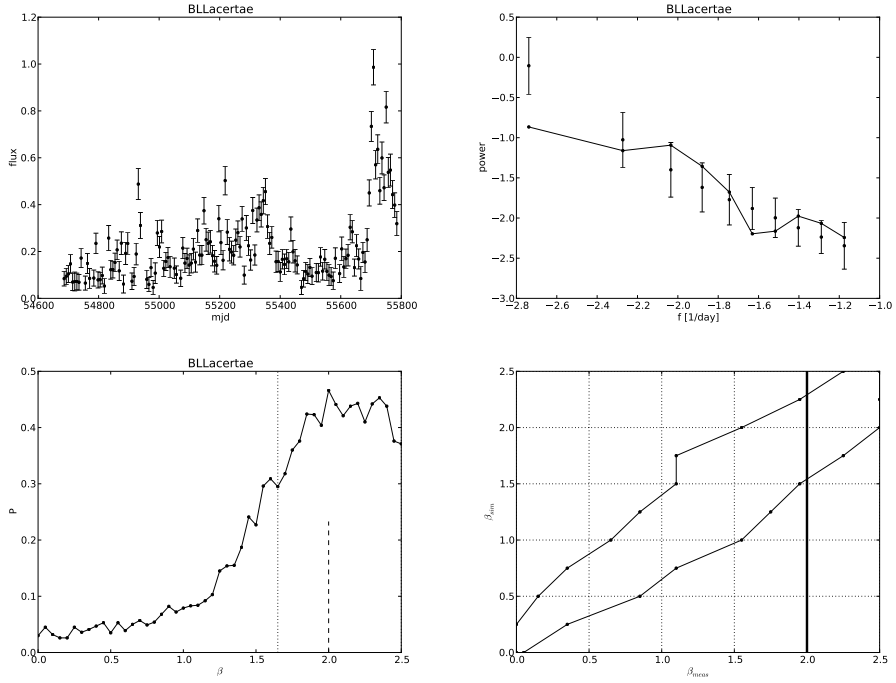

Figure E.85: PSD fit summary for BLLacertae. The best fit is $\beta = 2.0$ with 1σ limits $\beta^{lower} = 1.5$ and $\beta^{upper} = 2.3$.

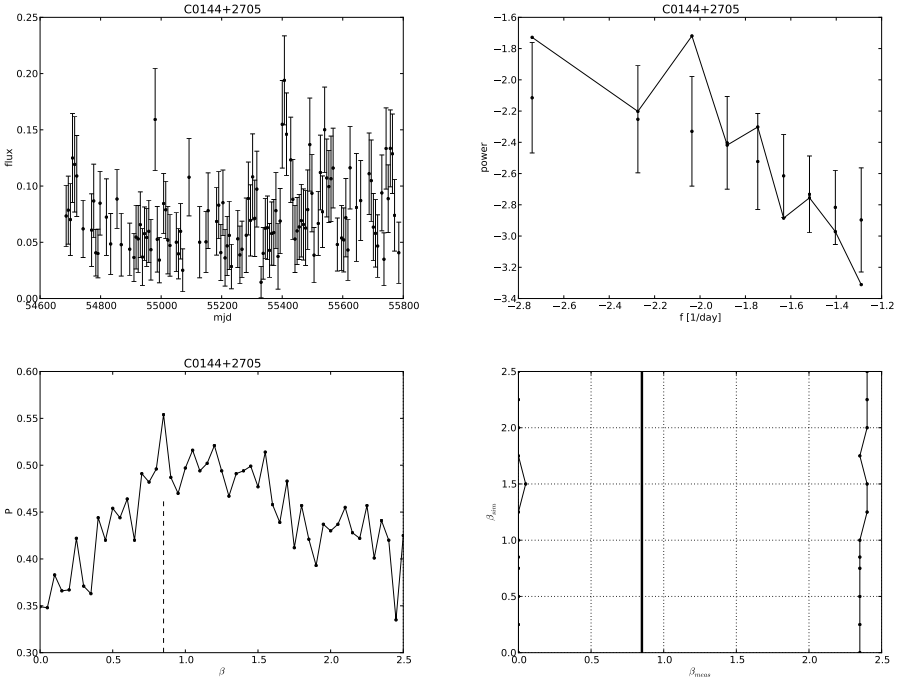

Figure E.86: PSD fit summary for C0144+2705. The best fit is $\beta = 0.8$ with 1σ limits $\beta^{lower} = 0.0$ and an undetermined upper limit.

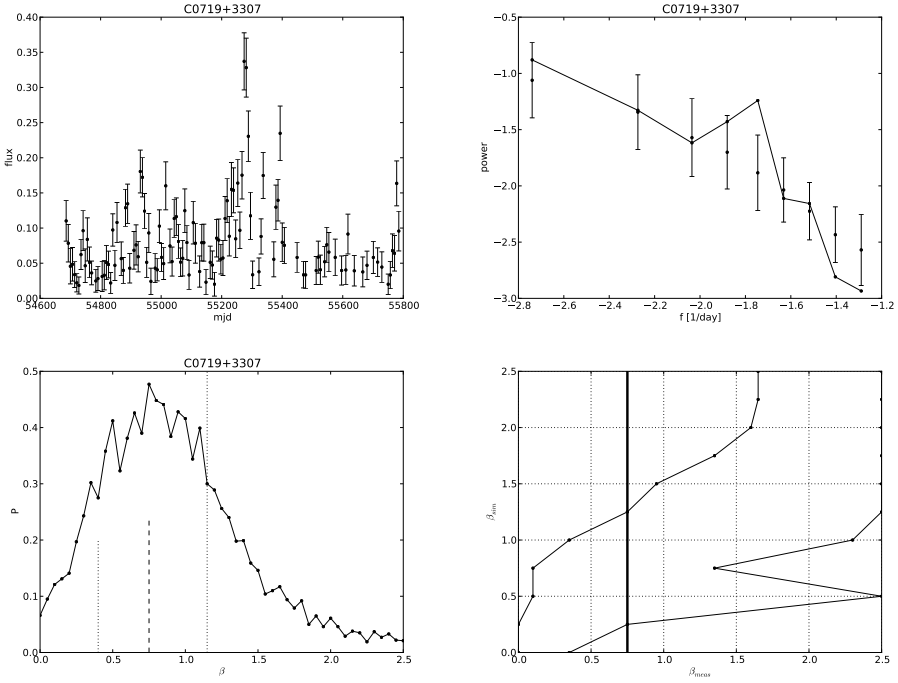

Figure E.87: PSD fit summary for C0719+3307. The best fit is $\beta = 0.8$ with 1σ limits $\beta^{lower} = 0.2$ and $\beta^{upper} = 1.2$.

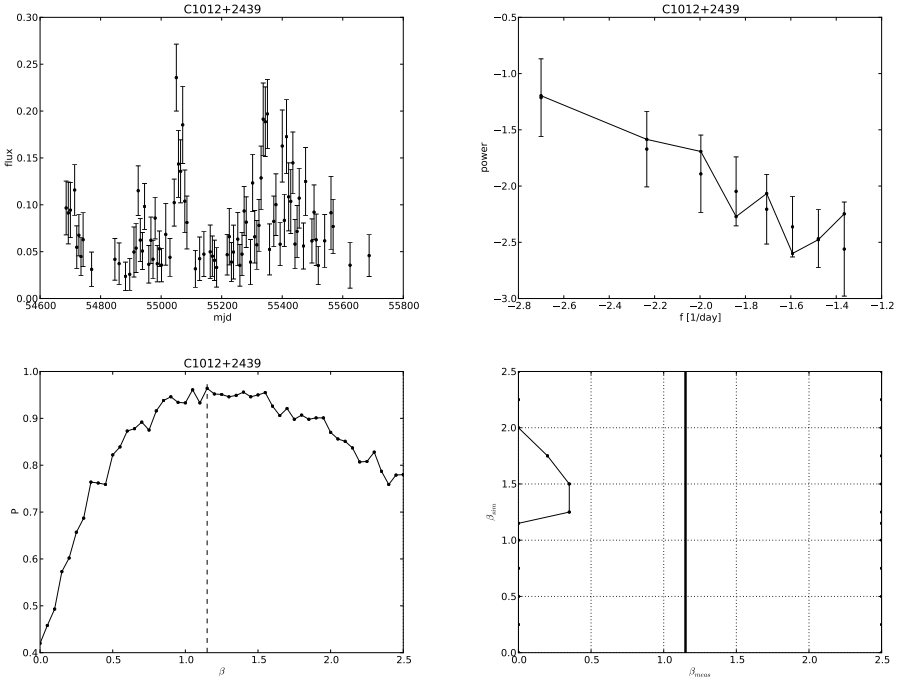

Figure E.88: PSD fit summary for C1012+2439. The best fit is $\beta = 1.1$ with 1σ limits $\beta^{lower} = 0.0$ and an undetermined upper limit.

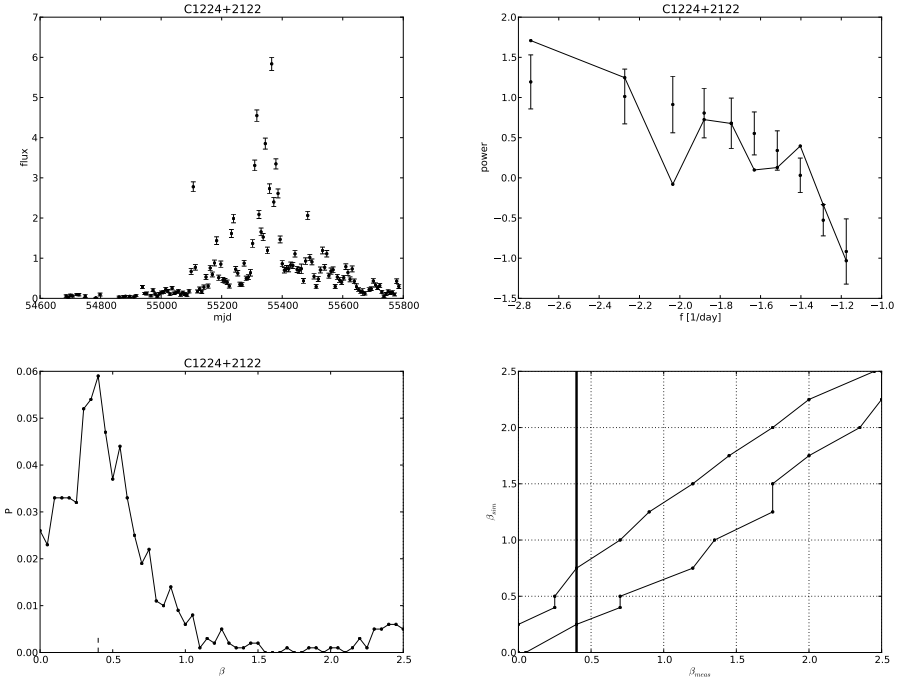

Figure E.89: PSD fit summary for C1224+2122. The best fit is $\beta = 0.4$ with 1σ limits $\beta^{lower} = 0.2$ and $\beta^{upper} = 0.8$.

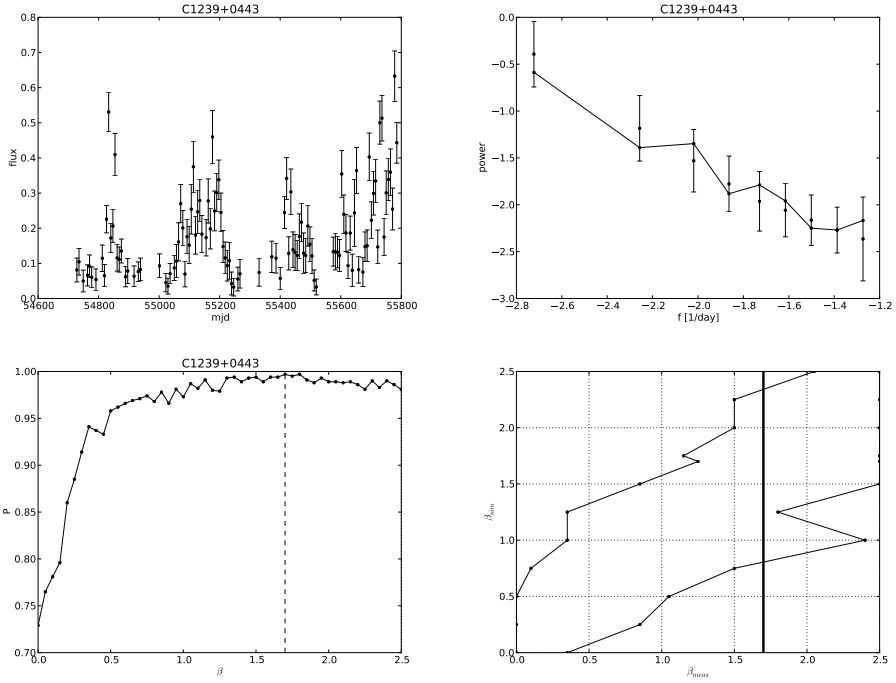

Figure E.90: PSD fit summary for C1239+0443. The best fit is $\beta = 1.7$ with 1σ limits $\beta^{lower} = 0.8$ and $\beta^{upper} = 2.3$.

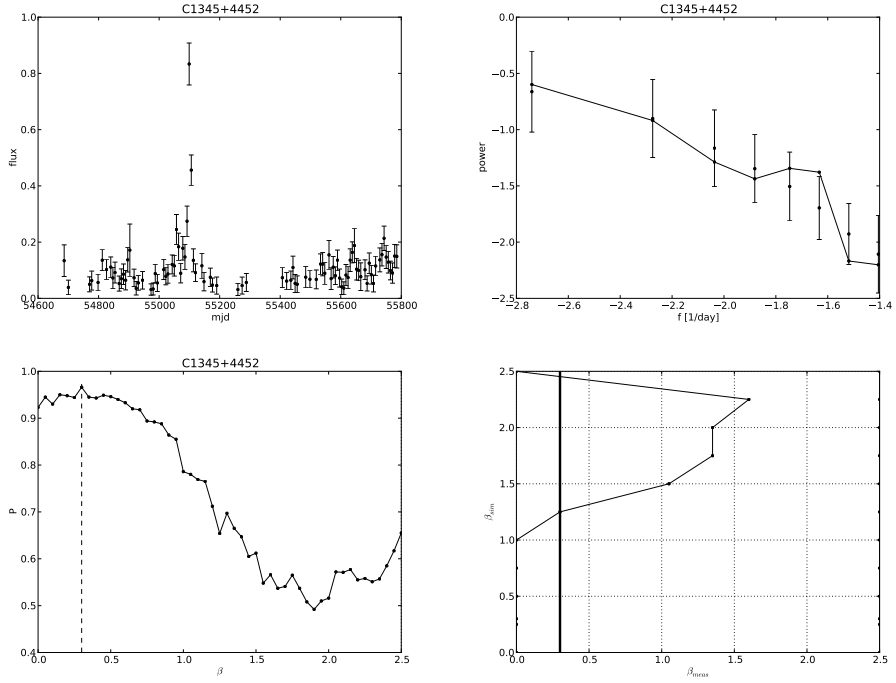

Figure E.91: PSD fit summary for C1345+4452. The best fit is $\beta = 0.3$ with 1σ limits $\beta^{lower} = 0.0$ and an undetermined upper limit.

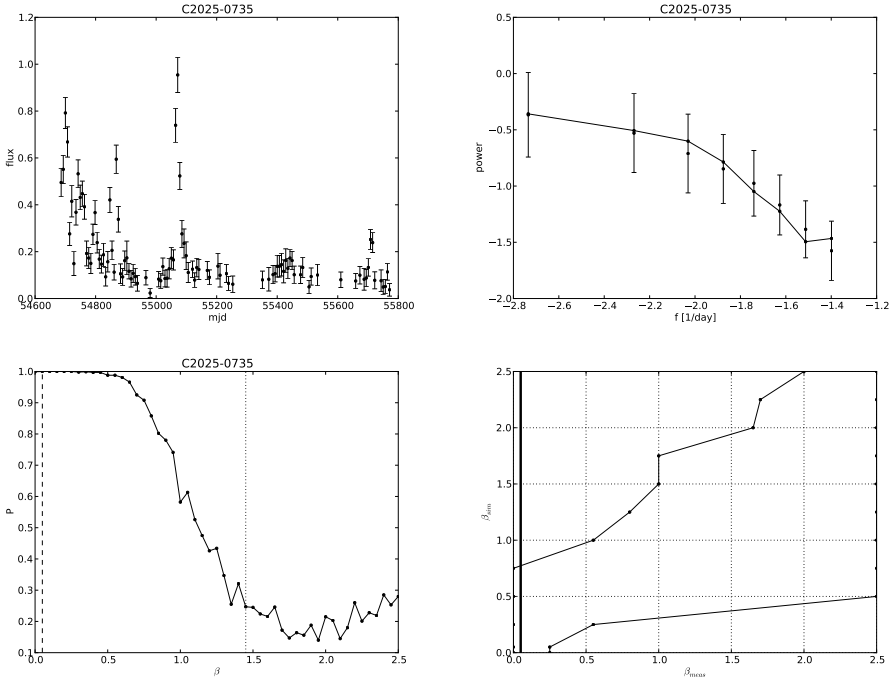

Figure E.92: PSD fit summary for C2025-0735. The best fit is $\beta = 0.1$ with 1σ limits $\beta^{lower} = 0.0$ and $\beta^{upper} = 0.8$.

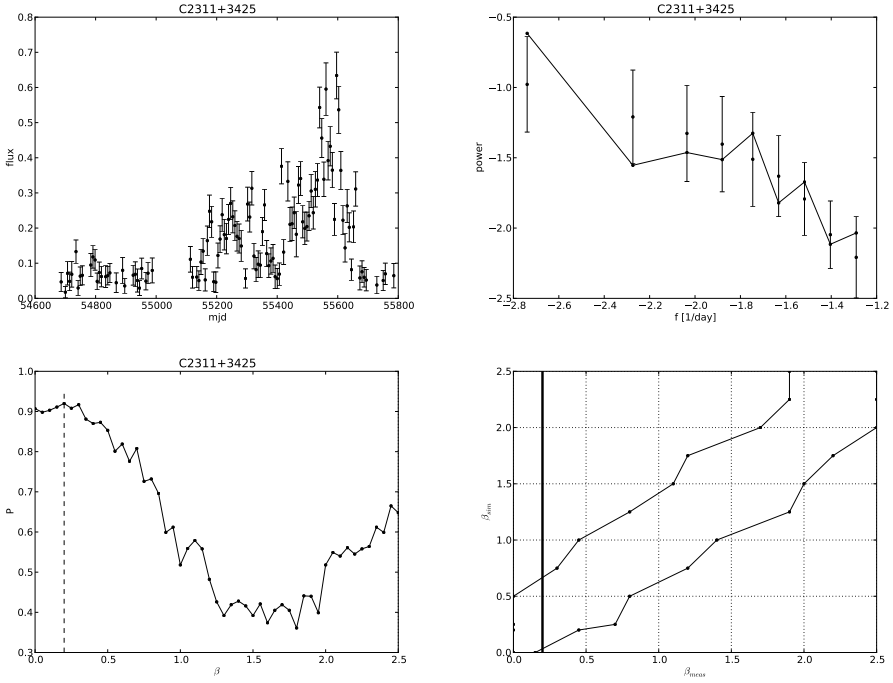

Figure E.93: PSD fit summary for C2311+3425. The best fit is $\beta = 0.2$ with 1σ limits $\beta^{lower} = 0.0$ and $\beta^{upper} = 0.7$.

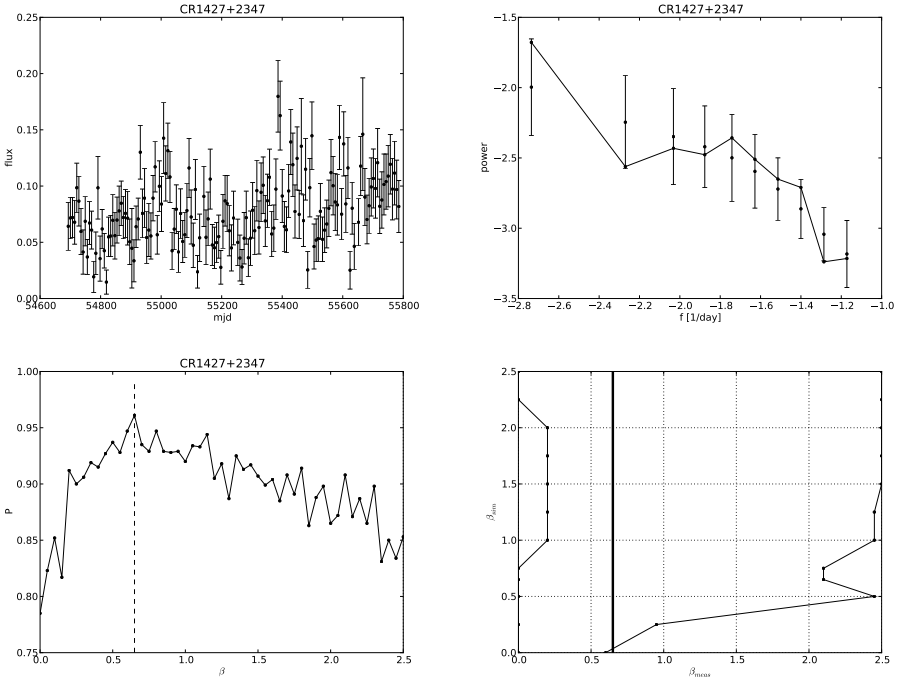

Figure E.94: PSD fit summary for CR1427+2347. The best fit is $\beta = 0.7$ with 1σ limits $\beta^{lower} = 0.0$ and an undetermined upper limit.

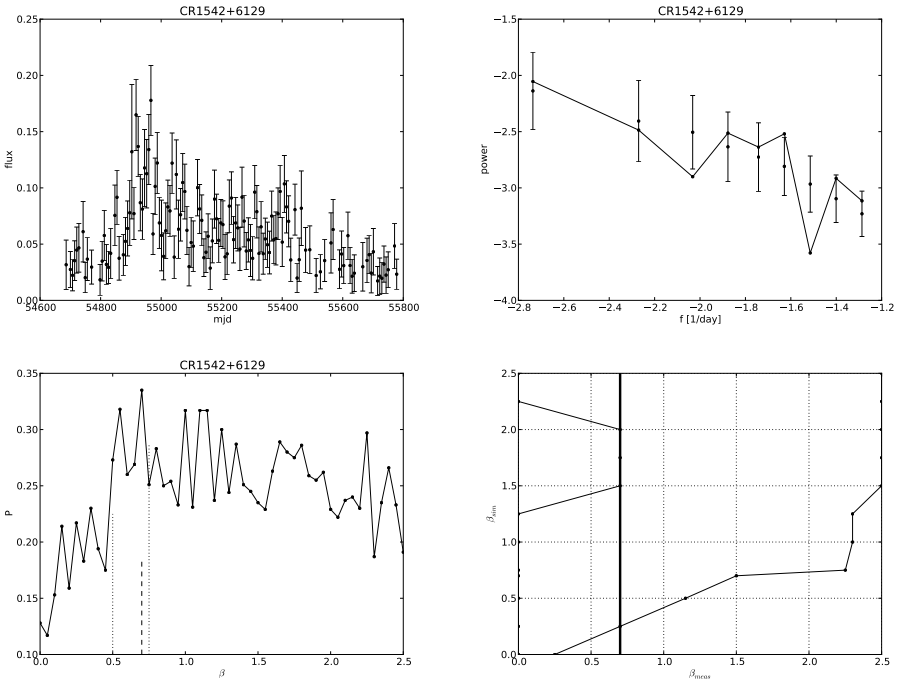

Figure E.95: PSD fit summary for CR1542+6129. The best fit is $\beta = 0.7$ with 1σ limits $\beta^{lower} = 0.2$ and an undetermined upper limit.

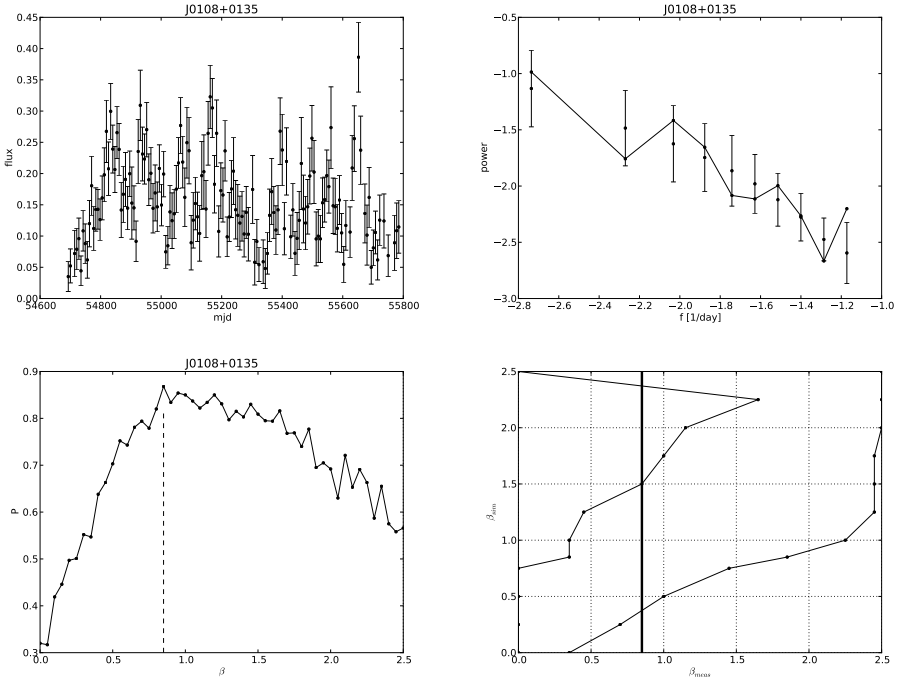

Figure E.96: PSD fit summary for J0108+0135. The best fit is $\beta = 0.8$ with 1σ limits $\beta^{lower} = 0.4$ and an undetermined upper limit.

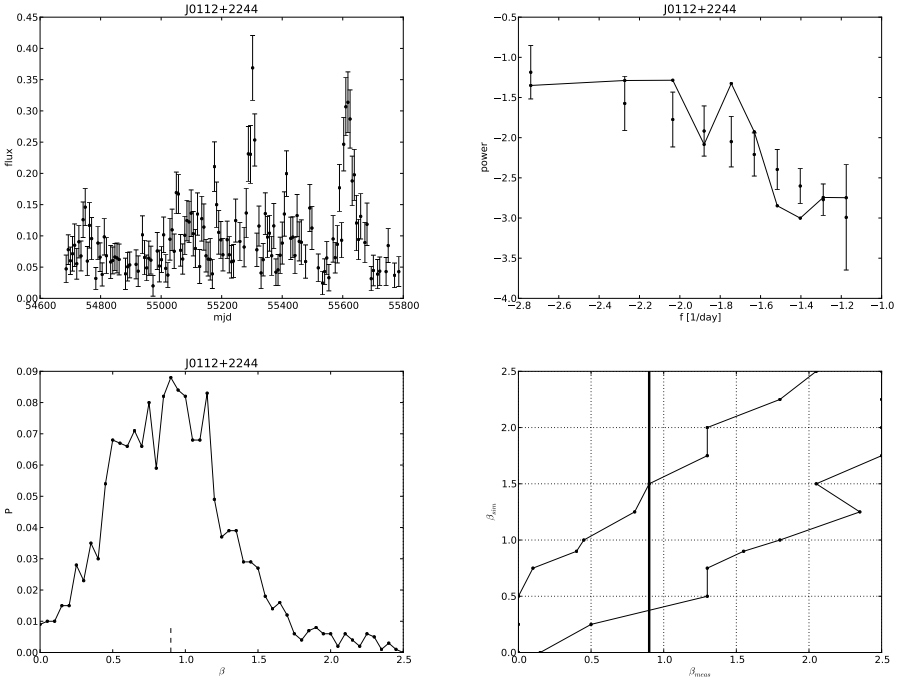

Figure E.97: PSD fit summary for J0112+2244. The best fit is $\beta = 0.9$ with 1σ limits $\beta^{lower} = 0.4$ and $\beta^{upper} = 1.5$.

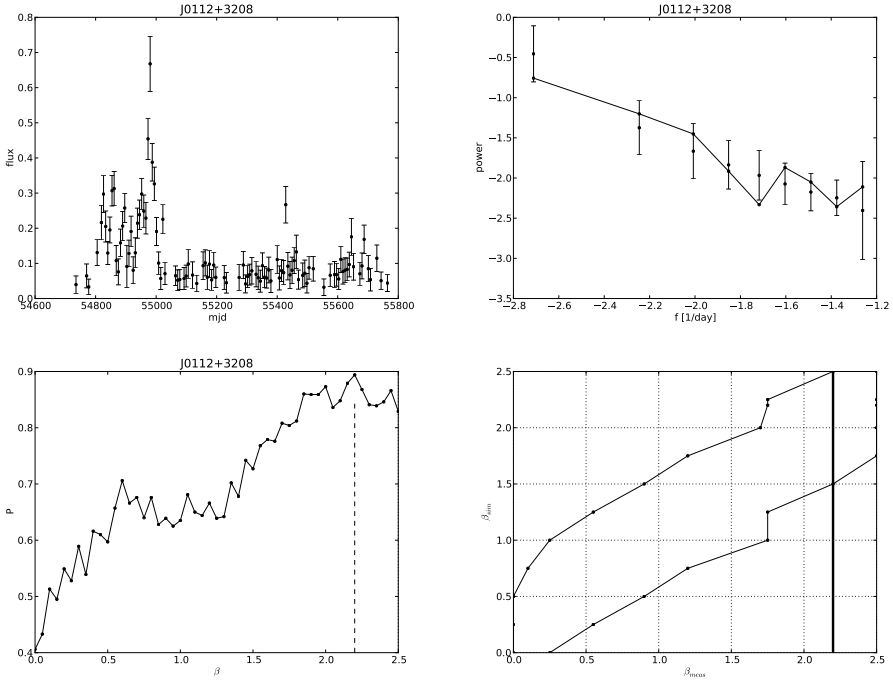

Figure E.98: PSD fit summary for J0112+3208. The best fit is $\beta = 2.2$ with 1σ limits $\beta^{lower} = 1.5$ and an undetermined upper limit.

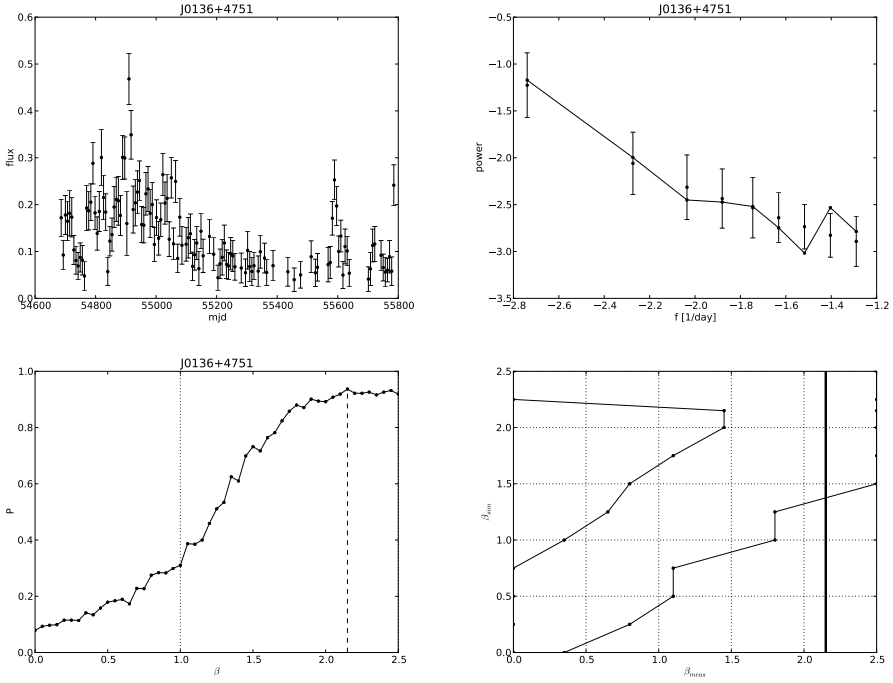

Figure E.99: PSD fit summary for J0136+4751. The best fit is $\beta = 2.1$ with 1σ limits $\beta^{lower} = 1.4$ and an undetermined upper limit.

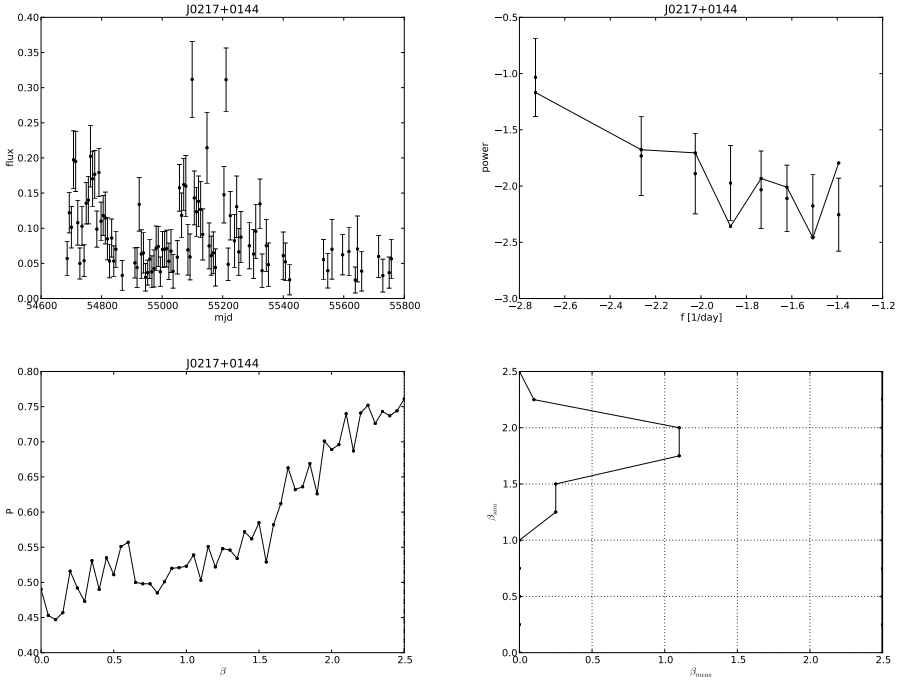

Figure E.100: PSD fit summary for J0217+0144. The best fit is $\beta = 2.5$ with 1σ limits $\beta^{lower} = 0.0$ and an undetermined upper limit.

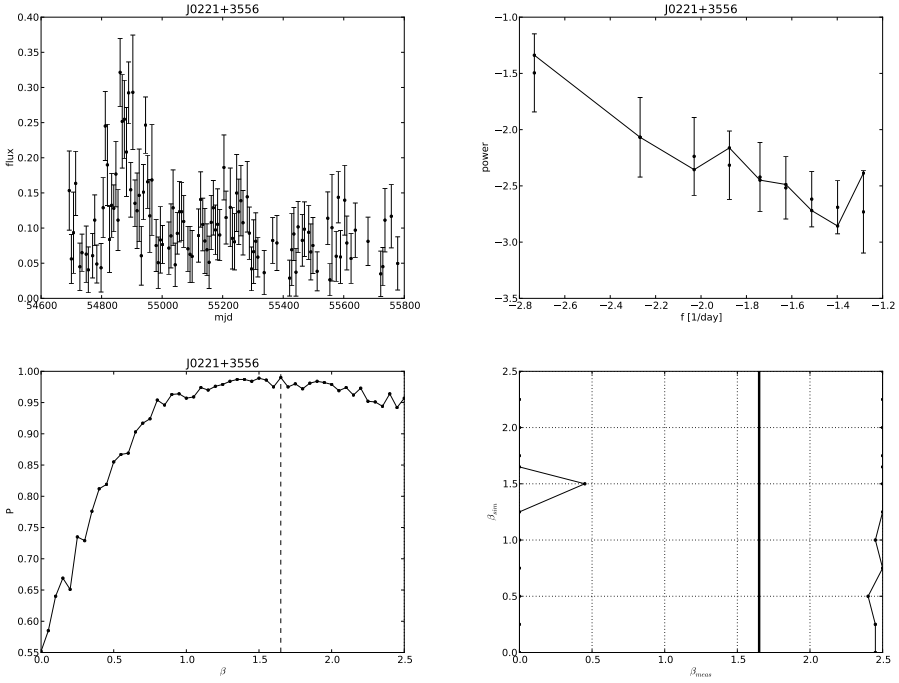

Figure E.101: PSD fit summary for J0221+3556. The best fit is $\beta = 1.6$ with 1σ limits $\beta^{lower} = 0.0$ and an undetermined upper limit.

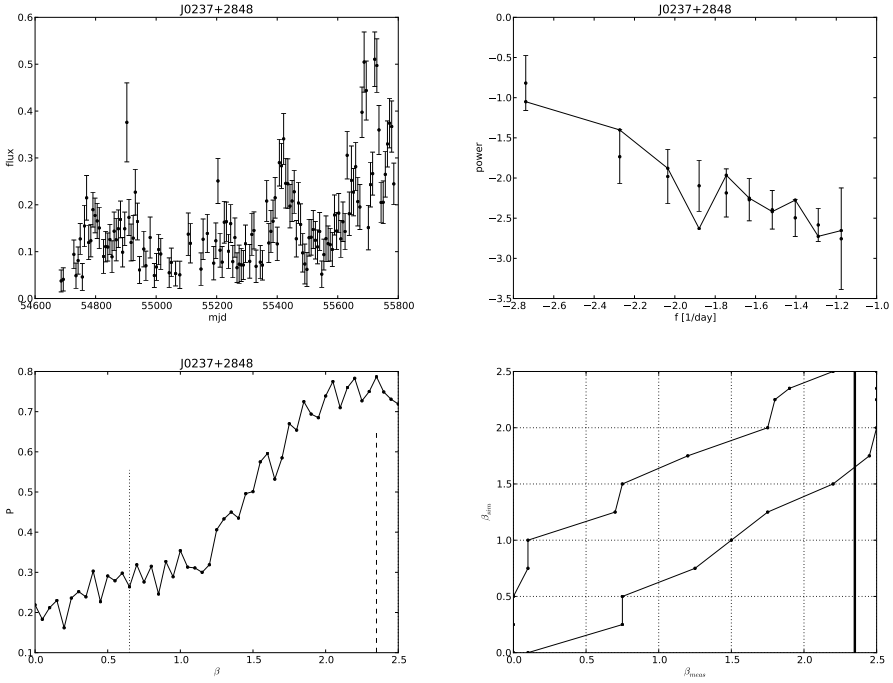

Figure E.102: PSD fit summary for J0237+2848. The best fit is $\beta = 2.4$ with 1σ limits $\beta^{lower} = 1.6$ and an undetermined upper limit.

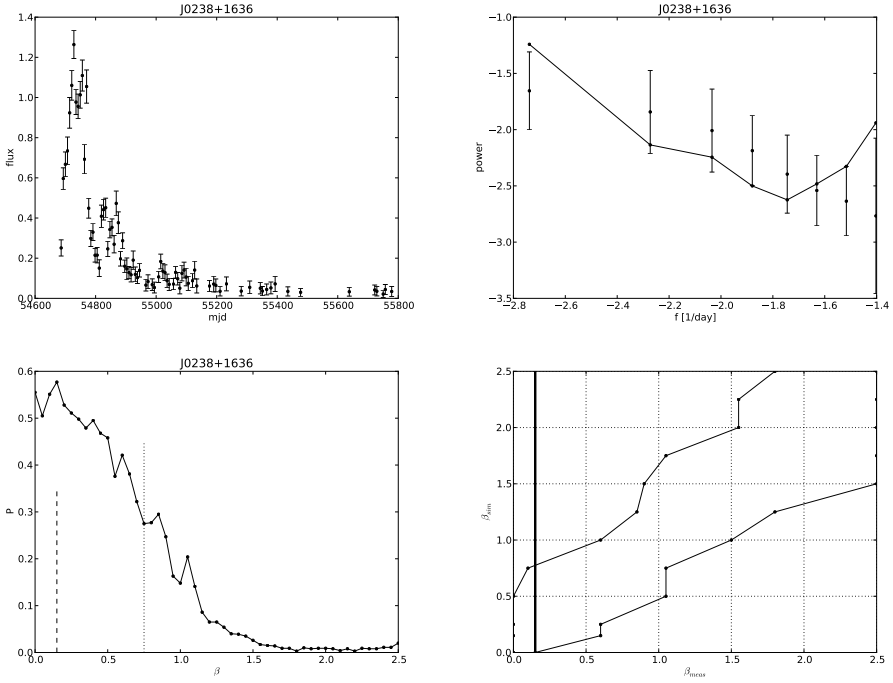

Figure E.103: PSD fit summary for J0238+1636. The best fit is $\beta = 0.1$ with 1σ limits $\beta^{lower} = 0.0$ and $\beta^{upper} = 0.8$.

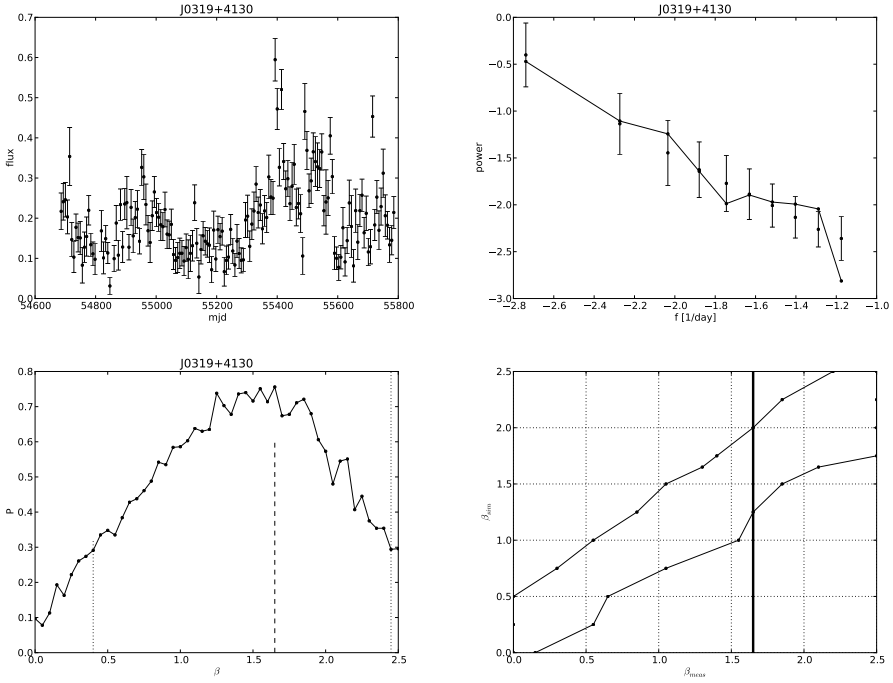

Figure E.104: PSD fit summary for J0319+4130. The best fit is $\beta = 1.6$ with 1σ limits $\beta^{lower} = 1.2$ and $\beta^{upper} = 2.0$.

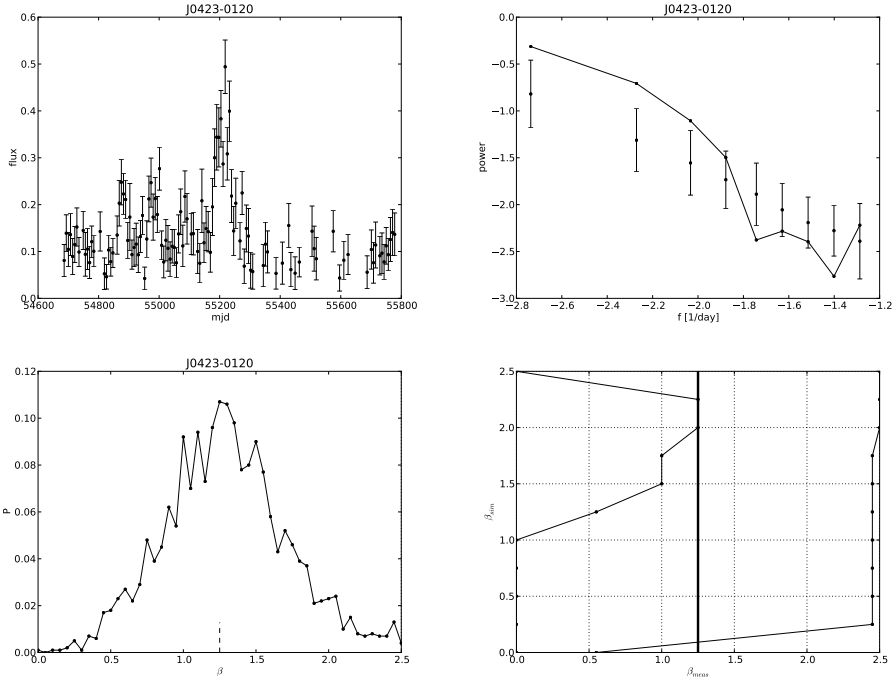

Figure E.105: PSD fit summary for J0423-0120. The best fit is $\beta = 1.2$ with 1σ limits $\beta^{lower} = 0.1$ and an undetermined upper limit.

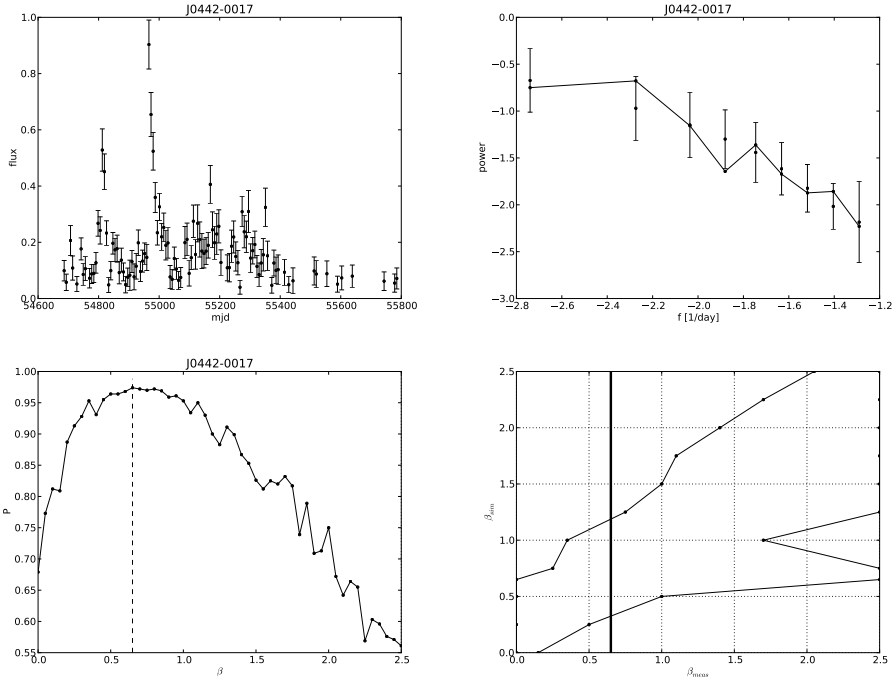

Figure E.106: PSD fit summary for J0442-0017. The best fit is $\beta = 0.7$ with 1σ limits $\beta^{lower} = 0.3$ and $\beta^{upper} = 1.2$.

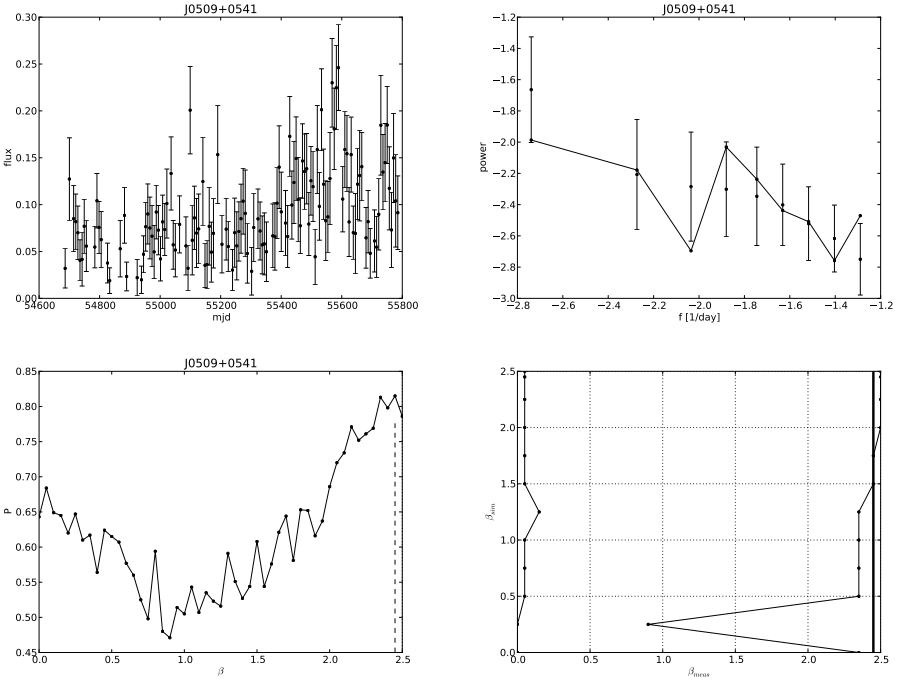

Figure E.107: PSD fit summary for J0509+0541. The best fit is $\beta = 2.5$ with 1σ limits $\beta^{lower} = 1.5$ and an undetermined upper limit.

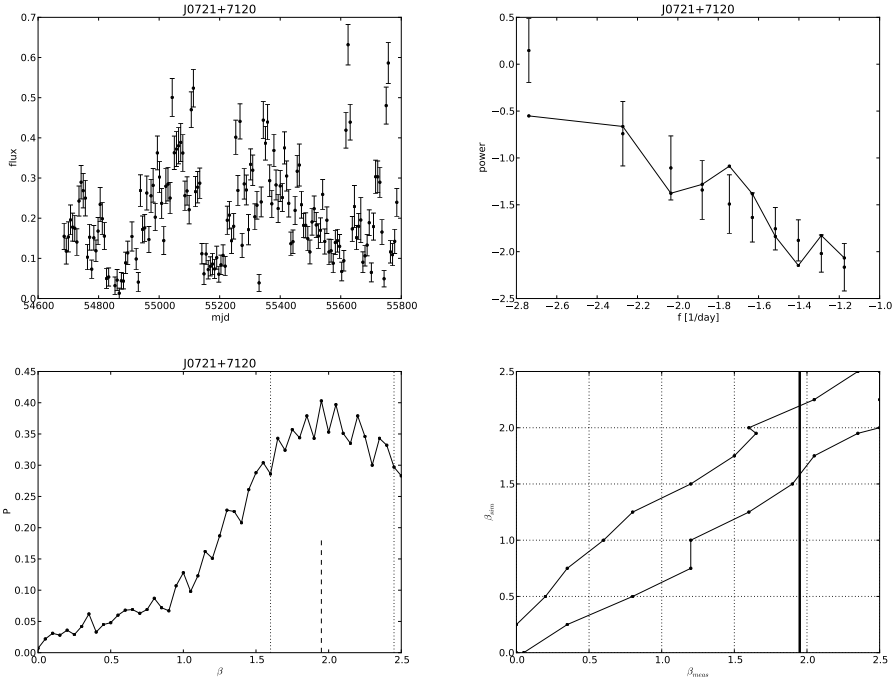

Figure E.108: PSD fit summary for J0721+7120. The best fit is $\beta = 1.9$ with 1σ limits $\beta^{lower} = 1.6$ and $\beta^{upper} = 2.2$.

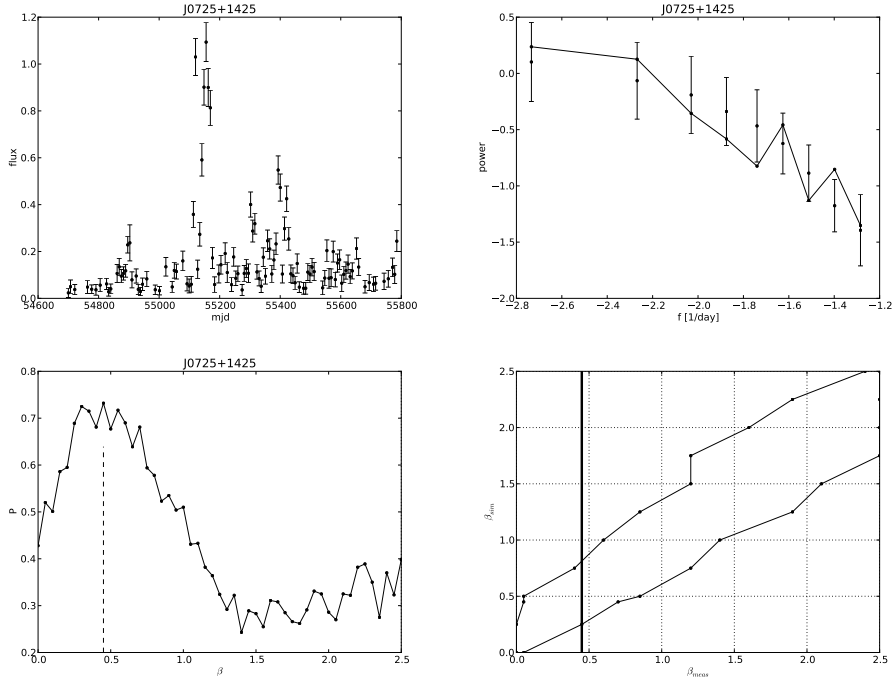

Figure E.109: PSD fit summary for J0725+1425. The best fit is $\beta = 0.5$ with 1σ limits $\beta^{lower} = 0.2$ and $\beta^{upper} = 0.8$.

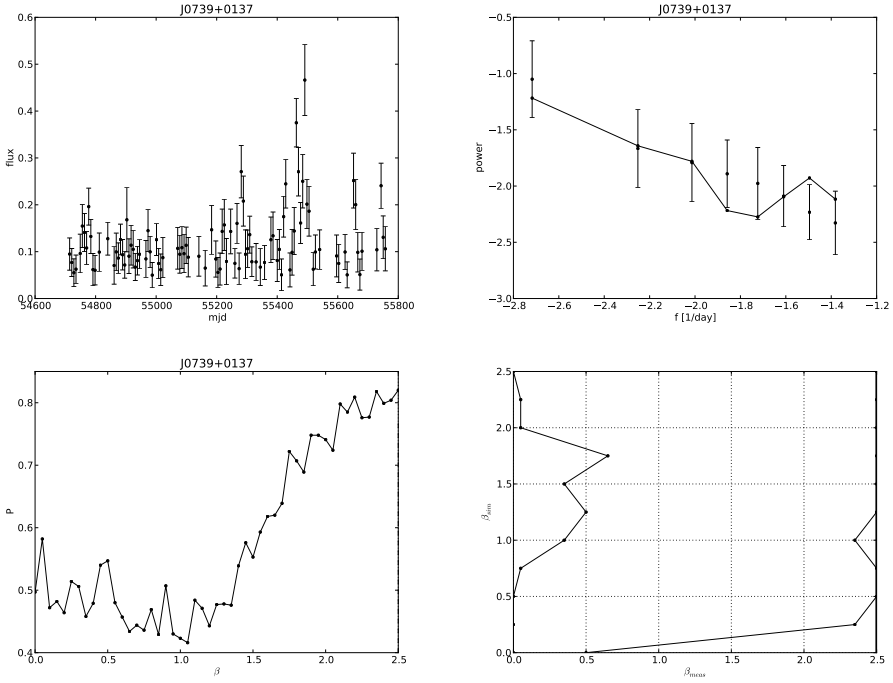

Figure E.110: PSD fit summary for J0739+0137. The best fit is $\beta = 2.5$ with 1σ limits $\beta^{lower} = 0.5$ and an undetermined upper limit.

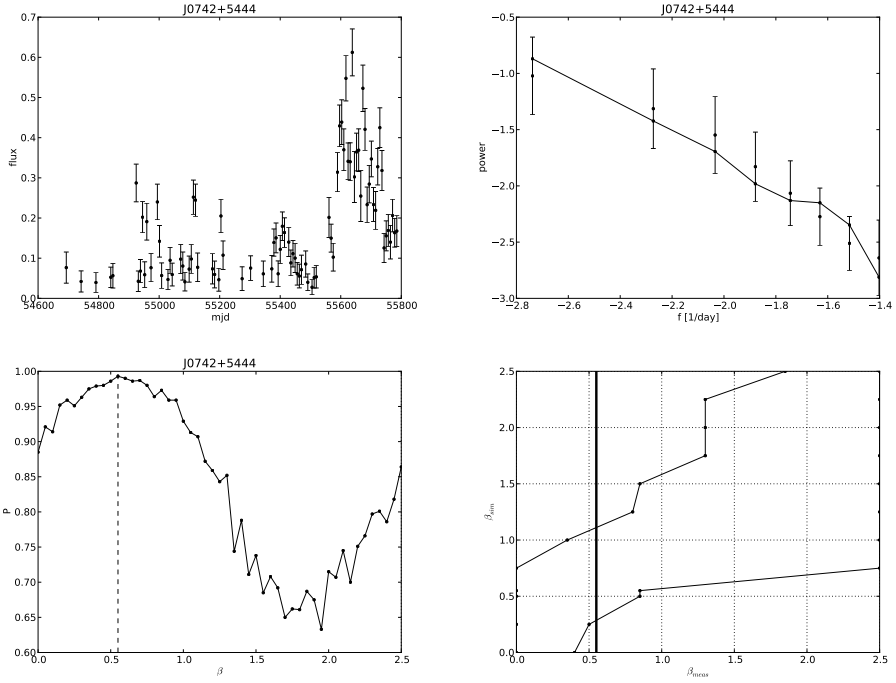

Figure E.111: PSD fit summary for J0742+5444. The best fit is $\beta = 0.6$ with 1σ limits $\beta^{lower} = 0.3$ and $\beta^{upper} = 1.1$.

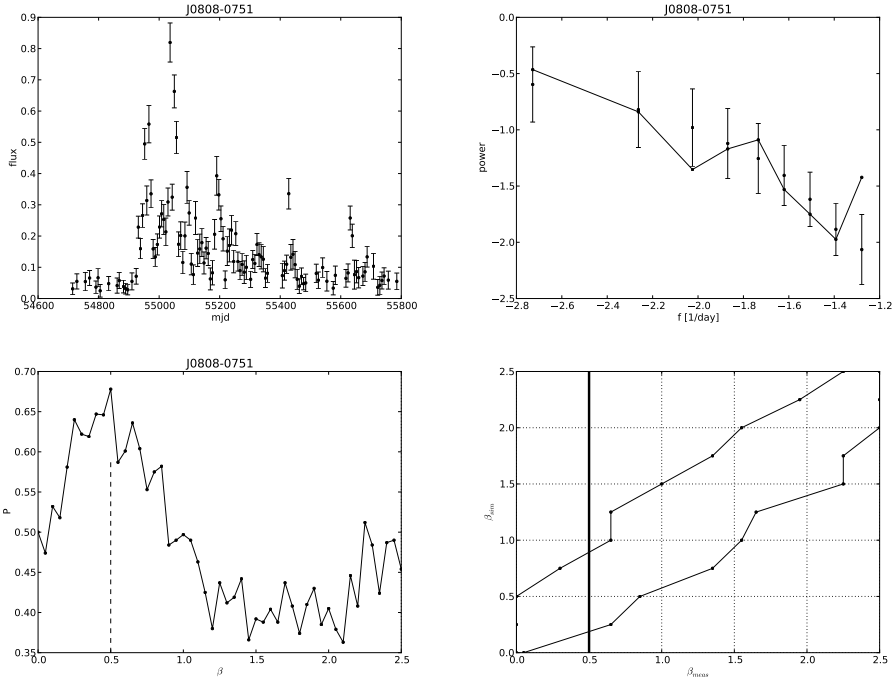

Figure E.112: PSD fit summary for J0808-0751. The best fit is $\beta = 0.5$ with 1σ limits $\beta^{lower} = 0.2$ and $\beta^{upper} = 0.9$.

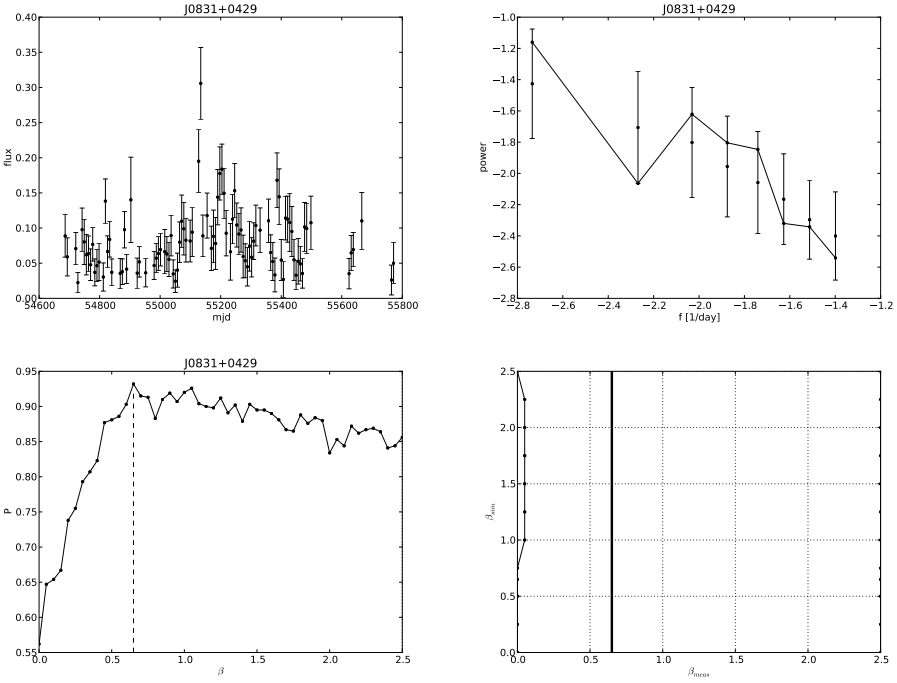

Figure E.113: PSD fit summary for J0831+0429. The best fit is $\beta = 0.7$ with 1σ limits $\beta^{lower} = 0.0$ and an undetermined upper limit.

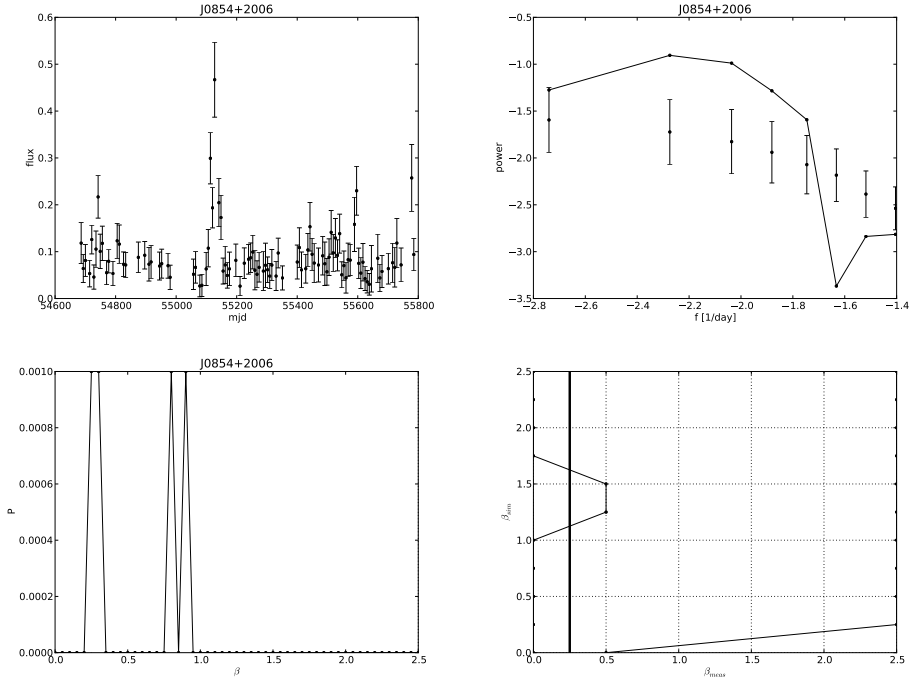

Figure E.114: PSD fit summary for J0854+2006. The best fit is $\beta = 0.2$ with 1σ limits $\beta^{lower} = 0.0$ and an undetermined upper limit.

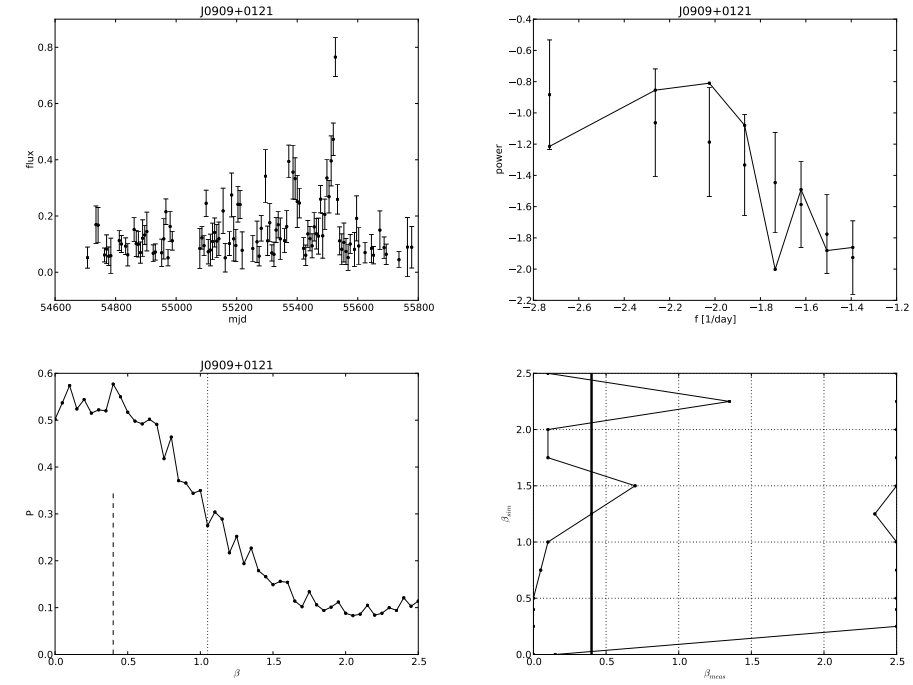

Figure E.115: PSD fit summary for J0909+0121. The best fit is $\beta = 0.4$ with 1σ limits $\beta^{lower} = 0.0$ and an undetermined upper limit.

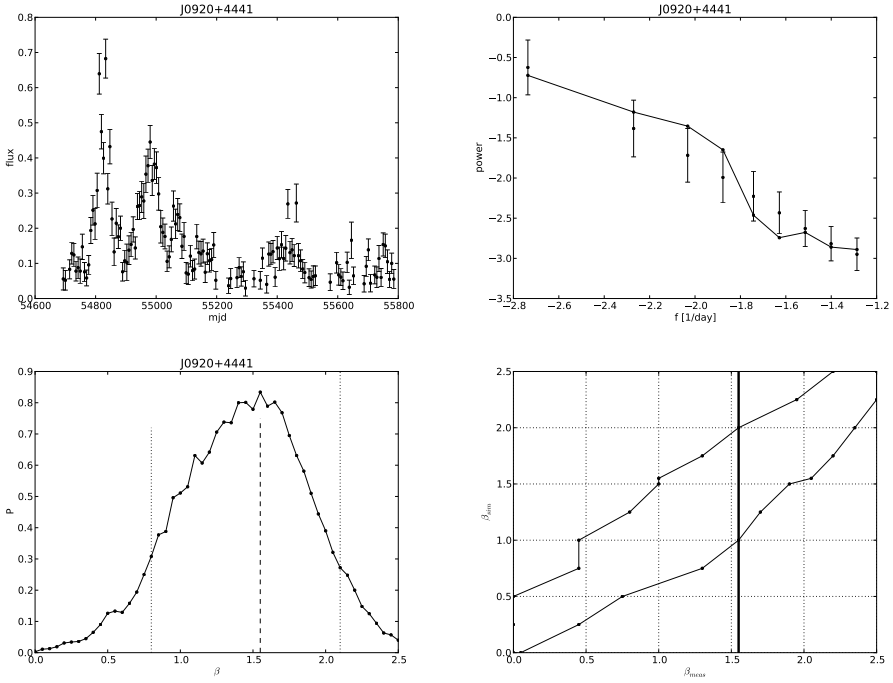

Figure E.116: PSD fit summary for J0920+4441. The best fit is $\beta = 1.6$ with 1σ limits $\beta^{lower} = 1.0$ and $\beta^{upper} = 2.0$.

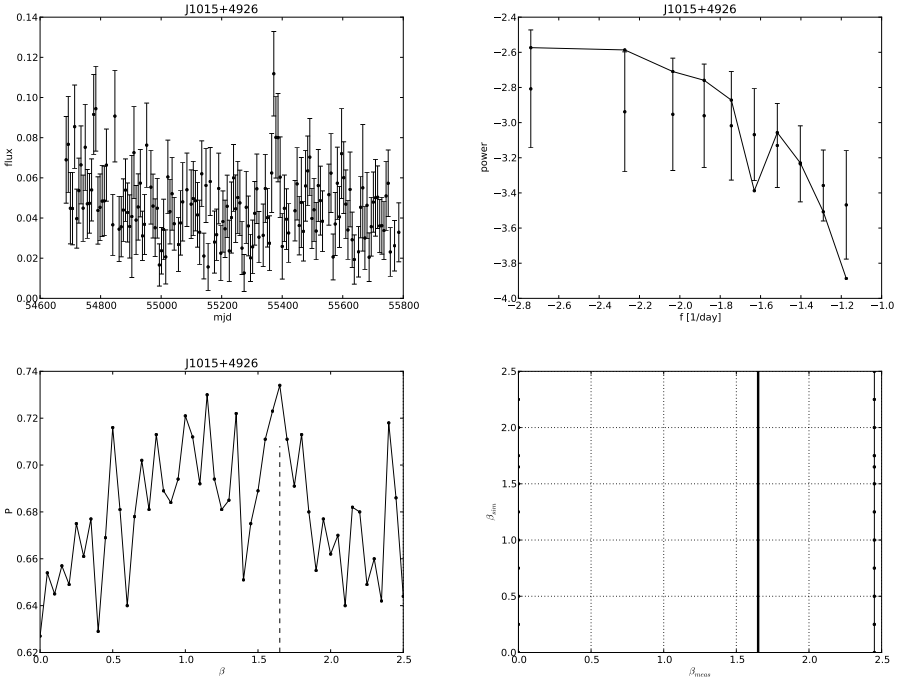

Figure E.117: PSD fit summary for J1015+4926. The best fit is $\beta = 1.6$ with 1σ limits $\beta^{lower} = 0.0$ and an undetermined upper limit.

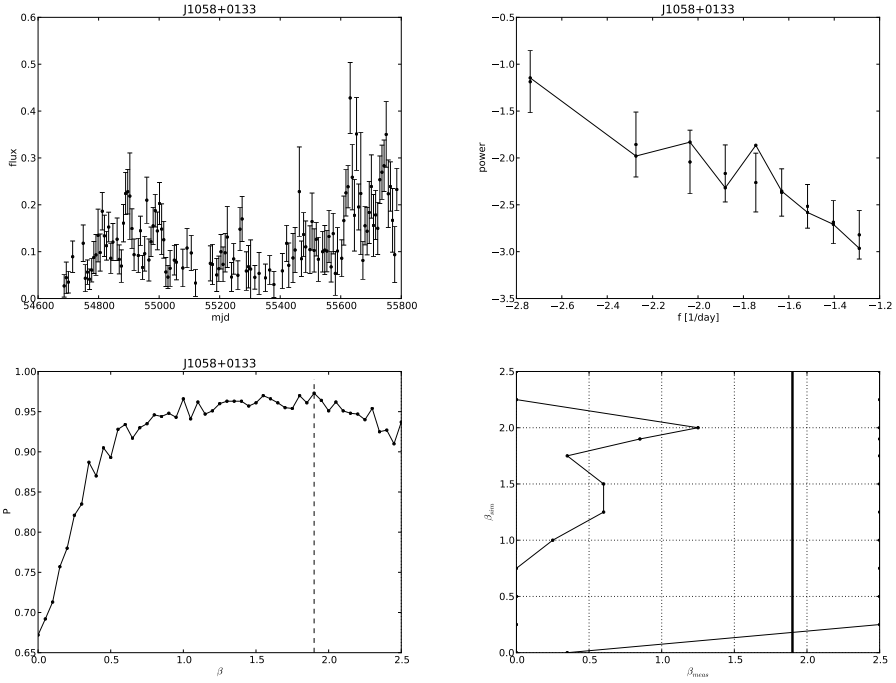

Figure E.118: PSD fit summary for J1058+0133. The best fit is $\beta = 1.9$ with 1σ limits $\beta^{lower} = 0.2$ and an undetermined upper limit.

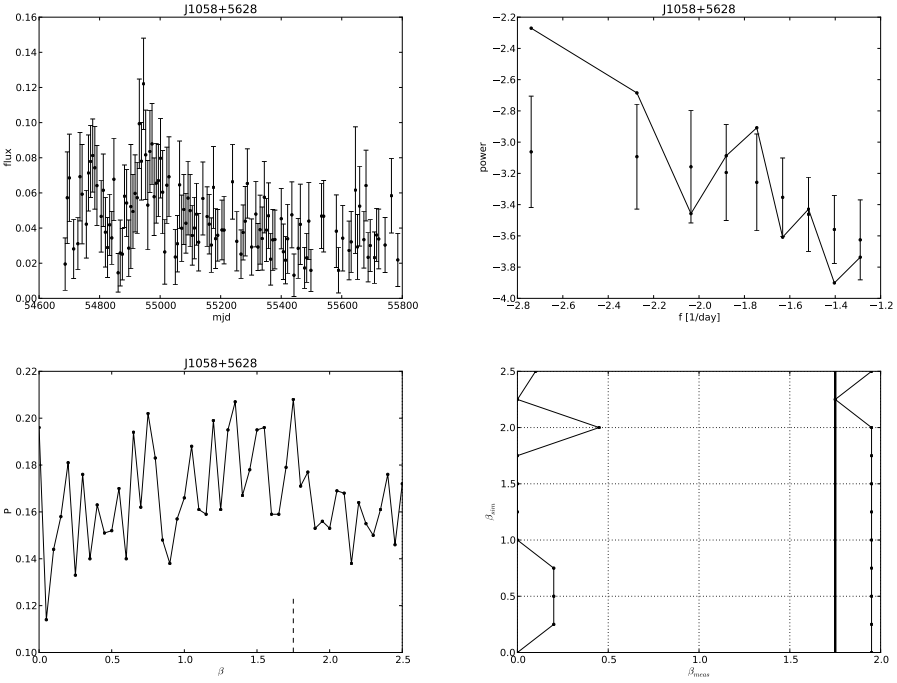

Figure E.119: PSD fit summary for J1058+5628. The best fit is $\beta = 1.8$ with 1σ limits $\beta^{lower} = 0.0$ and an undetermined upper limit.

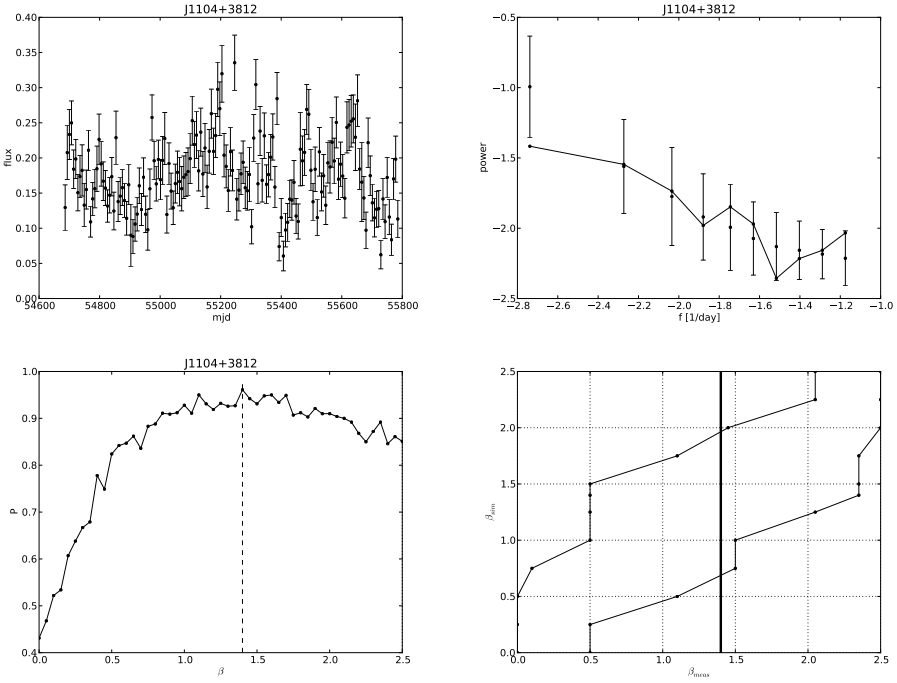

Figure E.120: PSD fit summary for J1104+3812. The best fit is $\beta = 1.4$ with 1σ limits $\beta^{lower} = 0.7$ and $\beta^{upper} = 2.0$.

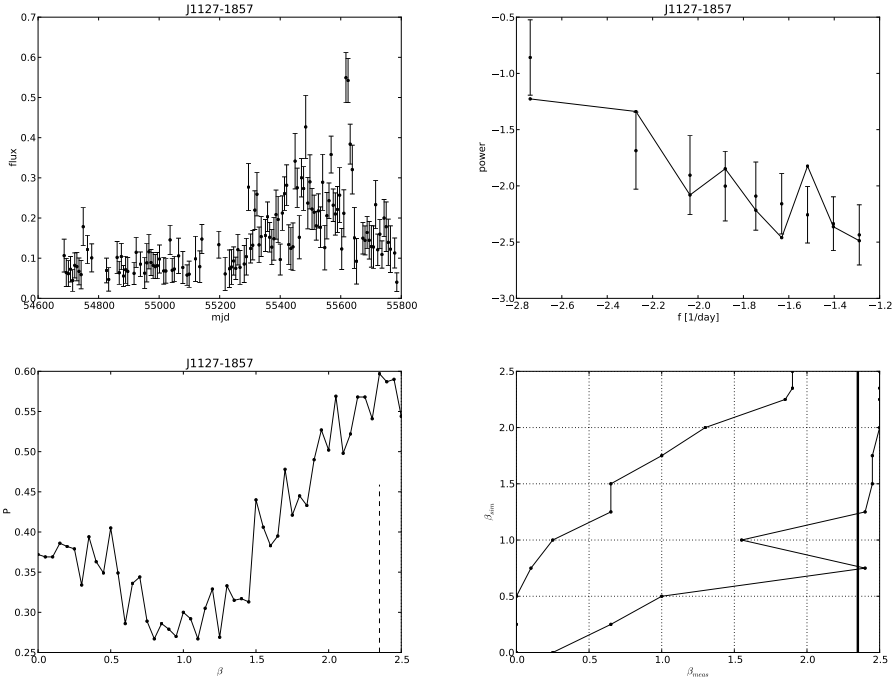

Figure E.121: PSD fit summary for J1127-1857. The best fit is $\beta = 2.4$ with 1σ limits $\beta^{lower} = 0.7$ and an undetermined upper limit.

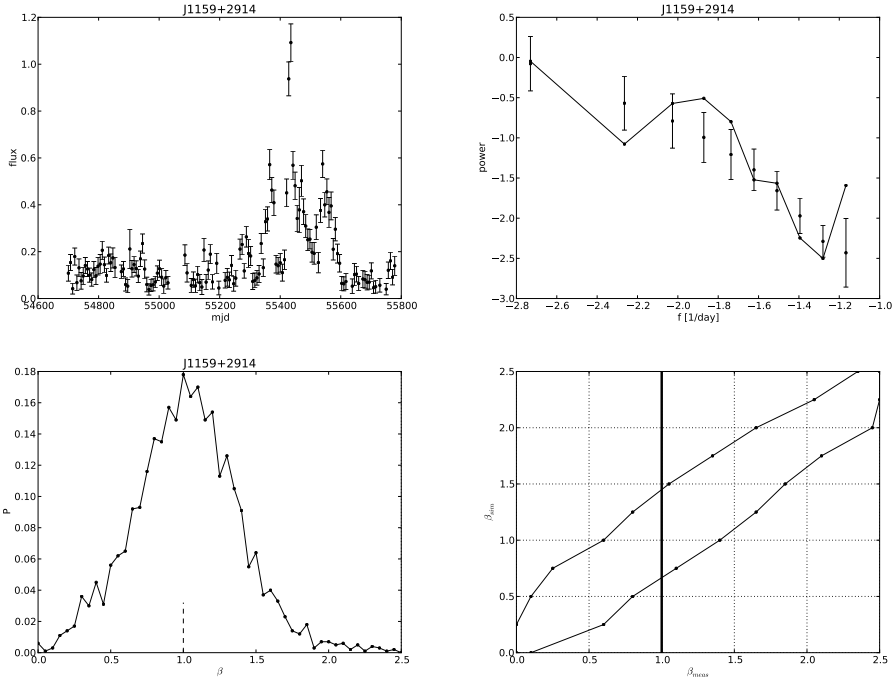

Figure E.122: PSD fit summary for J1159+2914. The best fit is $\beta = 1.0$ with 1σ limits $\beta^{lower} = 0.7$ and $\beta^{upper} = 1.4$.

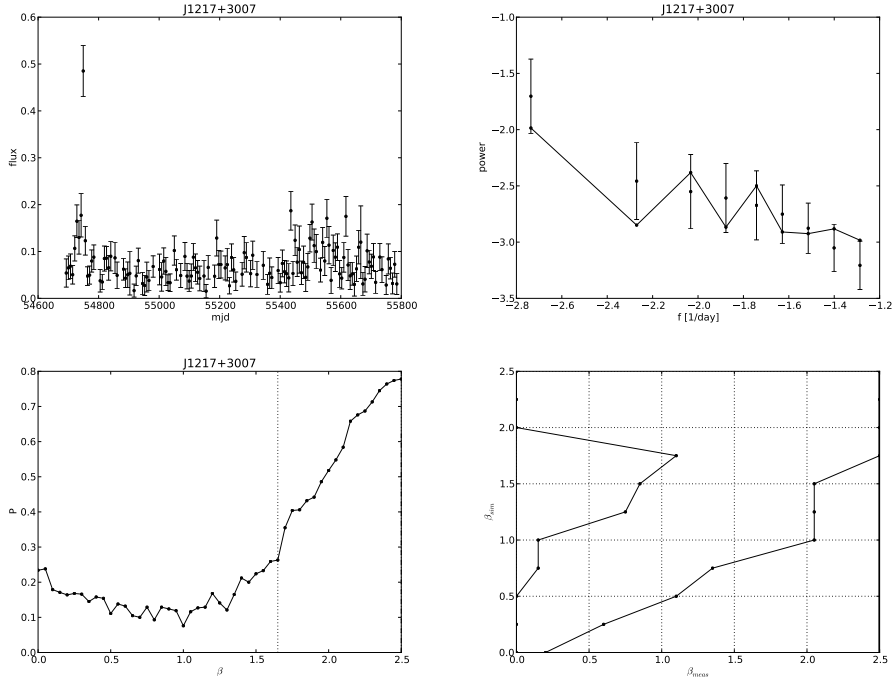

Figure E.123: PSD fit summary for J1217+3007. The best fit is $\beta = 2.5$ with 1σ limits $\beta^{lower} = 1.8$ and an undetermined upper limit.

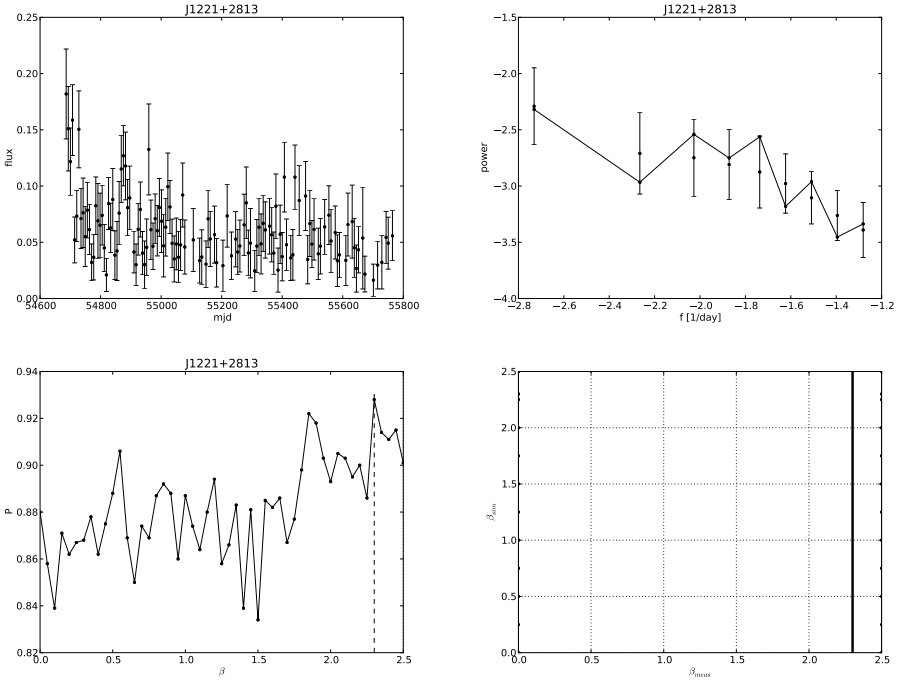

Figure E.124: PSD fit summary for J1221+2813. The best fit is $\beta = 2.3$ with 1σ limits $\beta^{lower} = 0.0$ and an undetermined upper limit.

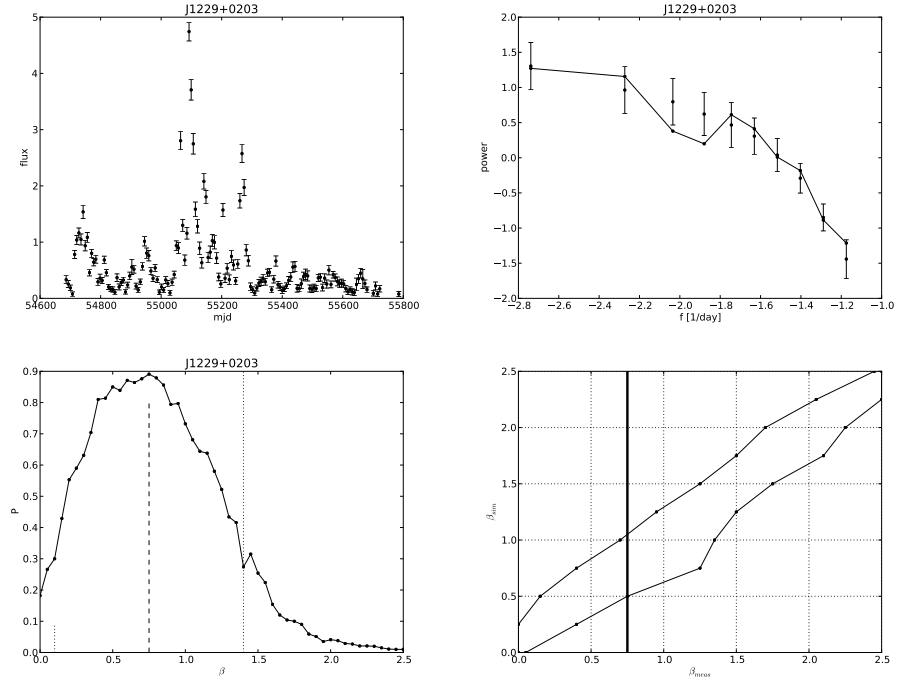

Figure E.125: PSD fit summary for J1229+0203. The best fit is $\beta = 0.8$ with 1σ limits $\beta^{lower} = 0.5$ and $\beta^{upper} = 1.0$.

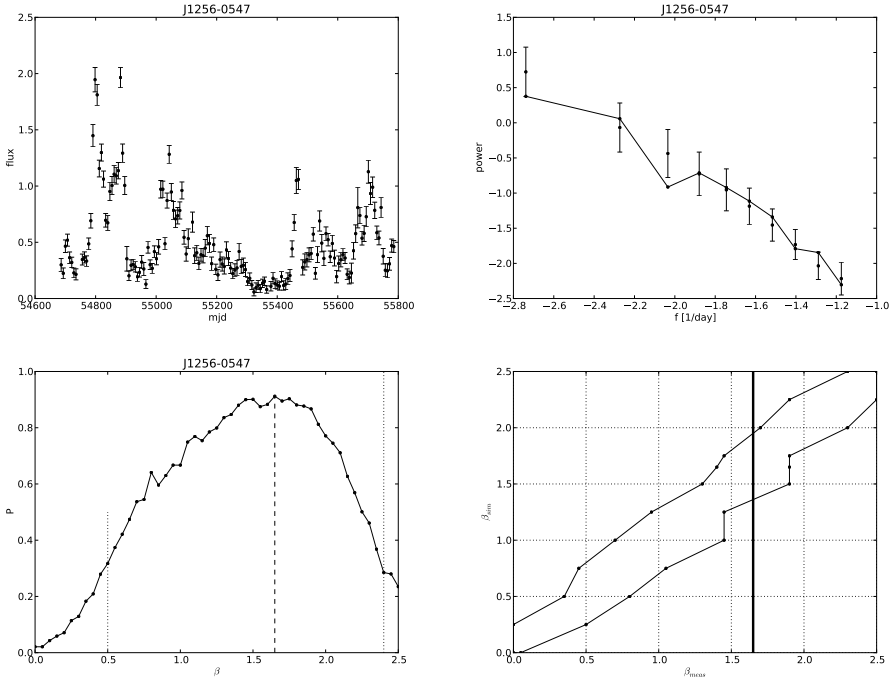

Figure E.126: PSD fit summary for J1256-0547. The best fit is $\beta = 1.6$ with 1σ limits $\beta^{lower} = 1.4$ and $\beta^{upper} = 1.9$.

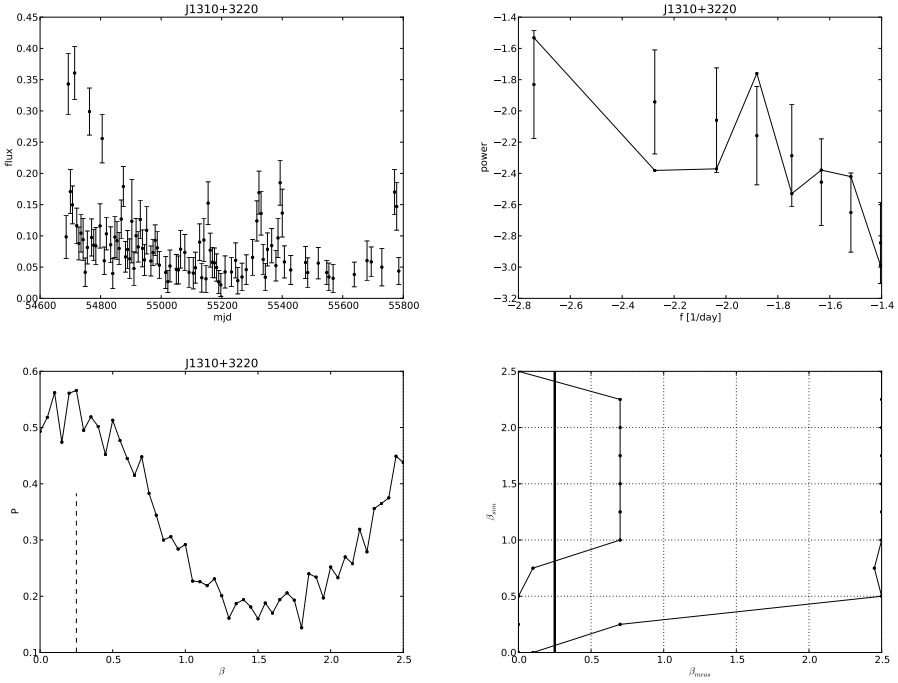

Figure E.127: PSD fit summary for J1310+3220. The best fit is $\beta = 0.2$ with 1σ limits $\beta^{lower} = 0.1$ and an undetermined upper limit.

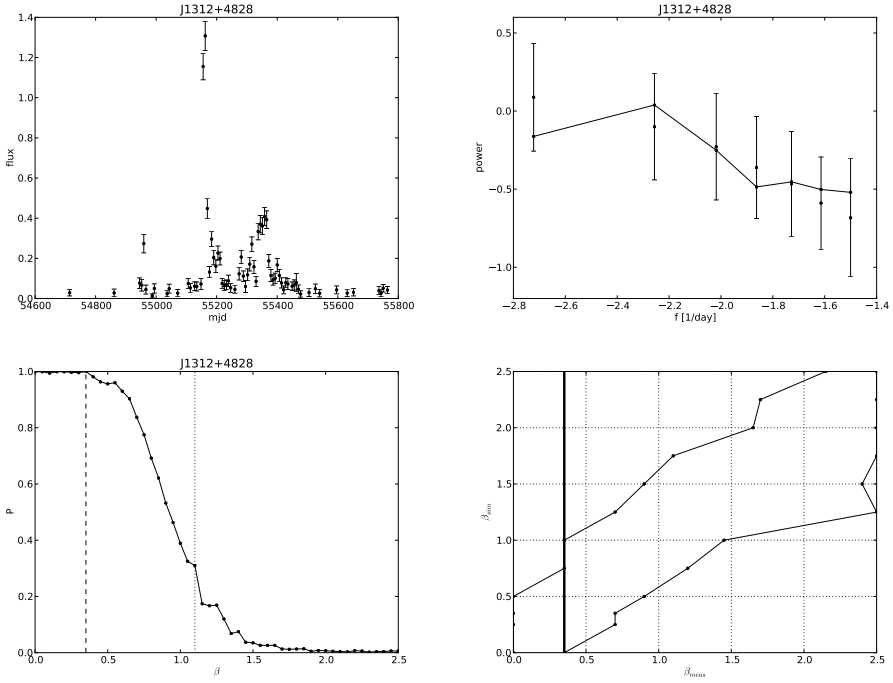

Figure E.128: PSD fit summary for J1312+4828. The best fit is $\beta = 0.3$ with 1σ limits $\beta^{lower} = 0.0$ and $\beta^{upper} = 1.0$.

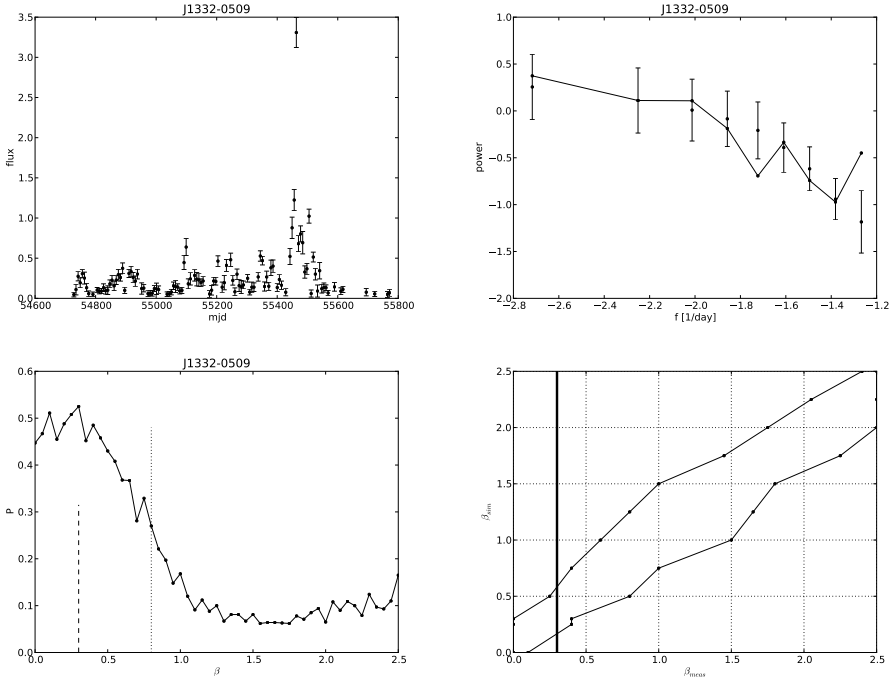

Figure E.129: PSD fit summary for J1332-0509. The best fit is $\beta = 0.3$ with 1σ limits $\beta^{lower} = 0.2$ and $\beta^{upper} = 0.6$.

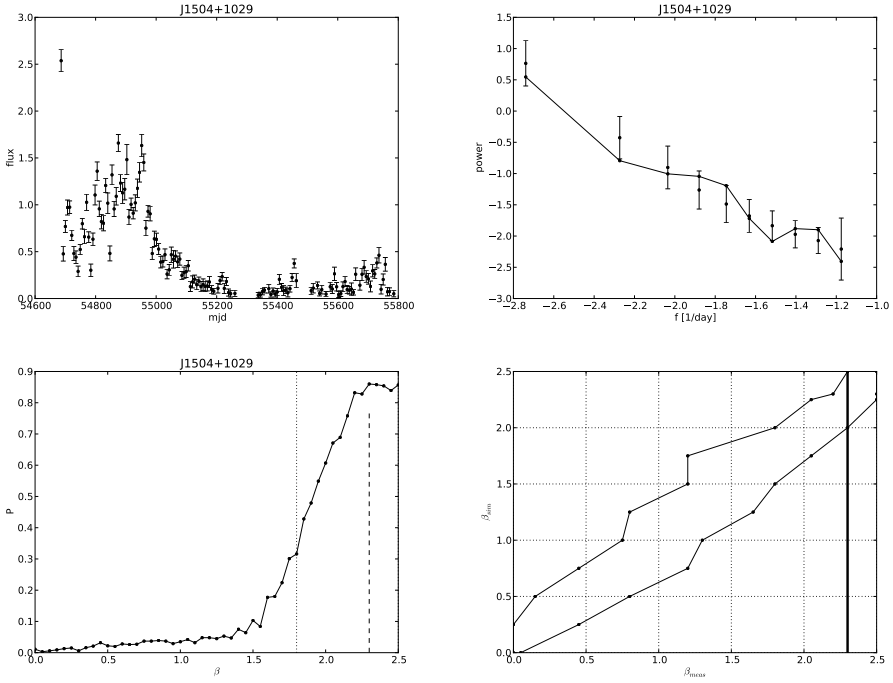

Figure E.130: PSD fit summary for J1504+1029. The best fit is $\beta = 2.3$ with 1σ limits $\beta^{lower} = 2.0$ and an undetermined upper limit.

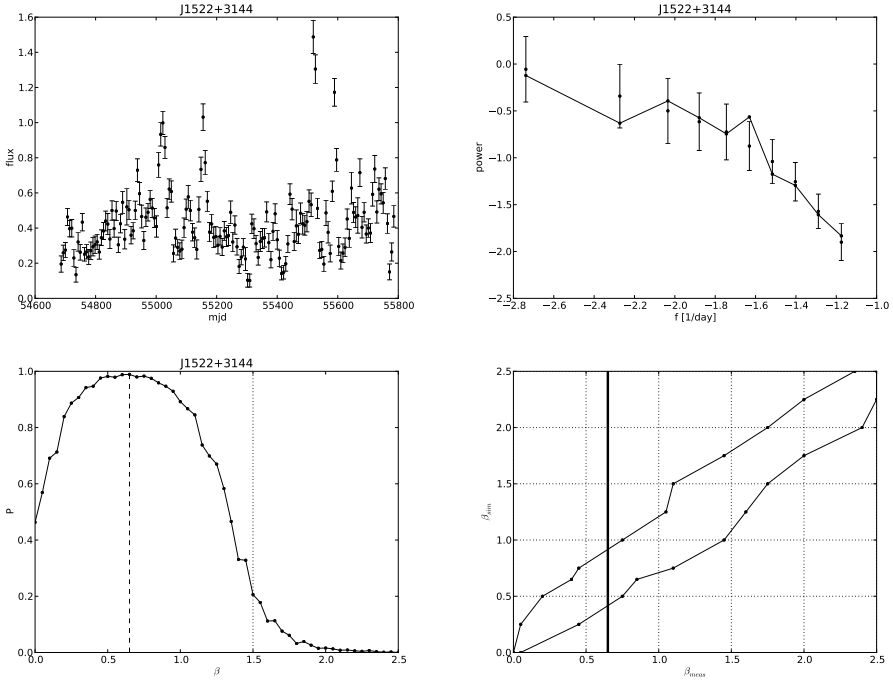

Figure E.131: PSD fit summary for J1522+3144. The best fit is $\beta = 0.7$ with 1σ limits $\beta^{lower} = 0.4$ and $\beta^{upper} = 0.9$.

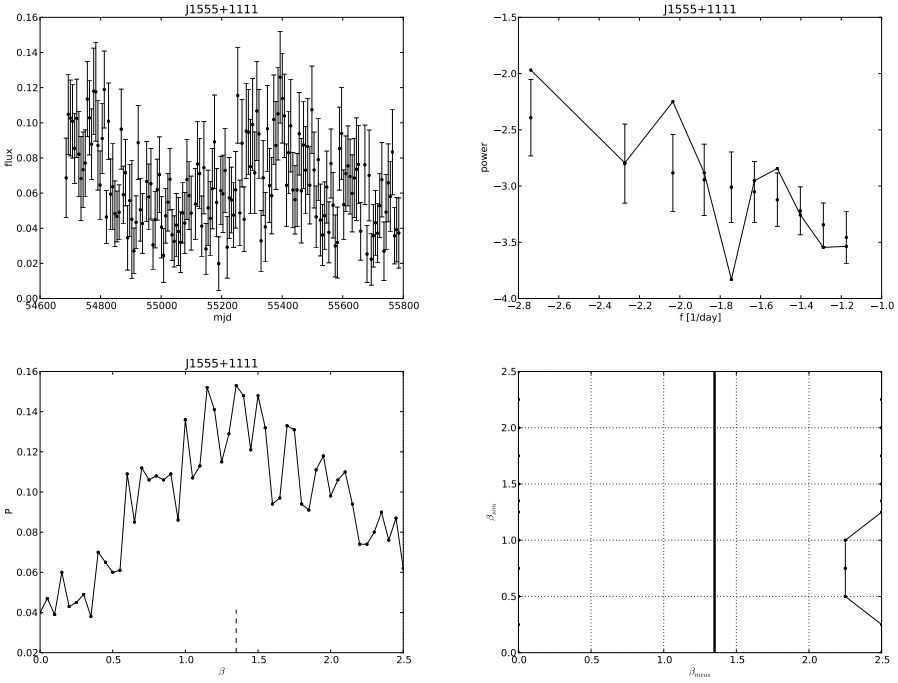

Figure E.132: PSD fit summary for J1555+1111. The best fit is $\beta = 1.4$ with 1σ limits $\beta^{lower} = 0.0$ and an undetermined upper limit.

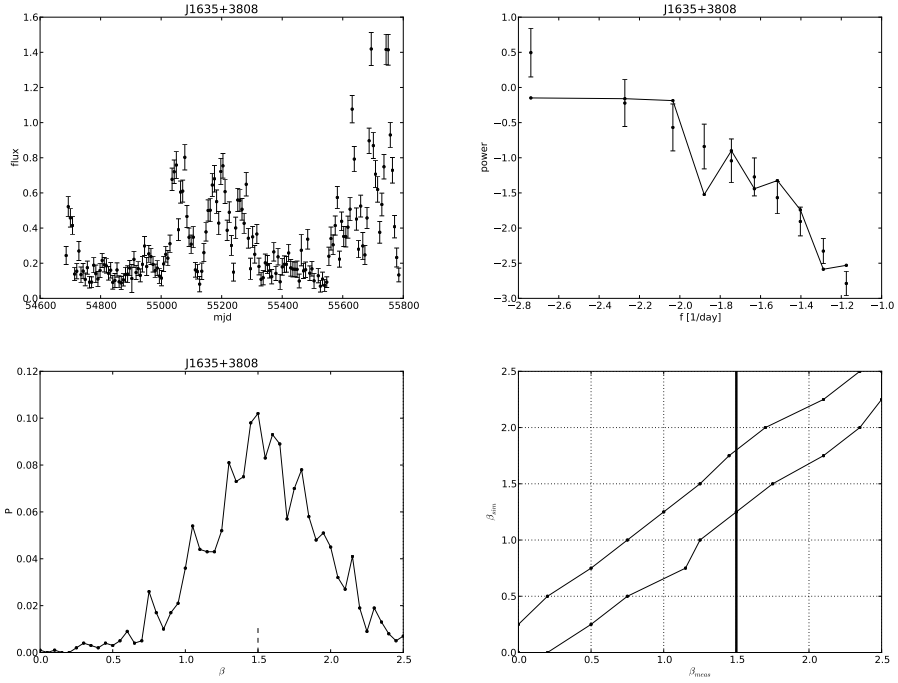

Figure E.133: PSD fit summary for J1635+3808. The best fit is $\beta = 1.5$ with 1σ limits $\beta^{lower} = 1.2$ and $\beta^{upper} = 1.8$.

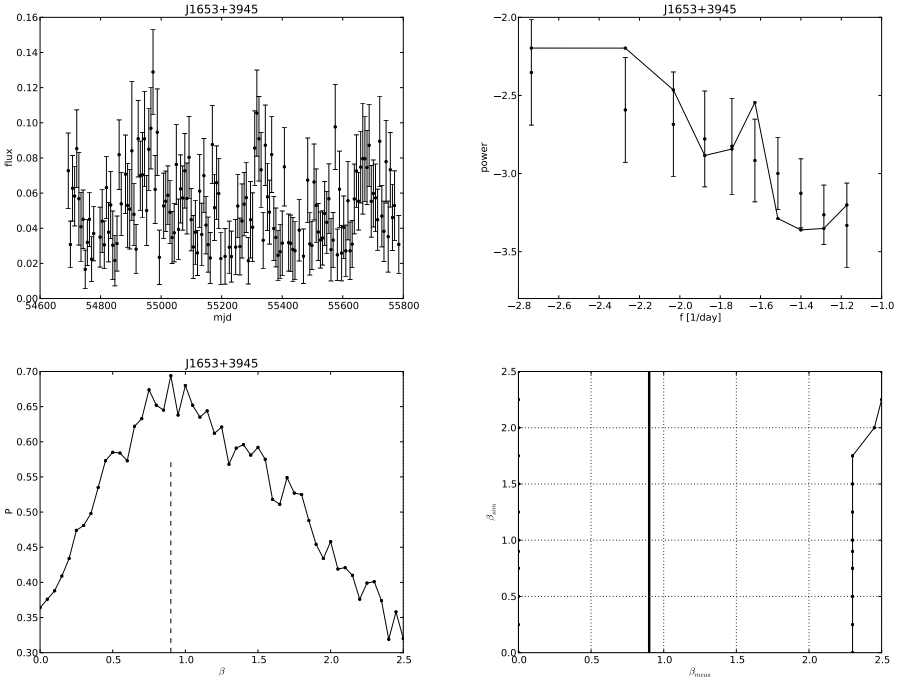

Figure E.134: PSD fit summary for J1653+3945. The best fit is $\beta = 0.9$ with 1σ limits $\beta^{lower} = 0.0$ and an undetermined upper limit.

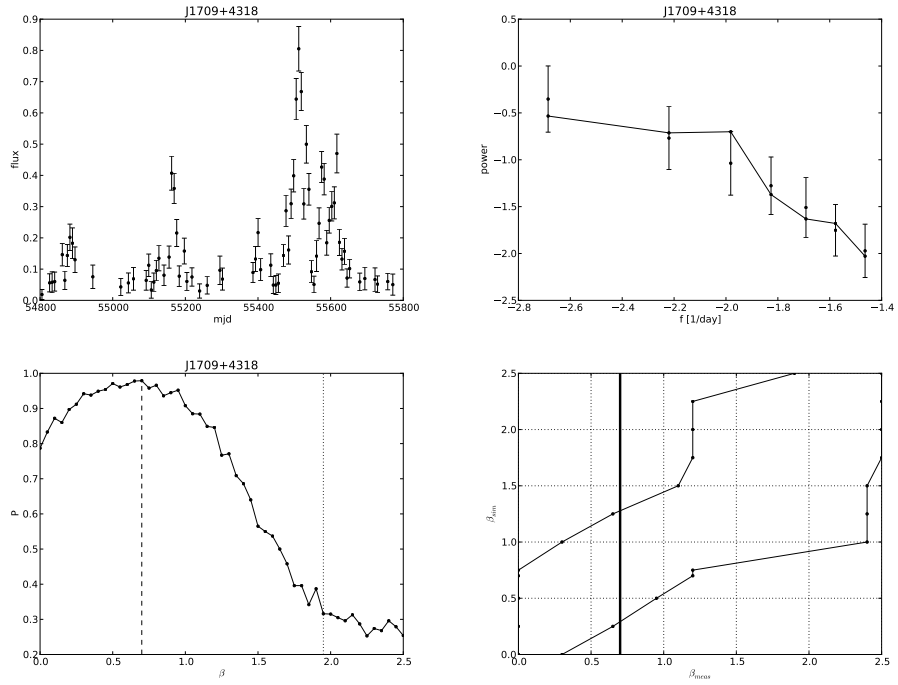

Figure E.135: PSD fit summary for J1709+4318. The best fit is $\beta = 0.7$ with 1σ limits $\beta^{lower} = 0.3$ and $\beta^{upper} = 1.3$.

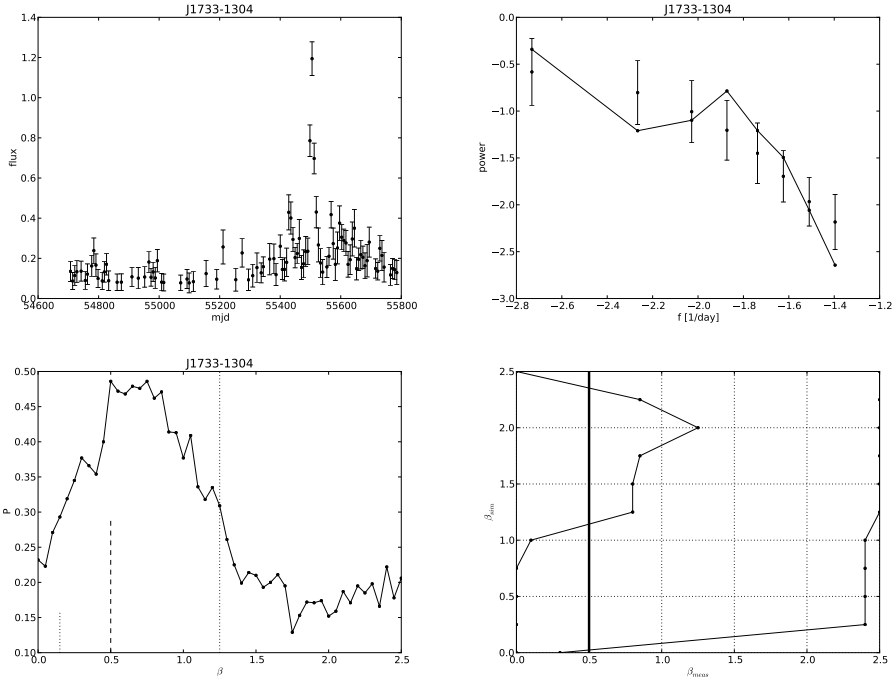

Figure E.136: PSD fit summary for J1733-1304. The best fit is $\beta = 0.5$ with 1σ limits $\beta^{lower} = 0.0$ and an undetermined upper limit.

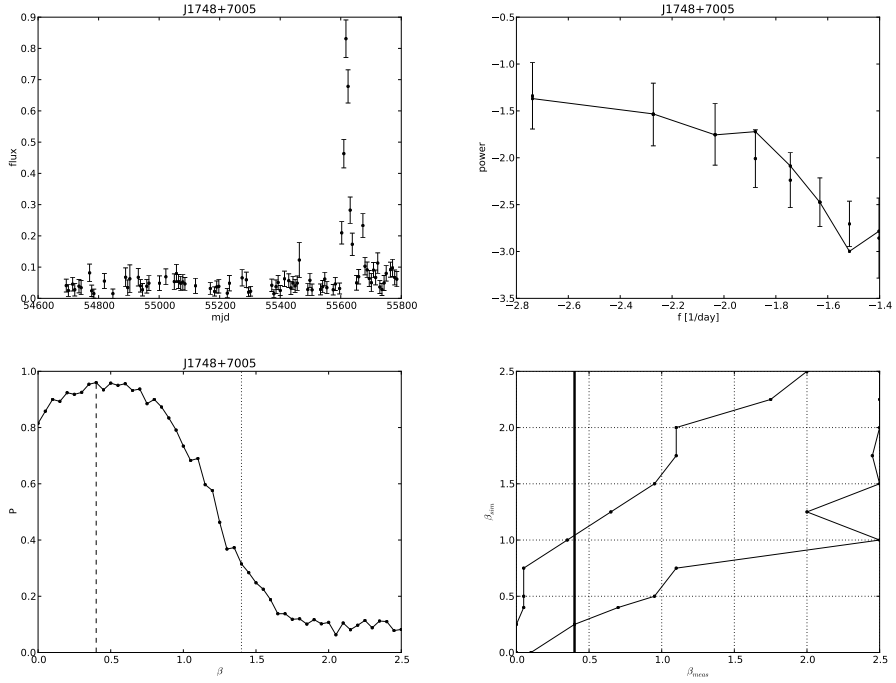

Figure E.137: PSD fit summary for J1748+7005. The best fit is $\beta = 0.4$ with 1σ limits $\beta^{lower} = 0.2$ and $\beta^{upper} = 1.0$.

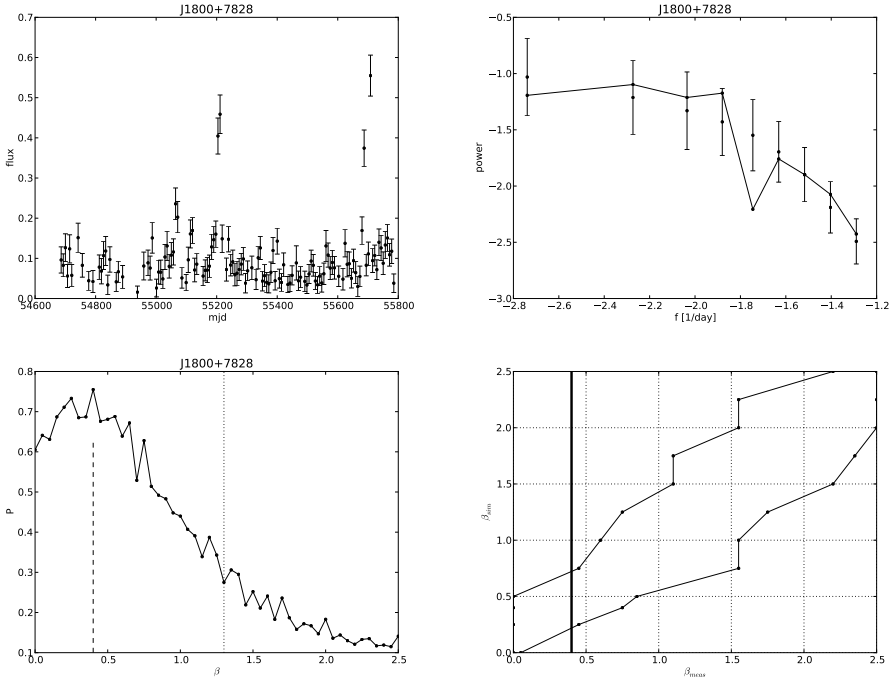

Figure E.138: PSD fit summary for J1800+7828. The best fit is $\beta = 0.4$ with 1σ limits $\beta^{lower} = 0.2$ and $\beta^{upper} = 0.7$.

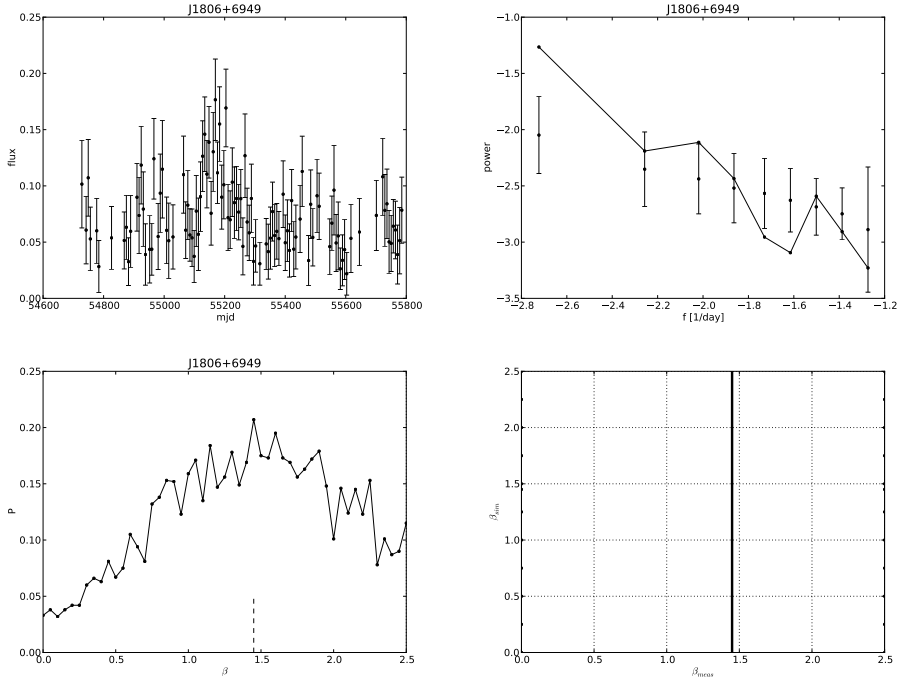

Figure E.139: PSD fit summary for J1806+6949. The best fit is $\beta = 1.4$ with 1σ limits $\beta^{lower} = 0.0$ and an undetermined upper limit.

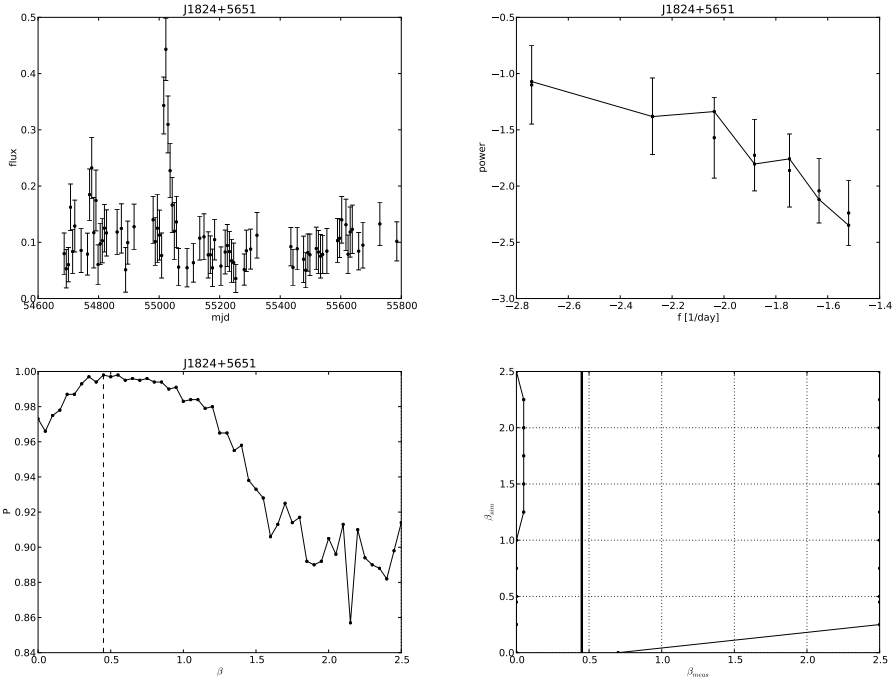

Figure E.140: PSD fit summary for J1824+5651. The best fit is $\beta = 0.5$ with 1σ limits $\beta^{lower} = 0.0$ and an undetermined upper limit.

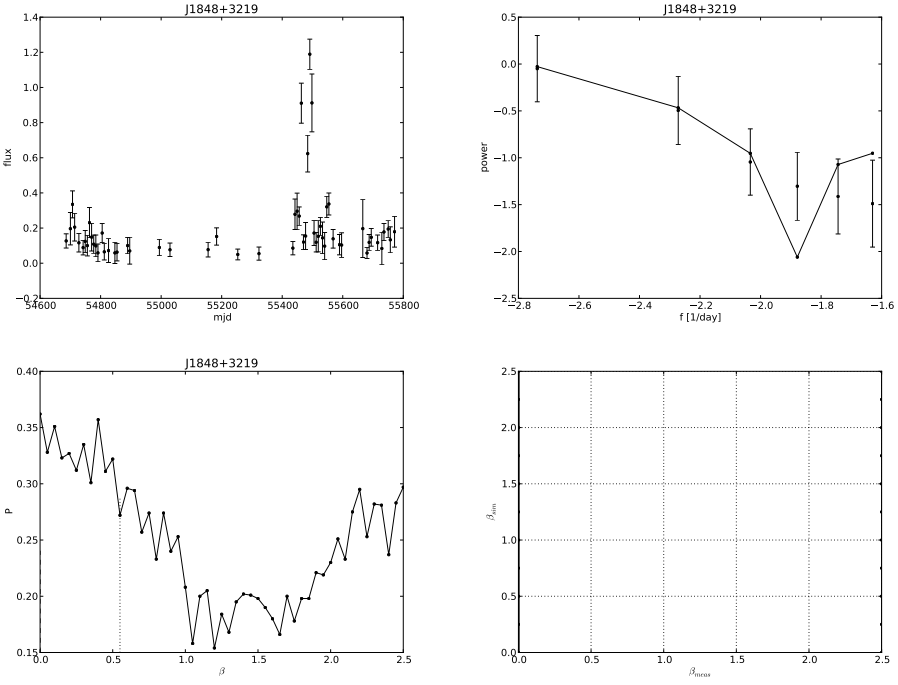

Figure E.141: PSD fit summary for J1848+3219. The best fit is $\beta = 0.0$ with 1σ limits $\beta^{lower} = 0.0$ and an undetermined upper limit.

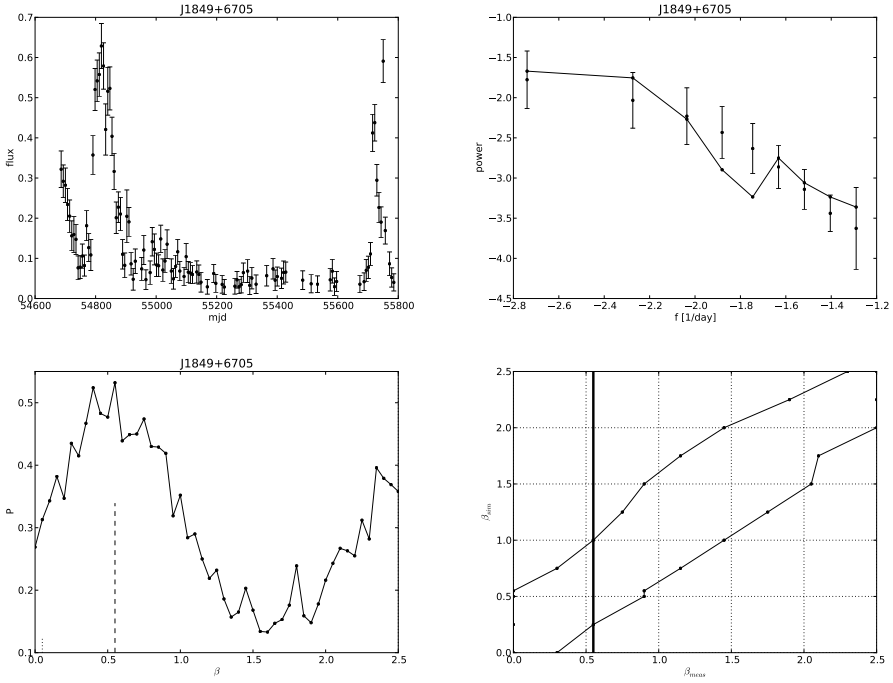

Figure E.142: PSD fit summary for J1849+6705. The best fit is $\beta = 0.6$ with 1σ limits $\beta^{lower} = 0.2$ and $\beta^{upper} = 1.0$.

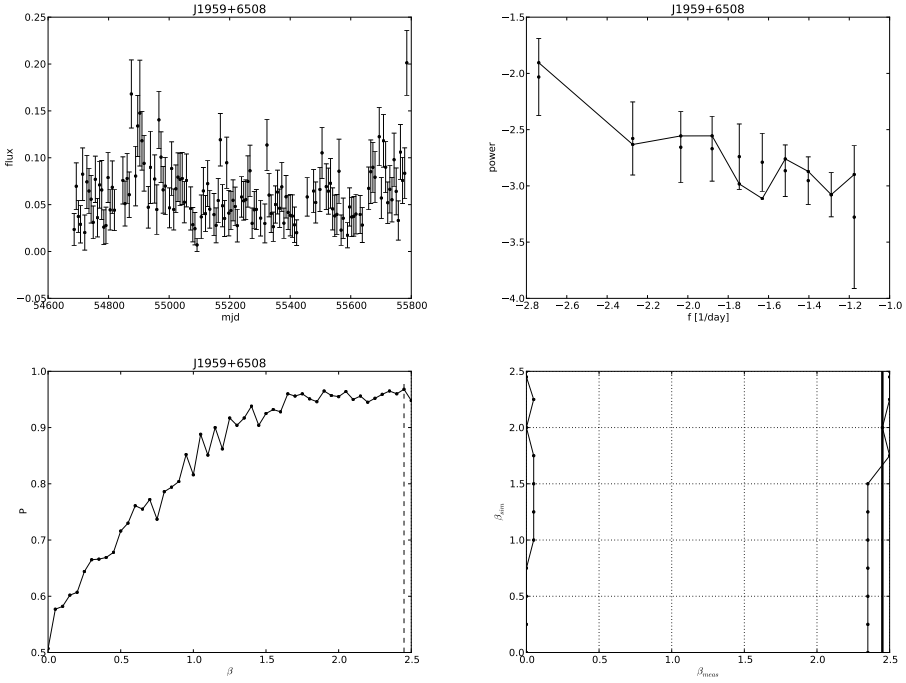

Figure E.143: PSD fit summary for J1959+6508. The best fit is $\beta = 2.5$ with 1σ limits $\beta^{lower} = 1.7$ and an undetermined upper limit.

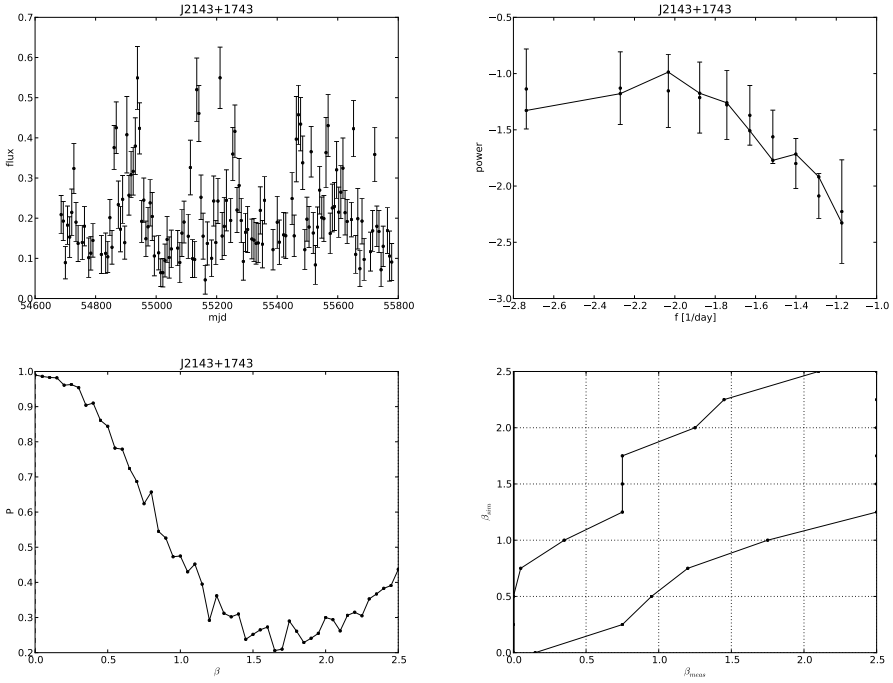

Figure E.144: PSD fit summary for J2143+1743. The best fit is $\beta = 0.0$ with 1σ limits $\beta^{lower} = 0.0$ and $\beta^{upper} = 0.5$.

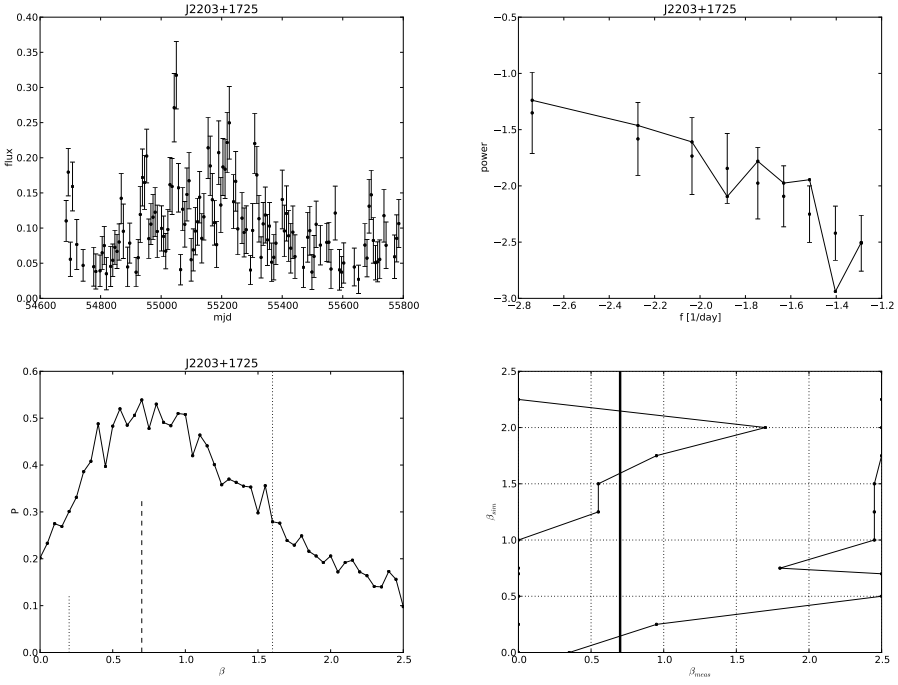

Figure E.145: PSD fit summary for J2203+1725. The best fit is $\beta = 0.7$ with 1σ limits $\beta^{lower} = 0.1$ and an undetermined upper limit.

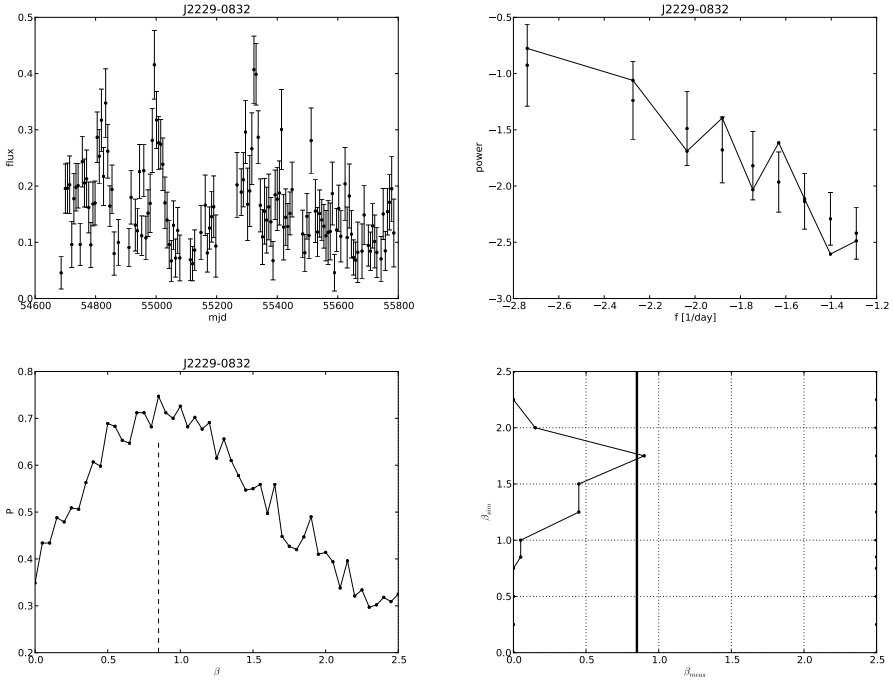

Figure E.146: PSD fit summary for J2229-0832. The best fit is $\beta = 0.8$ with 1σ limits $\beta^{lower} = 0.0$ and an undetermined upper limit.

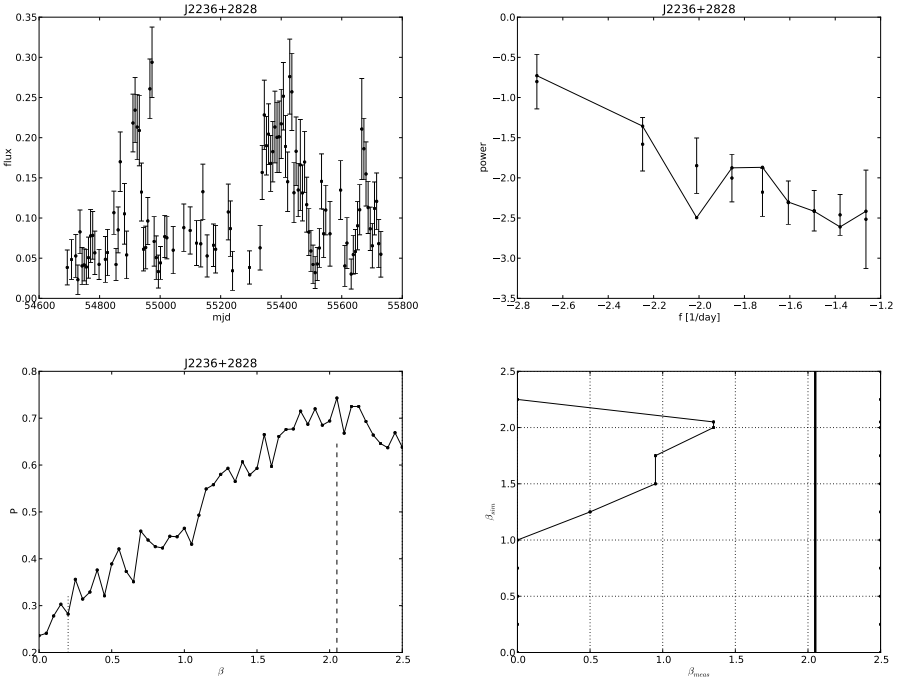

Figure E.147: PSD fit summary for J2236+2828. The best fit is $\beta = 2.0$ with 1σ limits $\beta^{lower} = 0.0$ and an undetermined upper limit.

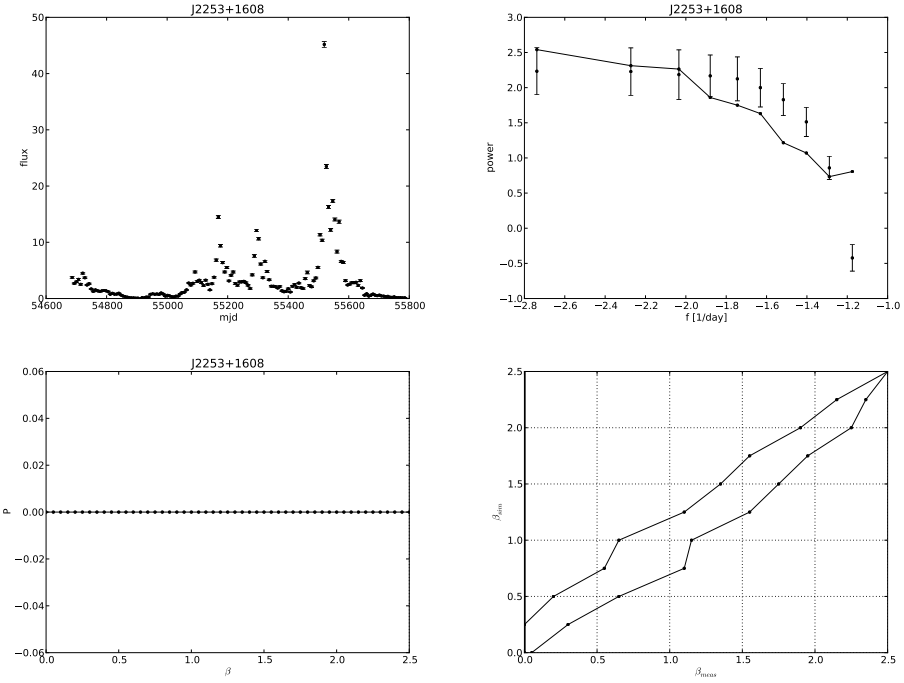

Figure E.148: PSD fit summary for J2253+1608. The best fit is $\beta = 0.0$ with 1σ limits $\beta^{lower} = 0.0$ and $\beta^{upper} = 0.2$.

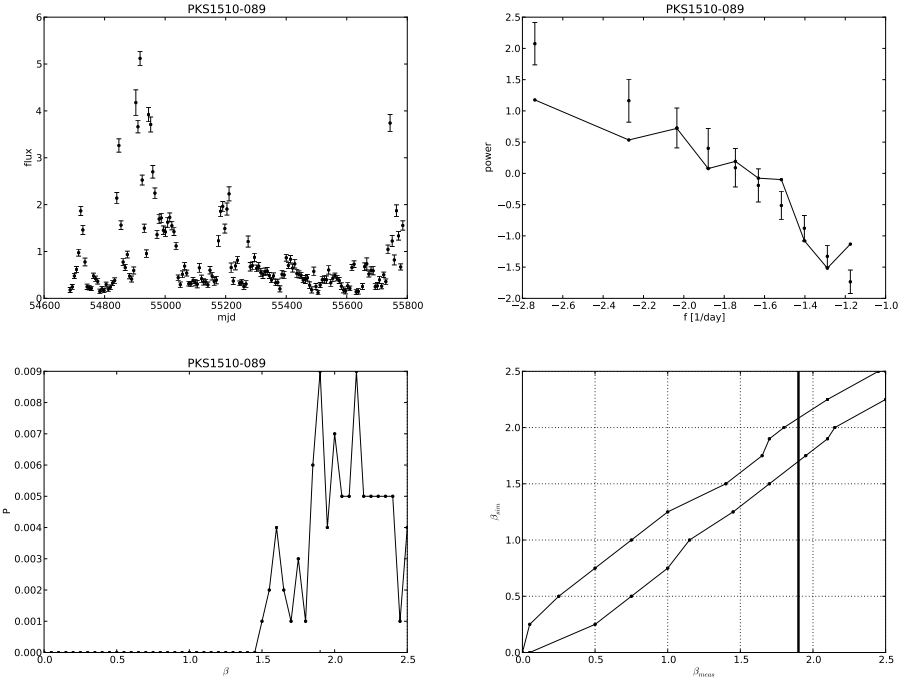

Figure E.149: PSD fit summary for PKS1510-089. The best fit is $\beta = 1.9$ with 1σ limits $\beta^{lower} = 1.7$ and $\beta^{upper} = 2.1$.

Appendix F

Cross-correlation summary figures and light curves for sources that are non-variable in at least one band

Figures summarizing the results of the cross-correlation analysis for the 63 sources in the cross-correlation sample that are found to be variable in both bands are presented. Each figure has three panels that show the data and the results of the cross-correlation significance analysis. The left panel show the radio light curve on top and gamma-ray light at the bottom. Central panel are the cross-correlation results with the black dots representing the cross-correlation for the data, while the color contours the distribution of random cross-correlations obtained by the Monte Carlo simulation with red for 1σ, orange for 2σ and green for 3σ significance. A time lag $\tau > 0$ indicates the gamma-ray emission lags the radio and $\tau < 0$ the opposite. The right panel shows the p-value of the measured cross-correlation and equivalent significance represented by the horizontal segmented lines and labeled at their right end. Notice that in the right panel the $p-$values are for positive and negative correlations, thus some of the troughs could represent anti-correlations that are considered in this discussion. The ambiguity can easily be resolved by looking at the cross-correlation plot on the middle panel.

F.1 Cross-correlation significance for $\beta_{radio} = 2.3$ and $\beta_{gamma} = 1.6$

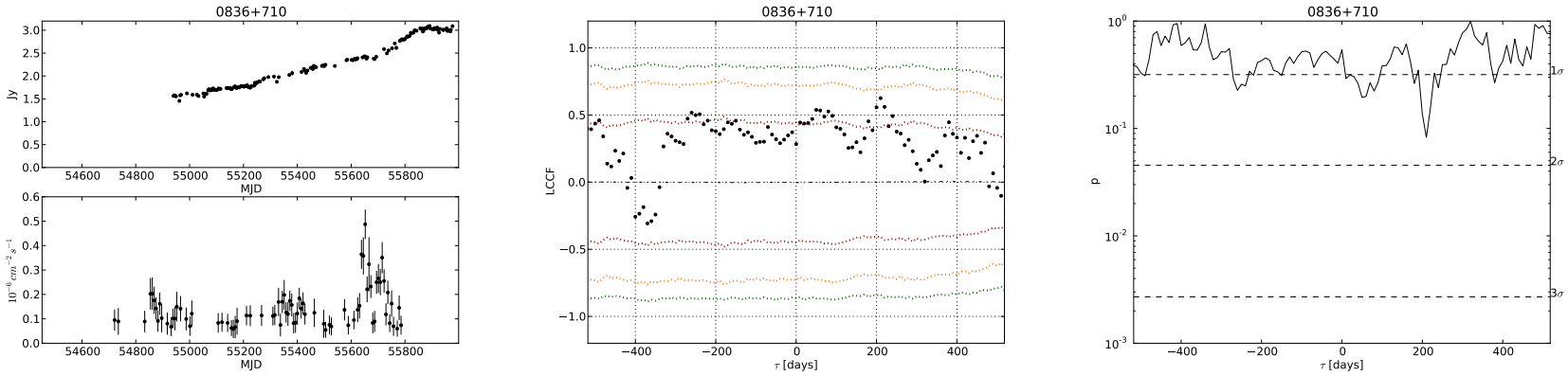

Figure F.1: Light curves and cross-correlation significance for 0836+710 in the case of $\beta_{radio} = 2.3$ and $\beta_\gamma = 1.6$. The most significant cross-correlation is at 210 ± 11 day with 91.74% significance.

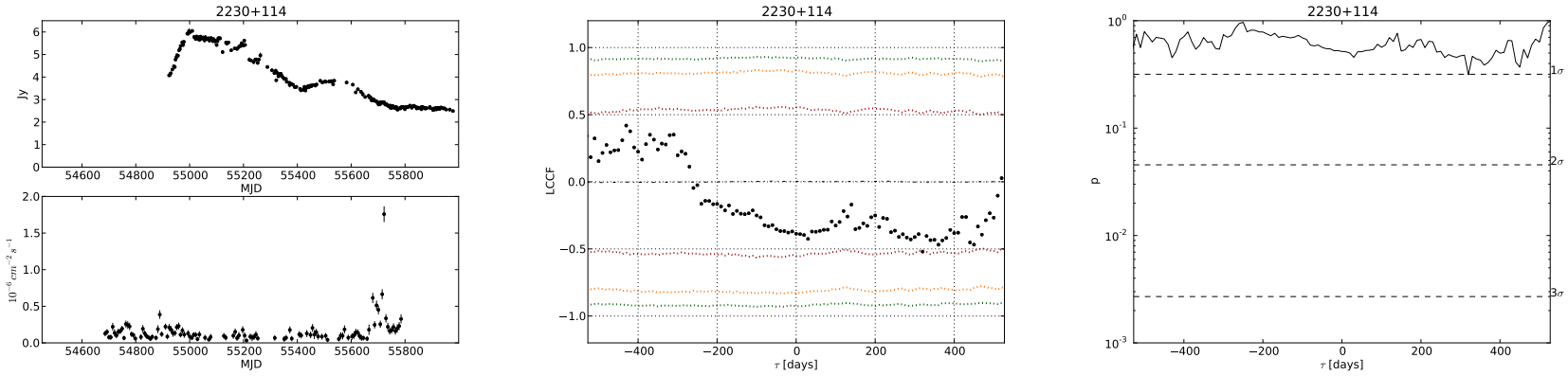

Figure F.2: Light curves and cross-correlation significance for 2230+114 in the case of $\beta_{radio} = 2.3$ and $\beta_\gamma = 1.6$. The most significant cross-correlation is at -430 ± 10 day with 54.75% significance.

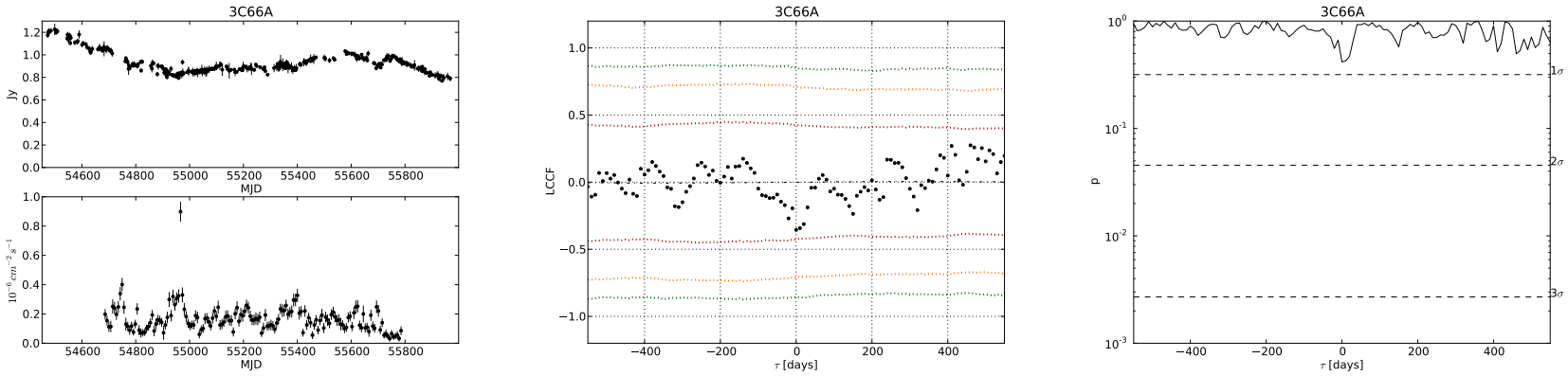

Figure F.3: Light curves and cross-correlation significance for 3C66A in the case of $\beta_{radio} = 2.3$ and $\beta_{\gamma} = 1.6$. The most significant cross-correlation is at 460 $\pm$ 16 day with 50.35% significance.

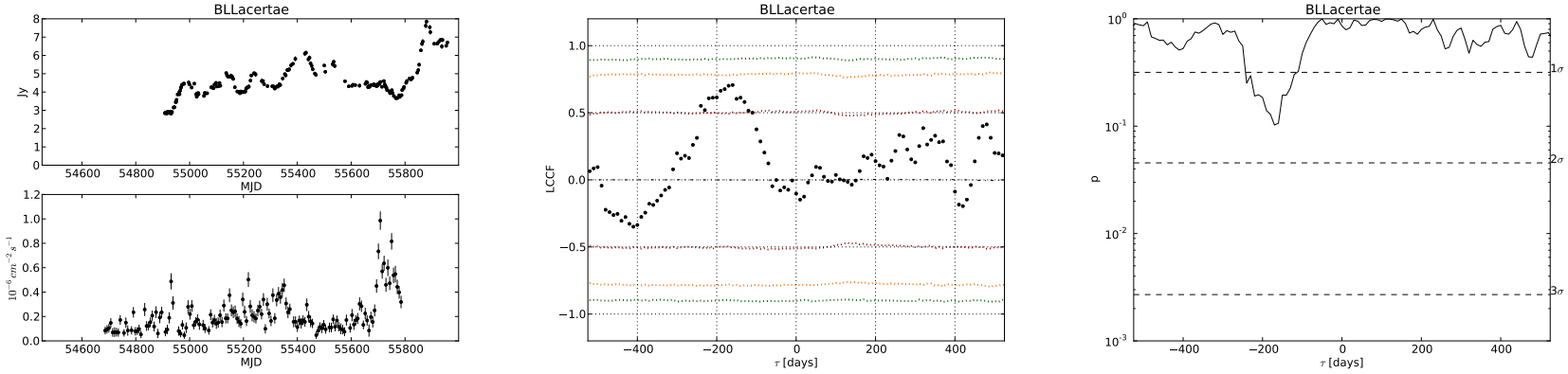

Figure F.4: Light curves and cross-correlation significance for BLLacertae in the case of $\beta_{radio} = 2.3$ and $\beta_{\gamma} = 1.6$. The most significant cross-correlation is at -160 $\pm$ 13 day with 89.33% significance.

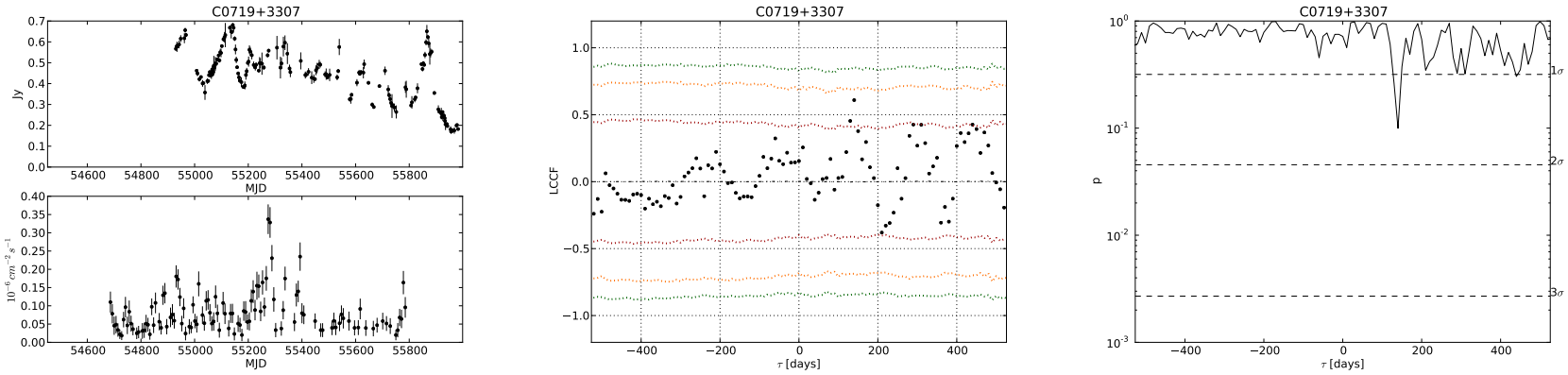

Figure F.5: Light curves and cross-correlation significance for C0719+3307 in the case of $\beta_{radio} = 2.3$ and $\beta_{\gamma} = 1.6$. The most significant cross-correlation is at 140 ± 8 day with 90.05% significance.

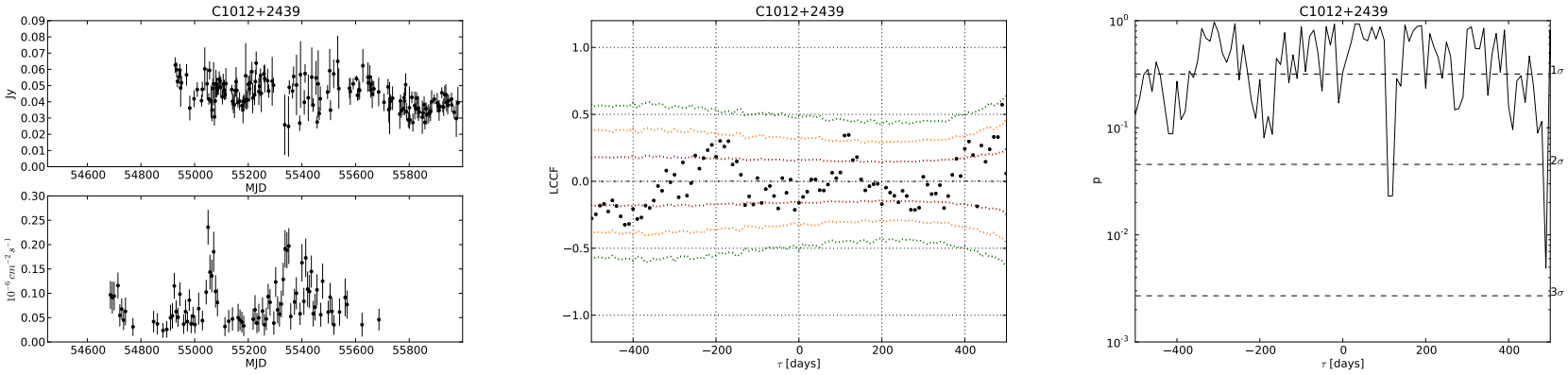

Figure F.6: Light curves and cross-correlation significance for C1012+2439 in the case of $\beta_{radio} = 2.3$ and $\beta_{\gamma} = 1.6$. The most significant cross-correlation is at 490 ± 49 day with 99.51% significance.

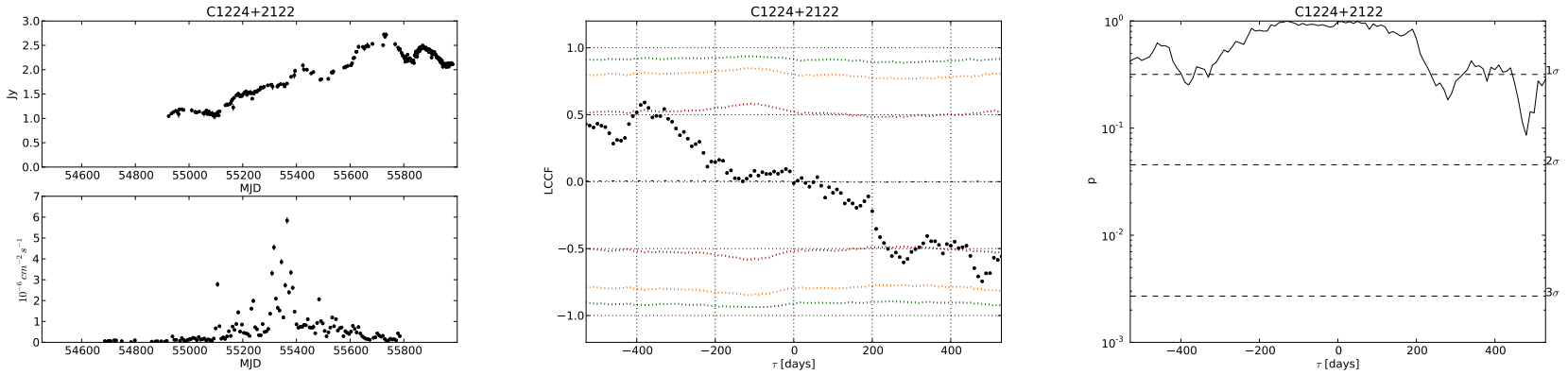

Figure F.7: Light curves and cross-correlation significance for C1224+2122 in the case of $\beta_{radio} = 2.3$ and $\beta_{\gamma} = 1.6$. The most significant cross-correlation is at -380 $\pm$ 10 day with 74.70% significance.

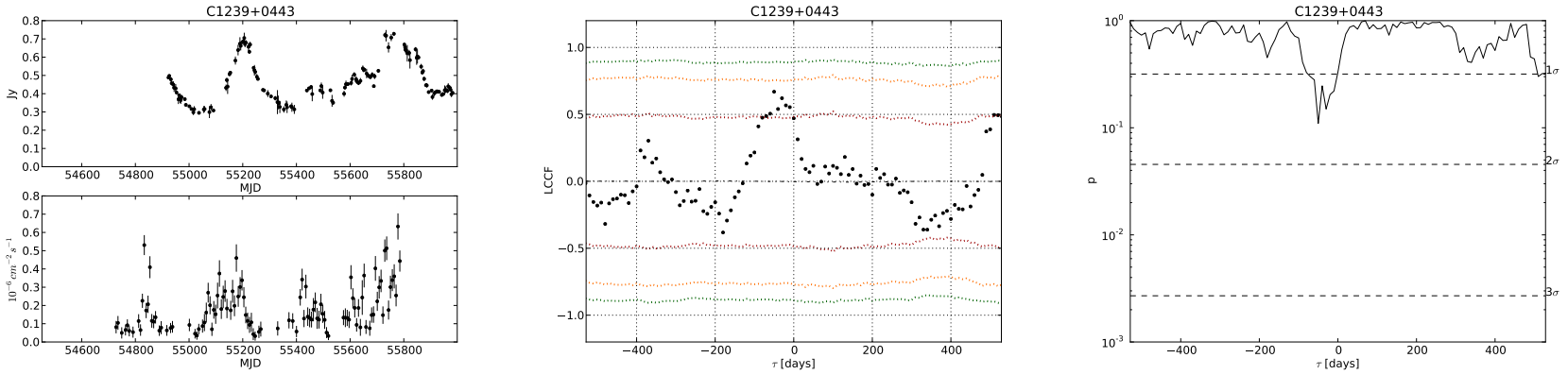

Figure F.8: Light curves and cross-correlation significance for C1239+0443 in the case of $\beta_{radio} = 2.3$ and $\beta_{\gamma} = 1.6$. The most significant cross-correlation is at -50 $\pm$ 15 day with 89.01% significance.

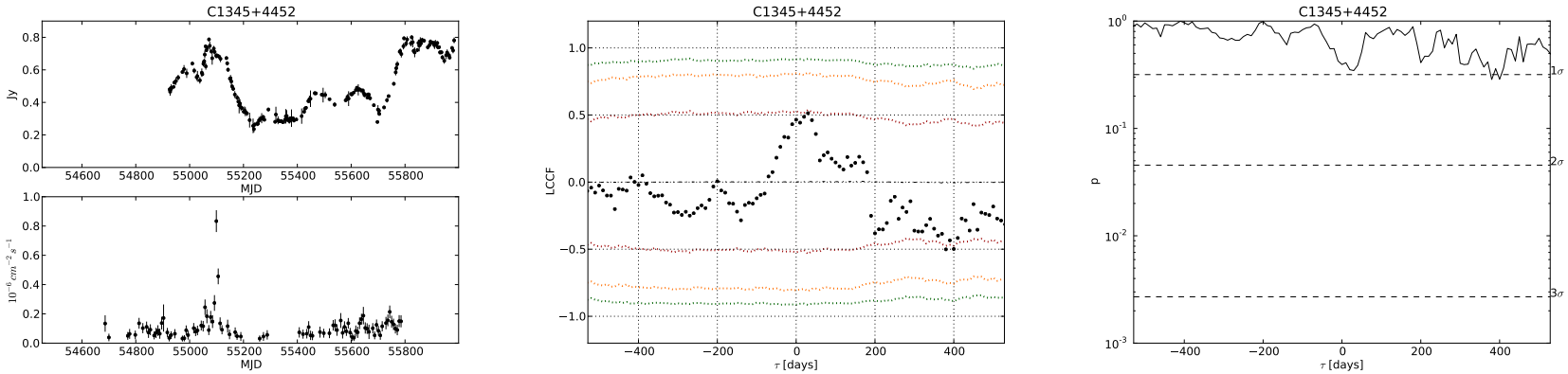

Figure F.9: Light curves and cross-correlation significance for C1345+4452 in the case of $\beta_{radio} = 2.3$ and $\beta_\gamma = 1.6$. The most significant cross-correlation is at 30 ± 14 day with 65.40% significance.

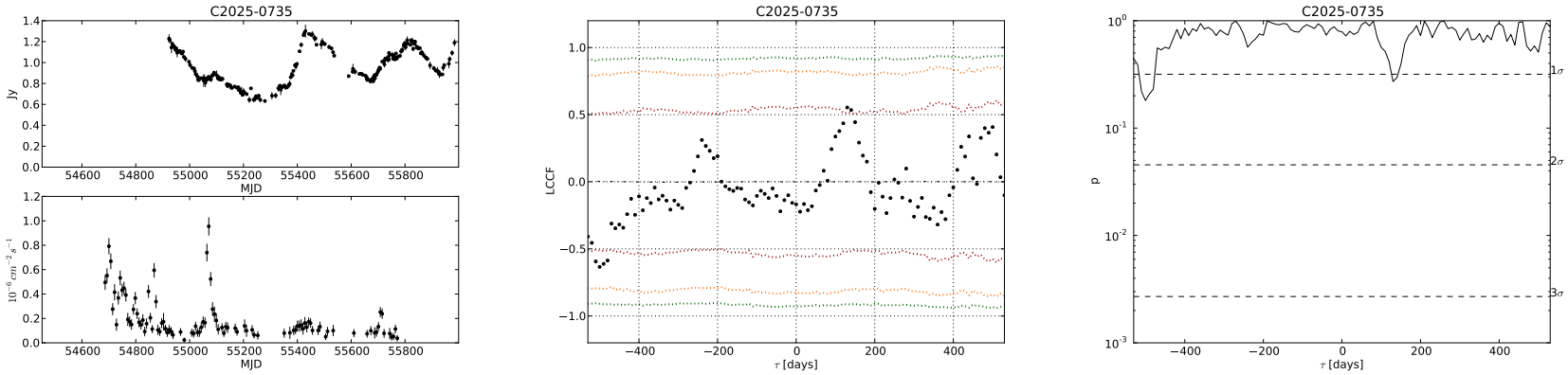

Figure F.10: Light curves and cross-correlation significance for C2025-0735 in the case of $\beta_{radio} = 2.3$ and $\beta_\gamma = 1.6$. The most significant cross-correlation is at 130 ± 12 day with 72.89% significance.

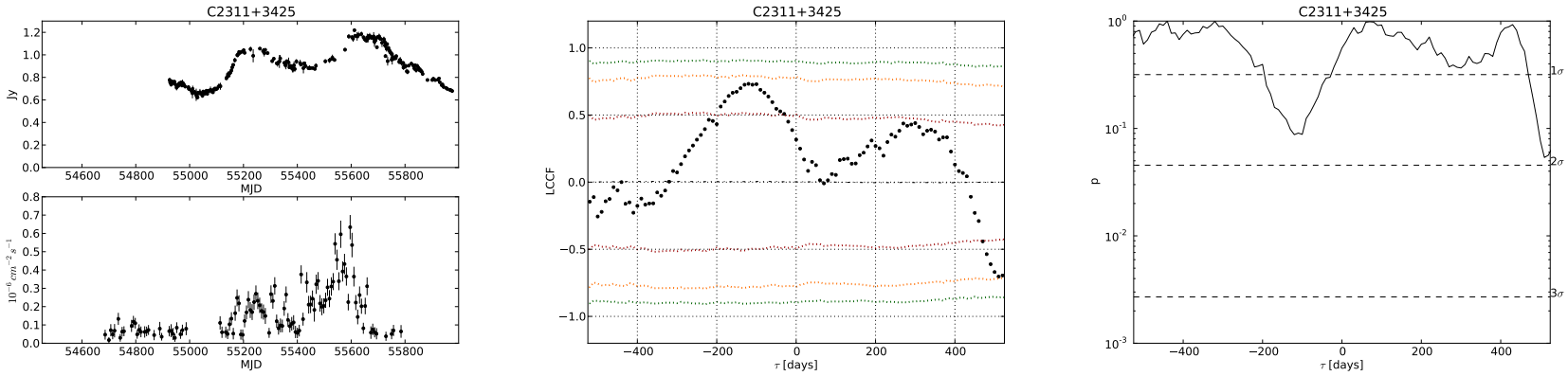

Figure F.11: Light curves and cross-correlation significance for C2311+3425 in the case of $\beta_{radio} = 2.3$ and $\beta_{\gamma} = 1.6$. The most significant cross-correlation is at -120 $\pm$ 14 day with 91.24% significance.

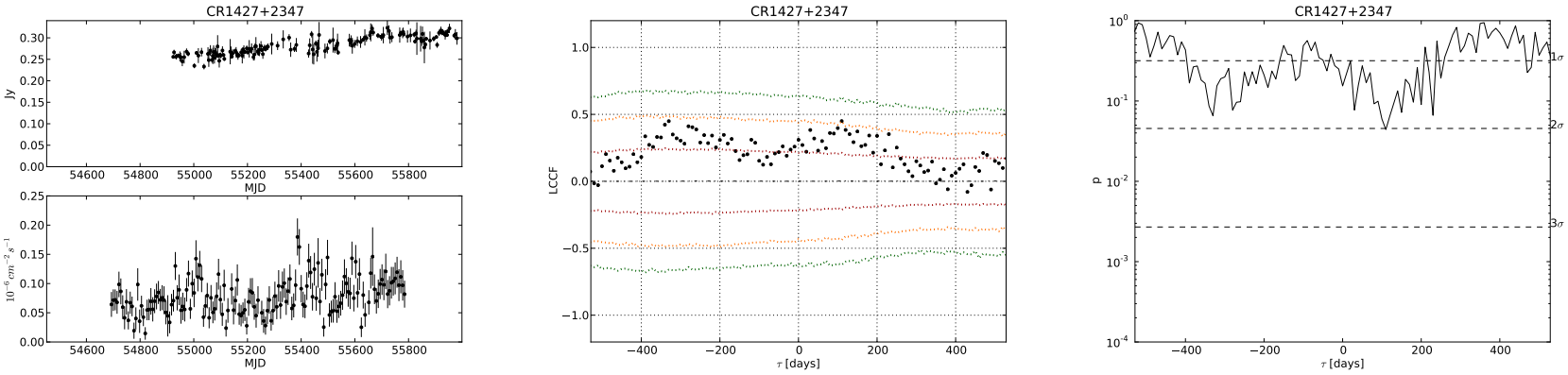

Figure F.12: Light curves and cross-correlation significance for CR1427+2347 in the case of $\beta_{radio} = 2.3$ and $\beta_{\gamma} = 1.6$. The most significant cross-correlation is at 110 $\pm$ 13 day with 95.59% significance.

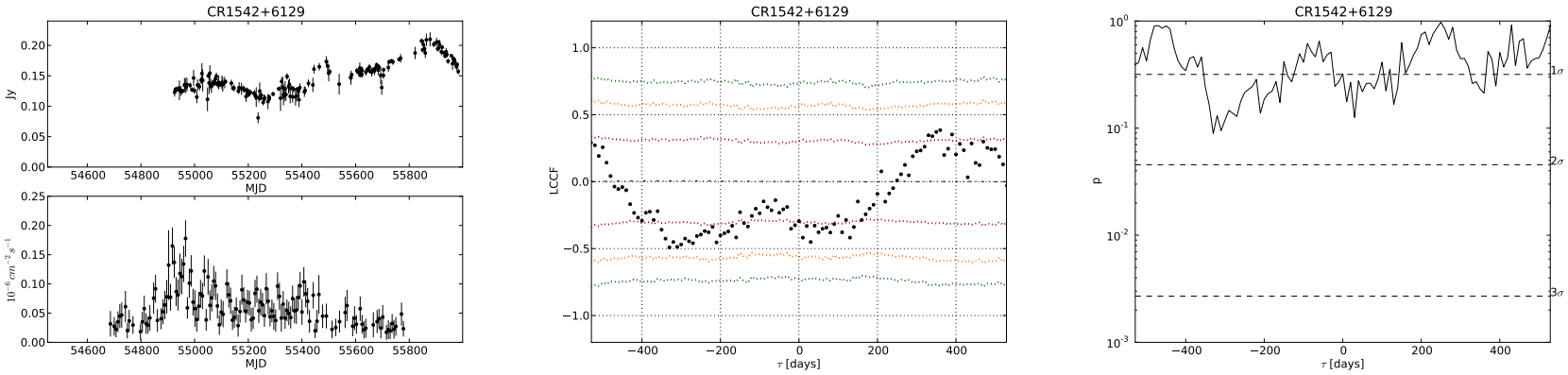

Figure F.13: Light curves and cross-correlation significance for CR1542+6129 in the case of $\beta_{radio} = 2.3$ and $\beta_{\gamma} = 1.6$. The most significant cross-correlation is at 360 $\pm$ 16 day with 78.75% significance.

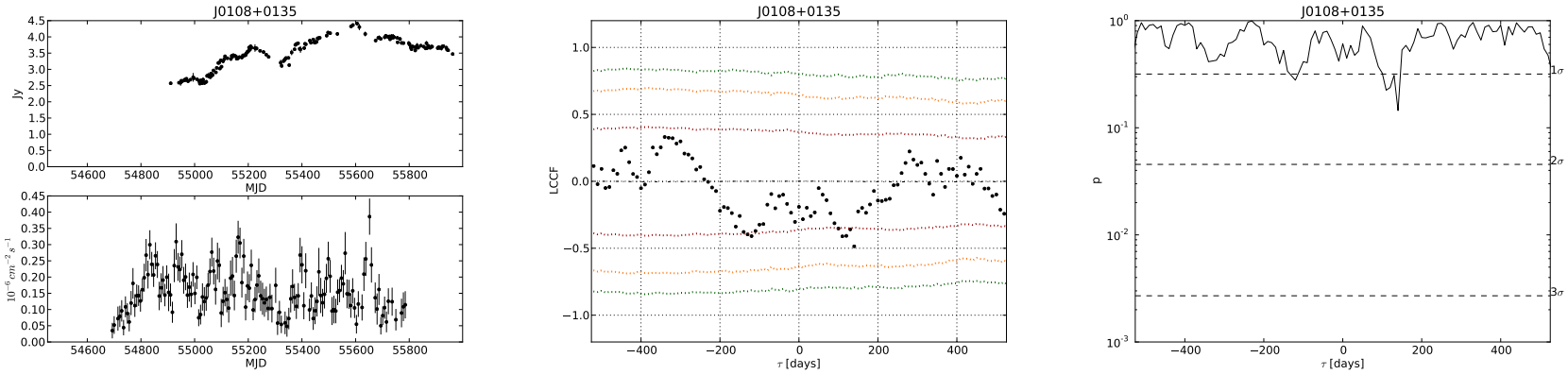

Figure F.14: Light curves and cross-correlation significance for J0108+0135 in the case of $\beta_{radio} = 2.3$ and $\beta_{\gamma} = 1.6$. The most significant cross-correlation is at -340 $\pm$ 16 day with 58.64% significance.

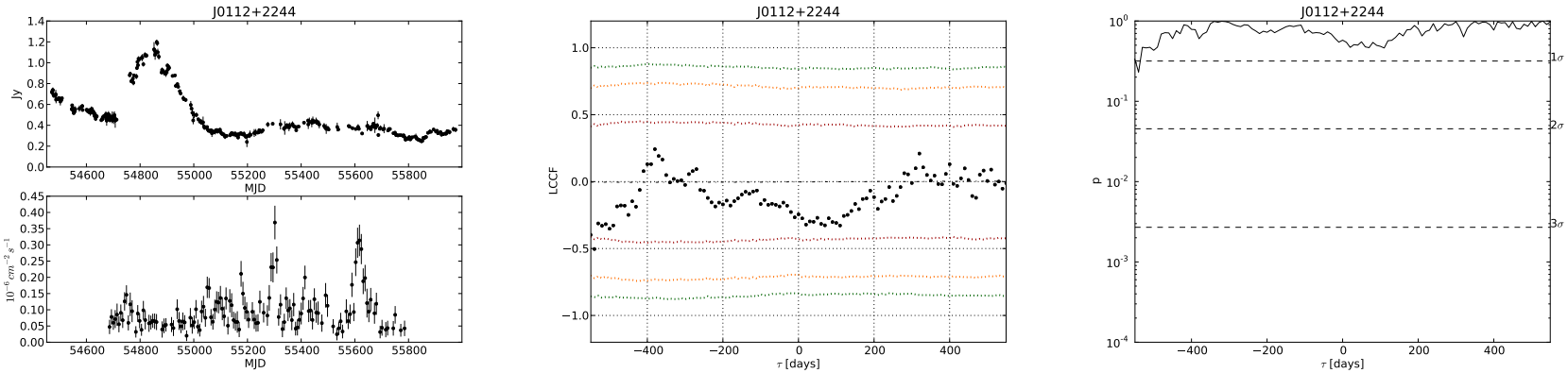

Figure F.15: Light curves and cross-correlation significance for J0112+2244 in the case of $\beta_{radio} = 2.3$ and $\beta_{\gamma} = 1.6$. The most significant cross-correlation is at -380 ± 14 day with 39.83% significance.

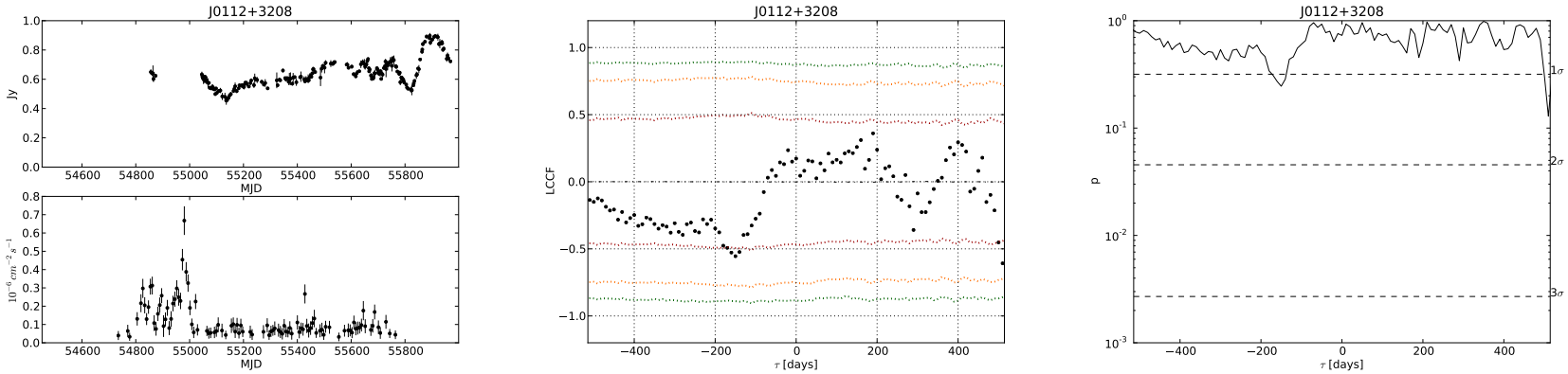

Figure F.16: Light curves and cross-correlation significance for J0112+3208 in the case of $\beta_{radio} = 2.3$ and $\beta_{\gamma} = 1.6$. The most significant cross-correlation is at 190 ± 12 day with 54.65% significance.

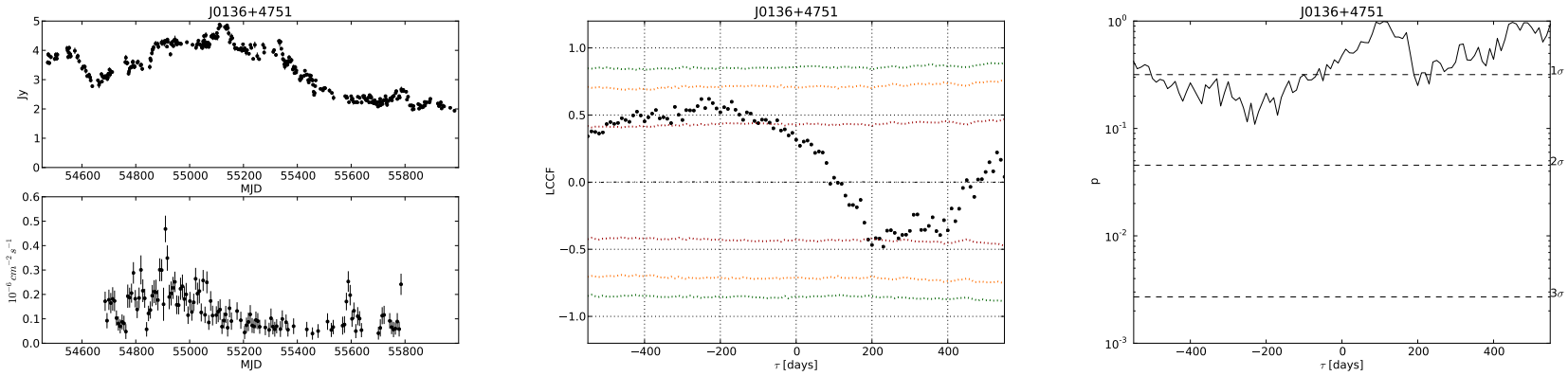

Figure F.17: Light curves and cross-correlation significance for J0136+4751 in the case of $\beta_{radio} = 2.3$ and $\beta_\gamma = 1.6$. The most significant cross-correlation is at -230 ± 13 day with 89.06% significance.

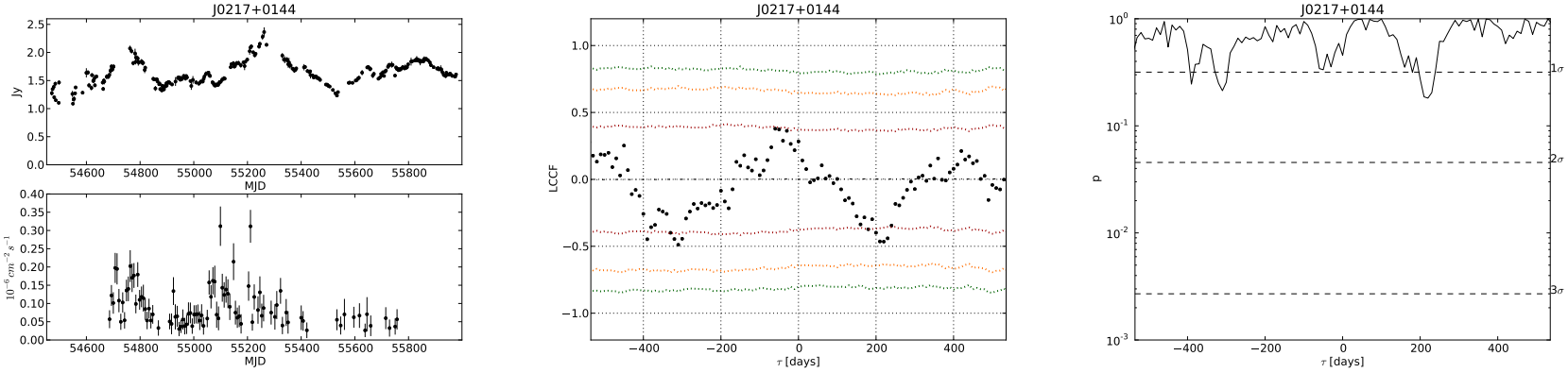

Figure F.18: Light curves and cross-correlation significance for J0217+0144 in the case of $\beta_{radio} = 2.3$ and $\beta_\gamma = 1.6$. The most significant cross-correlation is at -60 ± 15 day with 65.75% significance.

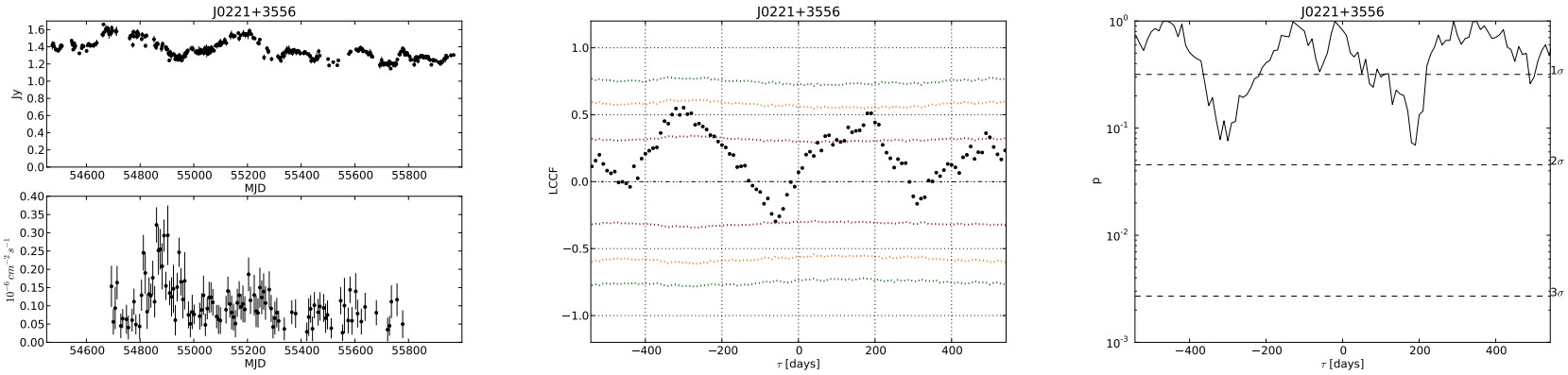

Figure F.19: Light curves and cross-correlation significance for J0221+3556 in the case of $\beta_{radio} = 2.3$ and $\beta_\gamma = 1.6$. The most significant cross-correlation is at 190 ± 12 day with 93.08% significance.

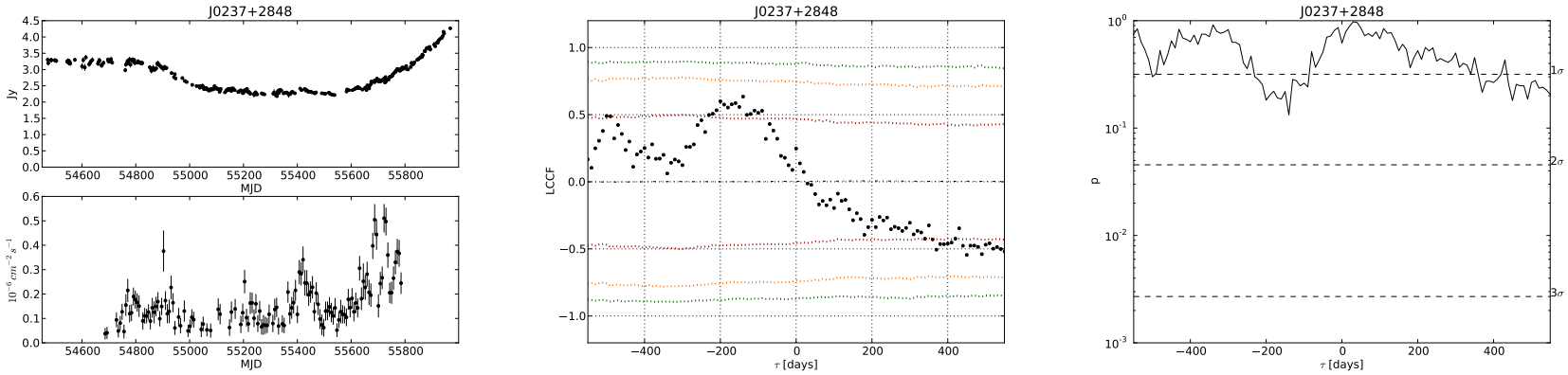

Figure F.20: Light curves and cross-correlation significance for J0237+2848 in the case of $\beta_{radio} = 2.3$ and $\beta_\gamma = 1.6$. The most significant cross-correlation is at -140 ± 12 day with 86.72% significance.

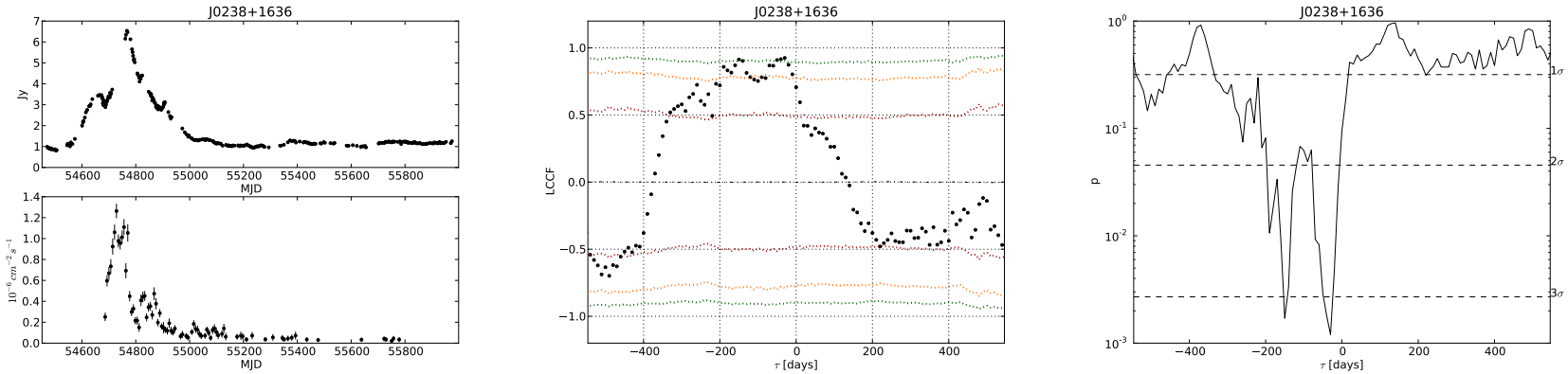

Figure F.21: Light curves and cross-correlation significance for J0238+1636 in the case of $\beta_{radio} = 2.3$ and $\beta_\gamma = 1.6$. The most significant cross-correlation is at -30 ± 8 day with 99.88% significance.

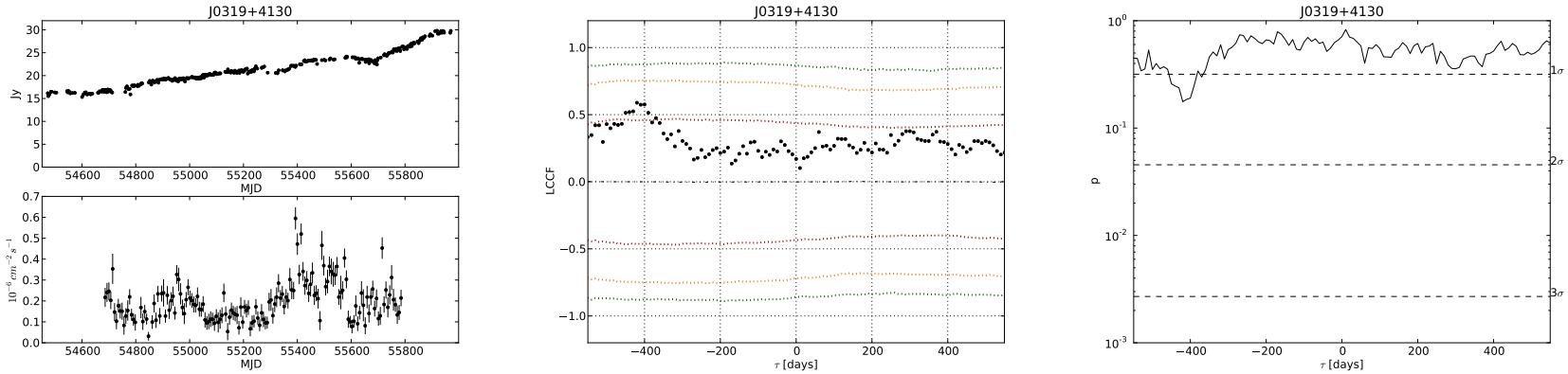

Figure F.22: Light curves and cross-correlation significance for J0319+4130 in the case of $\beta_{radio} = 2.3$ and $\beta_\gamma = 1.6$. The most significant cross-correlation is at -420 ± 13 day with 82.39% significance.

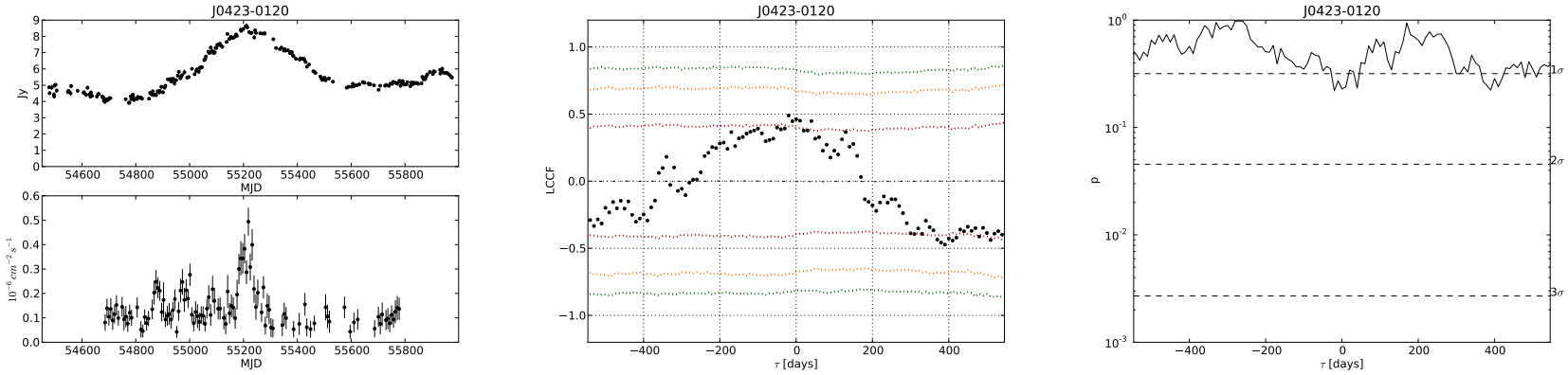

Figure F.23: Light curves and cross-correlation significance for J0423-0120 in the case of $\beta_{radio} = 2.3$ and $\beta_\gamma = 1.6$. The most significant cross-correlation is at -20 ± 16 day with 78.00% significance.

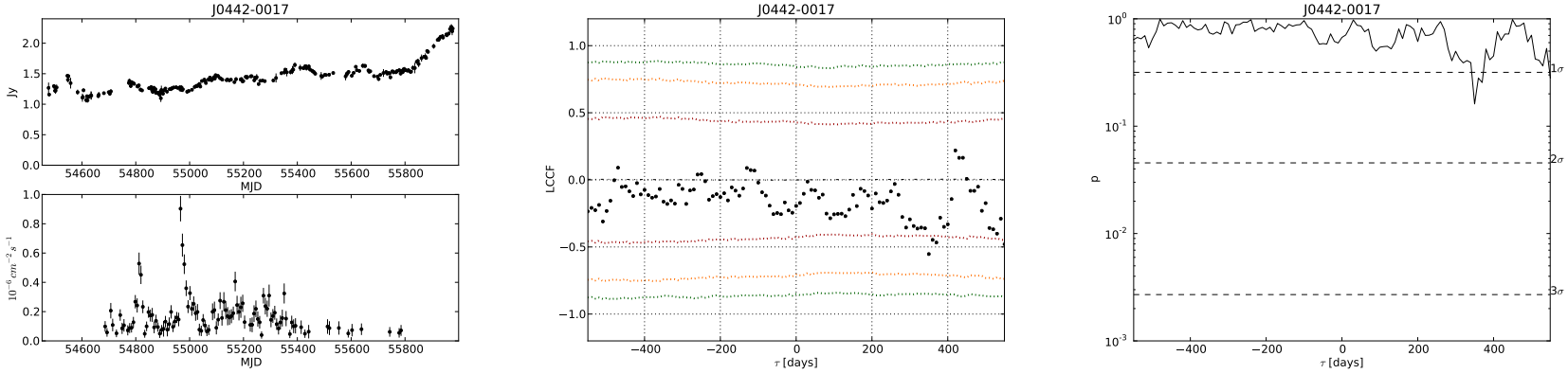

Figure F.24: Light curves and cross-correlation significance for J0442-0017 in the case of $\beta_{radio} = 2.3$ and $\beta_\gamma = 1.6$. The most significant cross-correlation is at 420 ± 29 day with 36.75% significance.

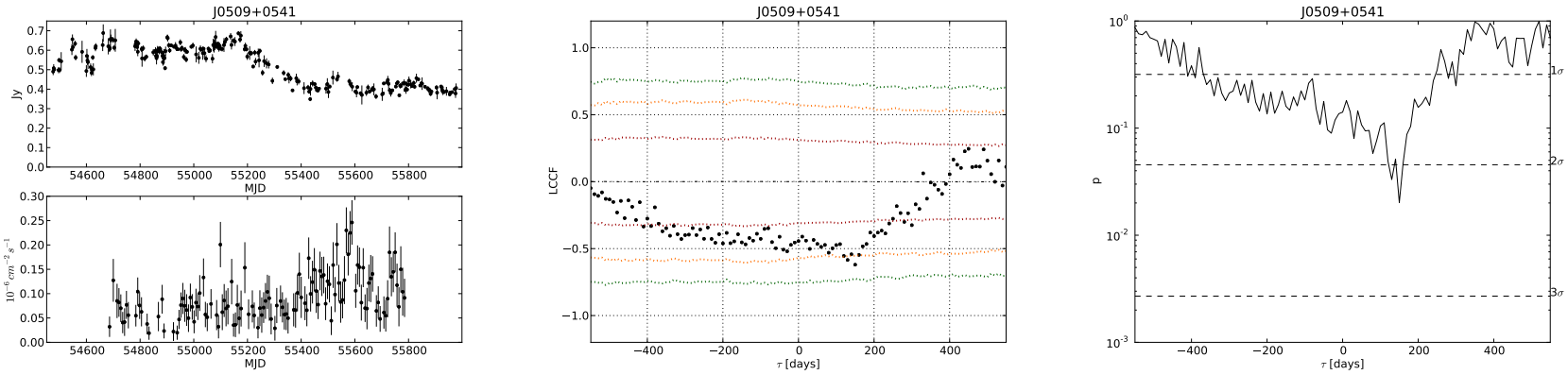

Figure F.25: Light curves and cross-correlation significance for J0509+0541 in the case of $\beta_{radio} = 2.3$ and $\beta_\gamma = 1.6$. The most significant cross-correlation is at 450 $\pm$ 14 day with 62.87% significance.

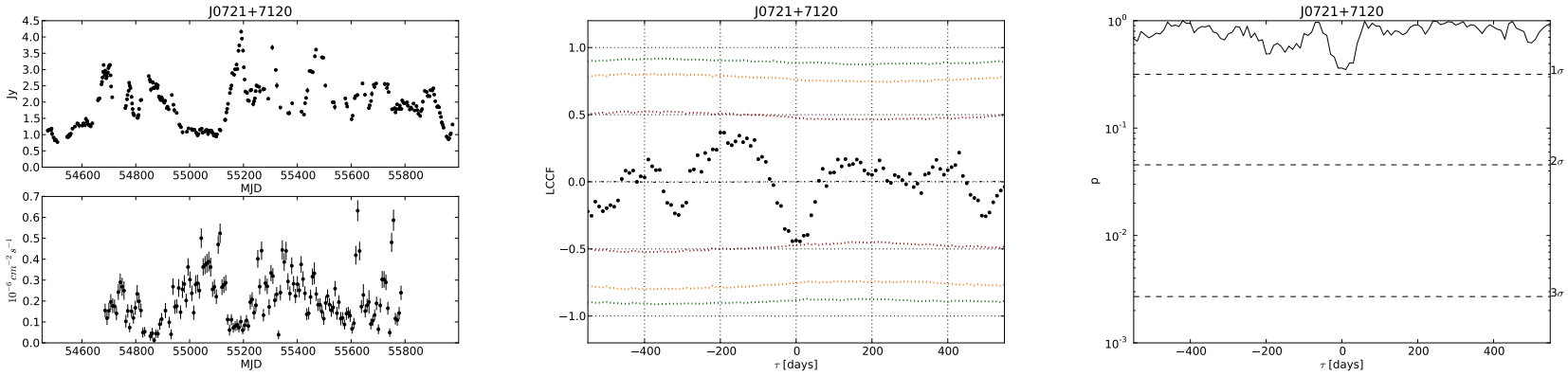

Figure F.26: Light curves and cross-correlation significance for J0721+7120 in the case of $\beta_{radio} = 2.3$ and $\beta_\gamma = 1.6$. The most significant cross-correlation is at -200 $\pm$ 12 day with 51.04% significance.

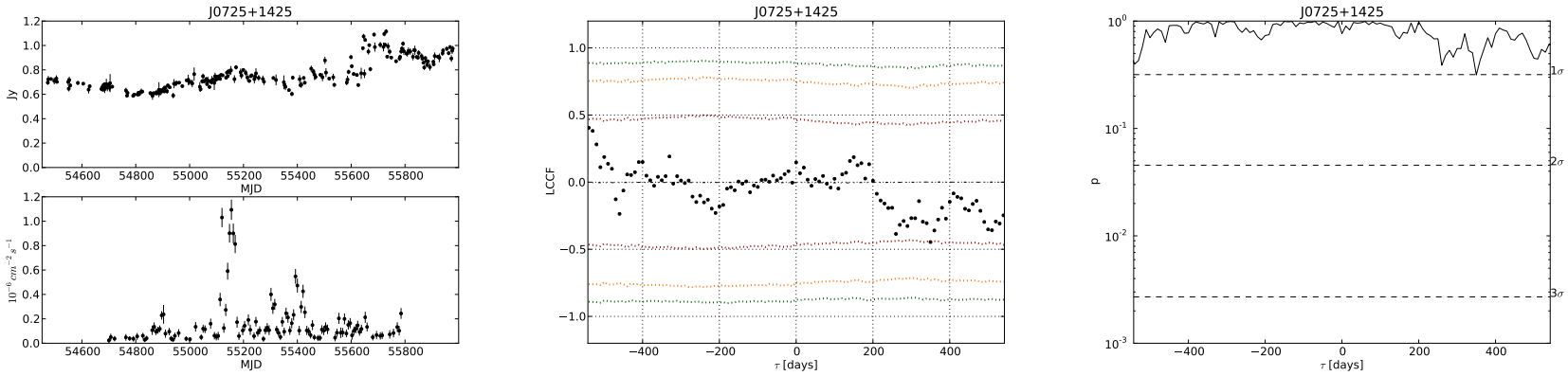

Figure F.27: Light curves and cross-correlation significance for J0725+1425 in the case of $\beta_{radio} = 2.3$ and $\beta_{\gamma} = 1.6$. The most significant cross-correlation is at 150 ± 13 day with 31.45% significance.

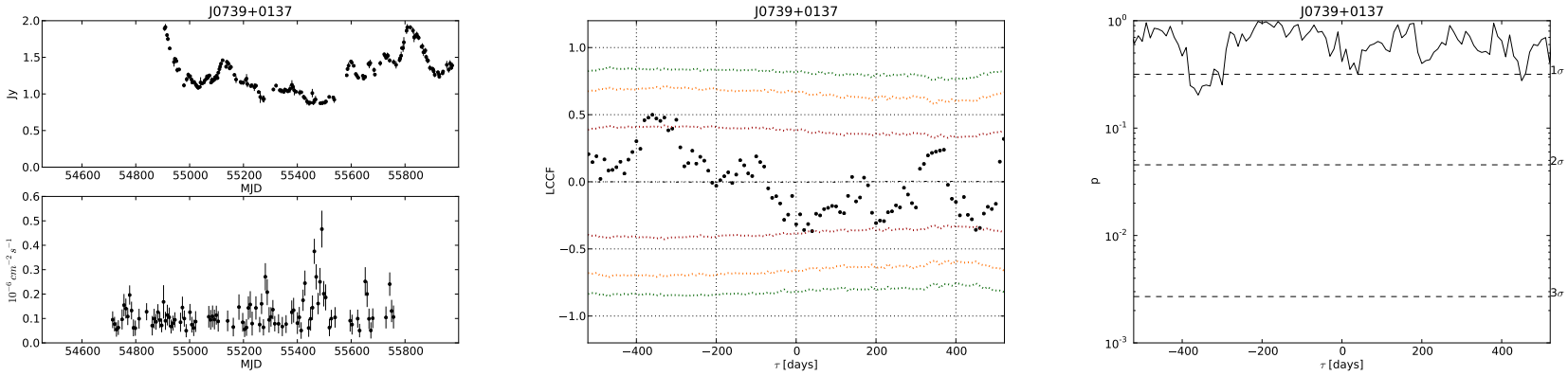

Figure F.28: Light curves and cross-correlation significance for J0739+0137 in the case of $\beta_{radio} = 2.3$ and $\beta_{\gamma} = 1.6$. The most significant cross-correlation is at -360 ± 15 day with 79.70% significance.

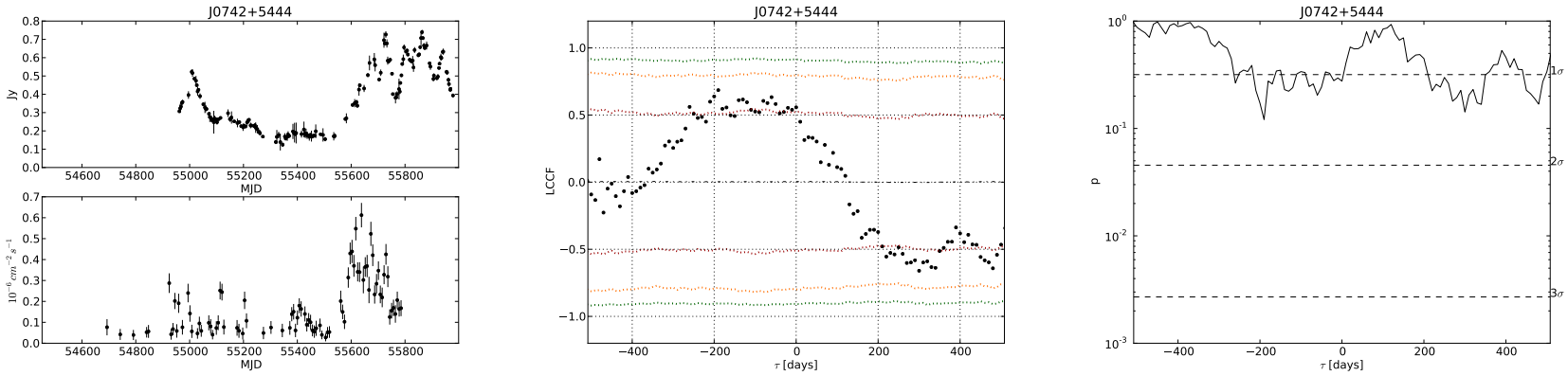

Figure F.29: Light curves and cross-correlation significance for J0742+5444 in the case of $\beta_{radio} = 2.3$ and $\beta_{\gamma} = 1.6$. The most significant cross-correlation is at -190 ± 9 day with 87.90% significance.

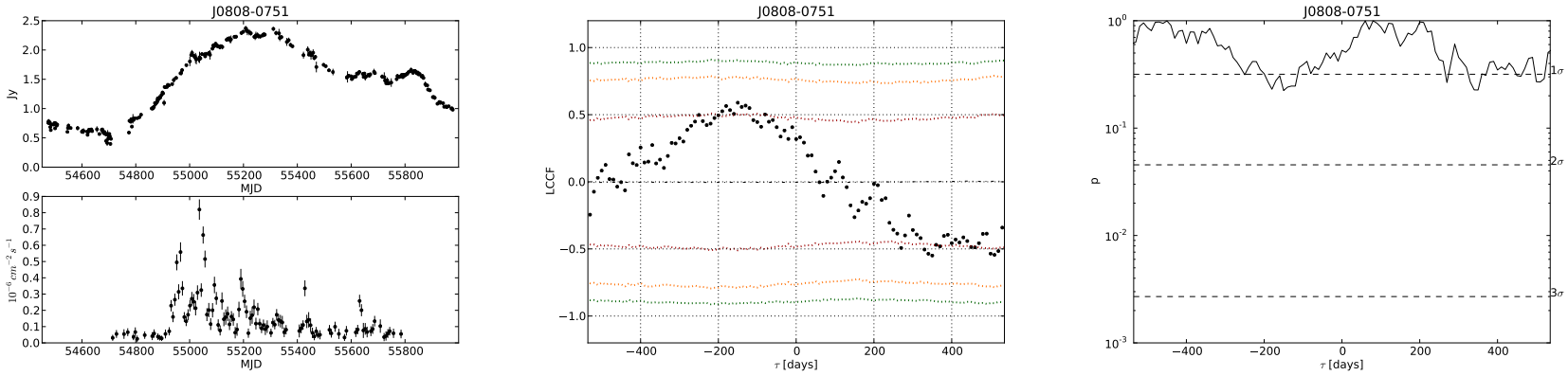

Figure F.30: Light curves and cross-correlation significance for J0808-0751 in the case of $\beta_{radio} = 2.3$ and $\beta_{\gamma} = 1.6$. The most significant cross-correlation is at -150 ± 15 day with 77.62% significance.

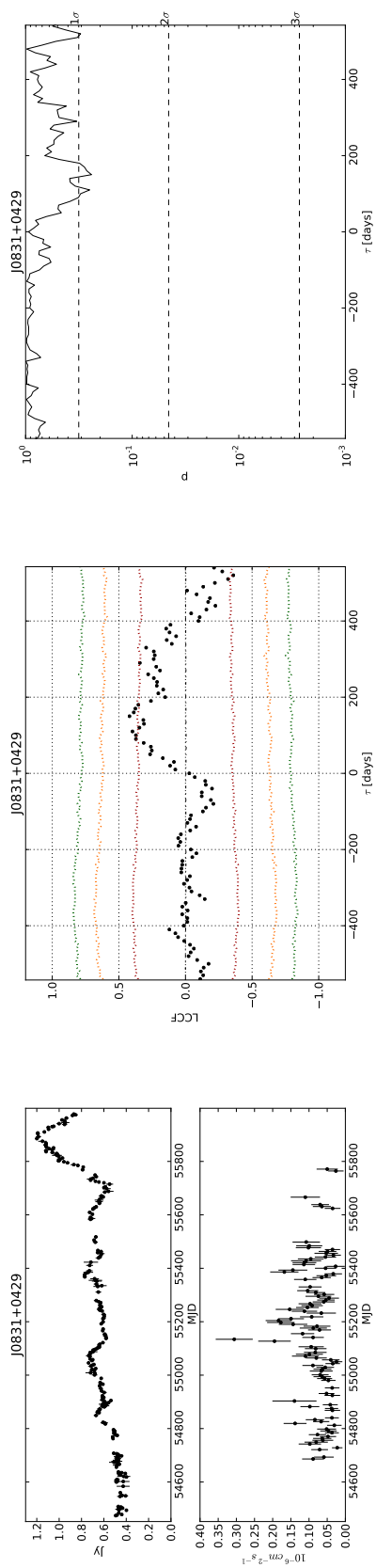

Figure F.31: Light curves and cross-correlation significance for J0831+0429 in the case of $\beta_{radio} = 2.3$ and $\beta_\gamma = 1.6$. The most significant cross-correlation is at 150 ± 16 day with 75.92% significance.

Figure F.32: Light curves and cross-correlation significance for J0854+2006 in the case of $\beta_{radio} = 2.3$ and $\beta_\gamma = 1.6$. The most significant cross-correlation is at -70 $\pm$ 16 day with 62.48% significance.

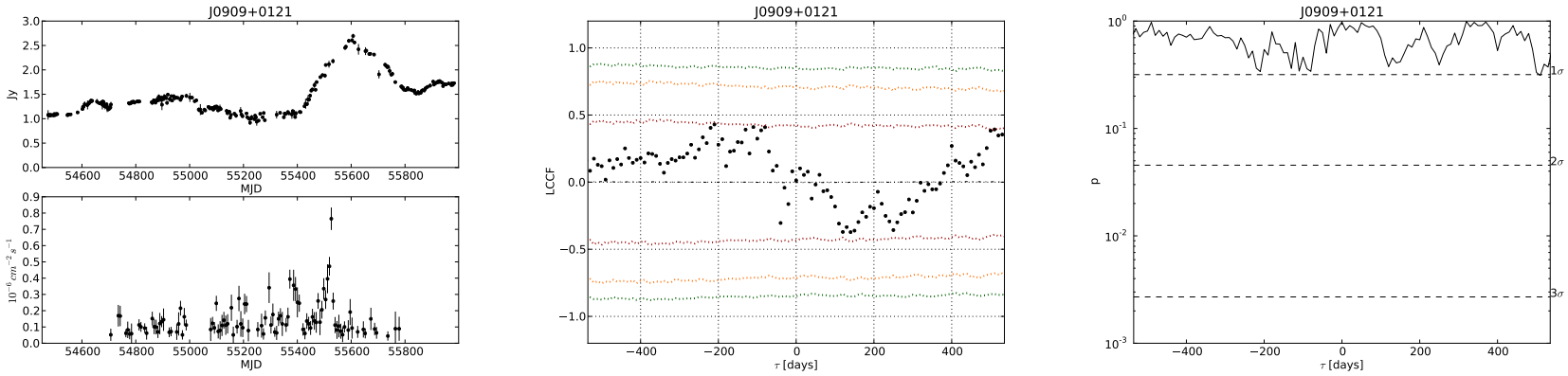

Figure F.33: Light curves and cross-correlation significance for J0909+0121 in the case of $\beta_{radio} = 2.3$ and $\beta_{\gamma} = 1.6$. The most significant cross-correlation is at 510 ± 16 day with 68.85% significance.

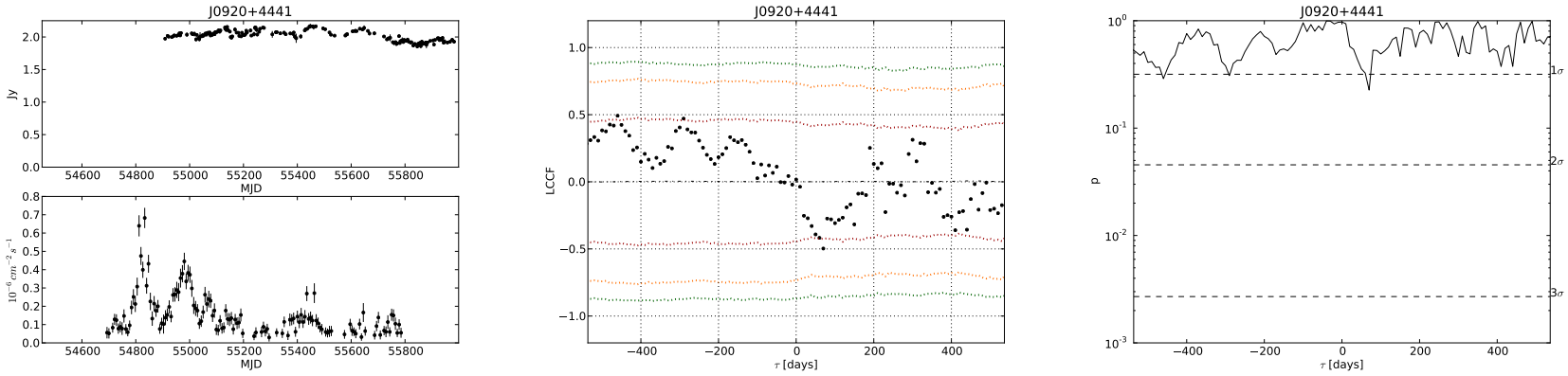

Figure F.34: Light curves and cross-correlation significance for J0920+4441 in the case of $\beta_{radio} = 2.3$ and $\beta_{\gamma} = 1.6$. The most significant cross-correlation is at -460 ± 13 day with 71.14% significance.

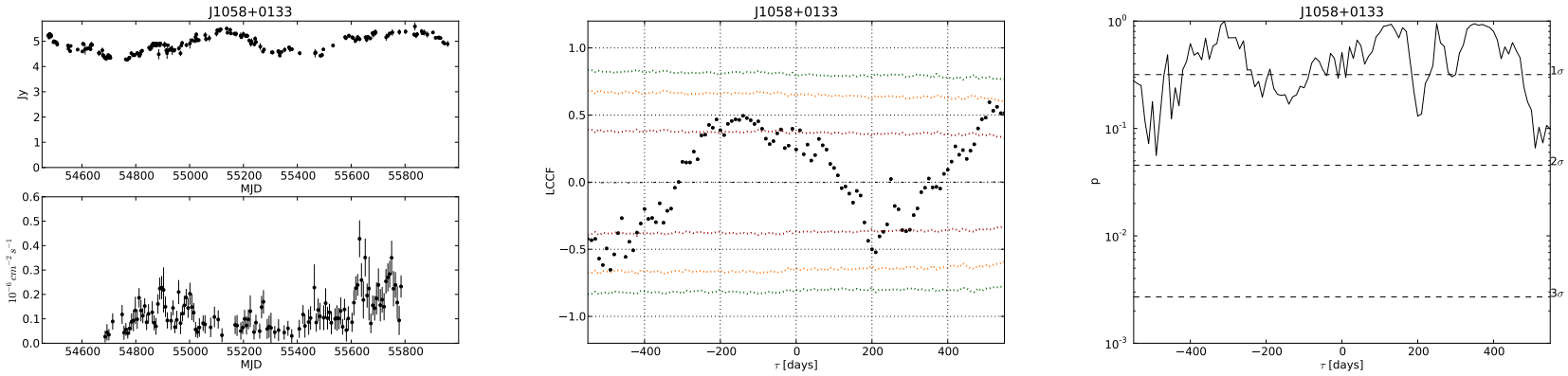

Figure F.35: Light curves and cross-correlation significance for J1058+0133 in the case of $\beta_{radio} = 2.3$ and $\beta_{\gamma} = 1.6$. The most significant cross-correlation is at 510 $\pm$ 15 day with 93.42% significance.

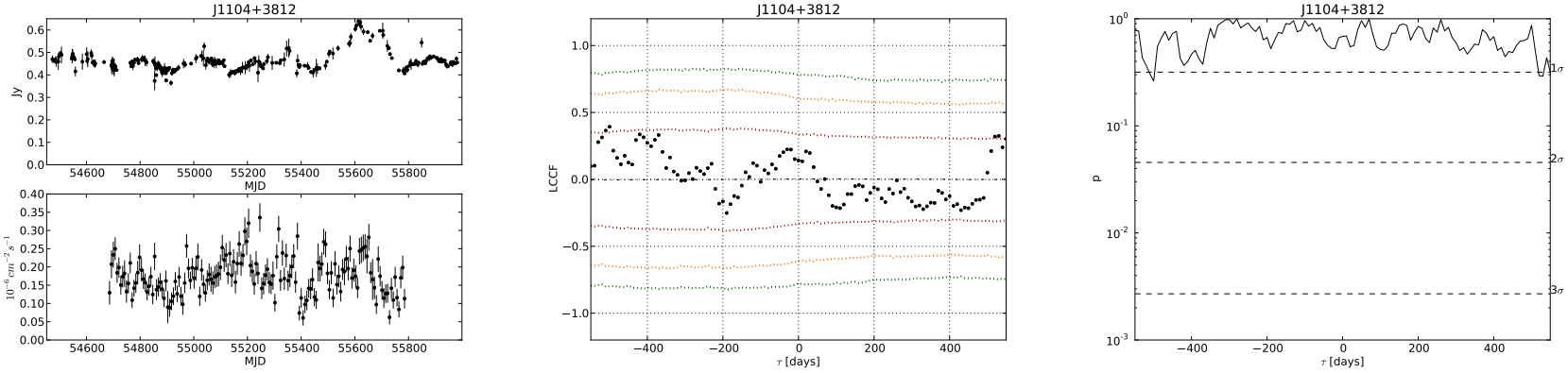

Figure F.36: Light curves and cross-correlation significance for J1104+3812 in the case of $\beta_{radio} = 2.3$ and $\beta_{\gamma} = 1.6$. The most significant cross-correlation is at -500 $\pm$ 10 day with 73.78% significance.

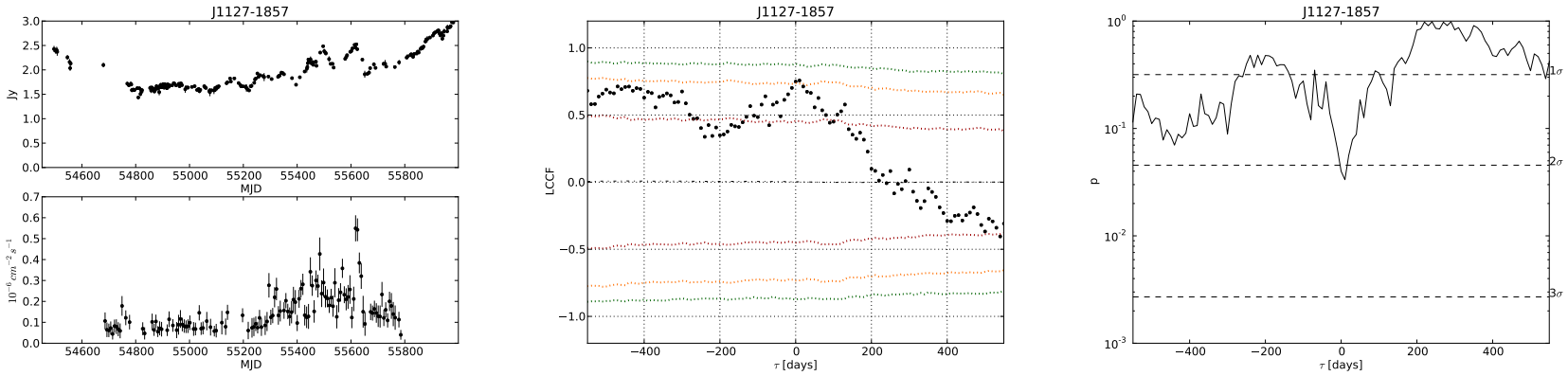

Figure F.37: Light curves and cross-correlation significance for J1127-1857 in the case of $\beta_{radio} = 2.3$ and $\beta_\gamma = 1.6$. The most significant cross-correlation is at 10 ± 11 day with 96.67% significance.

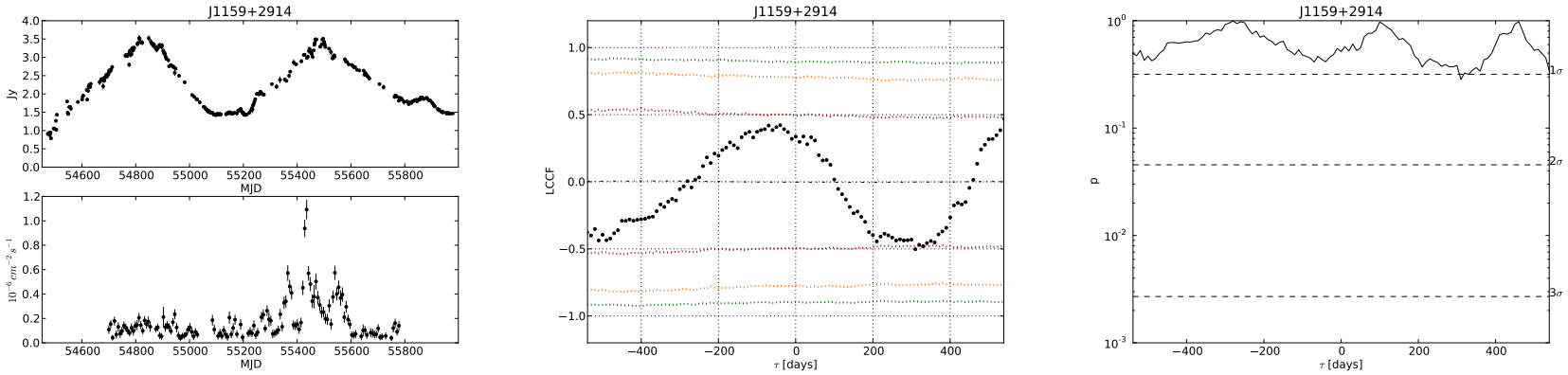

Figure F.38: Light curves and cross-correlation significance for J1159+2914 in the case of $\beta_{radio} = 2.3$ and $\beta_\gamma = 1.6$. The most significant cross-correlation is at -70 $\pm$ 17 day with 58.74% significance.

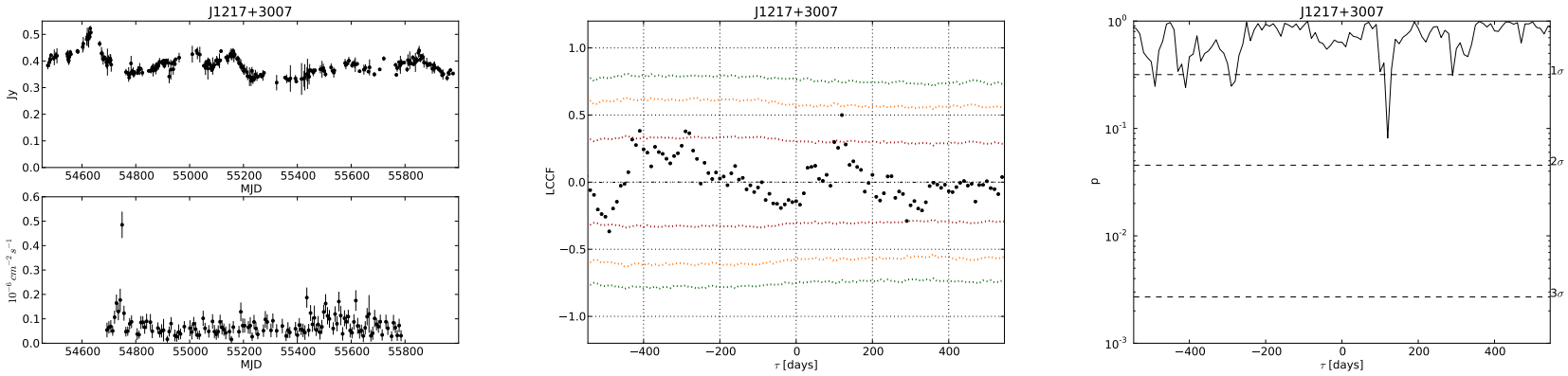

Figure F.39: Light curves and cross-correlation significance for J1217+3007 in the case of $\beta_{radio} = 2.3$ and $\beta_{\gamma} = 1.6$. The most significant cross-correlation is at 120 ± 9 day with 91.88% significance.

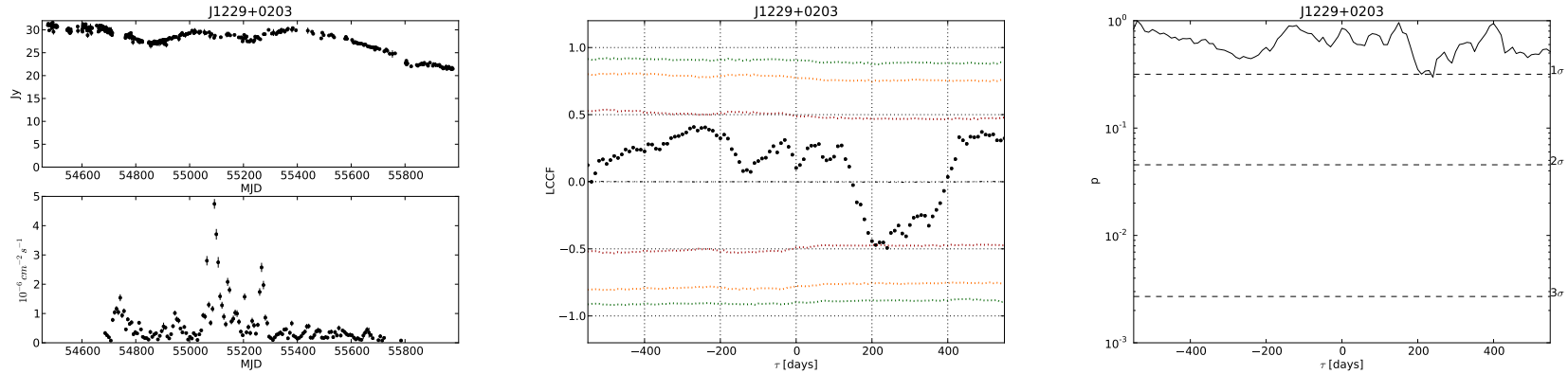

Figure F.40: Light curves and cross-correlation significance for J1229+0203 in the case of $\beta_{radio} = 2.3$ and $\beta_{\gamma} = 1.6$. The most significant cross-correlation is at -270 ± 16 day with 55.83% significance.

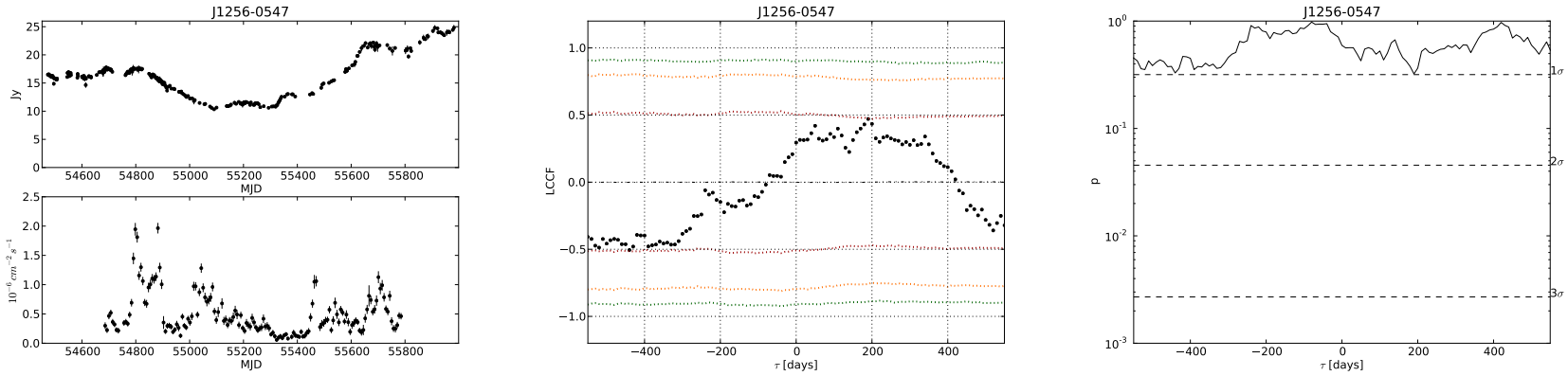

Figure F.41: Light curves and cross-correlation significance for J1256-0547 in the case of $\beta_{radio} = 2.3$ and $\beta_{\gamma} = 1.6$. The most significant cross-correlation is at 190 ± 10 day with 67.79% significance.

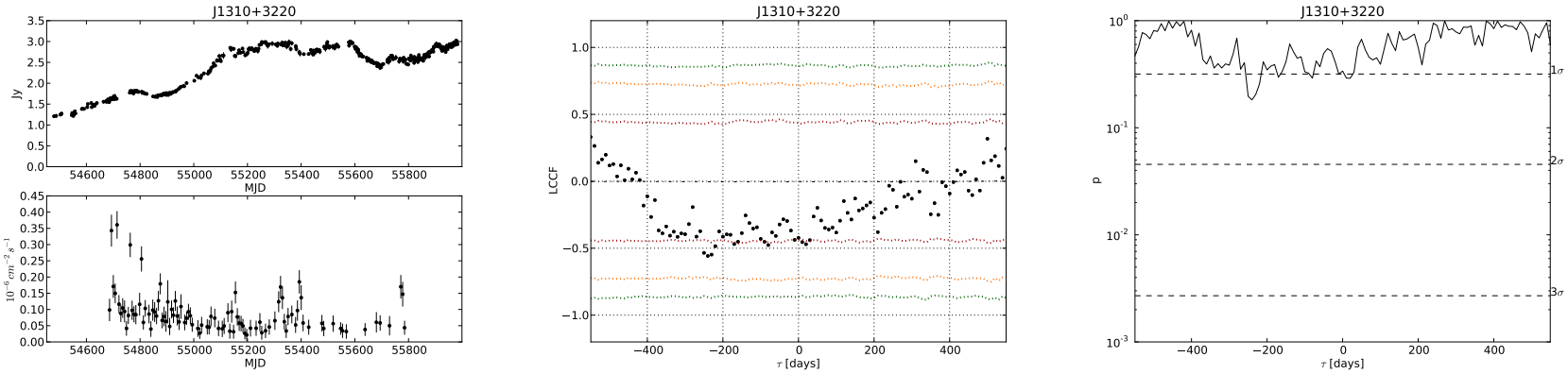

Figure F.42: Light curves and cross-correlation significance for J1310+3220 in the case of $\beta_{radio} = 2.3$ and $\beta_{\gamma} = 1.6$. The most significant cross-correlation is at 500 ± 56 day with 48.74% significance.

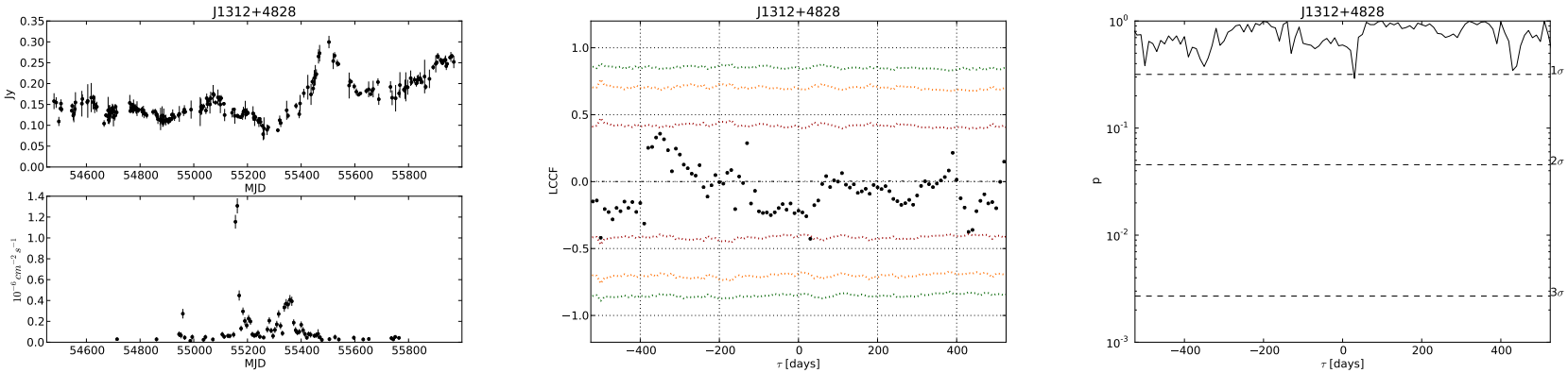

Figure F.43: Light curves and cross-correlation significance for J1312+4828 in the case of $\beta_{radio} = 2.3$ and $\beta_\gamma = 1.6$. The most significant cross-correlation is at -350 ± 16 day with 62.38% significance.

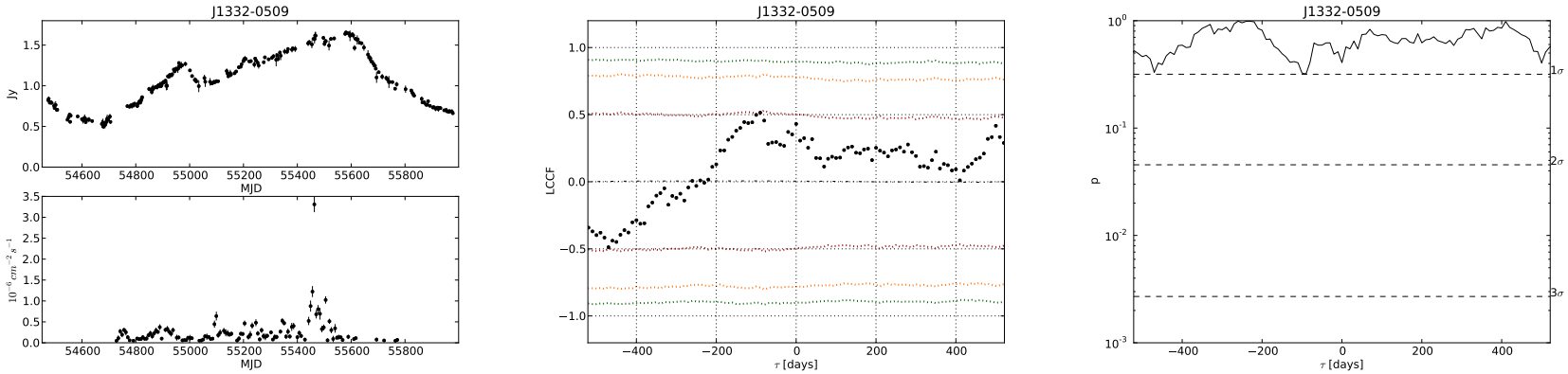

Figure F.44: Light curves and cross-correlation significance for J1332-0509 in the case of $\beta_{radio} = 2.3$ and $\beta_\gamma = 1.6$. The most significant cross-correlation is at -90 ± 15 day with 68.12% significance.

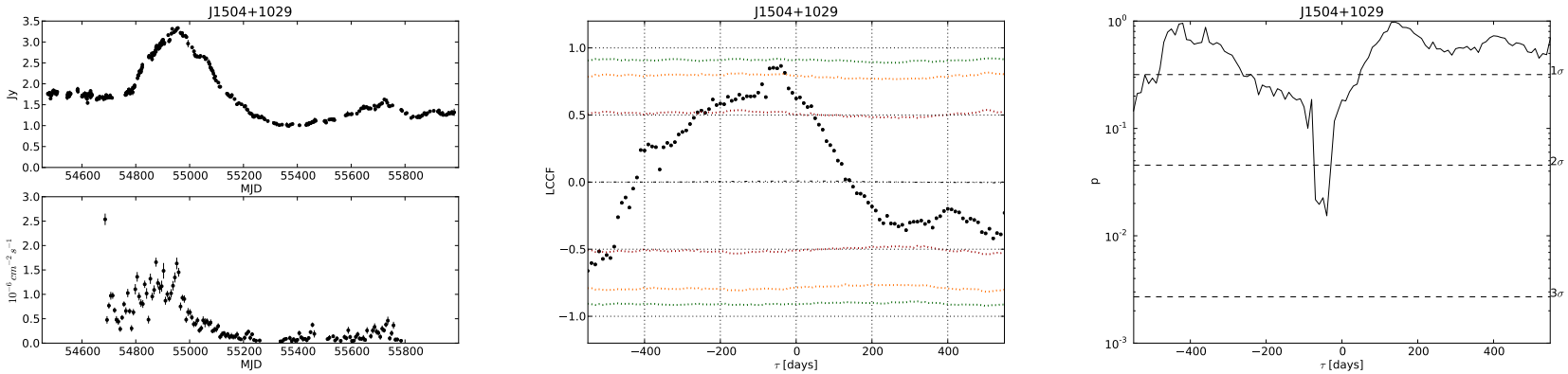

Figure F.45: Light curves and cross-correlation significance for J1504+1029 in the case of $\beta_{radio} = 2.3$ and $\beta_{\gamma} = 1.6$. The most significant cross-correlation is at -40 ± 13 day with 98.47% significance.

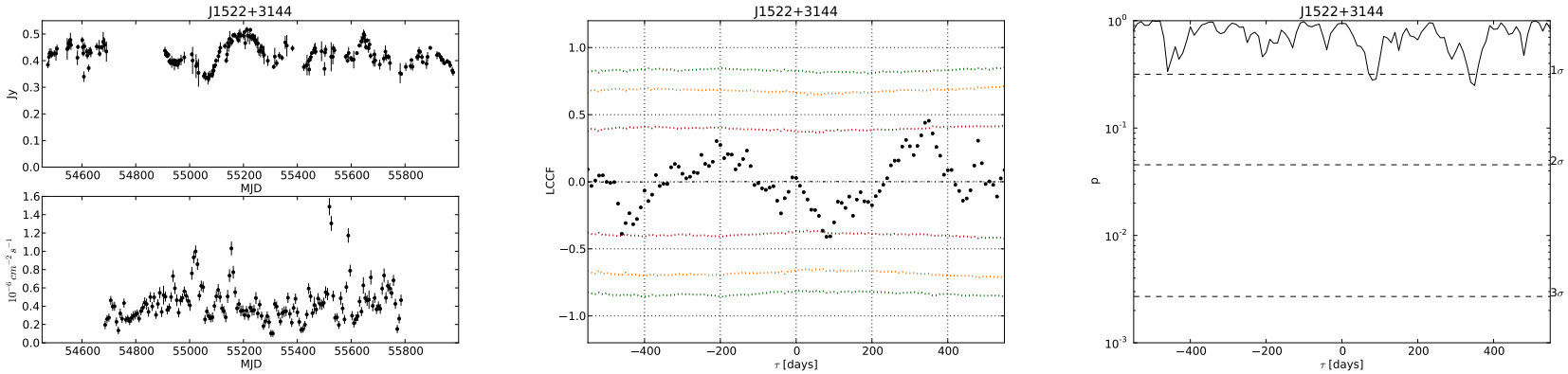

Figure F.46: Light curves and cross-correlation significance for J1522+3144 in the case of $\beta_{radio} = 2.3$ and $\beta_{\gamma} = 1.6$. The most significant cross-correlation is at 350 ± 9 day with 75.09% significance.

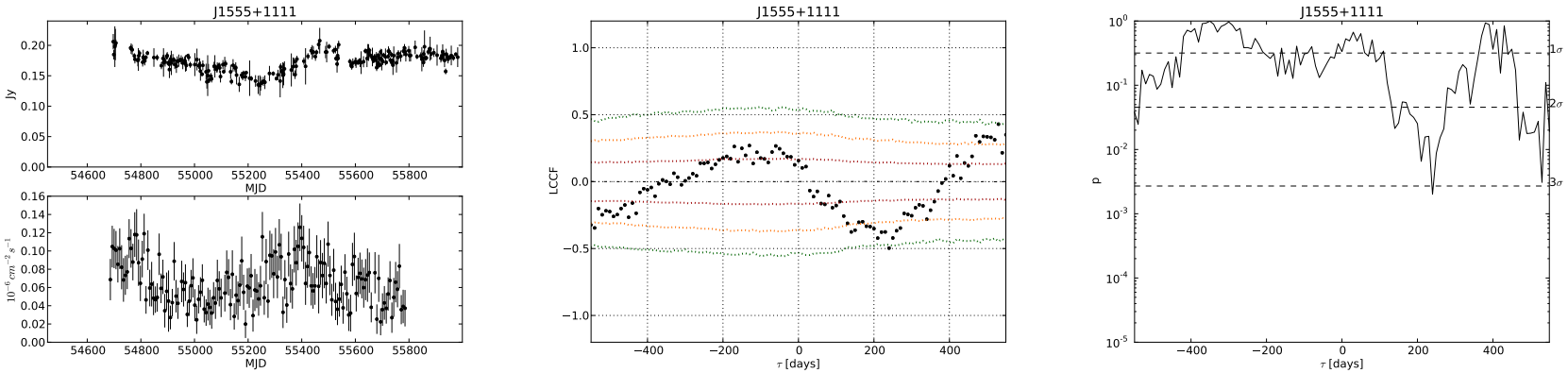

Figure F.47: Light curves and cross-correlation significance for J1555+1111 in the case of $\beta_{radio} = 2.3$ and $\beta_\gamma = 1.6$. The most significant cross-correlation is at 530 ± 17 day with 99.69% significance.

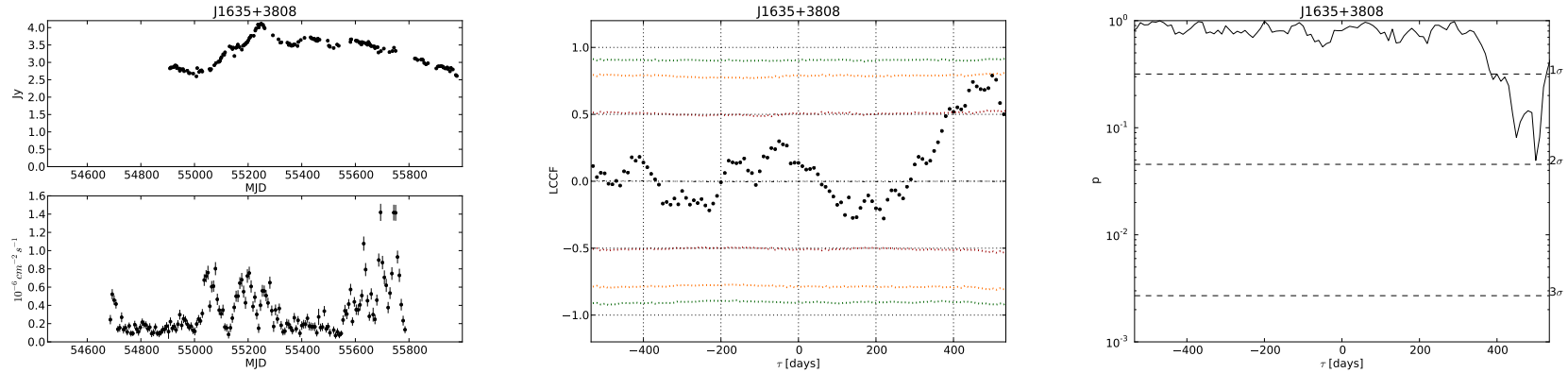

Figure F.48: Light curves and cross-correlation significance for J1635+3808 in the case of $\beta_{radio} = 2.3$ and $\beta_\gamma = 1.6$. The most significant cross-correlation is at 500 ± 9 day with 95.06% significance.

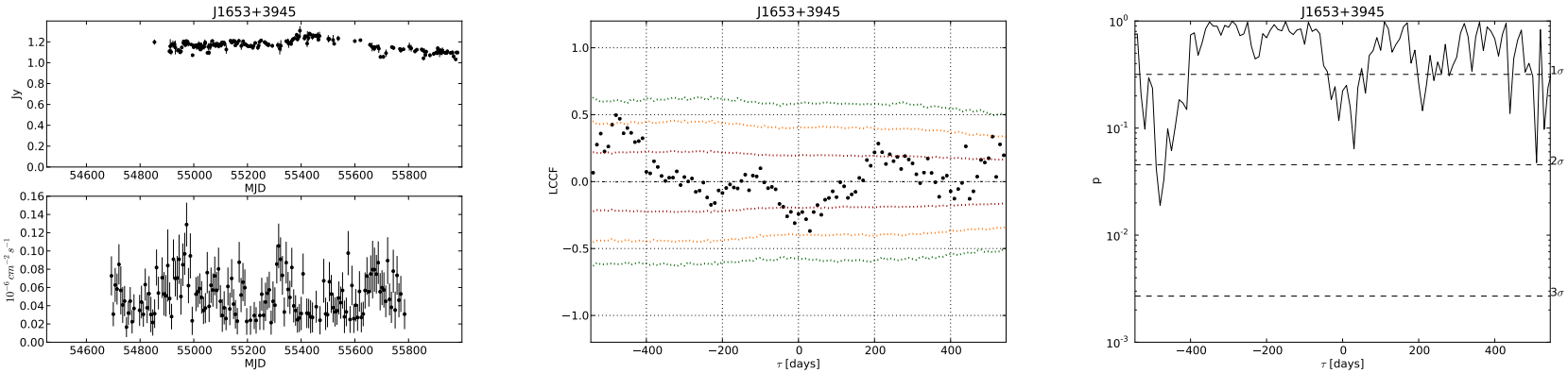

Figure F.49: Light curves and cross-correlation significance for J1653+3945 in the case of $\beta_{radio} = 2.3$ and $\beta_\gamma = 1.6$. The most significant cross-correlation is at -480 ± 12 day with 98.11% significance.

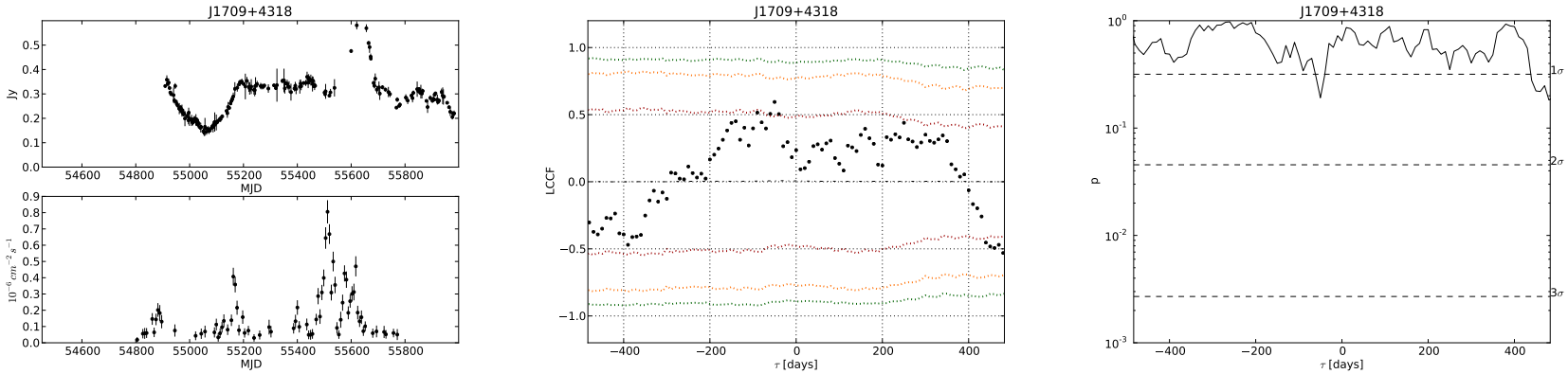

Figure F.50: Light curves and cross-correlation significance for J1709+4318 in the case of $\beta_{radio} = 2.3$ and $\beta_\gamma = 1.6$. The most significant cross-correlation is at -50 ± 12 day with 80.86% significance.

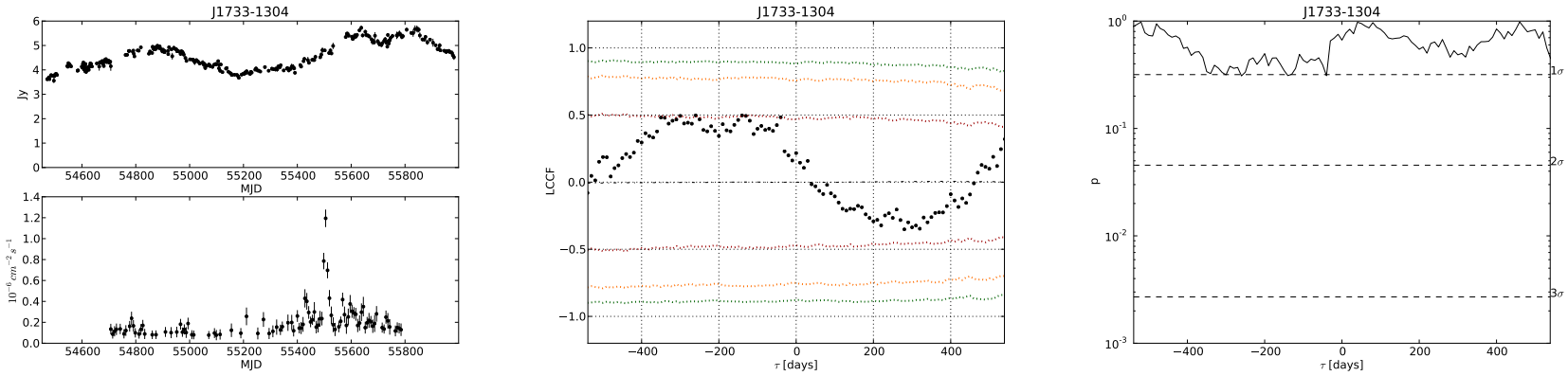

Figure F.51: Light curves and cross-correlation significance for J1733-1304 in the case of $\beta_{radio} = 2.3$ and $\beta_{\gamma} = 1.6$. The most significant cross-correlation is at -260 $\pm$ 14 day with 69.14% significance.

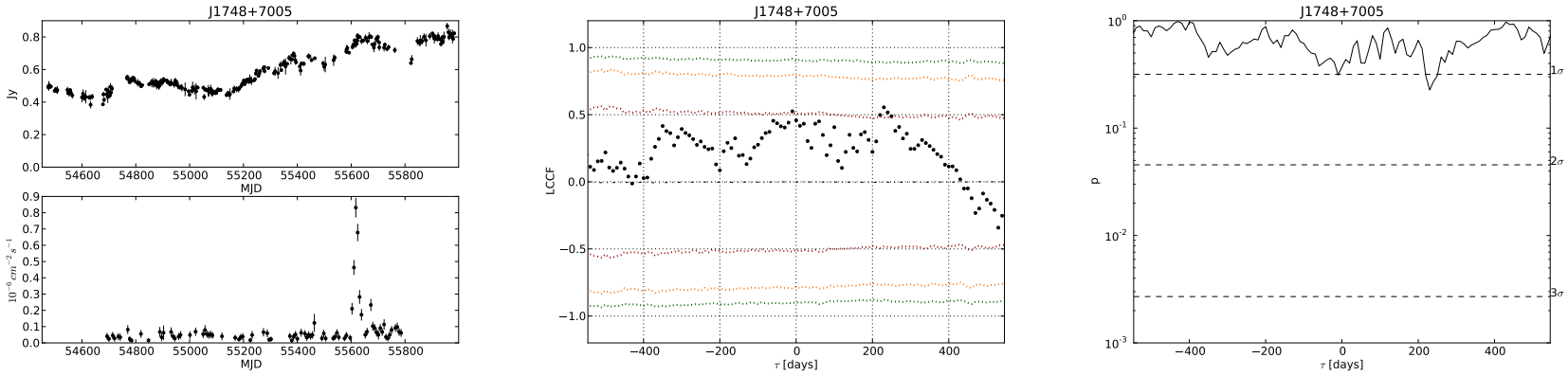

Figure F.52: Light curves and cross-correlation significance for J1748+7005 in the case of $\beta_{radio} = 2.3$ and $\beta_{\gamma} = 1.6$. The most significant cross-correlation is at 230 $\pm$ 10 day with 77.32% significance.

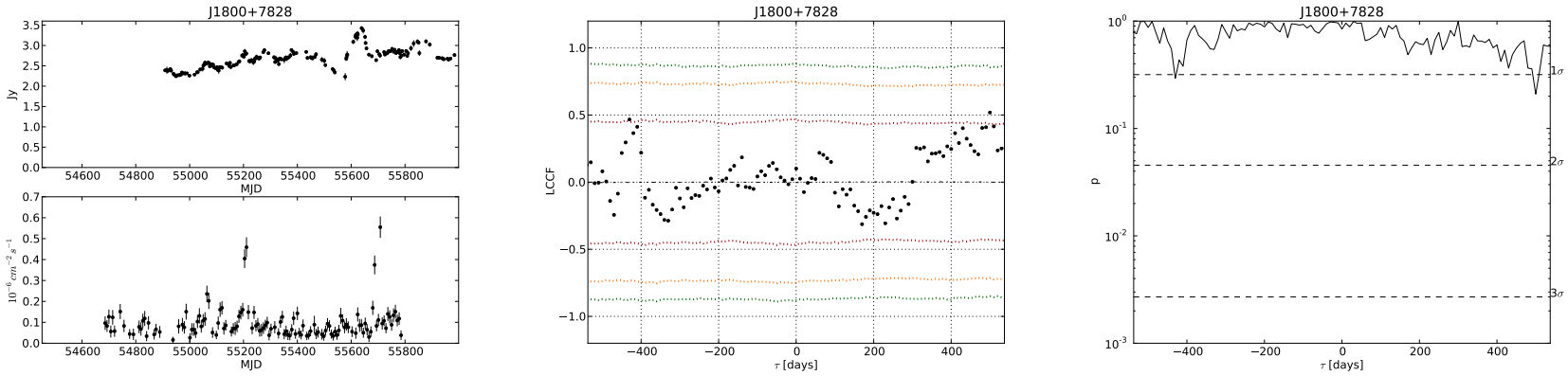

Figure F.53: Light curves and cross-correlation significance for J1800+7828 in the case of $\beta_{radio} = 2.3$ and $\beta_\gamma = 1.6$. The most significant cross-correlation is at 500 ± 10 day with 79.11% significance.

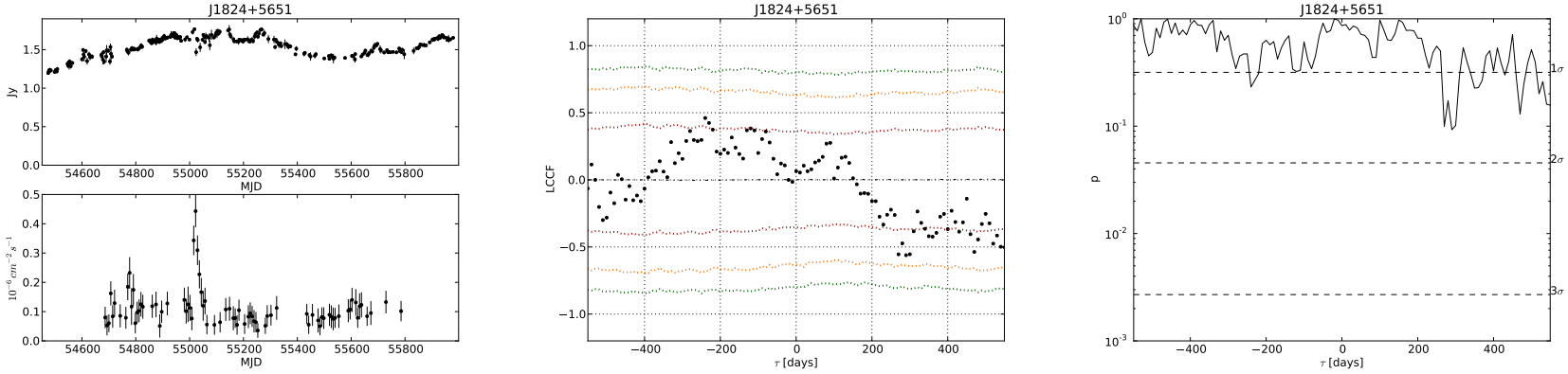

Figure F.54: Light curves and cross-correlation significance for J1824+5651 in the case of $\beta_{radio} = 2.3$ and $\beta_\gamma = 1.6$. The most significant cross-correlation is at -240 ± 12 day with 76.82% significance.

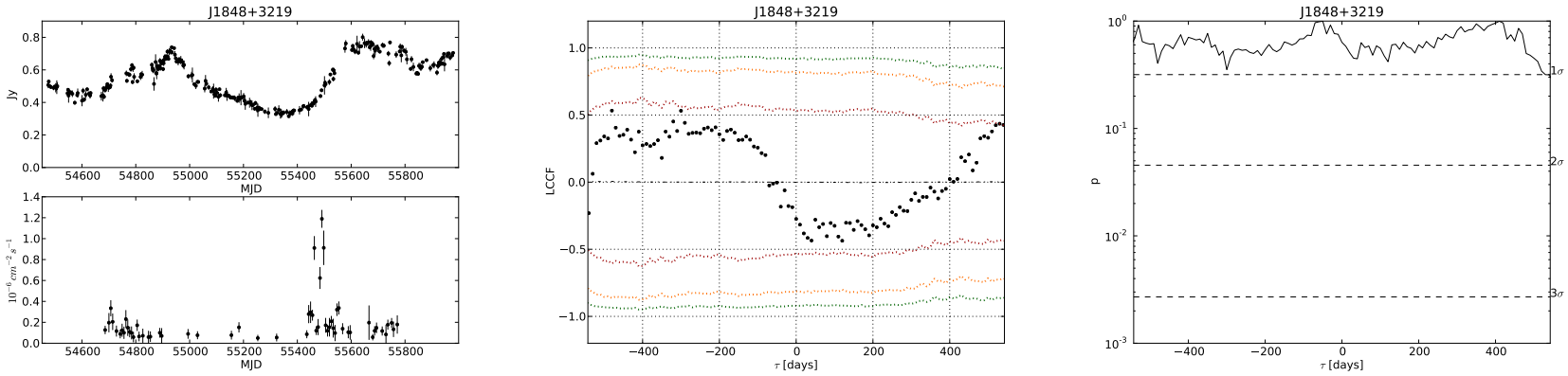

Figure F.55: Light curves and cross-correlation significance for J1848+3219 in the case of $\beta_{radio} = 2.3$ and $\beta_{\gamma} = 1.6$. The most significant cross-correlation is at -300 ± 12 day with 64.71% significance.

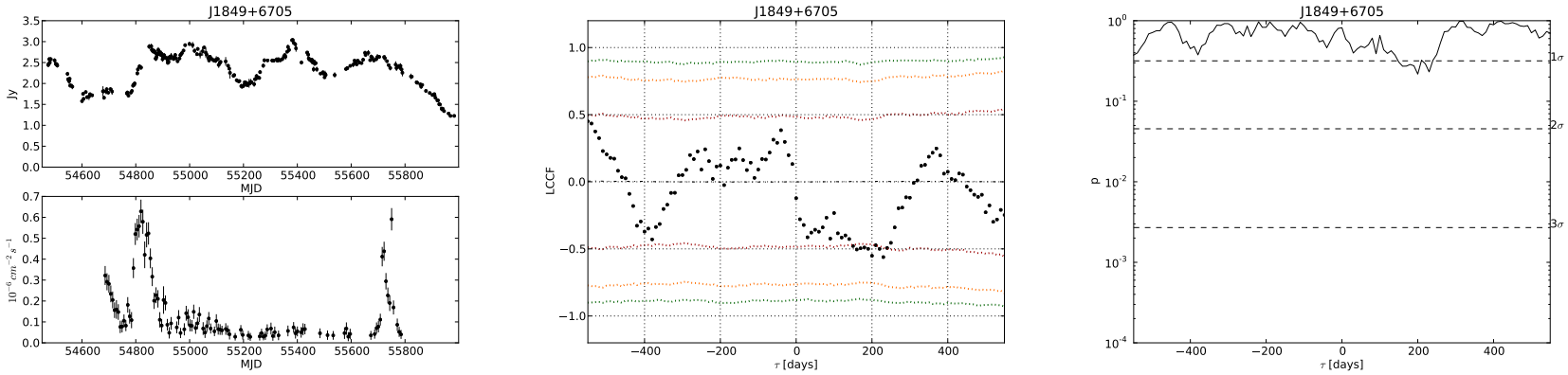

Figure F.56: Light curves and cross-correlation significance for J1849+6705 in the case of $\beta_{radio} = 2.3$ and $\beta_{\gamma} = 1.6$. The most significant cross-correlation is at -40 ± 9 day with 53.86% significance.

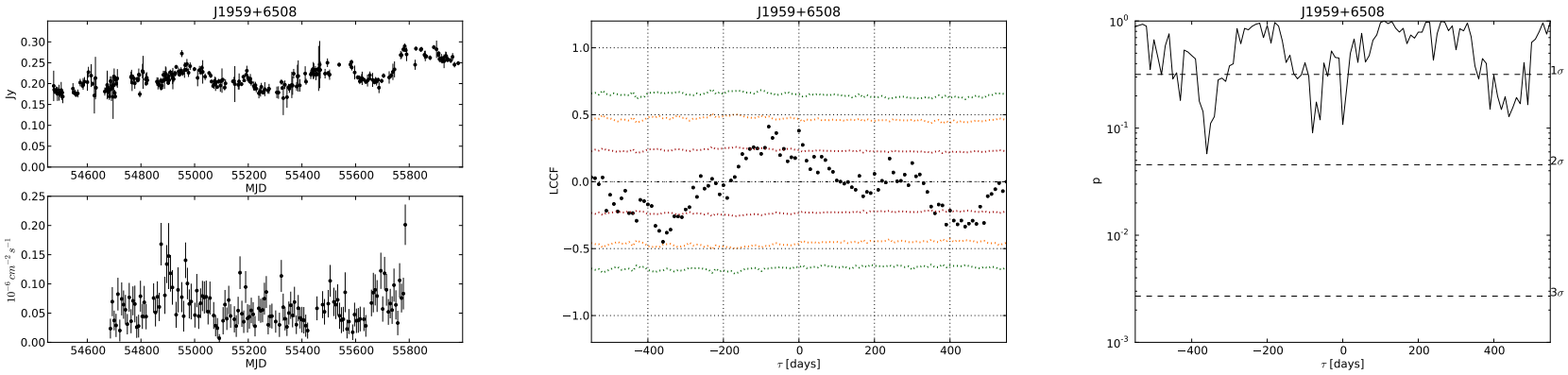

Figure F.57: Light curves and cross-correlation significance for J1959+6508 in the case of $\beta_{radio} = 2.3$ and $\beta_{\gamma} = 1.6$. The most significant cross-correlation is at -80 ± 13 day with 90.97% significance.

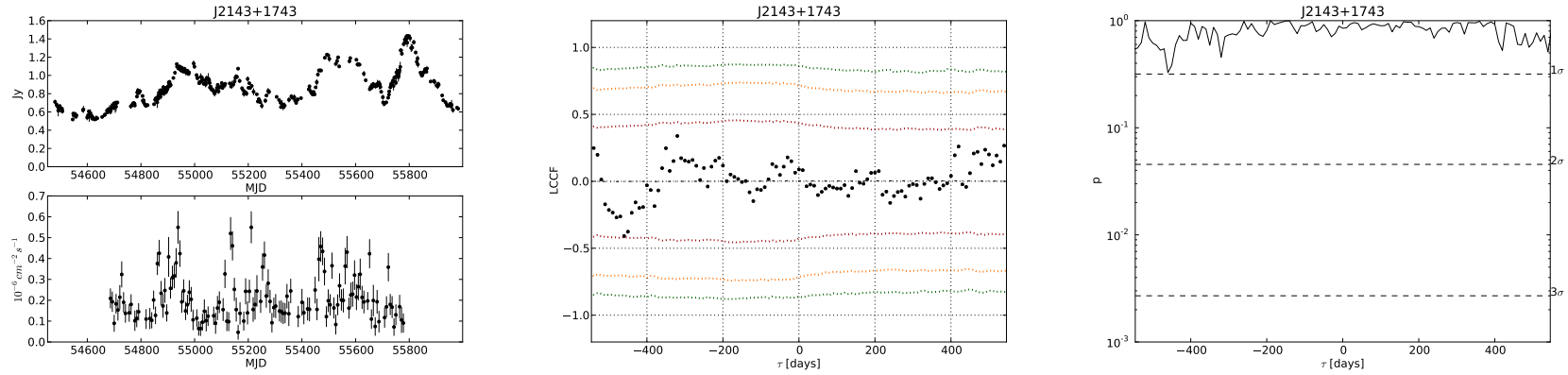

Figure F.58: Light curves and cross-correlation significance for J2143+1743 in the case of $\beta_{radio} = 2.3$ and $\beta_{\gamma} = 1.6$. The most significant cross-correlation is at -320 ± 11 day with 54.40% significance.

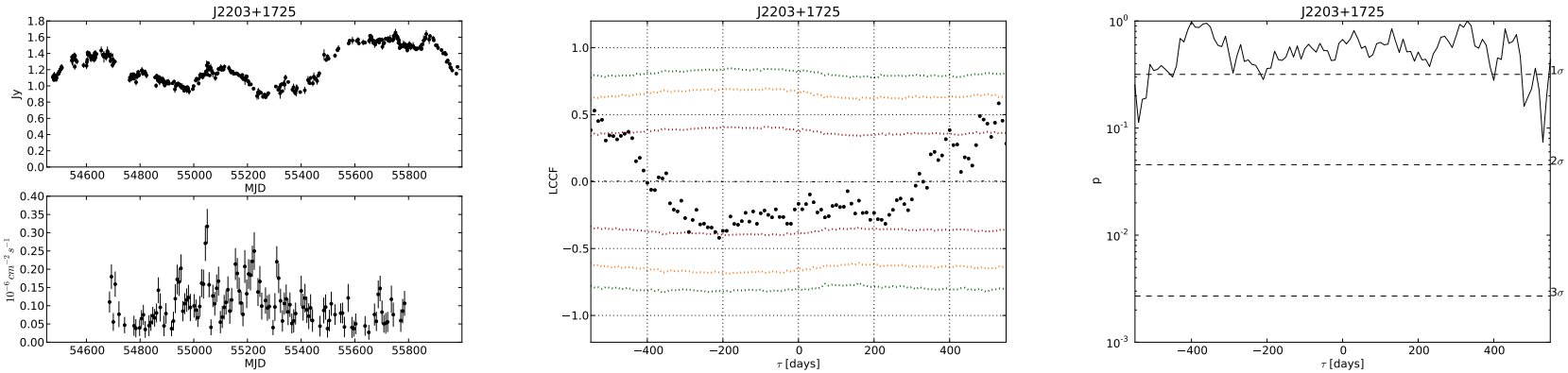

Figure F.59: Light curves and cross-correlation significance for J2203+1725 in the case of $\beta_{radio} = 2.3$ and $\beta_\gamma = 1.6$. The most significant cross-correlation is at 530 ± 9 day with 92.61% significance.

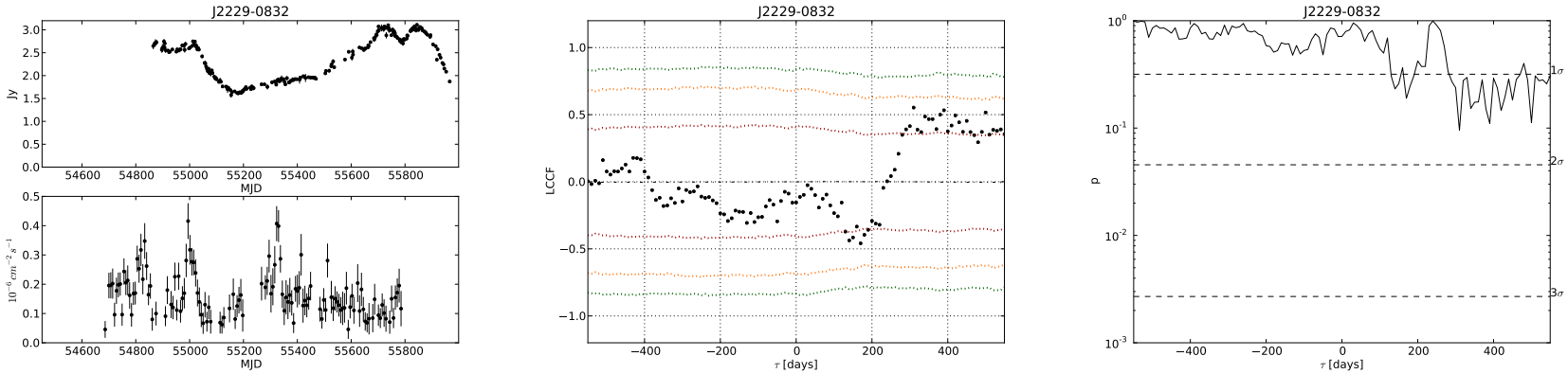

Figure F.60: Light curves and cross-correlation significance for J2229-0832 in the case of $\beta_{radio} = 2.3$ and $\beta_\gamma = 1.6$. The most significant cross-correlation is at 310 ± 13 day with 90.47% significance.

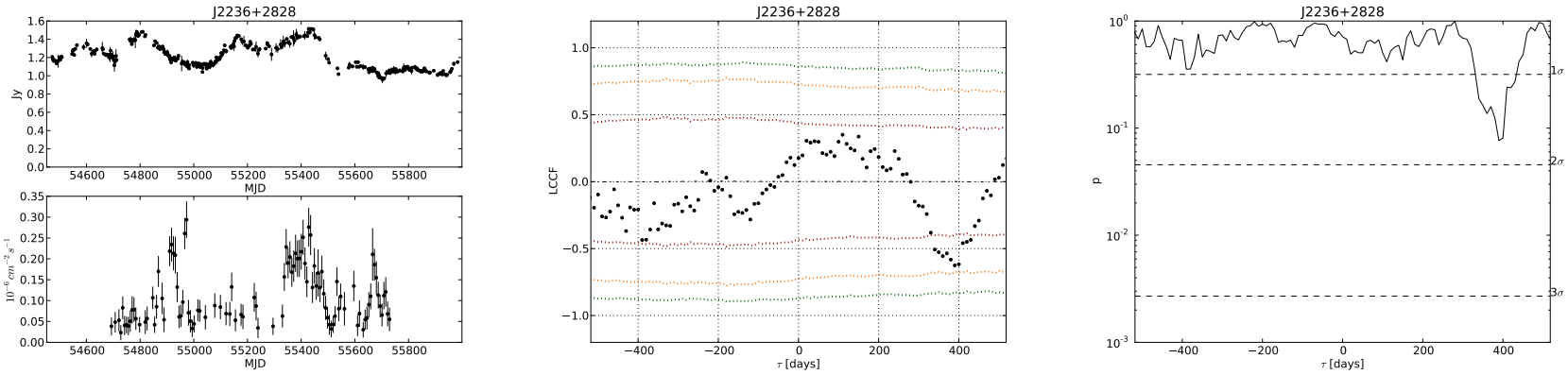

Figure F.61: Light curves and cross-correlation significance for J2236+2828 in the case of $\beta_{radio} = 2.3$ and $\beta_\gamma = 1.6$. The most significant cross-correlation is at 110 ± 14 day with 58.37% significance.

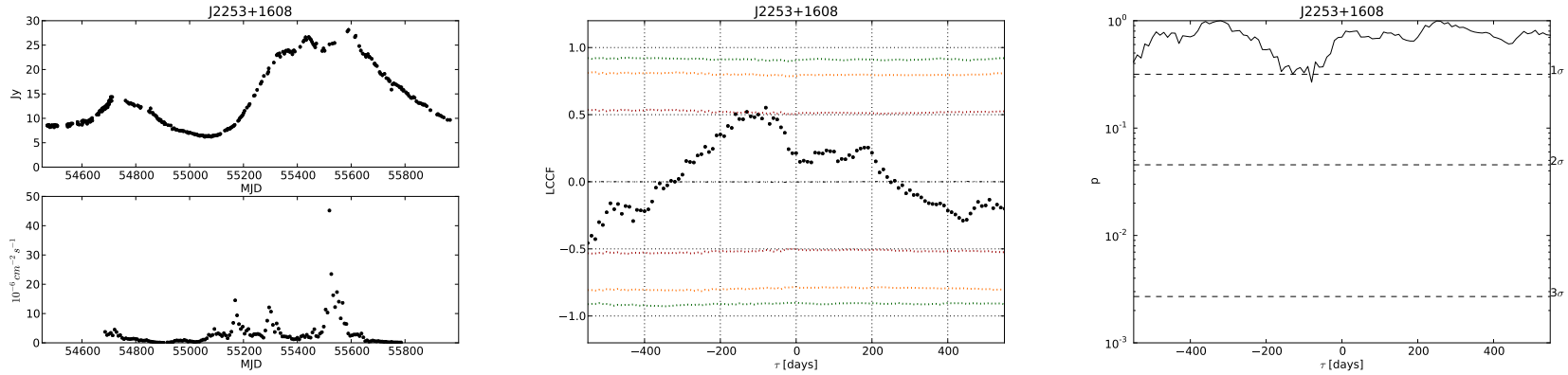

Figure F.62: Light curves and cross-correlation significance for J2253+1608 in the case of $\beta_{radio} = 2.3$ and $\beta_\gamma = 1.6$. The most significant cross-correlation is at -80 ± 17 day with 73.28% significance.

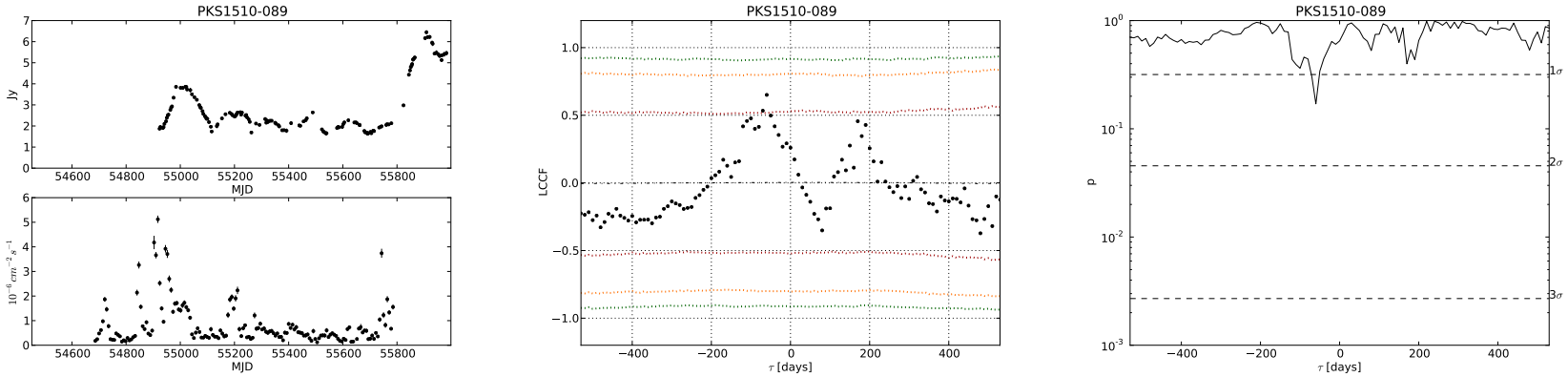

Figure F.63: Light curves and cross-correlation significance for PKS1510-089 in the case of $\beta_{radio} = 2.3$ and $\beta_{\gamma} = 1.6$. The most significant cross-correlation is at -60 ± 6 day with 83.02% significance.

F.2 Cross-correlation significance for $\beta_{radio} = 2.3$ and $\beta_{gamma} = 0.7$

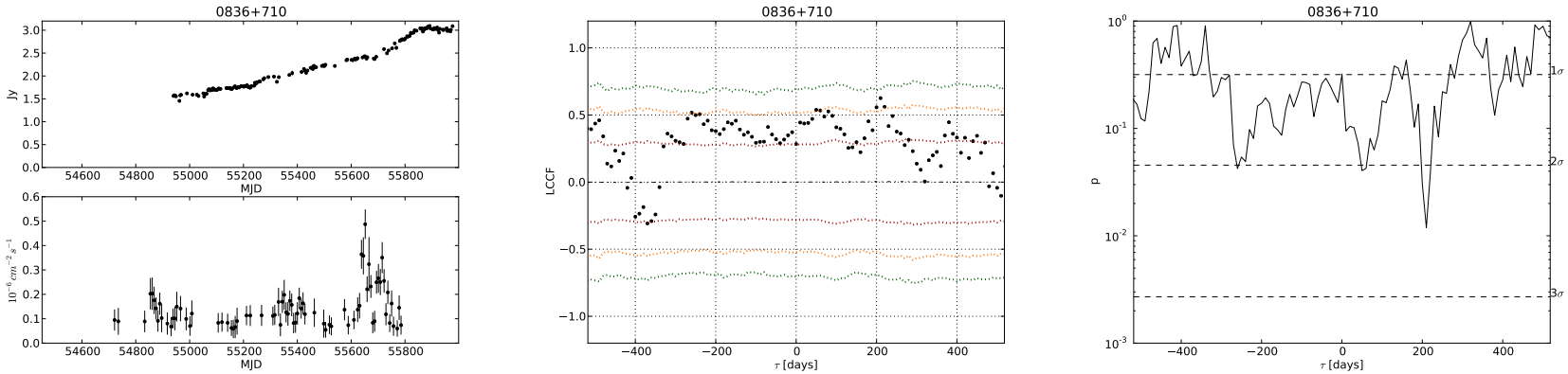

Figure F.64: Light curves and cross-correlation significance for 0836+710 in the case of $\beta_{radio} = 2.3$ and $\beta_\gamma = 0.7$. The most significant cross-correlation is at 210 $\pm$ 11 day with 98.81% significance.

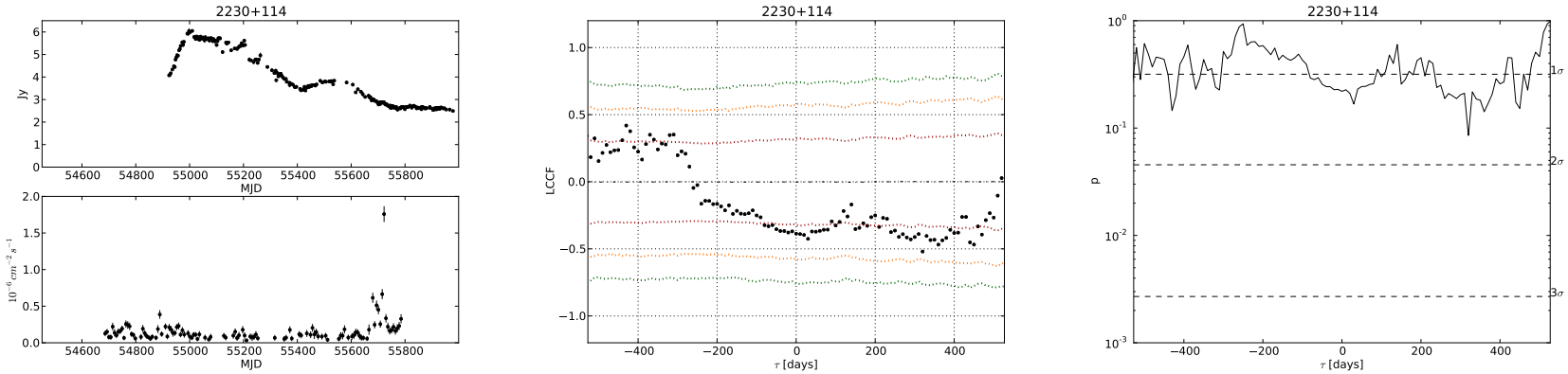

Figure F.65: Light curves and cross-correlation significance for 2230+114 in the case of $\beta_{radio} = 2.3$ and $\beta_\gamma = 0.7$. The most significant cross-correlation is at -430 $\pm$ 9 day with 85.47% significance.

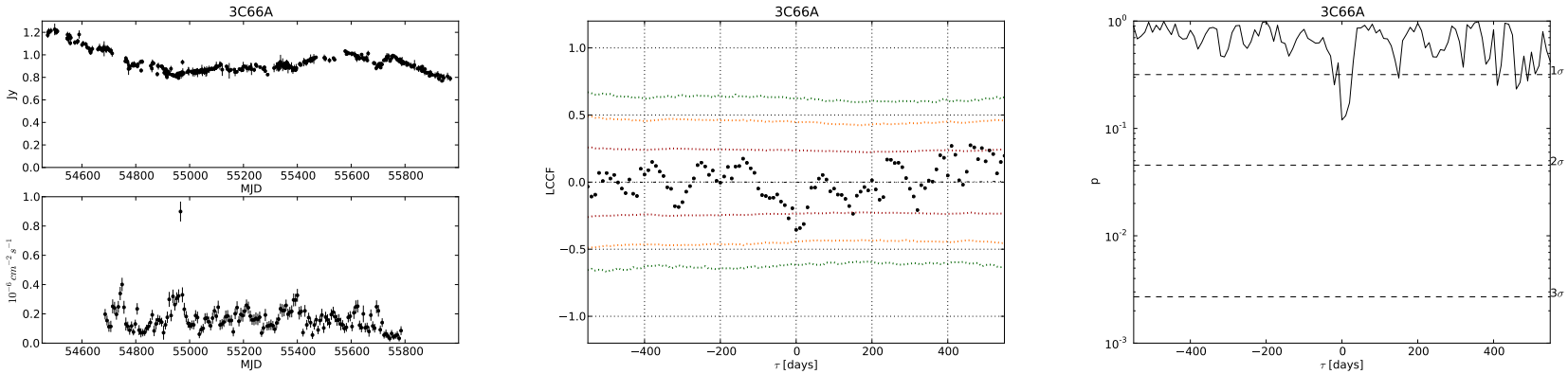

Figure F.66: Light curves and cross-correlation significance for 3C66A in the case of $\beta_{radio} = 2.3$ and $\beta_{\gamma} = 0.7$. The most significant cross-correlation is at 460 $\pm$ 15 day with 76.76% significance.

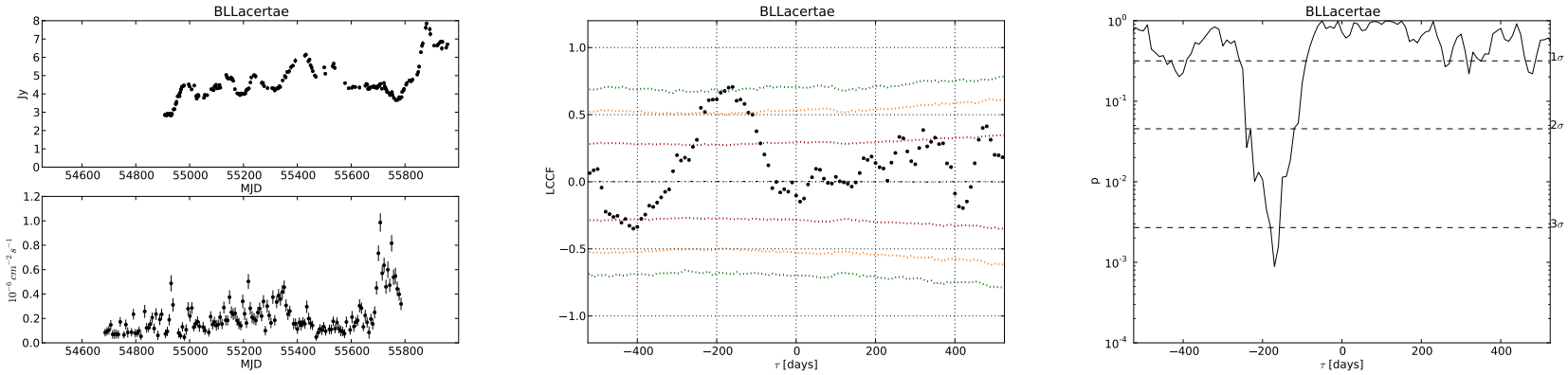

Figure F.67: Light curves and cross-correlation significance for BLLacertae in the case of $\beta_{radio} = 2.3$ and $\beta_{\gamma} = 0.7$. The most significant cross-correlation is at -160 $\pm$ 14 day with 99.84% significance.

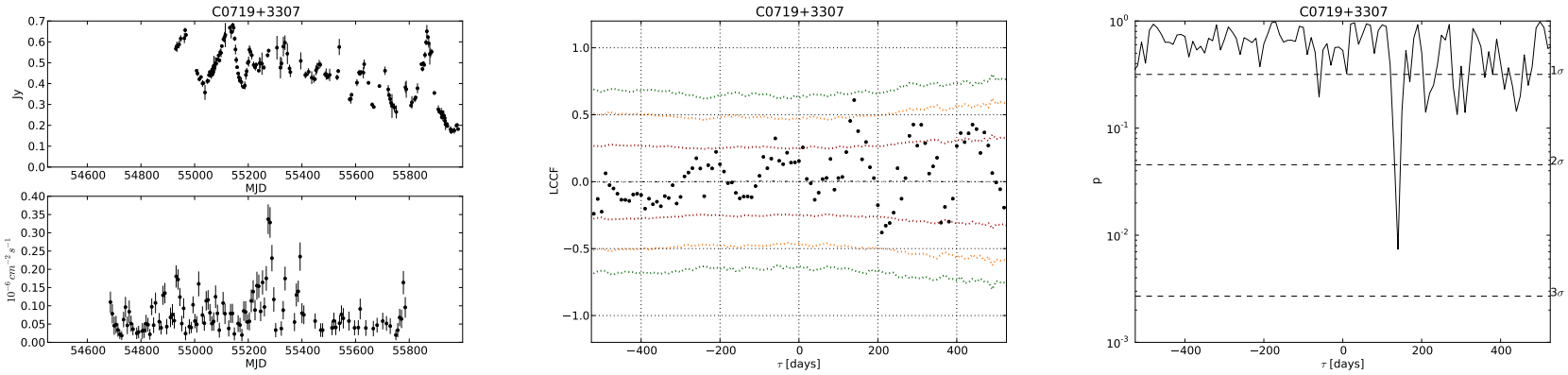

Figure F.68: Light curves and cross-correlation significance for C0719+3307 in the case of $\beta_{radio} = 2.3$ and $\beta_\gamma = 0.7$. The most significant cross-correlation is at 140 ± 8 day with 99.26% significance.

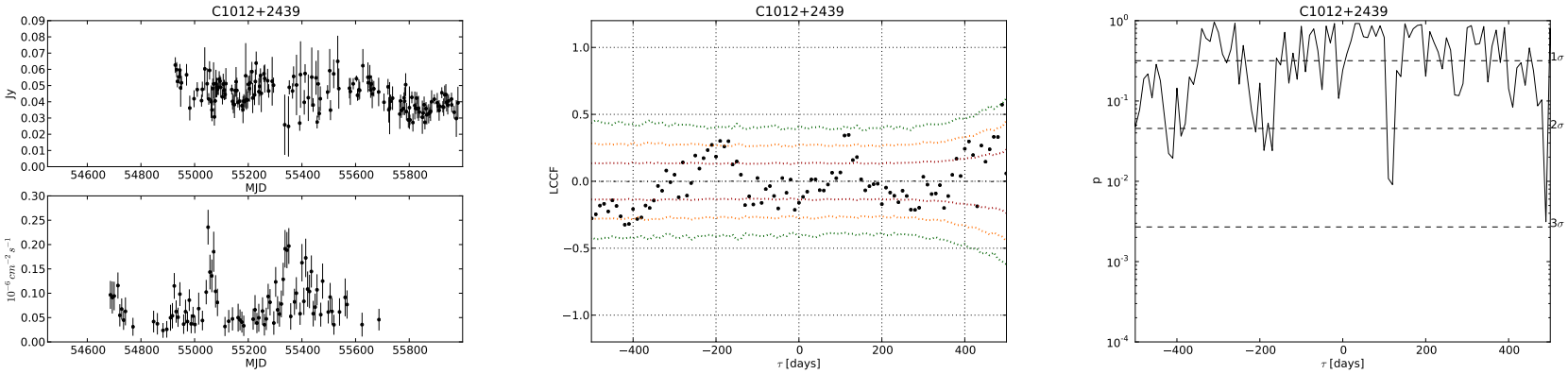

Figure F.69: Light curves and cross-correlation significance for C1012+2439 in the case of $\beta_{radio} = 2.3$ and $\beta_\gamma = 0.7$. The most significant cross-correlation is at 490 ± 47 day with 99.69% significance.

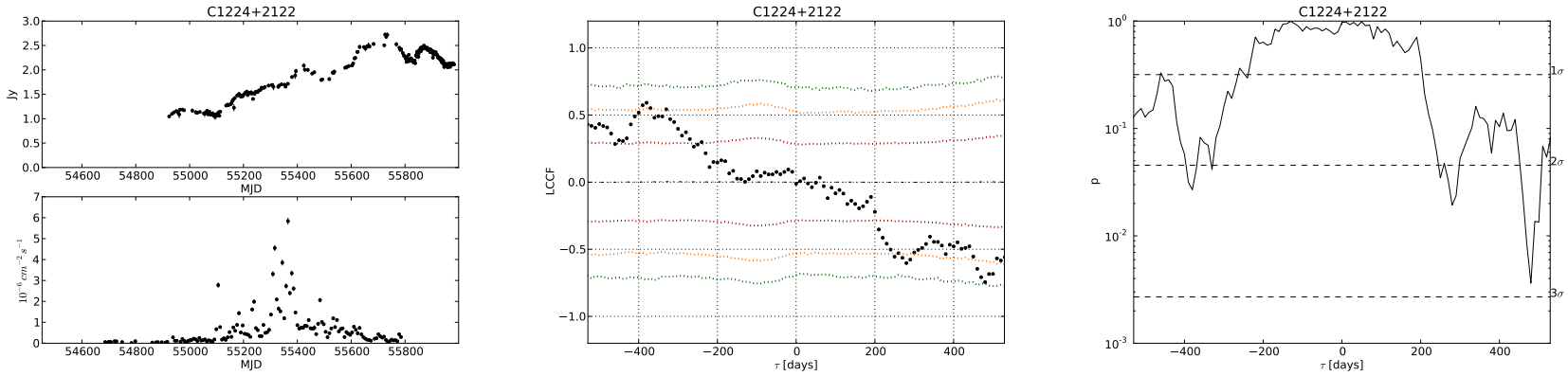

Figure F.70: Light curves and cross-correlation significance for C1224+2122 in the case of $\beta_{radio} = 2.3$ and $\beta_{\gamma} = 0.7$. The most significant cross-correlation is at -380 ± 9 day with 97.31% significance.

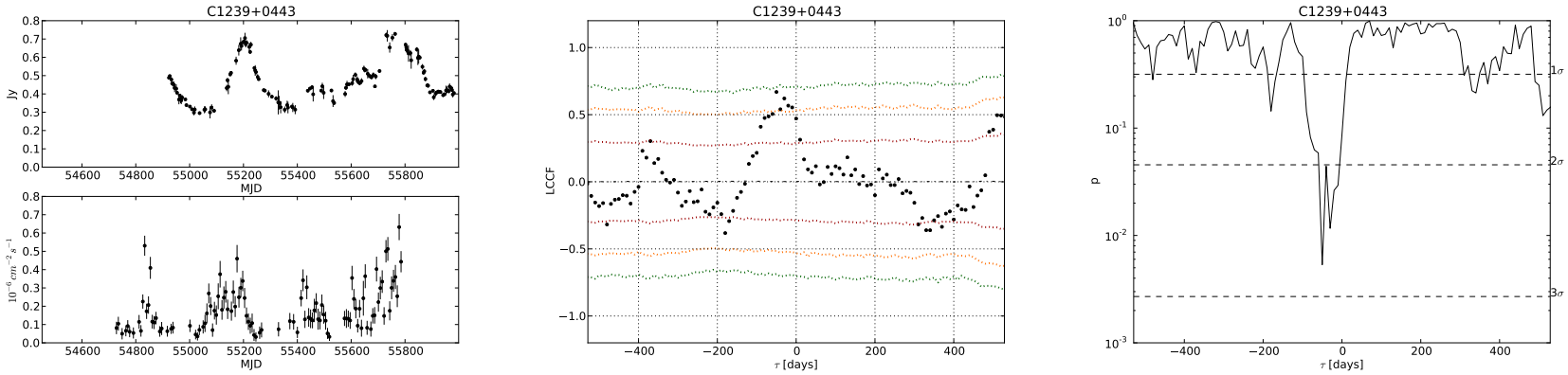

Figure F.71: Light curves and cross-correlation significance for C1239+0443 in the case of $\beta_{radio} = 2.3$ and $\beta_{\gamma} = 0.7$. The most significant cross-correlation is at -50 ± 15 day with 99.47% significance.

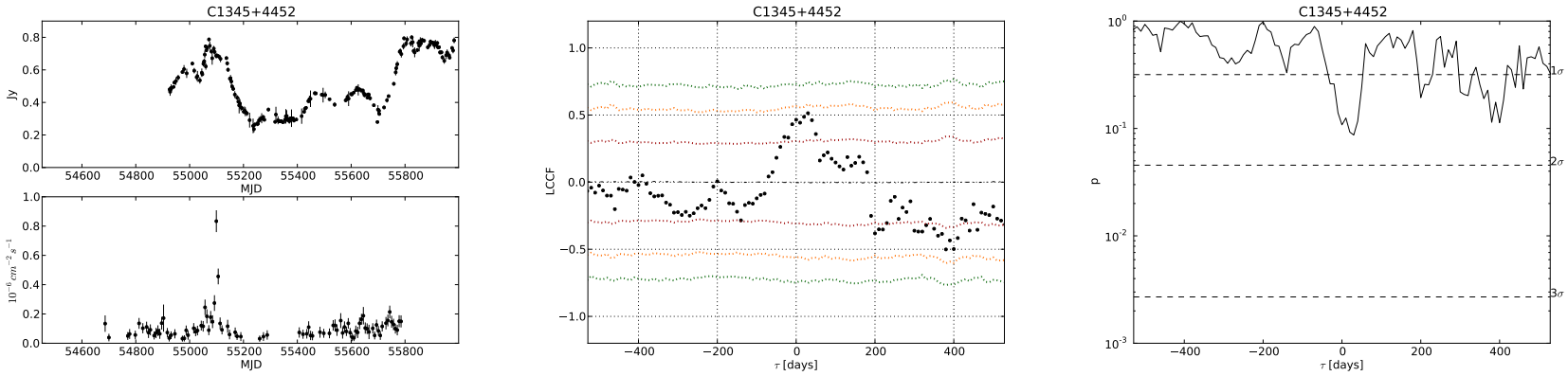

Figure F.72: Light curves and cross-correlation significance for C1345+4452 in the case of $\beta_{radio} = 2.3$ and $\beta_\gamma = 0.7$. The most significant cross-correlation is at 30 ± 14 day with 91.31% significance.

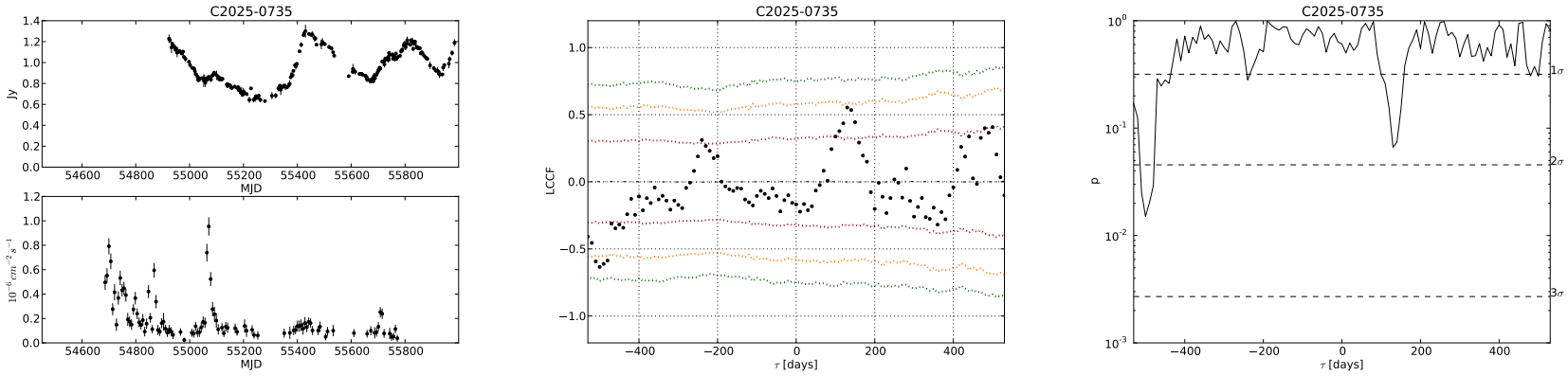

Figure F.73: Light curves and cross-correlation significance for C2025-0735 in the case of $\beta_{radio} = 2.3$ and $\beta_\gamma = 0.7$. The most significant cross-correlation is at 130 ± 9 day with 93.36% significance.

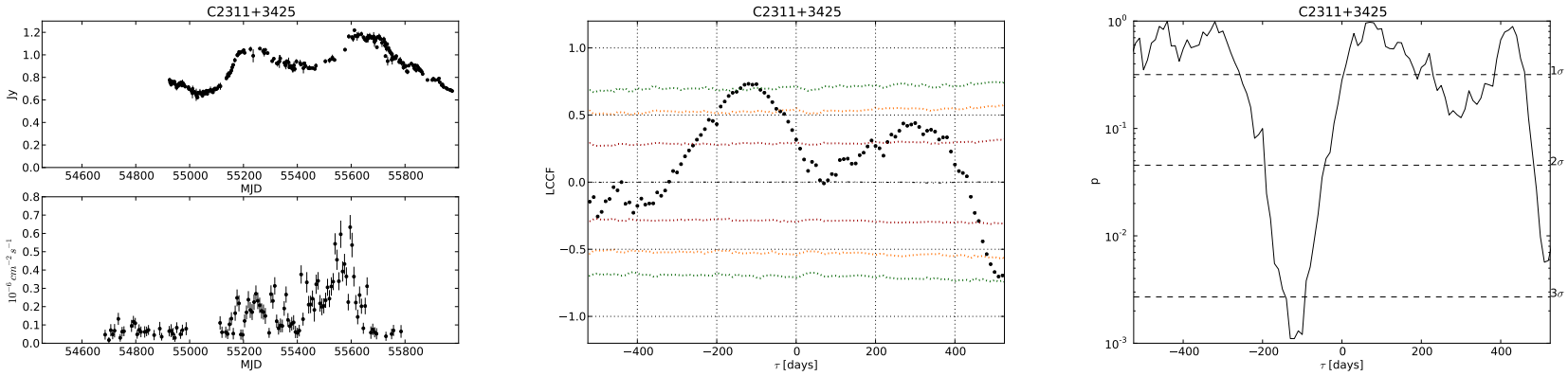

Figure F.74: Light curves and cross-correlation significance for C2311+3425 in the case of $\beta_{radio} = 2.3$ and $\beta_\gamma = 0.7$. The most significant cross-correlation is at -120 $\pm$ 14 day with 99.89% significance.

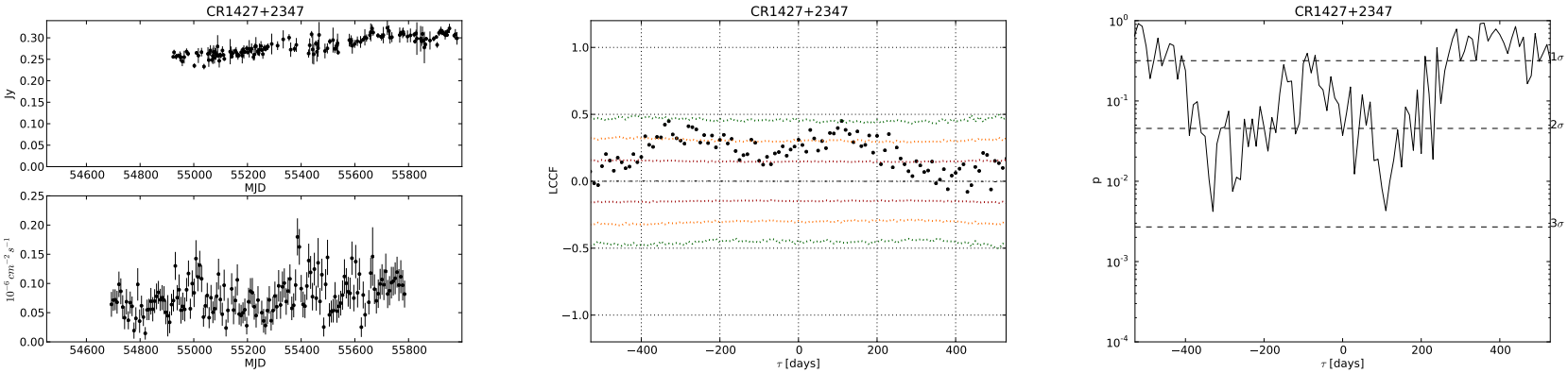

Figure F.75: Light curves and cross-correlation significance for CR1427+2347 in the case of $\beta_{radio} = 2.3$ and $\beta_\gamma = 0.7$. The most significant cross-correlation is at -330 $\pm$ 12 day with 99.58% significance.

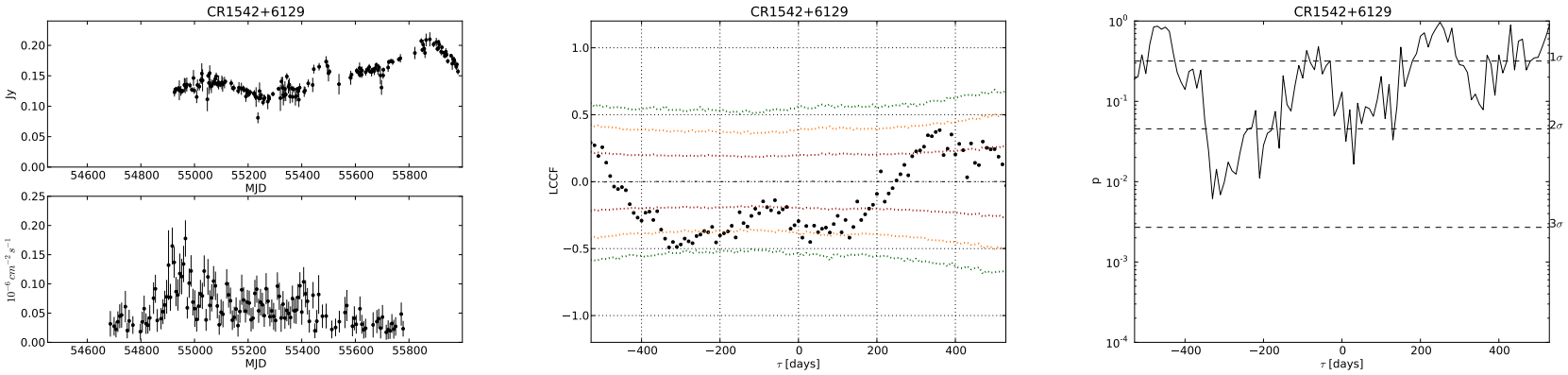

Figure F.76: Light curves and cross-correlation significance for CR1542+6129 in the case of $\beta_{radio} = 2.3$ and $\beta_{\gamma} = 0.7$. The most significant cross-correlation is at 360 ± 17 day with 92.15% significance.

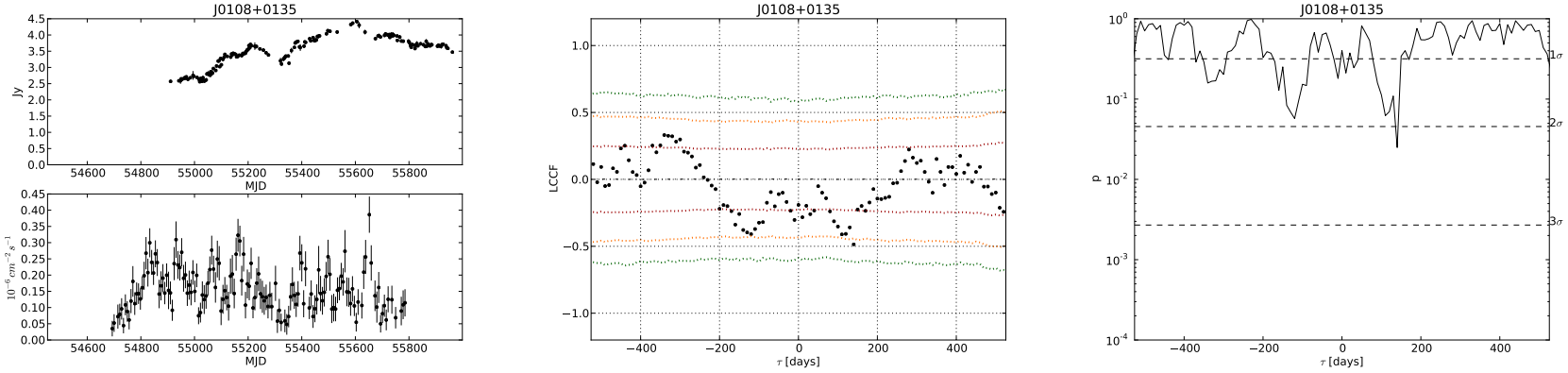

Figure F.77: Light curves and cross-correlation significance for J0108+0135 in the case of $\beta_{radio} = 2.3$ and $\beta_{\gamma} = 0.7$. The most significant cross-correlation is at -340 ± 16 day with 84.15% significance.

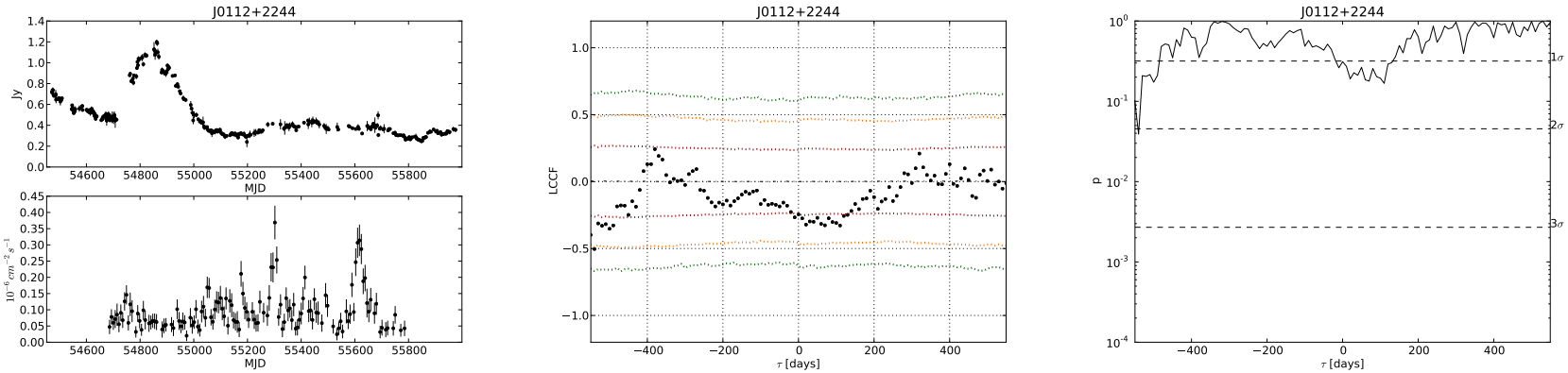

Figure F.78: Light curves and cross-correlation significance for J0112+2244 in the case of $\beta_{radio} = 2.3$ and $\beta_\gamma = 0.7$. The most significant cross-correlation is at -380 ± 13 day with 65.00% significance.

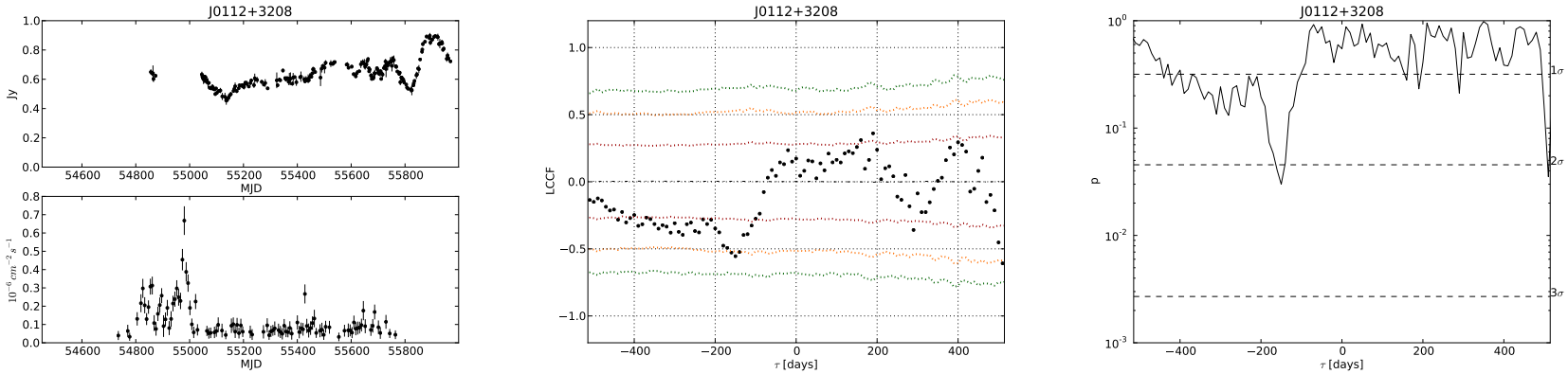

Figure F.79: Light curves and cross-correlation significance for J0112+3208 in the case of $\beta_{radio} = 2.3$ and $\beta_\gamma = 0.7$. The most significant cross-correlation is at 190 ± 12 day with 76.81% significance.

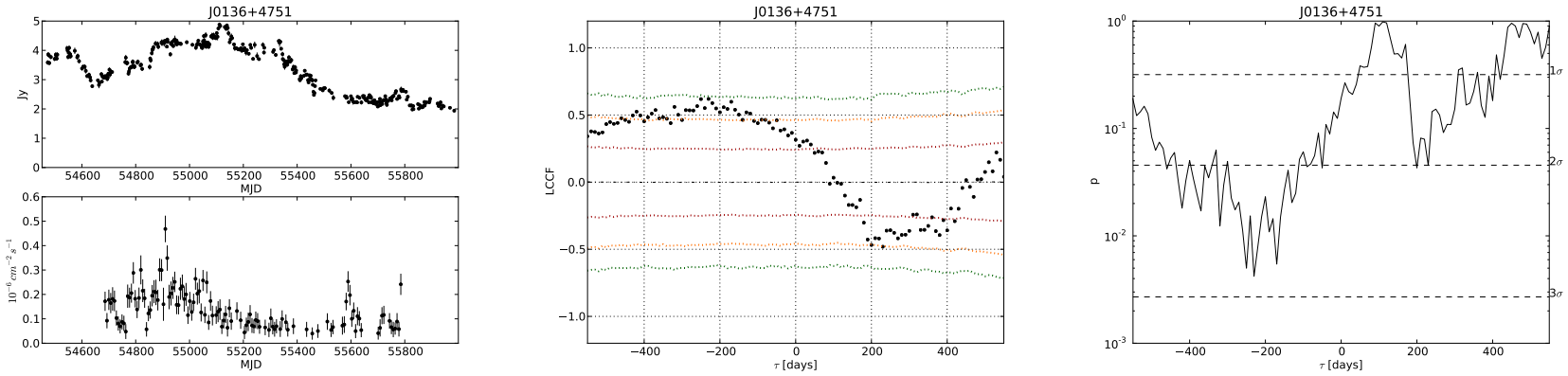

Figure F.80: Light curves and cross-correlation significance for J0136+4751 in the case of $\beta_{radio} = 2.3$ and $\beta_\gamma = 0.7$. The most significant cross-correlation is at -230 ± 14 day with 99.58% significance.

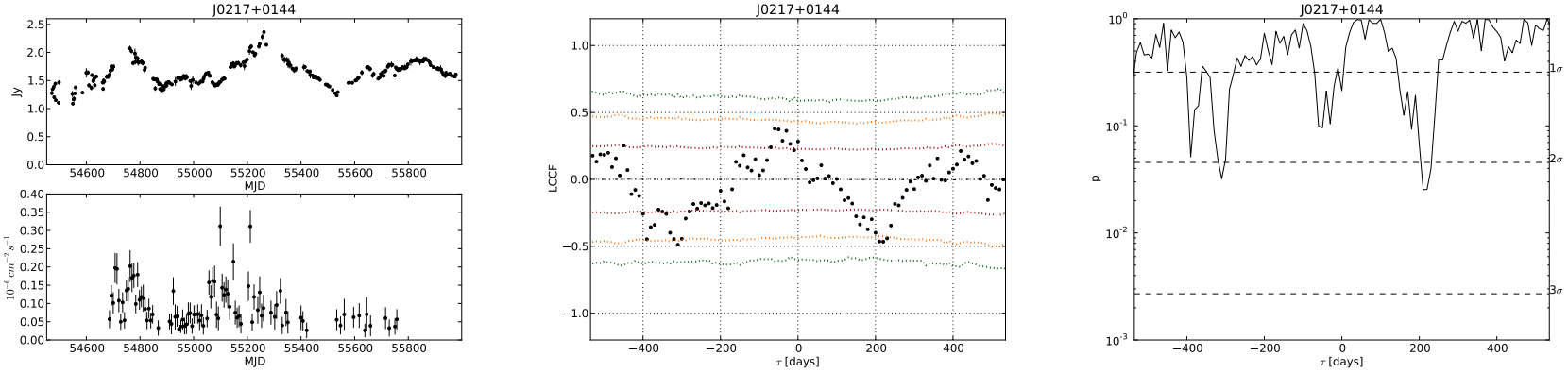

Figure F.81: Light curves and cross-correlation significance for J0217+0144 in the case of $\beta_{radio} = 2.3$ and $\beta_\gamma = 0.7$. The most significant cross-correlation is at -60 ± 15 day with 90.04% significance.

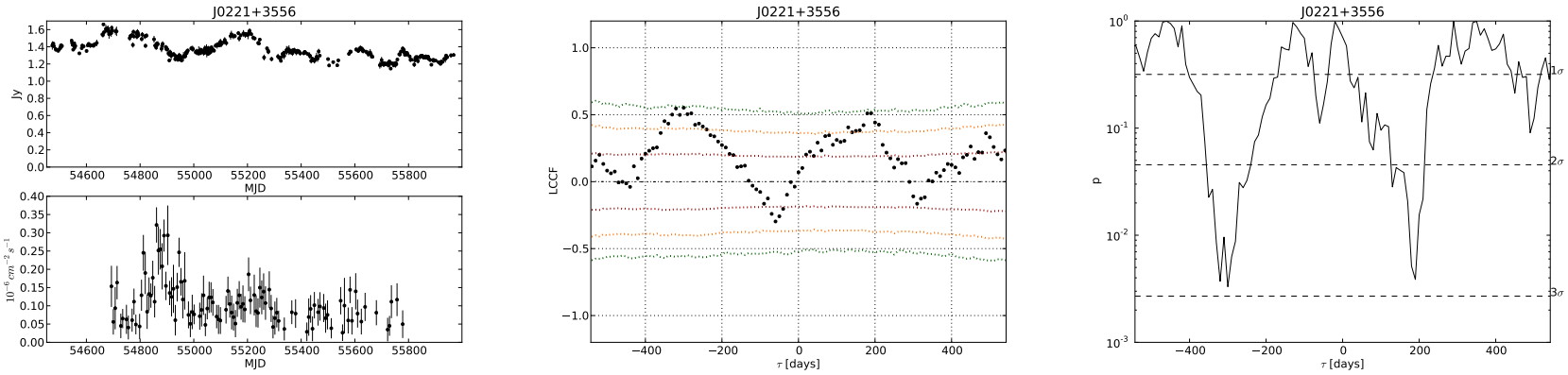

Figure F.82: Light curves and cross-correlation significance for J0221+3556 in the case of $\beta_{radio} = 2.3$ and $\beta_\gamma = 0.7$. The most significant cross-correlation is at -300 ± 15 day with 99.67% significance.

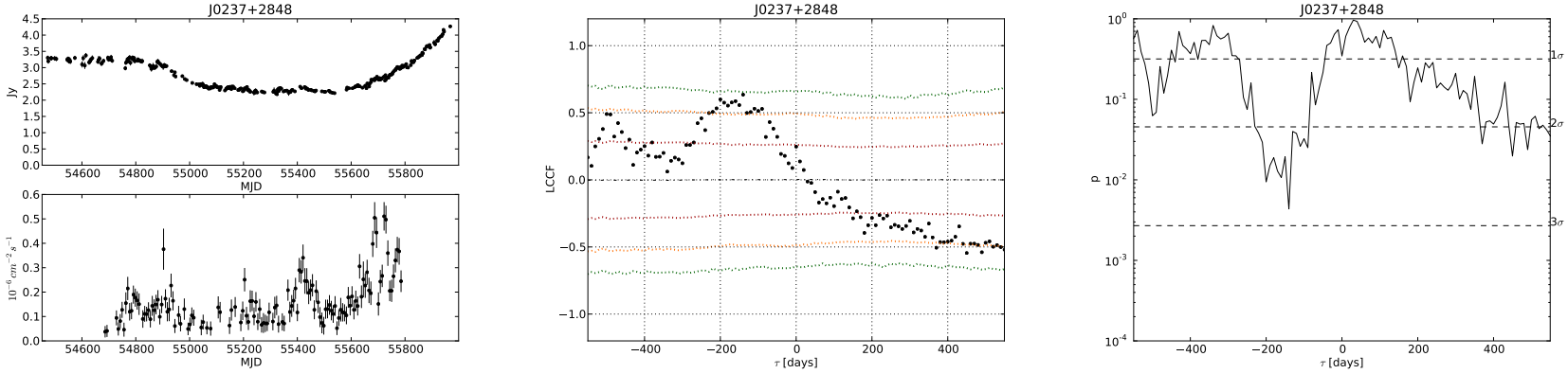

Figure F.83: Light curves and cross-correlation significance for J0237+2848 in the case of $\beta_{radio} = 2.3$ and $\beta_\gamma = 0.7$. The most significant cross-correlation is at -140 ± 12 day with 99.56% significance.

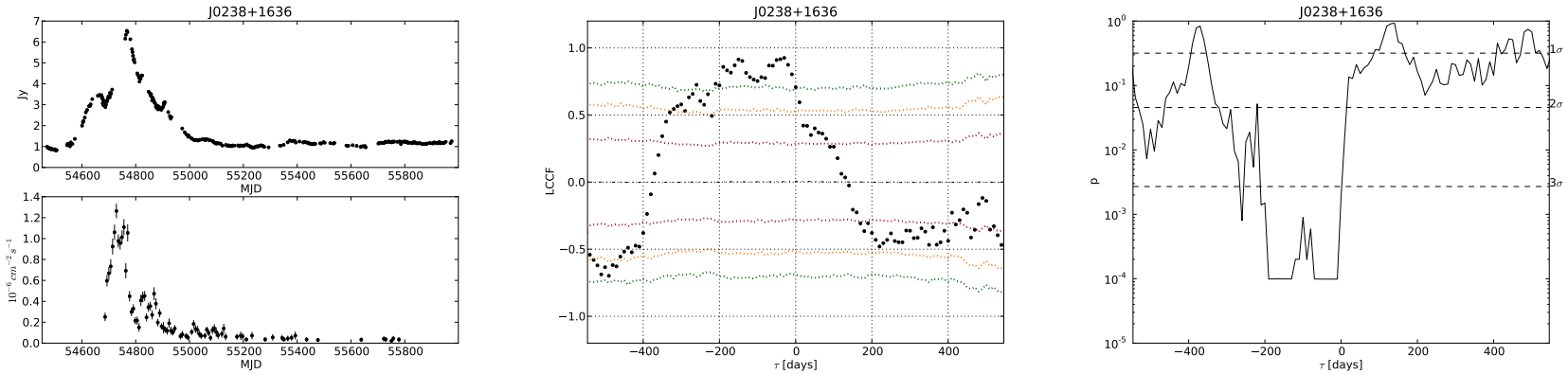

Figure F.84: Light curves and cross-correlation significance for J0238+1636 in the case of $\beta_{radio} = 2.3$ and $\beta_\gamma = 0.7$. The most significant cross-correlation is at -30 ± 9 day with 99.99% significance.

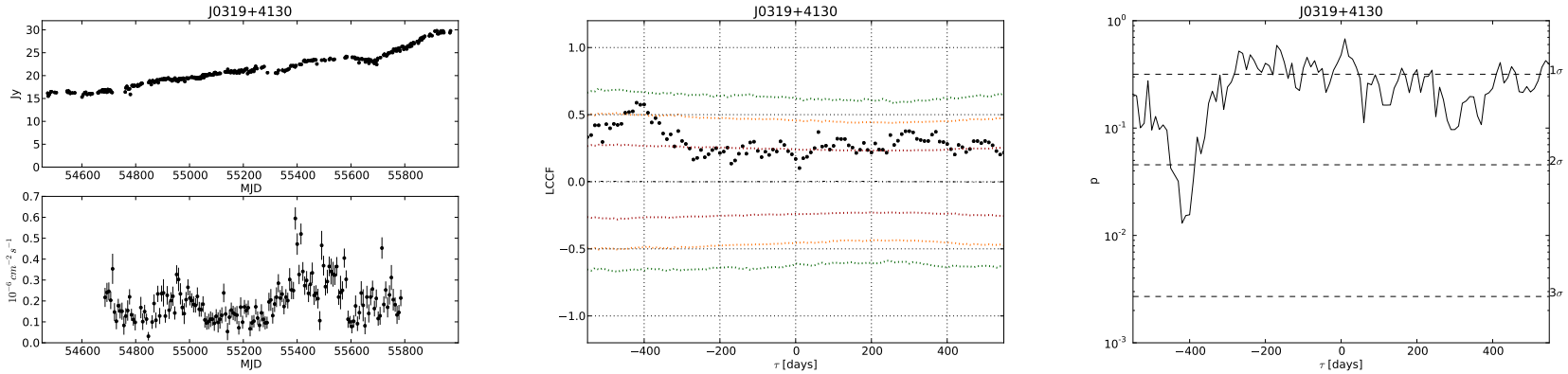

Figure F.85: Light curves and cross-correlation significance for J0319+4130 in the case of $\beta_{radio} = 2.3$ and $\beta_\gamma = 0.7$. The most significant cross-correlation is at -420 ± 13 day with 98.70% significance.

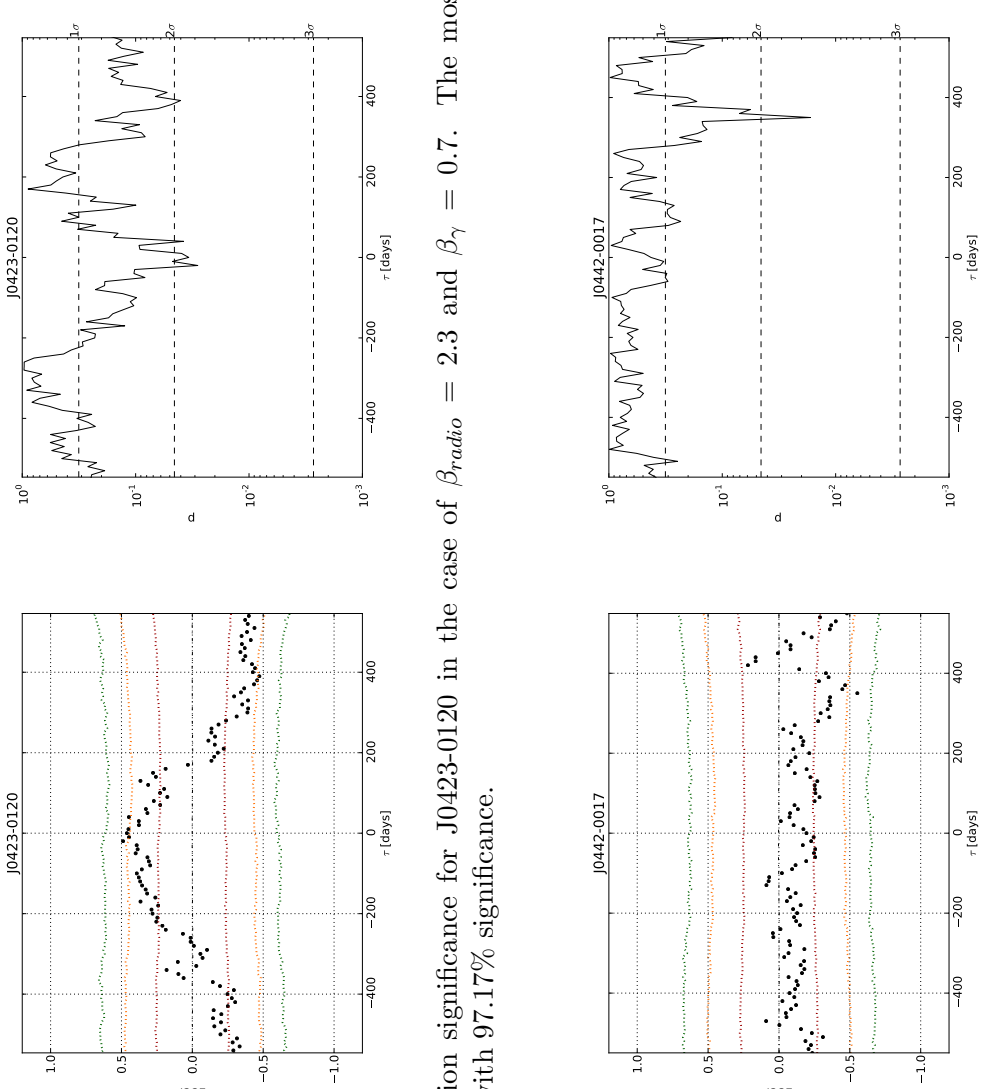

Figure F.86: Light curves and cross-correlation significance for J0423-0120 in the case of $\beta_{radio} = 2.3$ and $\beta_\gamma = 0.7$. The most significant cross-correlation is at -20 $\pm$ 16 day with 97.17% significance.

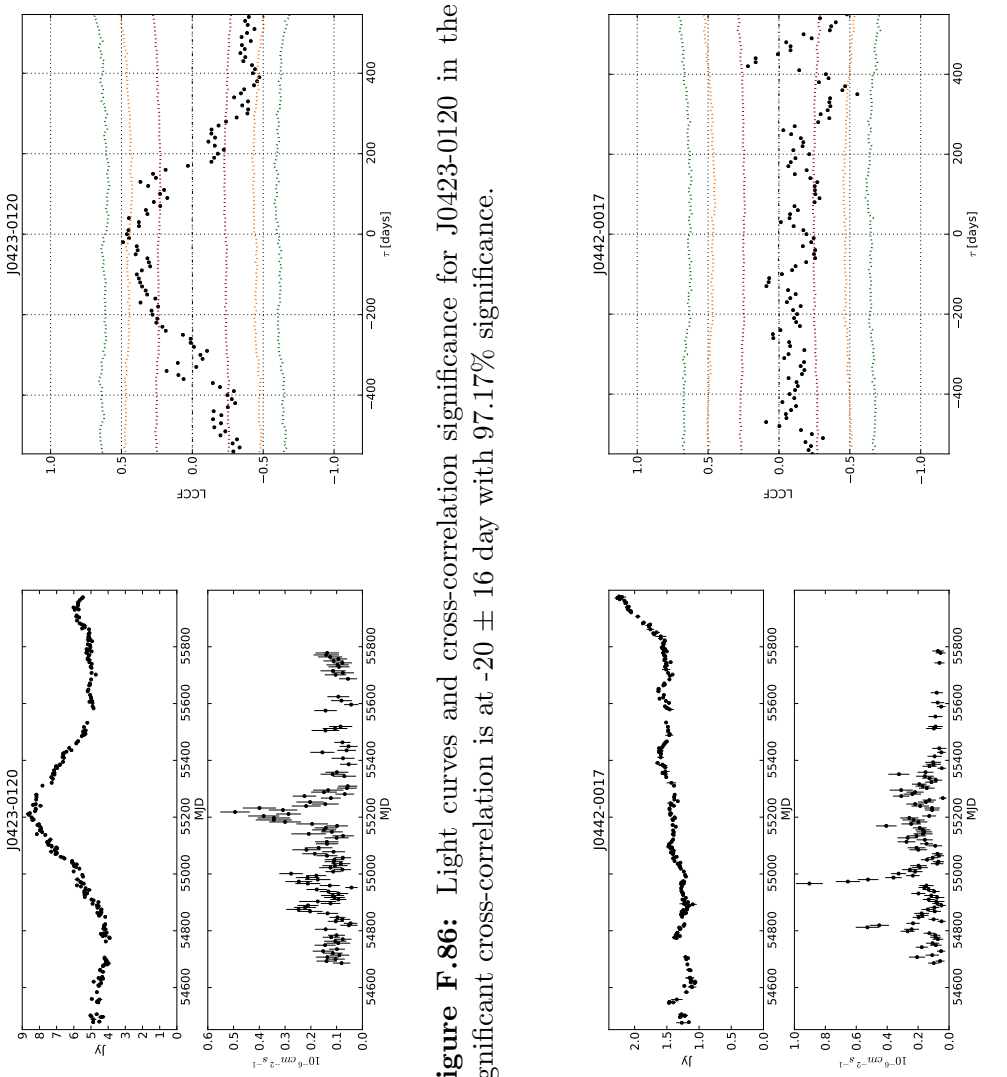

Figure F.87: Light curves and cross-correlation significance for J0442-0017 in the case of $\beta_{radio} = 2.3$ and $\beta_\gamma = 0.7$. The most significant cross-correlation is at 420 $\pm$ 30 day with 59.38% significance.

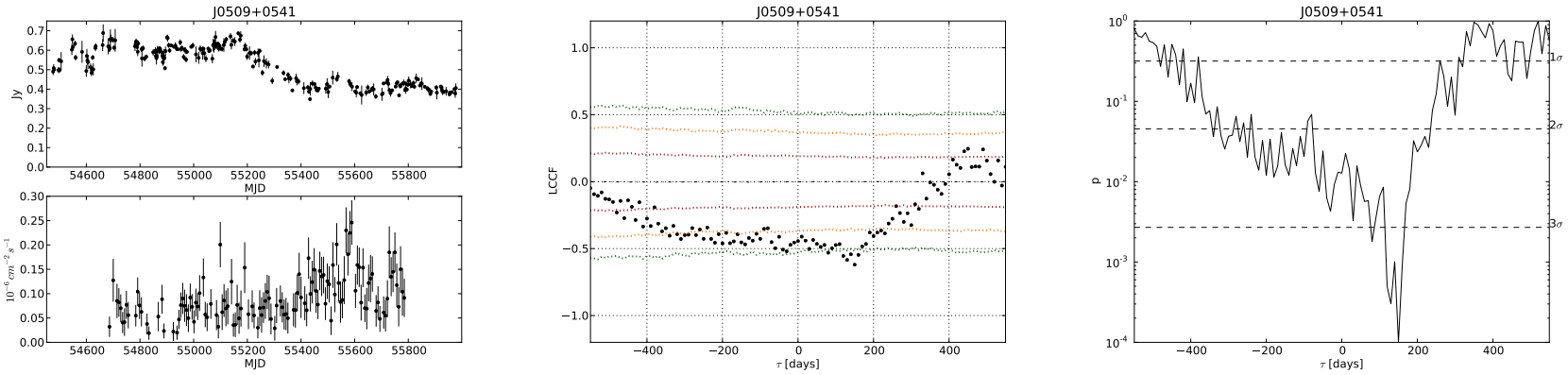

Figure F.88: Light curves and cross-correlation significance for J0509+0541 in the case of $\beta_{radio} = 2.3$ and $\beta_\gamma = 0.7$. The most significant cross-correlation is at 450 ± 15 day with 81.94% significance.

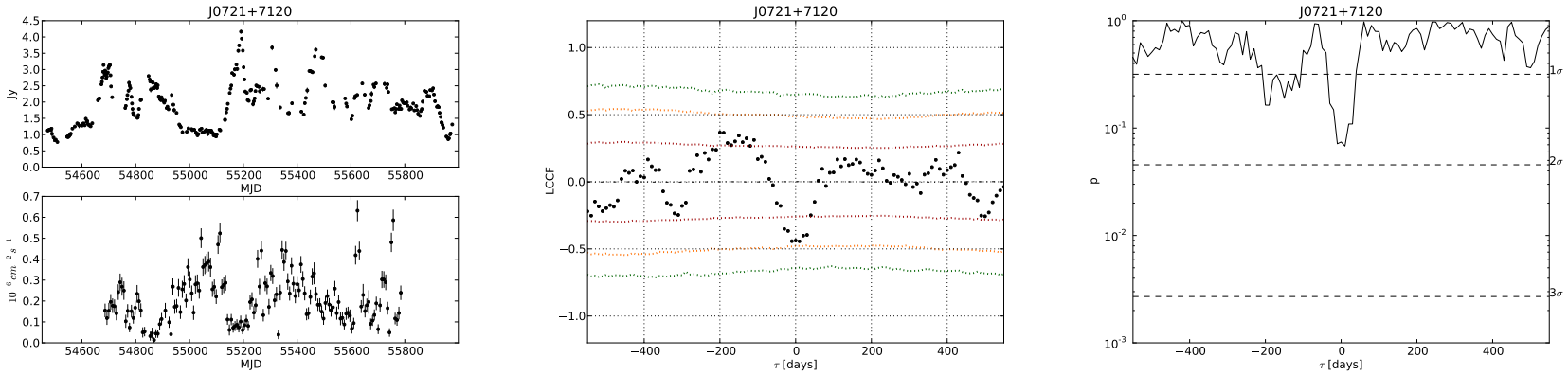

Figure F.89: Light curves and cross-correlation significance for J0721+7120 in the case of $\beta_{radio} = 2.3$ and $\beta_\gamma = 0.7$. The most significant cross-correlation is at -200 ± 12 day with 83.64% significance.

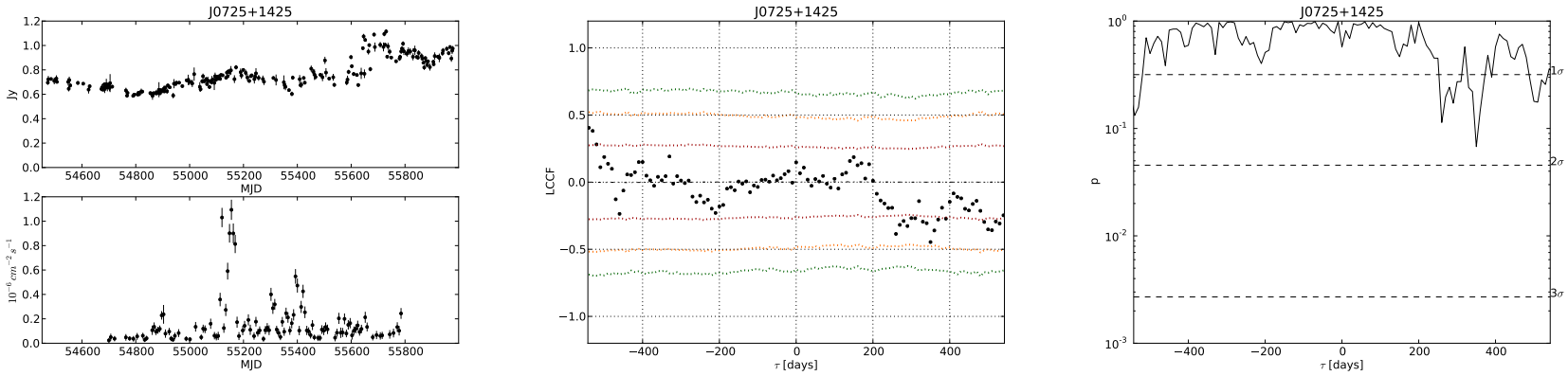

Figure F.90: Light curves and cross-correlation significance for J0725+1425 in the case of $\beta_{radio} = 2.3$ and $\beta_{\gamma} = 0.7$. The most significant cross-correlation is at 150 ± 13 day with 53.45% significance.

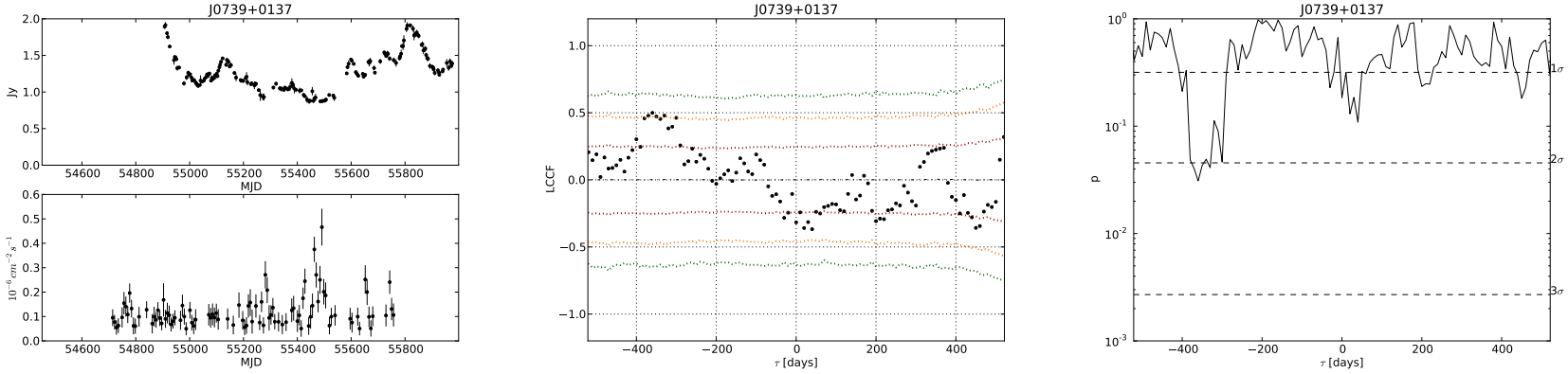

Figure F.91: Light curves and cross-correlation significance for J0739+0137 in the case of $\beta_{radio} = 2.3$ and $\beta_{\gamma} = 0.7$. The most significant cross-correlation is at -360 ± 14 day with 96.91% significance.

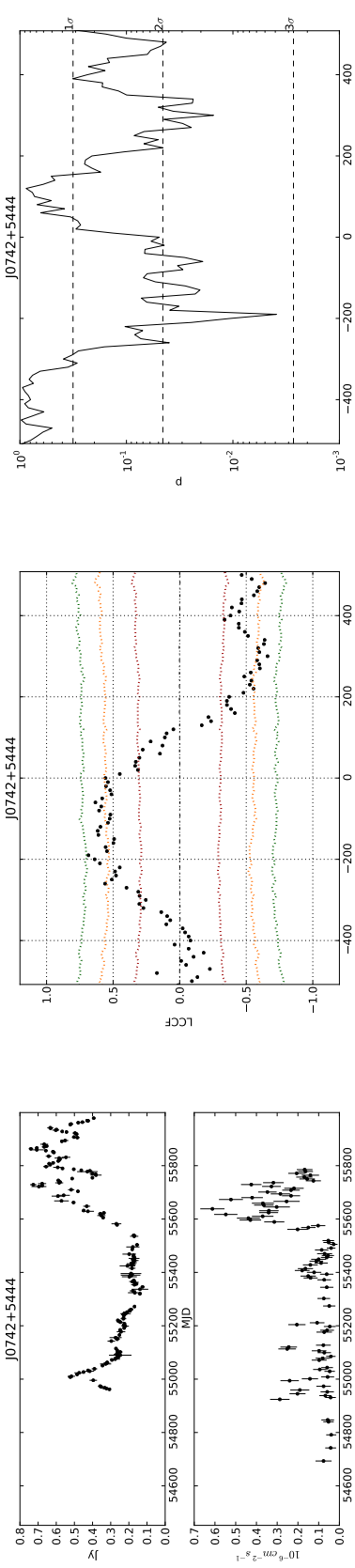

Figure F.92: Light curves and cross-correlation significance for J0742+5444 in the case of $\beta_{radio} = 2.3$ and $\beta_\gamma = 0.7$. The most significant cross-correlation is at -190 $\pm$ 9 day with 99.61% significance.

Figure F.93: Light curves and cross-correlation significance for J0808-0751 in the case of $\beta_{radio} = 2.3$ and $\beta_\gamma = 0.7$. The most significant cross-correlation is at -150 $\pm$ 15 day with 98.54% significance.

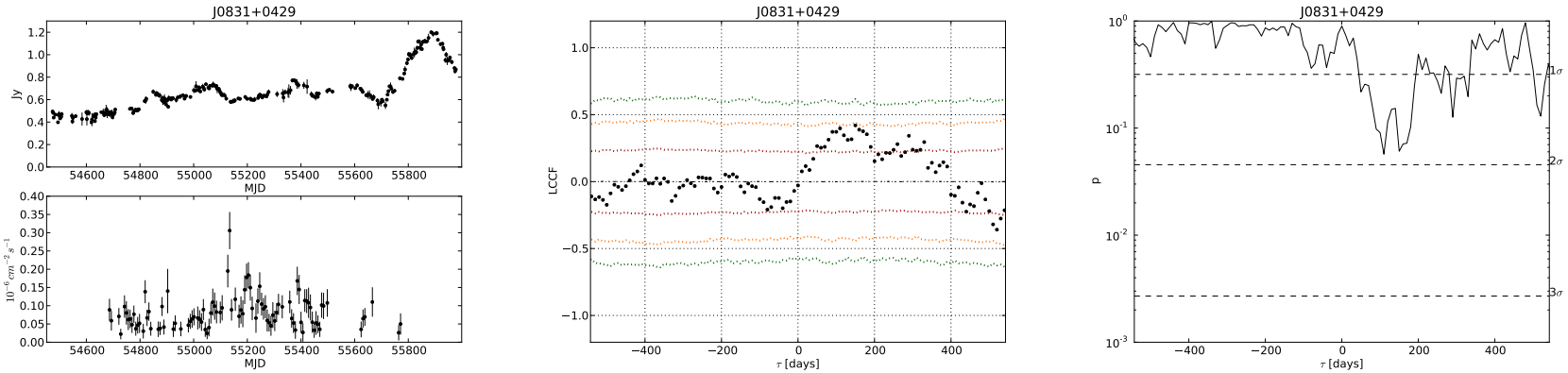

Figure F.94: Light curves and cross-correlation significance for J0831+0429 in the case of $\beta_{radio} = 2.3$ and $\beta_\gamma = 0.7$. The most significant cross-correlation is at 110 ± 16 day with 94.30% significance.

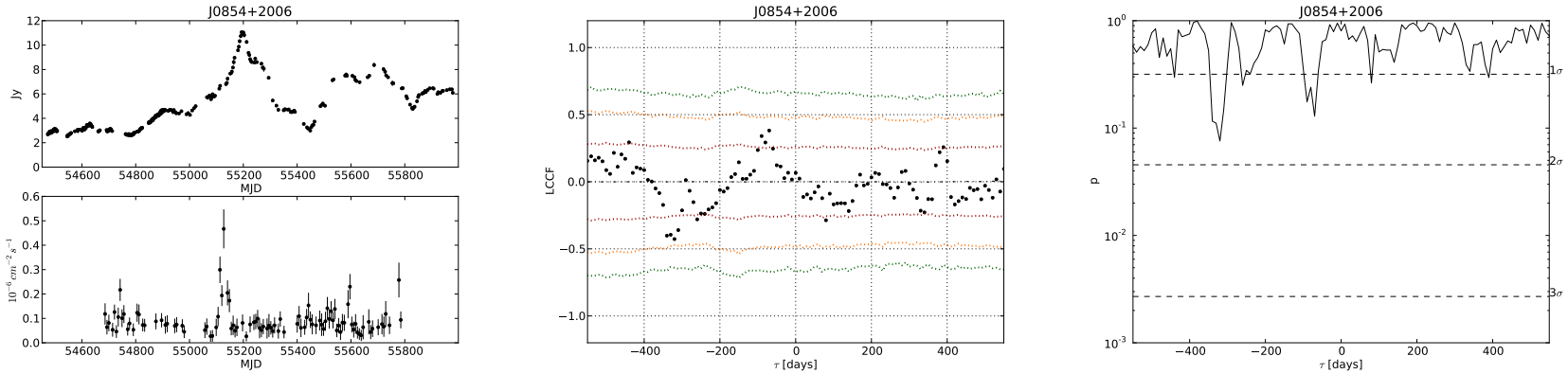

Figure F.95: Light curves and cross-correlation significance for J0854+2006 in the case of $\beta_{radio} = 2.3$ and $\beta_\gamma = 0.7$. The most significant cross-correlation is at -70 ± 16 day with 87.09% significance.

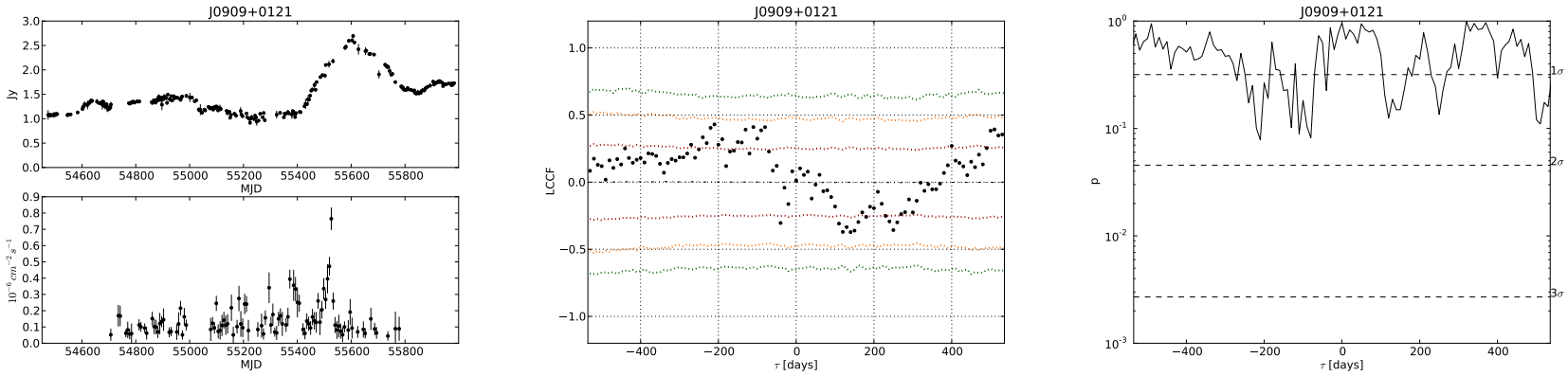

Figure F.96: Light curves and cross-correlation significance for J0909+0121 in the case of $\beta_{radio} = 2.3$ and $\beta_\gamma = 0.7$. The most significant cross-correlation is at -210 ± 11 day with 92.16% significance.

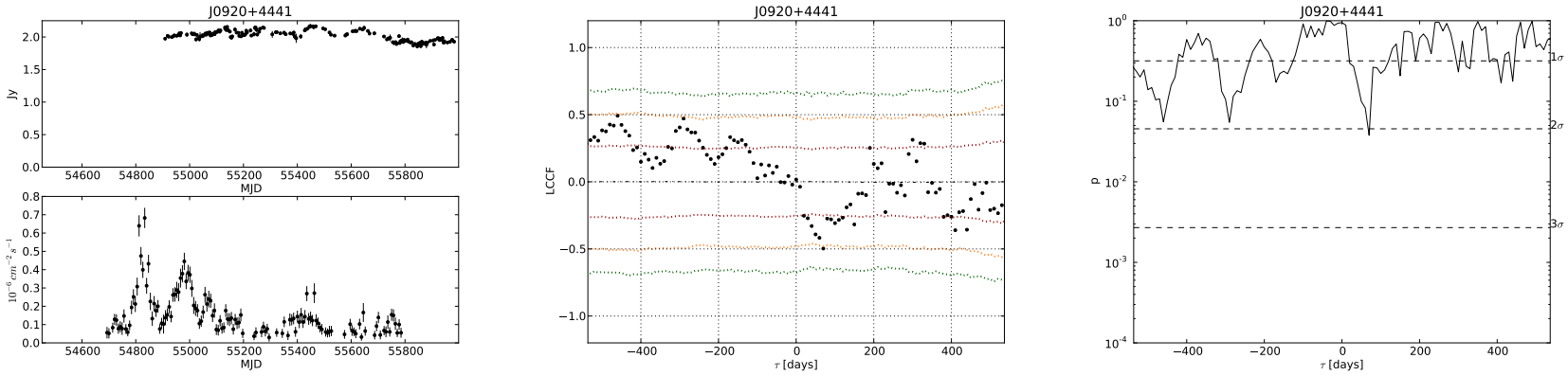

Figure F.97: Light curves and cross-correlation significance for J0920+4441 in the case of $\beta_{radio} = 2.3$ and $\beta_\gamma = 0.7$. The most significant cross-correlation is at -290 ± 12 day with 94.53% significance.

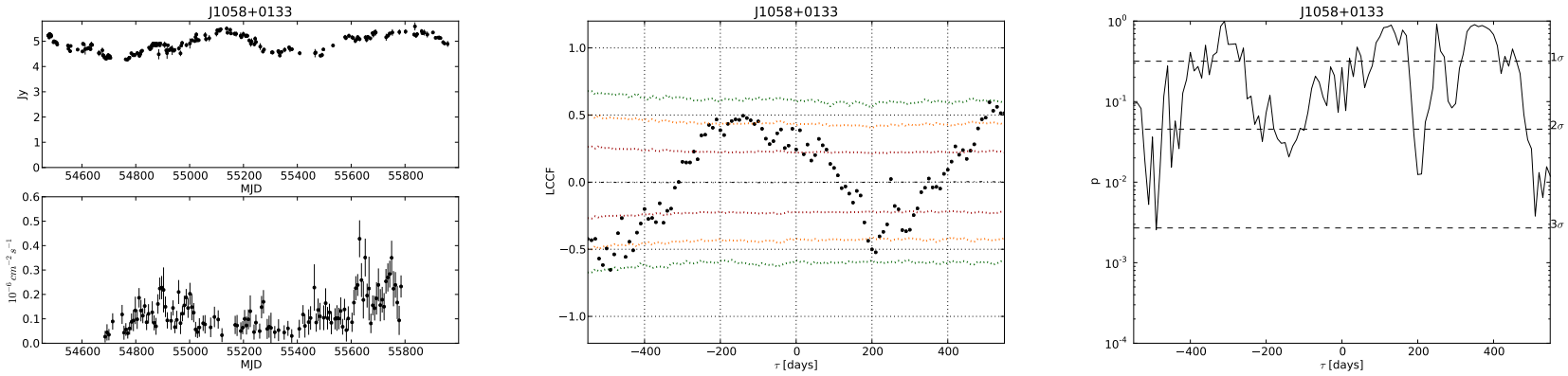

Figure F.98: Light curves and cross-correlation significance for J1058+0133 in the case of $\beta_{radio} = 2.3$ and $\beta_\gamma = 0.7$. The most significant cross-correlation is at 510 ± 15 day with 99.62% significance.

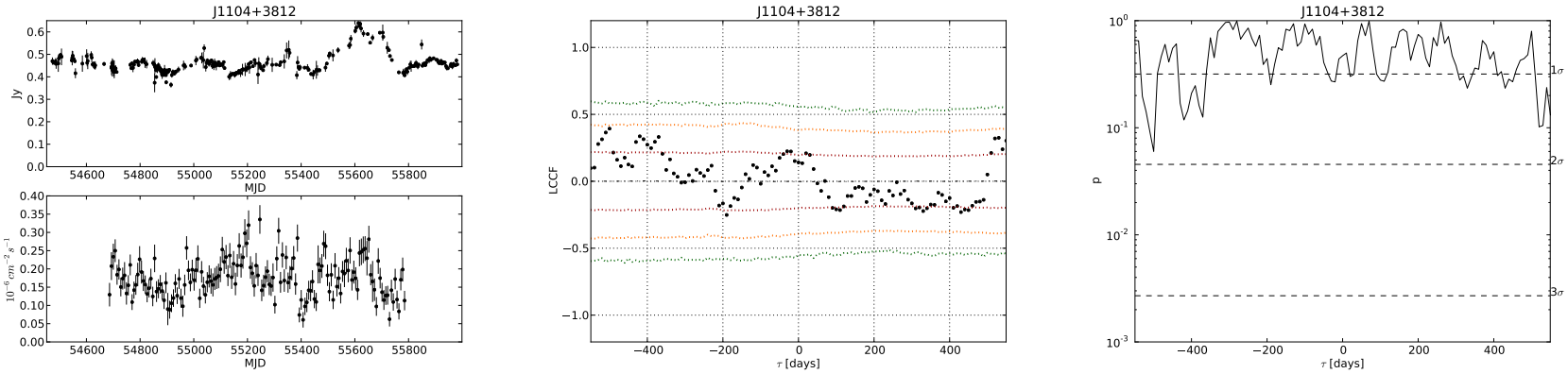

Figure F.99: Light curves and cross-correlation significance for J1104+3812 in the case of $\beta_{radio} = 2.3$ and $\beta_\gamma = 0.7$. The most significant cross-correlation is at -500 ± 11 day with 93.99% significance.

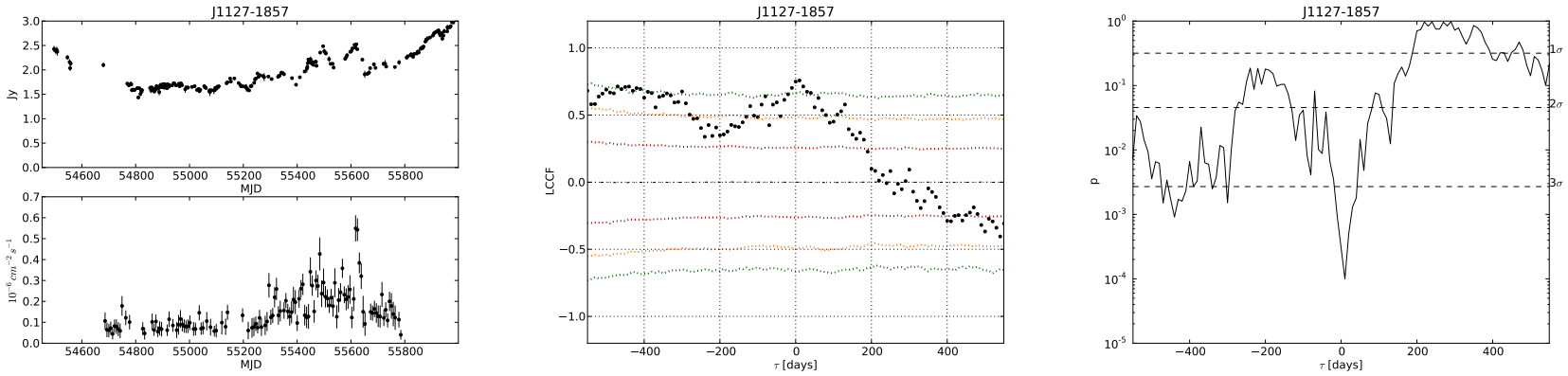

Figure F.100: Light curves and cross-correlation significance for J1127-1857 in the case of $\beta_{radio} = 2.3$ and $\beta_\gamma = 0.7$. The most significant cross-correlation is at 10 ± 11 day with 99.99% significance.

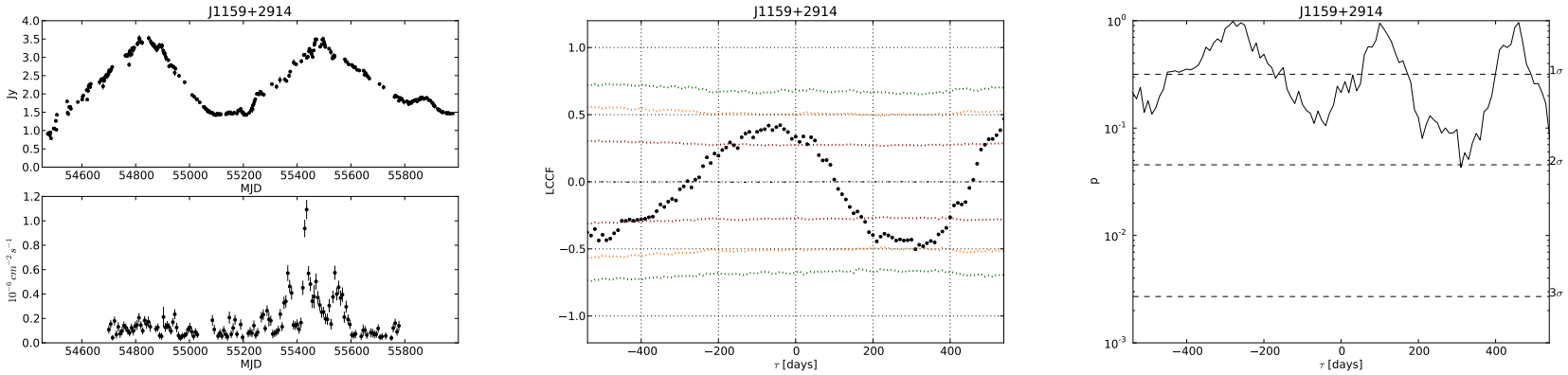

Figure F.101: Light curves and cross-correlation significance for J1159+2914 in the case of $\beta_{radio} = 2.3$ and $\beta_\gamma = 0.7$. The most significant cross-correlation is at -40 $\pm$ 15 day with 89.46% significance.

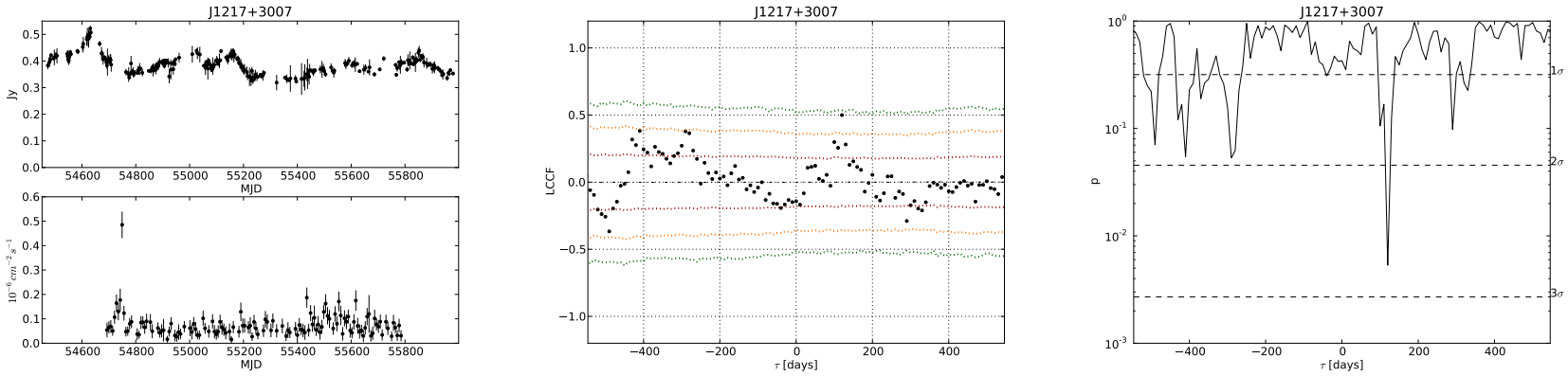

Figure F.102: Light curves and cross-correlation significance for J1217+3007 in the case of $\beta_{radio} = 2.3$ and $\beta_{\gamma} = 0.7$. The most significant cross-correlation is at 120 ± 10 day with 99.47% significance.

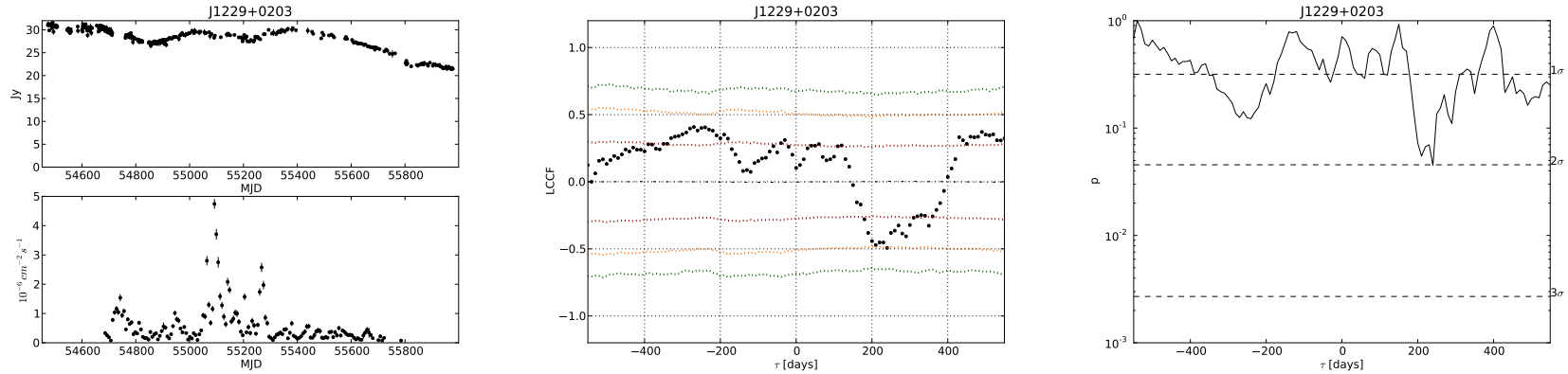

Figure F.103: Light curves and cross-correlation significance for J1229+0203 in the case of $\beta_{radio} = 2.3$ and $\beta_{\gamma} = 0.7$. The most significant cross-correlation is at -240 ± 15 day with 87.75% significance.

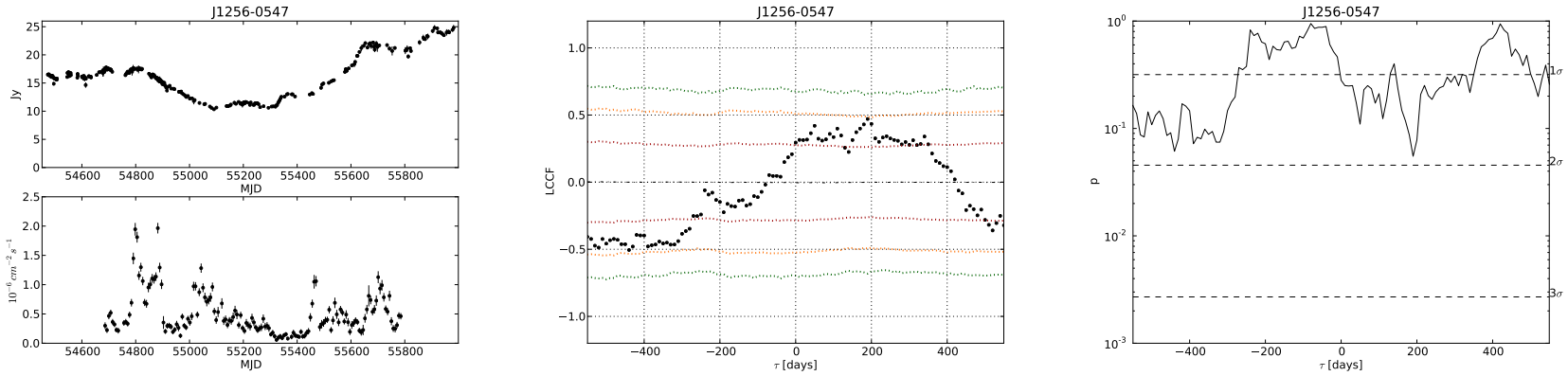

Figure F.104: Light curves and cross-correlation significance for J1256-0547 in the case of $\beta_{radio} = 2.3$ and $\beta_\gamma = 0.7$. The most significant cross-correlation is at 190 ± 9 day with 94.50% significance.

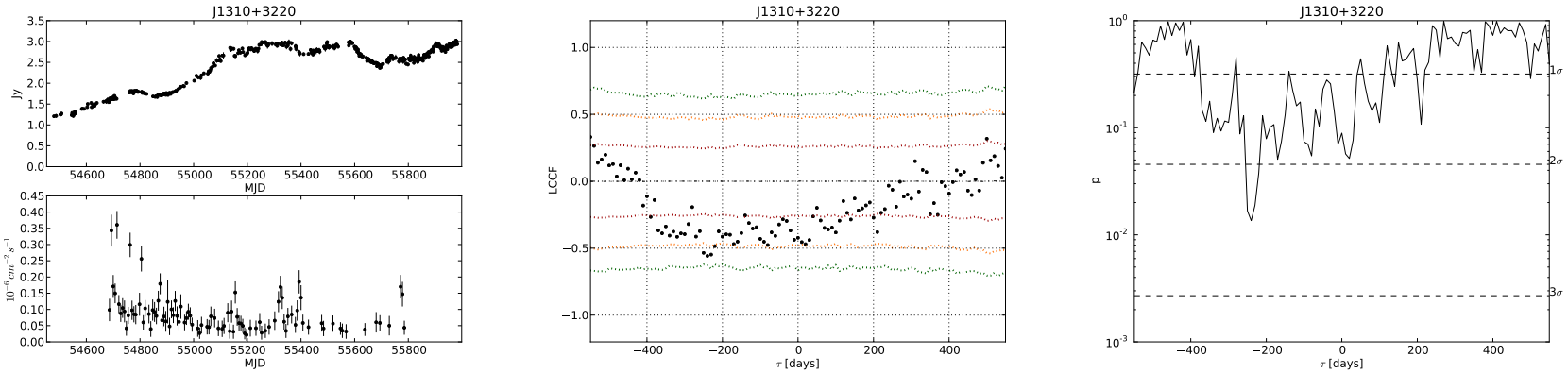

Figure F.105: Light curves and cross-correlation significance for J1310+3220 in the case of $\beta_{radio} = 2.3$ and $\beta_\gamma = 0.7$. The most significant cross-correlation is at 500 ± 57 day with 71.22% significance.

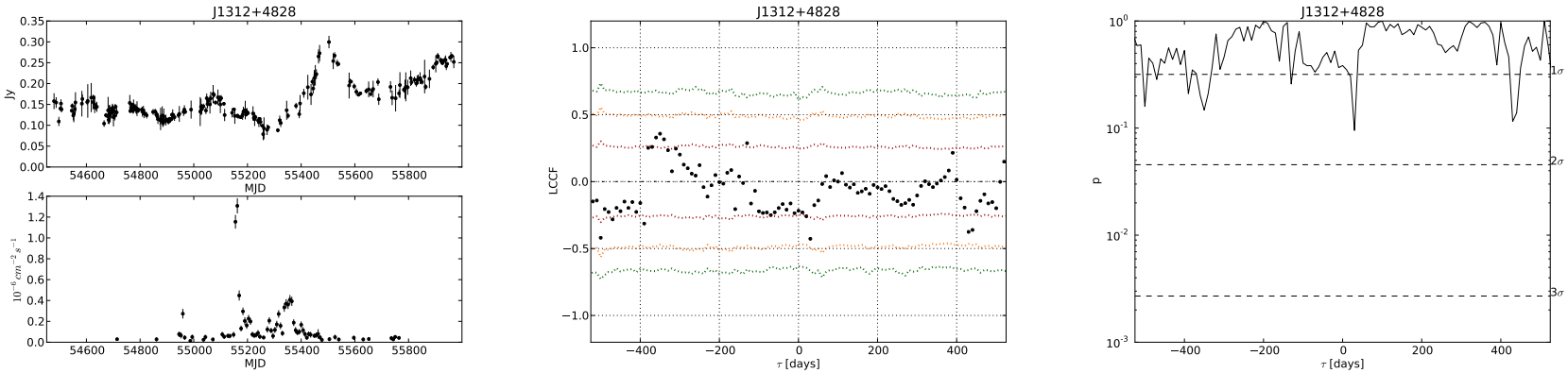

Figure F.106: Light curves and cross-correlation significance for J1312+4828 in the case of $\beta_{radio} = 2.3$ and $\beta_{\gamma} = 0.7$. The most significant cross-correlation is at -350 ± 15 day with 85.28% significance.

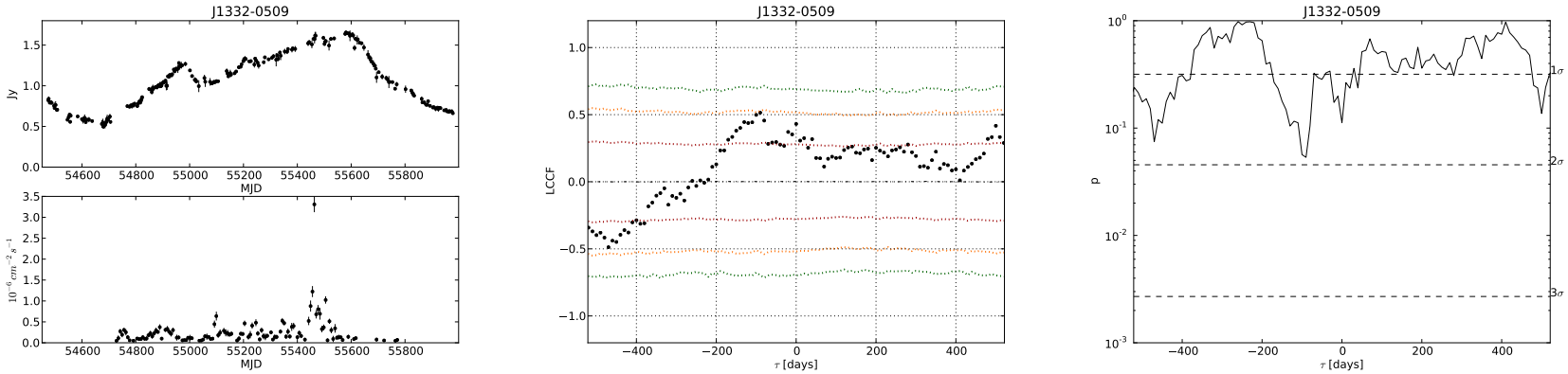

Figure F.107: Light curves and cross-correlation significance for J1332-0509 in the case of $\beta_{radio} = 2.3$ and $\beta_{\gamma} = 0.7$. The most significant cross-correlation is at -90 ± 15 day with 94.66% significance.

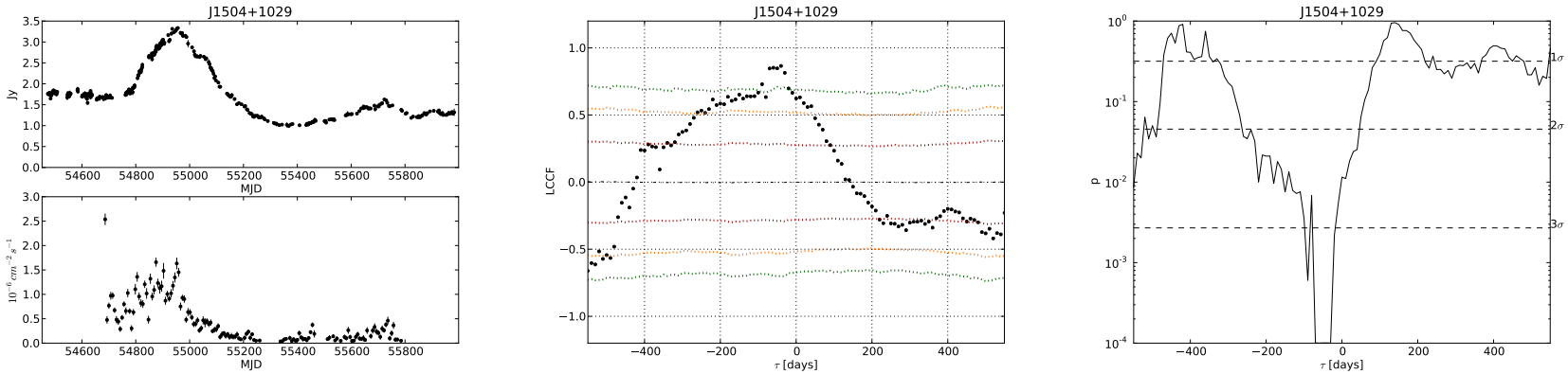

Figure F.108: Light curves and cross-correlation significance for J1504+1029 in the case of $\beta_{radio} = 2.3$ and $\beta_{\gamma} = 0.7$. The most significant cross-correlation is at -40 ± 13 day with 99.99% significance.

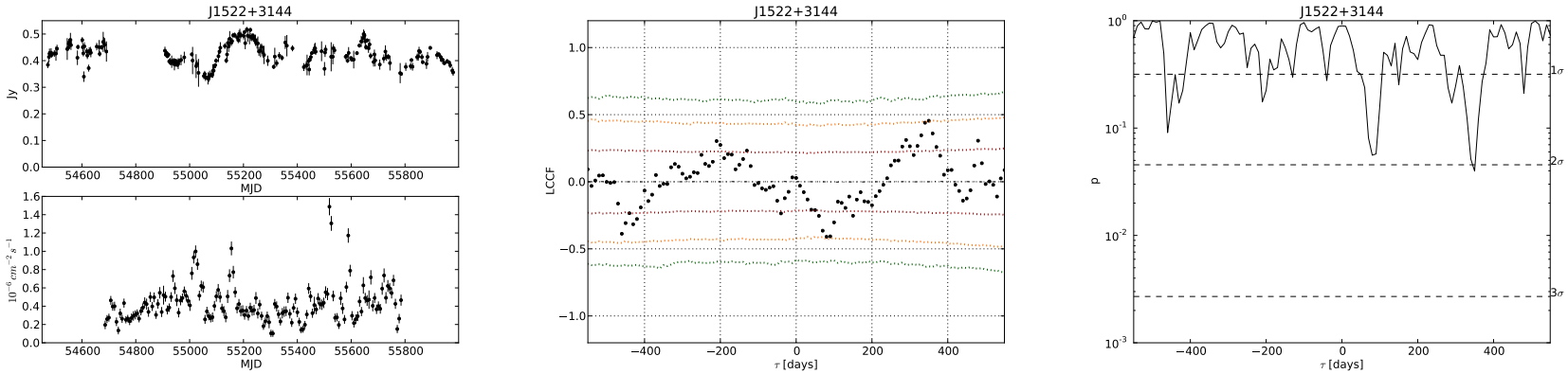

Figure F.109: Light curves and cross-correlation significance for J1522+3144 in the case of $\beta_{radio} = 2.3$ and $\beta_{\gamma} = 0.7$. The most significant cross-correlation is at 350 ± 9 day with 96.03% significance.

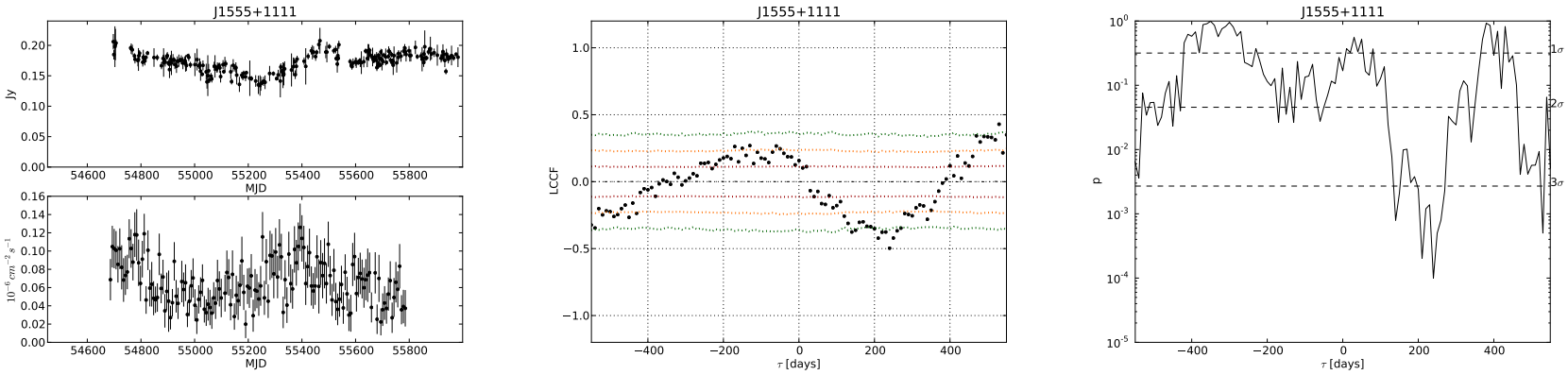

Figure F.110: Light curves and cross-correlation significance for J1555+1111 in the case of $\beta_{radio} = 2.3$ and $\beta_{\gamma} = 0.7$. The most significant cross-correlation is at 530 ± 17 day with 99.95% significance.

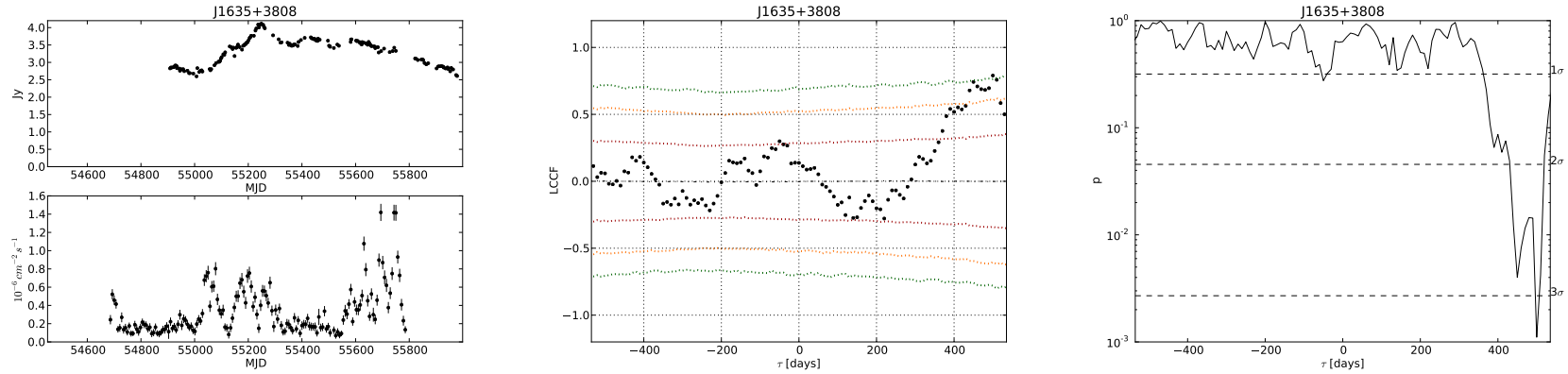

Figure F.111: Light curves and cross-correlation significance for J1635+3808 in the case of $\beta_{radio} = 2.3$ and $\beta_{\gamma} = 0.7$. The most significant cross-correlation is at 500 ± 9 day with 99.89% significance.

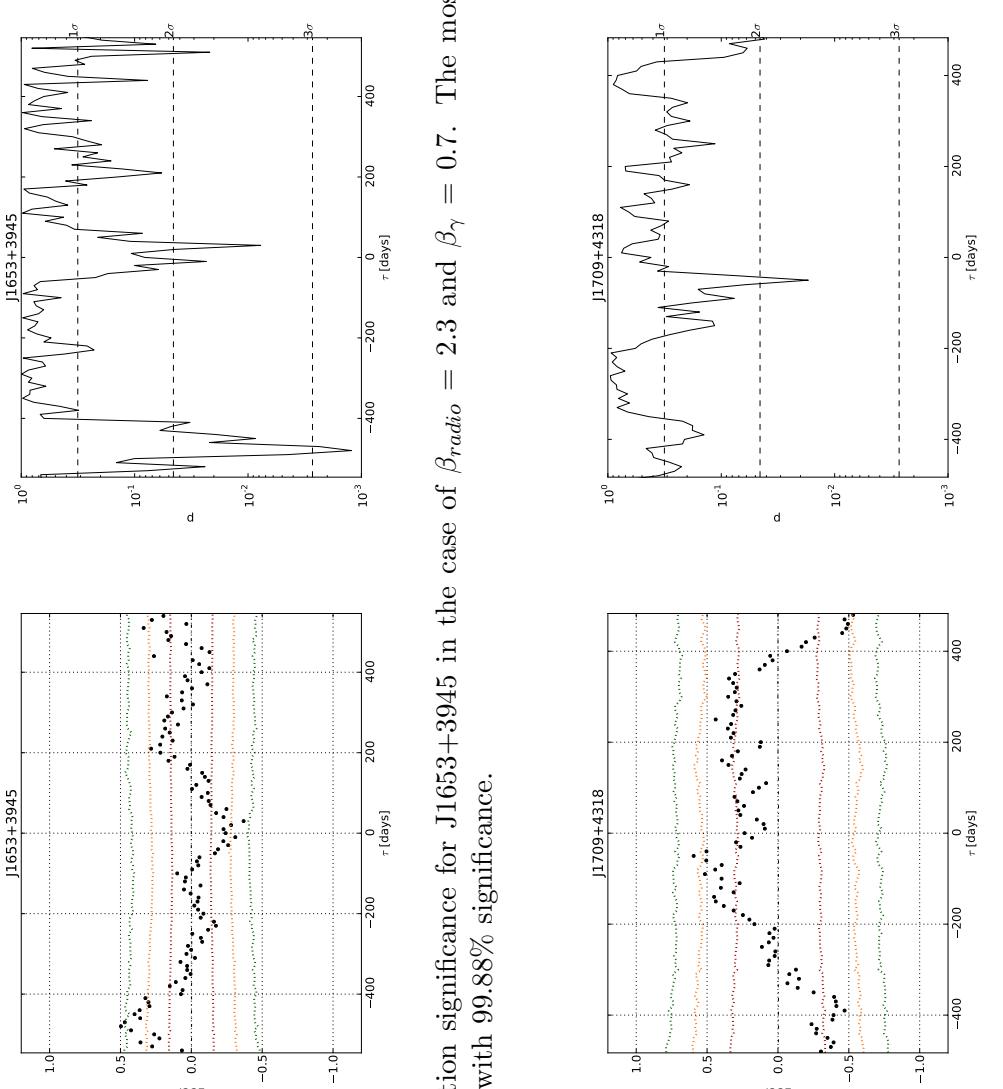

Figure F.112: Light curves and cross-correlation significance for J1653+3945 in the case of $\beta_{radio} = 2.3$ and $\beta_\gamma = 0.7$. The most significant cross-correlation is at -480 ± 13 day with 99.88% significance.

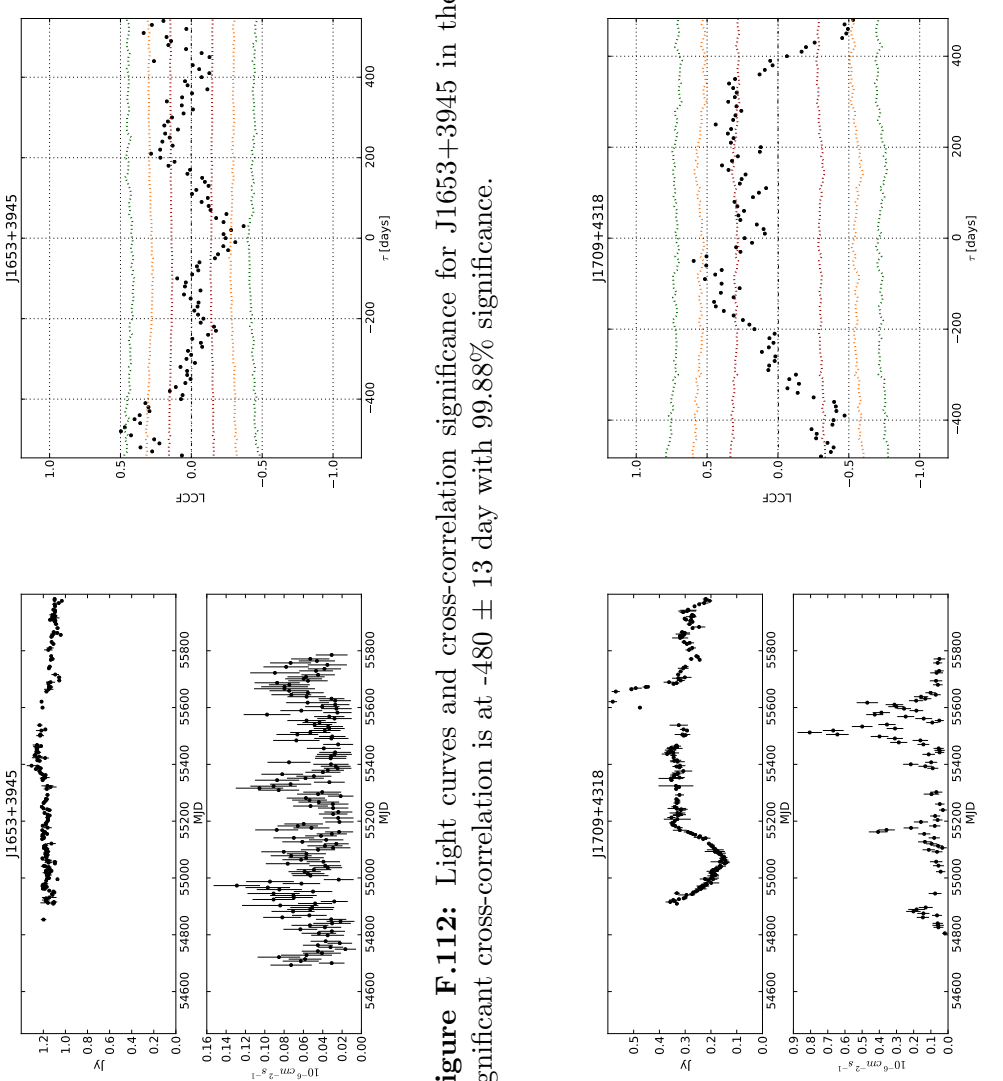

Figure F.113: Light curves and cross-correlation significance for J1709+4318 in the case of $\beta_{radio} = 2.3$ and $\beta_\gamma = 0.7$. The most significant cross-correlation is at -50 ± 12 day with 98.29% significance.

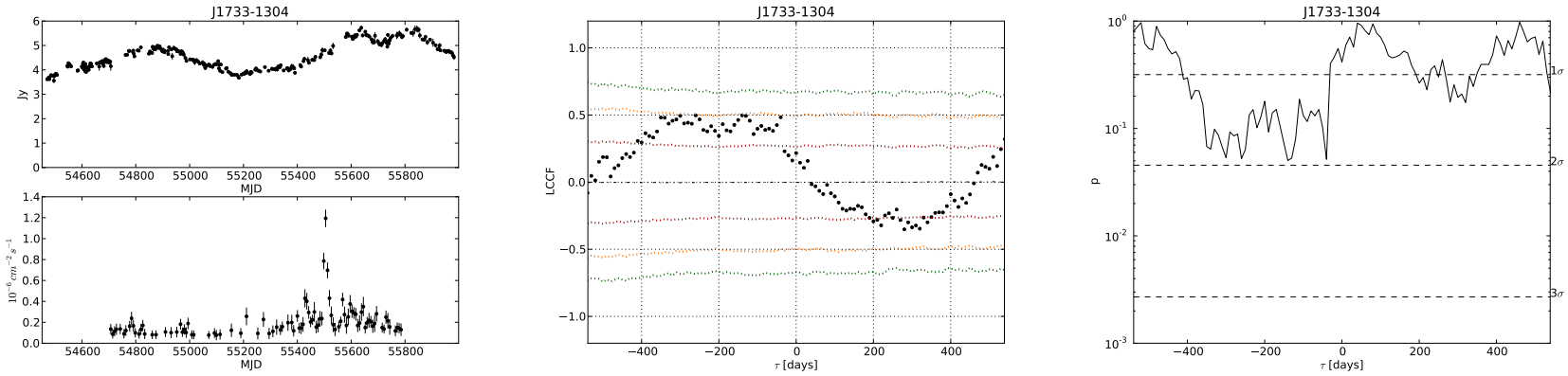

Figure F.114: Light curves and cross-correlation significance for J1733-1304 in the case of $\beta_{radio} = 2.3$ and $\beta_\gamma = 0.7$. The most significant cross-correlation is at -140 $\pm$ 11 day with 94.97% significance.

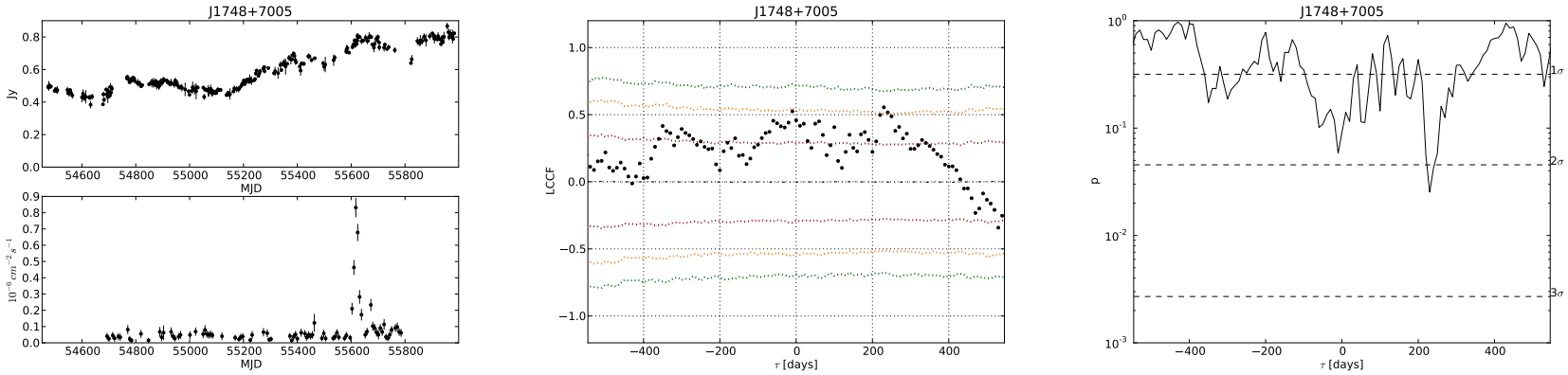

Figure F.115: Light curves and cross-correlation significance for J1748+7005 in the case of $\beta_{radio} = 2.3$ and $\beta_\gamma = 0.7$. The most significant cross-correlation is at 230 $\pm$ 10 day with 97.47% significance.

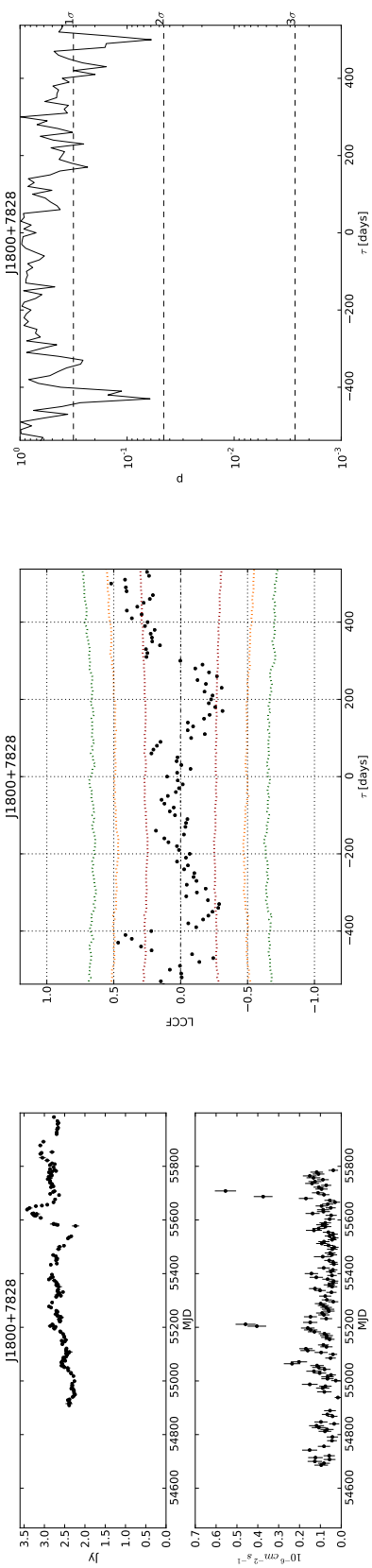

Figure F.116: Light curves and cross-correlation significance for J1800+7828 in the case of $\beta_{radio} = 2.3$ and $\beta_\gamma = 0.7$. The most significant cross-correlation is at 500 ± 10 day with 94.07% significance.

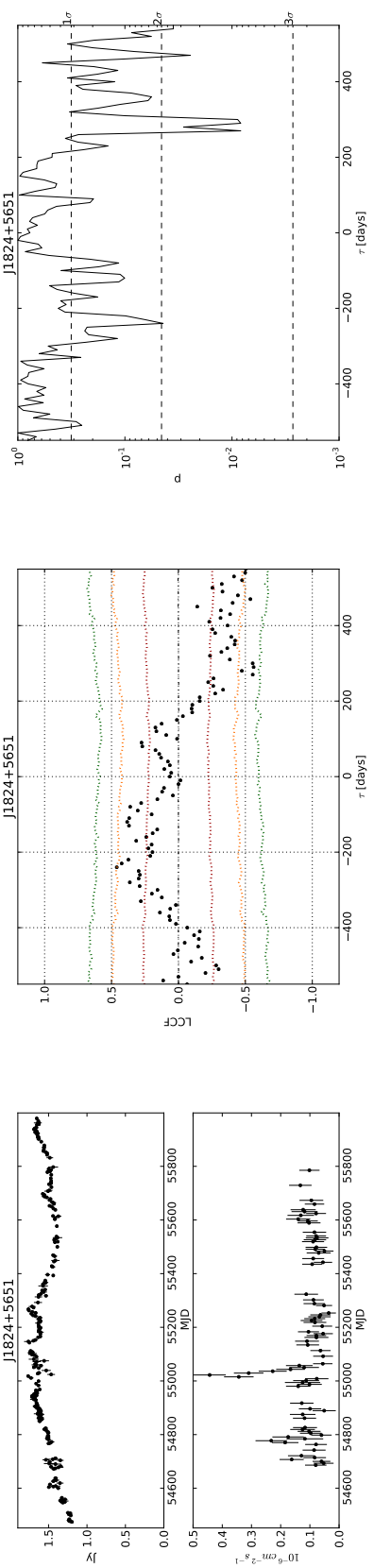

Figure F.117: Light curves and cross-correlation significance for J1824+5651 in the case of $\beta_{radio} = 2.3$ and $\beta_\gamma = 0.7$. The most significant cross-correlation is at -240 $\pm$ 11 day with 95.60% significance.

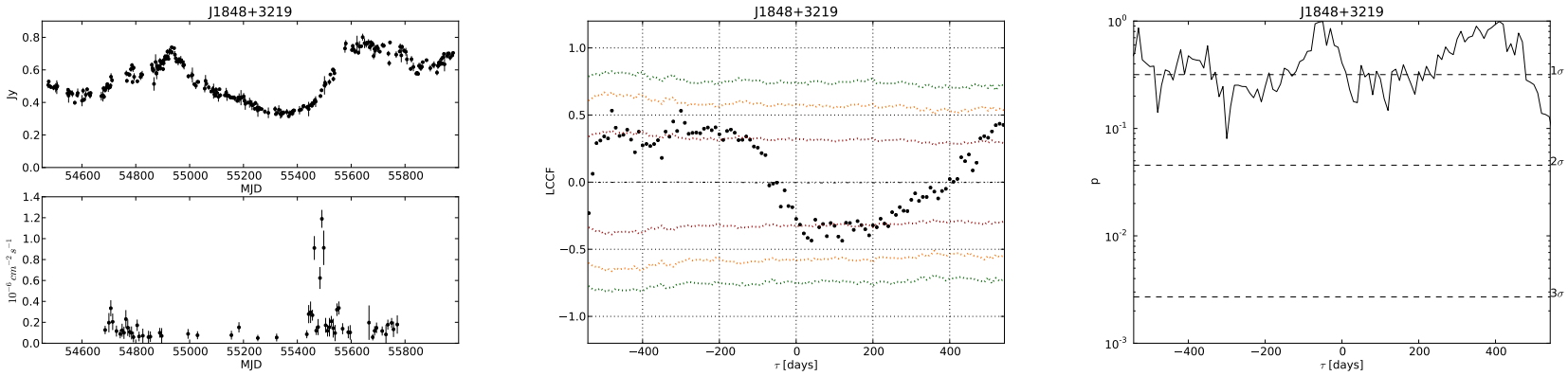

Figure F.118: Light curves and cross-correlation significance for J1848+3219 in the case of $\beta_{radio} = 2.3$ and $\beta_{\gamma} = 0.7$. The most significant cross-correlation is at -300 ± 11 day with 91.95% significance.

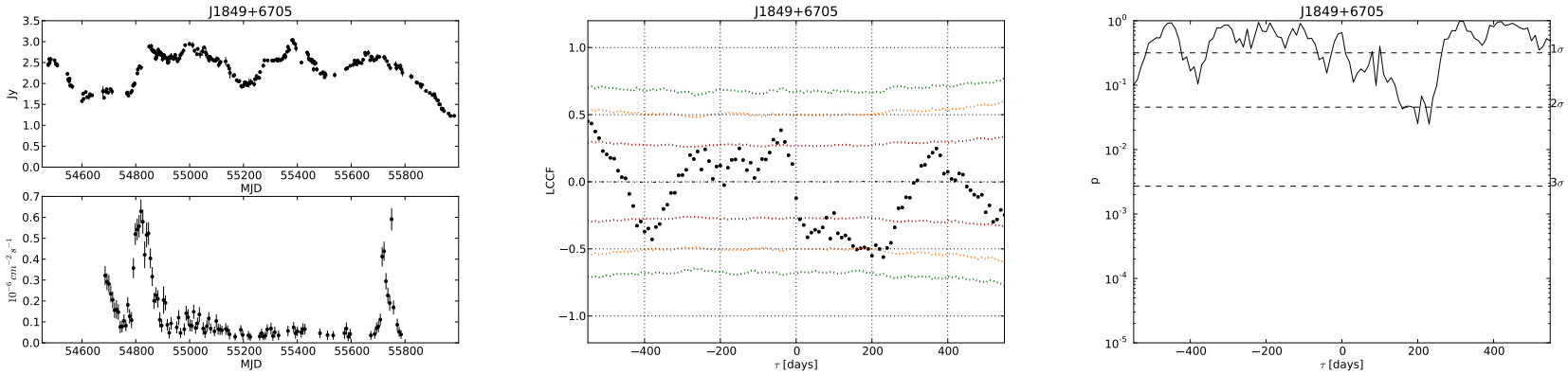

Figure F.119: Light curves and cross-correlation significance for J1849+6705 in the case of $\beta_{radio} = 2.3$ and $\beta_{\gamma} = 0.7$. The most significant cross-correlation is at -40 ± 10 day with 84.58% significance.

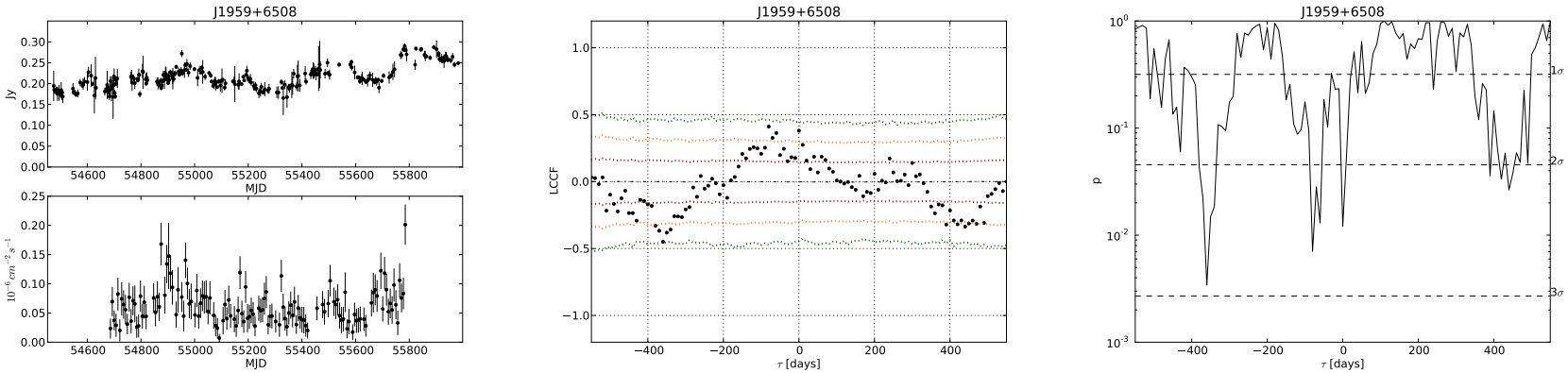

Figure F.120: Light curves and cross-correlation significance for J1959+6508 in the case of $\beta_{radio} = 2.3$ and $\beta_{\gamma} = 0.7$. The most significant cross-correlation is at -80 ± 13 day with 99.29% significance.

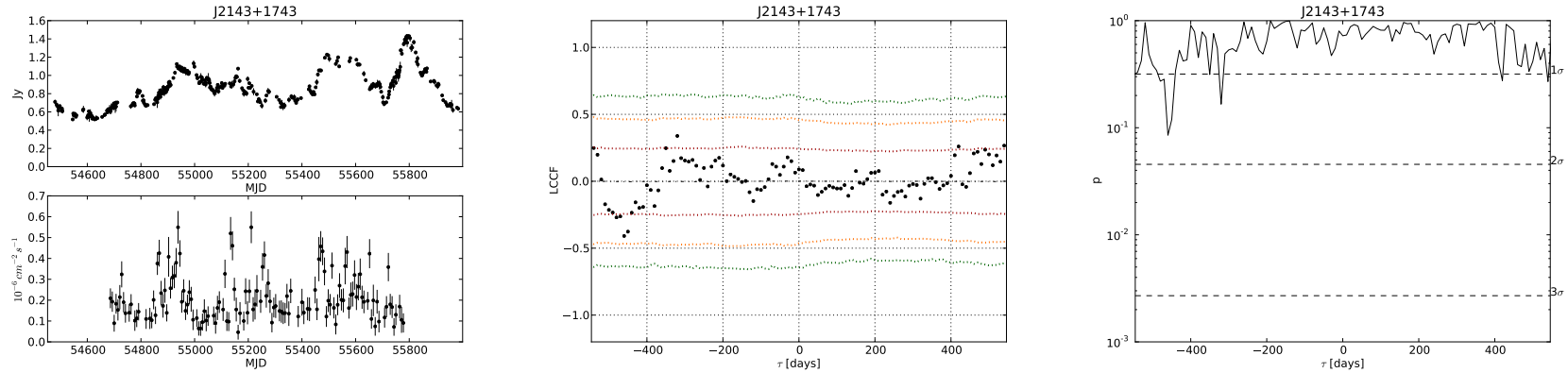

Figure F.121: Light curves and cross-correlation significance for J2143+1743 in the case of $\beta_{radio} = 2.3$ and $\beta_{\gamma} = 0.7$. The most significant cross-correlation is at -320 ± 11 day with 83.40% significance.

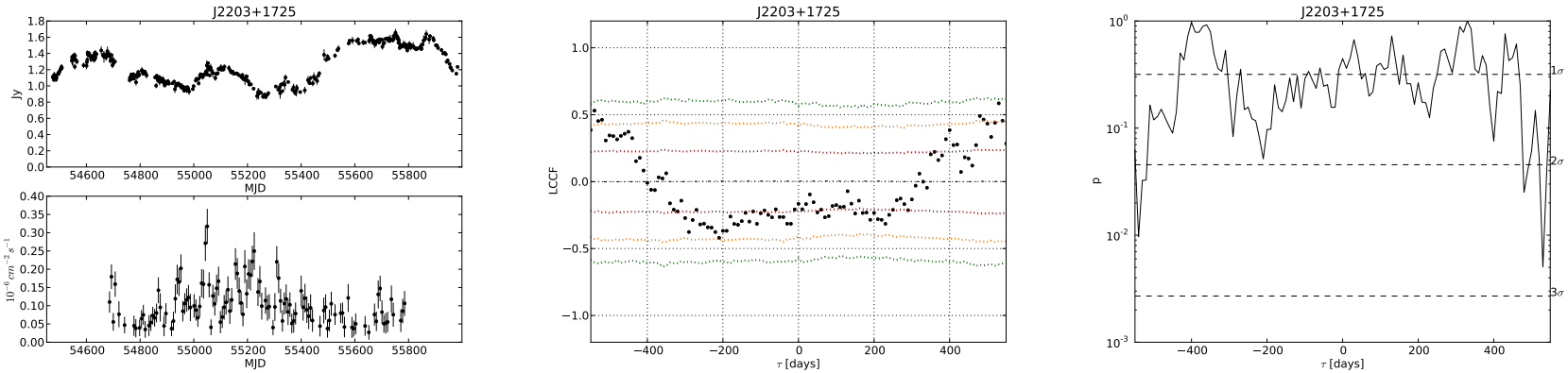

Figure F.122: Light curves and cross-correlation significance for J2203+1725 in the case of $\beta_{radio} = 2.3$ and $\beta_{\gamma} = 0.7$. The most significant cross-correlation is at 530 ± 9 day with 99.50% significance.

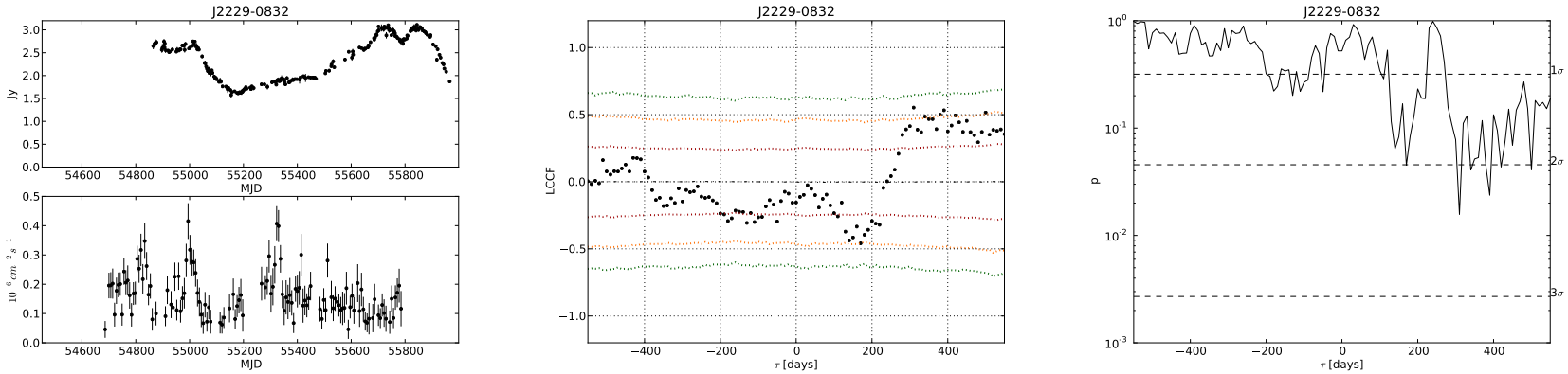

Figure F.123: Light curves and cross-correlation significance for J2229-0832 in the case of $\beta_{radio} = 2.3$ and $\beta_{\gamma} = 0.7$. The most significant cross-correlation is at 310 ± 13 day with 98.42% significance.

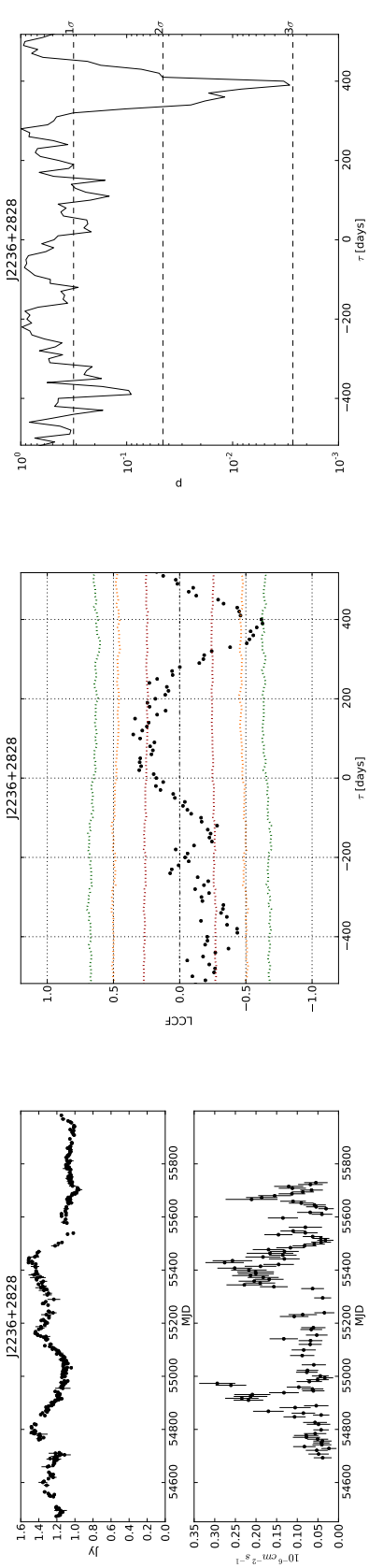

Figure F.124: Light curves and cross-correlation significance for J2236+2828 in the case of $\beta_{radio} = 2.3$ and $\beta_\gamma = 0.7$. The most significant cross-correlation is at 110 ± 13 day with 85.39% significance.

Figure F.125: Light curves and cross-correlation significance for J2253+1608 in the case of $\beta_{radio} = 2.3$ and $\beta_\gamma = 0.7$. The most significant cross-correlation is at -80 $\pm$ 17 day with 97.60% significance.

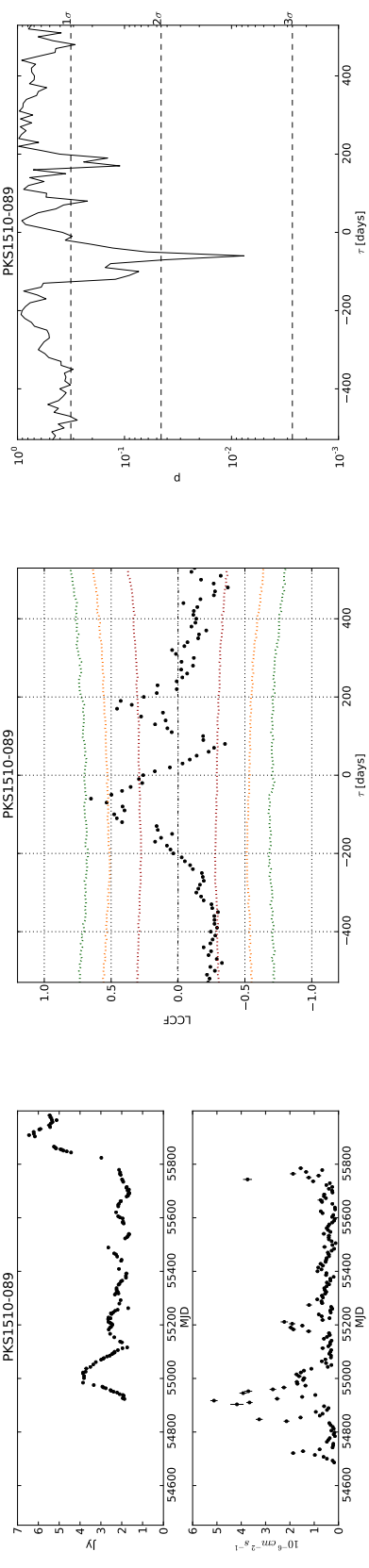

Figure F.126: Light curves and cross-correlation significance for PKS1510-089 in the case of $\beta_{radio} = 2.3$ and $\beta_\gamma = 0.7$. The most significant cross-correlation is at -60 $\pm$ 6 day with 99.24% significance.

F.3 Cross-correlation significance for best PSD fits

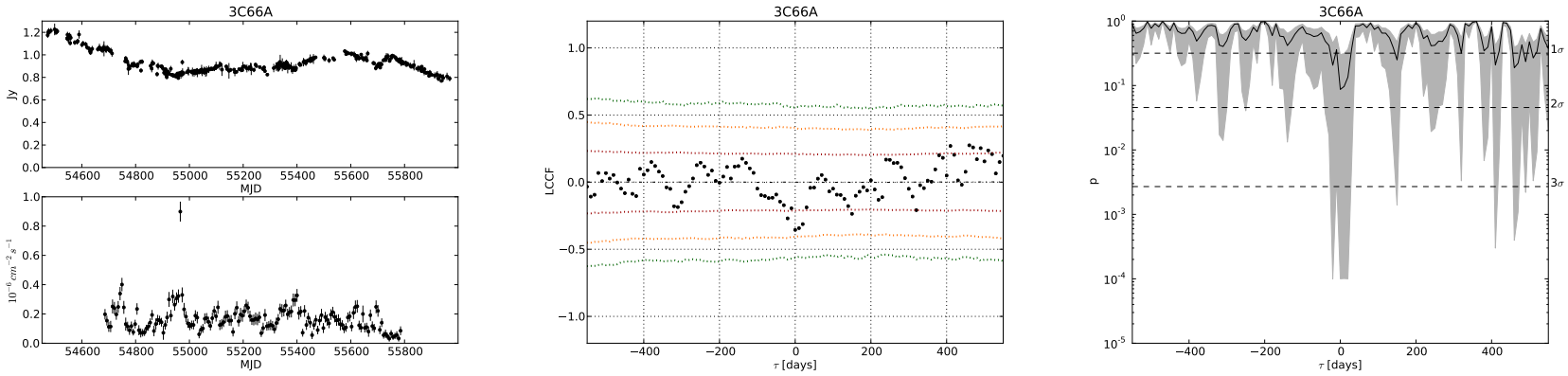

Figure F.127: Light curves and cross-correlation significance for 3C66A for the best fit PSD and limits at each band (shaded area on the right panel). The most significant cross-correlation is at 460 ± 14 day with 81.16% significance.

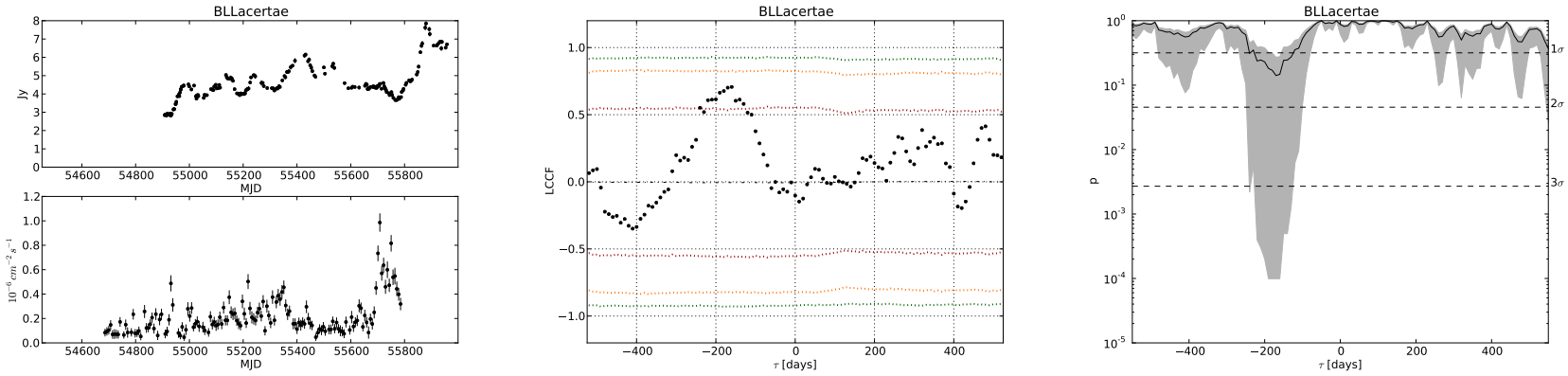

Figure F.128: Light curves and cross-correlation significance for BLLacertae for the best fit PSD and limits at each band (shaded area on the right panel). The most significant cross-correlation is at -160 ± 14 day with 85.27% significance.

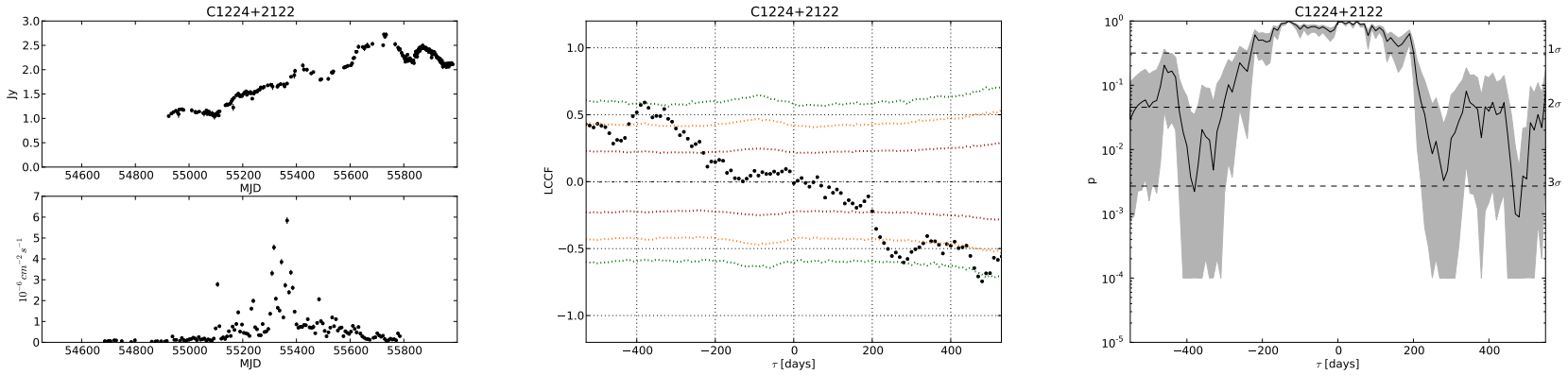

Figure F.129: Light curves and cross-correlation significance for C1224+2122 for the best fit PSD and limits at each band (shaded area on the right panel). The most significant cross-correlation is at -380 ± 10 day with 99.78% significance.

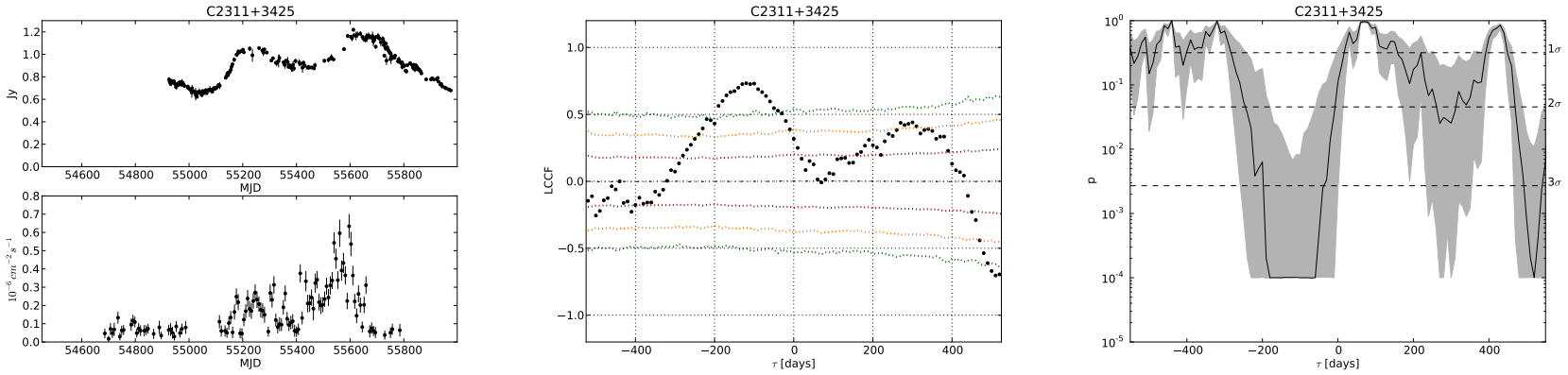

Figure F.130: Light curves and cross-correlation significance for C2311+3425 for the best fit PSD and limits at each band (shaded area on the right panel). The most significant cross-correlation is at -120 ± 14 day with 99.99% significance.

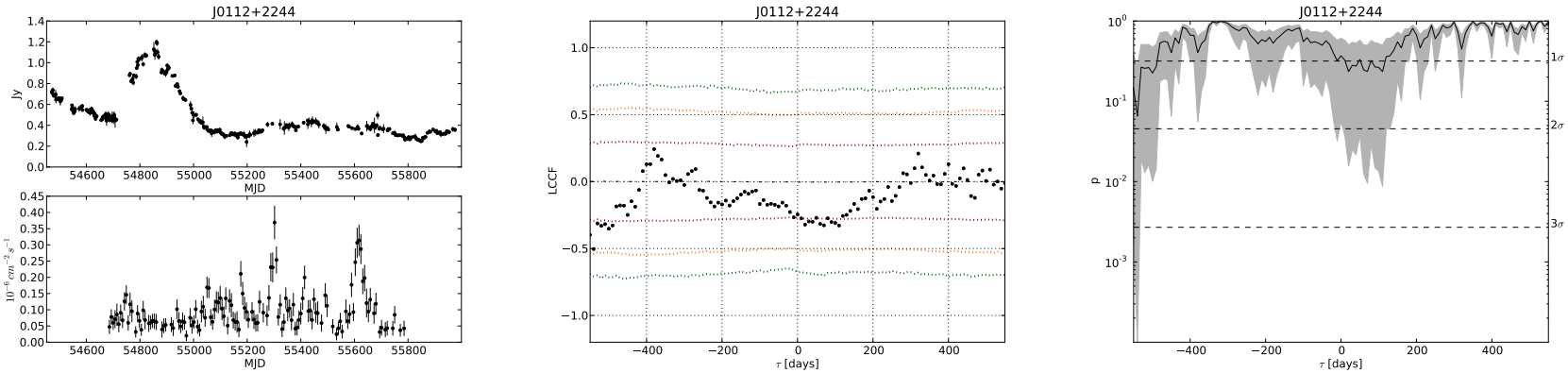

Figure F.131: Light curves and cross-correlation significance for J0112+2244 for the best fit PSD and limits at each band (shaded area on the right panel). The most significant cross-correlation is at -380 ± 13 day with 59.63% significance.

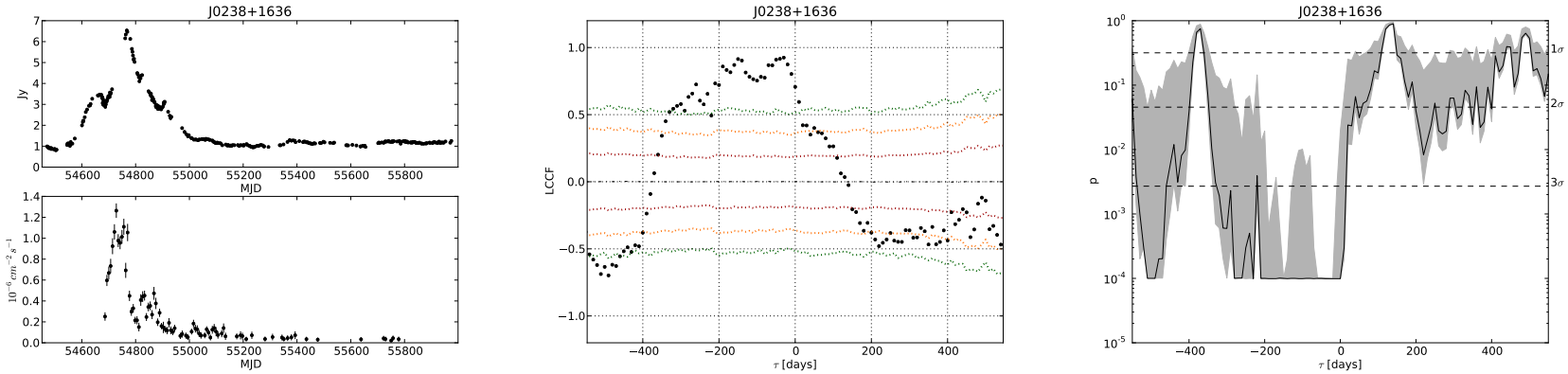

Figure F.132: Light curves and cross-correlation significance for J0238+1636 for the best fit PSD and limits at each band (shaded area on the right panel). The most significant cross-correlation is at -30 ± 9 day with 99.99% significance.

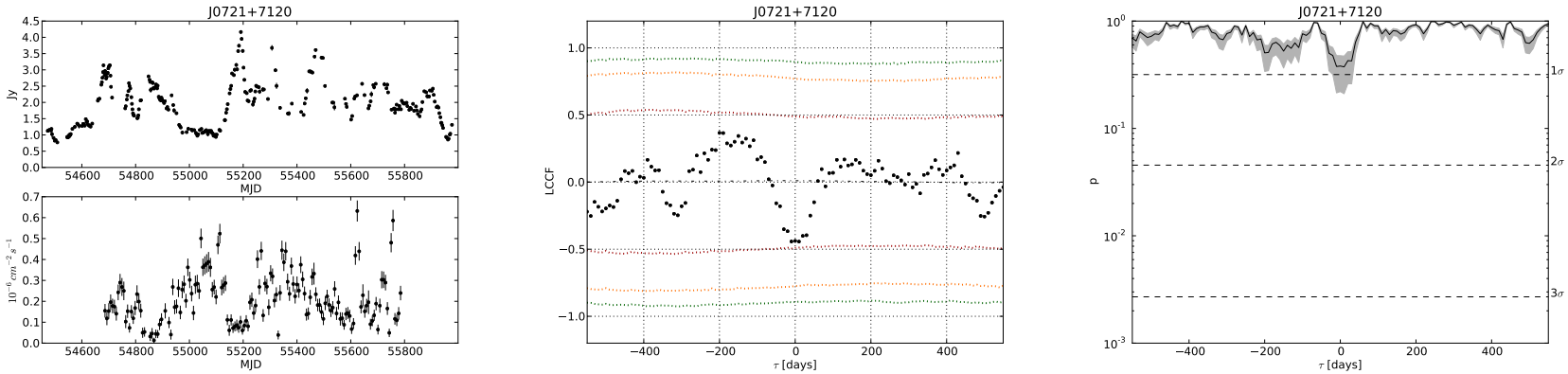

Figure F.133: Light curves and cross-correlation significance for J0721+7120 for the best fit PSD and limits at each band (shaded area on the right panel). The most significant cross-correlation is at -200 ± 11 day with 49.48% significance.

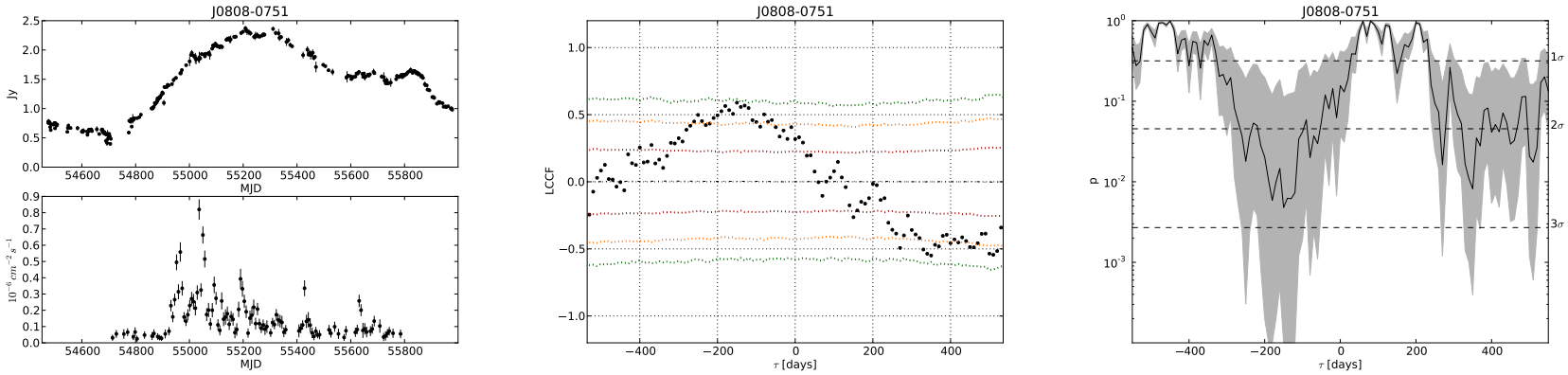

Figure F.134: Light curves and cross-correlation significance for J0808-0751 for the best fit PSD and limits at each band (shaded area on the right panel). The most significant cross-correlation is at -150 ± 16 day with 99.52% significance.

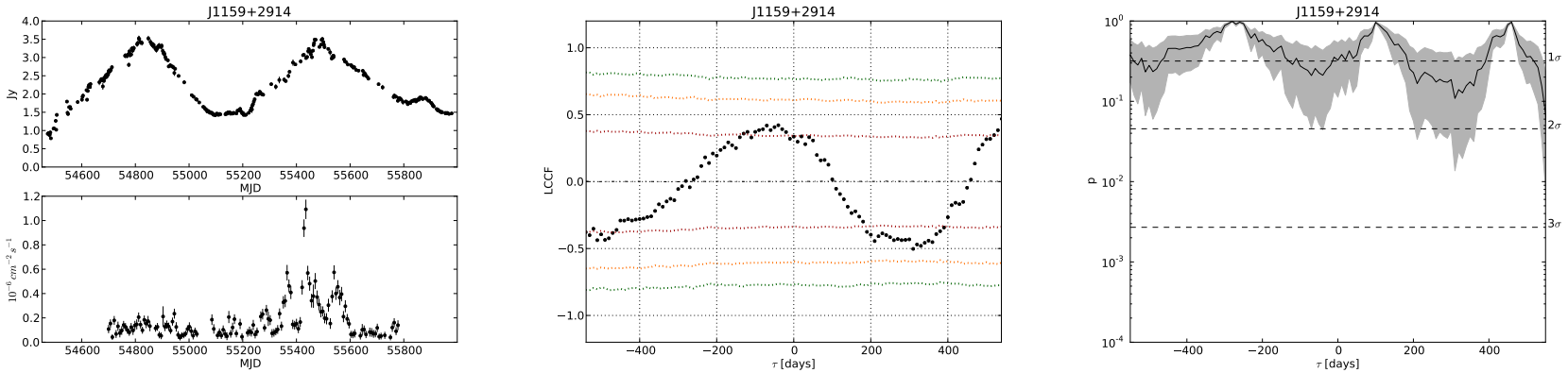

Figure F.135: Light curves and cross-correlation significance for J1159+2914 for the best fit PSD and limits at each band (shaded area on the right panel). The most significant cross-correlation is at -70 ± 18 day with 79.05% significance.

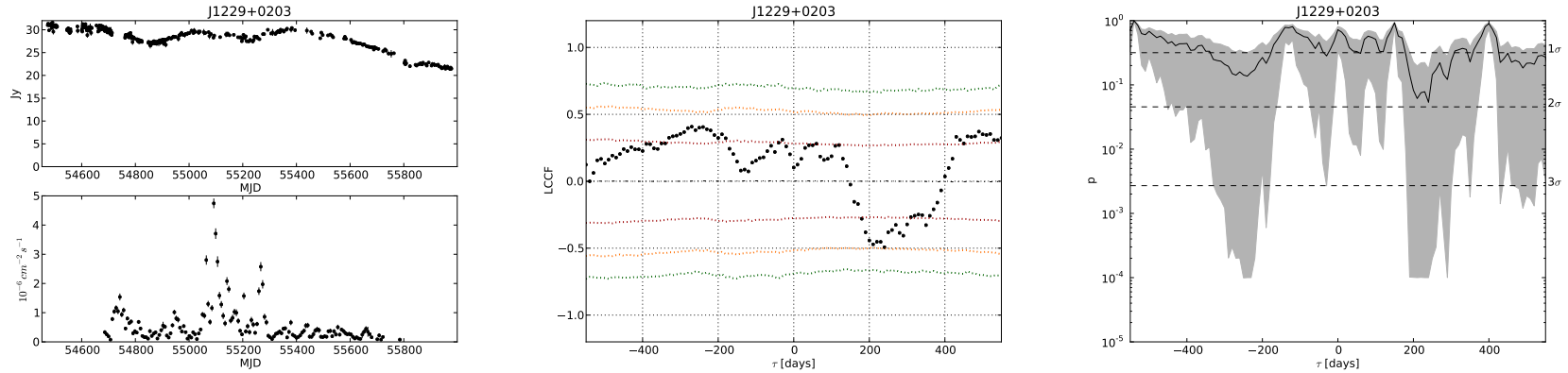

Figure F.136: Light curves and cross-correlation significance for J1229+0203 for the best fit PSD and limits at each band (shaded area on the right panel). The most significant cross-correlation is at -240 ± 16 day with 86.32% significance.

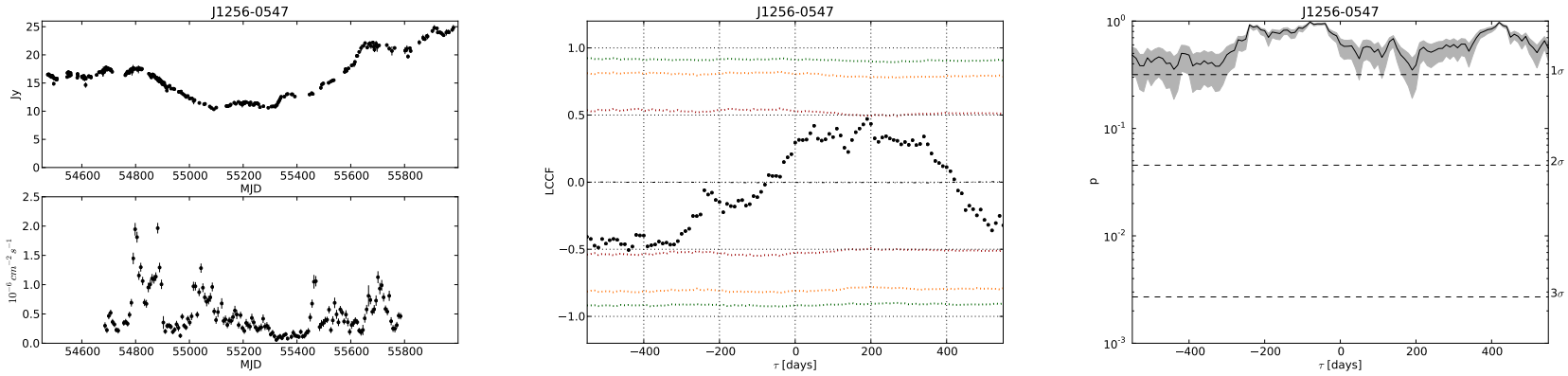

Figure F.137: Light curves and cross-correlation significance for J1256-0547 for the best fit PSD and limits at each band (shaded area on the right panel). The most significant cross-correlation is at 190 ± 10 day with 65.03% significance.

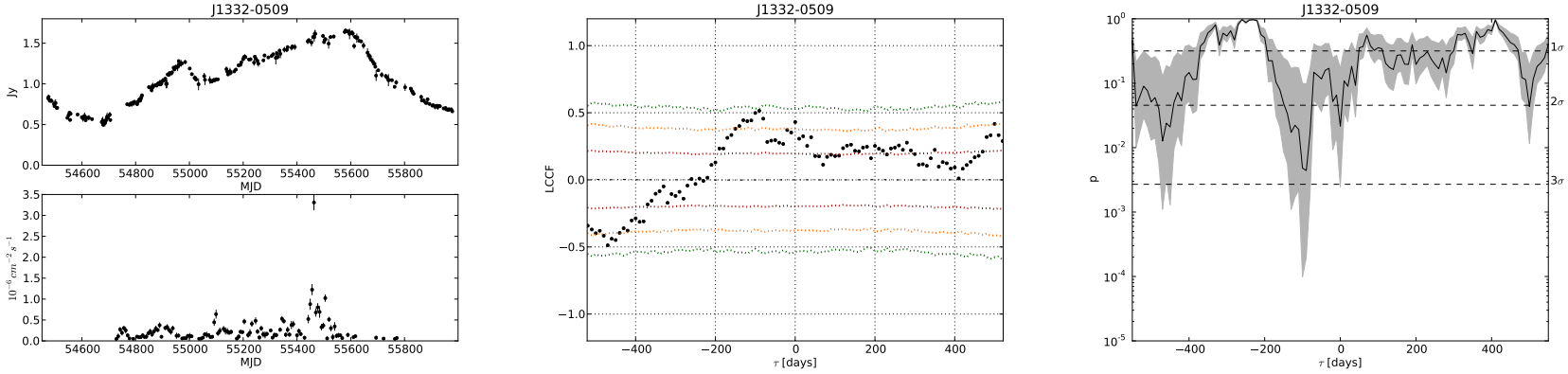

Figure F.138: Light curves and cross-correlation significance for J1332-0509 for the best fit PSD and limits at each band (shaded area on the right panel). The most significant cross-correlation is at -90 ± 15 day with 99.56% significance.

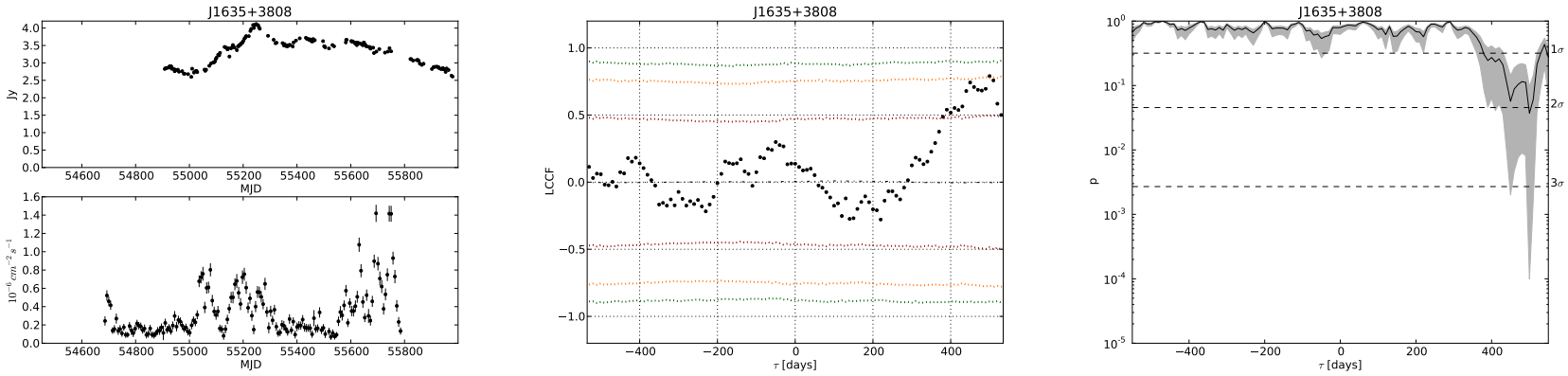

Figure F.139: Light curves and cross-correlation significance for J1635+3808 for the best fit PSD and limits at each band (shaded area on the right panel). The most significant cross-correlation is at 500 ± 8 day with 96.28% significance.

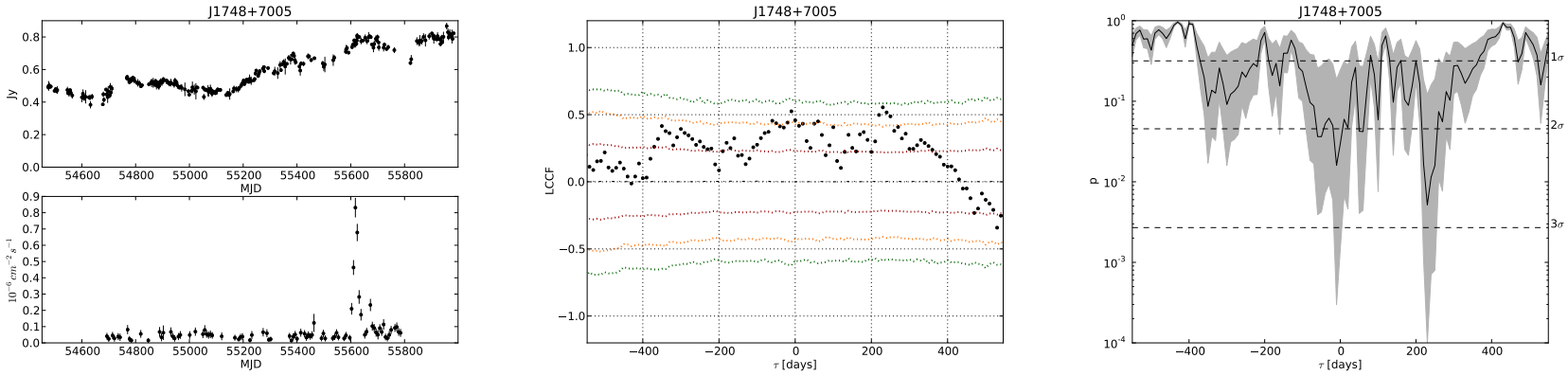

Figure F.140: Light curves and cross-correlation significance for J1748+7005 for the best fit PSD and limits at each band (shaded area on the right panel). The most significant cross-correlation is at 230 ± 10 day with 99.48% significance.

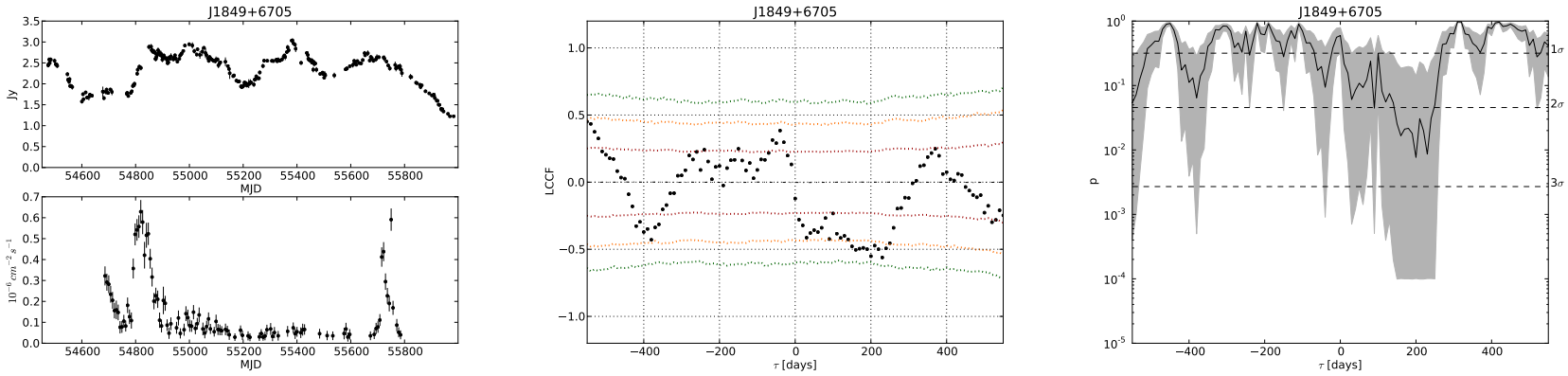

Figure F.141: Light curves and cross-correlation significance for J1849+6705 for the best fit PSD and limits at each band (shaded area on the right panel). The most significant cross-correlation is at -40 ± 10 day with 90.61% significance.

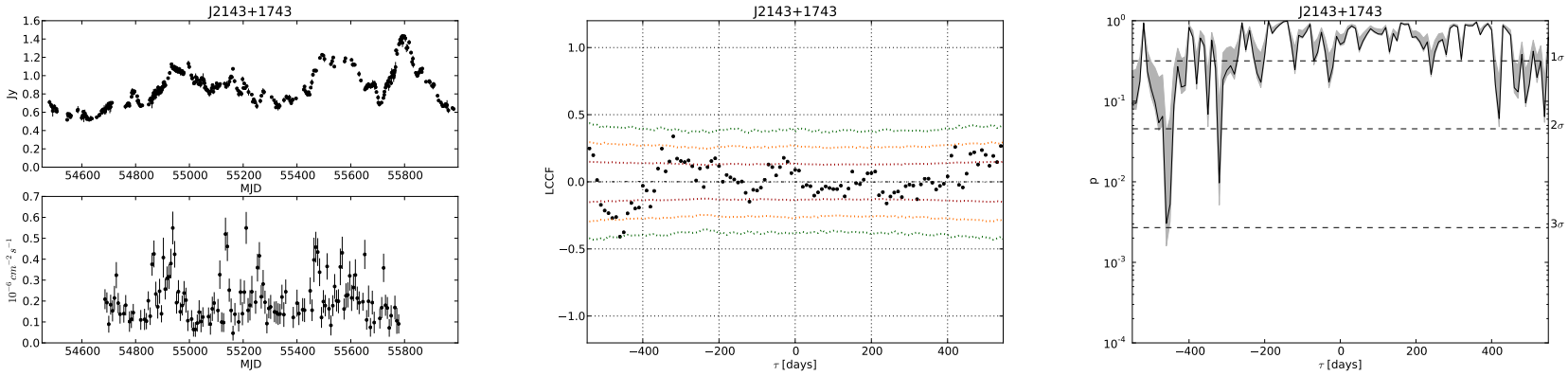

Figure F.142: Light curves and cross-correlation significance for J2143+1743 for the best fit PSD and limits at each band (shaded area on the right panel). The most significant cross-correlation is at -320 ± 11 day with 99.03% significance.

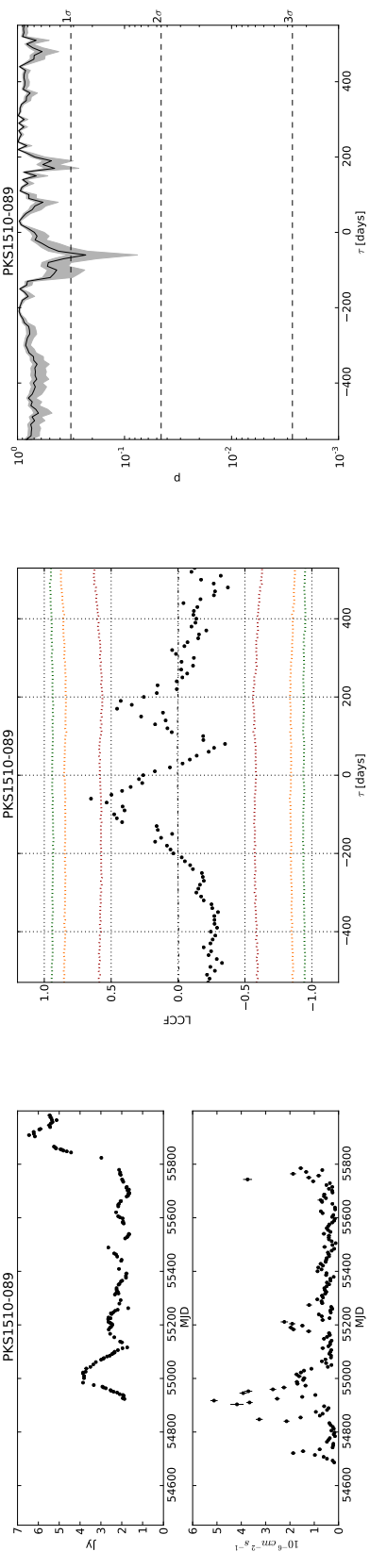

Figure F.143: Light curves and cross-correlation significance for PKS1510-089 for the best fit PSD and limits at each band (shaded area on the right panel). The most significant cross-correlation is at -60 $\pm$ 6 day with 76.99% significance.

F.4 Light curves for sources that are non-variable in at least one of the bands

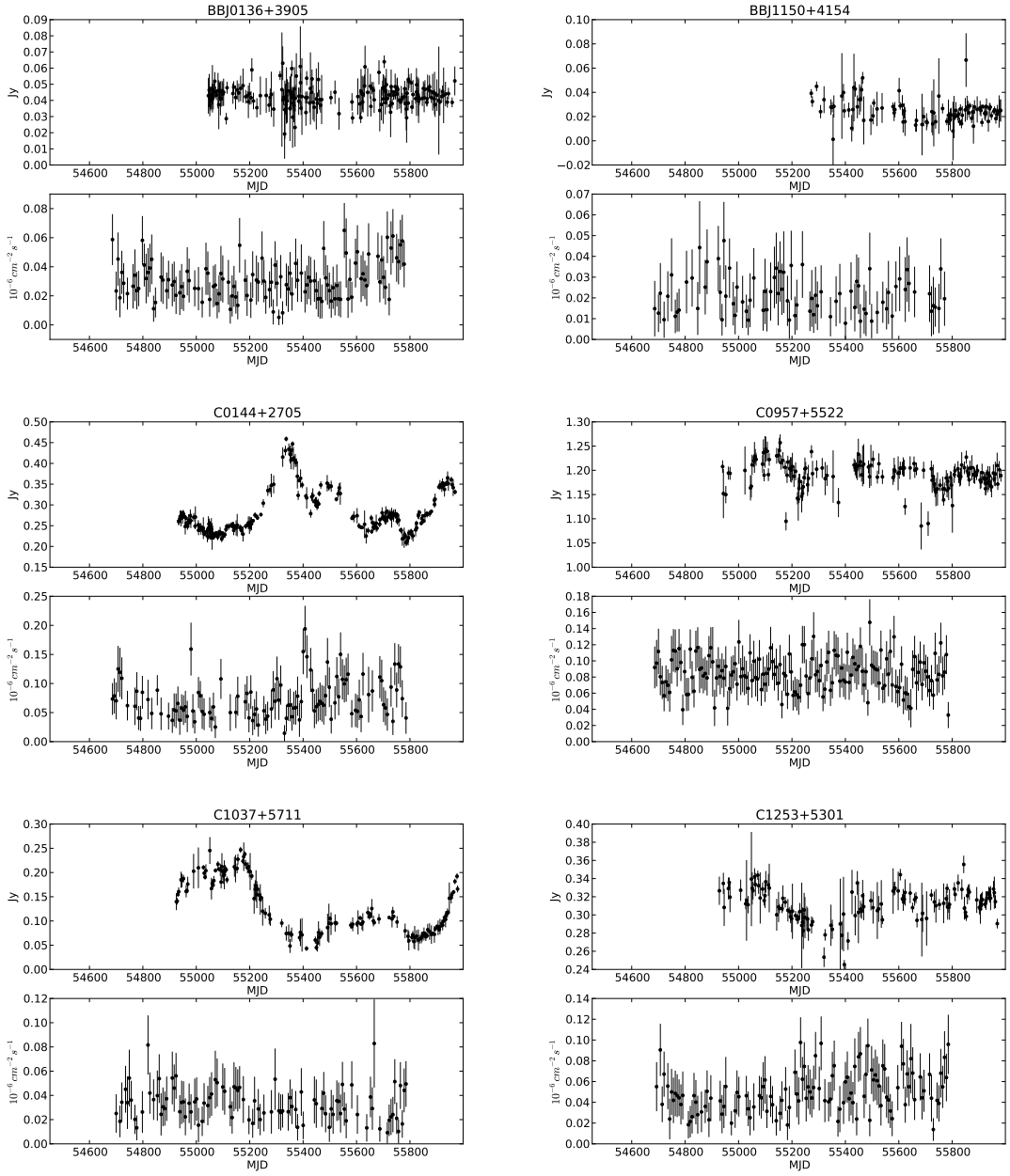

Figure F.144: Light curves for BBJ0136+3905, BBJ1150+4154, C0144+2705, C0957+5522, C1037+5711 and C1253+5301. For each source the upper panel is the radio light curve and the lower panel the gamma-ray light curve.

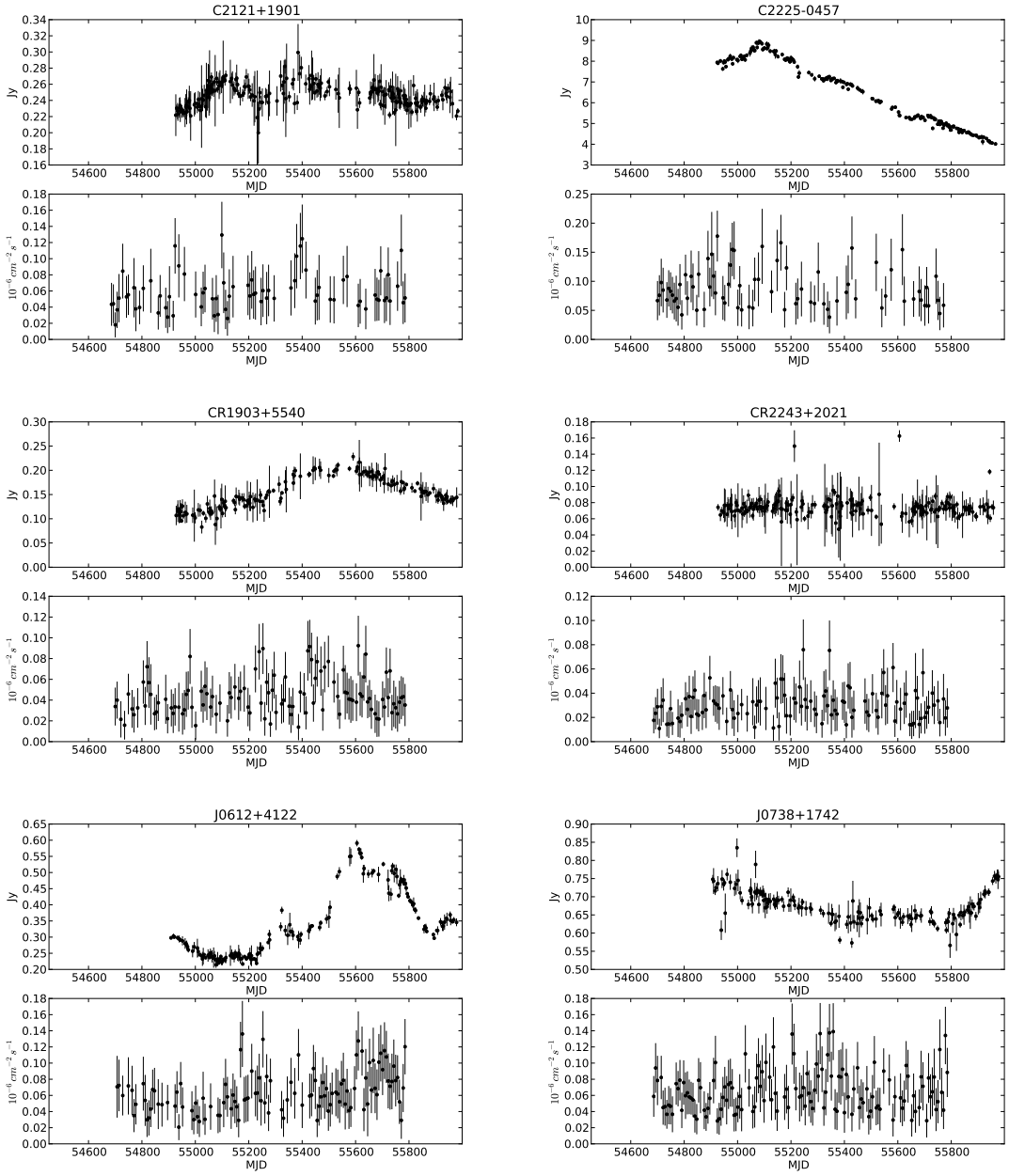

Figure F.145: Light curves for C2121+1901, C2225−0457, CR1903+5540, CR2243+2021, J0612+4122 and J0738+1742. For each source the upper panel is the radio light curve and the lower panel the gamma-ray light curve.

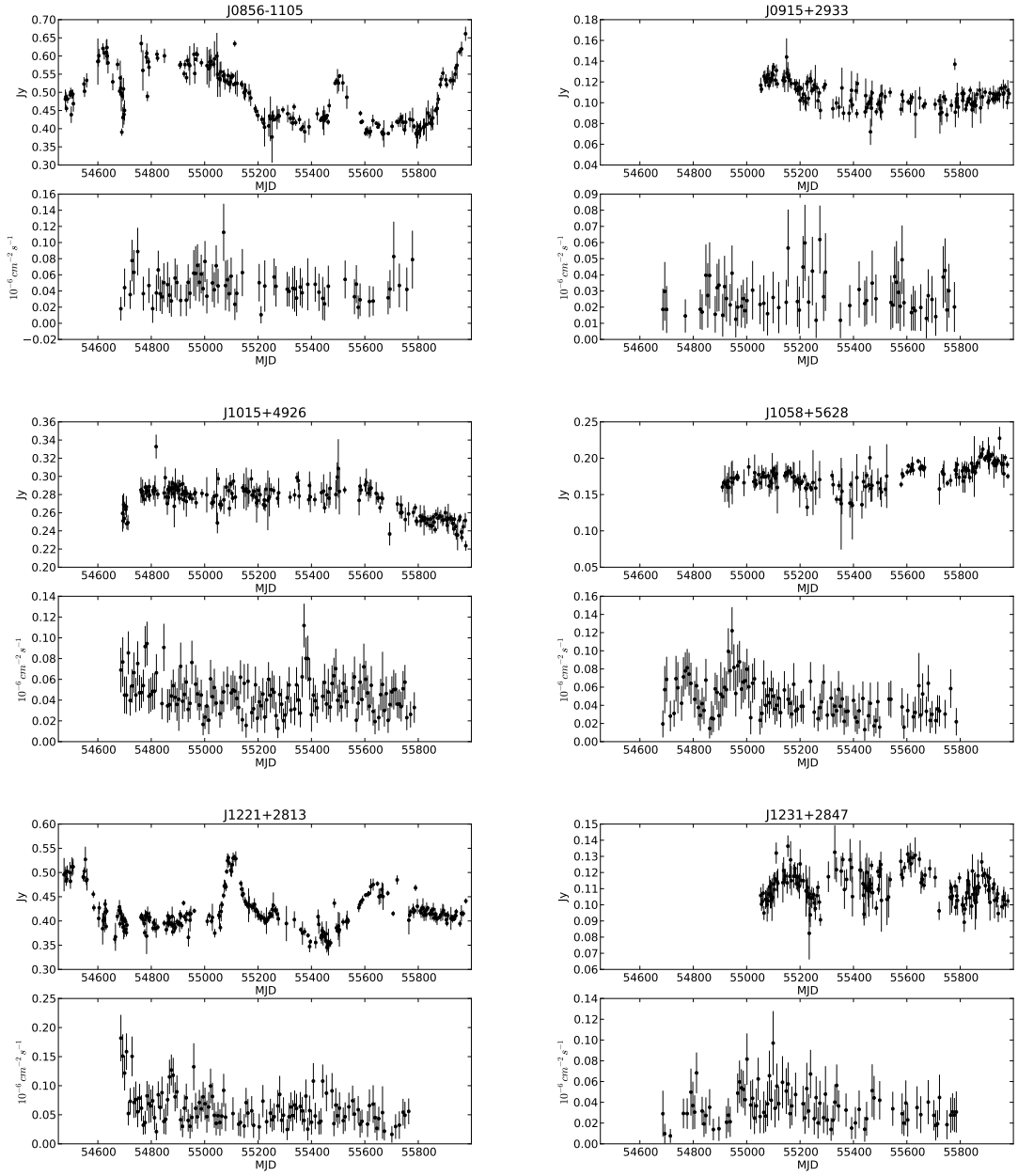

Figure F.146: Light curves for J0856−1105, J0915+2933, J1015+4926, J1058+5628, J1221+2813 and J1231+2847. For each source the upper panel is the radio light curve and the lower panel the gamma-ray light curve.

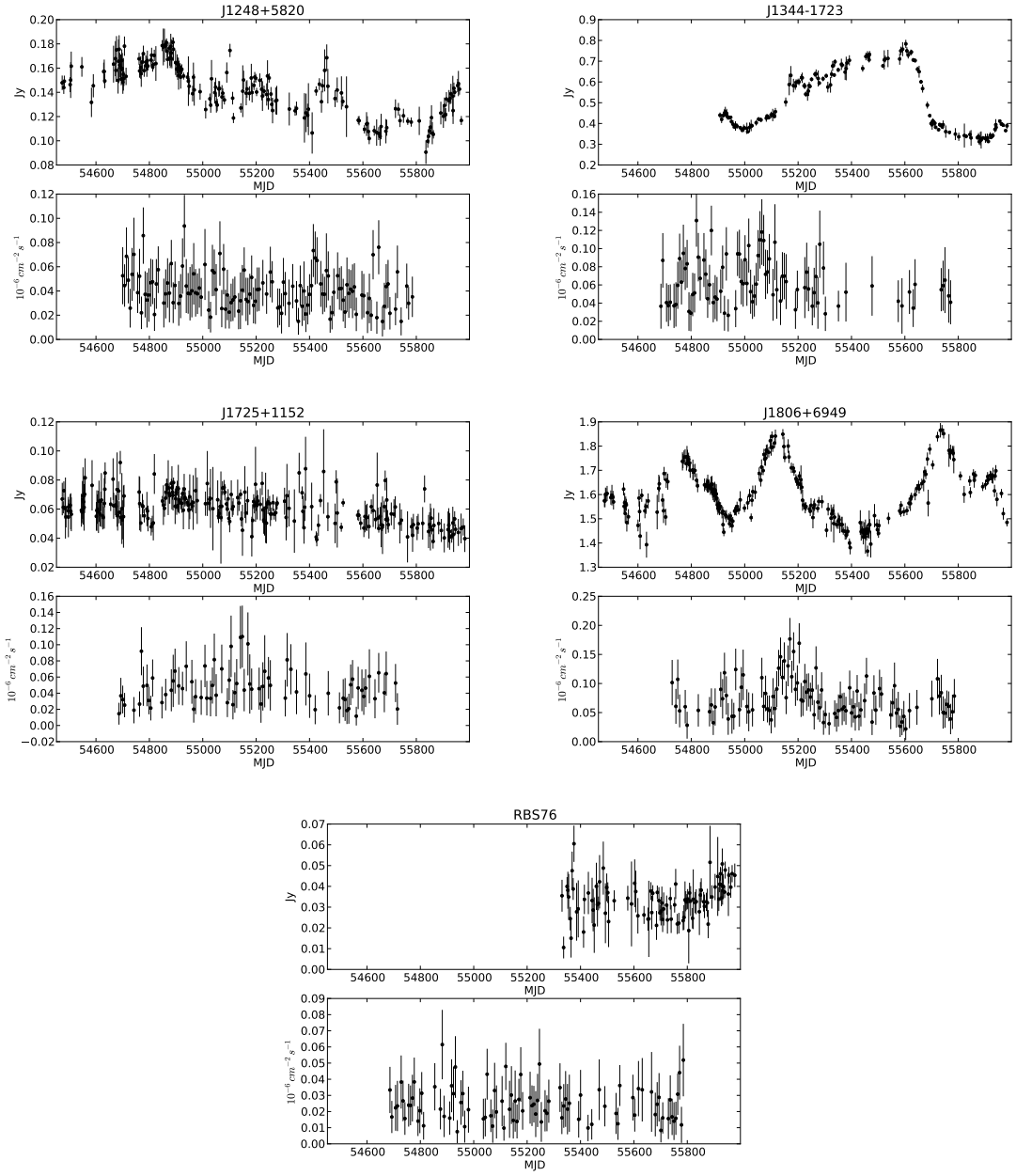

Figure F.147: Light curves for J1248+5820, J1344−1723, J1725+1152, J1806+6949 and RBS76. For each source the upper panel is the radio light curve and the lower panel the gamma-ray light curve.

Bibliography

Abdo, A. A., Ackermann, M., Ajello, M., et al. 2009, ApJS, 183, 46

Abdo, A. A., Ackermann, M., Ajello, M., et al. 2009, ApJ, 700, 597

Abdo, A. A., Ackermann, M., Ajello, M., et al. 2010, ApJS, 188, 405

Abdo, A. A., Ackermann, M., Ajello, M., et al. 2010, ApJ, 715, 429

Abdo, A. A., Ackermann, M., Ajello, M., et al. 2010, Nature, 463, 919

Abdo, A. A., Ackermann, M., Ajello, M., et al. 2010, ApJ, 722, 520

Abdo, A. A., Ackermann, M., Agudo, I., et al. 2010, ApJ, 716, 30

Ackermann, M., Ajello, M., Allafort, A., et al. 2011, ApJ, 743, 171

Ackermann, M., Ajello, M., Allafort, A., et al. 2011, ApJ, 741, 30

Ackermann, M., Ajello, M., Allafort, A., et al. 2012, Science, 338, 1190

Agudo, I., Jorstad, S. G., Marscher, A. P., et al. 2011, ApJ, 726, L13

Agudo, I., Marscher, A. P., Jorstad, S. G., et al. 2011, ApJ, 735, L10

Alexander, T. 1997, Astronomical Time Series, 218, 163

Aller, M. F., Aller, H. D., & Hughes, P. A. 1996, Extragalactic Radio Sources, 175, 283

Aller, M. F., Aller, H. D., & Hughes, P. A. 2009, arXiv:0912.3176

Aller, M. F., Hughes, P. A., & Aller, H. D. 2010, arXiv:1007.0258

Angelakis, E., Kraus, A., Readhead, A. C. S., et al. 2009, A&A, 501, 801

Angelakis, E., Fuhrmann, L., Nestoras, I., et al. 2012, Journal of Physics Conference Series, 372, 012007

Angel, J. R. P., & Stockman, H. S. 1980, ARA&A, 18, 321

Antonucci, R. 1993, ARA&A, 31, 473

Antonucci, R. R. J., & Miller, J. S. 1985, ApJ, 297, 621

Applegate, D. L., Bixby, R. E., Chvátal V., Cook, W. J. (2006), The Traveling Salesman Problem: A Computational Study. Princeton Series in Applied Mathematics. Princeton University Press.

Arévalo, P., Uttley, P., Kaspi, S., et al. 2008, MNRAS, 389, 1479

Asada, K., & Nakamura, M. 2012, ApJ, 745, L28

Atwood, W. B., Abdo, A. A., Ackermann, M., et al. 2009, ApJ, 697, 1071

Avni, Y. 1976, ApJ, 210, 642

Baars, J. W. M., Genzel, R., Pauliny-Toth, I. I. K., & Witzel, A. 1977, A&A, 61, 99

Begelman, M. C., Blandford, R. D., & Rees, M. J. 1984, Reviews of Modern Physics, 56, 255

Beringer et al.(PDG), PR D86, 010001 (2012), `http://pdg.lbl.gov`

Biggs, A. D., Browne, I. W. A., Helbig, P., et al. 1999, MNRAS, 304, 349

Blandford, R. 2008, Extragalactic Jets: Theory and Observation from Radio to Gamma Ray, 386, 3

Blandford, R. D., Königl, A. 1979, ApJ, 232, 34

Blandford, R. D., & Levinson, A. 1995, ApJ, 441, 79

Blandford, R. D., & Payne, D. G. 1982, MNRAS, 199, 883

Blandford, R. D., & Rees, M. J. 1978, In Pittsburgh Conference on BL Lac Objects, ed. AM Wolfe, pp. 32841. Pittsburgh: Univ. Pittsburgh Press

Blandford, R. D., & Znajek, R. L. 1977, MNRAS, 179, 433

Błażejowski, M., Sikora, M., Moderski, R., & Madejski, G. M. 2000, ApJ, 545, 107

Boettcher, M. 2012, arXiv:1205.0539

Brigham, E. O. 1988. *The fast Fourier transform and its applications*. Englewood Cliffs, N.J.: Prentice-Hall, 1988

Carlson, S. 1997, Scientific American, 276, 121

Chatterjee, R., Jorstad, S. G., Marscher, A. P., et al. 2008, ApJ, 689, 79

Cohen, M. H. (1994), The Owens Valley Radio Observatory: Early Years. Engineering and Science, 57 (3)

Cohen, M. H. (2007), A History of OVRO: Part II. Engineering and Science, 70 (3)

Cohen, M. H., Linfield, R. P., Moffet, A. T., et al. 1977, Nature, 268, 405

Coles, W., Hobbs, G., Champion, D. J., Manchester, R. N., & Verbiest, J. P. W. 2011, MNRAS, 418, 561

D'Ammando, F., & Orienti, M. 2012, The Astronomer's Telegram, 4261, 1

Deeming, T. J. 1975, Ap&SS, 36, 137

Dermer, C. D., & Schlickeiser, R. 1993, ApJ, 416, 458

Edelson, R., Krolik, J., Madejski, G., et al. 1995, ApJ, 438, 120

Edelson, R. A., & Krolik, J. H. 1988, ApJ, 333, 646

Emmanoulopoulos, D., McHardy, I. M., & Uttley, P. 2010, MNRAS, 404, 931

Fabian, A. C. 2012, ARA&A, 50, 455

Fermi-LAT Collaboration 2012, arXiv:1206.1896

Gaskell, C. M., & Peterson, B. M. 1987, ApJS, 65, 1

Ghisellini, G., Tavecchio, F., Foschini, L., et al. 2010, MNRAS, 402, 497

Górski, K. M., Hivon, E., Banday, A. J., et al. 2005, ApJ, 622, 759

Harris, F. J., Proc. IEEE, 66, 51

Hartman, R. C., Bertsch, D. L., Bloom, S. D., et al. 1999, ApJS, 123, 79

Hayashida, M., Madejski, G. M., Nalewajko, K., et al. 2012, ApJ, 754, 114

Healey, S. E., Romani, R. W., Taylor, G. B., et al. 2007, ApJS, 171, 61

Healey, S. E., Romani, R. W., Cotter, G., et al. 2008, ApJS, 175, 97

Herbig, T. 1994, Ph.D. Thesis, California Institute of Technology

Hovatta, T., Tornikoski, M., Lainela, M., et al. 2007, A&A, 469, 899

Hovatta, T., Valtaoja, E., Tornikoski, M., Lähteenmäki, A. 2009, A&A, 494, 527

Hovatta, T., Richards, J. L., Aller, M. F., et al. 2012, The Astronomer's Telegram, 4451, 1

Hufnagel, B. R., & Bregman, J. N. 1992, ApJ, 386, 473

Hughes, P. A., Aller, H. D., & Aller, M. F. 1992, ApJ, 396, 469

James, F. 2006, Statistical Methods in Experimental Physics: 2nd Edition, by Frederick James. Published by World Scientific Publishing Co., Pte. Ltd., Singapore, 2006.

Jones, T. W., O'Dell, S. L., & Stein, W. A. 1974, ApJ, 188, 353

Jorstad, S. G., Marscher, A. P., Mattox, J. R., et al. 2001, ApJ, 556, 738

Jorstad, S., Marscher, A., D'Arcangelo, F., & Harrison, B. 2009, arXiv:0912.5230

Kellermann, K. I., Sramek, R., Schmidt, M., Shaffer, D. B., & Green, R. 1989, AJ, 98, 1195

Komatsu, E., Smith, K. M., Dunkley, J., et al. 2011, ApJS, 192, 18

Kovalev, Y. Y., Kovalev, Y. A., Nizhelsky, N. A., & Bogdantsov, A. B. 2002, PASA, 19, 83

Kovalev, Y. Y., Kellermann, K. I., Lister, M. L., et al. 2005, AJ, 130, 2473

Kovalev, Y. Y., Aller, H. D., Aller, M. F., et al. 2009, ApJ, 696, L17

Peter J. M. Laarhoven, Aarts, E. H. L. (1987) Simulated Annealing: Theory and Applications, Volume 37 of Mathematics and Its Applications. Kluwer Academic Publishers.

Lawrence, A., & Papadakis, I. 1993, ApJ, 414, L85

Leitch, E. M. 1998, Ph.D. Thesis, California Institute of Technology

León-Tavares, J., Valtaoja, E., Tornikoski, M., Lähteenmäki, A., & Nieppola, E. 2011, A&A, 532, A146

Lico, R., Giroletti, M., Orienti, M., et al. 2012, A&A, 545, A117

Lilliefors, H. W. 1967, J. Am. Stat. Assoc., 62, 399

Lister, M. L., Cohen, M. H., Homan, D. C., et al. 2009, AJ, 138, 1874

Lister, M. L., Aller, M., Aller, H., et al. 2011, ApJ, 742, 27

Mahony, E. K., Sadler, E. M., Murphy, T., et al. 2010, ApJ, 718, 587

Mannheim, K., & Biermann, P. L. 1992, A&A, 253, L21

Marscher, A. P. 2006, Blazar Variability Workshop II: Entering the GLAST Era, 350, 155

Marscher, A. P., Jorstad, S. G., Gómez, J.-L., et al. 2002, Nature, 417, 625

Marscher, A. P., Jorstad, S. G., D'Arcangelo, F. D., et al. 2008, Nature, 452, 966

Mattox, J. R., Bertsch, D. L., Chiang, J., et al. 1996, ApJ, 461, 396

Meier, D. L. 2012, Black Hole Astrophysics: The Engine Paradigm, by David L. Meier. ISBN: 978-3-642-01935-7. Springer, Verlag Berlin Heidelberg, 2012

Nieppola, E., Tornikoski, M., Valtaoja, E., et al. 2011, A&A, 535, A69

Nolan, P. L., Abdo, A. A., Ackermann, M., et al. 2012, ApJS, 199, 31

Ojha, R., Kadler, M., Böck, M., et al. 2010, A&A, 519, A45

Orr, M. J. L., & Browne, I. W. A. 1982, MNRAS, 200, 1067

Paciesas, W. S., Meegan, C. A., von Kienlin, A., et al. 2012, ApJS, 199, 18

Paltani, S. 1999, BL Lac Phenomenon, 159, 293

Pavlidou, V., Richards, J. L., Max-Moerbeck, W., et al. 2012, ApJ, 751, 149

Pearson, T. J. 2009, Telescope Control System for the OVRO 40 m and 5.5-m antennas, http://www.astro.caltech.edu/~tjp/ovroman/manual.html

Peterson, B. M., Wanders, I., Horne, K., et al. 1998, PASP, 110, 660

Peterson, B. M., Ferrarese, L., Gilbert, K. M., et al. 2004, ApJ, 613, 682

Planck Collaboration, Ade, P. A. R., Aghanim, N., et al. 2011, A&A, 536, A13

Press, W. H. 1978, Comments on Astrophysics, 7, 103

Press, W. H., Teukolsky, S. A., Vetterling, W. T., & Flannery, B. P. 1992, Cambridge: University Press, —c1992, 2nd ed.

Protassov, R., van Dyk, D. A., Connors, A., Kashyap, V. L., & Siemiginowska, A. 2002, ApJ, 571, 545

Pushkarev, A. B., Kovalev, Y. Y., Lister, M. L., & Savolainen, T. 2009, A&A, 507, L33

Pushkarev, A. B., Kovalev, Y. Y., & Lister, M. L. 2010, ApJ, 722, L7

Rauch, M. 1998, ARA&A, 36, 267

Readhead, A. C. S. 1980, Objects of High Redshift, 92, 165

Readhead, A. C. S. 1994, ApJ, 426, 51

Readhead, A. C. S., Cohen, M. H., Pearson, T. J., & Wilkinson, P. N. 1978, Nature, 276, 768

Reinelt, G. (1994). The Traveling Salesman: Computational Solutions for TSP Applications. Springer-Verlag, Berlin, Heidelberg.

Remillard, R. A., & McClintock, J. E. 2006, ARA&A, 44, 49

Richards, J. L. 2011, PhD thesis, California Institute of Technology

Richards, J. L., Max-Moerbeck, W., Pavlidou, V., et al. 2011, ApJS, 194, 29

Rohlfs, K., & Wilson, T. L. 2004, Tools of radio astronomy, 4th rev. and enl. ed., by K. Rohlfs and T.L. Wilson. Berlin: Springer, 2004

Rolke, W. A., López, A. M., & Conrad, J. 2005, Nuclear Instruments and Methods in Physics Research A, 551, 493

Sargent, W. L. W., Young, P. J., Boksenberg, A., & Tytler, D. 1980, ApJS, 42, 41

Scargle, J. D. 1982, ApJ, 263, 835

Scargle, J. D. 1989, ApJ, 343, 874

Scheuer, P. A. G., & Readhead, A. C. S. 1979, Nature277, 182

Serabyn, E., Weisstein, E. W., Lis, D. C., & Pardo, J. R. 1998, Appl. Opt., 37, 2185

Shumway, R. H. and Stoffer, D. S. (2011). *Time Series Analysis and Its Applications*. Springer, New York.

Sikora, M., Begelman, M. C., & Rees, M. J. 1994, ApJ, 421, 153

Sikora, M., Stawarz, Ł., Moderski, R., Nalewajko, K., & Madejski, G. M. 2009, ApJ, 704, 38

Tavecchio, F., Ghisellini, G., Bonnoli, G., & Ghirlanda, G. 2010, MNRAS, 405, L94

Tchekhovskoy, A., Narayan, R., & McKinney, J. C. 2010, ApJ, 711, 50

Timmer, J., & Koenig, M. 1995, A&A, 300, 707

Ulrich, M.-H., Maraschi, L., & Urry, C. M. 1997, ARA&A, 35, 445

Urry, C. M., & Padovani, P. 1995, PASP, 107, 803

Uttley, P., McHardy, I. M., & Papadakis, I. E. 2002, MNRAS, 332, 231

Uttley, P., Edelson, R., McHardy, I. M., Peterson, B. M., & Markowitz, A. 2003, ApJ, 584, L53

Valtaoja, E., & Teräsranta, H. 1995, A&A, 297, L13

Valtaoja, E., & Teräsranta, H. 1996, A&AS, 120, 491

van der Klis, M. 1989, Timing Neutron Stars, 27

von Montigny, C., Bertsch, D. L., Chiang, J., et al. 1995, ApJ, 440, 525

Wall, J. V., Jenkins, C. R., Ellis, R., et al. 2003, Practical statistics for astronomers, by J.V. Wall and C.R. Jenkins. Cambridge observing handbooks for research astronomers, vol. 3. Cambridge, UK: Cambridge University Press, 2003

Welsh, W. F. 1999, PASP, 111, 1347

White, R. J., & Peterson, B. M. 1994, PASP, 106, 879

Wilks, S. S. 1938, Ann. Math. Stat., 9, 60

Zensus, J. A. 1997, ARA&A, 35, 607